Large Eddy Simulation of Transitional Separated-Reattached Flow over Geometries Characterized by Different Aspect Ratios and with Different Intensities of Free Stream Turbulence

Hayder Azeez Neamah Diabil

A Doctoral Thesis

Submitted in partial fulfilment of the requirements for the award of Doctor of Philosophy of De Montfort University, Department of Engineering and Physical Sciences Institute

May, 2018

To my parents and wife who support and motivate me. To my sons and little daughter with love

Abstract

In the current study, changes in the physics of transitional separated-reattached flow due to changes of a geometry nature and an increase of intensity of free stream turbulence have been investigated numerically using the large eddy simulation approach. Numerical simulations have been carried out using the Open FOAM tool box.

Six case studies are selected and divided into two groups of the flows: a low level of intensity of free stream turbulence (< 0.2%) and a high level of intensity of free stream turbulence (3.7%). Each group involves three geometrical shapes: a two-dimensional flat plate, a three-dimensional geometry with an aspect ratio value of 1 and a three-dimensional geometry with an aspect ratio value of 2. To the best of the author's knowledge, the current study is the first work to explore transitional separated-reattached flow over three-dimensional geometries.

In a comparison among the case studies, the separation bubble that formed on the flat plate is longer than that on other geometries, leading to longer temporal and spatial evolution of the transition. In addition, maximum values of the Reynolds stresses in the flat plate are larger than that in other geometries. Furthermore, all case studies show that the transition in the free shear layer is driven by the Kelvin-Helmholtz instability mechanism.

Spectral analysis is carried out to cover all the computational domains employing both Fourier transform and wavelet power transform methods. In the current geometries for both incoming flows (with high and low levels of intensity of free stream turbulence), the regular shedding frequencies are in a good agreement with that reported in the literature. In addition, these frequencies are compatible with the Kelvin-Helmholtz instability conditions. Moreover, the spectral analysis indicates that the low frequency of the free shear layer flapping is absent.

The evolution of coherent structures is identified by performing flow visualisation techniques. Different evolution processes of transformation of large-scale structures from Kelvin-Helmholtz rolls to hairpin structures are observed depending on the geometry shapes and on the level of intensity of free stream turbulence.

The development of the turbulent boundary layer after the reattachment is also examined. For all case studies used here, a dominant observation is that there is no apparent effect of the geometry nature on the delay in the recovery of the reattached turbulent boundary layer.

Acknowledgments

I wish to express my deep sense of gratitude to my supervisor Dr Xin Kai Li for giving me an opportunity to carry on my PhD study under his guidance. His helping nature, kindness and practical approach made me realize a lot of things. I would like to thank him for his valuable comments, which had kept me on the right path throughout this study. I also would like to thank my second supervisor Professor Mikhail Goman.

I wish to express my sincere thanks to Dr Ibrahim Elrayah Abdalla who was my supervisor before leaving the university. I am grateful to him for his encouragement and fruitful discussions.

I gratefully thank the Iraqi government for the financial support.

Publications

Diabil, H. A., Li, X. K., and Abdalla, I. E. 2017. Coherent Structures and Flow Topology of Transitional Separated-Reattached Flow over Two and Three Dimensional Geometrical Shapes. *Mathematical Methods and Computational Techniques in Science and Engineering, AIP Conf. Proc., 1872*: 020019, *American Institute of Physics*. http://dx.doi.org/10.1063/1.4996676

Diabil, H. A., Li, X. K., and Abdalla, I. E. 2017. Numerical Study of a Separated Boundary Layer Transition over Two and Three Dimensional Geometrical Shapes. *WSEAS TRANSACTIONS on SYSTEMS and CONTROL*, 12: 45-72. http://www.wseas.org/multimedia/journals/control/2017/a125803-084.pdf

Prepared for publication

Diabil, H. A., Li, X. K., and Abdalla, I. E. 2018. Coherent Structures Evolution in Transitional Separated-reattached flows. *Prepared to submit to International Journal of Computers & Fluids.*

Diabil, H. A., Li, X. K., and Abdalla, I. E. 2018. On Instability Mechanisms of Transition in Transitional Separated-Reattached Flows over Geometries Characterised with Different Aspect Ratios. 2018. *Prepared to submit to Physics of Fluids.*

Contents

List of Figures

List of Tables

Nomenclature

Roman letters

B	geometry width
C_f	skin friction coefficient
C_{ij}	cross terms
C_s	Smagorinsky constant
D	geometry thickness
G	Clauser parameter
L_{ij}	Leonard stresses
Ls	geometry length
Lx	streamwise length of computational domain
Ly	wall-normal length of computational domain
Lz	spanwise length of computational domain
p	pressure
Re	Reynolds number
R_{ij}	subgride-scale Reynolds stresses
S_{ij}	grid-scale strain rate
u	instantaneous streamwise velocity
U_0	inlet velocity
U_m	mean streamwise velocity
u'_{rms}	root mean square fluctuating streamwise velocity
u_τ	frictional velocity
v	instantaneous wall-normal velocity

V_m	mean wall-normal velocity
v'_{rms}	root mean square fluctuating wall-normal velocity
w	instantaneous spanwise velocity
x	distance along the streamwise axis
x^+	dimensionless distance along the streamwise axis
x_R	mean reattachment length
y	distance along the wall-normal axis
y^+	dimensionless distance along the wall-normal axis
z	distance along the spanmwise axis
z^+	dimensionless distance along the spanwise axis

Greek Letters

Δ	grid filter scale
Δt	time step
Δx^+	streamwise mesh size in wall units
Δy^+	wall-normal mesh size in wall units
Δz^+	spanwise mesh size in wall units
μ	dynamic viscosity
υ	kinematic viscosity
υ_t	subgrid-scale eddy viscosity
ρ	Density
τ_{ij}	subgride-scale stress
τ_w	wall shear stress

Abbreviations

CFL	Courant-Friedrich-Lewy number
FST	Elevated level of intensity of free stream turbulence case
LES	Large Eddy Simulation
NFST	Low level of intensity of free stream turbulence case
OF	Open FOAM
PISO	Pressure-Implicit with Splitting of Operators
SGS	Sub grid scale model
3D_case1	Three-dimensional geometry with a width to thickness ratio (aspect ratio) of 1
3D_case2	Three-dimensional geometry with a width to thickness ratio (aspect ratio) of 2

Chapter One

Introduction

1.1 Background

The transition from laminar flow to turbulence is an interesting physical phenomenon which requires a good understanding in order to control the transition. Although there is considerable knowledge regarding this phenomenon in the attached flow, comprehensive aspects of the transition in a separated shear layer remain poorly understood, and thus represent a considerable research challenge (Taghinia et al., 2015).

Due to dramatic changes in the drag force, lift force and heat transfer rate in separated flows, study and analysis of these flows are important in many practical engineering applications where either the flow is internal, such as in diffusers, combustors and channels with sudden expansions, or it is external, such as flow around aerofoils, aircraft, projectiles, vehicles, and buildings. In addition, the location where transition starts and the spatial extent within which it takes place are of crucial interest in engineering design and in predicting the performance of engineering applications (Yang, 2013).

In aerodynamic applications, a separation bubble that forms within a separated-reattached flow is considered parasitic because it increases drag that reduces aerodynamic efficiency and causes aerodynamic instability. Consequently, such an instability has been experimentally observed to reduce aerodynamic performance as well as result in potentially dangerous dynamic structural loading in aerospace structures (Schreck and Robinson, 2007; Bak et al., 1999). Tani (1964) reported that the separation bubble is undesirable and negatively affects aerofoil performance, leading to catastrophic failures in aerodynamic systems.

There are two principal causes for separation of flow: the boundary layer encounters a sufficiently adverse pressure gradient ($\frac{\partial p}{\partial x} > 0$) (applied, or due to change in geometry), or the flow faces some particular obstacle. In the first separation case, the momentum in the boundary layer is not high enough to overcome the pressure gradient and both separation and reattachment locations can change as flow parameters vary (Alving and

Fernholz, 1996). In this case, the adverse pressure gradient leads to an increased thickness of the boundary layer by decelerating the flow. However, a favourable pressure gradient ($\frac{\partial p}{\partial x} < 0$) accelerates the flow and leads to the formation of a stable boundary layer by retarding the growth of this layer (Sharpe, 1994). In the second separation case, the separation point is fixed in the space where obstacles may be flat plates, humps, forward-/backward-facing steps and other forms of localised surface curvature variations.

A separated boundary layer may or may not reattach to a solid surface, leading to the generation of a large recirculation zone. In the former case, a separated-reattached flow will be formed and characterised by an interaction between the separated shear layer and the nearby solid surface. In the latter case, the flow is characterised by an interaction between two shear layers, which are emanated from separation lines and usually developed to a fully turbulent flow after the transition region (Versteeg and Malalasekera, 2007).

There are three types of separated-reattached flows which can be generated depending on the flow nature at the points of separation and reattachment:

- Turbulent separated-reattached flow: the separated and reattached flows are turbulent.
- Laminar separated-reattached flow: the separated and reattached flows are laminar.
- Transitional separated-reattached flow: the separated flow is laminar, and the reattached flow is turbulent. In this flow, the separated shear layer will usually undergo a rapid transition to turbulence.

Generally, a laminar boundary layer is more likely to be separated than a turbulent boundary layer because in turbulent flow, faster outer particles energize the slower particles near the surface due to an extensive mixing process (Sharpe, 1994). However, in transitional separation, laminar separated flow is characterised as it usually involves unsteadiness due to its instability, even at relatively low Reynolds numbers. Hence, the flow is likely to undergo a transition to turbulence (Sharpe, 1994).

Kiya et al. (1993) reported that various attempts have been carried out to reduce or eliminate the separation bubble, such as deformation of the separation edge, the use of an elevated level of free-stream turbulence intensity, sound waves, oscillation of the separation edge and forcing the shear layer to be near the edge via an oscillating jet, in addition, the sinusoidal disturbances method which was proposed by Kiya et al. (1993). However, in the literature it seems that employing an elevated intensity of free stream turbulence is more appropriate for controlling the separation bubble.

Horton (1967) presented a description of the structure of a time-averaged separation bubble for an aerofoil, as shown in Fig. 1-1 (Lin and Pauley, 1996). It can be seen that the fluid, which is close to the wall and downstream of the separation point, is virtually stationary and this region is called the dead air region. The separated shear layer, which is highly unstable, undergoes a transition to turbulence and reattaches behind a vortical structure known as the reverse flow vortex.

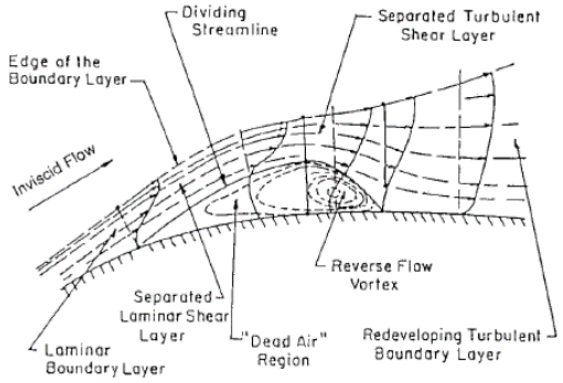

Fig. 1-1. Phenomenological features of a laminar separation bubble, as presented in Lin and Pauley (1996)

Jahanmiri (2011) stated that transitional separated-reattached flow can be divided into two main regions. The first region is bounded by the mean dividing streamline and the solid surface called the separation bubble. The mean dividing streamline is the line that passes through the zero value points in successive velocity profiles, whilst the separation bubble is represented by a recirculation flow. Immediately after the separation, there is a dead air region followed by a strong recirculation zone. The second region of the flow is a free shear layer between the free stream and the mean dividing streamline. Due to flow instability, the laminar separated layer undergoes a transition at the location of

unsteadiness. After the transition, the turbulent separated layer reattaches to the solid surface because of the effects of momentum transfer of a high turbulent mixing that eliminates the reverse flow near the wall. After the reattachment, the development of a turbulent boundary layer takes place.

Generally, the transition to turbulence is not a sudden event. It takes place gradually, although it may be fairly rapid (Sharpe, 1994). There are many methods to enhance the transition to turbulence such as an increase of turbulence intensity in the free stream, an increase of roughness of the solid surface and high adverse pressure gradients, all of which advance the transition (Sharpe, 1994).

Mayle (1991) considered that transitional separation is very complicated, and the identification of a precise transition location is very important. He reported that the transition can be divided into three modes as follows:

- *Natural* or *Classical* transition: This mode occurs within an attached laminar boundary layer that starts with a weak instability and increases to a fully turbulent flow through sequential stages such as flow over a flat plate. In this mode, the level of free-stream turbulence intensity is less than 1%.

- *Bypassed* transition: This mode occurs when the transition takes place earlier due to the effect of an external flow, such as a high intensity of free stream turbulence on the laminar boundary layer. This external flow will provide a high level of disturbance which leads to the first stages of the natural transition being bypassed and a reduction in the associated interval. So here, the transition to turbulence takes place quickly.

- *Separated-flow* transition: This mode occurs within a laminar free shear layer through sequential stages, which leads to a turbulent free shear layer, such as a transitional separated boundary layer, mixing layers, jet flow and wakes. This mode of transition can be as a natural or bypassed transition.

The *Natural or Classical* transition mode of attached flow starts as linear oscillations which are developed in a laminar boundary layer due to presence of very low freestream turbulence intensity (< 1%). These oscillations are two-dimensional and called Tollmien-Schlichting (TS) waves. An increase in the disturbance amplitude of TS waves leads to a

distortion of their spanwise similarity. Distorted TS waves develop into three-dimensional structures. Vortical structures burst into turbulent spots leading to the boundary layer alternating between laminar and turbulent states. Eventually, the turbulent spots that originate from different locations merge to form a fully developed turbulent boundary layer (Versteeg and Malalasekera, 2007).

In process of *bypassed* transition mode, influence of the freestream disturbances leads to produce turbulent spots directly bypassing linear instability stages of the boundary layer (Blair, 1992). No formation of Tollmien-Schlichting waves in this case of the flow.

There are three modes of the *Separated-flow* transition classified in Hatman and Wang (1999) as follows:

- *Transitional separation*: In this mode, the transition onset takes place prior to the boundary layer separation point and the transition development is essentially similar to the natural transition in attached boundary layers. This mode occurs if the boundary layer separates at relatively high Reynolds numbers and with low adverse pressure gradients.

- *Laminar separation / short bubble*: In this mode, the transition occurs downstream from the separation point by inflexional instability. This mode is characterized by a quick transition due to the complex interaction between the separated shear layer and the reverse flow vortex, and it is also characterized by distinctive vortex shedding. This mode is induced if the separation of the laminar boundary layer occurs at moderate Reynolds numbers and with mild adverse pressure gradients.

- *Laminar separation / long bubble*: In this mode the transition onset takes place downstream of the separation point through inflexional instability. This mode is characterised by a delayed completion of the transition and it is no longer accompanied by vortex shedding. This mode occurs when the laminar boundary layer separation occurs at low Reynolds numbers due to strong adverse pressure gradients. In this mode, the shear layer may fail to reattach.

In transitional separated-reattached flow induced due to flow around obstacles, as in the current study, a separation bubble is formed when a laminar flow with a relatively low

Reynolds number separates to form a laminar free shear layer. The separated laminar layer becomes unstable and tends to undergo the transition to turbulence. The turbulent separated layer reattaches to the solid surface. After the reattachment, a rapid development of a turbulent boundary layer occurs, and thus, fundamental aspects of transitional separated-reattached flow can be summarized as a primary instability mechanism of the laminar free shear layer that leads to the onset of the transition, different shedding frequency modes, formation of large scale structures and their development that is associated with a secondary instability mechanism of the transition and the development of a turbulent boundary layer after the reattachment (Manneville, 1990). In this type of separated-reattached flows, the separation bubble is susceptible to instability due to its sensitivity to small fluctuations in the upstream flow (Bak et al., 1999; Rist and Augustin, 2006).

Yang (2013) reported that accurate modelling of this flow is limited both experimentally and theoretically. In experimental studies, measurement techniques provide limited temporal and spatial resolution of flow parameters, and hence there is no inclusive description of the transition process within these studies. He also stated that theoretical studies suffer from the limitation imposed by the nonlinearity of the transition process at later stages. In addition, instability mechanisms of transitional separated flows, especially for the secondary instability mechanism, are still far from being fully understood.

1.2 Turbulent flow and its simulation methods

Turbulent flow is a random fluctuating motion of the fluid when its flow velocity increases suddenly. Turbulent flow can be described by solving flow equations, the so-called Navier-Stokes equations (NSE), numerically using Computational Fluid Dynamics (CFD) techniques. There are many non-dimensional quantities used to parameterize the turbulence, and the Reynolds number (*Re*) is the most often, which is the ratio of inertial forces to viscous forces and is equal to

$$Re = \frac{UL}{\upsilon} \tag{1-1}$$

where L is the characteristic length of the flow domain.

Viscous forces dominate at low Reynolds number and they damp disturbances rapidly where the flow is considered to be laminar. When Reynolds number increases, the effect of viscous forces decays and disturbances grow, leading to fully turbulent flow.

Turbulent flow is characterised as three-dimensional, unsteady, non-linear, random, and diffusive in nature.

Diffusiveness of the turbulence leads to increased rates of mass, momentum, and heat transfer and enhances the mixing of flow properties. The disadvantage of diffusiveness of the turbulence is the creation of boundary layers and shear layers that are much thicker than that of the laminar flow.

Turbulence involves a wide range of length and time scales. To understand these scales, the basic entities of turbulent flow should be identified. These entities are lumps of rotating fluid called eddies. The sizes of these eddies are different, and the variation of such falls within a wide range. However, the length scale of the largest eddy is equal to the system length scale, whilst the length scale of the smallest eddy is equal to Kolmogorov scale.

Large eddies extract kinetic energy from the mean flow due to its instability in the energy production region of the turbulence spectrum. The kinetic energy cascades through different-sized eddies until it is moped up by the smallest eddies due to viscous dissipation leading to the conversion of the kinetic energy into heat. The kinetic energy cannot be moped up by viscous dissipation at the large eddies because the inertial forces are dominant in this situation and the effect of viscous forces is thus neglected.

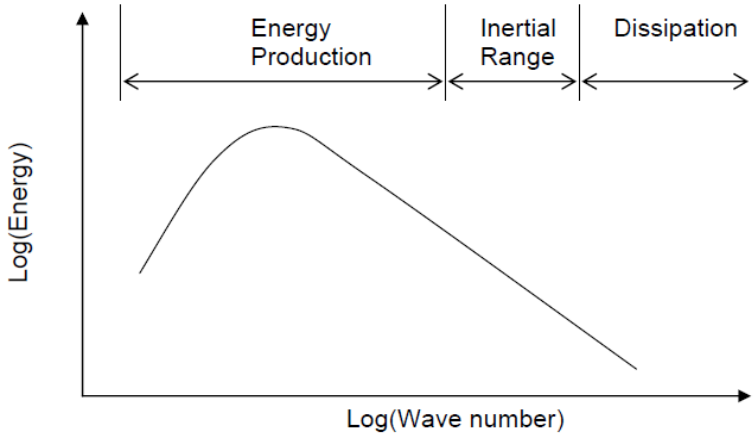

Fig. 1-2. Turbulent energy spectrum related to wave number (Nichols)

Fig. 1-2 shows the turbulent energy spectrum related to wave number. It is shown that most of the kinetic energy is contained in large turbulent eddies (low wave numbers), which is then transferred in a cascading process by the inertial range to the scales of the dissipation range, where the energy is eventually dissipated (Nichols).

1.2.1 Turbulence length and time scales

The maximum and minimum length and time scales of the eddies of the turbulent flow are defined in terms of the turbulent kinetic energy (k), turbulent dissipation (ε), and the kinematic viscosity (υ). The length scale (L) and the time scale (T) of the largest eddies (turbulence-producing eddies) and the length scale (λ) and the time scale (τ) of the smallest scale eddies (Kolmogorov scale), or dissipative eddies, are characterized, respectively, as follows (Nichols)

$$L = \frac{k^{\frac{3}{2}}}{\varepsilon} \tag{1-2}$$

$$T = \frac{k}{\varepsilon} \tag{1-3}$$

$$\lambda = \left(\frac{\upsilon^3}{\varepsilon}\right)^{\frac{1}{4}} \tag{1-4}$$

$$\tau = \left(\frac{\upsilon}{\varepsilon}\right)^{\frac{1}{2}} \tag{1-5}$$

Ratios of length and time scales of the smallest eddy to the largest eddy are characterized by the turbulent Reynolds number (Re_t) as

$$\frac{\lambda}{L} = (Re_t)^{-\frac{3}{4}} \tag{1-6}$$

$$\frac{\tau}{T} = (Re_t)^{-\frac{1}{2}} \tag{1-7}$$

where

$$Re_t = \frac{k^2}{\upsilon\varepsilon} \tag{1-8}$$

1.2.2 Turbulence simulation approaches

As mentioned above, CFD is used to predict flow characteristics, saving the time and the cost of conducting the analogous experiments. The unsteady three-dimensional Navier-Stokes equations (NSE) are used to simulate and describe numerically the turbulent flow. There are three basic approaches for the numerical simulation of turbulence: Direct

Numerical Simulation (DNS), Reynolds-Averaged Navier-Stokes (RANS) and Large Eddy Simulation (LES).

The highest accuracy approach is DNS, which resolves all scales with no modelling of the flow. DNS is employing a simulation mesh which has a cell space that is smaller than the Kolmogorov scale to capture all turbulent kinetic energy which cascades from the largest scale eddies to the smallest scale eddies. As shown in equation (1-6), the range of turbulent length scales may span orders of magnitude for high Reynolds number flows. Since these turbulent length scales are much smaller than the physical scales (i.e. wing chord, channel height) associated with a flow of interest, it is easy to see that large amounts of mesh points would be required to fully simulate a high Reynolds number turbulent flow. Therefore, computational time is increased and the required computational resources are high. This is considered to be one of the principal drawbacks of using DNS. In general, this approach is impractical for complex geometries with high Reynolds number flows.

The RANS approach involves modelling and solving for time-averaged quantities of the flow, which drastically reduces the computational time. In this approach, the flow is decomposed into two parts: the mean part and the fluctuating part. The mean part is a function of space only, whilst the fluctuating part is a function of space and time. A time-averaging process used to remove the necessity to simulate all turbulent scales by using one length scale to characterize all turbulent spectra. In RANS, the unsteadiness is assumed to be at scales that are below the computational mesh size and the flow is treated as a steady flow. Thus, RANS equations are time-averaged Navier-Stokes equations.

A large number of RANS models have been presented and applied for different problems. However, due to the low accuracy of this approach – since it only predicts the time-or ensemble averaged flow field – employing it to gain any meaningful prediction of the physics of complex flows, such as the transition in transitional separated-reattached flow, is extremely hard, if not impossible (Yang, 2012; 2015).

LES is based on the idea of scale separation or filtering with a mathematically well-established formalism. The separation process is carried out using a spatial filter for the turbulence spectrum. Thus, LES equations are space-filtered Navier-Stokes equations.

The strategy underlying LES is one of resolving the flow of large structures and modelling the effects of the flow of small structures on the large structures. In this way, the spatial filtering of LES is employed to separate the resolved large scales from the unresolved small scales. More details about LES are presented in Chapter 3.

LES is able to simulate transitional / turbulent flow aspects better than RANS, but requires a very high space and time resolutions especially for modelling close to walls which consequently requires long computational times and considerable computational resources (Yang, 2015). In order to provide a very accurate solution, it needs to create a very fine mesh to reduce the number of modelled scales. Therefore, LES approaches DNS in terms of modelling and computational resources. Fig. 1-3 shows region of the turbulent energy spectrum modelled by different turbulence model approaches.

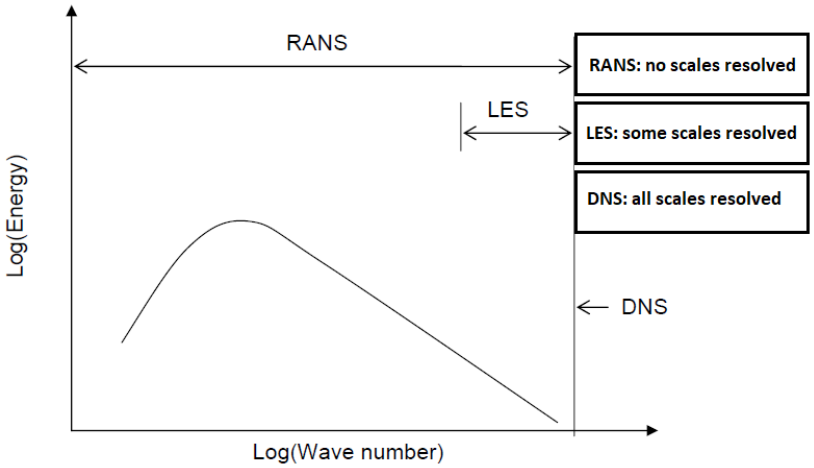

Fig. 1-3. Region of the turbulent energy spectrum modelled by different turbulence model approaches. (Nichols)

1.3 Open FOAM framework

Recently, Open FOAM (Open Source Field Operation and Manipulation) has become widely used in academic research and industrial engineering (Lysenko et al., 2013). Open FOAM (hereafter OF) is, foremost, a set of C++ libraries. It is designed to solve and create executable applications. OF is completely free and employs a finite volume formulation. OF includes two main groups: solvers and utilities, which can potentially cover a wide range of problems. Solvers are designed to solve specific problems in continuum mechanics and the utilities to perform tasks that involve data manipulation.

OF involves many standard fields such as incompressible flow, compressible flow, combustion, solid-body stress analysis, etc. Each field includes several solvers that deal with different features of specific problems. As an example, Table 1-1 describes some of the available incompressible flow solvers.

solver	discretion
icoFoam	transient, incompressible, and laminar flow solver for Newtonian fluids
pimpleFoam	transient, incompressible flow, and large time-step solver using the PIMPLE (merged PISO-SIMPLE) algorithm
pisoFoam	transient, and incompressible flow solver
simpleFoam	steady-state, incompressible, and turbulent flow solver

Table 1-1 Description of some of incompressible flow solvers as detailed in the OF user guide

To create and solve any problem by OF, three main directories must be generated. These directories are **0**, **constant**, and **system.** Each directory involves numerous files in order to prepare the mesh, initial conditions, boundary conditions, and numerical schemes that will be used to solve the problem. The **0** directory is to identify initial conditions for the problem variables such as velocity, pressure, etc. The **constant** directory is to create the numerical simulation mesh, identify boundary conditions, and choose the turbulence simulation approach and its modelling method. The **system** directory is to select simulation runtime, time step, properties of parallel computing and the numerical scheme and solving methods. OF directories and their files are shown in Fig. 1-4.

For more details about available turbulence models, solvers, numerical schemes, and the utilities available through OF, the reader is referred to Robertson et al. (2015), Jasak et al. (2007) and also the OF user and programmer guides.

In many numerical simulation studies, OF has been used to simulate different problems. In addition, many studies present comparisons between the results of OF and ANSYS FLUENT (hereafter AF). Balogh et al. (2012) and Lopez et al. (2015) employed these two commercial CFD codes to simulate different problems. They observed minor differences between the results of these two codes. However, they concluded that OF is sufficiently accurate to simulate complicated applications.

Lysenko et al. (2013) showed that OF is more effective than AF because there are no limitations to parallel computing and no black boxes in OF. In addition, there are no limitations for detailed-chemistry modelling in OF compared with AF with regards to

combustion applications. Lysenko et al. (2013) reported that there is an extensive list of numerical schemes and mathematical models provided by OF, making this technology perfect to simulate a wide range of fluid dynamics problems. Lysenko et al. (2013) recommended that the researchers should present more studies employing OF to further validate this technology. Robertson et al. (2015) validated OF by comparing its simulated data with the experimental results of a turbulent flow passing several types of shapes. Reynolds-Averaged Navier-Stokes (RANS) and a hybrid RANS/LES method were used as numerical simulation methods. In this study, excellent agreement between simulated data and experimental results were reported. Robertson et al. (2015) concluded that OF can be considered as a reliable solver for different applications.

Because of the high accuracy and reliability of OF, as demonstrated extensively in the literature, this code has been selected for use in the present study. It is worth noting that, to the best of the author's knowledge, there are no studies that have investigated transitional separated-reattached flow using OF. So, the current study may represent the first work to attempt to validate OF and presents its ability to simulate this type of flow.

1.4 Motivation

The phenomenon of transition flow from laminar to turbulence is common and important feature in many practical engineering applications. Motivation of study this phenomenon is to understand the transition process and to apply the knowledge of this study in order to reduce, accurately predict, and control the transition. Study and analyses of transitional separated-reattached flows are particularly useful and important for flows on many environmental and industrial applications. The industrial applications involve a wide range of appliances from sheets of cooling fins of small electronic devices to turbomachines blades and airfoils, where the transition plays a significant role in heat transfer and aerodynamics characteristics of these appliances.

The engineering significance of the results of the present work is to shed a light on physics of such flow on two groups of engineering applications, which are two-dimensional geometries and three-dimensional geometries.

The two-dimensional geometry that is chosen in the current study is a blunt flat plate in order to have good knowledge and understanding of the flow physics of the separation

bubble that forms on many practical applications such as wind turbines rotor blades, blades of low-pressure turbines, wings of airplanes and small unmanned aerial vehicles, blades of jet engines and fans, inboard section of helicopter rotors, and other engineering applications that include a flow over a flat plate.

Two three-dimensional geometry models, characterised with different aspect ratios, are used in the current study. The purpose of using these geometries is to understand physics of the transitional separated-reattached flow over them. It is believed that the current study is the first work that presents aspects of such flow on a three-dimensional geometry.

Simulated results of the flow over the three-dimensional geometry offer knowledge about transitional separated-reattached flows that occur in many engineering applications such as wind loads on structures, river flows, humps and other forms of localized obstacles, spread of pollutants in the vicinity of buildings, aerodynamics of aircrafts and road vehicles (cars, trucks and trains), different parts in instruments of meteorology, and wind energy applications.

It is worth pointing out that the separated-reattached flows over three-dimensional geometries are quite complicated when compared with flows over two-dimensional geometries, such as a flat plate. The complication is a result of additional two separation bubbles that form on the side surfaces of the three-dimensional geometry and the relations between these separation bubbles and other separation bubbles that form on the top and bottom surfaces of this geometry. This issue will be revealed for the first time in the current study. Another goal of the current study is to understand effect of the aspect ratio of the three-dimensional geometry on characteristics of the transitional separated-reattached flows.

1.5 Organization of the thesis

Chapter one: Background to transitional separated-reattached flow, turbulente flow, and Open FOAM are presented.

Chapter two: Literature review of transitional separated-reattached flows; the objectives of the research are also presented.

Chapter three: Governing equations, methodology, and numerical computation are discussed in detail.

Chapter four: Open FOAM code validation and the flow variables, with and without elevated intensity of free stream turbulence, are presented.

Chapter five: Primary instability mechanism, with and without elevated intensity of free stream turbulence, is discussed.

Chapter six: Spectral analyses, with and without elevated intensity of free stream turbulence, are presented.

Chapter seven: Coherent structure development, with and without elevated intensity of free stream turbulence, are exhibited.

Chapter eight: Reattached turbulent boundary layer development, with and without elevated intensity of free stream turbulence, is discussed.

Chapter nine: Conclusions from the current study and scope for future work are described.

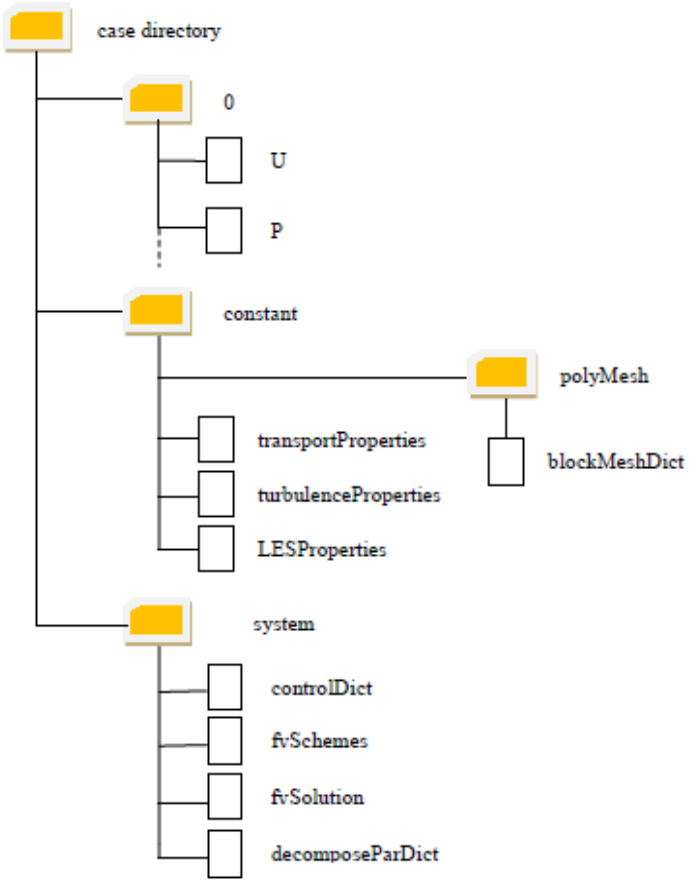

Fig. 1-4. Directory structure of a turbulent flow case simulated using LES and run in parallel using OF

Chapter Two

Literature Review

2.1 Aspects of transitional separated-reattached flow

It has been recognised that transitional separated-reattached flow is characterised by four important features:

- Primary instability mechanism that causes the separated laminar layer to be unstable, leading to the start of a transition.
- Characteristic (regular) vortex shedding frequency.
- Large-scale structures (coherent structures) development, which is the change of vortices shapes from being two-dimensional to three-dimensional in nature. This phenomenon is associated with a secondary instability mechanism.
- Breakdown of three-dimensional structures to turbulent structures and development of the reattached turbulent boundary layer.

The following literature review sheds light on the above features of transitional separated-reattached flows.

2.2 Instability mechanisms

It has been documented in many studies that the separated shear layer, which is formed due to flow separation, is mostly inviscidly unstable and the transition is driven by the inviscid Kilven-Helmholtz instability mechanism. The amplification of this invicid instability is larger than that in the case of viscous instabilities (Tollmien-Schlichting waves). This is presented for mixing layer and jet studies conducted by Ho and Huerre (1984), Rogers and Moser (1993), Danaila et al. (1997) and Urbain and Metais (1997).

The Kilven-Helmholtz instability mechanism for the separated shear layer has also been reported by Abdalla and Yang (2004a) for a blunt flat plate, by Yang and Voke (2001) for a flat plate with a semi-circular leading edge, by Neto et al. (1993) for a backward-

facing step and Abdalla et al. (2009) for a surface-mounted obstacle and forward-facing step.

The findings of these studies are consistent with the theoretical and experimental results of Dovgal et al. (1994), who argued that since an inflection point exists in local velocity profiles, such profiles are inviscidly unstable; hence, it is understood that the transition onset in the free shear layer is due to action of the Kilven-Helmholtz instability. However, knowledge about the other aspects of the transition, including breakdown to turbulence, coherent structure development and unsteady behaviour of the flow around the mean reattachment line, is still not fully understood.

Free shear layer instability can be characterised as convective or absolute. Convective instability is characterised by disturbances of the flow that develop in space and move away from the source. However, if these disturbances develop in time and spread everywhere, the flow is absolutely unstable. Absolute instability is characterised by a strong reverse flow in the separation bubble (Niew, 1993).

For backward-facing step flows, Niew (1993) suggested that the absolute instability occurs with a reverse flow intensity of more than 20%. Hammond and Redekopp (1998) reported that absolute instability exists if the strength of the reverse flow within the separation bubble approaches (roughly) 30% of the ambient stream speed.

Huerre and Monkewitz (1985) attributed the spatial growth of waves to be a consequence of presence of the convective instability in free shear layers for a mixing layer from a theoretical standpoint. Jones et al. (2008) employed classical linear stability analysis for time-averaged flow fields based on a separation bubble formed on a NACA-0012 aerofoil at 5^0 incidence. It was concluded that the separation bubble is connectively unstable without any region of absolute instability. A similar conclusion was reached by Yang and Voke (2001) for a transitional separation on a flat plate with a semi-circular leading edge. In this study, there was less than 3% maximum reverse flow in the separation bubble. Therefore, there was no evidence of the absolute instability. So, the separation bubble was connectively unstable.

Alam and Sandham (2000) carried out a numerical simulation for a transitional separated-reattached flow induced by an adverse pressure gradient on a flat plate. They clarified the

fact that the separated shear layer is absolutely unstable when the maximum negative value of the local velocity profile is within a range between 15% and 20%. This range depends on the values of the Reynolds numbers. Alam and Sandham (2000) showed that with high Reynolds number, the absolute instability initiates when reverse flow intensity is as low as 15%. They concluded that the inviscid instability of the separated shear layer can be dominated by the viscous Tollmien-Schlichting instability when the reverse flow intensity is about 15% - 20%, i.e., if the absolute instability is present. Furthermore, Alam and Sandham (2000) identified that the transition in the separated shear layer is started by an oblique mode and the instability was convective in nature due to the low rate of the reverse flow, which was less than 8% of the local free stream velocity.

For such flow, Spalart and Strelets (2000) found that the Kilven-Helmholtz instability was the primary instability mechanism in the separated shear layer. They noted that absence of the absolute instability is due to an insufficient rate of reverse flow, which is necessary to enhance the absolute instability. McAuliffe and Yaras (2008) also found that Kilven-Helmholtz rolls formed in the separated shear layer in the first half of the separation bubble. The authors observed that growth of a linear Tollmien-Schlichting instability after the separation led to the roll-up of spanwise vorticity into discrete vortical structures. They noted that the transition sheared features from both viscous and inviscid instability mechanisms because the instability growth in their study was similar to Kelvin-Helmholtz instability growth.

Roberts and Yaras (2006) and McAuliffe and Yaras (2008) concluded that frequency of instability due to the Kelvin-Helmholtz mode in the separated layer was close to the frequency of the Tollmien-Schlichting instability mode in the attached layer before the separation point. Marxen et al. (2003; 2004) reported that the transition was driven by convective amplification of two-dimensional Tollmien-Schlichting waves, and the absolute instability was the second instability mechanism.

Brinkerhoff and Yaras (2011; 2013) observed an interaction between inviscid and viscous instability mechanisms in the separated layer. The dominant instability in the separated layer is inviscid Kelvin-Helmholtz instability. The authors stated that streamwise-oriented vortices, as formed by the Tollmien-Schlichting instability mode in the attached boundary layer before the separation, moved inside the separation bubble. These vortices

amplified in the separated shear layer and produced hairpin-like structures in the transient region, where there was a strong interaction between these vortices and the inviscid Kelvin-Helmholtz instability.

McAuliffe and Yaras (2009), Yaras (2012), Dahnert et al. (2012) and Ducoin et al. (2016) noticed that the Kilven-Helmholtz instability was the dominant primary instability mechanism of the transition. Roberts and Yaras (2006) noted that there was an interaction between the Kilven-Helmholtz and the Tollmien-Schlichting modes in the transition of the separation bubble. They observed that the formation of vortical structures by shear layer roll-up in the inner part of flow was dominated by the Tollmien-Schlichting frequency and the transition was driven by a Kilven-Helmholtz instability.

Lang et al. (2004) reported that the viscous Tollmien-Schlichting instability mechanism may have a considerable effect on the transition in the separated-reattached flow. Gungora and Simens (2015) found that a viscous Tollmien-Schlichting instability was a dominant primary instability mechanism for separation under the effect of an adverse pressure gradient. The inviscid Kelvin-Helmholtz instability is the primary instability mechanism in the separated shear layer with a strong adverse pressure gradient, which can be seen in Serna and Lazaro (2015a; 2015b) and Hosseinverdi and Fasel (2015).

In the early stages of the transition in the separation bubble, the onset of spanwise structures (primary structures) is associated with a primary instability mechanism. These structures, which are two-dimensional across the spanwise direction, are broken down into smaller scale streamwise structures (secondary structures) leading to spanwise deformation of the vortex. This process is associated with a secondary instability mechanism (Yang and Voke, 2001; Abdalla and Yang, 2004a; Jones et al., 2008; Marxen et al., 2013; Kurelek et al., 2016).

In a mixing layer, it has been found that the vortex pairing process is a governing secondary instability mechanism which involves a merging of spanwise vortices by the roll-up of two such vortices around each other to form a large single vortex (Huang and Ho, 1990). In the plain free shear layers, Lasheras and Choi (1988) observed a perturbed vorticity was formed as a braid between two Kelvin-Helmholtz rolls. This vorticity stretched in the axial direction, leading to the formation of three-dimensional streamwise structures. Jones et al. (2008) performed a numerical simulation for a flow over an

aerofoil. They found that after the shedding of two-dimensional spanwise vortices, three-dimensional streamwise vortices are formed within the braid region along the successive spanwise vortices.

Although the flow visualization for a separation bubble on a blunt flat plate in Yang and Abdalla (2008) did not capture the merging of two separated Kelvin-Helmholtz rolls in a pairing process to form a double helix structure, the characteristics of origin and new coherent structures gave evidence of the occurrence of a helical-pairing instability. The authors proposed that the pairing process might take place on a very short timescale. Yang and Abdalla (2008) indicated that the Kelvin-Helmholtz rolls themselves evolve into three-dimensional hairpin and rib-like structures around the reattachment zone and in reattached turbulent boundary layer. The authors concluded based on their numerical simulation that transformation from two-dimensional to three-dimensional coherent structures was most likely due to the helical instability, which is associated with the helical pairing of vortices that was considered to be a secondary instability mechanism of the transition. Yang and Abdalla (2008) stated that the helical pairing instability mechanism was similar to that presented by Delcayre (1997) for a backward-facing step. Yang and Abdalla (2008) showed that the hairpin vortices became part of the core of the spanwise vortices, which were formed from the pairing instability, and this instability distorted Kelvin-Helmholtz rolls to form three-dimensional coherent vortices.

A helical-pairing instability was reported by Comte et al. (1992) to be a secondary instability mechanism that transformed two-dimensional Kelvin-Helmholtz rolls to three-dimensional coherent structures in mixing layers. The vortex pairing phenomenon was observed in mixing layers by Winant and Browand (1974). Chandrsuda et al. (1978) documented that the helical pairing was the process of localized pairing of vortices by them winding up around each other to form a quasi-spanwise double helix vortex structure. Merging of spanwise rolls within the transitional separated flow was reported in Hwang et al. (2000) and Marxen et al. (2013) for a blunt flat plate, and by Burgmann et al. (2006) for the suction side of an aerofoil SD7003.

Yang and Voke (2001) found that large structures, which were formed from a pairing of two spanwise vortices, were subjected to an undulation process associated with a secondary instability mechanism that led to the formation of spanwise peak-valley

structures. These structures developed into hairpin structures around the reattachment region.

Recently, Kurelek et al. (2016) and Kirk and Yarusevych (2017) experimentally investigated vorticity development in the later stages of the transition in a separation bubble formed on a NACA 0018 aerofoil. They showed that rolled-up vortices, which were strongly coherent in the spanwise direction, underwent significant and rapid deformations leading to their breakdown into smaller-scale structures; occasional vortex merging was also observed in this study. Rapid breakdown of spanwise structures into smaller-scale structures prior to reattachment was also reported in Alam and Sandham (2000) and Spalart and Strelets (2000).

Spanwise undulations of spanwise rolls that shed from the separated layer were observed by Kurelek et al. (2017) for a transitional separated flow on a NACA 0018 aerofoil. Spanwise undulations were developed in the vortex filaments, forming hairpin-like structures. Formation of these streamwise structures involved two stages: the first stage was re-orientation of spanwise vorticity into the streamwise direction; the second one was by a lifting-up action that reoriented the vorticity into the wall-normal direction. Then, the hairpin-like structures broke down into turbulent structures.

Recently, Lambert and Yarusevych (2017) observed that after the free shear layer roll-up region, a non-periodic merging of two or more consecutive vortices occurred. The authors hypothesized the merging process to be produced by a perturbation in the shedding cycle, leading to a critical change in vortex spacing and / or strength. Then, it was observed that two adjacent vortices rounded on each other, where the leading vortex moved toward the wall and the trailing vortex moved away from the wall, forming a new structure that moved downstream and broke down into turbulent structures.

It is clearly shown in the literature that the transition stages in the first half of the separation bubble include receptivity and linear and weakly non–linear instability amplification. These stages can be accurately predicted for many receptivity mechanisms or instabilities. The principal challenge is to accurately predict the non-linear intermittency transition region that takes place in the second half of the separation bubble. This will be key for the designers due to the maximum skin friction that occurs in this

region. In addition, this region involves the presence of a large number of scales that will need to be resolved. However, Marxen et al. (2013) reported that the formation and evolution of coherent structures in the separation bubble are far from being completely understood. In other words, the physical nature of secondary instability mechanisms for the transitional separated-reattached flow is unclear, and several scenarios related to the phenomenon remained to be explored (Robinet, 2013).

It is worth pointing out that the above studies, which identified primary and secondary instability mechanisms of transitional separated-reattached flow, were carried out without an elevated level of intensity of free stream turbulence. There are relatively few studies available in the literature that have investigated the effects of high levels of disturbances in the incoming flow on its resultant characteristics. It has been shown that there are dramatic influences due to high levels of intensity of free stream turbulence on the properties of this flow which may lead to the bypassed transition, which was successfully simulated using LES for an attached flow by Voke and Yang (1995).

Bearman and Morel (1983) reviewed the effect of high levels of intensity of free stream turbulence on the mean separated flow. They defined free stream turbulence as the background level of random and three-dimensional velocity fluctuations in the flow. Free stream turbulence is present in the natural wind and it is generated by different methods. For example, free stream turbulence exists in road vehicles encountering the turbulence generated by the natural effects of wind and also by flows over other vehicles. High levels of intensity of free stream turbulence can be found in the incoming flow to blades rows in turbomachines. Buildings may be subject to turbulence from many sources. Bearman and Morel (1983) reported that additional high intensity of free stream turbulence accelerates the transition to turbulence and enhances mixing and entrainment of the flow.

Yang and Abdalla (2008) documented that the primary instability mechanism of the transition is still the Kelvin-Helmholtz instability mechanism, even at a 2% intensity of free stream turbulence. In their study, the two-dimensional Kelvin-Helmholtz rolls are present in the early stages of the separated shear layer. It should be noted that this study was carried out for transitional separated-reattached flow induced by a blunt flat plate with a Reynolds number of 6.5×10^3, as based on the plate thickness and inlet velocity. The authors postulated that the increase in the randomness in the incoming flow, which

is a consequence of an elevated intensity of free stream turbulence, leads to a different secondary instability mechanism forming. A complementary study was presented in Abdalla and Yang (2004a) for a similar geometry and Reynolds number, but without free stream turbulence. Yang and Abdalla (2008) recommended that further investigations are needed.

For a similar geometry and Reynolds number, Yang and Abdalla (2009) investigated the influence of a 2% intensity of free stream turbulence on characteristic shedding frequency. They reported that the value of this frequency is close to that of the characteristic shedding frequency observed in a case without free stream turbulence. Yang and Abdalla (2009) concluded that the primary instability in the free shear layer is still the Kelvin-Helmholtz instability, even with a 2% intensity of free stream turbulence.

Hosseinverdi and Fasel (2015), in their DNS study, investigated the effects of four levels of intensity of free stream turbulence (0.1, 0.5, 1, and 2%) on the instability mechanism of transition in transitional separated-reattached flow generated on a flat plat due to effects of an adverse pressure gradient. The authors documented that there are different instability modes in the free share layer depending on levels of intensity of free stream turbulence. At 0.1%, the transition starts via the Kelvin-Helmholtz instability. When the intensity of free stream turbulence increases to 0.5% and 1%, the transition is accelerated, and the Kelvin-Helmholtz instability and the Klebanoff mode (K-mode) instability blend together, simultaneously contributing to the transition process. For the highest intensity of free stream turbulence (2%), the dominant transition mechanism is the K-mode. Hosseinverdi and Fasel (2015) reported that the Klebanoff mode is characterized by low frequency, three-dimensional perturbations.

McAuliffe and Yaras (2010) studied the effects of elevated-disturbance environments on the instability mechanism for the transition of a separated laminar boundary layer formed by an adverse pressure gradient. In this study, a 1.45% intensity of free stream turbulence led to the transition being bypassed. The authors showed that for a similar flow, but with a lower intensity of free stream turbulence (0.1%), the transition was driven by the Kelvin-Helmholtz instability. McAuliffe and Yaras (2010) reported that with a high intensity of free stream turbulence, streamwise streaks are formed in the laminar boundary

layer. These streamwise streaks produce turbulent spots in the separated shear layer. The turbulent spots grow, merge and shed to the reattached turbulent boundary layer.

The findings of McAuliffe and Yaras (2010) are comparable with the results of an experiment carried out by Coull and Hodson (2011). In this experimental work, Klebanoff streaks were observed to form in the laminar boundary layer due to an elevated intensity of free stream turbulence. When these streaks arrived at the separation region, the transition was induced more rapidly and the separated shear layer becomes three-dimensional. Kelvin-Helmholtz structures, which were observed in instances of no free stream turbulence, become shorter in the spanwise direction and more distorted due to an interaction with Klebanoff streaks in the case of a high level of intensity of free stream turbulence.

A bypassed transition was also reported by Langari and Yang (2013), who studied transitional separated-reattached flow on a flat plate with a semi-circular leading edge with a high intensity of free stream turbulence (5.6%). The authors also studied the effects of a lower intensity of free stream turbulence (< 0.2%) and compared the results with the data of Yang and Voke (2001) for a similar geometry and Reynolds number (3450), as based on the inlet flow velocity and plate thickness. For a low level of disturbances, there was good agreement between the results of both the above LES studies. Both showed that the free shear layer was inviscidly unstable via a two-dimensional Kelvin-Helmholtz instability mechanism. Two-dimensional Kelvin-Helmholtz rolls were clearly visible in the early stages of the transition which distorted / deformed due to three-dimensional motion; three-dimensional hairpin vortices were then formed around the mean reattachment line.

Due to an elevated intensity of free stream turbulence (5.6%) in the work conducted by Langari and Yang (2013) at a plate edge, it was noted that the stage at which two-dimensional Kelvin-Helmholtz rolls exists was bypassed and that these rolls were irregular in the spanwise direction, forming three-dimensional hairpin structures. In this case, a 5.6% intensity of free stream turbulence led to an earlier breakdown to turbulence. Langari and Yang (2013) concluded that due to the effects of a high intensity of free stream turbulence, the Kelvin-Helmholtz instability mechanism, which was dominant in the free shear layer at low levels of disturbance, was bypassed.

Volino and Hultgren (2000) experimentally generated an elevated free-stream turbulence (7%) to reveal its influence on transitional separated-reattached flow induced by an adverse pressure gradient. This study also investigated the transition with a low disturbance level (0.2%). They found that the transition occurred through the bypassed mode with a high intensity of free stream turbulence, and the transition location became closer to the plate edge compared with that in the low disturbance case.

The effects of various levels of intensity of free stream turbulence (0, 0.05, 0.5, and 2.5%) on the instability mechanism in laminar boundary layers, which was separated from a flat plate due to a presence of an adverse pressure gradient, was investigated by Balzer and Fasel (2016). With a non-zero intensity of free stream turbulence, streamwise elongated streaks were observed inside the boundary layer. These streaks were formed by a Klebanoff instability mode. When intensity of free stream turbulence increased, these streaks appeared with a higher amplitude and a distinct spanwise scaling. The authors noted the strong growth of these streaks inside the separation bubble. In general, the separated layer was inviscidly unstable at all levels of intensity of free stream turbulence.

Recently, Istvan and Yarusevych (2017) experimentally investigated the instability mechanism of the transition in a separation bubble formed over the suction side of a NACA 0018 aerofoil with a 1.92% intensity of free stream turbulence. Experimental tests detected a reduction in the separation bubble length and increase of amplitude of fluctuating velocities, leading to an earlier transition by shifting the transition location towards the aerofoil edge. The authors noted that as a consequence of the elevated level of intensity of free stream turbulence, shear layer roll-up became less organized, spanwise coherence was distorted, and streamwise streaks, that originated in the attached flow before the separation bubble, were formed. Istvan and Yarusevych (2017) concluded that the transition in the separation bubble altered to the bypassed transition.

Using different intensities of free stream turbulence, Simoni et al. (2017) investigated the characteristics of a separation bubble formed on a flat plate due to an adverse pressure gradient, where the intensity of free stream turbulence levels were 0.65%, 1.2%, and 2.87%. It was reported that the transition to turbulence was driven by the Kelvin-Helmholtz instability mechanism for all chosen levels of intensity of free stream

turbulence. In addition, a strong reduction in the length and height of the separation bubble was observed with increasing levels of disturbance.

2.3 Shedding frequency

Basically, there are two frequency modes in separated-reattached flows: a low frequency mode and a high frequency mode. The low frequency mode is related to the dynamics of the separation bubble growth / decay, referred to in the literature as the low frequency shear layer flapping (Kiya and Sasaki, 1983; Cherry et al., 1984; Tafti and Vanka, 1991). The high frequency mode is related to the shedding of large-scale structures from the free shear layer and can be divided into two types: characteristic (regular) shedding frequency and selective high frequency. The selective high frequency is about seven times as large as the characteristic shedding frequency (Tafti and Vanka, 1991; Abdalla and Yang, 2005).

The power spectra for the velocity and surface pressure fluctuation of an experimental study allowed Kiya and Sasaki (1983) to estimate the low frequency shear layer flapping value to be of the order of 0.12 U_0/x_R (where U_0 is the free stream velocity and x_R is the mean reattachment length) at a position close to the separation line. In this experiment, the separated-reattached flow was turbulent over a blunt flat plate. The authors suggested that the flapping of the shear layer was a result of large-scale unsteadiness in the separation bubble (i.e., shrinkage and enlargement of the separation bubble). They documented that this low frequency motion occurred close to the separation line rather than more distal positions. In addition, Kiya and Sasaki (1983) reported that smaller-scale unsteadiness was related to the regular shedding frequency. However, they showed that frequency of the large-scale unsteadiness was much lower than the frequency of the smaller-scale unsteadiness. In this experiment, the characteristic shedding frequency was detected within the range 0.6 - 0.8 U_0/x_R.

Similarly, Hillier and Cherry (1981 a) and Cherry et al. (1984) showed 0.12 U_0/x_R as a reasonable value for the low frequency shear layer flapping. Cherry et al. (1984) noted that the fundamental shedding frequency in the separation bubble was 0.7 U_0/x_R. They concluded that the low frequency shear layer flapping was an integral feature of the fully turbulent separated flow.

For turbulent separated-reattached flows over different geometries, shear layer flapping has been reported extensively: Suksangpanomrung et al. (2000) and Tenaud et al. (2016) for a blunt flat plate, Eaton and Johnston (1982) and Lee and Sung (2001) for a backward-facing step, Cherry et al. (1983) and Castro and Haque (1987; 1988) and Hudy et al. (2003) for a flat plate associated with a long central splitter plate, and Orellano and Wengle (2000) for a fence geometry. However, for such flows, the low frequency motion was noted to be absent by Ruderich and Fernholz (1986) for the flow over a flat plate associated with a long central splitter plate and Dimaczek et al. (1989) for a surface-mounted obstacle flow.

Eaton and Johnston (1982) showed that the shear layer flapping was a result of an instantaneous imbalance between the entrainment rate from the recirculation region and the reinjection near the reattachment.

Abdalla and Yang (2005) investigated spectra for instantaneous velocity and pressure in transitional separated-reattached flow on a blunt flat plate. They emphasised that there was no low frequency shear layer flapping in their study, attributing this absence to be due to the action of the laminar part of separation bubble which acted as a filter to absorb and damp this low frequency.

For transitional separated-reattached flow over a forward-facing step and surface mounted obstacle, Abdalla et al. (2009) did not observe the shear layer flapping when analysing spectra for instantaneous velocity components. However, they noticed a high peak frequency close to the separation line, and they attributed this to the Kilven-Helmholtz instability mechanism of the separation bubble that formed before the leading edge of the geometry.

Laminar symmetric separated wakes were addressed in Castro (2005). It was concluded that the shear layer flapping phenomenon does not occur if the ratio of the backflow velocity to the free stream velocity is less than 20%.

Transitional separation studies in Yang and Voke (2001), Hosseinverdi and Fasel (2015) and Ducoine et al. (2016), which were carried out numerically, may disprove the conclusion drawn by Cherry et al. (1984), who emphasised that fully turbulent separation is a condition of the low frequency shear layer flapping.

Yang and Voke (2001) revealed low frequency shear layer flapping with a value of 0.104 U_0/x_R took place close to the separation line of a transitional separated-reattached flow generated on a flat plate with a semi-circular leading edge. In this study, the separated flow was laminar in nature. The authors suggested that the presence of this phenomenon was due to a larger shrinkage of the separation bubble caused by a big vortex shedding which occurred at a lower frequency. They reported in this study that the regular shedding frequency varied from 0.35 U_0/x_R to 1.14 U_0/x_R. However, the averaged frequency was estimated at about 0.77 U_0/x_R.

Ducoine et al. (2016) investigated the transition to turbulence over a wing section with the effects of an adverse pressure gradient. They showed that a Setrouhal number of 0.08 was estimated to be the magnitude of the shear layer flapping in the laminar separation part. In this study, it was shown that there were two characteristic shedding frequencies, which were associated with Setrouhal numbers of 0.12 and 0.248. With a similar separation on a flat plate, Hosseinverdi and Fasel (2015) noticed a low frequency in the fluctuating wall normal velocity spectrum. They reported that this low frequency was related to the flapping, as resulting from a vertical oscillation in the free shear layer.

As shown in the literature, the low frequency shear layer flapping is still not fully understood. It is not clear yet if this low frequency motion is an integral feature of the fully turbulent separated flow or if the transitional separated-reattached flow can involve this motion. Therefore, more effort is needed in this regard.

Tafti and Vanka (1991) identified 0.15 U_0/x_R as the value of the low frequency shear layer flapping in a turbulent separated shear layer on a blunt flat plate with a Reynolds number of 1×10^3, as based on the inlet velocity and flat plat thickness. They suggested that this phenomenon was due to the periodic enlargement and shrinkage of the separation bubble. In addition to the low frequency, there were two high frequencies: the characteristic shedding frequency and the selective high frequency. The characteristic shedding frequency was 0.6 U_0/x_R and the selective high frequency was 4.2 U_0/x_R. Tafti and Vanka (1991) showed that the selective high frequency occurred with a period equal to that of the low frequency unsteadiness, and the selective high frequency was seven times that of the characteristic shedding frequency. They documented that the selective high frequency was more notable at low Reynolds numbers; whilst they expected that the selective high

frequency should also be notable at higher Reynolds numbers, they were unable to confirm this hypothesis because of measurement difficulties.

For a higher Reynolds number (6.5×10^3) based on the inlet velocity and flat plat thickness, Abdalla and Yang (2005) revealed that there was a selective high frequency in their transitional separated-reattached flow. Based on spectra for instantaneous pressure and velocity components, Abdalla and Yang (2005) observed that there is a high frequency peak in the range of 5 - 6.5 U_0/x_R, which is approximately seven times the regular shedding frequency (0.7 - 0.875 U_0/x_R).

The vortex shedding frequency for a transitional separation on a blunt flat plate with a 2% intensity of free stream turbulence was investigated in numerical simulations conducted by Yang and Abdalla (2009). The Reynolds number in this study was 6.5×10^3, as based on the inlet velocity and flat plat thickness. The authors found that there was no relationship between the presence of a high level of intensity of free stream turbulence and the low frequency shear layer flapping, where this low frequency motion was absent. They showed that the characteristic shedding frequency range was 0.8 - 0.9 U_0/x_R. There was good agreement between the characteristic shedding frequency range reported in this study and that reported by Abdalla and Yang (2005) for a case without free stream turbulence.

Castro and Haque (1988) experimentally studied the effects of free stream turbulence, which varied in intensity between 3.25% to 3% over the length of the reversed flow region of a turbulent separated-reattached flow over a flat plate placed normal to the free stream. This plate was associated with a splitter plate. The Reynolds number for this experiment was 20×10^3. The authors reported that high levels of intensity of free stream turbulence enhanced the entrainment rates of the free shear layer and modified the relatively low-frequency flapping motion in this same layer at a location just after the separation point.

2.4 Coherent structures

In many – if not all – separated turbulent and transitional flows, the presence of large-scale structures (coherent structures) is common (Na and Moin, 1998). Coherent structures are defined as spatially coherent and temporally evolving vortical structures (Cantwell, 1981). Hussain (1986) defined coherent structures as connected large-scale

turbulent fluid masses with a phase-correlated vorticity over their spatial extent. Coherent structures were described by Robinson (1991a) as being "a three-dimensional region of the flow over which at least one fundamental flow variable (velocity component, density, etc.) exhibited significant correlation with itself or with another variable over a range of space and / or time that was significantly larger than the smallest local scales of the flow". Berkooz et al. (1992) defined coherent structures as "organized spatial features which repeatedly appear (often in flows dominated by local shear) and undergo a characteristic temporal life cycle".

Lesieur (1997) showed that there are three conditions which should be available in the region of coherent vortices:

- Concentration of the vorticity (ω) should be high enough so that a local roll-up of the surrounding fluid is possible.
- They should approximately keep their shape during a time far enough in front of the local turnover time (ω^{-1}).
- Coherent vortices should be unpredictable.

Many types of coherent structures have been presented in the literature, such as Kelvin-Helmholtz rolls, streaks, lambda-shaped (hairpin), horseshoe, counter-rotating and ribs. Head and Bandyopadhyay (1981) defined hairpin vortices as a combination of two legs, which are quasi-streamwise vortex pairs with opposite signs, and a tip, which is a spanwise vorticity. Hairpin vortices (also known as horseshoe vortices), lambda-shaped vortices, and ring-like vortices, are considered to be key structures in a turbulent boundary layer (Robinson, 1991a; Robinson, 1991b; Svizher and Cohen, 2006; Adrian, 2007).

An understanding of the generation of coherent structures and their evolution, interaction and coupling with a background of turbulence may improve our knowledge of the associated transition mechanisms, as well as the development of turbulence after the transition (Hussain and Melander, 1992). Good knowledge of coherent structures' dynamics leads to a better insight into turbulence phenomena such as mixing, heat and mass transfer, chemical reactions, combustion and can develop models applicable to turbulence (Hussain and Melander, 1992). Hence, great effort to study coherent structures is needed.

Scales and shapes of coherent structures are different from flow to flow depending on flow geometries, flow conditions and locations with respect to a solid surface (Yang, 2013). Brown and Roshko (1974), Browand and Trout (1985), Comte et al. (1998), and McMullan and Garrett (2016) found that large-scale spanwise vortices were regular coherent structures in a plane mixing layer. Perry and Chong (1982) and Robinson (1991a; 1991b) reported that hairpin, or horseshoe, vortices were the dominant large-scale motions in a turbulent boundary layer. For a similar flow, streaky structures that appeared to be coherent were observed by Chernyshenko and Baig (2005), Schlatter et al. (2008), Watmuff et al. (2010), Schrader et al. (2010), Deguchi and Hall (2015), and Brinkerhoff and Yaras (2015).

Jeong and Hussain (1997) showed that lambda-shaped vortices and low-speed streaks were coherent structures in a transitional boundary layer. Brinkerhoff and Yaras (2014) observed the development of hairpin vortices in transition and turbulent regions in the transitional boundary layer. Dominant structures of flow dynamics in wakes were counter-rotating vortices, as found by Hussain and Hayakawa (1987), Giralt and Ferre (1993), and Scarano et al. (1999). Kelvin-Helmholtz rolls were found in transitional separated-reattached flow for different geometries such as a backward-facing step in Neto et al. (1993), a flat plate with a semi-circular leading edge in Yang and Voke (2001), a blunt flat plate in Yang and Abdalla (2008), and a two-dimensional surface-mounted obstacle and forward-facing step in Abdalla et al. (2009).

In the literature, many techniques have been presented to extract coherent structures from turbulent and transitional flows: conditional, non-conditional, pattern recognition and flow visualisation (Yang, 2002). Conditional techniques include a sampling of the flow only during those intervals of time that satisfy some predetermined criterion that is deemed dynamically significant and is related to the presence of the coherent structure being sought. The disadvantage of these techniques is a lack of objectivity in the sense that one must have some predetermined idea regarding the likely structural topology in order to set the sampling criterion (Yang, 2002).

An example of the conditional techniques is the particle image velocimetry method (PIV) that was used by Adrian et al. (2000) to identify vortex organization in the outer region of a turbulent boundary layer. They observed the existence of large-scale motions (LSMs)

as a result of an alignment of hairpin packets. The authors reported that LSMs moved with a common convective velocity and they were characterized by a region of low-momentum fluid between the legs of hairpin structures.

Another example of conditional techniques is the variable interval time-average method (VITA) that was applied by Wei and Ning (1988) to study bursting frequency in turbulent boundary layers using different Reynolds numbers.

Kiya and Sasaki (1985) experimentally educed large-scale vortices of a turbulent separated-reattached flow formed on a blunt flat plate. Conditional sampling techniques were employed for this purpose using surface-pressure fluctuations as a conditional signal. At the reattachment zone, hairpin vortices were observed as the dominant structures in the flow. These structures were generated from a successive amalgamation of Kelvin-Helmholtz vortices formed in the separated shear layer. The authors concluded that there was a relationship between the large-scale motions and unsteadiness of the forward part of the turbulent bubble (shrinkage / enlargement), i.e., shear layer flapping.

The objectivity and lack of bias of non-conditional techniques make them more accurate than conditional techniques (Yang, 2002). An example of a non-conditional technique is proper orthogonal decomposition analysis (POD) which is based on two-point correlation. This technique was used by Gordeyev and Thomas (2000; 2002) to examine coherent structures in the similarity region of a turbulent planar jet. POD was employed also by Hosseinverdi and Fasel (2016) to present large-scale structures in a laminar-turbulent transition.

Hellstorm et al. (2015) applied the POD technique to present coherent structures of a turbulent pipe flow with a high Reynolds number. They recognized four distinct types of large-scale motion: the near-wall streaks, hairpin or horseshoe vortices, large-scale motions (LSMs) and very large-scale motions (VLSMs). In this study, agreement was reported with the study of Adrian et al. (2000) regarding the properties of LSMs. VLSMs are defined as a temporal manifestation of repeating LSMs that can extend up to 30R (R is the pipe radius), where there are no actual spatial structures referred to as VLSMs. For more details about these types of large-scale motion, the reader is referred to Hellstorm et al. (2015).

The pattern recognition technique was employed by Giralt and Ferre (1993) to detect coherent structures in turbulent wakes behind a cylinder. The pattern recognition analysis of the streamwise and spanwise velocities in the horizontal plane of the wake demonstrated that large-scale structures were counter-rotating vortices. Analysis of the streamwise velocity and wall-normal velocity in the vertical plane showed that these counter-rotating vortices were connected at their top to form a horseshoe vortex.

Coherent structures of a turbulent separated-reattached flow passing a backward-facing step were observed through the use of pattern recognition techniques in Scarano et al. (1999). The presence of a significant number of counter-rotating structures was observed inside the free shear layer; these structures were the result of an early three-dimensional breakdown of primary spanwise rolls. Scarano et al. (1999) indicated that a low field sampling frequency did not allow for a detailed investigation of the flow time-evolution and dynamical processes of coherent structures. So, this is considered one of the limitations of using the pattern recognition technique.

Flow visualization has been applied to reveal coherent structures within the flow in many studies. Mainly, there are three flow visualization schemes: low-pressure isosurface, vorticity field isosurface and Q-criterion isosurface. Comte et al. (1998) employed a streamwise vorticity isosurface to investigate the development of coherent structures in a turbulent mixing layer flow. Similar work presented by Robinson (1991a) by using low pressure isosurface for a turbulent boundary layer. They showed that the low pressure isosurface is superior to the vorticity field isosurface in identifying coherent structures in flows, which are associated with a presence of a solid surface. This is due to a high shear compared with vortical intensity of vortices, which are close to the solid surface. Additionally, the vorticity isosurface method cannot differentiate swirling motions from shearing motions (Kida and Miura, 1998).

The Q-criterion scheme, which shares some properties with vorticity and pressure criteria, was used by Gungor and Simens (2015) and Karaca and Gungor (2016) to reveal the effect of the spanwise perturbation generated from a surface roughness, at the location of coherent structure breakdown. The flow in these studies was a transitional-separated reattached flow induced due to effect of an adverse pressure gradient on an aerofoil. The aim of these studies was merely to focus on effect of surface roughness on the breakdown

location of large structures within the separation bubble. However, a description of coherent structures and their spatial and temporal evolution was not given in these studies.

For a similar separation flow, Ducoin et al. (2016) studied the physics of transition mechanisms in a separated boundary layer generated over an aerofoil with a low angle of attack using an SD7003 wing section. They reported that the transition was driven by the Kelvin-Helmholtz instability. The first appearance of coherent structures was in the form of two-dimensional Kelvin-Helmholtz rolls, which then moved a certain distance before their deformation to form C-shaped structures. C-shaped structures were shown to be filaments within the braid breakdown region. C-shaped vortex filaments were also reported by Burgmann and Schroder (2008) as a result of the evolution of Kelvin-Helmholtz rolls in a separation bubble formed on a SD7003 aerofoil.

For a transitional separation induced by an adverse pressure gradient, Roberts and Yaras (2006) summarized a periodic shedding of coherent structures that occurred at the trailing edge of the separation bubble. They observed that the transient roll-up of vorticity in the separated shear layer takes place before the maximum thickness of the separation bubble. Resultant vortices gradually grow when they move along a path, which follow the time-averaged dividing streamline before shedding at the maximum thickness of the separation bubble. The shedding process is accompanied by the entrainment of small three-dimensional structures which are formed within the separation bubble.

In a numerical simulation for a turbulent separated-reattached flow on a blunt flat plate, Tafti and Vanka (1991) showed that the existent coherent structures were three-dimensional in nature with a spanwise size that varied from 20% to 30% of the mean reattachment length. For a similar geometry but with higher Reynolds number, Kiya and Sasaki (1985) reported in their experimental work that turbulent separated-reattached flow was characterised by three-dimensional hairpin vortices. These vortices were pairs of counter-rotating vortices.

Yang and Voke (2000; 2001), in their numerical simulations, observed the formation of hairpin structures in a transitional separated-reattached flow induced on a flat plate with a semi-circular leading edge. The Reynolds number was 3450, based on the inlet velocity and plate leading edge diameter. The authors found that large-scale structures started as two-dimensional Kelvin-Helmholtz rolls; when these rolls travelled toward the mean

reattachment line, they grew and distorted to form spanwise peak-valley structures via a secondary instability process. At about the mid-distance of the mean reattachment length, where a significant development of three-dimensional motions of the flow started, an irregular shedding of large-scale structures with a roll-up of the free shear layer occurred. Further downstream, the formation of hairpin vortices took place around and after the mean reattachment line. Eventually, the streamwise structures broke down into relatively smaller turbulent structures within the reattached turbulent boundary layer. It should be noted that the flow visualization method used by Yang and Voke (2000; 2001) was the low pressure isosurface.

In addition to the two- and three-dimensional structures that were revealed in Yang and Voke (2000; 2001), Yang (2002) observed streaky structures in the last third of the separation bubble and after the mean reattachment line. The appearance of these structures is common in turbulent boundary layers and its formation is associated with counter-rotating streamwise vortices. Yang (2002) reported that streaky structures can obviously be observed close to the wall and gradually disappear when moving upward.

The low-pressure isosurface flow visualization technique was used in Abdalla and Yang (2008) to present coherent structures in transitional separated-reattached flow over a blunt flat plate with a Reynolds number of 6.5×10^3, based on the inlet flow and plate thickness. The authors showed that two-dimensional spanwise rolls are shed from the free shear layer. The spatial and temporal evolution of those rolls are based on their pairing with each other and stretching in the streamwise direction to form three-dimensional hairpin and rib structures. The transformation of two-dimensional structures to three-dimensional structures is via a secondary instability mechanism, namely the helical pairing instability. New three-dimensional structures were shed from the separation bubble into reattached turbulent flow, and then broke down into smaller structures further downstream.

For a similar geometry with a turbulent separated flow, but with a higher Reynolds number (50×10^3), Suksangpanomrung et al. (2000) observed horseshoe vortices when employing the streamwise vorticity isosurface method.

For both works on transitional separated-reattached flow, on a two-dimensional surface-mounted obstacle in Abdalla et al. (2007) and a forward-facing step in Abdalla et al. (2009), the low-pressure isosurface method was performed to discover shapes of existing

coherent structures. The Reynolds number for both studies was 4.5×10^3, as based on the inlet flow velocity and geometry height. It was observed that there were structures that initiated as two-dimensional spanwise vortices, then these structures grew and merged with each other when convicting downstream. There was the formation of a large-size structure by the pairing of two Kelvin–Helmholtz rolls. Direct or rapid breakdown of the large-size structure was found to form horseshoe vortices. The authors observed the weak presence of hairpin structures, unlike that observed for the flat plate flow. They documented that the instability mechanism that resulted in the formation of the three-dimensional structures was different from that in the flat plate case. Therefore, further research is needed to reveal the secondary instability mechanism.

Sasaki and Kiya (1991) and Hwang et al. (2000) experimentally visualized the coherent structures generated in a separated-reattached flow over a blunt flat plate with a low Reynolds number.

Sasaki and Kiya (1991) used dye and hydrogen bubbles to visualize the flow with three ranges of Reynolds number: *Regime I* for $80 < Re < 320$, *Regime II* for $320 < Re < 380$ and *Regime III* for $380 < Re < 800$. In *Regime I* and up to $Re = 300$, they found that the separated shear layer remained laminar without roll-up up to the reattachment line and there was no significant spanwise distortion of the vortex filaments. The lack of roll-up of the free shear layer was due to the dominant viscous force. With $Re = 320$, an instability wave in the free shear layer was observed. In *Regime II*, the free shear layer rolled-up to form large-scale vortices via a Kelvin-Helmholtz instability. These vortices were subjected to spanwise deformation to transform into hairpin structures shortly downstream from the reattachment line. In *Regime III*, the roll-up location of the free shear layer was further upstream than one in *Regime II*. Two or three rolled-up vortices amalgamated in the middle of the separation bubble to form large-scale three-dimensional structures, which then transformed to hairpin structures that had a less regular appeared than that in *Regime II*.

Hwang et al. (2000) carried out their experiment with a Reynolds number of 560. Roll-up and shedding of large-scale vortices from the separated shear layer were observed. These vortices moved toward the separation line, grew and shed from the separation bubble. Further downstream, a merging of two neighbouring large structures occurred.

With the effect of an elevated level of intensity of free stream turbulence (2% at the leading edge of a blunt flat plate), Yang and Abdalla (2008) showed that there were two-dimensional Kelvin-Helmholtz rolls in the first half of the separation bubble. The authors compared this case of the flow with a case without intensity of free stream turbulence. They observed that Kelvin-Helmholtz rolls in the former case were less regular than those in the latter. Hairpin structures were rarely observed with a high level of intensity of free stream turbulence. The authors stated that additional intensity of free stream turbulence led to the degraded coherency of the two-dimensional structures along both the spanwise and streamwise directions. Additionally, hairpin structures seemed to be larger in the spanwise direction and shorter in the streamwise direction.

Chandrasuda et al. (1978) reported that a high intensity of free stream turbulence reduced the spanwise coherency of structures in turbulent mixing layers. However, in transitional mixing layers, quasi-two-dimensional large-scale Kelvin–Helmholtz rolls were observed, even in the presence of strong external disturbances (Comte et al., 1992).

2.5 Development of the reattached turbulent boundary layer

After the reattachment, the turbulent boundary layer develops slowly within the developing boundary layer region. The evidence for the slow development of the turbulent boundary layer is a dip in the streamwise velocity profile below the standard log law, as shown in the experiments of Bradshow and Wong (1972) and numerical simulations of Le et al. (1997), for the turbulent separated reattached flow over a backward-facing step.

Under the influence of an adverse pressure gradient, Alam and Sandham (2000) reported that the boundary layer downstream of the reattachment is initially quite different from an equilibrium turbulent boundary layer. They showed that the boundary layer takes about seven separation bubble lengths to be re-established with the log-law velocity profile.

For transitional separated-reattached flow on a blunt flat plate, the slow development of a reattached turbulent boundary layer was observed in experiments of Castro and Epik (1996). They found that the log-law velocity profile was re-established after a distance of 75 thicknesses of the boundary layer at the reattachment, while turbulence structures had not developed normally even at this considerable distance. Castro and Epik (1996)

concluded that slow decay of the outer layer was preventing the inner layer from reaching its canonical form.

Delay in the recovery of the turbulent boundary layer after the reattachment was reported in Le et al. (1997), who studied a turbulent separated-reattached flow over a backward-facing step with a Reynolds number of 5100 based on the inlet velocity and the step height. They showed that with a distance of 20 step heights after the separation, there was no full recovery of the turbulent boundary layer, where velocity profiles were below the log-law profile.

Yang and Voke (2001) reported in their numerical simulation of transitional separated flow over a flat plate with a semi-circular leading edge and a low intensity of free stream turbulence (< 0.2%) that a long distance is required for the turbulent boundary layer to attain the log-law profile (to reach its canonical form) and for the inner layer turbulence structure to re-establish. They attribute that the recovery delay of turbulent boundary layer is due to high unsteadiness of the flow around the mean reattachment line and the presence of two and three-dimensional flow structures within the turbulent flow after the reattachment. These structures take some time to break down into small turbulent structures. The small turbulent structures then need time to develop in the inner layer and interact with structures of the outer layer.

There are few studies in the literature that deal with the enhancement of the recovery of the turbulent boundary layer after the reattachment by using elevated intensities of free stream turbulence. Castro and Epik (1996, 1998) experimentally investigated the development of the turbulent boundary layer after the reattachment of the transitional separated-reattached flow formed on a blunt flat plate. These studies were performed at two intensities of free stream turbulence at the leading edge of the plate: a low level with a value of 0.2% and a high level with a value of 5.1%. The results of these experiments showed that the Clauser parameter value at x/x_R = 20 downstream from the mean reattachment is 5.9 with a low intensity of free stream turbulence and 5.4 with a high intensity of free stream turbulence. Castro and Epik (1996, 1998) concluded that there is no significant effect due to a high intensity of free stream turbulence on the development of the reattached turbulent boundary layer where, with and without a high intensity of free stream turbulence, the Clauser parameter value is still below the standard value (6.8).

It is worth pointing out that reattached turbulent boundary layer satisfies its canonical form when the Clauser parameter profile of this layer reaches its standard value (6.8) (Alam and Sandham, 2000).

For transitional separated-reattached flow that forms on a flat plate with an adverse pressure gradient, McAuliffe and Yaras (2010) numerically tested the influence of adding free stream turbulence to the recovery of the reattached turbulent boundary layer to equilibrium. They used two intensities of free stream turbulence (0.1% and 1.45%) at the separation point. McAuliffe and Yaras (2010) stated that for both intensities of free stream turbulence, large-scale structures associated with the transition still survived in the turbulent boundary layer after the reattachment. These structures provide a source of production of turbulent kinetic energy in the outer region of the boundary layer. The authors concluded that the interaction between the large-scale structures and the outer region of the reattached turbulent boundary layer delays re-establishment of the reattached turbulent boundary layer.

2.6 Summary

In the present literature review, aspects of transitional separated-reattached flow that formed due to flow over geometries or the effects of an adverse pressure gradient in the presence of low (close to zero) or high levels of intensity of free stream turbulence are discussed. To the best of the author's knowledge, there is no agreed description for aspects of this flow in the literature. In addition, only a few studies have employed a relatively elevated level of intensity of free stream turbulence to reveal its effects on the transition features and the entire flow.

In general, it is well known that in the presence of high levels of intensity of free stream turbulence, the separation distance decreases and the transition takes place closer to the separation point, leading to an early breakdown of the free shear layer to turbulence (Hillier and Cherry, 1981b; Nakamura and Ozono, 1987; Volino and Hultgren, 2000; Kalter and Fernholz, 2001; Volino, 2002; Halfon et al., 2004; Yang and Abdalla, 2008; Lardeau et al., 2012; Langari and Yang, 2013; Balzer and Fasel, 2016; and others).

Other aspects of the transitional separation flow such as instability mechanisms that drive the transition, the shape of coherent structures and their development, and the low frequency shear layer flapping phenomenon are still not fully understood.

As shown in the literature, the transition starts with different instability mechanisms depending on turbulence intensity levels. It is not currently clear if there is a threshold of intensity of free stream turbulence that might control the transition instability mechanisms and help identify their types. Therefore, great effort is needed for this issue.

2.7 Research objectives

It seems that all geometries chosen as case studies in the literature were two-dimensional. If the transitional separated-reattached flow is around a three-dimensional geometrical shape, the questions that this raises are:

- Will transitional separated-reattached flow around a three-dimensional geometry impose aspects that are similar to, or different from, that generated on a two-dimensional geometry?
- For a three-dimensional geometry, is there any effect of changing the width to thickness ratio on features of transitional separated-reattached flow?
- If the change in width to thickness ratio is combined with an elevated intensity of free stream turbulence, what will happen to characteristics of transitional separated-reattached flow?

The current study is the first work to attempt to answer these questions by elucidating the entire transitional separated-reattached flow from the laminar separation to the developed turbulent boundary layer after the reattachment involving instability mechanisms, vortex-shedding frequency modes, and coherent structures and their evolution. In addition, comparisons of transitional separated-reattached flow for the two-dimensional blunt flat plate and two three-dimensional geometries are presented.

The chosen three-dimensional geometry in the current study with a width to thickness ratio (aspect ratio) of 1 is referred to as 3D_case1, whilst geometry with a width to thickness ratio of 2 is referred to as 3D_case2.

In the current study, transitional separated-reattached flow is investigated in the presence of a near zero low level of intensity of free stream turbulence (< 0.2%), denoted NFST, and an elevated level of intensity of free stream turbulence (3.7%), denoted FST.

It is worth noting that for a transitional separated-reattached flow formed on a blunt flat plate, Yang and Abdalla (2009) showed that even with a 2% intensity of free stream turbulence, the transition was driven by the Kelvin-Helmholtz instability. This study was carried out with a Reynolds number of 6.5×10^3, as based on the inlet velocity and plate thickness.

Langari and Yang (2013) examined a higher level of intensity of free stream turbulence (5.6%) to investigate the transitional separated-reattached flow formed on a semi-circular leading edge flat plate with a Reynolds number of 3450 based on the inlet velocity and leading edge diameter. They reported that the primary instability in the free shear layer, which was the Kelvin-Helmholtz instability at low level of disturbances, was bypassed.

If the effect of the difference in Reynolds number and geometrical shape used in Yang and Abdalla (2009) and Langari and Yang (2013) is ignored, it can be said that the threshold for the occurrence of the bypassed transition is within a range of intensity of free stream turbulence of 2% > to 5.6%., which is a relatively wide range. Hence, the use of a 3.7% intensity of free stream turbulence in the current study is to reduce this range. This is an additional objective of the current study.

To clarify the above points, the following characteristics of transitional separated-reattached flow formed on a blunt flat plate, 3D_case1, and 3D_case2 in the presence of a < 0.2% and a 3.7% intensities of free stream turbulence can be identified in the current study:

1- Primary instability mechanism of the transition.

2- Vortex-shedding frequency modes.

3- Large-scale motions and their development.

4- Turbulent boundary layer development after the reattachment.

In addition, the current study presents an extensive database for transitional separated-reattached flows, most of them are presented for the first time.

Chapter Three

Methodology

3.1 Governing equations

Navier-Stokes equations govern the motion of all Newtonian fluids. To solve these equations by using direct numerical simulation methods, a very high-resolution mesh is required to capture all length scales and a very small time step is employed to capture all the time scales of the flow. For relatively high Reynolds number and / or complex geometries, this method is computationally expensive and sometimes it is impossible to do simulations due to the broad range of length and time scales encompassed within certain problems.

To reduce the computational cost, the large eddy simulation (LES) method is employed. In this approach, large eddies or large-scale motions (grid-scale) are computed directly and small eddies (subgrid-scale) are modelled. A spatial filter is used to separate the flow into resolved (grid-scale) and unresolved (subgrid-scale) parts. Hence, the instantaneous velocity can be expressed as (Yang, 2013):

$$u_i = \bar{u}_i + u_i' \tag{3-1}$$

where $\bar{u}_i$ is the filtered or resolved scale velocity and u_i' is the subgrid-scale velocity.

When the finite volume method is used to solve the LES equations, these equations are integrated over control volumes and the governing equations can be regarded as implicitly filtered through the equivalent of imposing a top-hat filter. In this case, the local mesh space is considered the equivalent of a local filter (Yang, 2013). The filtered continuity and Navier-Stokes equations for incompressible Newtonian fluids in LES are:

$$\frac{\partial \overline{u}_j}{\partial x_j} = 0 \tag{3-2}$$

$$\frac{\partial \overline{u}_i}{\partial t} + \frac{\partial \overline{u}_i \overline{u}_j}{\partial x_j} = -\frac{1}{\rho}\frac{\partial \overline{p}}{\partial x_i} + \upsilon \frac{\partial^2 \overline{u}_i}{\partial x_j \partial x_j} - \frac{\partial \tau_{ij}}{\partial x_j} \tag{3-3}$$

where u_i, u_j $(i, j = 1, 2, 3)$ are the three velocity components in the Cartesian form, ρ denotes density, p denotes pressure and υ denotes kinematic viscosity, respectively.

Overbar notation denotes application of the spatial filtering which is called the grid-scale filter. The unresolved subgrid-scale stress (τ_{ij}) is an unknown stress tensor that refers to the effect of subgrid-scale motions on the resolved fields of the LES.

$$\tau_{ij} = \overline{u_i u_j} - \overline{u}_i \overline{u}_j = L_{ij} + C_{ij} + R_{ij} \tag{3-4}$$

where L_{ij} are the Leonard stresses, C_{ij} are the cross terms, and R_{ij} are the subgrid-scale Reynolds stresses, which are defined, respectively, as follows (Piomelli 1999):

$$L_{ij} = \overline{\overline{u}_i \overline{u}_j} - \overline{u}_i \overline{u}_j \tag{3-5}$$

$$C_{ij} = \overline{\overline{u}_i u'_j} + \overline{u'_j \overline{u}_i} \tag{3-6}$$

$$R_{ij} = \overline{u'_i u'_j} \tag{3-7}$$

The Leonard stresses represent interactions between resolved scales that result in subgrid-scale contributions and can be computed explicitly. The cross terms represent interactions between the resolved and unresolved scales. The subgrid-scale Reynolds stresses represent interactions between small (unresolved) scales (Piomelli 1999).

The subgrid-scale Reynolds stresses are invariant with respect to a Galilean transformation. However, the same does not hold for either the Leonard stresses or the cross term. Hence, the correlations that are used to model these stresses are approximations only. Thus, any attempt at decomposition of subgrid-scale stress is abandoned in preference of modelling whole subgrid-scale stresses (Piomelli 1999).

The unresolved subgrid-scale stress (τ_{ij}) is modelled via an eddy viscosity model. According to the Boussinesq approximation, there is a relationship between the grid-scale strain rate tensor and the unresolved subgrid-scale stress (τ_{ij}) that refers to the effect of subgrid-scale motions on the resolved fields, which can be expressed as:

$$\tau_{ij} = -2\,\upsilon_t\,\overline{S}_{ij} + \frac{1}{3}\,\delta_{ij}\,\tau_{kk}, \qquad \overline{S}_{ij} = \frac{1}{2}\left(\frac{\partial \overline{u}_i}{\partial x_j} + \frac{\partial \overline{u}_j}{\partial x_i}\right) \tag{3-8}$$

where δ_{ij} is the Kronecker delta which is 1 if $i = j$ and zero if $i \neq j$, υ_t is the subgrid-scale eddy viscosity, $\overline{S}_{ij}$ is the grid-scale strain rate tensor, and τ_{kk} is the isotropic part of the stress tensor that not modelled and instead added to the pressure term. Equation (3-3) can be re-written as:

$$\frac{\partial \overline{u}_i}{\partial t} + \frac{\partial \overline{u}_i \overline{u}_j}{\partial x_j} = -\frac{1}{\rho}\frac{\partial p^*}{\partial x_i} + \upsilon \frac{\partial^2 \overline{u}_i}{\partial x_j \partial x_j} + 2\frac{\partial \upsilon_t \overline{S}_{ij}}{\partial x_j}, \qquad p^* = \overline{p} - \frac{1}{3}\rho\, \delta_{ij}\, \tau_{kk} \tag{3-9}$$

The remaining problem in equation (3-9) is to solve the subgrid-scale eddy viscosity, υ_t. The oldest and simplest model by which to achieve this was proposed by Smagorinsky in 1963:

$$\upsilon_t = C\, \Delta^2 \left|\overline{S}\right|, \qquad \left|\overline{S}\right| = \sqrt{2\, \overline{S}_{ij}\, \overline{S}_{ij}} \tag{3-10}$$

where *C* is a parameter in the model and Δ is the grid filter scale (filter width) that is equal to the cubic root of the cell volume $(\Delta x \Delta y \Delta z)^{\frac{1}{3}}$. From equations (3-8) and (3-10), the subgrid-scale stress (τ_{ij}) can be written now as:

$$\tau_{ij} = -2\, C\, \Delta^2 \left|\overline{S}\right| \overline{S}_{ij} + \frac{1}{3}\, \delta_{ij}\, \tau_{kk} \tag{3-11}$$

In the Smagorinsky model, $C = C_s^2$, where C_s is the Smagorinsky constant. Specification of a proper value for the Smagorinsky constant is a controversial topic. There is no entirely satisfactory value for this constant. Despite this, the majority of work reported in the literature assumes that the Smagorinsky constant is 0.18 for isotropic turbulent flow and 0.1 for a flow near the solid wall (Yang, 2015).

However, there are many shortcomings to the Smagorinsky model. For example, it is too dissipative (so it is not suitable for simulating transitional flows) and the Smagorinsky constant needs to be adjusted for different flows (Piomellli, 1999; Yang, 2015).

To overcome these shortcomings, a dynamic subgrid-scale model was proposed by Germano et al. (1991). In this model, the constant *C* is computed as a function of space and time, i.e., it is determined locally in space and time during the calculation and hence the need to artificially adjust the model coefficient is avoided. The procedure for calculating the dynamic subgrid-scale coefficient and its further improvement are described by Germano et al. (1991) and Lilly (1992).

The limitation to the utility of Germano et al. (1991) model is a restriction to flows that are statistically homogenous in at least one direction, where the model coefficient is averaged over all homogeneous directions due to mathematical inconsistency in the formulation of the dynamic subgrid-scale model (Ghosal et al., 1995). Thereby, the averaging process completely removes the mathematical inconsistency. Ghosal et al. (1995) performed an integral formulation of the dynamic subgrid-scale model of Germano et al. (1991) that rigorously removes the mathematical inconsistency at the expense of having to solve an integral equation at each time step to avoid the limitation that one direction must be statistically homogeneous. The improved model is called the dynamic localization model and is detailed in Ghosal et al. (1995). In the dynamic localization model, the coefficient in this model is a function of the position and time. So, this model can be applied to general inhomogeneous flows and it does not suffer from the mathematical inconsistency which is in the dynamic subgrid-scale model (Ghosal et al., 1995). Huai et al. (1997) reported that the dynamic localization subgrid-scale model can adjust itself locally both in terms of space and time according to the characteristics of the flow field. This is essential for the LES of transitional flows, since the intermittency is the dominant phenomenon during the transition.

The dynamic localization subgrid-scale model was successfully used by Ghosal et al. (1995) to simulate an isotropic turbulence and turbulent flow over a backward-facing step. A good agreement between simulated and experimental results was found in this study. This model was also used to simulate rotating channel flows by Piomelli and Liu (1995) and a transitional boundary layer by Huai et al. (1997).

The dynamic localization subgrid-scale model was used within an OF code by Baba-Ahmadi and Tabor (2008; 2009) to simulate different applications. In these studies, good agreements between simulated and experimental results were shown.

In the present study, the commercial OF 3.0.0 CFD toolbox is used with LES, employing the dynamic localization subgrid-scale model to simulate transitional separated-reattached flow over the three geometries detailed in Chapter 2.

As shown previously, it is believed that the current study is the first research to consider the use of OF technology to predict aspects of transitional separated-reattached flow. It is useful to use this technology, which is developing rapidly, to simulate this difficult and

complicated flow. The good agreement between the results of the current study and other studies will motivate researchers to employ and develop this new technology to simulate more complicated problems.

In OF, the governing equations of LES are discretised using the finite volume method. In the current study, the second-order implicit backward Euler time scheme is used for the time advancement. A full explanation of the backward Euler time scheme implementations in OF, and hence the finite volume approach, is provided in Jasak (1996). The second-order central differencing scheme, which is widely used in LES owing to its non-dissipative and conservative properties, is used for the spatial discretisation.

In OF, mass conservation is imposed through the pressure-velocity by a coupling method which is performed based on the PISO algorithm (Pressure-Implicit with Splitting of Operators) proposed by Issa (1986). In OF, a collocated (non-staggered) mesh arrangement is used, hence, Rhie and Chow pressure smoothing is performed to couple the velocity and pressure solutions with the PISO (Baba-Ahmadi and Tabor, 2008).

The PISO algorithm is an implicit time-marching scheme first developed by Issa (1986). It uses operator splitting to separate the solution of the velocity and pressure equations, such that the solutions of each field are close approximations of the exact solution with formal second-order temporal accuracy (Jasak, 1996). It has been shown that the PISO algorithm is both accurate and robust (Barton, 1998; Baba-Ahmadi and Tabor, 2008). Bressloff (2001) used the PISO algorithm to simulate numerous flow cases, showing that the use of this algorithm presents good agreement with experimental results. A flow chart of the PISO algorithm is shown in Fig. 3-1.

The solution procedure for the PISO algorithm is stated in Kimbrell (2012) as follows:

1. Set the boundary conditions.
2. Solve the discretized momentum equation to compute a predictor velocity field.
3. Compute the mass fluxes based on the predictor velocity.
4. Solve the pressure equation using the predictor velocity field.
5. Correct the mass fluxes to be divergence-free.
6. Correct the predictor velocity on the basis of the new pressure field.

7. Update the boundary conditions.
8. Repeat from 3 using the new velocity field as a predictor velocity for a set number of iterations. It is recommended that a minimum of two predictor-corrector iterations are performed to achieve an accurate solution (Issa, 1986).
9. Increase the time step and repeat from 1.

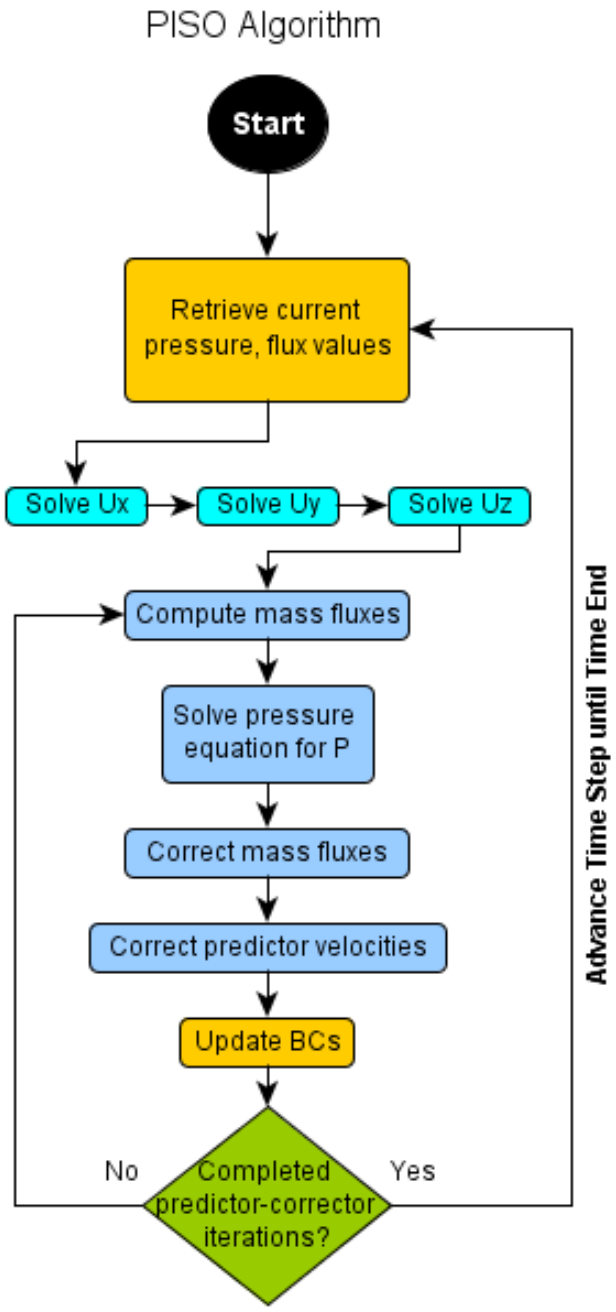

Fig. 3-1. Flow chart of the PISO algorithm (Kimbrell, 2012)

3.2 Computational details for NFST

Computational domains for the flat plate and three-dimensional geometries are shown in Figs. 3-2 and 3-3 respectively. For all geometries used in the current study with NFST, computational domain dimensions are 25*D* × 16*D* × 4*D* along the streamwise *x*, wall-normal *y*, and spanwise *z* directions, respectively. *D* denotes the geometry thickness and equals 1 cm. The velocity components corresponding to the above directions are *u*, *v* and *w*, respectively. The dimensions of the computational domain with NFST and geometry parameters are detailed in Table 3-1.

The origin of the streamwise direction is located at the leading edge of the geometry, which is centred at the origin of the wall-normal coordinate. For all geometries, the streamwise direction extends from the inflow boundary at -4.5*D* to the outflow boundary at 20.5*D*. The lateral boundaries are located at -8*D* and 8*D* in the wall-normal direction, corresponding to a blockage ratio of 16.

Structured mesh, as shown in Fig. 3-4, is employed for all geometries with NFST. Mesh cell spaces are uniform in the spanwise direction, while non-uniform mesh distributions are used in the other directions with finer resolution in the vicinity of the solid surface in order to resolve the separated shear layer that develops at the separation line and the recirculation zone downstream of the geometry leading edge. Mesh refinement tests were carried out and a mesh of 198 × 220 × 84 cells along the streamwise, wall-normal and spanwise directions, respectively, was selected. In terms of wall units, based on the frictional velocity at *x/D* = 18 for the flat plate, which is approximately equal to that in 3D_case1 and 3D_case2, the mesh sizes vary from $\Delta x^+ = 4.86$ to $\Delta x^+ = 26.417$, $\Delta y^+ = 0.739$ to $\Delta y^+ = 30.49$, and $\Delta z^+ = 4.88$. Wall units are calculated as follows:

$$x^+ = \frac{x\, u_\tau}{\upsilon} \tag{3-12}$$

$$u_\tau = \sqrt{\frac{\tau_w}{\rho}} \tag{3-13}$$

$$\tau_w = \mu \left(\frac{\partial u}{\partial y}\right)_w \tag{3-14}$$

where u_τ is the fractional velocity, υ is the kinematic viscosity, τ_w is the wall shear stress, ρ is the fluid density and μ is the dynamic viscosity.

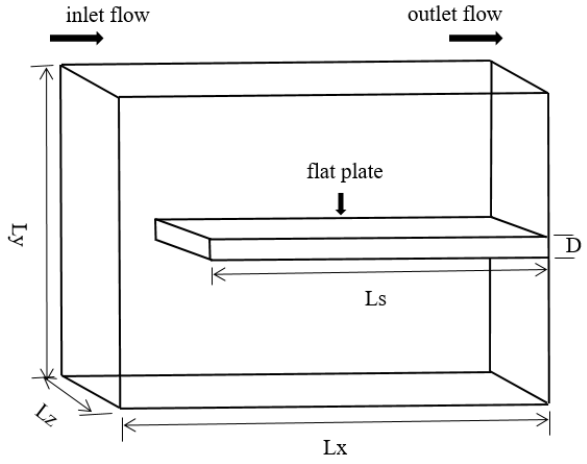

Fig. 3-2. Conceptual representation of the domain for the two-dimensional flat plate

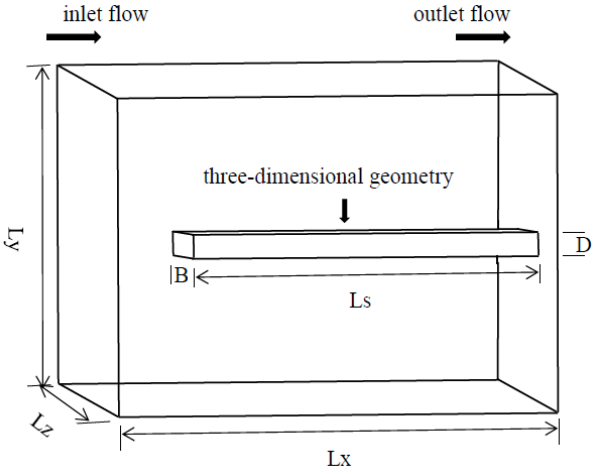

Fig. 3-3. Conceptual representation of the domain for the three-dimensional geometry

Computational domain size for all geometrical shapes		Geometrical shape dimensions			
Lx	25 cm		flat plate	3D_case1	3D_case2
Ly	16 cm	thickness (D)	1 cm	1 cm	1 cm
Lz	4 cm	Length (Ls)	20.5 cm	20.5 cm	20.5 cm
blockage ratio	16	width (B)	-	1 cm	2 cm

Table 3-1. Details of the computational domain size with NFST and dimensions for all geometrical shapes

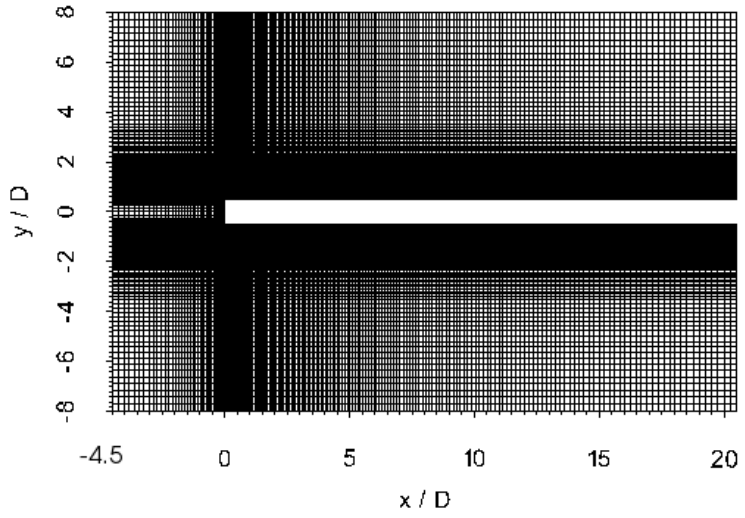

Fig. 3-4. Computational mesh at the mid-distance of the spanwise direction for all geometrical shapes with NFST

The time step used for the time iterations is $\Delta t = 2\times10^{-6}$ s, which is equivalent to 0.001885 D/U_0, where U_0 is the inflow velocity corresponding to the CLF_{max} number of 0.32 for the flat plate, 0.26 for 3D_case1 and 0.28 for 3D_case2. The Courant-Friedrich-Lewy (CFL) number is defined as:

$$CFL = \Delta t \left(\frac{|u|}{\Delta x} + \frac{|v|}{\Delta y} + \frac{|w|}{\Delta z}\right) \tag{3-15}$$

For all geometries used in the current study, the simulation ran for about 8 flow passes through the domain (100,000 time steps) to allow the transition and reattached turbulent boundary layer to be well-established, i.e., the flow reaches the statistically stationary state. The time-averaged results are gathered over approximately 30 further flow passes through the domain (400,000 time steps) with the averaging process carried out for samples at each time step. The total runtime for the simulation is 1 s (942.5 D/U_0) corresponding to about 38 flow passes or residence times.

The Reynolds number in the current study is 6.5×10^3 based on the thickness of the geometry and the inflow velocity, which is 9.425 m/s, and is uniform and aligned with the geometry. A zero velocity gradient is taken at the outflow boundary. No-slip boundary conditions are imposed for the walls of the geometries. On the lateral boundaries, free-slip boundary conditions are imposed. For the flat plate, periodic boundary conditions are

applied in the spanwise direction. These boundary conditions are changed to be free-slip for both three-dimensional geometries.

It is worth pointing out that the length of the spanwise dimension in the computational domain for the flat plate, which is 4*D*, is sufficient to resolve the flow characteristics. For a separation bubble formed on a flat, semi-circular leading edge plate, Yang and Voke (2001) performed two simulations with spanwise lengths of 2*D* and 4*D*. They compared the results of each of these simulations and reported that there was no appreciable change in the flow behaviour in either. The difference in the time-averaged statistics was less than 5%. For similar geometry and Reynolds number, Langari and Yang (2013) used the spanwise dimension of 8*D*. In this study, it was good agreement between magnitudes of the flow mean variables in Yang and Voke (2001), who used 2*D* as the spanwise length, and Langari and Yang (2013), who used 8*D* as the spanwise length, indicating that there is no notable effect of the spanwise length on the flow properties.

In addition, Cherry et al. (1984) reported that effect of the spanwise length is weak on the mean reattachment length, where Reynolds number plays a significant role. So, 4*D*, as the spanwise length for the flat plate, is sufficient to simulate transitional separated-reattached flow.

To determine whether the spanwise length (4*D*) in the computational domain for 3D_case1 and 3D_case2 is sufficient to predict the flow features, two additional lengths were added to the spanwise dimension in the computational box to perform two additional simulations with longer spanwise lengths of 8*D* and 10*D*. Additional cells were added to the mesh to maintain the cells sizes between the two simulations, i.e. cells number in the spanwise direction became 168 for the spanwise length of 8*D* and 210 for the spanwise length of 10*D*.

Comparisons among the flow mean variables in the three simulations, which were with 4*D*, 8*D* and 10*D* as the spanwise lengths of the computational domains, for both 3D_case1 and 3D_case2 showed that there was no discernible difference in the mean first-order quantities and the mean second-order quantities presented a maximum difference of around 3%. Clearly, these comparisons indicated that there was no particular difference

between the magnitudes of the mean flow variables for the spanwise lengths of 8*D* and 10*D*.

This indicates that there is no appreciable effect of spanwise length on the flow characteristics of the three-dimensional geometry. Hence, 4*D*, as the spanwise dimension in the computational domain for 3D_case1 and 3D_case2, is sufficient in the current study.

3.3 Turbulent inflow generation methods

The accurate numerical generation of free-stream turbulence, which provides realistic turbulent fluctuations at the inlet of the computational domain for LES, is a difficult task (Yang and Abdalla, 2009; Yang, 2013; 2015). Achieving the desired free-stream turbulence is a considerable challenge because the inlet flow must include a stochastically-varying component: ideally this component should 'look' like turbulence whilst at the same time be as simple as possible to implement and modify (Tabor and Baba-Ahmadi, 2010). Yang (2013; 2015) reported that in LES at inflow boundary, unlike the RANS computations where only time-averaged information is required that can be usually specified according to experimental data, three components of instantaneous velocity need to be specified at each time step, which should have characteristics, such as stochastically varying, with scales down to the filter scale (spatially and temporally), compatible with the Navier–Stokes equations and turbulent structures (turbulence intensities, length scales, spectrum etc.).

In General, the current methods to generate turbulent inflow boundary conditions in LES can be classified into two basic categories: precursor methods and synthesis methods (Tabor and Baba-Ahmadi, 2010; Yang, 2013; 2015).

In synthesis methods, some form of random fluctuation is generated / manipulated and combined with the given mean flow at the inlet. For more details about available synthesis methods, the reader is referred to Tabor et al. (2004), Keating et al. (2004), Tabor and Baba-Ahmadi (2010), Pokora et al. (2011), and Yang (2013; 2015). However, Yang (2013; 2015) reported that no one of the synthesis methods can generate inflow free

stream turbulence with all the desired characteristics, such as intensity, shear stresses, length scales and a power spectrum.

In precursor methods (pre-prepared library generation), an additional simulation (precursor simulation) is performed as a source of turbulence and the required data are extracted from this simulation, stored, and fed as the input for the main simulation. Tabor and Baba-Ahmadi (2010) and Yang (2013; 2015) showed that the precursor technique generates highly realistic turbulence information at the inflow boundary, though a high computational cost is still a major disadvantage to use this technique.

To save computational cost compared with the precursor method by avoiding the problem of large data storing, Lund et al. (1998) presented a method called the recycling-rescaling technique (concurrent library generation) that is applicable for incompressible flow. Lund et al. (1998) proposed to run the precursor calculation continuously in parallel with the main simulation. The basic idea of this method consists of taking a plane of velocity field from a location several boundary-layer thicknesses downstream of the inflow, and rescaling the velocity profiles. The rescaled velocity profiles are then reintroduced at the inlet.

Tabor and Baba-Ahmadi (2010) reported that one disadvantage of the precursor methods, either a priori or concurrently, is the necessity to set up and run a separate calculation involving a separate mesh with the main computation. However, there is no reason why the precursor calculation cannot be integrated into the main domain with sampling downstream of the inlet being mapped back into the inlet, leading to avoid using an auxiliary calculation. This method is called the internal mapping, where in this method, the velocity a short distance downstream of the inlet to the main domain is sampled and the flow velocity data are reintroduced back into the domain inlet, creating an inlet section integrated into the main domain in which turbulence can develop. Merging the auxiliary calculation into the main domain as a mapping method, and using sophisticated feedback control techniques to drive the flow towards a desired state make this technique usable for LES simulations. This can easily be provided by correcting the mapped velocities within the inlet section of the main domain to ensure a constant target flux by a number of computational manipulations, including the introduction of artificial body forces,

modification of the mapped data, and direct correction of the velocity data (Villiers, 2006; Baba-Ahmadi and Tabor, 2009).

It is worth pointing out that Baba-Ahmadi and Tabor (2009) referred that the internal mapping technique was implemented by de Villiers (2006). This method was used in Tabor et al. (2004), Baba-Ahmadi and Tabor (2009), and Tabor and Baba-Ahmadi (2010) within OF codes to simulate different applications. In these studies, good agreements between experimental results and simulated data were found.

3.3.1 Turbulent inflow generation methods in OF

In OF, there are two methods to generate turbulent inflow conditions: random inflow generator method and internal mapping method. In the current study, both methods are performed.

In the case of a low intensity of free stream turbulence, the random inflow generator method is used by adding 0.01 as a small random disturbance to the inlet velocity to generate the low turbulence level (< 0.2%) in the incoming flow.

To generate an elevated intensity of free-stream turbulence, the internal mapping method is used to generate a 3.7% intensity of free stream turbulence at the leading edge of the current geometries. This is carried out using additional streamwise length (8*D*) in the mesh of NFST, i.e., the distance from the inlet boundary to the leading edge of all geometries becomes 12.5*D* instead of 4.5*D*. In the additional region (inlet section), the mapping process takes place where remapping of the velocity from the end of the inlet section back to the domain inlet.

Extension of the computational domain leads to the introduction of additional cells in the streamwise direction. In this case, the number of streamwise cells is increased from 198 to 278, i.e., additional 80 streamwise cells are used in the inlet section and distributed uniformly in both the streamwise and spanwise directions whilst maintaining the original wall-normal distribution.

A similar time step, $\Delta t = 2\times10^{-6}$ s, that is used in the simulation for NFST is applied here. The simulation ran for about 8 flow passes through the domain (140,000 time steps)

before gathering the time-averaged results. The time-averaged results are gathered over approximately 23 further flow passes through the domain (400,000 time steps). The total runtime for the simulation is 1.08 s corresponding to about 31 flow passes or residence times.

Chapter Four

OF Code Validation and Results

4.1 OF code validation

In order to validate the current OF code, mean values of the flow variables over the flat plate for NFST are compared with available experimental results and numerical simulated data. The geometry and Reynolds number of the flat plate are similar to those used in the experimental work of Castro and Epik (1998) and the numerical study of Yang and Abdalla (2009).

In the work of Castro and Epik (1998), the blockage ratio was higher than the present blockage ratio and a flap was used to control the reattachment length. It should be noted that the main purpose of the experimental work of Castro and Epik (1998) was to study the recovery of the turbulent boundary layer after the reattachment, where the results for the separation bubble were limited. So, the results of another piece of experimental work, as reported by Kiya and Sasaki (1983), were also chosen for the comparison. Kiya and Sasaki (1983) investigated turbulent separated-reattached flow on a blunt flat plate with a Reynolds number of 26×10^3, which is higher than the current Reynolds number. There was no transition within this experimental work and the blockage ratio was also higher than the current blockage ratio.

An important parameter in the separated-reattached flow is the mean reattachment length (x_R), which is a distance bounded by the separation and mean reattachment points. Le et al. (1997) defined the mean reattachment point as the streamwise location at the first grid point away from the wall where the value of the mean streamwise velocity equals zero ($U_m = 0$). The mean velocity is defined as

$$U_m = \frac{1}{n} \sum_{i=1}^{n} u_i \tag{4-1}$$

where n is the number of time steps.

The profile of the mean streamwise velocity at the first cell away from the wall along the streamwise direction for the flat plate is shown in Fig. 4-1. It is clear from this figure that the mean reattachment length is $x_R = 6D$.

The mean reattachment length can also be identified by investigating skin friction coefficient C_f, where the separation and reattachment points are the locations of the zero mean skin friction coefficient. Skin friction coefficient is defined by:

$$C_f = \frac{\tau_w}{\frac{1}{2}\rho U_0^2} \tag{4-2}$$

where ρ is the fluid density, U_0 is the free stream velocity, and τ_w is the wall shear stress, which given in equation (3-14).

The distribution of the mean skin friction coefficient as a function of streamwise distance for the flat plate, which is normalized by both the geometry thickness and the mean reattachment length, is shown in Fig. 4-2. The initial flat part of the mean skin friction coefficient profile after the separation point refers to the dead air region in the separation bubble. A larger negative mean skin friction coefficient corresponds to the reverse flow vortex region. The mean skin friction coefficient attains a minimum value of -0.74×10^{-2} at $x/x_R = 0.745$ and increases rapidly thereafter. Its value becomes zero at about $x/D = 6$ indicating that the time-averaged reattachment length is $6D$ for the flat plate.

For a turbulent separated-reattached flow, Djilali and Gartshore (1991) and Tafti and Vanka (1991) reported that the minimum mean skin friction coefficient was at $x/x_R = 0.63$ and 0.7, respectively. This is in good agreement with the current location if the difference in the separated flow nature is considered.

The mean reattachment length ($6D$) for the flat plate in the current study is lower than $7.7D$, which was the separation bubble mean length found by Castro and Epik (1998). This can be considered as constituting good agreement between each of these studies, taking into account the effects of the flap and higher blockage ratio in Castro and Epik (1998).

The mean reattachment length of the flat plate is also lower than $6.5D$, which was the predicted mean reattachment length in Yang and Abdalla (2009). However, good agreement can be shown between these studies if the different characteristics of the

current OF code and the FORTRAN code that was used by Yang and Abdalla (2009) are taken into considered. In addition, the simulated time-averaged variables of the flow in Yang and Abdalla (2009) were collected by an averaging process for the samples taken every 10 time steps, while in the current OF code this averaging process is carried out for samples taken at each time step. Hence, the current results may be more accurate than those reported by Yang and Abdalla (2009). Moreover, the difference between the numerical schemes of the current PISO algorithm and the algorithm used by Yang and Abdalla (2009) may be another reason for the difference in the mean reattachment lengths in each of these studies.

The mean reattachment length in the experiment of Kiya and Sasaki (1983) was 5.05*D*, which is lower than the mean reattachment length of the flat plate. However, this experimental work was conducted for a fully turbulent separated flow with a higher Reynolds number (26×10^3).

It is interesting to note that by decreasing the Reynolds number below of 30×10^3, the separation bubble's mean length increases (Cherry et al., 1984). Sasaki and Kiya (1991) found in their experiment that within a range of Reynolds numbers between 80 and 800, the mean reattachment length was as a function of the Reynolds number. Moreover, Lane and Loehrke (1980) concluded that with a range of low Reynolds numbers, the mean reattachment length decreases with increasing Reynolds number. With a high Reynolds number was held in the range of $3.2 \times 10^4 \pm 0.2 \times 10^4$, Cherry et al. (1984) reported a value of $4.9D \pm 0.05D$ as the mean reattachment length. This length was 6.3*D* in Tafti and Vanka (1991) with a lower Reynolds number (1×10^3). Djilali and Gartshore (1991) measured 4.7*D* as the mean reattachment length on a flat plate with a splitter plate with a Reynolds number of 50×10^3.

In general, the above studies refer to the fact that the mean reattachment length decreases as Reynolds number increases. Accordingly, there is excellent agreement between this fact and the mean reattachment length for the flat plate in terms of the comparison between the study conducted by Tafti and Vanka (1991) (with a Reynolds number of 1×10^3), the current study (with a Reynolds number of 6.5×10^3) and the work of Kiya and Sasaki (1983) (with a Reynolds number of 26×10^3). The mean reattachment lengths found in these studies are 6.3*D*, 6*D*, and 5.05*D*, respectively. It can be observed that the

mean reattachment length decreases with increasing Reynolds number in these studies. This indicates that the mean reattachment length of the flat plate is comparable to the relationship between its value and the Reynolds numbers presented in the literature.

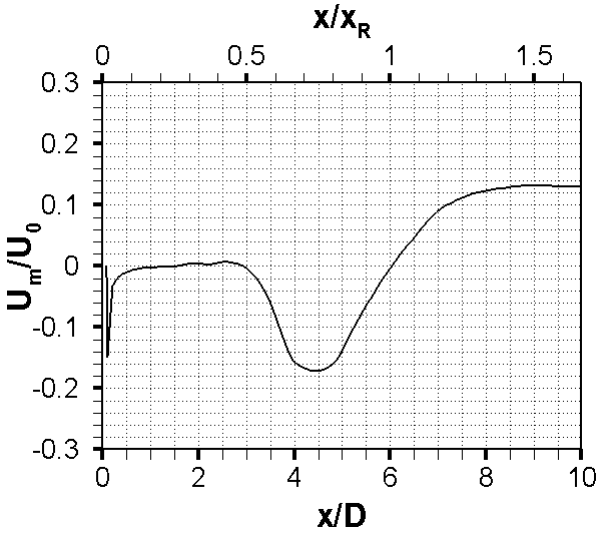

Fig. 4-1. Profile of the mean streamwise velocity at the first cell away from the wall normalized by the inflow velocity along the streamwise direction for the flat plate with NFST

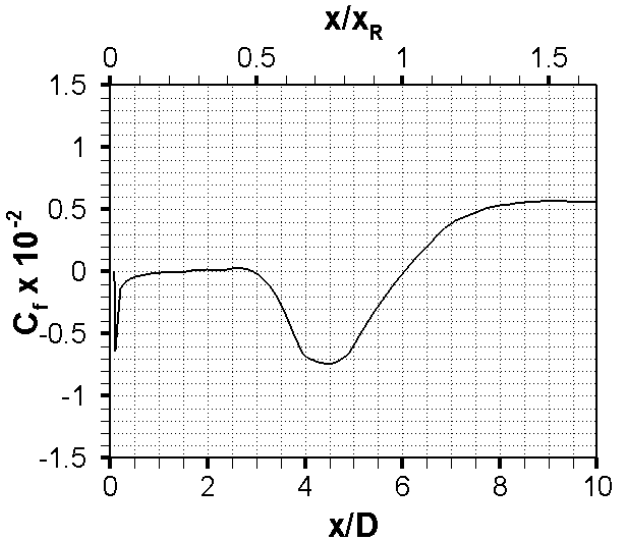

Fig. 4-2. Profile of the mean skin friction coefficient along the streamwise direction for the flat plate with NFST

Profiles of the time-averaged values of the flow for all geometries used in the current study are plotted at six corresponding values of x/x_R = 0.2, 0.4, 0.6, 0.8, 1, and 1.2. The vertical axis is the wall-normal direction normalized by the mean reattachment length, which starts from the geometry surface. As shown in Fig. 3-4, the origin of wall-normal direction is the centre of the geometry. This location is shifted to be at the upper wall for all geometries in the present study.

It is worth pointing out that comparisons of the results of the current study and other studies employ profiles that are plotted as functions of y/x_R at corresponding values of x/x_R, i.e., these comparisons are carried out at the same non-dimensionalized location (x/x_R) but not at the same geometric location (x).

For the flat plate, the profile of the time-averaged streamwise velocity, as normalized by the inlet velocity (U_m/U_0), is compared with results of Yang and Abdalla (2009) and Kiya and Sasaki (1983), as shown in Fig. 4-3. Despite the current peak at x/x_R = 0.2 being slightly lower than the peak given by Yang and Abdalla (2009) at the same position, the current results are in good agreement with results of Yang and Abdalla (2009) at all other positions.

However, there are some differences between the current results and experimental results in Kiya and Sasaki (1983). Three factors contribute to this difference. The first is the difference in nature of the separated flow, where in the current study it is laminar, it is turbulent in Kiya and Sasaki (1983). The second is the difference in the blockage ratios, where the current blockage ratio of 16 took a value of 20 in Kiya and Sasaki (1983). The third is the current Reynolds number is lower than the Reynolds number used in the experiment of Kiya and Sasaki (1983). The current low Reynolds number may lead to a stronger back flow in the recirculation region. This is shown at x/x_R = 0.6 and 0.8, where the experimental minimum mean streamwise velocities are slightly higher than the current minimum mean streamwise velocities.

In general, there is good agreement between the magnitudes of the current mean streamwise velocity and that presented in Yang and Abdalla (2009) and Kiya and Sasaki (1983).

Mean square fluctuating velocity is defined by (for example in the streamwise direction):

$$u_m'^2 = \frac{1}{n}\sum_{i=1}^{n}(u_i - U_m)^2 \quad (4\text{-}3)$$

The root mean square fluctuating streamwise velocity is normalized by the inlet velocity (u'_{rms}/U_0) profiles for the flat plate, as shown in Fig. 4-4. Despite there being slight differences in the peaks at the fourth and fifth positions, it can be observed that the current results for u'_{rms}/U_0 are in good agreement with the results of Yang and Abdalla (2009) at all locations. Experimental data reported by Kiya and Sasaki (1983) showed that the peak of u'_{rms}/U_0 is higher than the current peak at the first and second locations as shown in Fig. 4-4. This may be due to the reason of the nature of the separated flows, the blockage ratios and Reynolds numbers.

Overall, the current results are close to the experimental results, indicating the acceptable prediction of the turbulence by the current OF code.

The current maximum value of u'_{rms}/U_0 is 0.288 at x/x_R = 0.8. At the same streamwise location, Yang and Abdalla (2009) reported 0.285 as the maximum value of u'_{rms}/U_0, whilst the measured maximum value of u'_{rms}/U_0 was reported as 0.26 in Kiya and Sasaki (1983). For a turbulent separated-reattached flow with a low Reynolds number, Tafti and Vanka (1991) showed that the maximum value of u'_{rms}/U_0 was 0.32 at x/x_R = 0.7. With a higher Reynolds number, Djilali and Gartshore (1991) measured the maximum value of u'_{rms}/U_0 as being 0.3, at a point that was located upstream the mean reattachment line. Hence, it can be seen that the current maximum value of u'_{rms}/U_0 is within the range reported in the literature cited above.

Profiles of root mean square fluctuating wall-normal velocity (v'_{rms}) and Reynolds shear stress normalized by the inlet velocity for the flat plate are shown in Figs. 4-5 and 4-6, respectively. It is worth pointing out that the profiles of these time-averaged variables were presented only at the reattachment point (x/x_R = 1) in Yang and Abdalla (2009), Kiya and Sasaki (1983) and Castro and Epik (1998). Therefore, the associated profiles in the current study are plotted without comparison at the other streamwise locations, as shown in Figs. 4-5 and 4-6.

There is good agreement between the maximum current value of v'_{rms}/U_0 and that reported in Yang and Abdalla (2009) and Kiya and Sasaki (1983) at the mean reattachment point, especially for Yang and Abdalla (2009), as shown in Fig. 4-5. At this location, the

maximum value of v'_{rms}/U_0 in the current study is 0.21, which took a reported maximum value of about 0.2 in Yang and Abdalla (2009) and Kiya and Sasaki (1983). The current maximum value of this turbulent intensity is 0.211 at $x/x_R = 0.8$, as shown in Fig. 4-5.

The current Reynolds shear stress normalized by $(U_0)^2$ is slightly higher than that in Yang and Abdalla (2009) and lower than that in Kiya and Sasaki (1983) at the mean reattachment point, as shown in Fig. 4-6. At this location, the current maximum value of this shear stress is $0.017(U_0)^2$, while it is $0.015(U_0)^2$ in Yang and Abdalla (2009) and $0.021(U_0)^2$ in Kiya and Sasaki (1983). The current maximum value of the Reynolds shear stress is about $0.02(U_0)^2$ at $x/x_R = 0.8$ as shown in Fig. 4-6.

In Figs. 4-4, 4-5, and 4-6, the current Reynolds normal and shear stresses at the mean reattachment point are also compared with the experimental data reported by Castro and Epik (1998), which were measured with the same current Reynolds number using the same current geometry. In this comparison, it can be seen that the current Reynolds stresses peaks are higher than those in Castro and Epik (1998). However, the difference between the current results and the experimental results of Castro and Epik (1998) probably arises for three reasons. The first is the different blockage ratios, where in Castro and Epik (1998) the blockage ratio is larger than the current blockage ratio by a factor of about four. The second is the flap that was used in Castro and Epik (1998) to control the reattachment length. The third is the data measured at the reattachment point in Castro and Epik (1998) were for a Reynolds number of 3.68×10^3 because of the upper velocity limit (6 m/s) on the miniature pulsed-wire probe.

Castro and Epik (1998) noted that the value of the Reynolds stresses at a Reynolds number of 6.5×10^3 at the reattachment point were higher than those presented in Figs. 4-4, 4-5, and 4-6 by 12%. So, there is fair agreement between the current results and the data reported by Castro and Epik (1998). In addition, Hancock (1995) and Hillier and Cherry (1981a) reported that an increase in Reynolds number leads to an increase in Reynolds stresses values at the reattachment. This confirms the agreement between results in the current study and Castro and Epik's (1998) work.

Overall, the agreement between the current OF results and other studies' results used for the above comparisons for the flat plate are reasonably good. This is encouraging, as we

can conclude that the current OF code gives reasonably accurate results and can thus be reliably used to simulate transitional separated-reattached flows, and can be expected to extend to three-dimensional geometries.

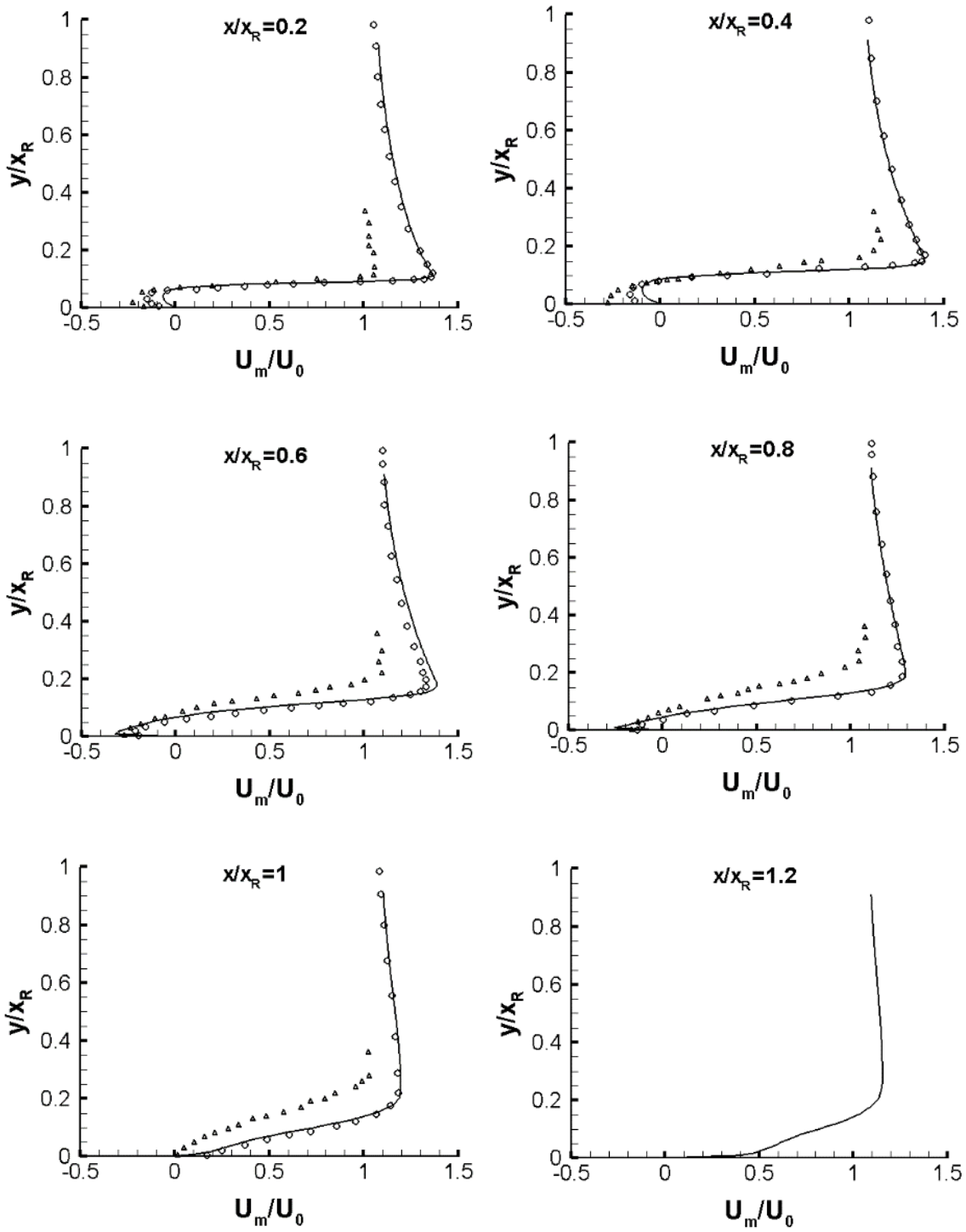

Fig. 4-3. Profiles of the mean streamwise velocity for the flat plate with NFST. Present results: solid line; Yang and Abdalla (2009): circles; Kiya and Sasaki (1983): triangles

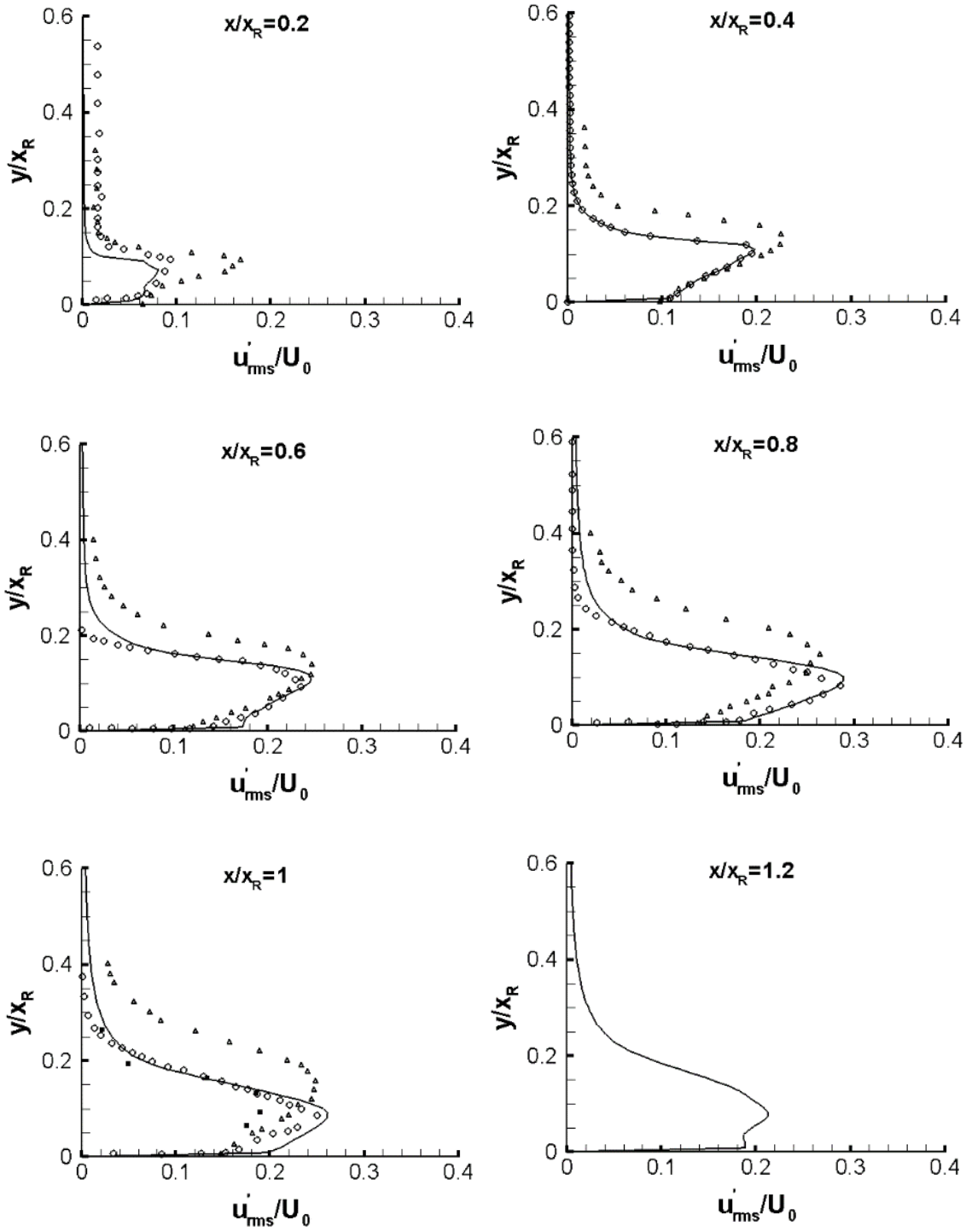

Fig. 4-4. Profiles of the root mean square fluctuating streamwise velocity for the flat plate with NFST. Present results: solid line; Yang and Abdalla (2009): circles; Kiya and Sasaki (1983): triangles; Castro and Epik (1998): squares

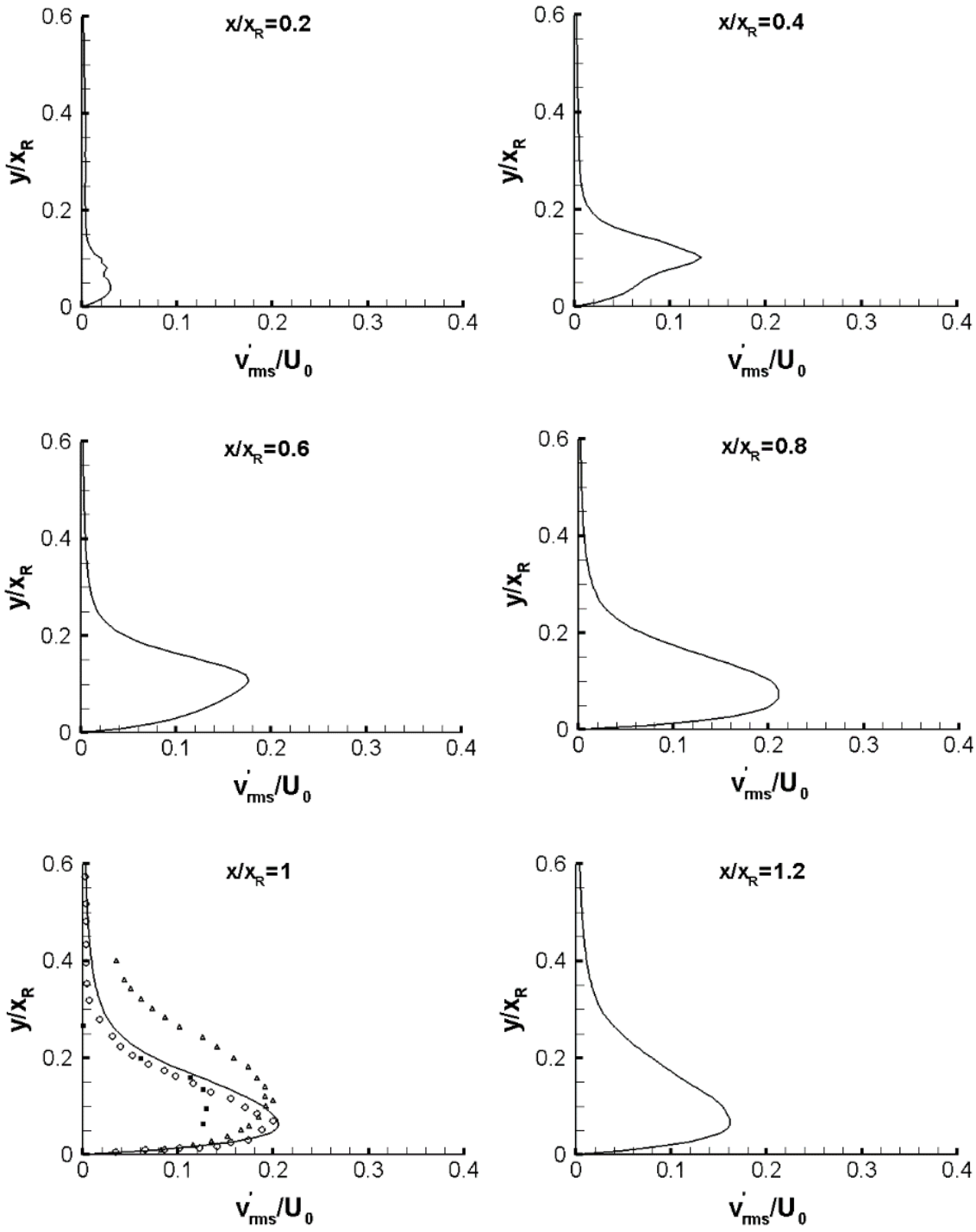

Fig. 4-5. Profiles of the root mean square fluctuating wall-normal velocity for the flat plate with NFST. Present results: solid line; Yang and Abdalla (2009): circles; Kiya and Sasaki (1983): triangles; Castro and Epik (1998): squares

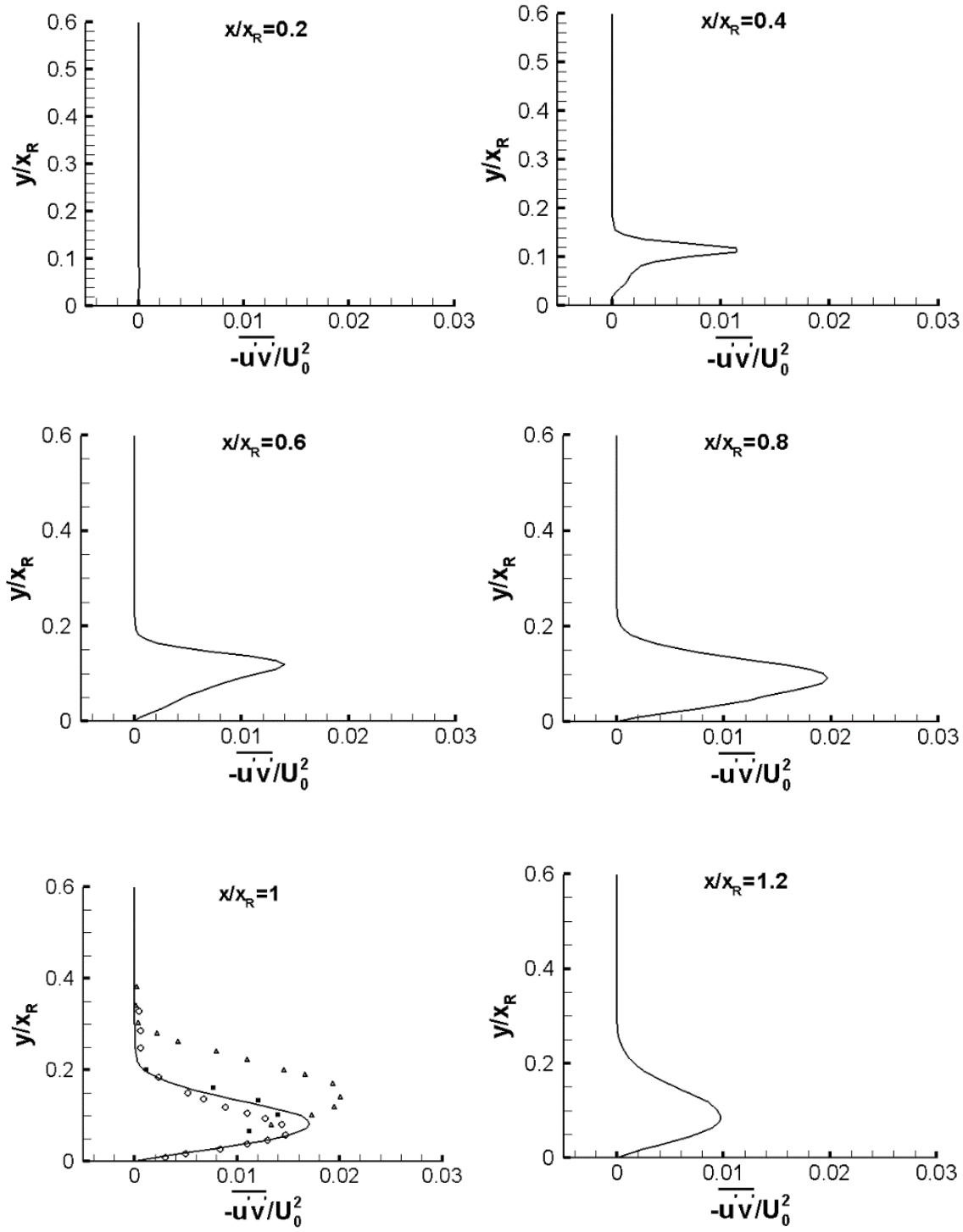

Fig. 4-6. Profiles of the Reynolds shear stress for the flat plate with NFST. Present results: solid line; Yang and Abdalla (2009): circles; Kiya and Sasaki (1983): triangles; Castro and Epik (1998): squares

4.2 Results for NFST

4.2.1 Mean variables of the flow

As shown in the literature review, the current study is the first to present the results of a transitional separated-reattached flow over a three-dimensional geometry. To the best of the author's knowledge, there are no results of such a geometry being presented in the literature to date. Therefore, the mean values of variables of the flow for 3D_case1 and 3D_case2 are presented here without the possibility for any comparison with other work. In addition, the other mean values of variables of transitional separated-reattached flow for the flat plate that are not presented in the previous section will be presented herein, such as the mean wall-normal velocity and the mean pressure coefficient. The aims of this section are to present a database by which subsequent studies can be validated, as well as to compare the flow mean variables for all geometries used in the current study.

The distribution of the mean streamwise velocity at the first cell away from the wall along the streamwise direction for 3D_case1 and 3D_case2 are plotted in Figs. 4-7 and 4-8, respectively. It is clear shown that the mean reattachment length is x_R = 3.4D for 3D_case1 and x_R = 3.95D for 3D_case2. Therefore, it can be concluded that the increase in aspect ratio of the three-dimensional geometry from 1 to 2 leads to an increase of the mean reattachment length by about 0.55D.

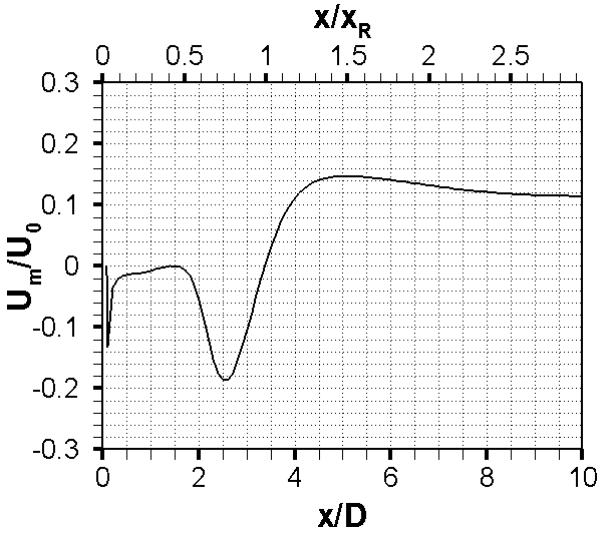

Fig. 4-7. Profile of the mean streamwise velocity at the first cell away from the wall normalized by the inflow velocity along the streamwise direction for 3D_case1 with NFST

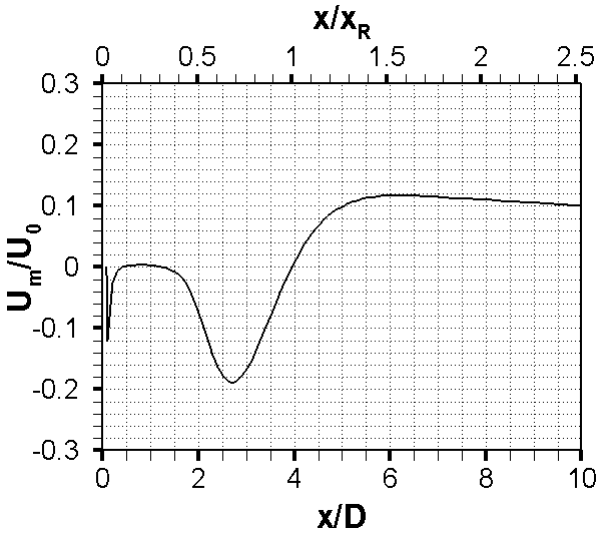

Fig. 4-8. Profile of the mean streamwise velocity at the first cell away from the wall normalized by the inflow velocity along the streamwise direction for 3D_case2 with NFST

The mean reattachment length magnitude can be also shown by profile for the mean skin friction coefficient, which is presented in Fig. 4-9 for 3D_case1 and Fig. 4-10 for 3D_case2.

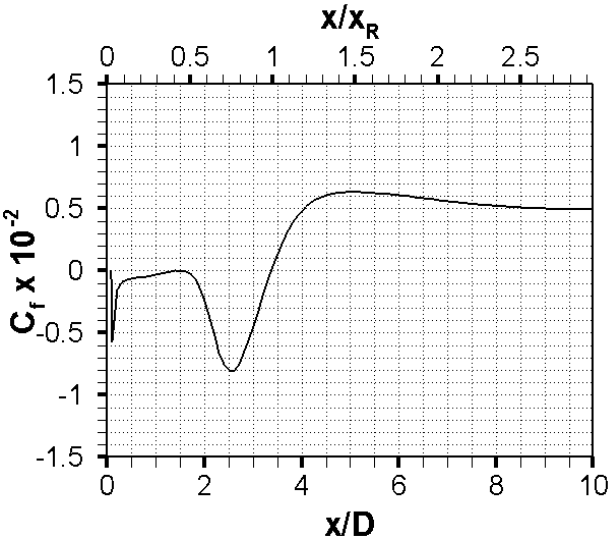

Fig. 4-9. Profile of the mean skin friction coefficient along the streamwise direction for 3D_case1 with NFST

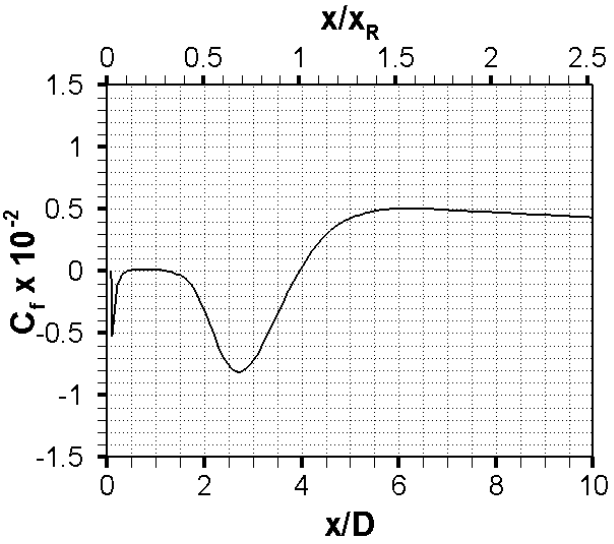

Fig. 4-10. Profile of the mean skin friction coefficient along the streamwise direction for 3D_case2 with NFST

The minimum value of the mean skin friction coefficient is -0.8 $\times 10^{-2}$ at x/x_R = 0.764 for 3D_case1, which decreases to -0.81 $\times 10^{-2}$ at x/x_R = 0.7 for 3D_case2, as shown in Figs. 4-9 and 4-10. For the flat plate, the profile of the mean skin friction coefficient attains the bottom with a value of -0.74 $\times 10^{-2}$ at x/x_R = 0.745, as shown in Fig. 4-2. This is in relatively good agreement regarding the minimum value of the mean skin friction coefficient and the location at which it occurs among the three geometries indicating that there is no considerable effect of the nature of the geometry on the mean skin friction coefficient.

It is worth pointing out that the symbol (x_R) shown in all figures of the current study denotes different values depending on the geometry, i.e., x_R is 6D for the flat plate figures, 3.4D for 3D_case1 figures, and 3.95D for 3D_case2 figures with NFST.

Mean streamwise velocity profiles for 3D_case1 and 3D_case2 are shown in Figs. 4-11 and 4-12, respectively. For both three-dimensional geometries, the minimum mean streamwise velocity in the vicinity of the wall and within the recirculation zone is approximately similar to that for the flat plate. However, the minimum mean streamwise velocity is within the range from -0.3U_0 to - 0.32U_0 in the region extending from x/x_R = 0.6 to x/x_R = 0.8 for all geometries. Despite the minimum mean streamwise velocity for the flat plate being slightly lower than this for both three-dimensional geometries, the

current study indicates that there is no noticeable effect of the nature of the geometry on the back-flow magnitude.

Reynolds stresses profiles for 3D_case1 and 3D_case2 are presented in Figs. 4-13 and 4-14 for u'_{rms}/U_0, Figs. 4-15 and 4-16 for v'_{rms}/U_0 and Figs. 4-17 and 4-18 for the shear stress. It can be seen that the maximum values of these variables for 3D_case2 are slightly higher than those for 3D_case1.

For all geometries, peaks in profiles of Reynolds normal and shear stresses along the streamwise direction are zero at the separation, after which they start to grow downstream. The highest peaks are for Reynolds normal stresses in the streamwise direction. However, the highest peaks in the profiles of Reynolds stresses are in the second half of the separation bubble at a position just before the mean reattachment line. This indicates that violent three-dimensional motions and nonlinear flow development take place in the second half of the separation bubble. This behaviour is comparable to that described in Yang and Voke (2001) for transitional separated-reattached flow over a flat plate with a semi-circular leading edge.

Inspection of Reynolds stresses profiles for all geometries reveals that the maximum values of these variables for the flat plate are higher than those for both three-dimensional geometries by about 20% - 25%. So, it can be concluded that the intensities of breakdown to turbulence, which is associated with violent three-dimensional motions and nonlinear flow development, in 3D_case1 and 3D_case2 are lower than that for the flat plate.

Time-averaged wall-normal velocity normalized by the inlet velocity (V_m/U_0) profiles for the flat plate, 3D_case1 and 3D_case2 are presented in Figs. 4-19, 4-20, and 4-21, respectively. It is believed that no measured or simulated results of the mean wall-normal velocity for a flat plate have to date been presented in the literature. So, the mean wall-normal velocity for the flat plate is presented without comparison with other data.

For all geometries, the minimum values of the mean wall-normal velocity are within the region bounded by $x/x_R = 0.6$ to $x/x_R = 0.8$, referring to the strong recirculation part of the separation bubble occurs in this region. However, the maximum mean wall-normal velocities for the flat plate are slightly higher than that for the other geometries.

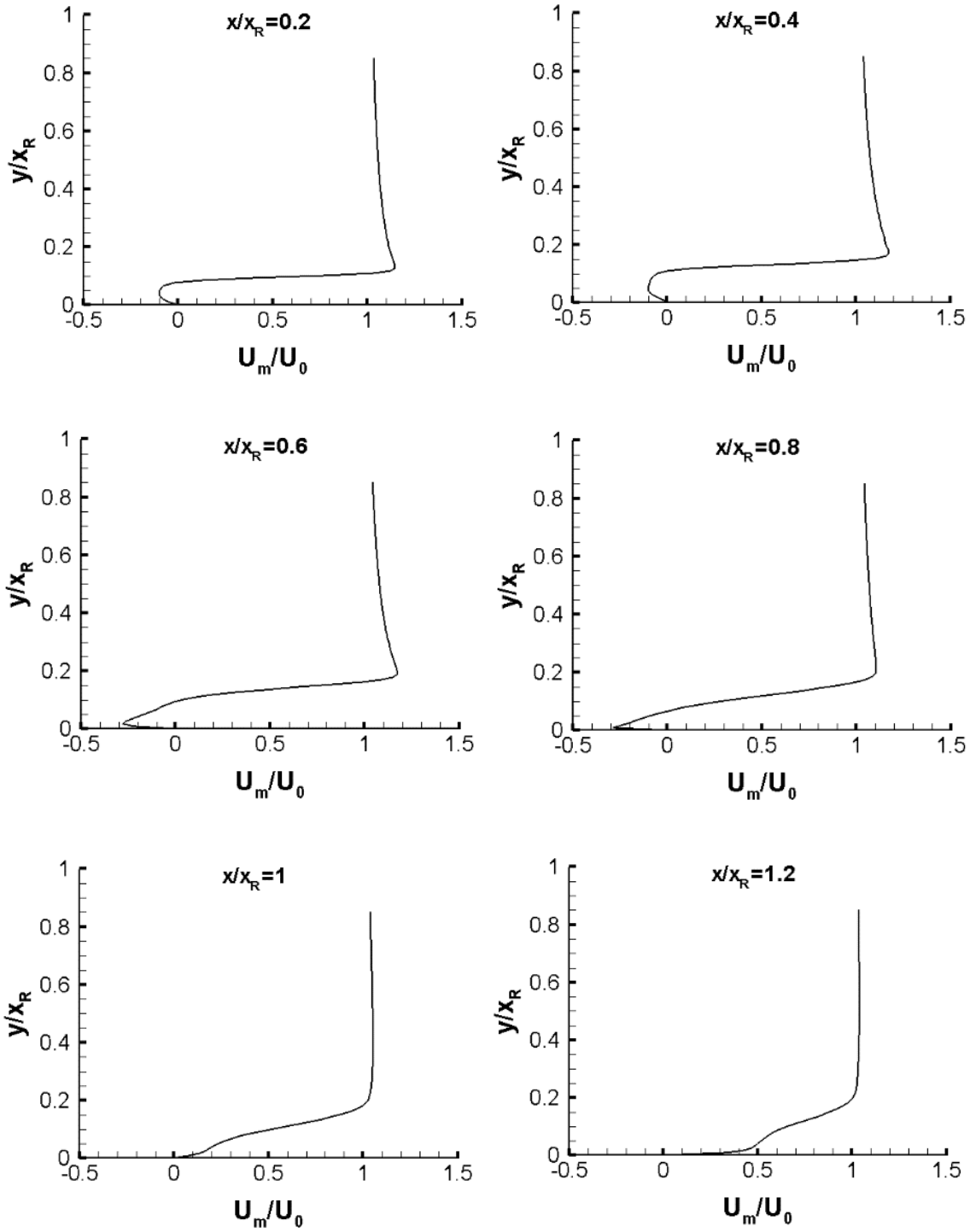

Fig. 4-11. Profiles of the mean streamwise velocity for 3D_case1 with NFST

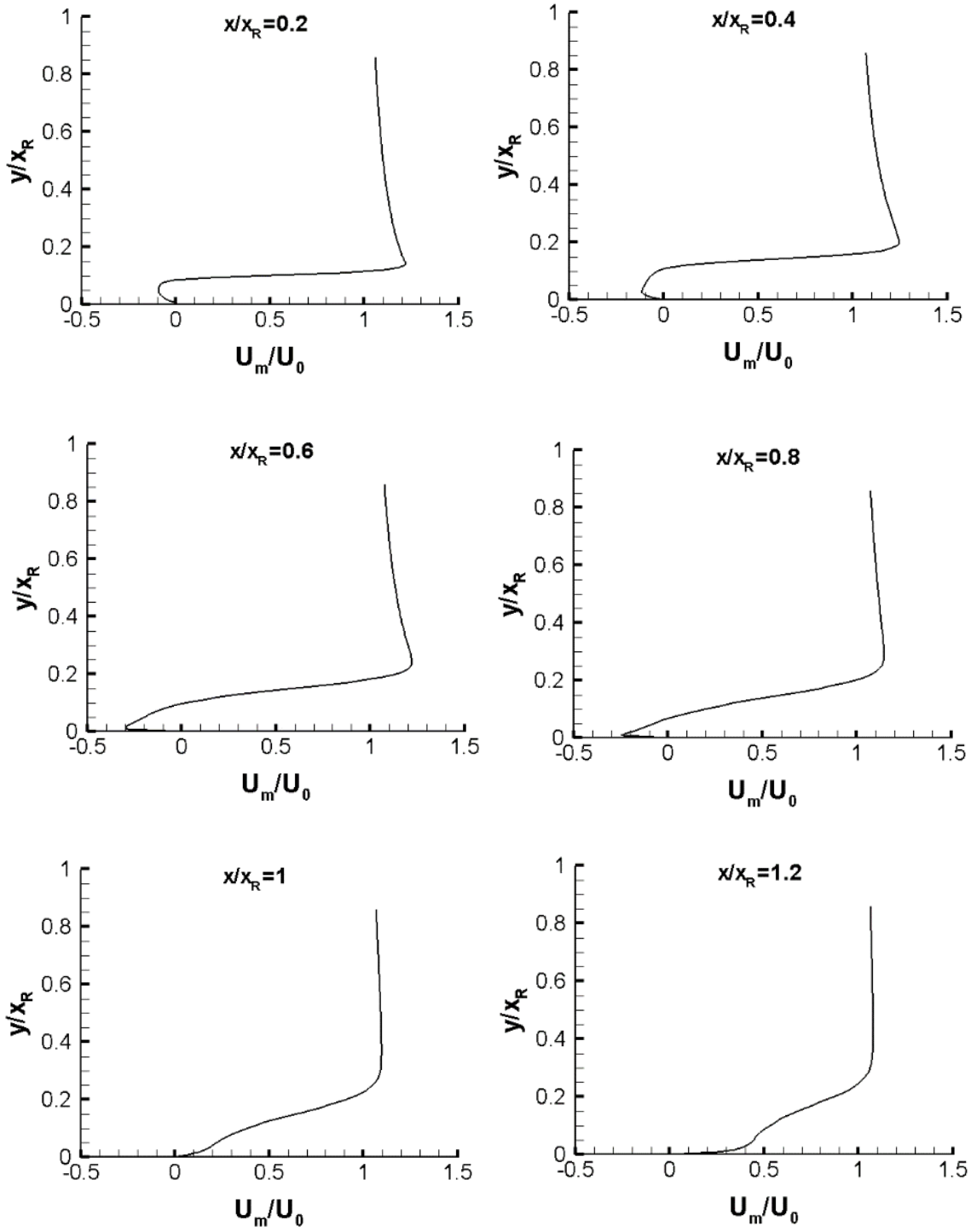

Fig. 4-12. Profiles of the mean streamwise velocity for 3D_case2 with NFST

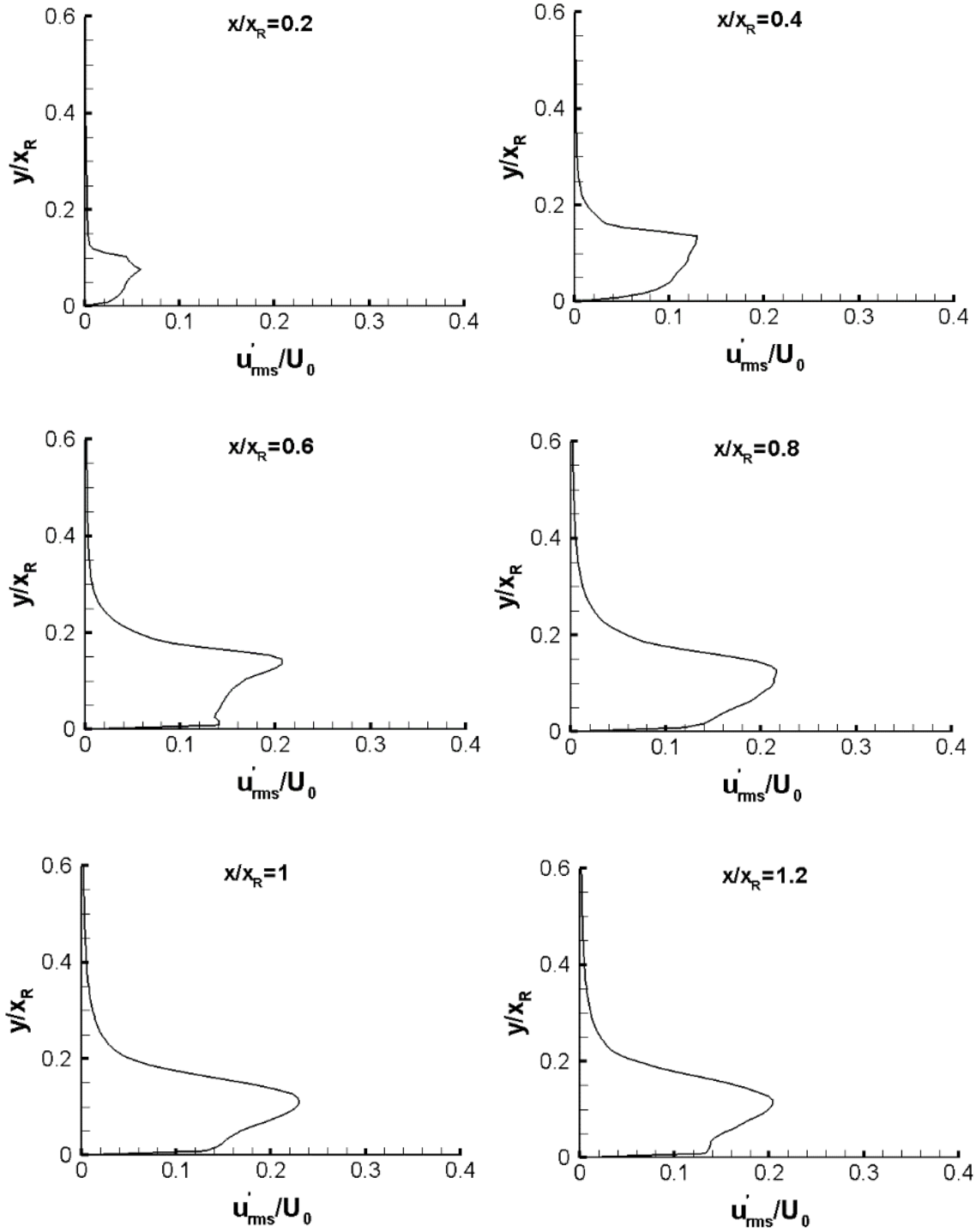

Fig. 4-13. Profiles of the root mean square fluctuating streamwise velocity for 3D_case1 with NFST

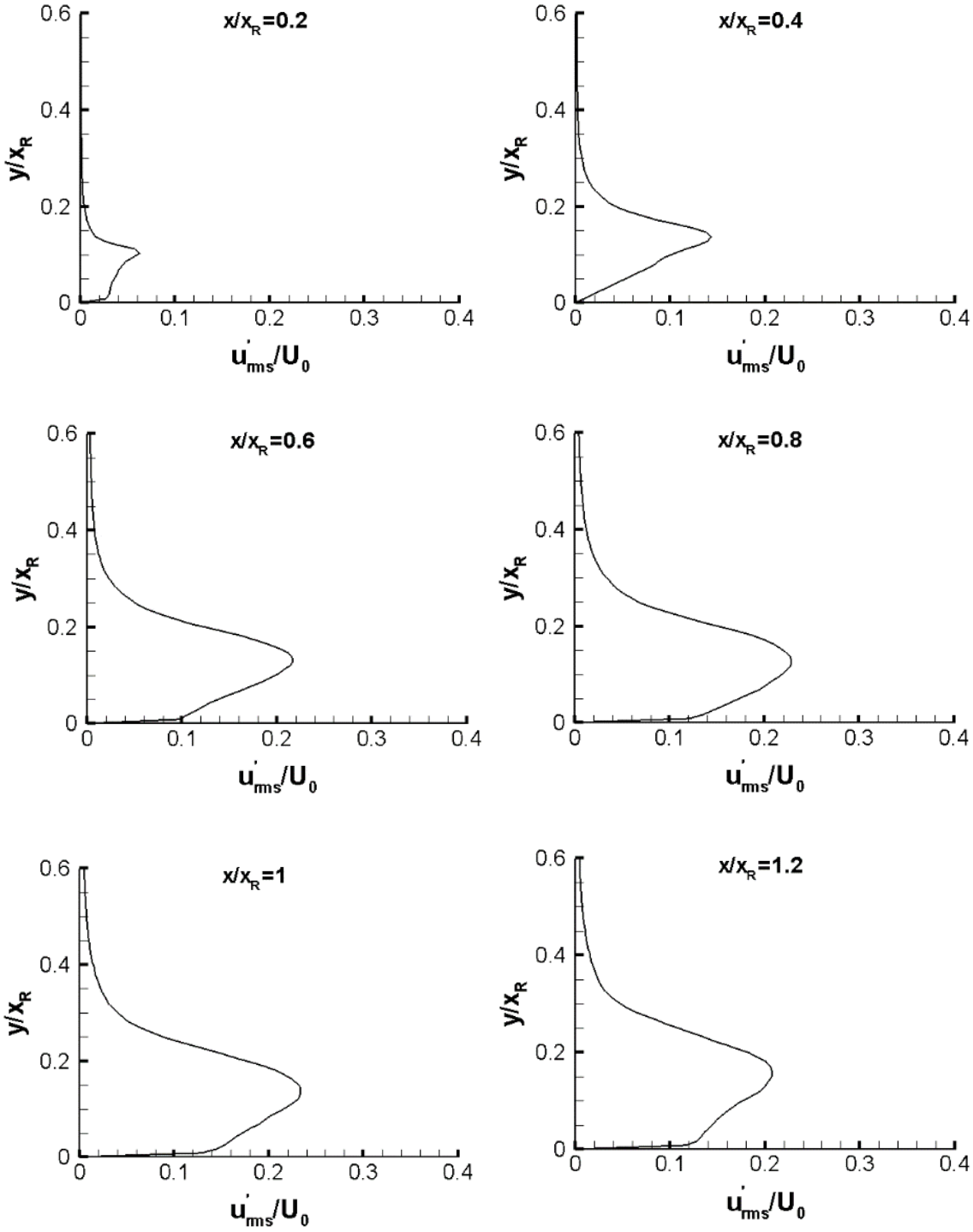

Fig. 4-14. Profiles of the root mean square fluctuating streamwise velocity for 3D_case2 with NFST

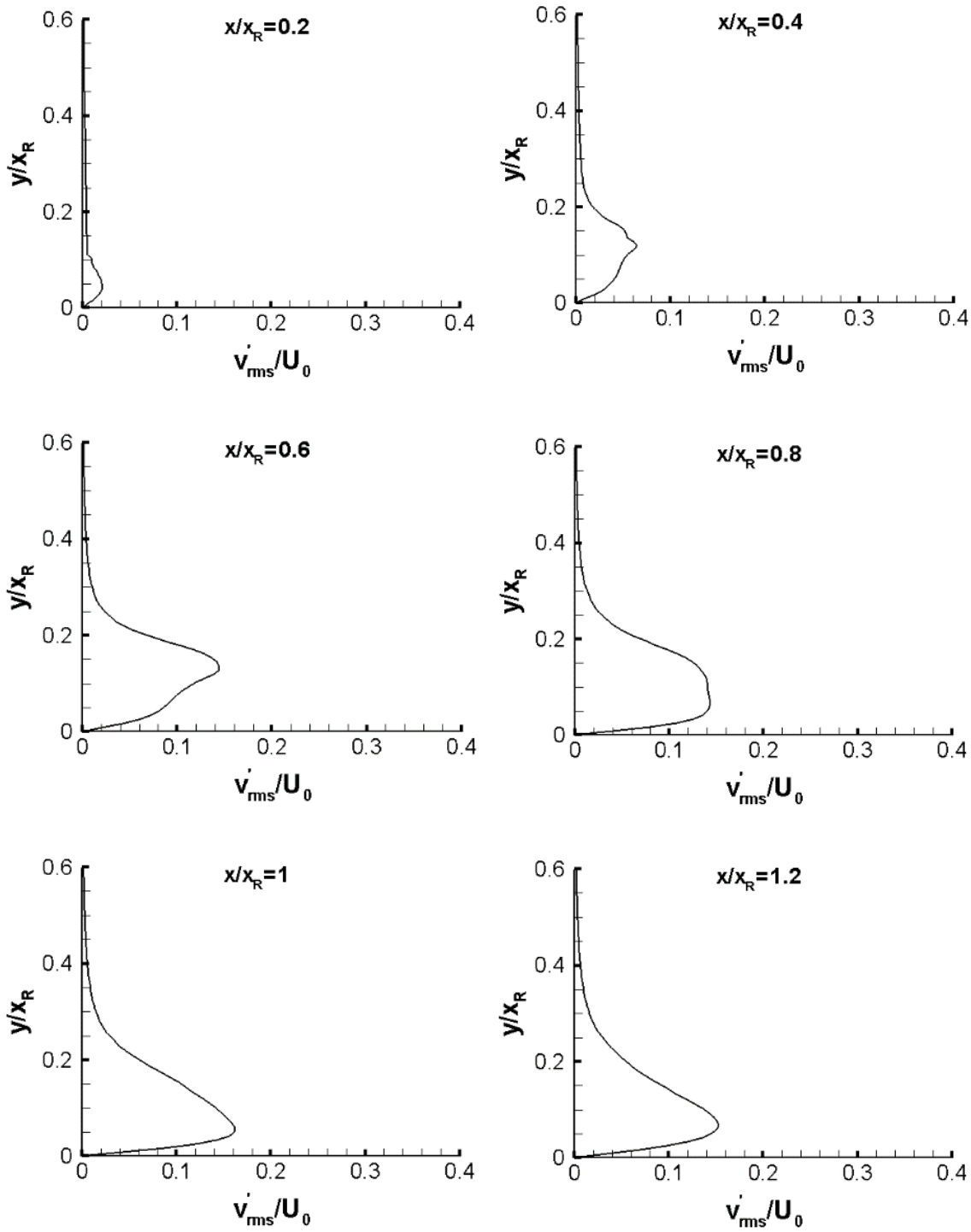

Fig. 4-15. Profiles of the root mean square fluctuating wall-normal velocity for 3D_case1 with NFST

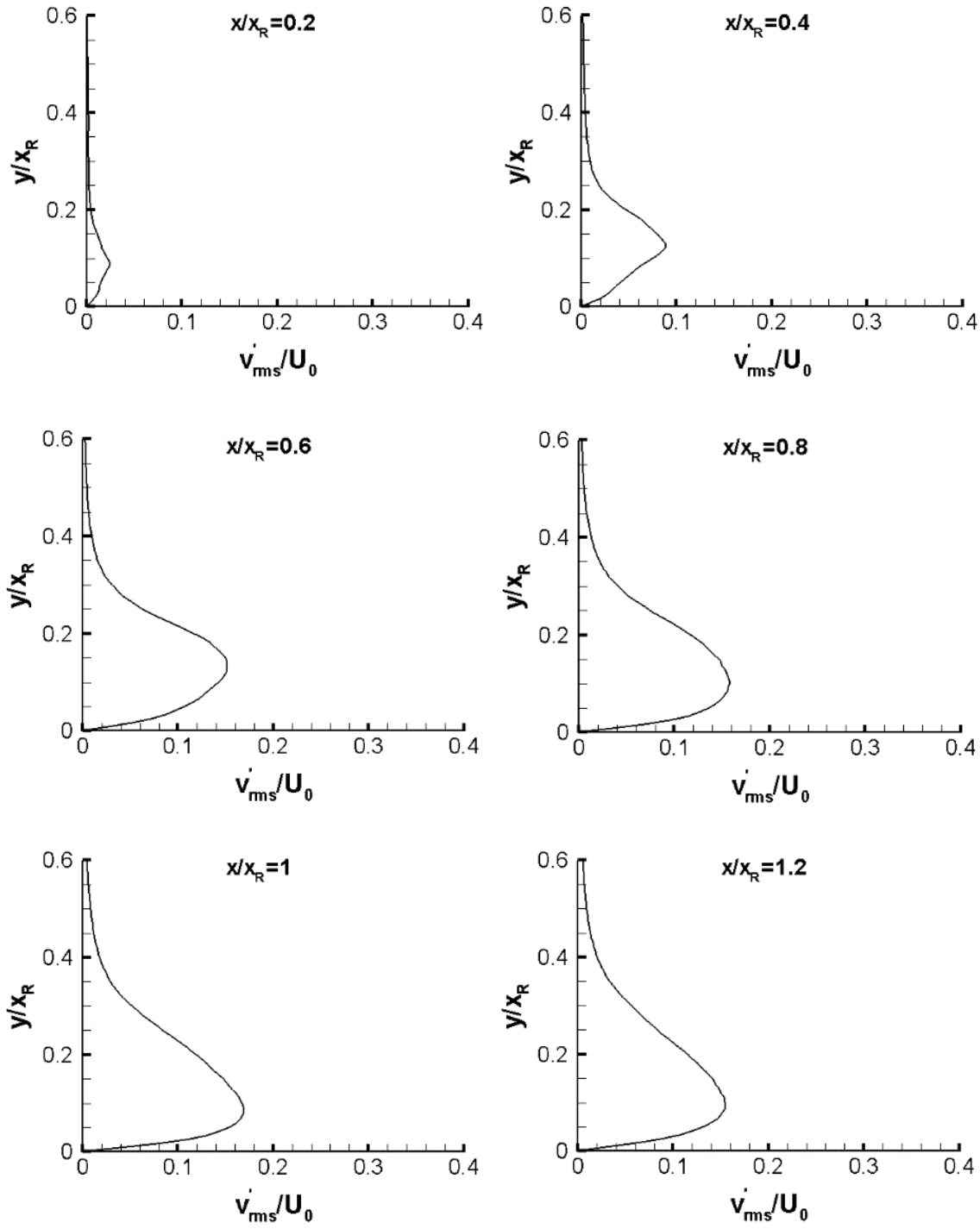

Fig. 4-16. Profiles of the root mean square fluctuating wall-normal velocity for 3D_case2 with NFST

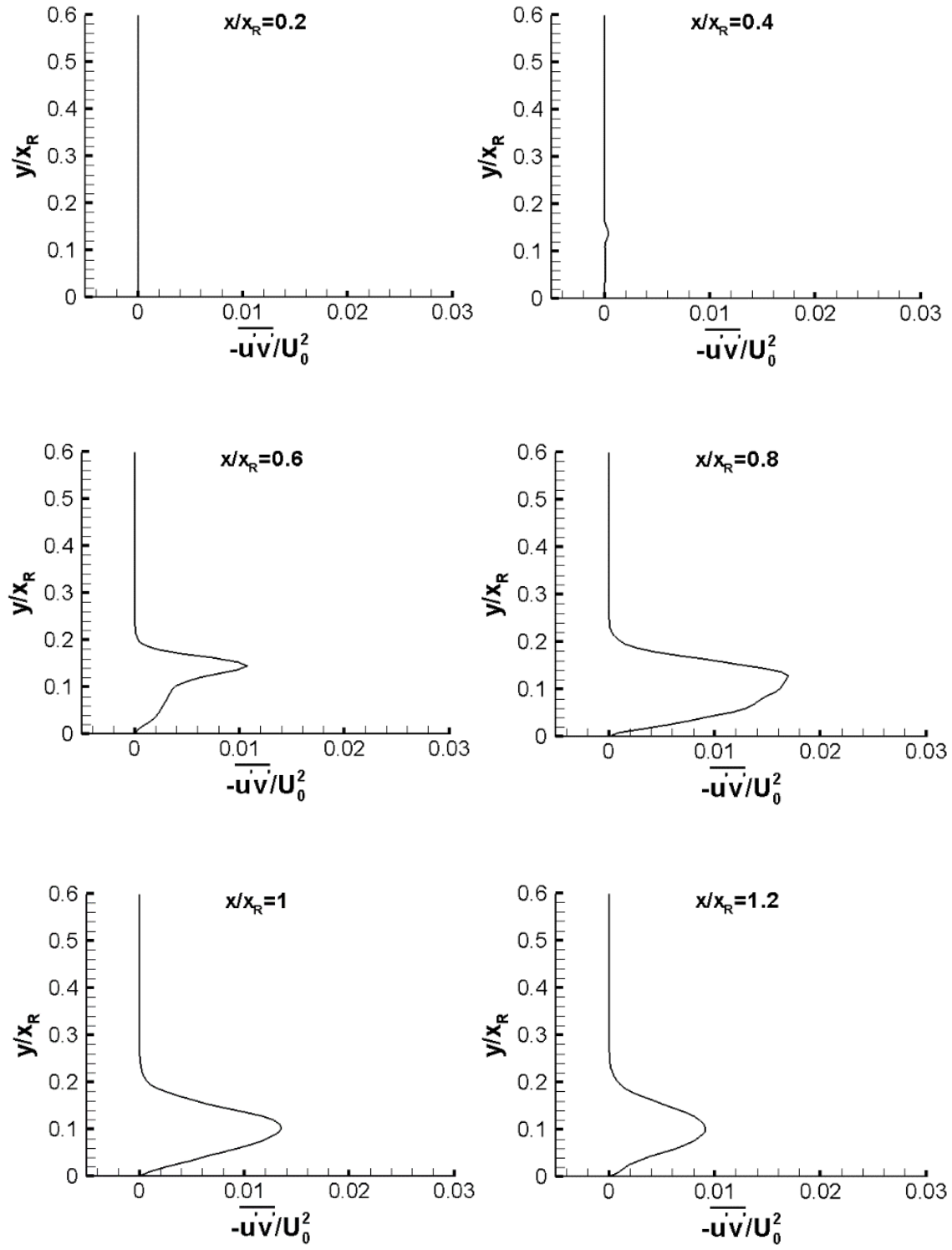

Fig. 4-17. Profiles of the Reynolds shear stress for 3D_case1 with NFST

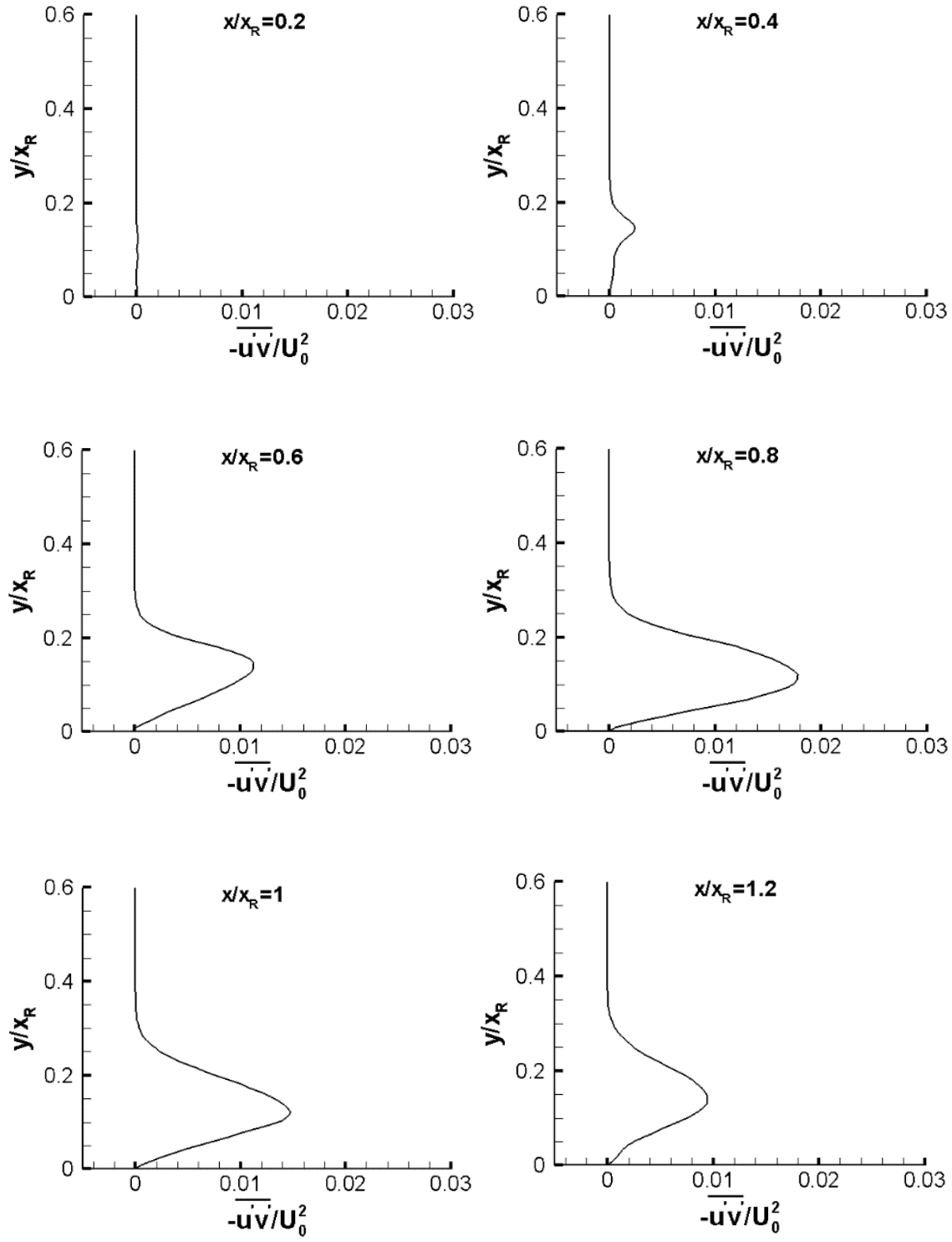

Fig. 4-18. Profiles of the Reynolds shear stress for 3D_case2 with NFST

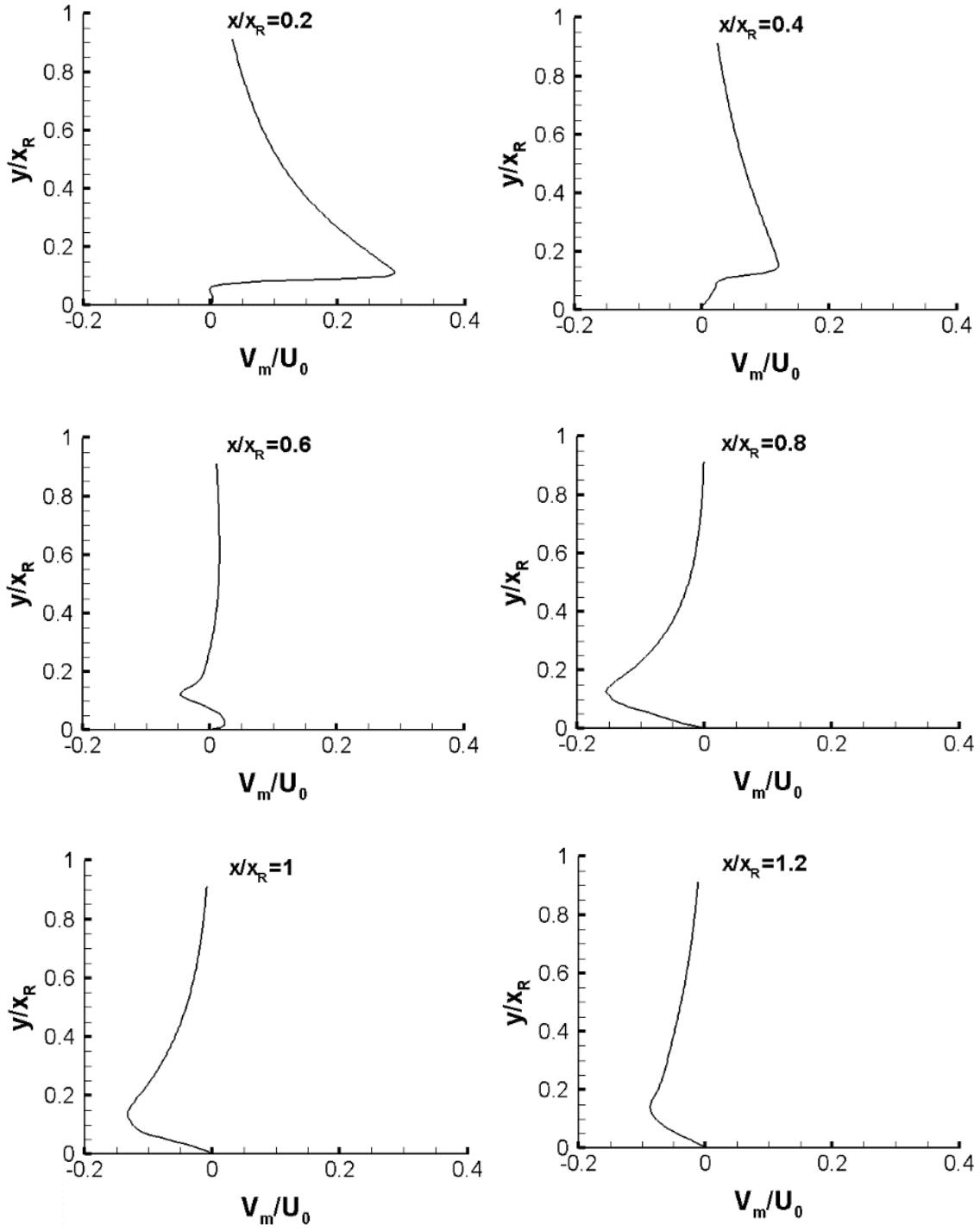

Fig. 4-19. Profiles of the mean wall-normal velocity for the flat plate with NFST

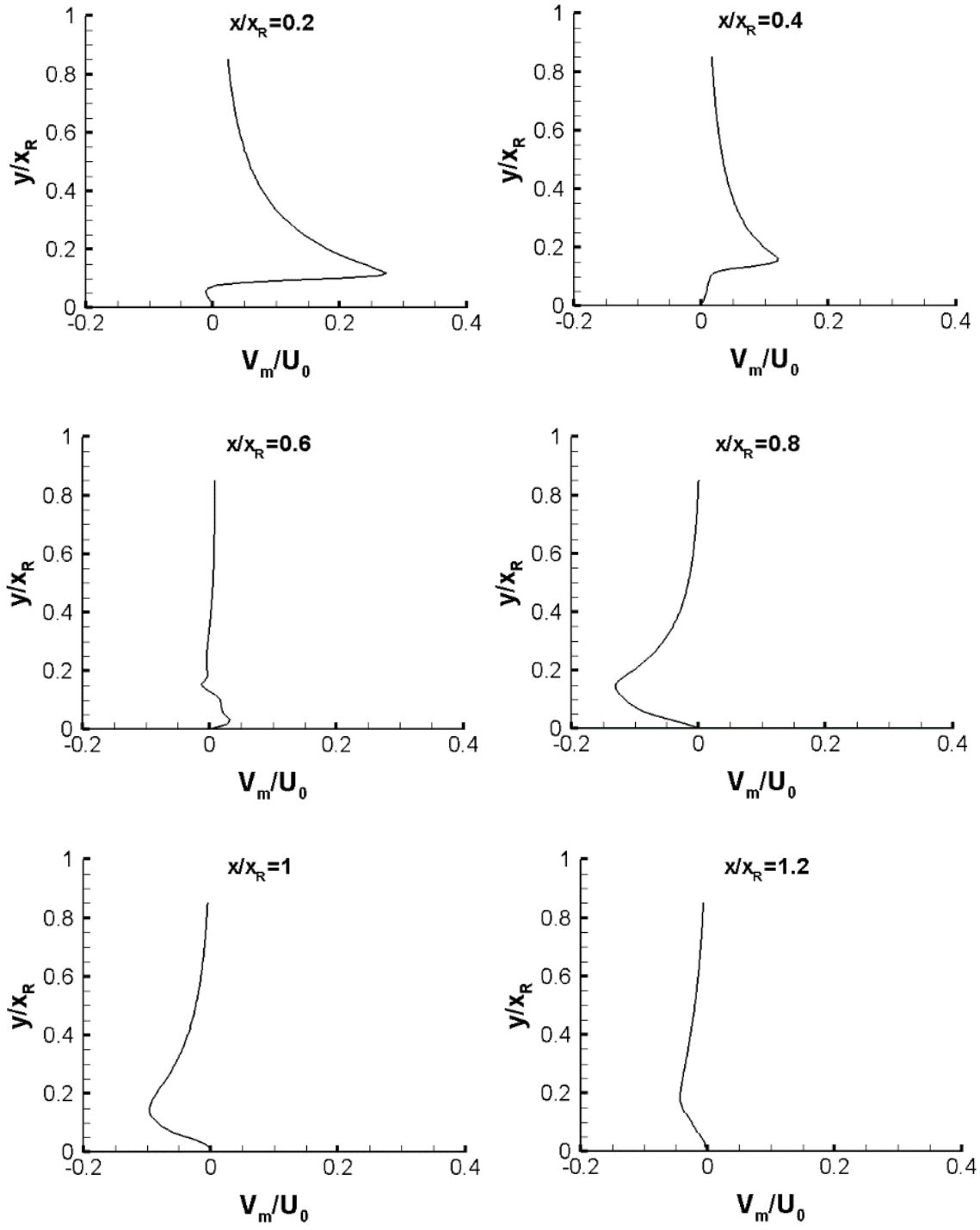

Fig. 4-20. Profiles of the mean wall-normal velocity for 3D_case1 with NFST

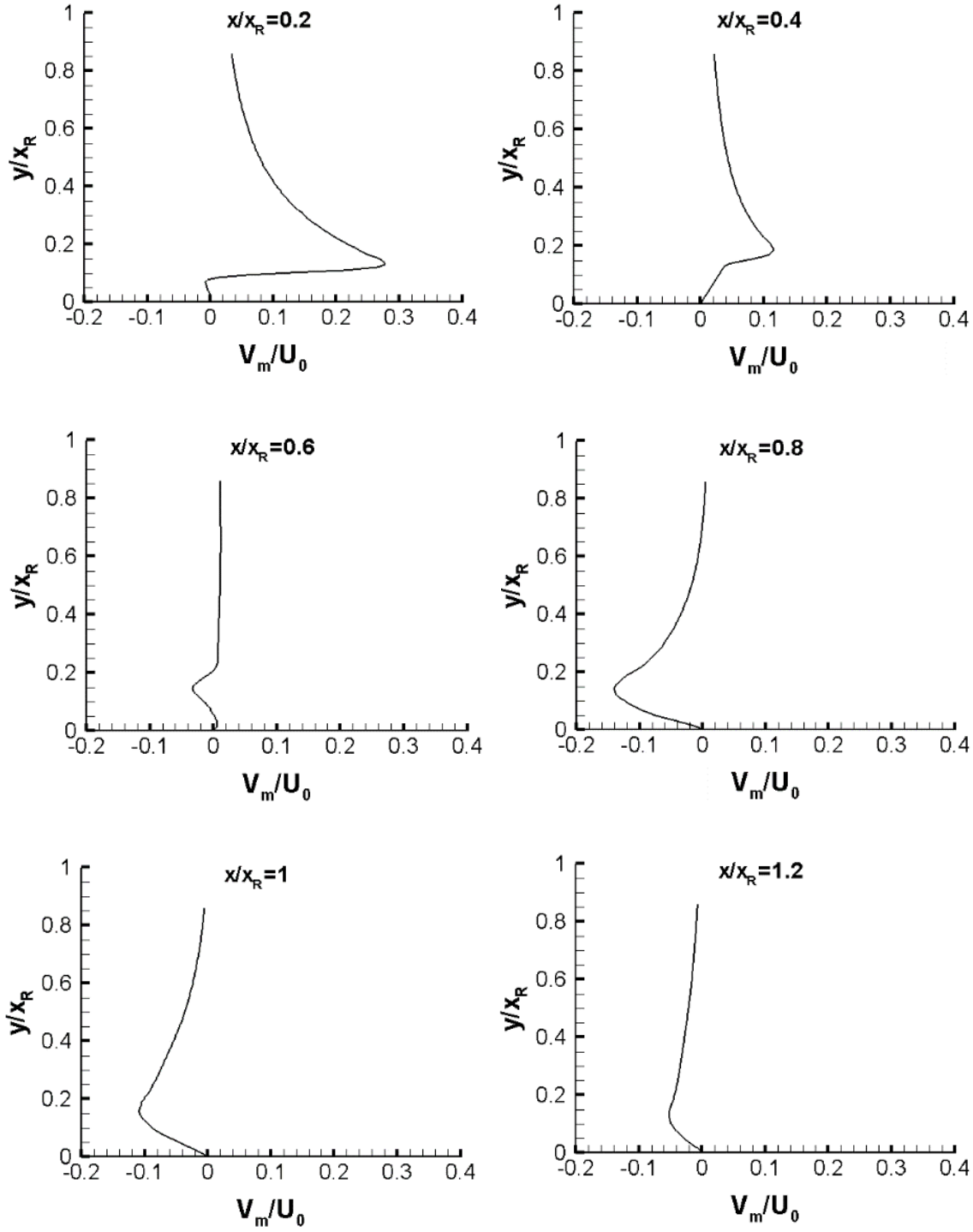

Fig. 4-21. Profiles of the mean wall-normal velocity for 3D_case2 with NFST

The distribution of the mean surface pressure coefficient along the streamwise direction for the flat plate is shown in Fig. 4-22. The pressure coefficient (C_P) is defined as:

$$C_P = \frac{P - P_\infty}{0.5\rho U_0^2} \tag{4-4}$$

where P is the static pressure at the point at which the pressure coefficient is being calculated and P_∞ is the static pressure in the free stream.

Although the experimental results for the mean surface pressure coefficient for transitional separated-reattached flow are not available in the literature, the current mean surface pressure coefficient is compared with the experimental results of Cherry et al. (1981b) for a turbulent separated-reattached flow on a flat plate with higher Reynolds number (32×10^3) based on the inflow velocity and plate thickness.

Despite the current mean surface pressure coefficient being lower than that reported by Cherry et al. (1981b), its distribution along the streamwise direction is nevertheless comparable as shown in Fig. 4-22. However, this difference may be due to the different Reynolds numbers and the nature of the separated flow that lead to the current results showing larger pressure losses.

The minimum mean surface pressure coefficient for the flat plate is at $x/x_R = 0.6$, after which a rapid recovery takes place. The recovery completes after the mean reattachment at approximately $x/x_R = 1.3$.

Babu and Sarkar (2012) employed LES to simulate transitional separated-reattached flow over a similar geometry, and with a similar Reynolds number in Yang and Voke (2001). There was good agreement with the results of both studies. Babu and Sarkar (2012) presented the profile of the mean surface pressure coefficient which is very similar to the current profile of this coefficient, enhancing our belief in the accuracy of the provided results from the current OF code.

For 3D_case1 and 3D_case2, the mean surface pressure coefficient profiles are plotted in Figs. 4-23 and 4-24, respectively. For 3D_case1, the minimum mean surface pressure coefficient is found at $x/x_R = 0.6$, after which a rapid recovery takes place. The recovery completes after the mean reattachment at approximately $x/x_R = 1.5$ as shown in Fig. 4-23.

For 3D_case2, the minimum mean surface pressure coefficient is at x/x_R = 0.5 and whose magnitude is lower than that for 3D_case1, but higher than for the flat plate. Rapid recovery takes place after x/x_R = 0.5, completes after the mean reattachment at approximately x/x_R = 1.5 as shown in Fig. 4-24.

For all geometries, the maximum mean surface pressure coefficient is located at about the mean reattachment point and its value in 3D_case2 is lower than that for 3D_case1 and higher than that for the flat plate.

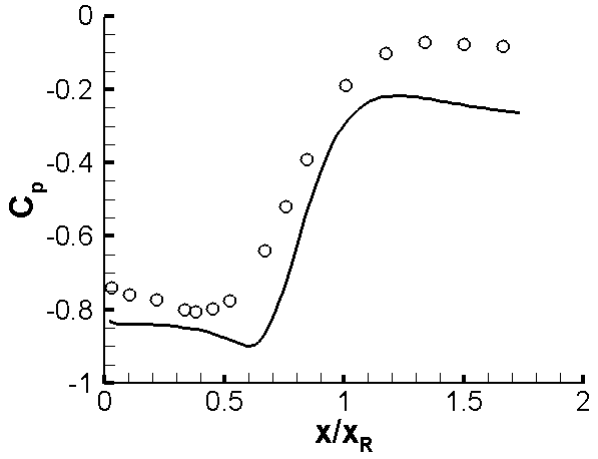

Fig. 4-22. Distribution of the mean surface pressure coefficient for the flat plate with NFST. Present results: solid line; Cherry et al. (1981b): circles

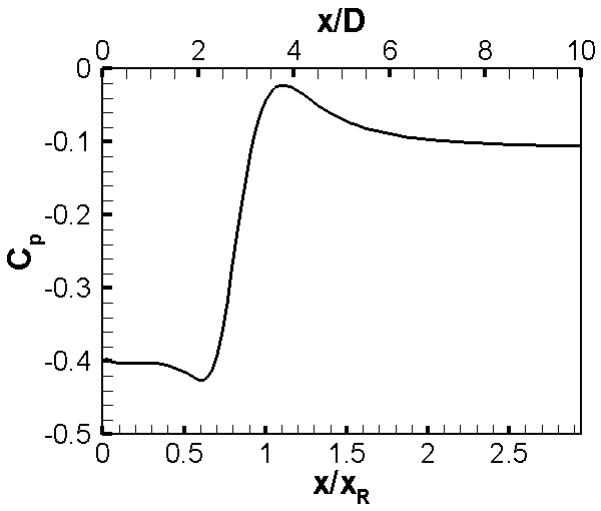

Fig. 4-23. Distribution of the mean surface pressure coefficient for 3D_case_1 with NFST

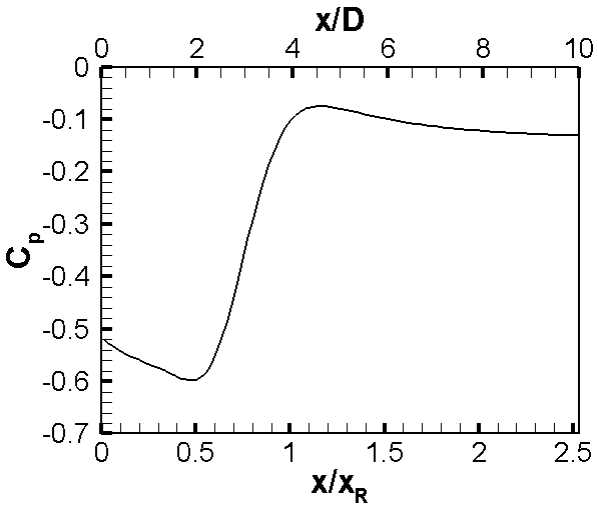

Fig. 4-24. Distribution of the mean surface pressure coefficient for 3D_case_2 with NFST

The simulated mean pressure coefficient profiles across the shear layer at different streamwise locations for the flat plate are compared with those presented by Tafti and Vanka (1991) as shown in Fig. 4-25. The numerical simulation performed by Tafti and Vanka (1991) was for a turbulent separated-reattached flow on a blunt flat plate with Reynolds number of 1×10^3. Excellent agreement between the current results and results of Tafti and Vanka (1991) can be seen at $x/x_R = 0.2$ as shown in Fig. 4-25. However, at the other streamwise positions, peaks in the current mean pressure coefficient profiles are slightly higher than those in Tafti and Vanka (1991). This may be due to the difference of the Reynolds numbers and the nature of the separated flow in each of these studies. It is clear shown that the mean pressure coefficient profile becomes much more uniform after the reattachment and the mean pressure coefficient recovery is nearly complete after $x/x_R = 1.2$ as shown in Fig. 4-25.

A similar scenario is found for 3D_case1 and 3D_case2, where the mean pressure coefficient profile becomes much more uniform after the mean reattachment location, as shown in Fig. 4-26 for 3D_case1 and Fig. 4-27 for 3D_case2.

It is interesting to note that the maximum pressure losses in the flat plate are higher than those in 3D_case2. However, the maximum pressure losses in 3D_case2 are higher than those in 3D_case1 as shown in Figs. 4-25, 4-26 and 4-27.

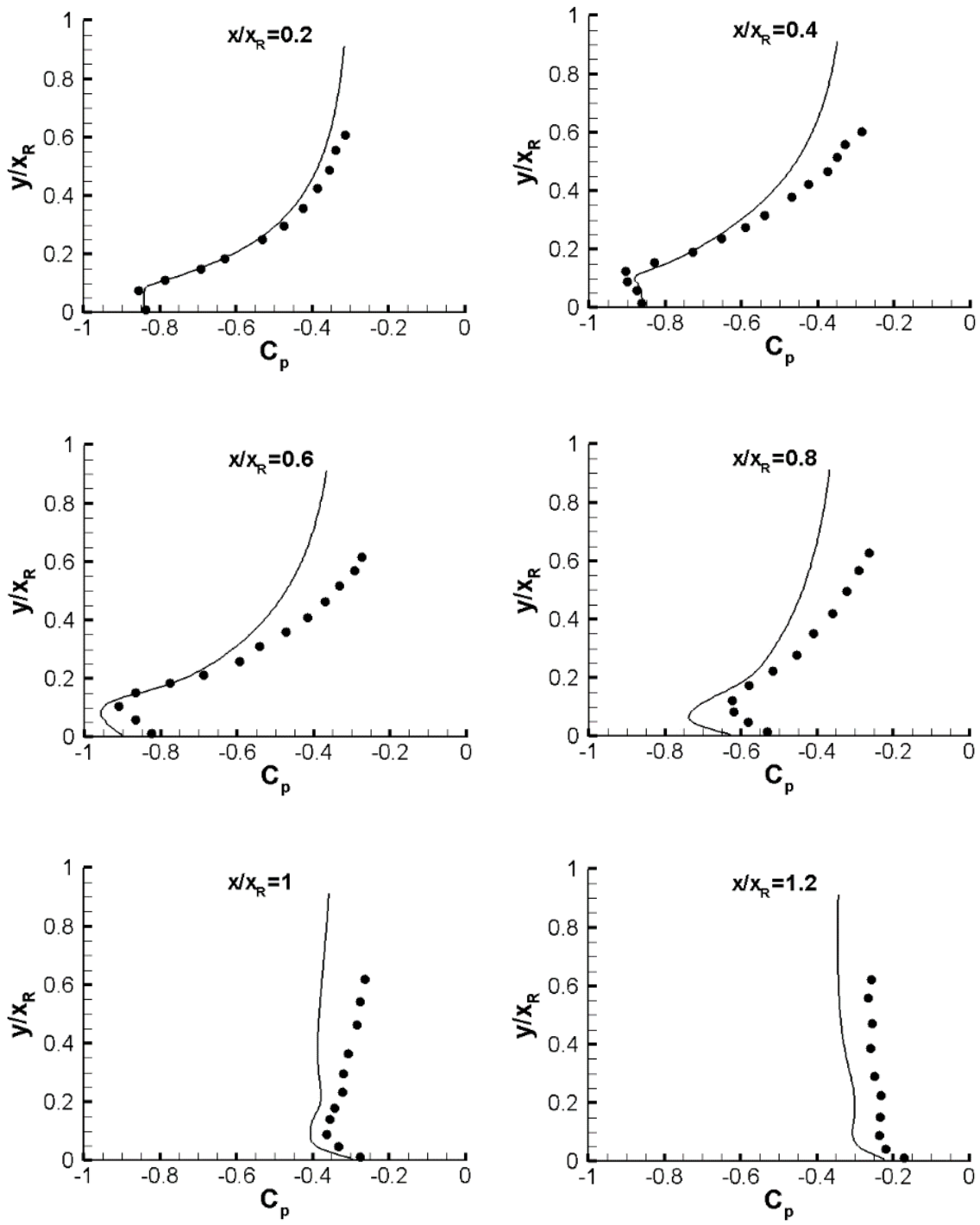

Fig. 4-25. Profiles of the mean pressure coefficient for the flat plate with NFST. Present results: solid line; Tafti and Vanka (1991): circles

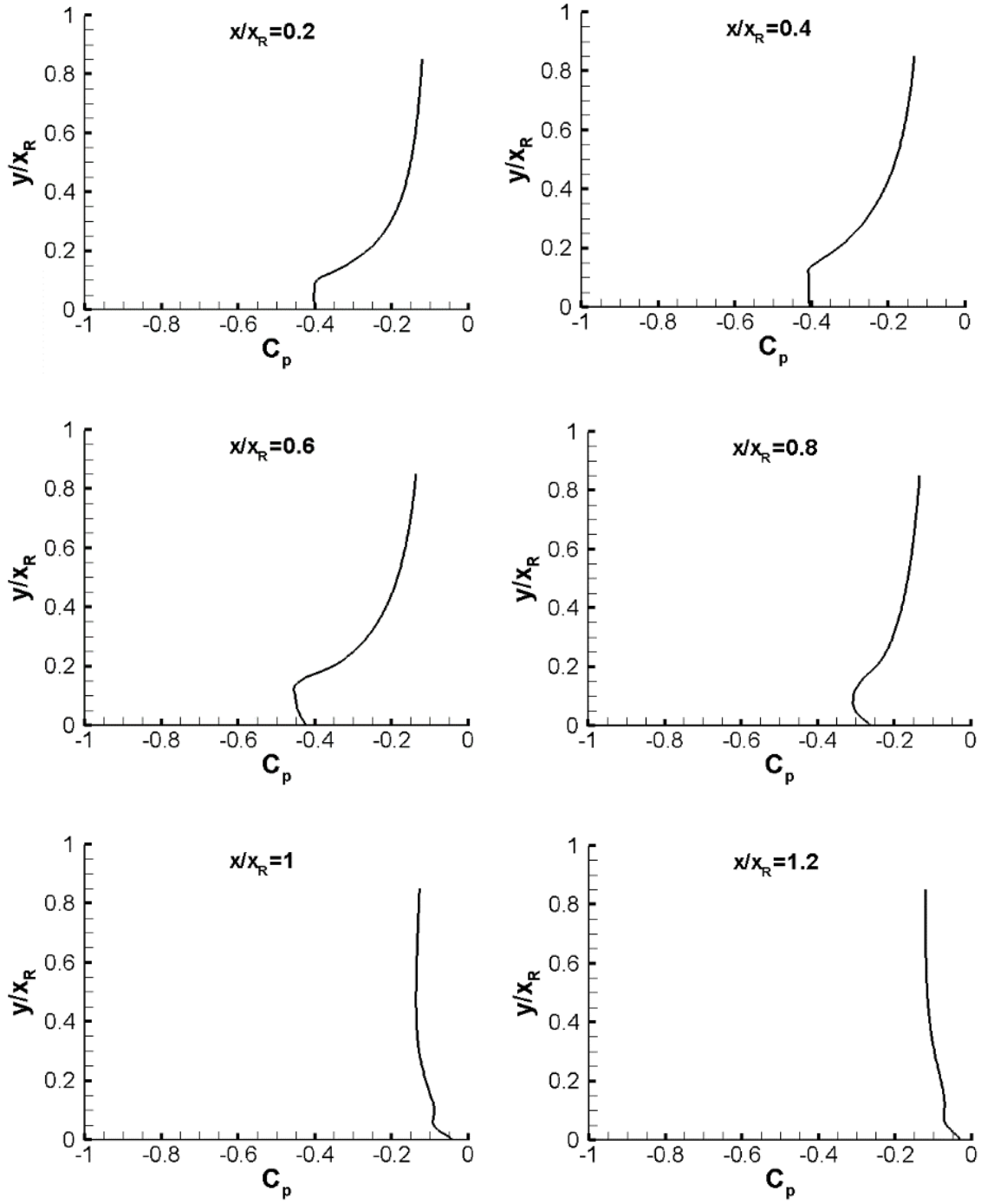

Fig. 4-26. Profiles of the mean pressure coefficient for 3D_case1 with NFST

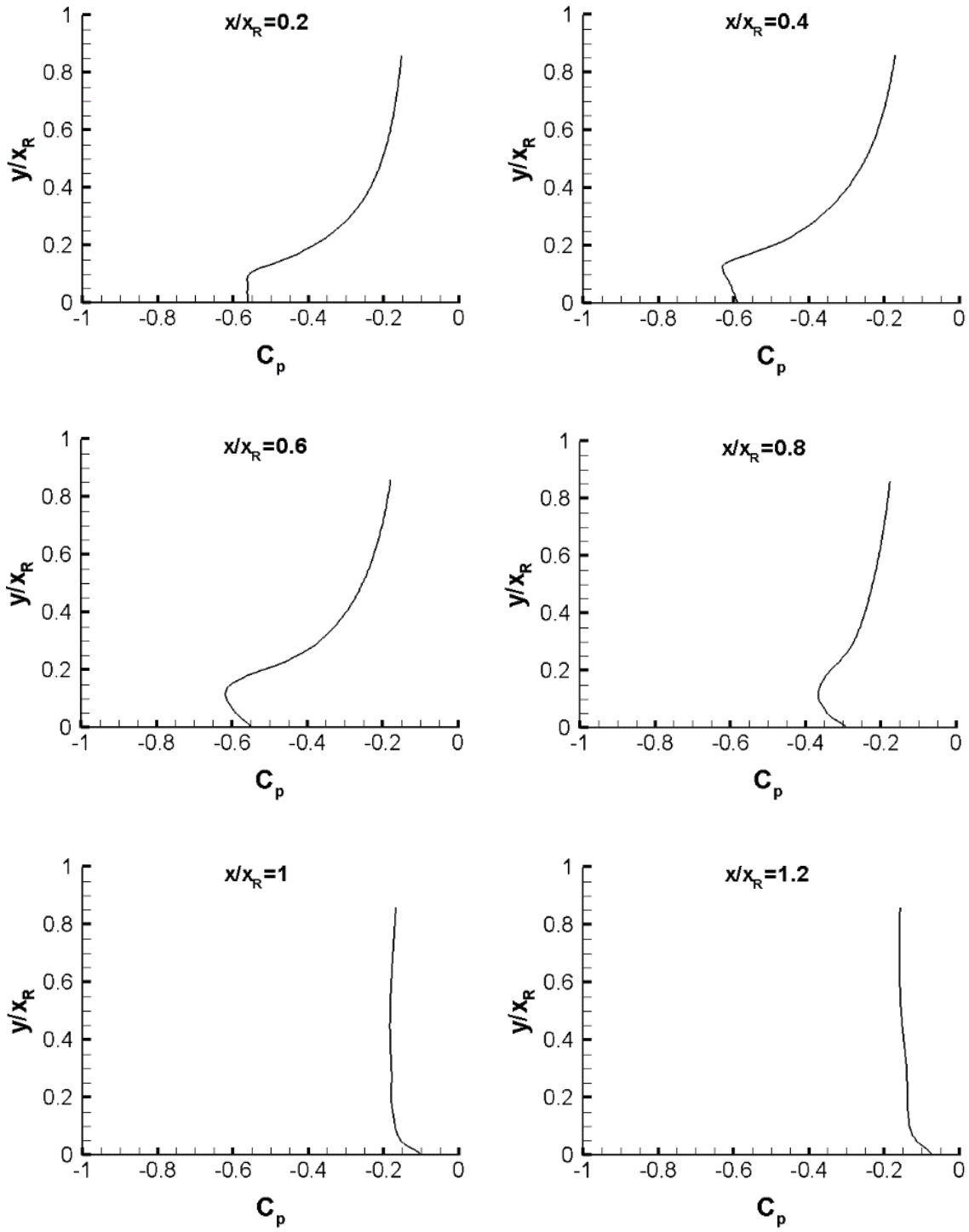

Fig. 4-27. Profiles of the mean pressure coefficient for 3D_case2 with NFST

The time-averaged velocity streamlines, velocity vectors, and streamwise velocity contours for the flat plate, 3D_case1, and 3D_case2 at the mid-distance of the spanwise direction ($z/D = 2$) are shown in Figs. 4-28, 4-29, and 4-30, respectively.

For all geometries used in the current study, the mean separation bubble is similar to a separation bubble for separated-reattached steady laminar flow with different reattachment lengths. It is clear to see that a single separation bubble starts from the leading edge at $x/D = 0$ and ends downstream at about $x/D = 6$ for the flat plate, $x/D = 3.4$ for 3D_case1, and $x/D = 3.95$ for 3D_case2.

In general, the size of the separation bubble in terms of height and length for the flat plate is much larger than that in each of the three-dimensional geometries. Despite the reattachment length being close in 3D_case1 and 3D_case2, where the difference is just $x/D = 0.55$, the separation bubble size in 3D_case2 is still larger than that for 3D_case1.

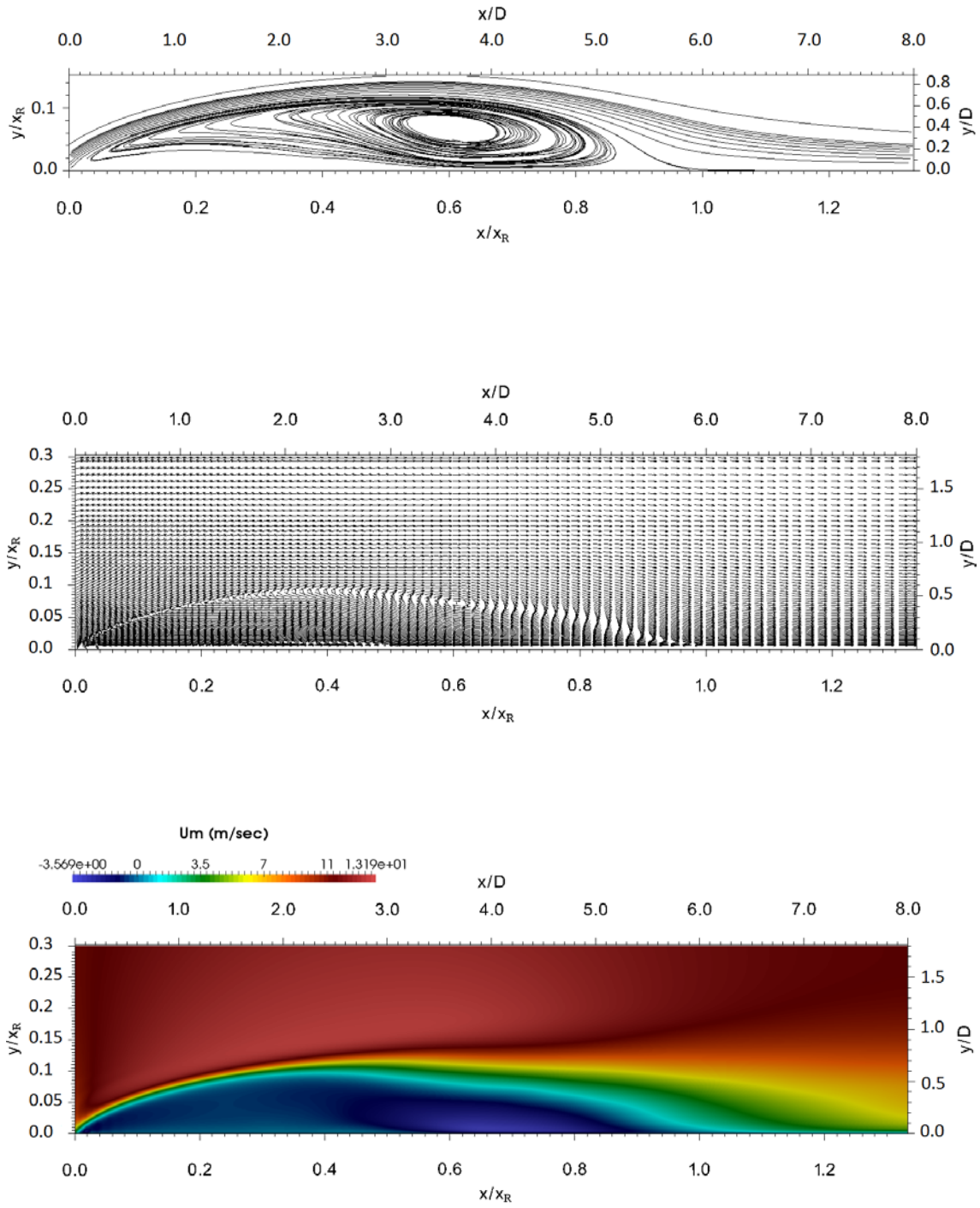

Fig. 4-28. Mean velocity streamlines, velocity vectors, and streamwise velocity contours for the flat plate with NFST

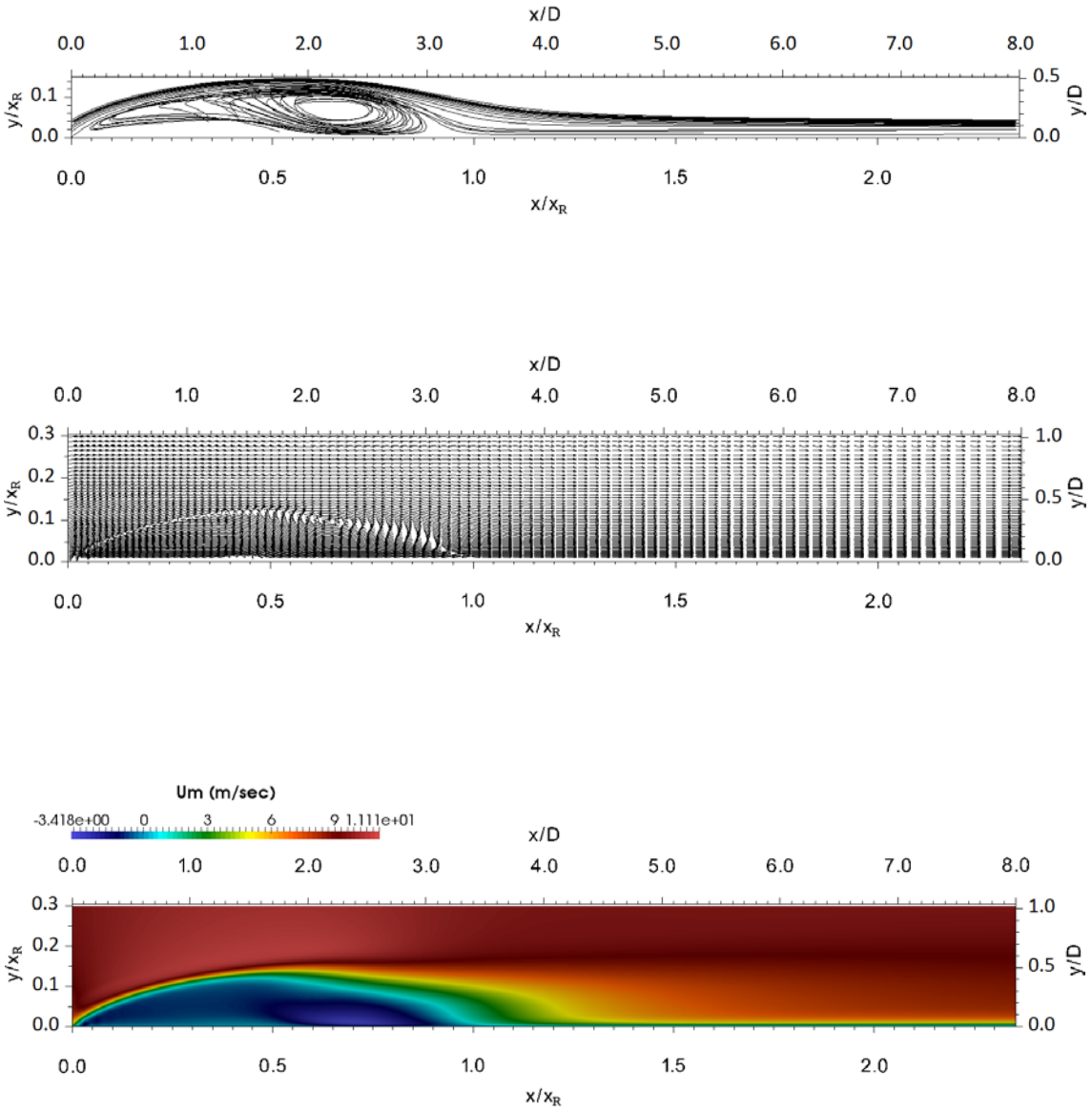

Fig. 4-29. Mean velocity streamlines, velocity vectors, and streamwise velocity contours for 3D_case1 with NFST

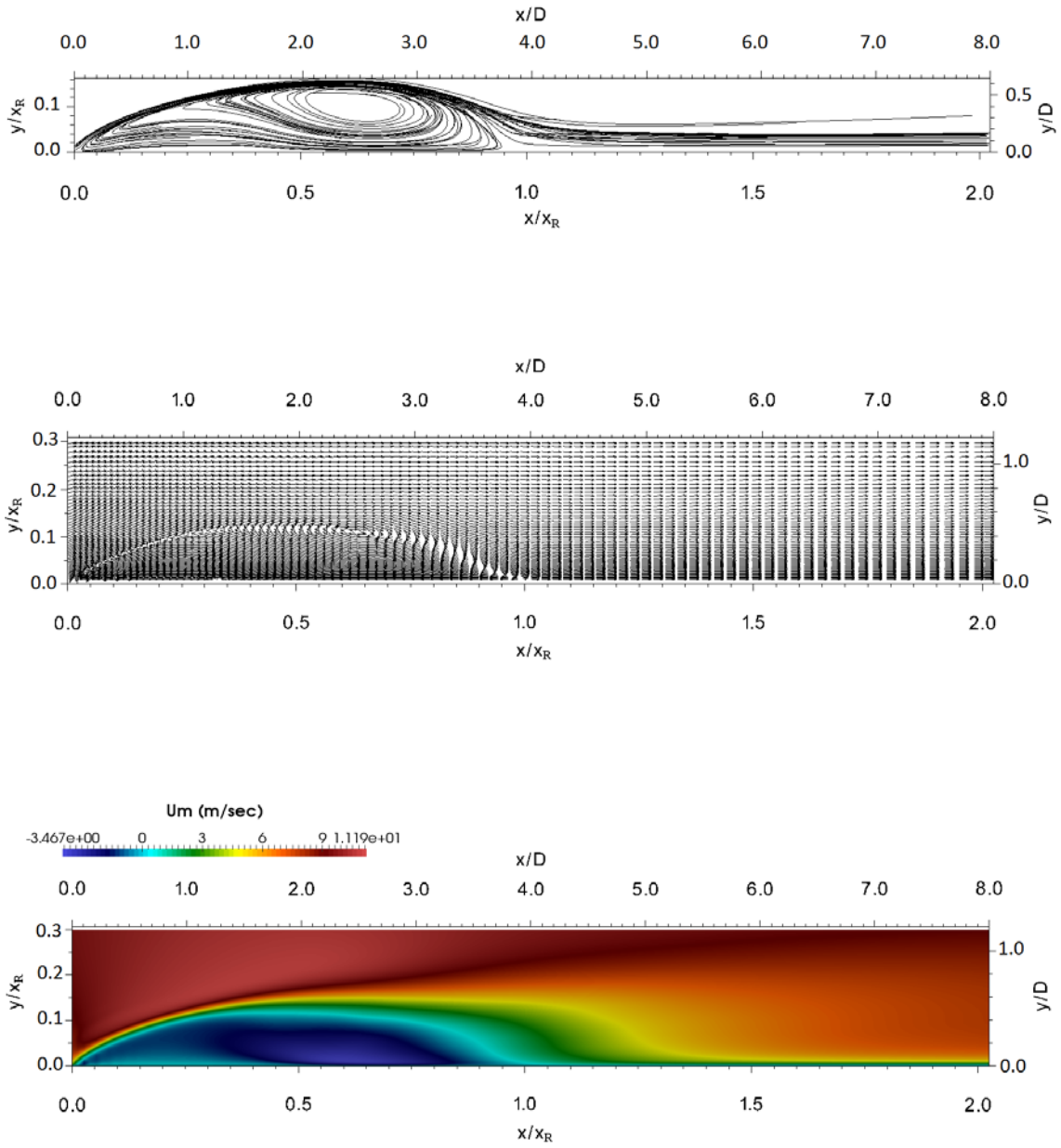

Fig. 4-30. Mean velocity streamlines, velocity vectors, and streamwise velocity contours for 3D_case2 with NFST

4.2.2 Transition process

The transition process for the flat plate and the other two geometries are illustrated in Figs. 4-31, 4-32, and 4-33 using the *x*-*y* plane of the instantaneous spanwise vorticity at the mid spanwise distance, as taken at three arbitrary times. The vorticity snapshot at different *z*-planes looks very similar.

At the beginning of the separation bubble that formed for all geometries, a two-dimensional laminar free shear layer starts at the geometry leading edge and develops with the formation of a two-dimensional spanwise vorticity. Instability in the free shear layer via an inviscid Kelvin-Helmholtz instability mechanism (will be shown in Chapter 5) leads to the formation of two-dimensional spanwise structures called Kelvin-Helmholtz rolls. The growth rates of a Kelvin-Helmholtz instability are typically much higher than the growth rates of a Tollmien-Schlichting instability in an attached boundary layer.

Further downstream, the free shear layer rolls up and Kelvin-Helmholtz rolls develop and distort to form the three-dimensional streamwise vortices associated with significant three-dimensional motions of the flow. Furthermore, at close to the reattachment location, the three-dimensional structures break down into smaller turbulent structures and shed to the turbulent reattached boundary layer, which develops rapidly.

In the case of three-dimensional geometries, four separation bubbles are constructed on the top, down, and sides surfaces of these geometries. Instantaneous magnitude vorticity isosurfaces for both three-dimensional geometries are plotted in Figs. 4-34 for 3D_case1 and 4-35 for 3D_case2. It is clear to show that there is a two-dimensional laminar separated layer that starts from the leading edge of each surface. Similarly, each of these layers distorts at the location where the transition starts. Distortion of the free shear layers grows gradually and at a specific location, these layers break down into a violent three-dimensional flow. Further downstream, the reattachment takes place and a turbulent reattached boundary layer develops toward the outlet boundary of the computational box.

It is observed that there is no considerable difference in locations of the flow development stages for each surface of each of the three-dimensional geometries. Further details about the flow development on the flat plate and on the top and side surfaces of both three-dimensional geometries are given in Chapter 7.

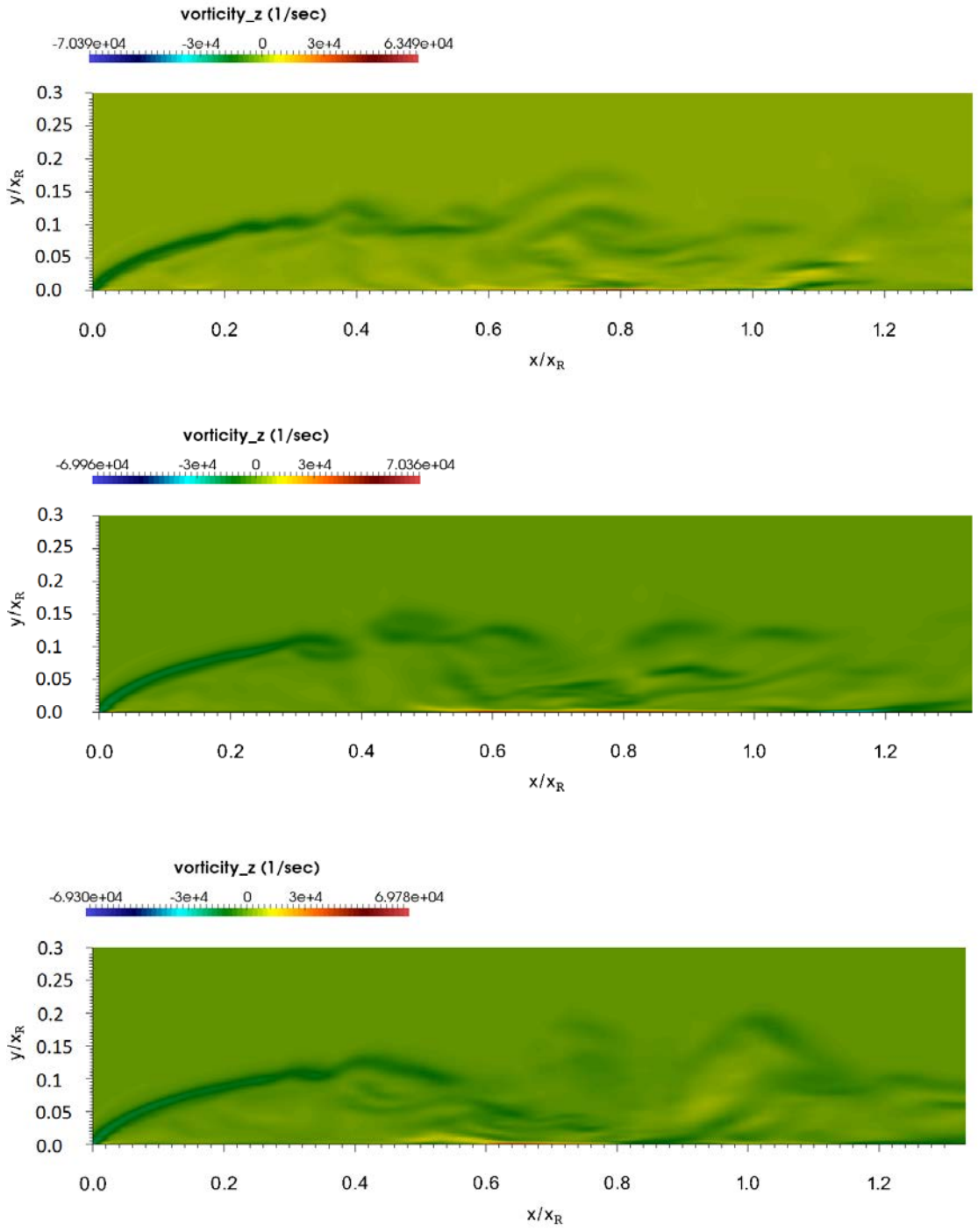

Fig. 4-31. The *x-y* plane of instantaneous spanwise vorticity at three arbitrary times for the flat plate with NFST

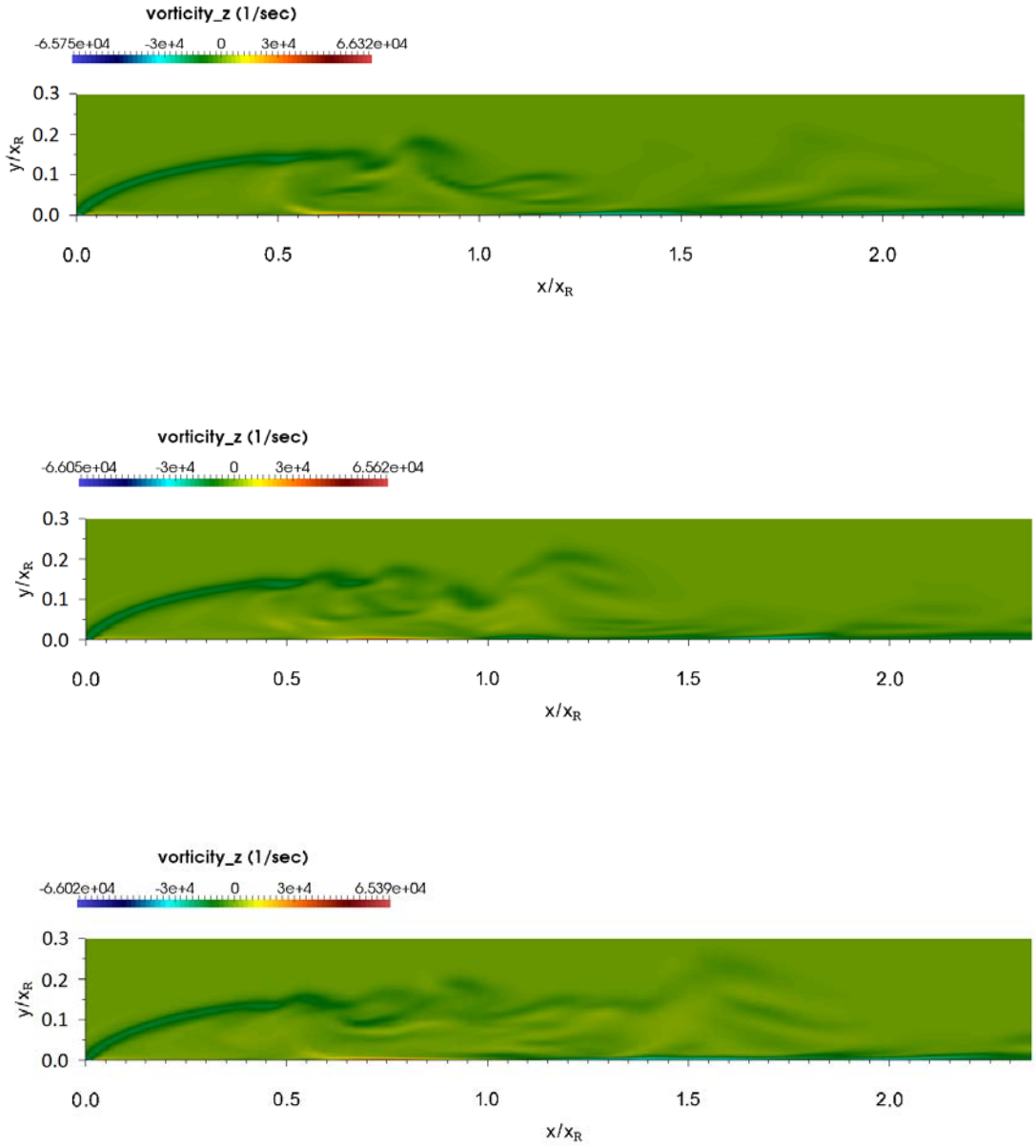

Fig. 4-32. The *x*-*y* plane of instantaneous spanwise vorticity at three arbitrary times for 3D_case1 with NFST

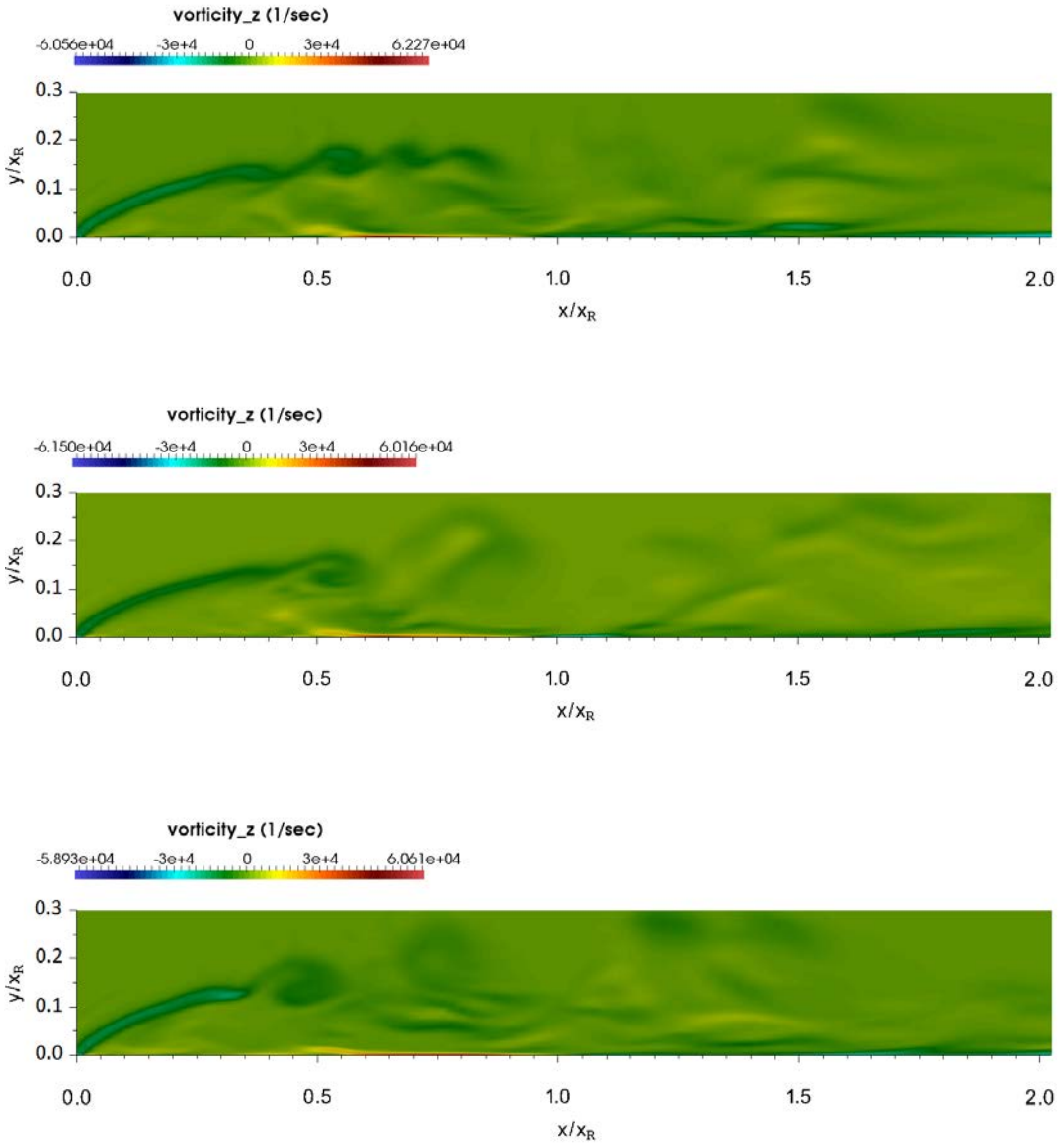

Fig. 4-33. The *x-y* plane of instantaneous spanwise vorticity at three arbitrary times for 3D_case2 with NFST

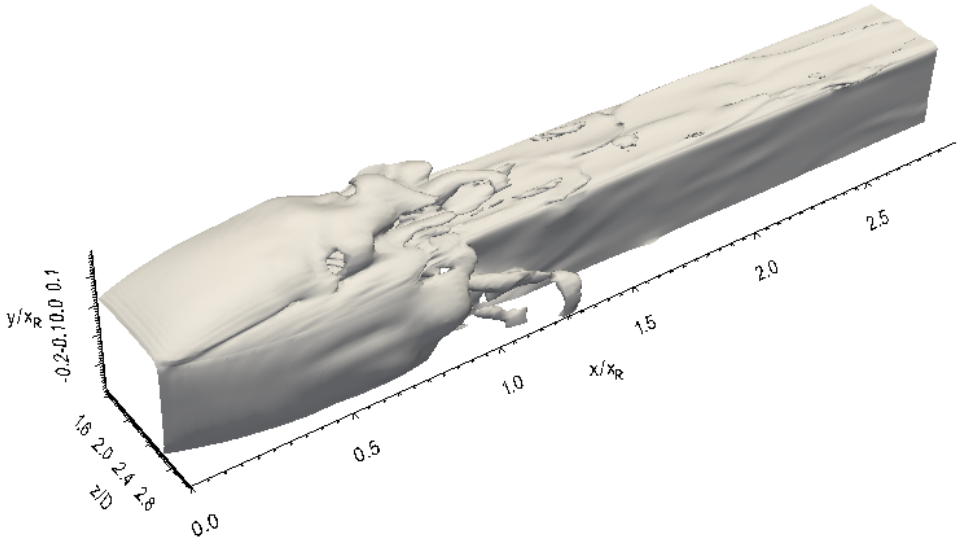

Fig. 4-34. Vorticity magnitude isosurface on the top and side surfaces of 3D_case1 with NFST

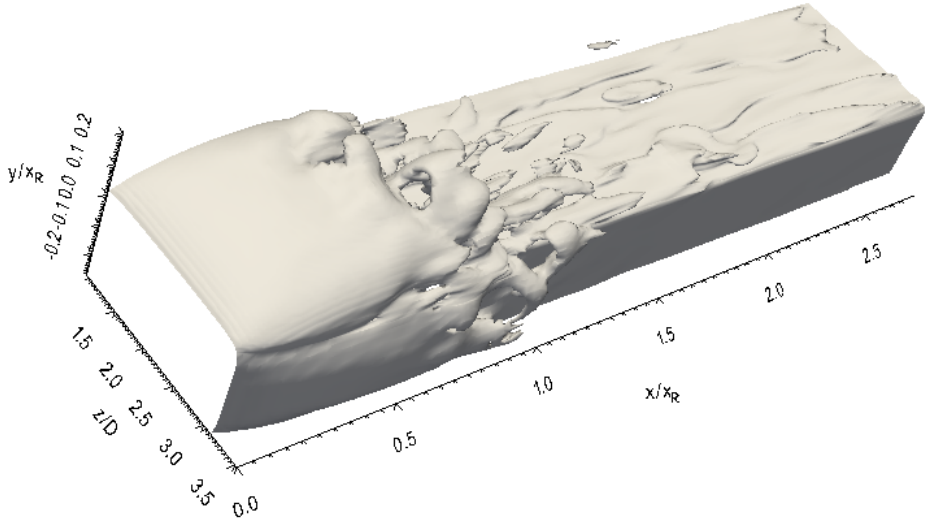

Fig. 4-35. Vorticity magnitude isosurface on the top and side surfaces of 3D_case2 with NFST

4.2.3 Instantaneous reattachment length

Instantaneous streamwise velocity contours in the *x*-*y* plane at *z*/*D* = 2, as taken at three arbitrary times for the flat plate, 3D_case1, and 3D_case2, are shown in Figs. 4-36, 4-37, and 4-38, respectively. It can be found that the instantaneous flow is particularly unsteady

around the time-averaged reattachment line and that the instantaneous reattachment point is highly random.

Variation of the instantaneous reattachment length (x_i) normalised by the mean reattachment length (x_R) is shown in Fig. 4-39 for the flat plate, Fig. 4-40 for 3D_case1 and Fig. 4-41 for 3D_case2. The maximum and minimum instantaneous reattachment lengths are approximately $x_{imax.} = 1.33x_R$ and $x_{imin.} = 0.81x_R$ for the flat plate, $x_{imax.} = 1.15x_R$ and $x_{imin} = 0.79x_R$ for 3D_case1, and $x_{imax.} = 1.22x_R$ and $x_{imin} = 0.75x_R$ for 3D_case2. Hence, the difference between the maximum and minimum instantaneous reattachment lengths is $0.52x_R$ (52% of the mean reattachment length) for the flat plate, $0.36x_R$ (36% of the mean reattachment length) for 3D_case1, and $0.47x_R$ (47% of the mean reattachment length) for 3D_case2.

Eaton and Johnston (1981) showed that there is a difference in the instantaneous reattachment length for a separated flow over a backward-facing step. Gartshore and Savill (1982) reported a variation in the instantaneous reattachment length for a separated flow over a flat plat combined with a splitter plate geometry. They found that the instantaneous reattachment length can be increased up to 50% of the mean length of the separation bubble.

The current ratios of the movement of the instantaneous reattachment length to the mean reattachment length for the flat plate and 3D_case2 are in good agreement with the results of Gartshore and Savill (1982) and Yang and Voke (2001).

However, the unsteadiness in the instantaneous reattachment length in both three-dimensional geometries is lower than that for the flat plate. In addition, the movement of the instantaneous reattachment length in 3D_case2 is greater than that in 3D_case1, indicating that the width to thickness ratio of the three-dimensional geometry may have an influence on the unsteadiness in the instantaneous reattachment length. This may be due to the difference in the shape and size of the existing flow structures being shed from the separation bubble in both geometries. Further details about flow structures are discussed in Chapter 7.

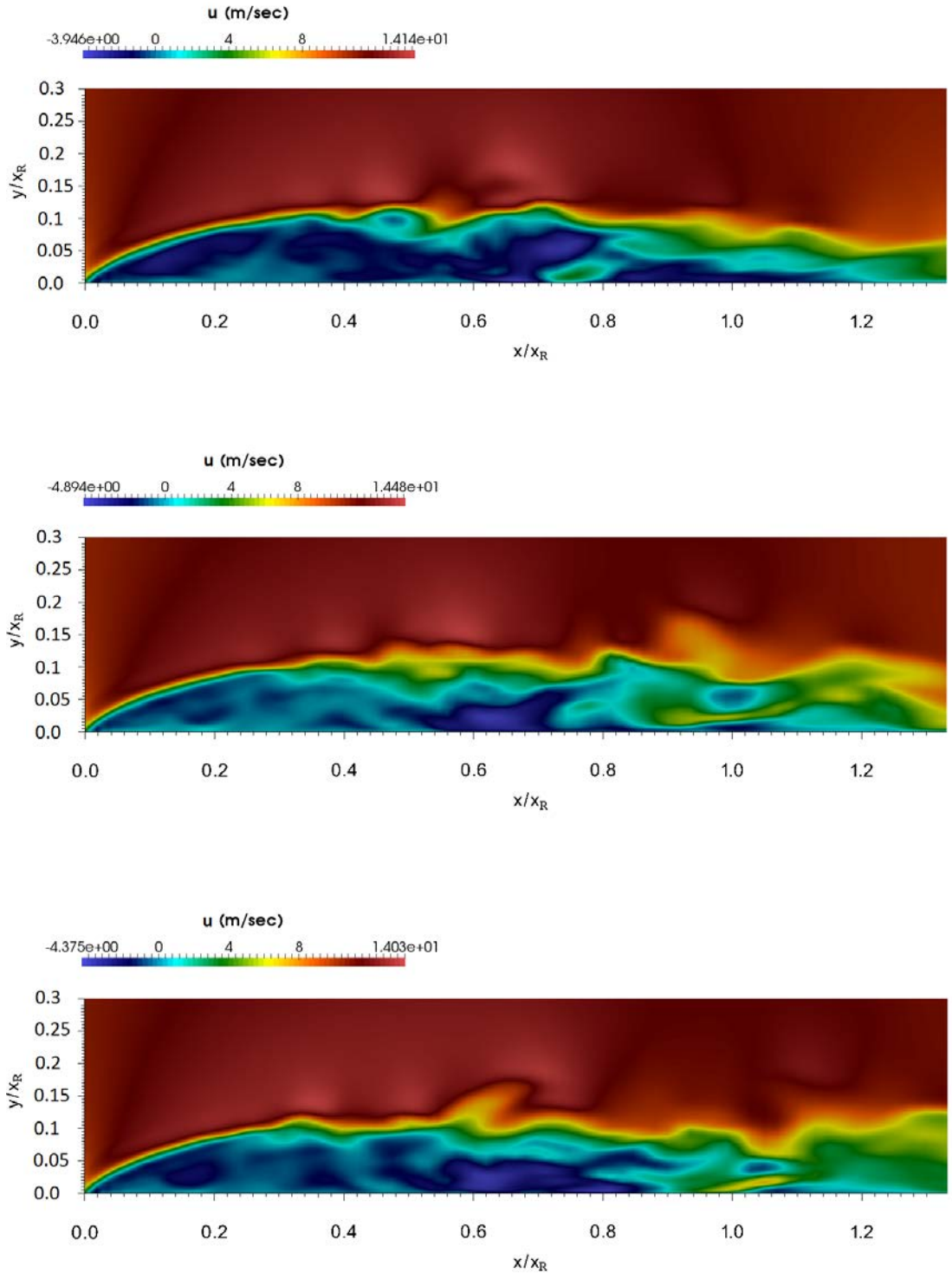

Fig. 4-36. Instantaneous streamwise velocity contours at three arbitrary times for the flat plate with NFST

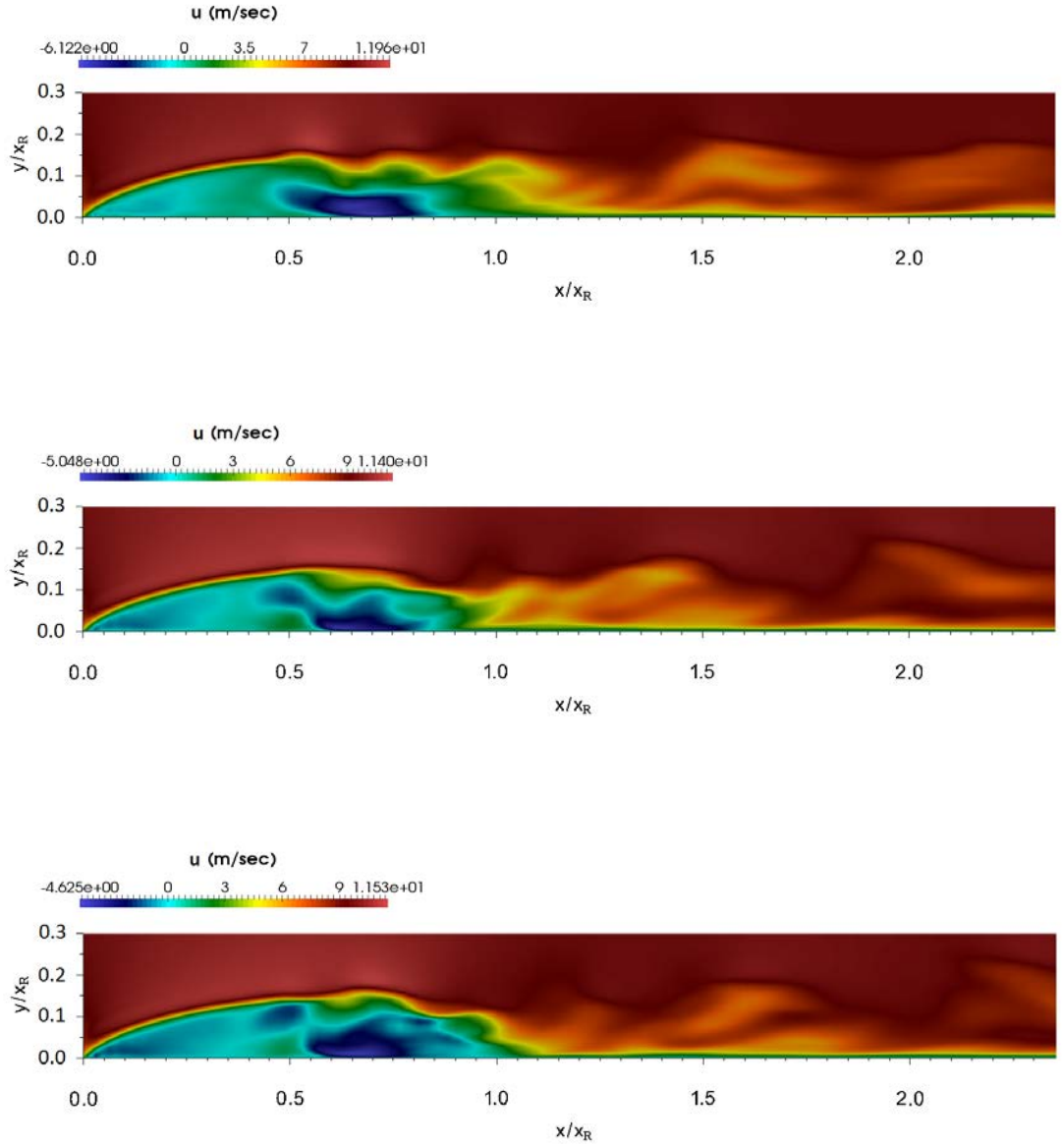

Fig. 4-37. Instantaneous streamwise velocity contours at three arbitrary times for 3D_case1 with NFST

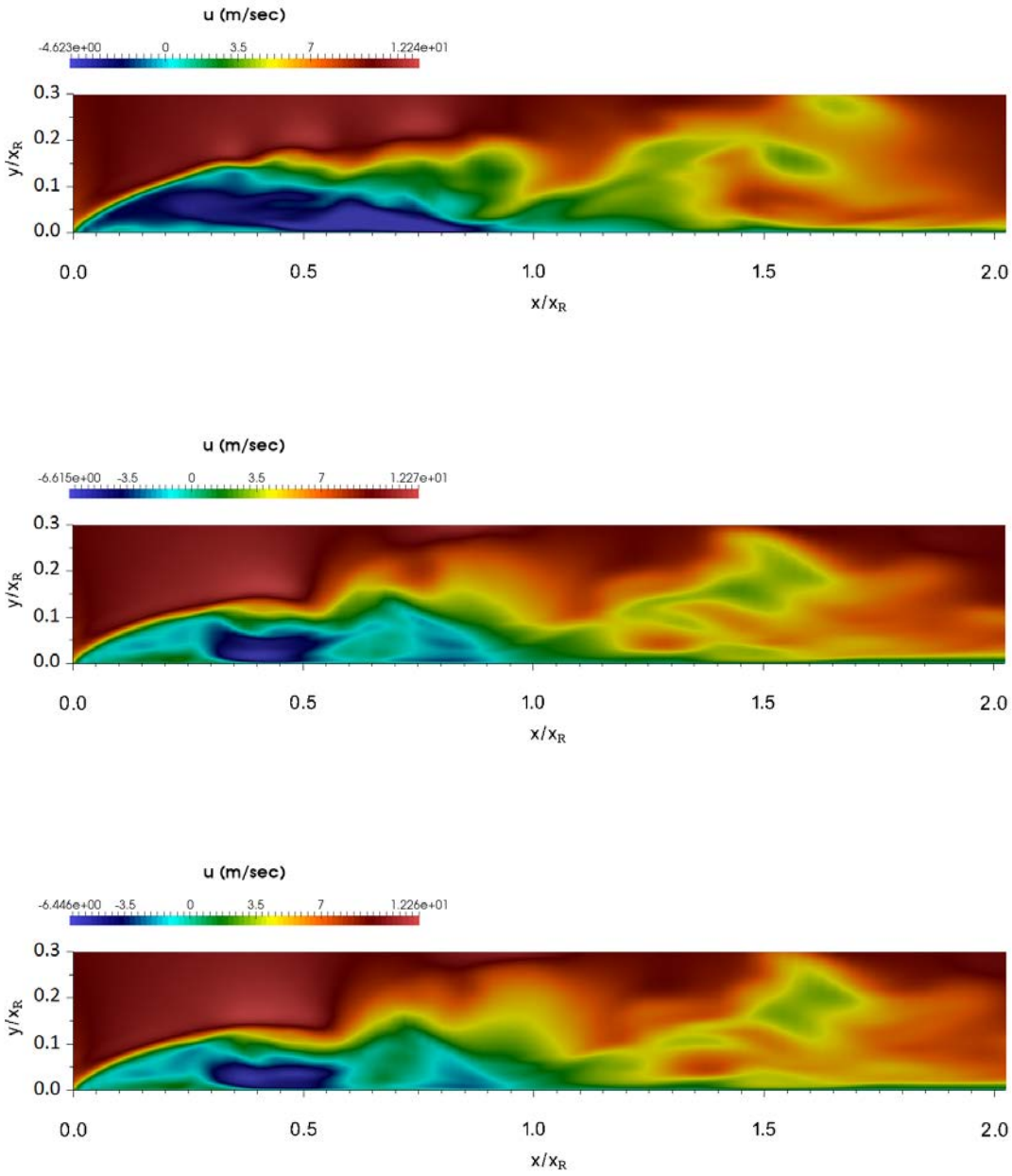

Fig. 4-38. Instantaneous streamwise velocity contours at three arbitrary times for 3D_case2 with NFST

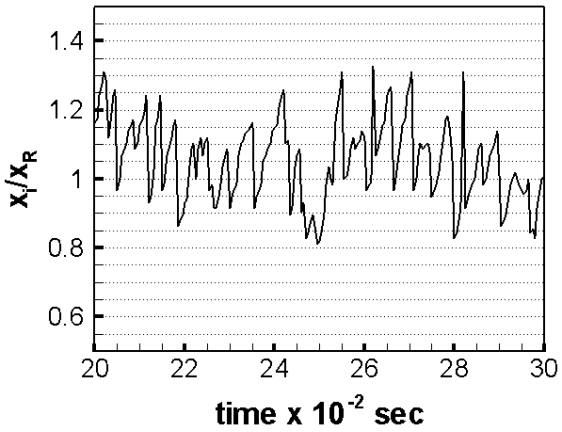

Fig. 4-39. Variation of the instantaneous reattachment length for the flat plate with NFST

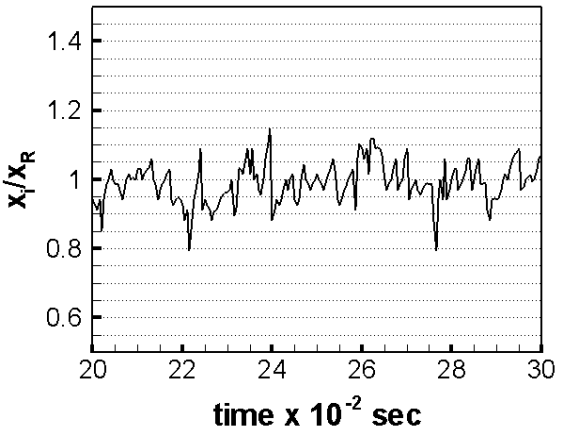

Fig. 4-40. Variation of the instantaneous reattachment length for 3D_case1 with NFST

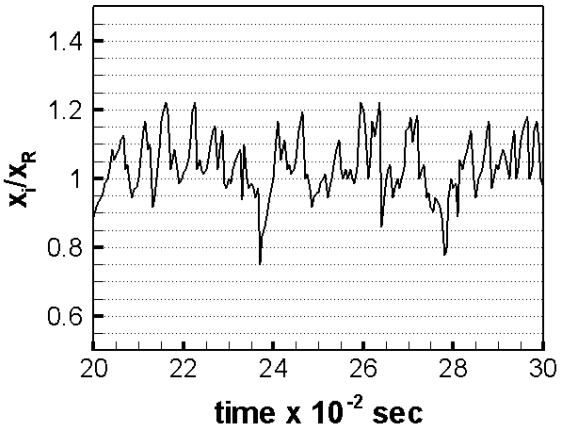

Fig. 4-41. Variation of the instantaneous reattachment length for 3D_case2 with NFST

4.3 Results for FST

4.3.1 Mean variables of the flow

The mean reattachment length for the flat plate in the presence of a 3.7% intensity of free stream turbulence is *4.2D*, as shown in Fig. 4-42 that respectively presents the profiles of the mean streamwise velocity at the first cell away from the wall for the flat plate. Hence, the current elevated intensity of free stream turbulence leads to a reduction in the mean length of the separation bubble by 30%, which is consistent with that reported in the literature.

Due to the presence of an elevated intensity of free stream turbulence, a reduction in the mean reattachment length has been reported in numerous studies. Nakamura and Ohys (1983; 1984; 1986) demonstrated this for a flow over different geometries. For a flow over a blunt flat plate, upstream movement of the location of the mean reattachment line was presented in Hillier and Cherry (1981b), Nakamura and Ozono 1987, Yang and Abdalla (2009), Kurelek and Yarusevych (2016). Castro and Haque (1988) observed the reduction of the mean reattachment length for a separated-reattached flow over a flat plate connected to a splitter plate. A similar observation was documented in Langari and Yang (2013) for the flow separation observed over a semi-circular leading edge of a flat plate.

For a separated-reattached flow induced by effect of an adverse pressure on a flat plate, the reduction in the mean reattachment length was documented by Kalter and Fernholz (2001), Halfon et al. (2004) and Simoni et al. (2017).

All these studies support the idea that an elevated intensity of free stream turbulence reduces the separation bubble mean length.

Abdalla and Yang (2009) reported a 14% reduction in the separation bubble mean length for a transitional separated-reattached flow on a blunt flat plate when intensity of free stream turbulence increased from less than 0.2% to 2%. For a similar flow but over a flat plate with a semi-circular leading edge, an increase in intensity of free stream turbulence from less than 0.2% to 5.6% reduced the mean reattachment length by about 60% in Langari and Yang (2013). This is considered to be in good agreement with the current study and Abdalla and Yang (2009) and Langari and Yang (2013) because the current elevated intensity of free stream turbulence (3.7%) is between the values used in these

two studies and the reduction of the current separation bubble mean length (30%) is also between the values reported in these two studies. So, it can be concluded that the current OF code can account for a high intensity of free stream turbulence and predict transitional separated-reattached flow accurately.

A comparison between the mean skin friction coefficient distribution for the flat plate with NFST and FST is presented in Fig. 4-43. It is clear that in the FST separation bubble, the dead air region distance is shorter, and the minimum mean skin friction coefficient is slightly lower than that with NFST.

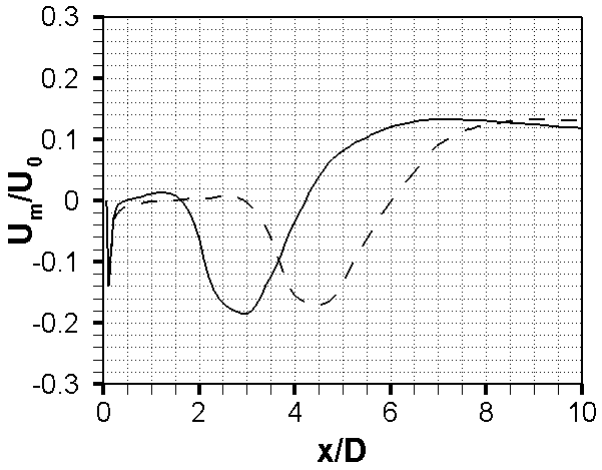

Fig. 4-42. Distribution of the mean streamwise velocity at the first cell away from the wall normalized by inflow velocity along the streamwise direction for the flat plate. With FST: solid line; with NFST: dashed line

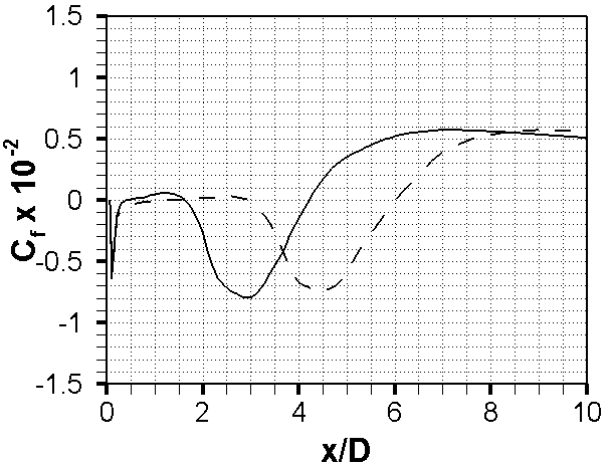

Fig. 4-43. Distribution of the mean skin friction coefficient along the streamwise direction for the flat plate. With FST: solid line; with NFST: dashed line

For 3D_case1, the mean reattachment length for FST becomes 2.5*D* with a reduction of 26.47% compared with NFST, as shown in Fig. 4-44 that presents the profile of the mean streamwise velocity at the first cell away from the wall for this geometry.

The distribution of the mean skin friction coefficient for 3D_case1, as shown in Fig. 4-45, shows that for FST the dead air region length is shorter, and the minimum mean skin friction coefficient is slightly lower, than those for NFST.

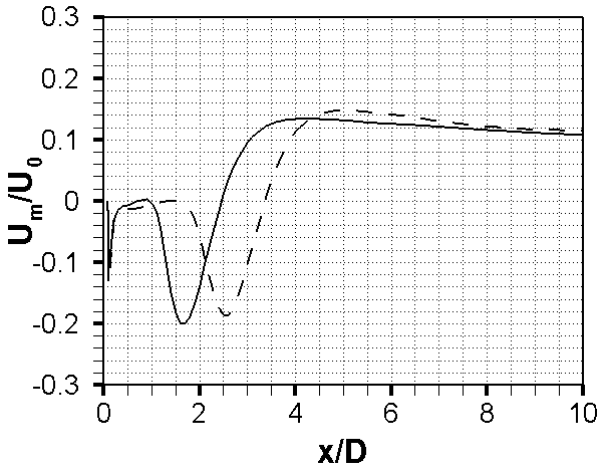

Fig. 4-44. Distribution of the mean streamwise velocity at the first cell away from the wall normalized by inflow velocity along the streamwise direction for 3D_case1. With FST: solid line; with NFST: dashed line

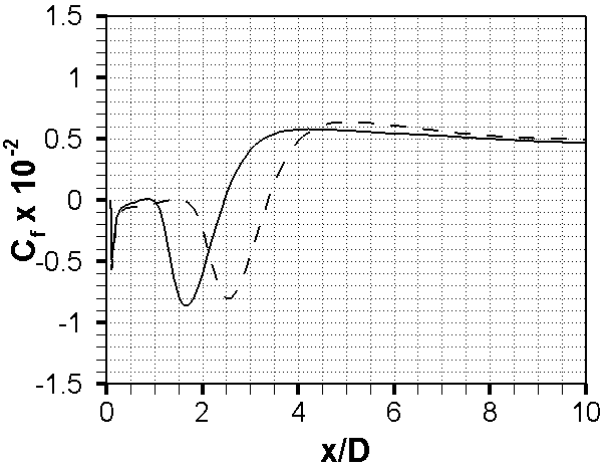

Fig. 4-45. Distribution of the mean skin friction coefficient along the streamwise direction for 3D_case1. With FST: solid line; with NFST: dashed line

For 3D_case2, the separation bubble mean length for FST reduces to 3.1*D*, i.e., there is a reduction in the mean reattachment length of about 21.5% compared with NFST as shown in Fig. 4-46, that presents the profile of the mean streamwise velocity at the first cell away from the wall.

The distribution of the mean skin friction coefficient for 3D_case2 with FST, as shown in Fig. 4-47, illustrates a reduction in the dead air region length and the minimum value of the mean skin friction coefficient compared with NFST.

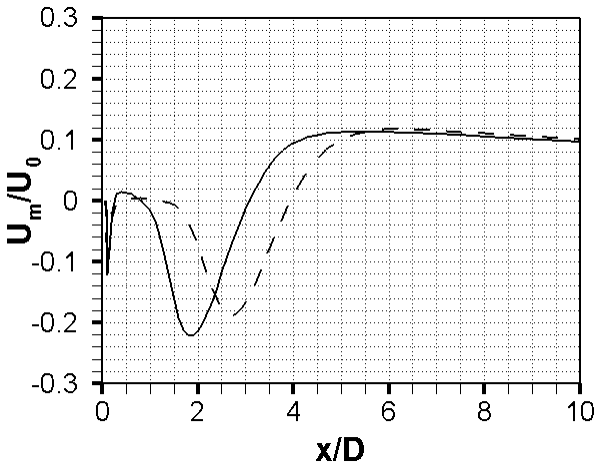

Fig. 4-46. Distribution of the mean streamwise velocity at the first cell away from the wall normalized by inflow velocity along the streamwise direction for 3D_case2. With FST: solid line; with NFST: dashed line

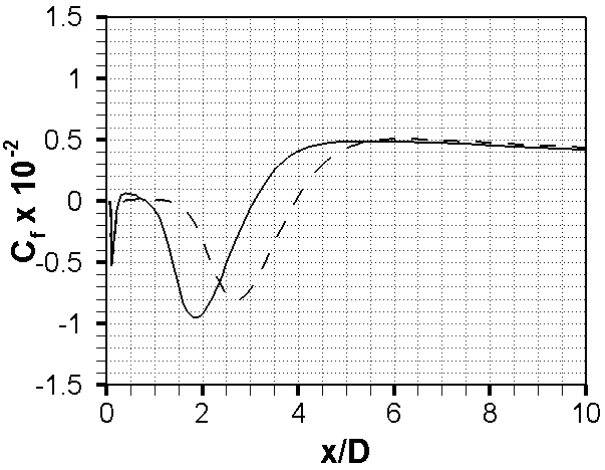

Fig. 4-47. Distribution of the mean skin friction coefficient along the streamwise direction for 3D_case2. With FST: solid line; with NFST: dashed line

In general, a 3.7% intensity of free stream turbulence decreases the separation by about 30% for the flat plate, 26.47% for 3D_case1 and 21.5% for 3D_case2. In addition, the presence of this high level of disturbances reduces the dead air region distance and also the minimum value of the mean skin friction coefficient for all geometries.

Time-averaged variables of the flow with FST are compared with the analogous results with NFST for all geometries as shown below. For the flat plate, a comparison with available published results is also carried out. This comparison is made with the results of simulations carried out by Yang and Abdalla (2009) and the experimental results recorded by Kiya and Sasaki (1983). Yang and Abdalla (2009) studied a transitional separation on a blunt flat plate with a 2% intensity of free stream turbulence and a Reynolds number of 6.5×10^3. For a similar geometry, Kiya and Sasaki (1983) performed an experiment for a turbulent separated-reattached flow with a Reynolds number of 26×10^3.

Mean variables for the flow associated with the flat plate are presented first in this section. As shown above, these variables are compared reasonably with the results of Yang and Abdalla (2009) and Kiya and Sasaki (1983) to confirm the veracity of the current OF code in simulating transitional separated-reattached flow in the presence of an elevated intensity of free stream turbulence.

Results for 3D_case1 and 3D_case2 are presented with a comparison between just FST and NFST due to absence of any equivalent results for such geometries in the literature.

It is worth pointing out that mean variables of the flow are presented here as functions of (y/x_R) at streamwise positions normalized by (x_R), i.e., comparisons are performed at the same non-dimensional streamwise locations (x/x_R) but not at the same geometric locations (x).

For the flat plate, the mean streamwise velocity normalized by the inlet velocity profiles at the six streamwise positions shown in Fig. 4-48. Despite the presence of a 3.7% intensity of free stream turbulence, there is no noticeable impact of this parameter on the mean streamwise velocity. In addition, it can be seen that there is good agreement between the current results and results of Yang and Abdalla (2009). However, in the first and second streamwise positions, the minimum mean streamwise velocity in Kiya and

Sasaki (1983) is lower than that reported in the current results as shown in Fig. 4-48. The reason for this difference is due to the separated turbulent flow in Kiya and Sasaki (1983) and also due to a higher Reynolds number. Moreover, the blockage ratio in Kiya and Sasaki (1983) was higher than the current blockage ratio.

The root mean square fluctuating streamwise velocity normalized by the inlet velocity (u'_{rms}/U_0) profiles for the flat plate are shown in Fig. 4-49. At all streamwise positions, the maximum value of (u'_{rms}) for FST is found to be higher than that for NFST. There is excellent agreement between the current results for FST and the results of Kiya and Sasaki (1983) at the first streamwise position as shown in Fig. 4-49. However, at the other streamwise positions, the current maximum value of (u'_{rms}) is higher than that reported by Kiya and Sasaki (1983). Furthermore, it can be seen that at $x/x_R = 0.4$ and beyond, the maximum value of (u'_{rms}) in Kiya and Sasaki (1983) tends towards the current maximum value of (u'_{rms}) for NFST more than for FST, especially, at $x/x_R = 0.4$ as shown in Fig. 4-49.

A comparison between current FST results and the data recorded by Yang and Abdalla (2009) shows that the current maximum values of (u'_{rms}) are higher than that in Yang and Abdalla (2009) at all streamwise positions, as shown in Fig. 4-49. This difference comes from different intensities of free stream turbulence in each of these studies. The current intensity of free stream turbulence is 3.7%, and is higher than that used by Yang and Abdalla (2009), which was 2%. Due to the higher intensity of free stream turbulence the flow becomes more chaotic in the current study, leading to an increase in intensity of (u'_{rms}). Overall, good agreement is found between both studies.

For all streamwise positions, the addition of a 3.7% intensity of free stream turbulence increases the maximum root mean square fluctuating wall-normal velocity (v'_{rms}) by about 10% - 40% as shown in Fig. 4-50.

It is worth pointing out that v'_{rms} was presented at just $x/x_R = 1$ in Kiya and Sasaki (1983) and Yang and Abdalla (2009). So, a comparison of v'_{rms} between these studies and the current study is carried out at just this location, as shown in Fig. 4-50. Despite the maximum value of the current v'_{rms} being higher than that reported in Kiya and Sasaki (1983), good agreement can be seen in Fig. 4-50 between the current results and results of Yang and Abdalla (2009).

In the current study, the maximum Reynolds shear stress increases by about 35% at x/x_R = 0.8 due to the increase of intensity of free stream turbulence as shown in Fig. 5-51.

Reynolds shear stress in Kiya and Sasaki (1983) and Yang and Abdalla (2009) was also presented at just x/x_R = 1, so a comparison of the Reynolds shear stress profile is performed at the same location only, as shown in Fig. 5-51. It can be seen that good agreement between the current results and results of Yang and Abdalla (2009) is achieved, while the maximum Reynolds shear stress in Kiya and Sasaki (1983) is lower than that in the current study by about 27% as shown in Fig. 5-51.

The comparison between the mean wall-normal velocity (V_m) from FST and NFST is shown in Fig. 5-52. Unfortunately, there are no studies available in the literature that present this variable as a basis for comparison. However, it can be seen that the maximum value V_m for FST is slightly higher than that for NFST at the first and second streamwise positions as shown in Fig. 5-52. At the other streamwise locations, the current study shows that there is no considerable difference in V_m when intensity of free stream turbulence increases to 3.7%.

In general, the good agreement demonstrated in the above comparisons carried out between the results of the current study and those of Kiya and Sasaki (1983) and Yang and Abdalla (2009) is encouraging in terms of extending our investigation to the combined effects of elevated intensity of free stream turbulence and change of geometry aspect ratio on transitional separated-reattached flow.

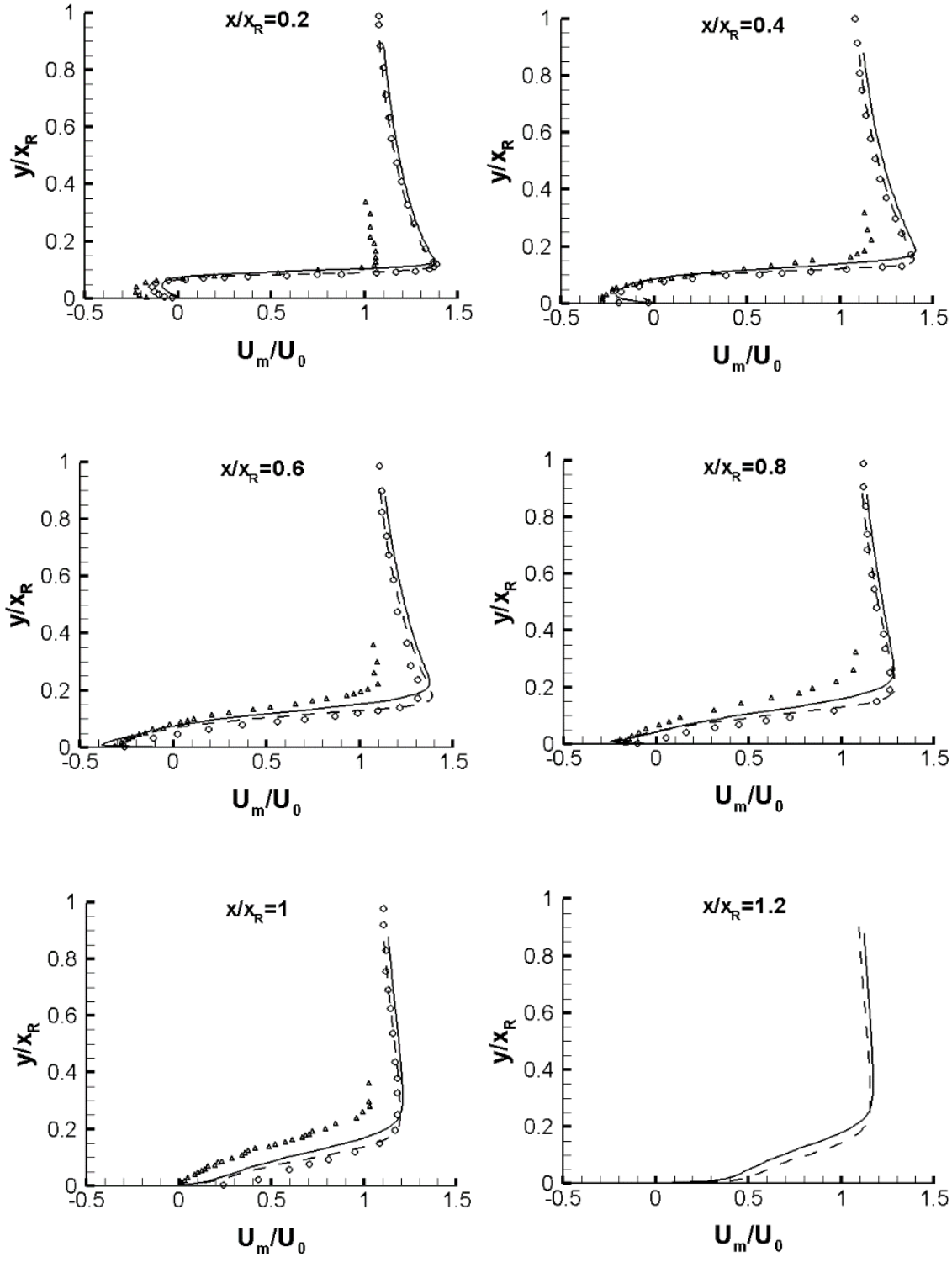

Fig. 4-48. Profiles of the mean streamwise velocity for the flat plate. Present results with FST: solid line; present results with NFST: dashed line; Yang and Abdalla (2009) with 2% FST: circles; Kiya and Sasaki (1983): triangles

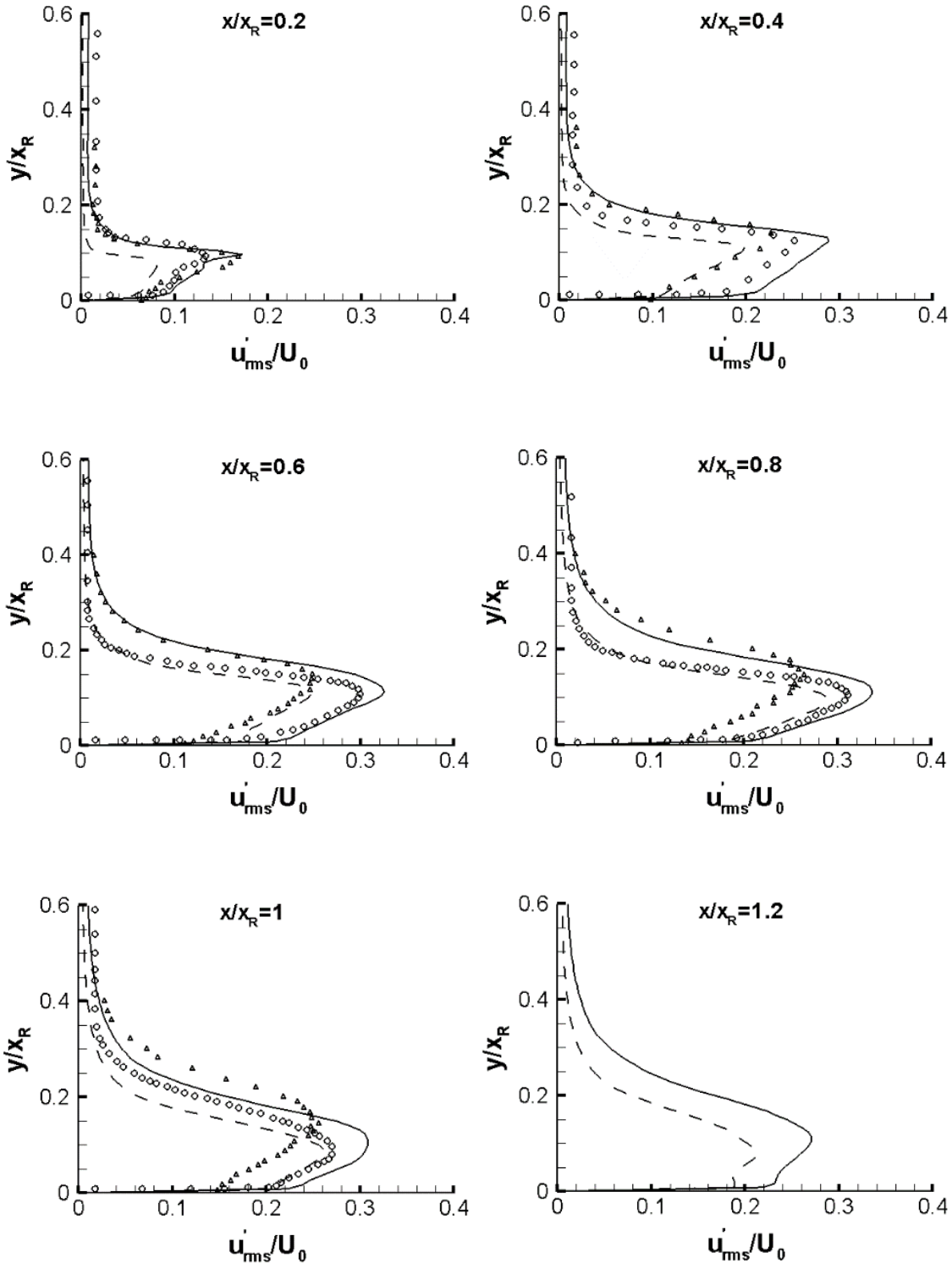

Fig. 4-49. Profiles of the root mean square fluctuating streamwise velocity for the flat plate. Present results with FST: solid line; present results with NFST: dashed line; Yang and Abdalla (2009) with 2% FST: circles; Kiya and Sasaki (1983): triangles

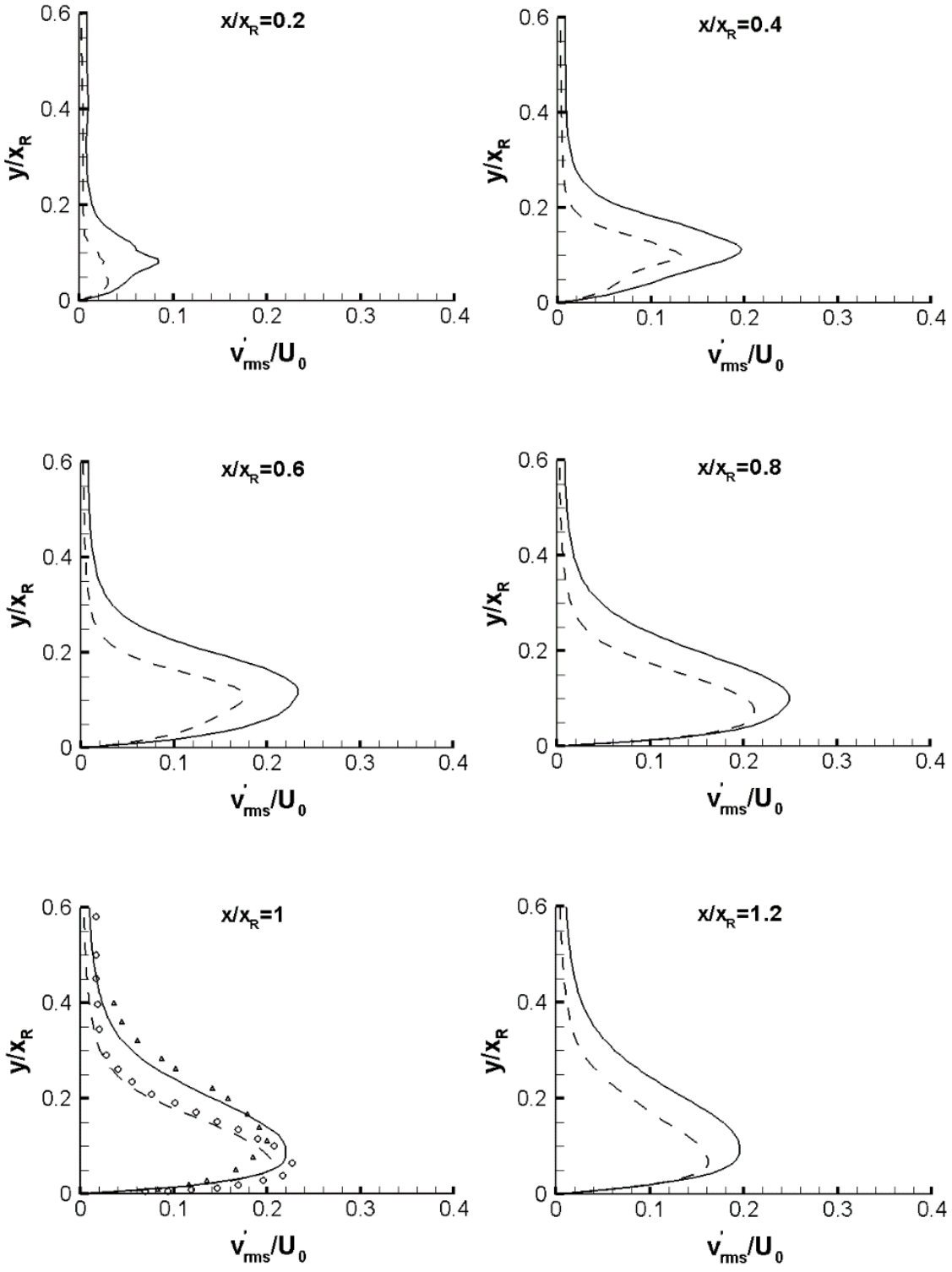

Fig. 4-50. Profiles of the root mean square fluctuating wall-normal velocity for the flat plate. Present results with FST: solid line; present results with NFST: dashed line; Yang and Abdalla (2009) with 2% FST: circles; Kiya and Sasaki (1983): triangles

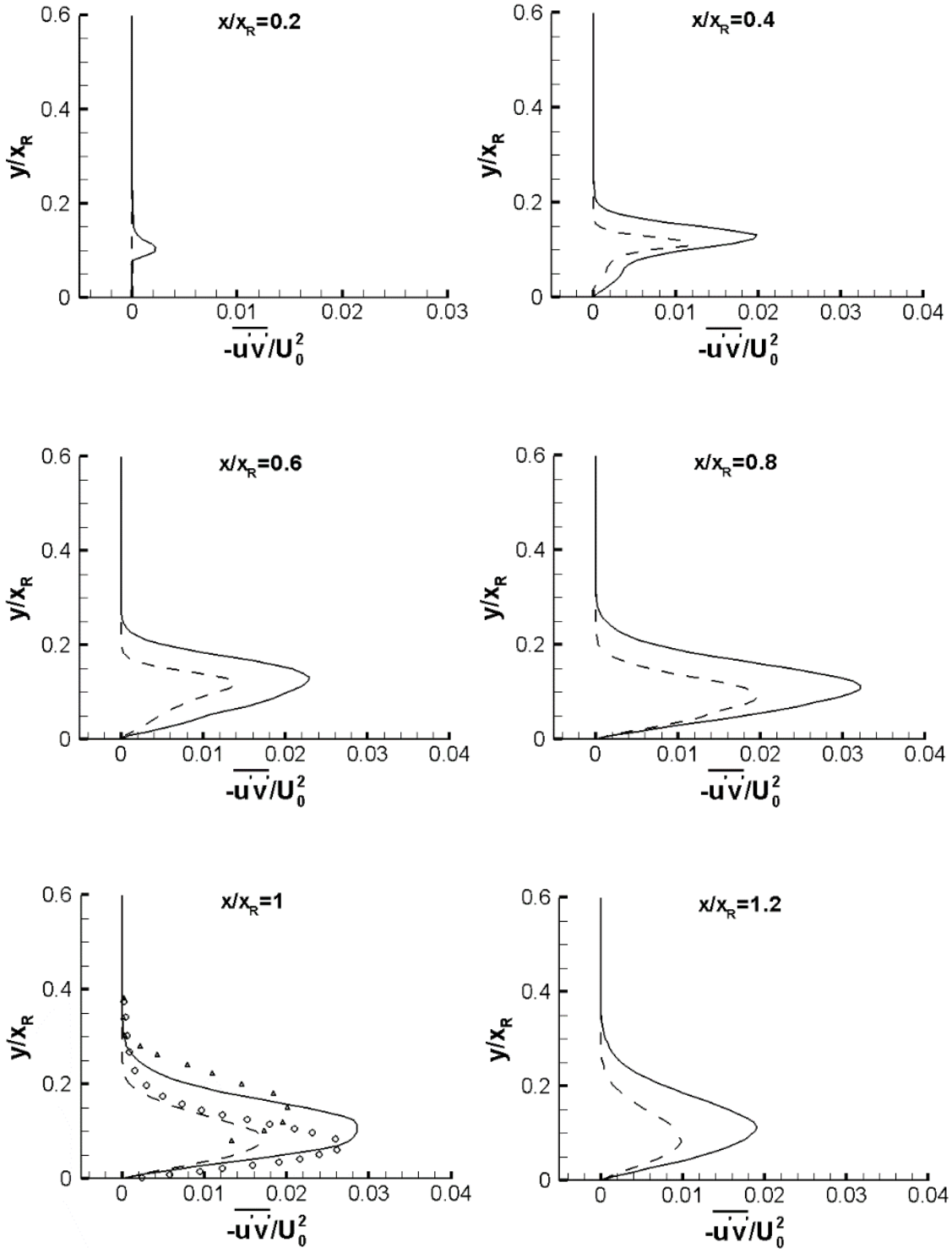

Fig. 4-51. Profiles of the Reynolds shear stress for the flat plate. Present results with FST: solid line; present results with NFST: dashed line; Yang and Abdalla (2009) with 2% FST: circles; Kiya and Sasaki (1983): triangles

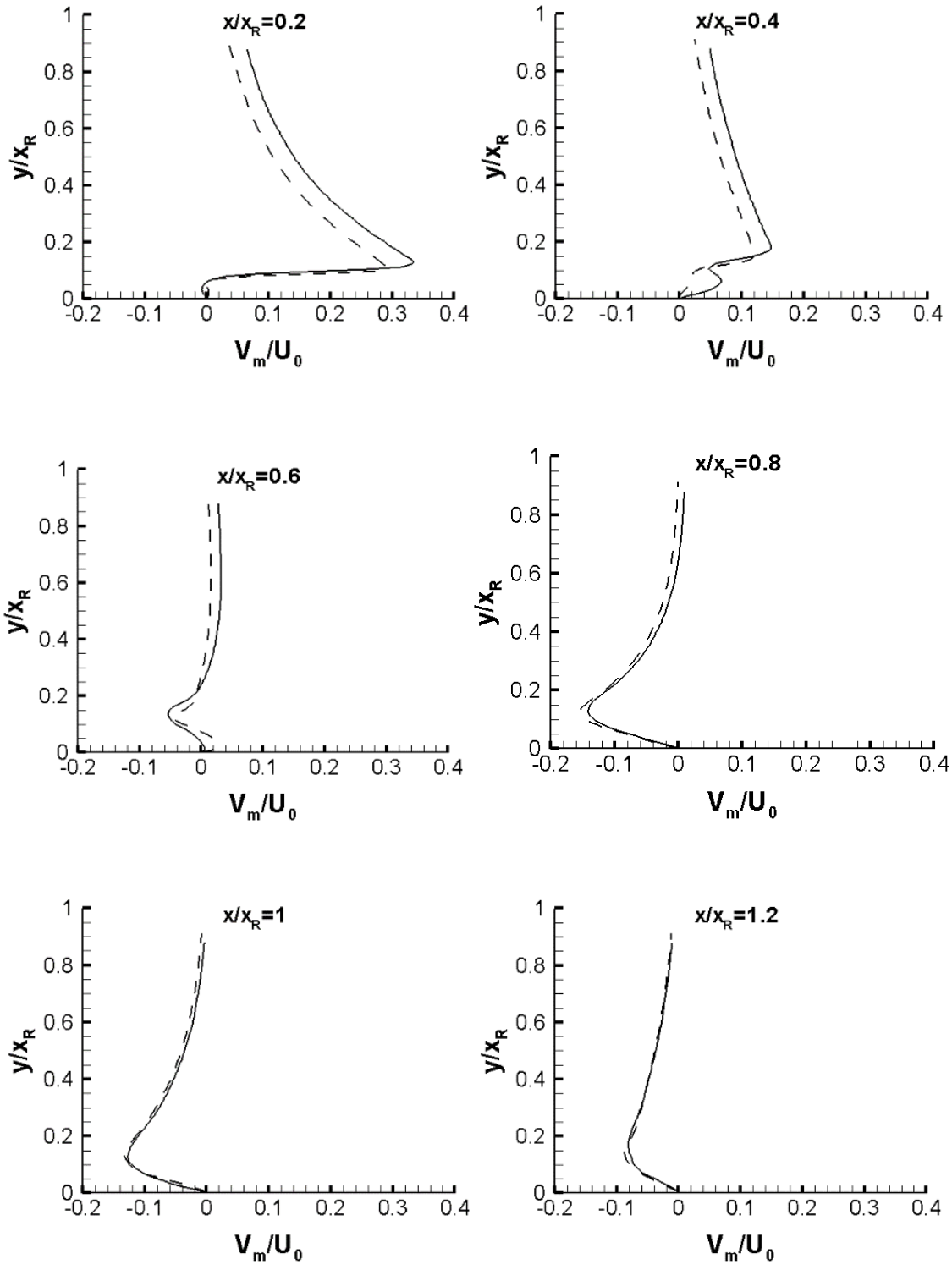

Fig. 4-52. Profiles of the mean wall-normal velocity for the flat plate. With FST: solid line; with NFST: dashed line

The mean streamwise velocities calculated from FST and NFST are presented in Fig. 4-53 for 3D_case1 and Fig. 4-54 for 3D_case2. For both geometries, there is no a noticeable difference in the mean streamwise velocities with increasing intensity of free stream turbulence.

For both three-dimensional geometries, an increase in intensity of free stream turbulence leads to only slight difference in the maximum value of the mean wall-normal velocity, as shown in Fig. 4-55 for 3D_case1 and Fig. 4-56 for 3D_case2.

An increase in the maximum Reynolds stresses, due to the presence of a 3.7% intensity of free stream turbulence, for 3D_case1 is lower than that in 3D_case2 at all streamwise positions. As an example, the increase in u'_{rms} is about 18% at $x/x_R = 0.8$ for 3D_case1 and about 22% for 3D_case2 at the same location, as shown in Fig. 4-57 for 3D_case1 and Fig. 4-58 for 3D_case2, where a comparison between u'_{rms} with high and low levels of intensity of free stream turbulence is illustrated.

For v'_{rms}, it can be observed that the increase in the maximum magnitude of this variable for 3D_case1 is about 14% at $x/x_R = 0.8$, as shown in Fig. 4-59. For 3D_case2 at the same position, the increase in the maximum v'_{rms} is about 30% as shown in Fig. 4-60.

At $x/x_R = 0.8$, the increase in the Reynolds shear stress for 3D_case1 is about 35% as shown in Fig. 4-61, and about 60% for 3D_case2 as shown in Fig. 6-62.

Overall, for FST it can be seen that the maximum Reynolds normal and shear stresses for both three-dimensional geometries are lower than those presented for the flat plate by about 25% - 35%. Generally speaking, for the comparisons carried out for time-averaged variables of the flow with and without a high intensity of free stream turbulence for all geometries there is no noticeable increase in the mean velocities, whilst, the Reynolds stresses increase considerably.

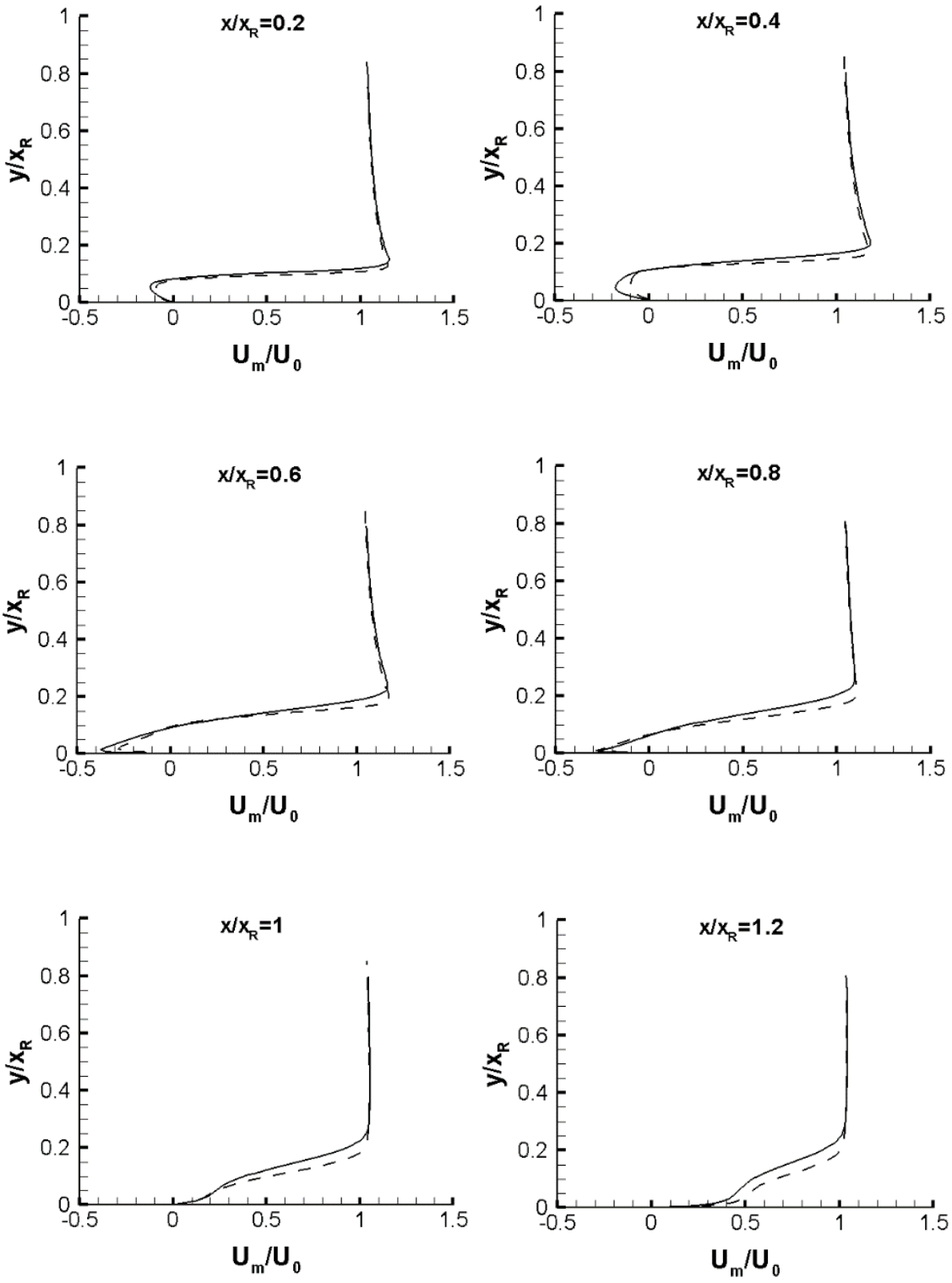

Fig. 4-53. Profiles of the mean streamwise velocity for 3D_case1. With FST: solid line; with NFST: dashed line

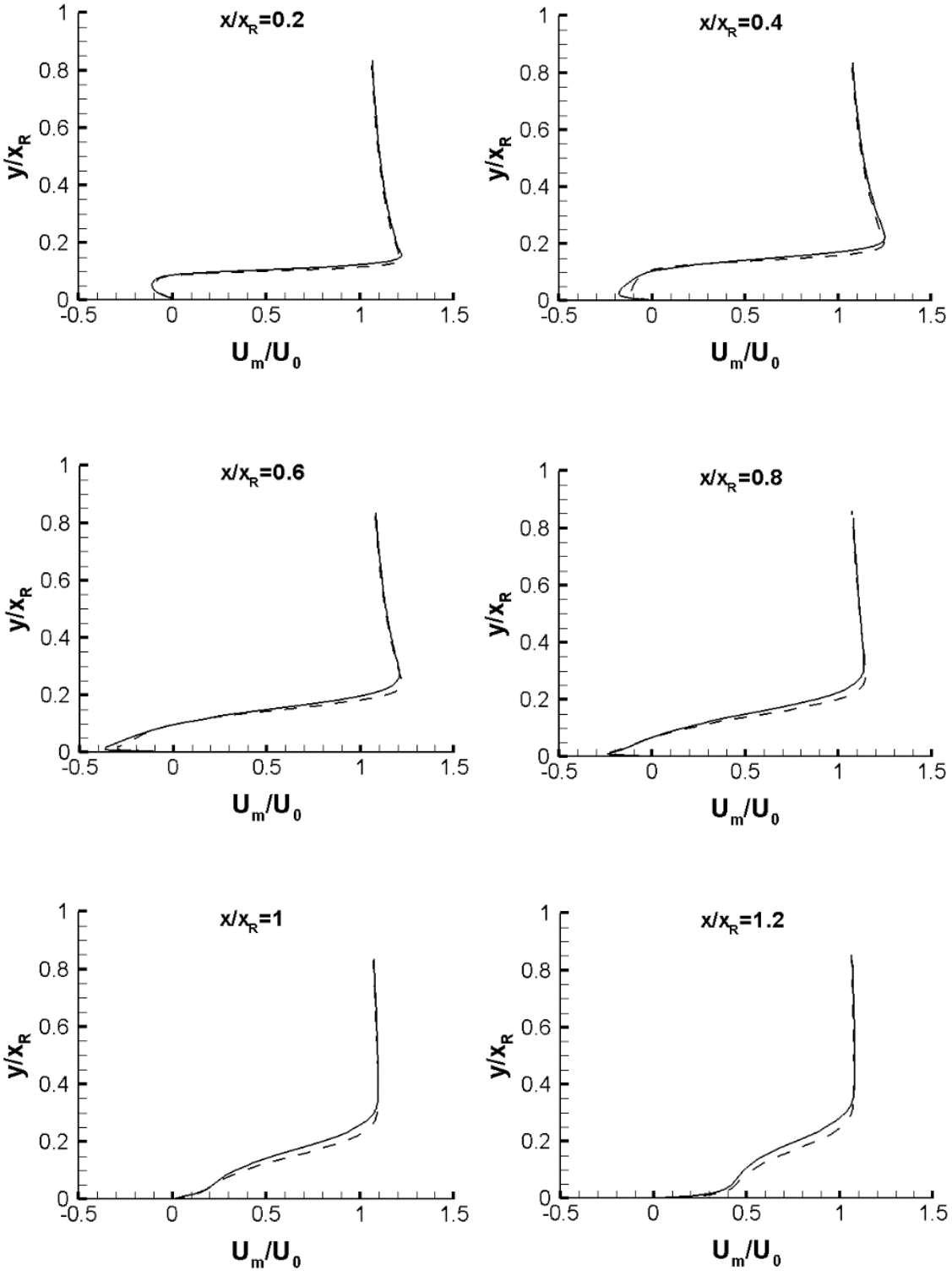

Fig. 4-54. Profiles of the mean streamwise velocity for 3D_case2. With FST: solid line; with NFST: dashed line

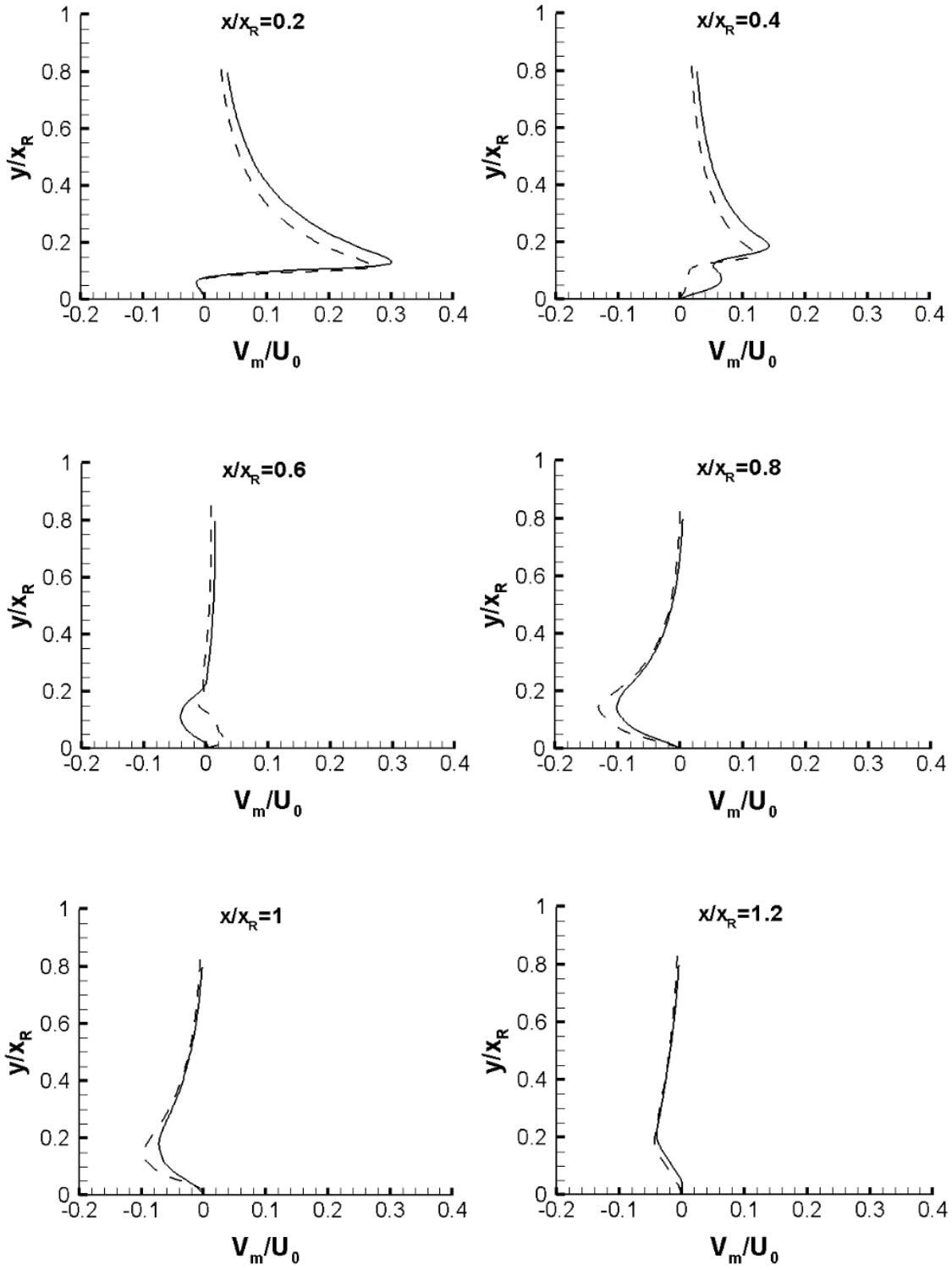

Fig. 4-55. Profiles of the mean wall-normal velocity for 3D_case1. With FST: solid line; with NFST: dashed line

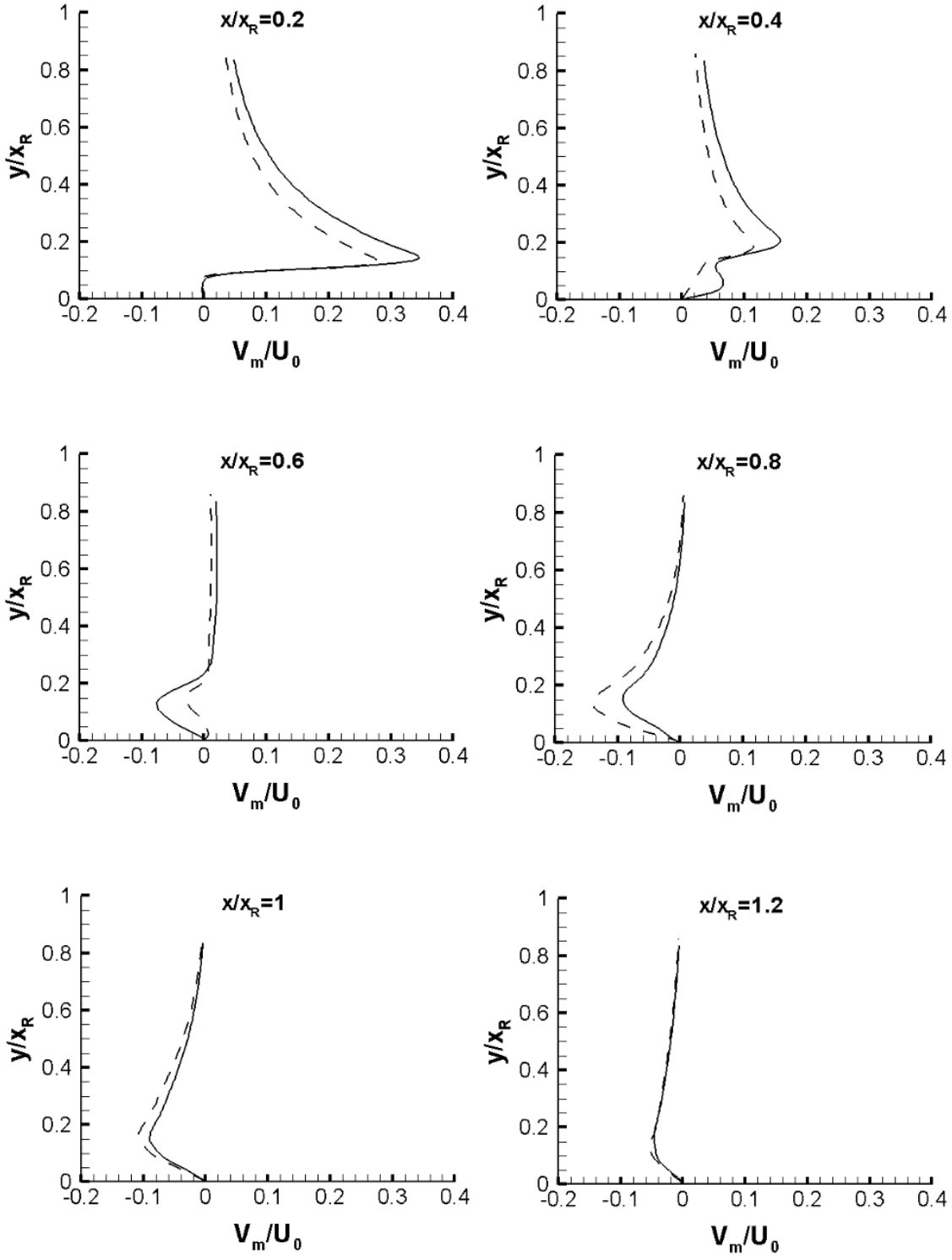

Fig. 4-56. Profiles of the mean wall-normal velocity for 3D_case2. With FST: solid line; with NFST: dashed line

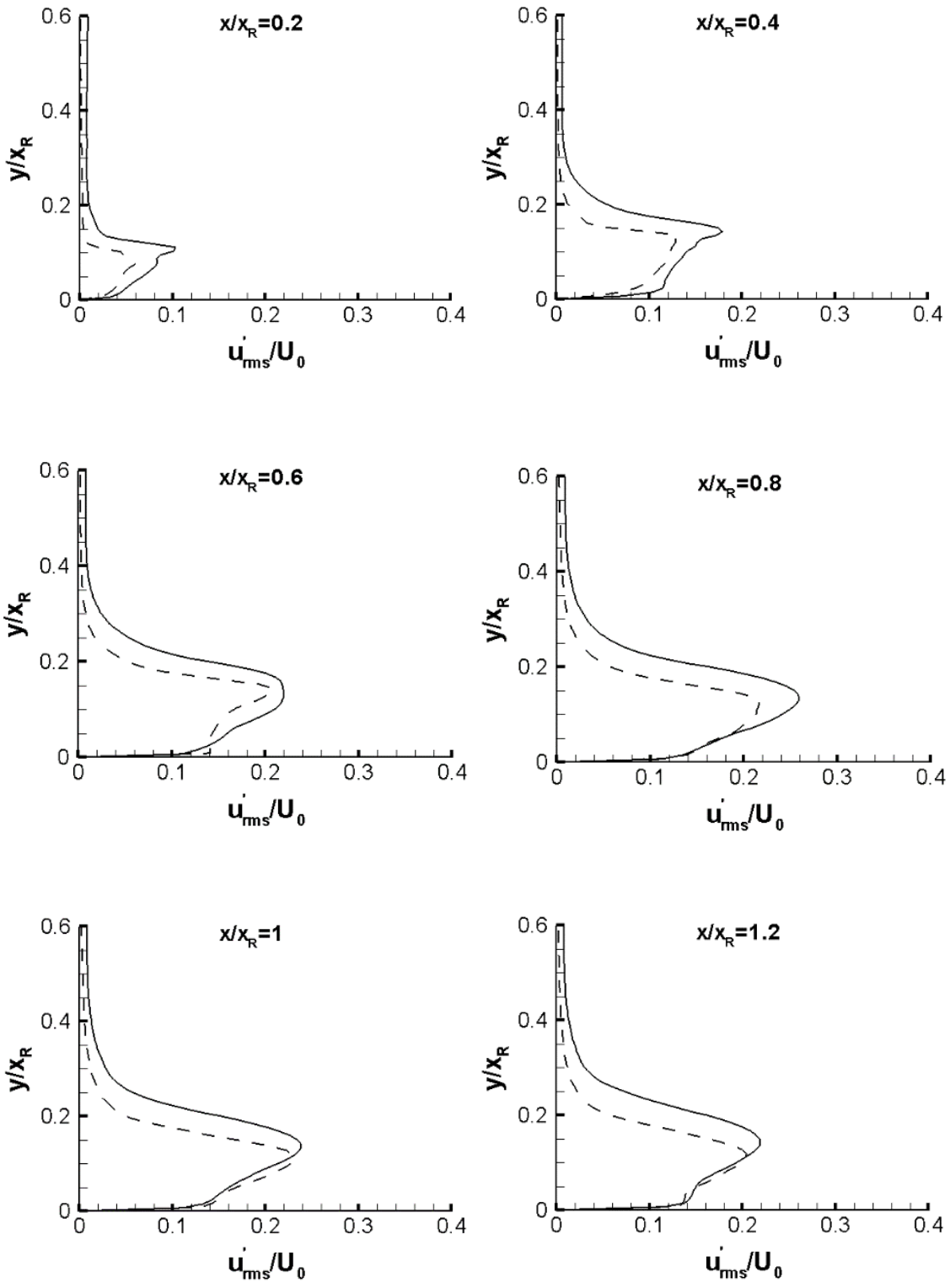

Fig. 4-57. Profiles of the root mean square fluctuating streamwise velocity for 3D_case1. With FST: solid line; with NFST: dashed line

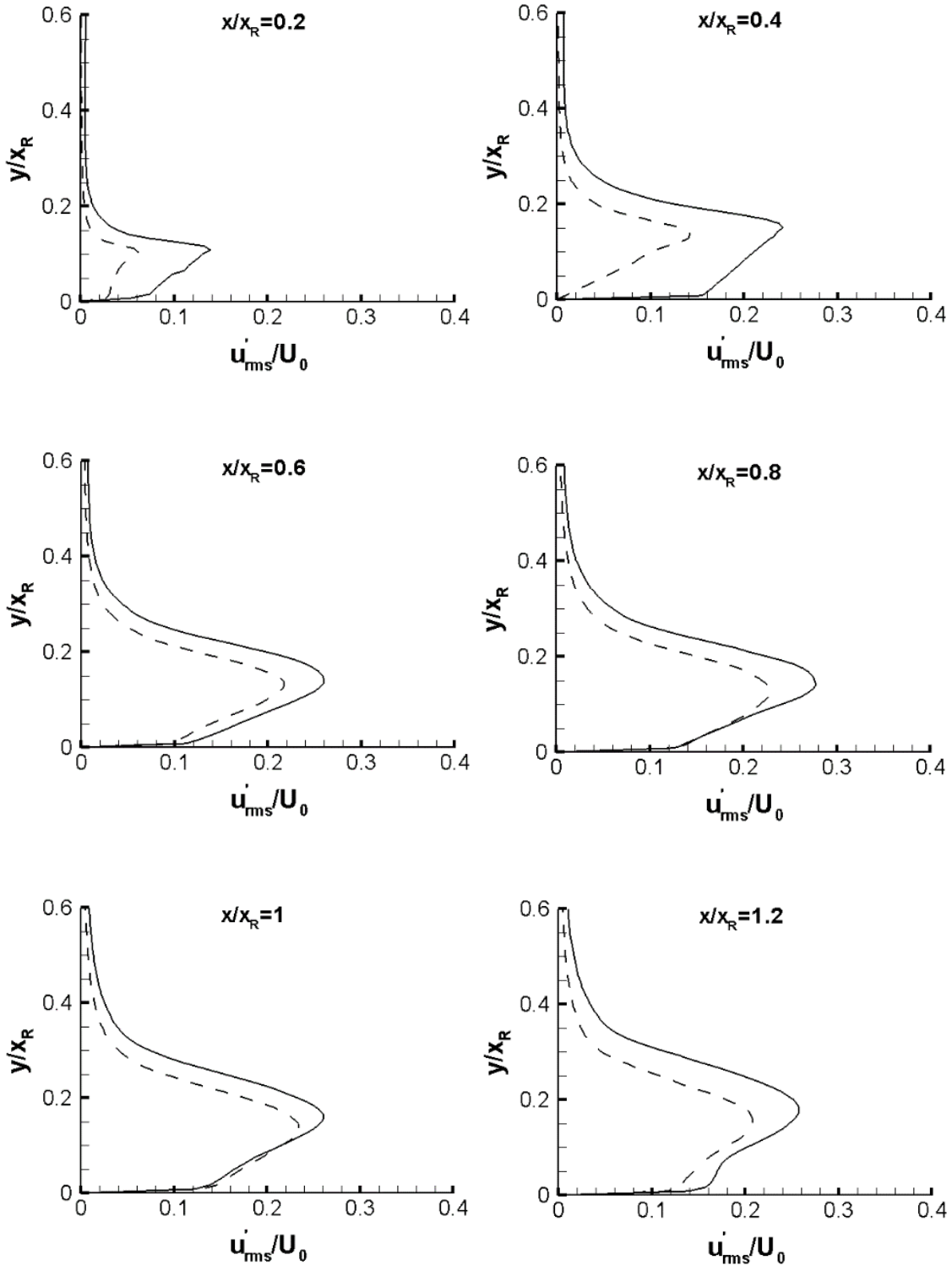

Fig. 4-58. Profiles of the root mean square fluctuating streamwise velocity for 3D_case2. With FST: solid line; with NFST: dashed line

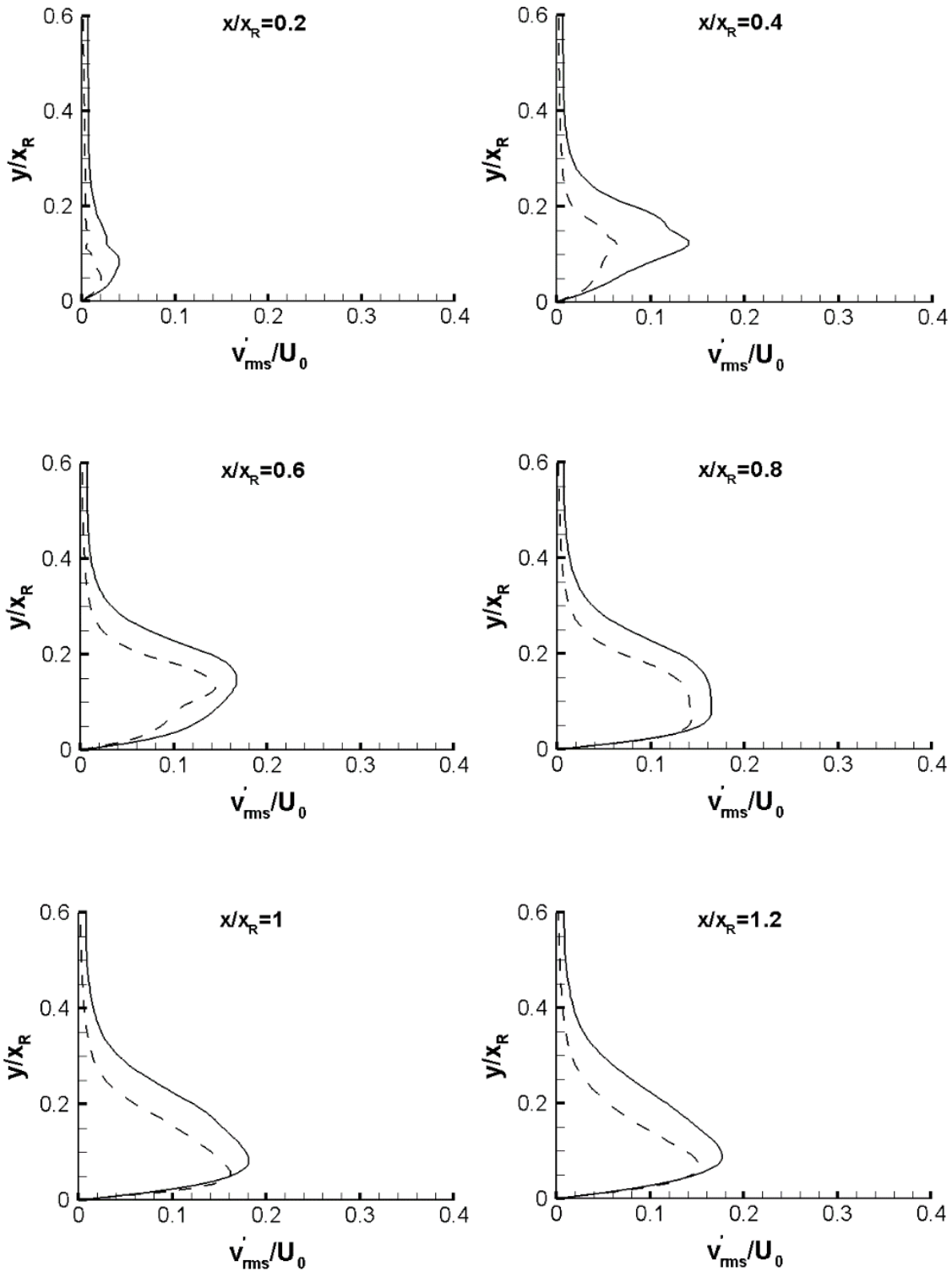

Fig. 4-59. Profiles of the root mean square fluctuating wall-normal velocity for 3D_case1. With FST: solid line; with NFST: dashed line

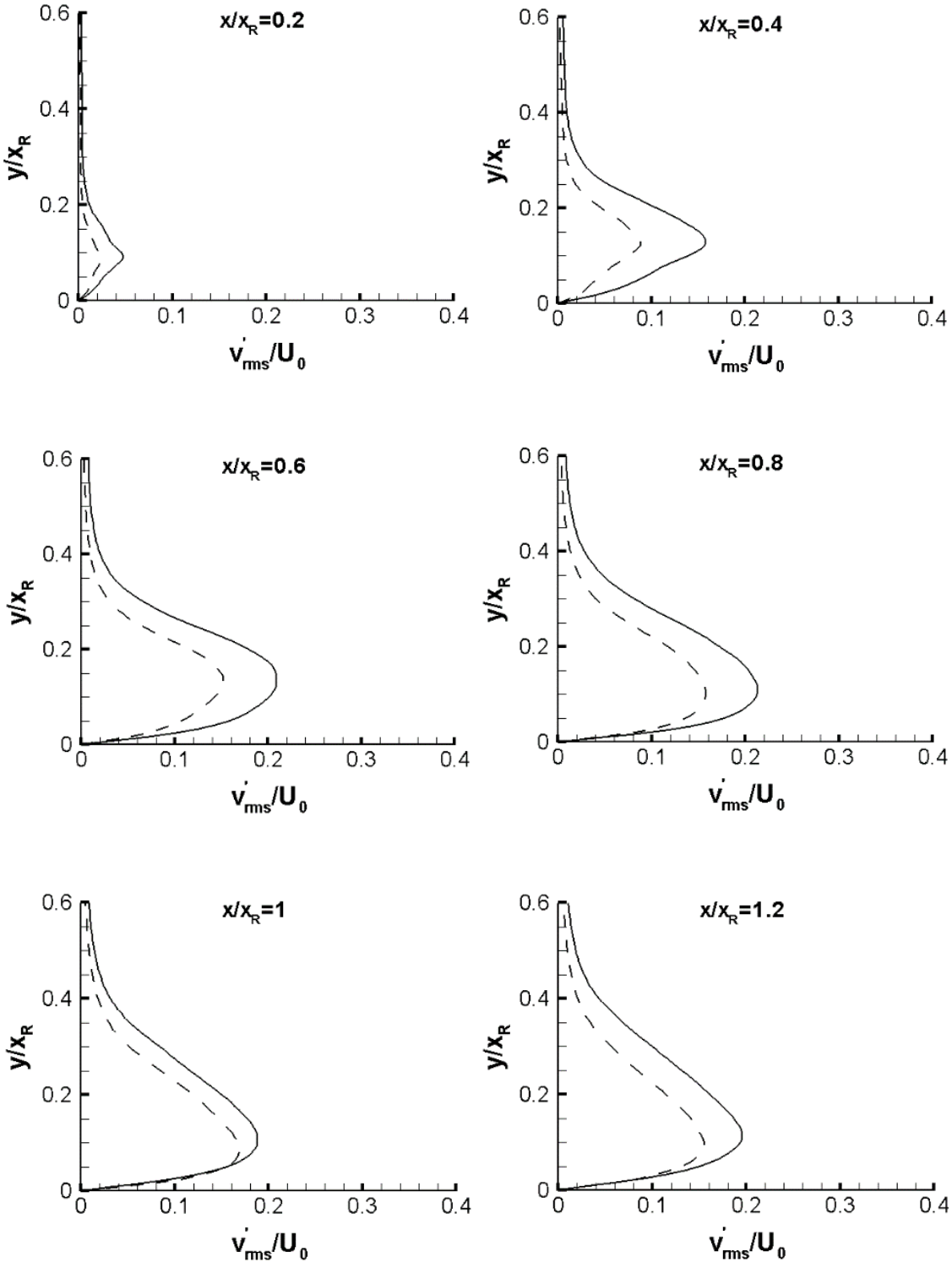

Fig. 4-60. Profiles of the root mean square fluctuating wall-normal velocity for 3D_case2. With FST: solid line; with NFST: dashed line

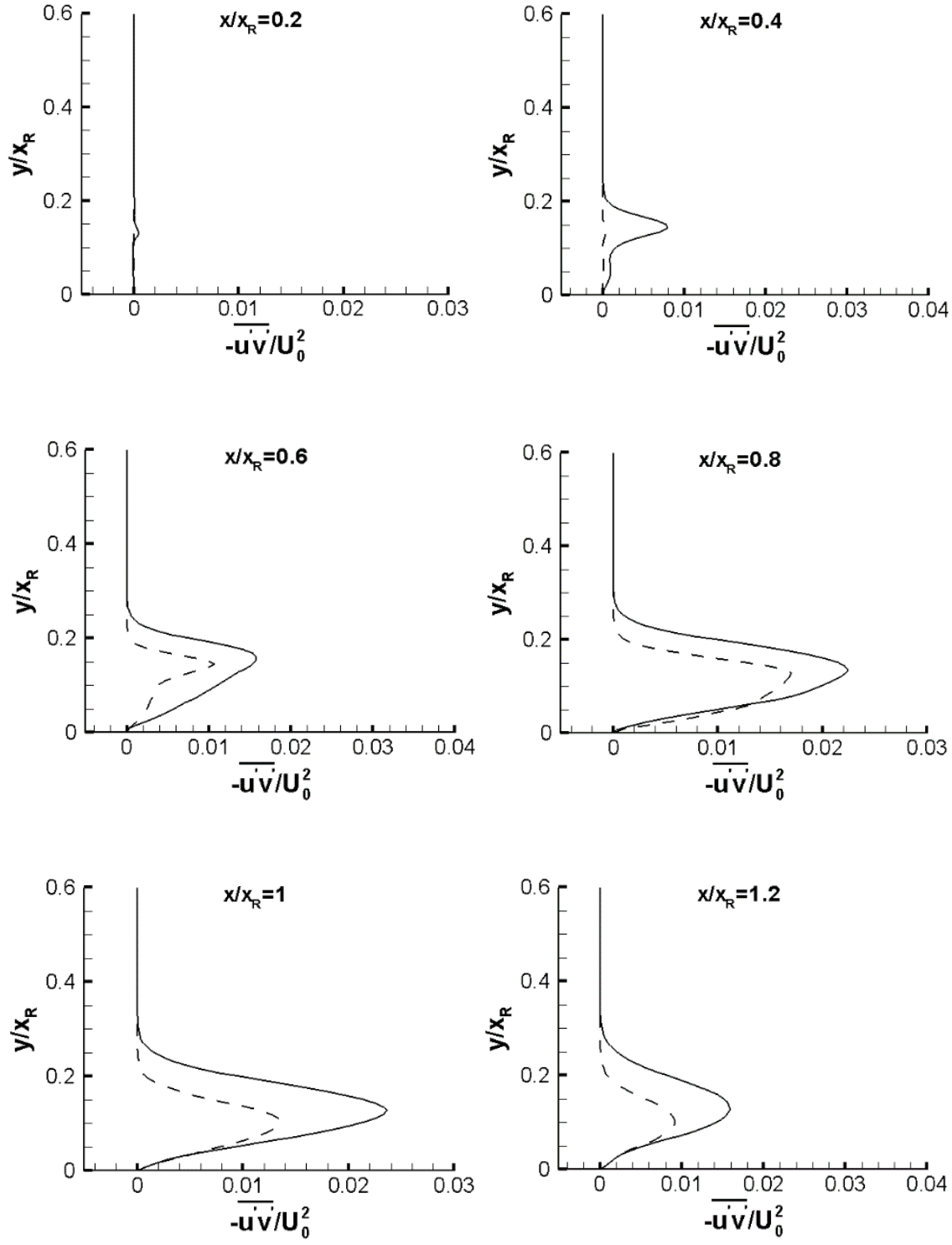

Fig. 4-61. Profiles of the Reynolds shear stress for 3D_case1. With FST: solid line; with NFST: dashed line

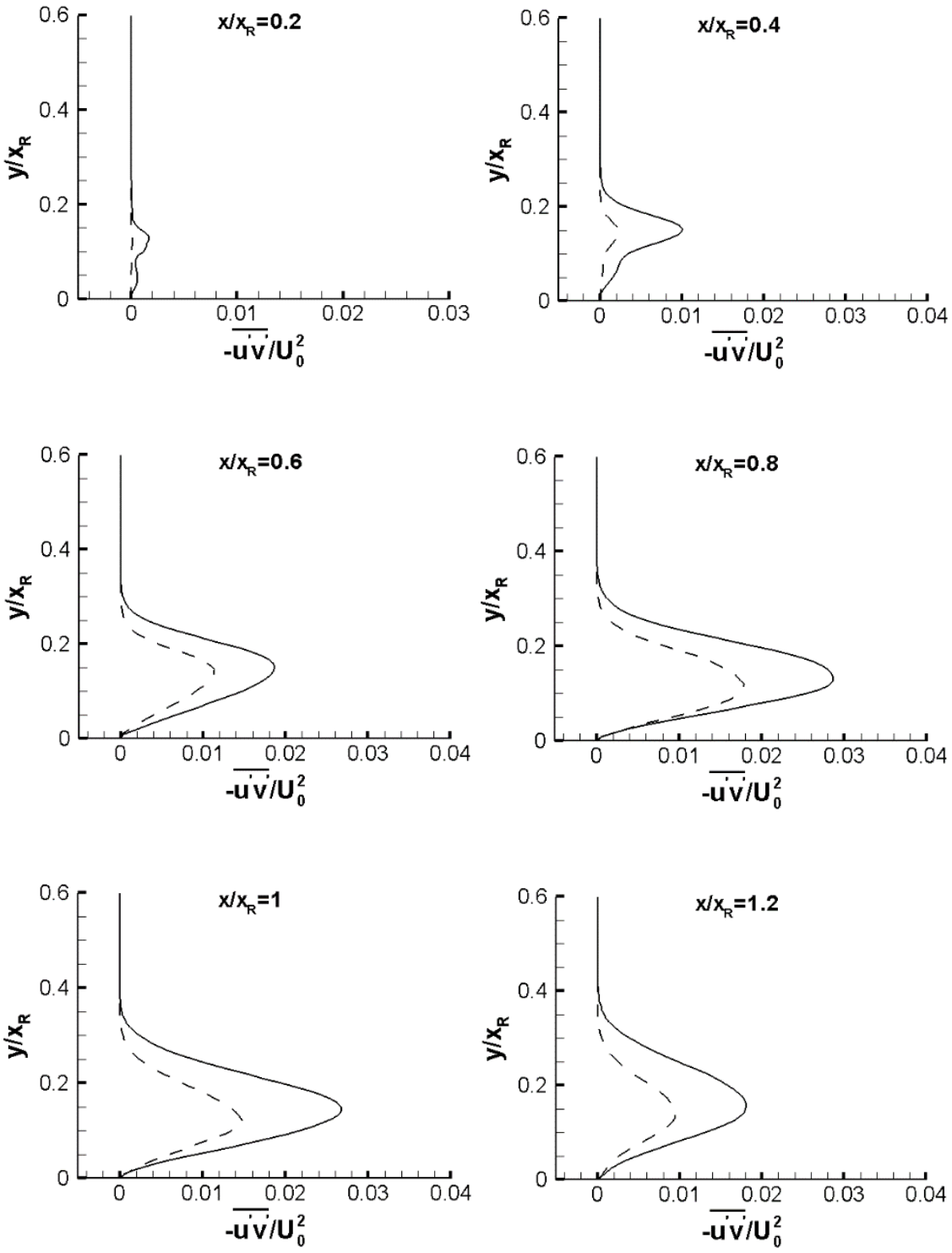

Fig. 4-62. Profiles of the Reynolds shear stress for 3D_case2. With FST: solid line; with NFST: dashed line

In the previous figures, which illustrate the Reynolds shear stress with an elevated intensity of free stream turbulence for the current geometries, it is clear shown that the Reynolds shear stress is not zero at the first selected streamwise position (x/x_R = 0.2) indicating that the flow in this location is not purely laminar. In order to present evidence to support a laminar flow at the separation line, the Reynolds stresses are plotted at a position very close to the separation line (x/x_R = 0.075) as shown in Figs. 4-63, 4-64 and 4-65 for the flat plate, 3D_case1 and 3D_case2, respectively. In these figures, it is clearly observed that value of the Reynolds shear stress is zero at x/x_R = 0.075, which is certainly indicated that the flow is laminar at this streamwise position for all geometries.

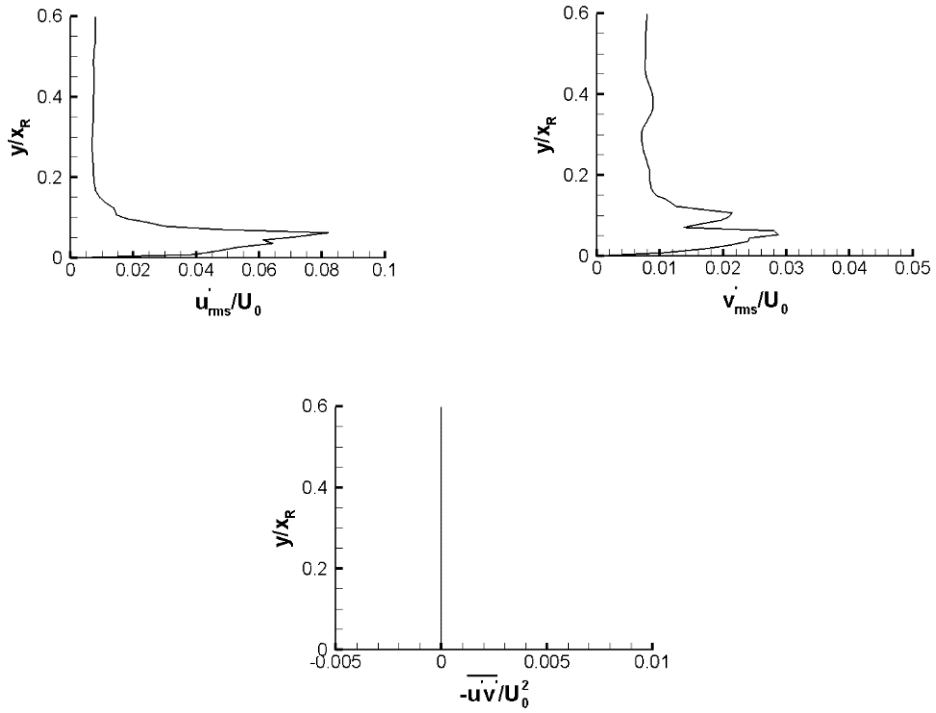

Fig. 4-63. Profiles of Reynolds stresses at x/x_R = 0.075 for the flat plate with FST

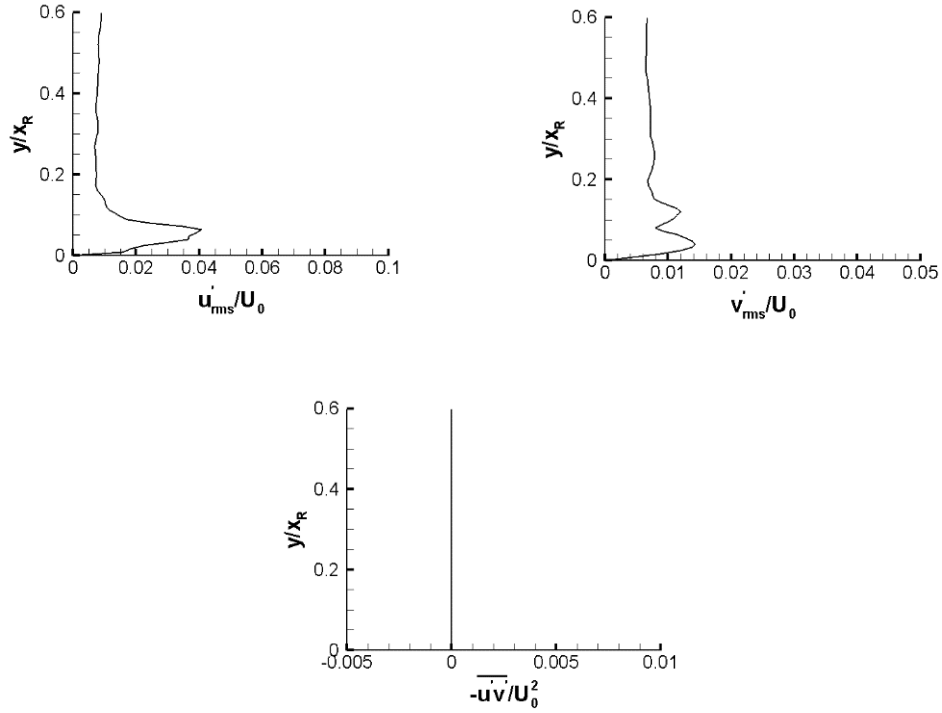

Fig. 4-64. Profiles of Reynolds stresses at x/x_R = 0.075 for 3D_case1 with FST

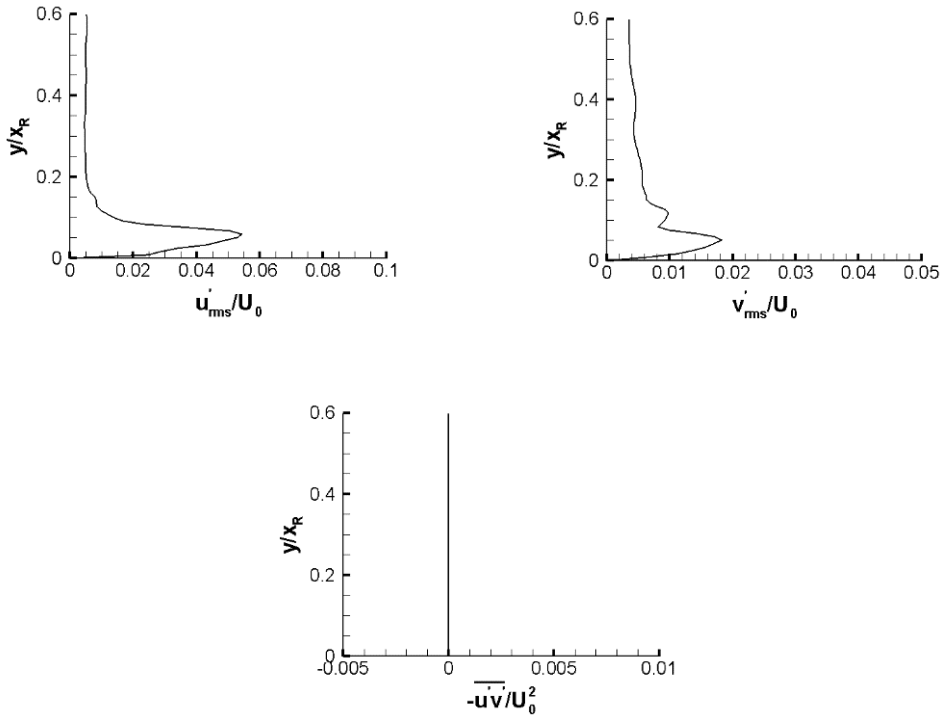

Fig. 4-65. Profiles of Reynolds stresses at x/x_R = 0.075 for 3D_case2 with FST

The mean surface pressure coefficient for the flat plate in the current study is compared with that presented in the experimental work of Cherry et al. (1981b) for FST and NFST cases. It is worth pointing out that in Cherry et al. (1981b), a turbulent separation on a blunt flat plate with a Reynolds number of 32×10^3 was investigated for FST and NFST. In this study, the disturbance level at the incoming flow was 6.5%. It should be noted that there are no experimental results for the mean surface pressure coefficient for a transitional separated-reattached flow available in the literature. So, even though in Cherry et al. (1981b) separated flow is turbulent and intensity of free stream turbulence is higher than that in the current study, the current mean surface pressure coefficient is compared with experimental results of Cherry et al. (1981b) for FST and NFST as shown in Fig. 4-66.

Although there is good agreement between the distribution of the mean surface pressure coefficient with FST presented in the current study and the experimental work of Cherry et al. (1981b), the minimum value of the mean surface pressure coefficient in Cherry et al. (1981b) is much lower than that found in the current study as shown in Fig. 4-66. This difference comes from the difference in Reynolds numbers, intensity of free stream turbulence and the nature of the separated flow in each of these studies. However, there is no a noticeable difference in the current maximum and minimum mean surface pressure coefficients when the flow is studies via NFST or FST as shown in Fig. 4-66. In addition, in both instances of the flows, a rapid recovery of the profile of the mean surface pressure coefficient occurs before the mean reattachment point, and completes after the reattachment.

Similar behaviour is observed for the profiles of the mean surface pressure coefficient, as can be seen for both three-dimensional geometries in Fig. 4-67 for 3D_case1 and Fig. 4-68 for 3D_case2.

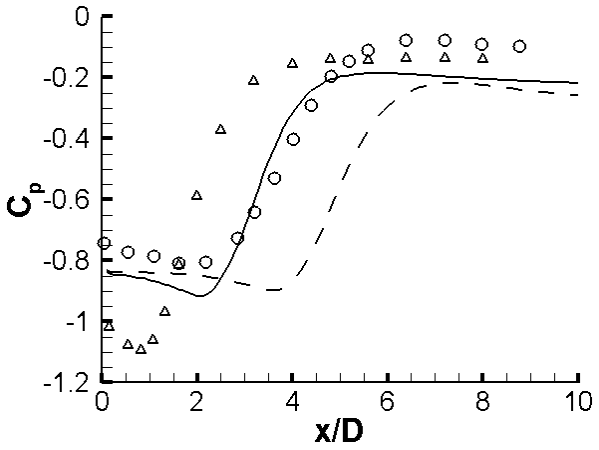

Fig. 4-66. Distribution of the mean surface pressure coefficient for the flat plate. Present results with FST: solid line; present results with NFST: dashed line; Cherry et al. (1981b) with NFST: circles; Cherry et al. (1981b) with 6.5% FST: triangles

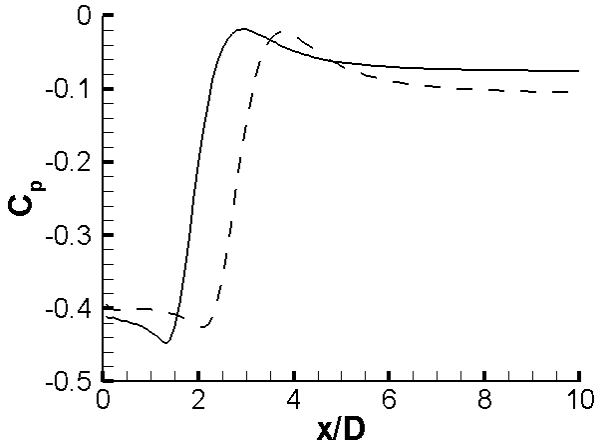

Fig. 4-67. Distribution of the mean surface pressure coefficient for 3D_case_1. With FST: solid line; with NFST: dashed line

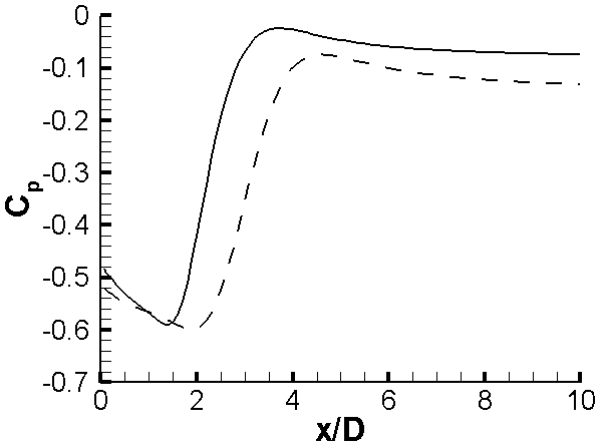

Fig. 4-68. Distribution of the mean surface pressure coefficient for 3D_case_2. With FST: solid line; with NFST: dashed line

Predicted mean pressure coefficient profiles across the shear layer at different streamwise locations for FST and NFST are shown in Fig. 4-69 for the flat plate, Fig. 4-70 for 3D_case1, and Fig. 4-71 for 3D_case2. In general, the maximum difference in the mean pressure coefficient due to effects of a high intensity of free stream turbulence occurs at x/x_R = 0.8 for all geometries, where a strong recirculation takes place. Further downstream, the mean pressure coefficient profile starts to recover.

The time-averaged velocity streamlines, velocity vectors, and streamwise velocity contours with FST at the mid-distance of the spanwise direction (z/D = 2) are shown in Fig. 4-72 for the flat plate, Fig. 4-73 for 3D_case1, and Fig. 4-74 for 3D_case2. From a comparison with that found from NFST presented in Section 4.2.1 for all geometries, it can be seen that the reduction in the separation bubble mean length and height due to the presence of a 3.7% intensity of free stream turbulence are clearly visible.

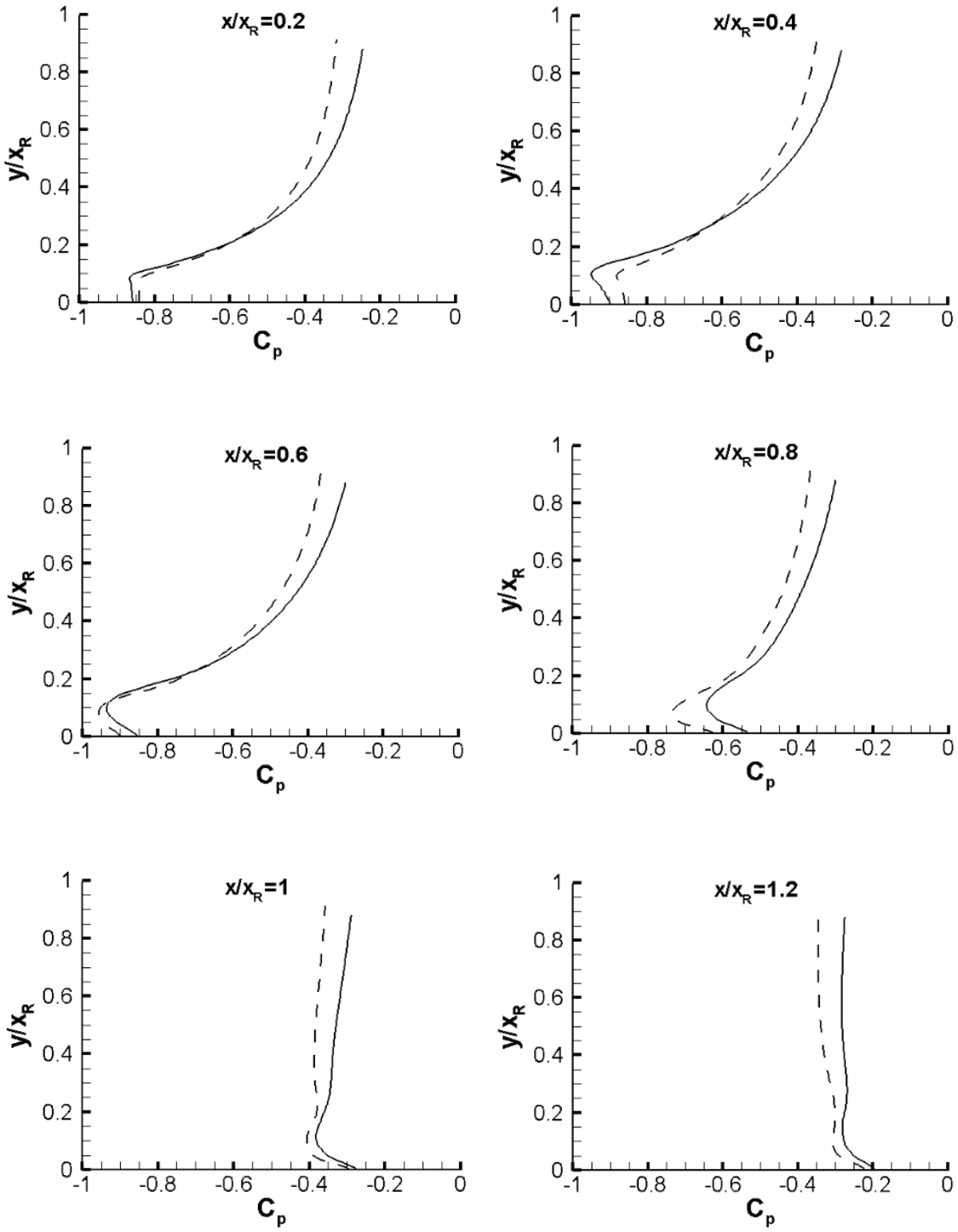

Fig. 4-69. Profiles of the mean pressure coefficient for the flat plate. With FST: solid line; with NFST: dashed line

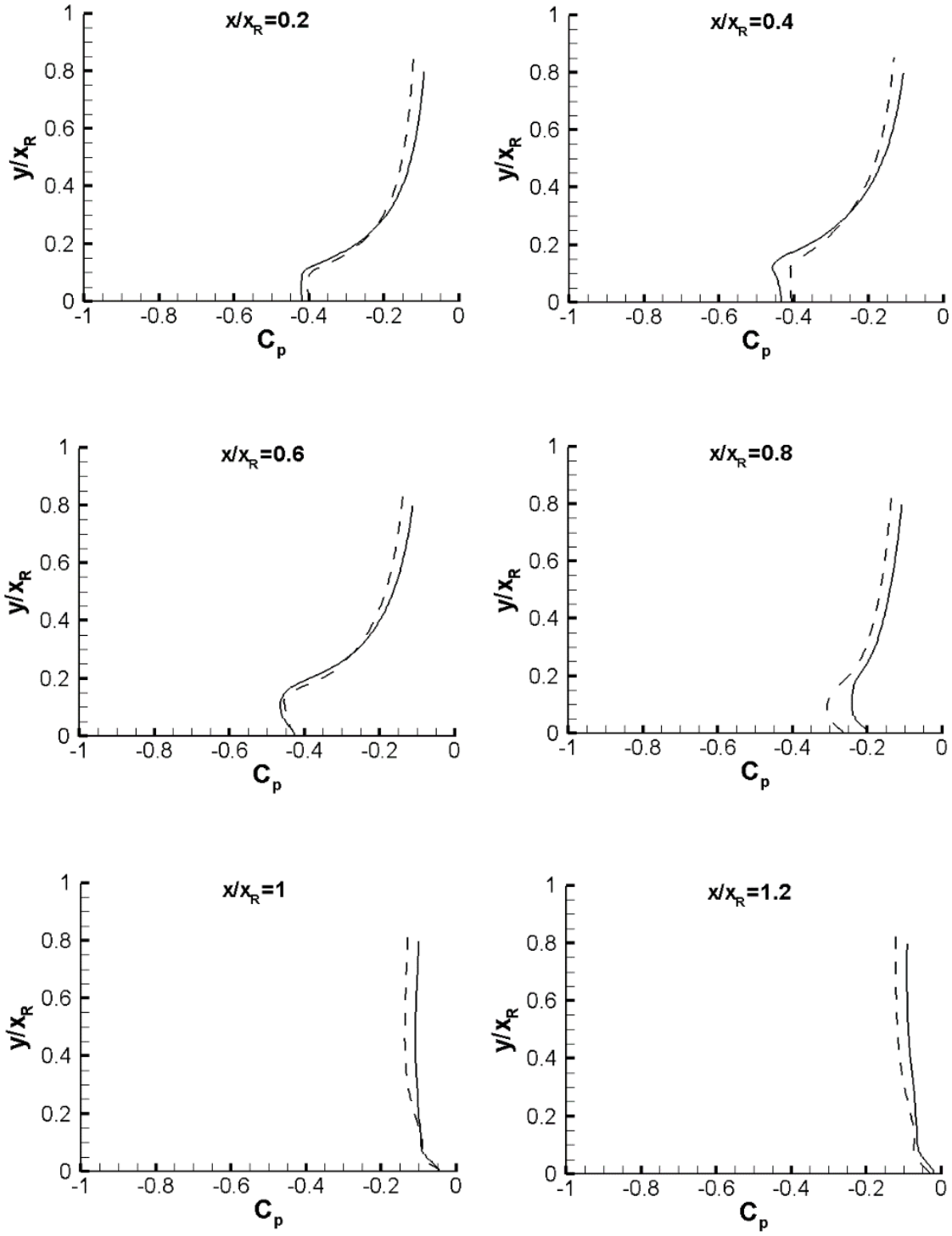

Fig. 4-70. Profiles of the mean pressure coefficient for 3D_case1. With FST: solid line; with NFST: dashed line

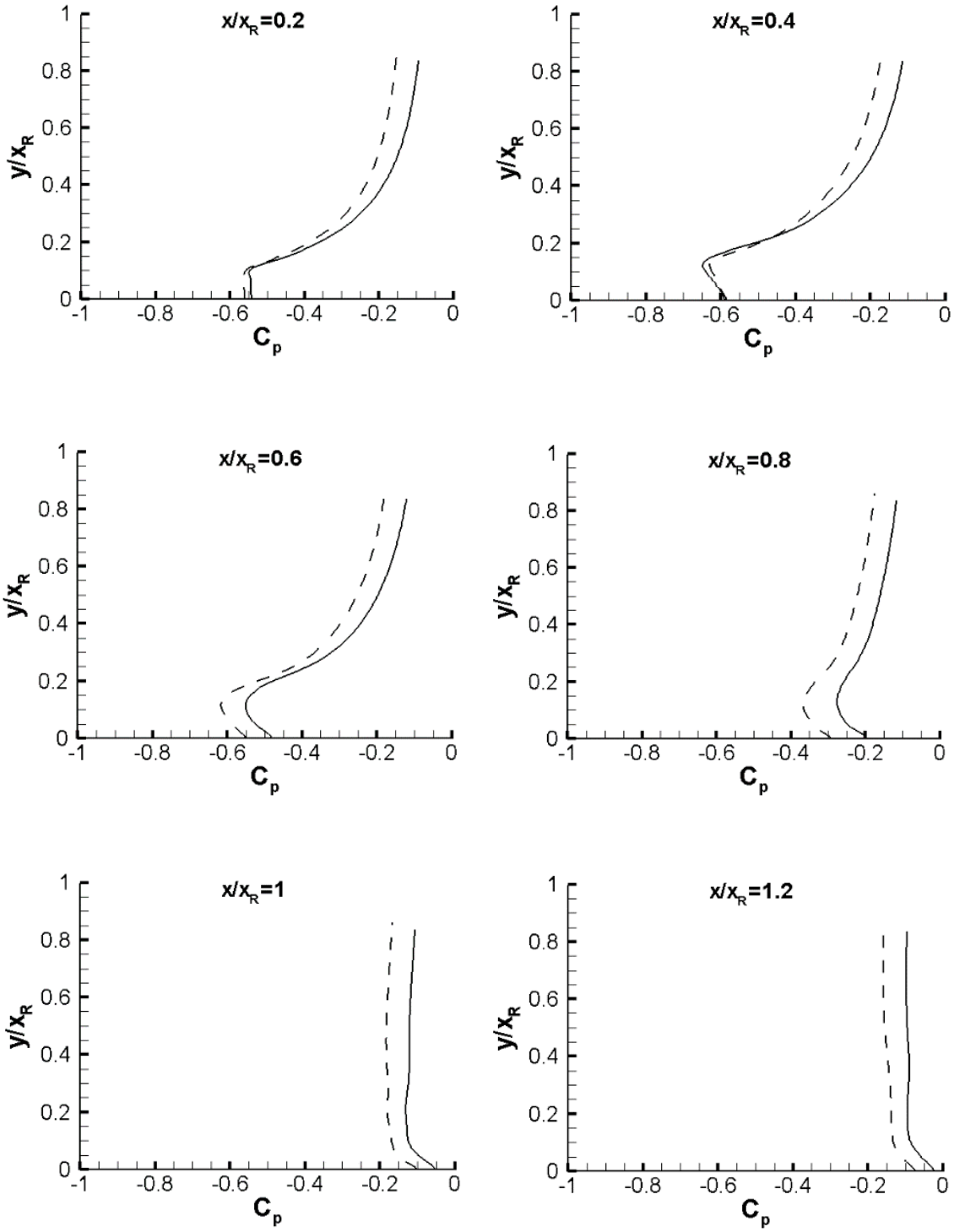

Fig. 4-71. Profiles of the mean pressure coefficient for 3D_case2. With FST: solid line; with NFST: dashed line

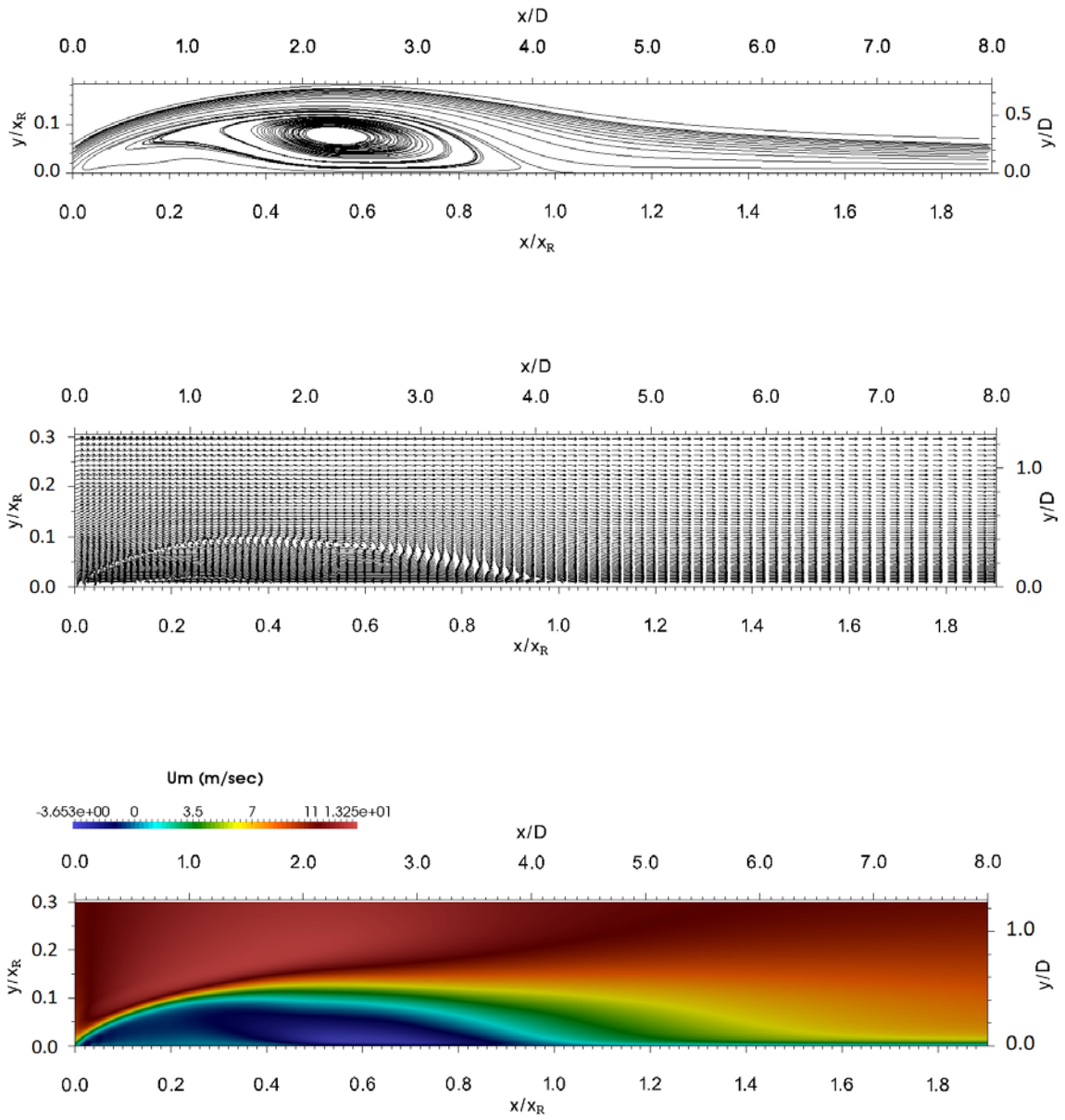

Fig. 4-72. Mean velocity streamlines, velocity vectors, and streamwise velocity contours for the flat plate with FST

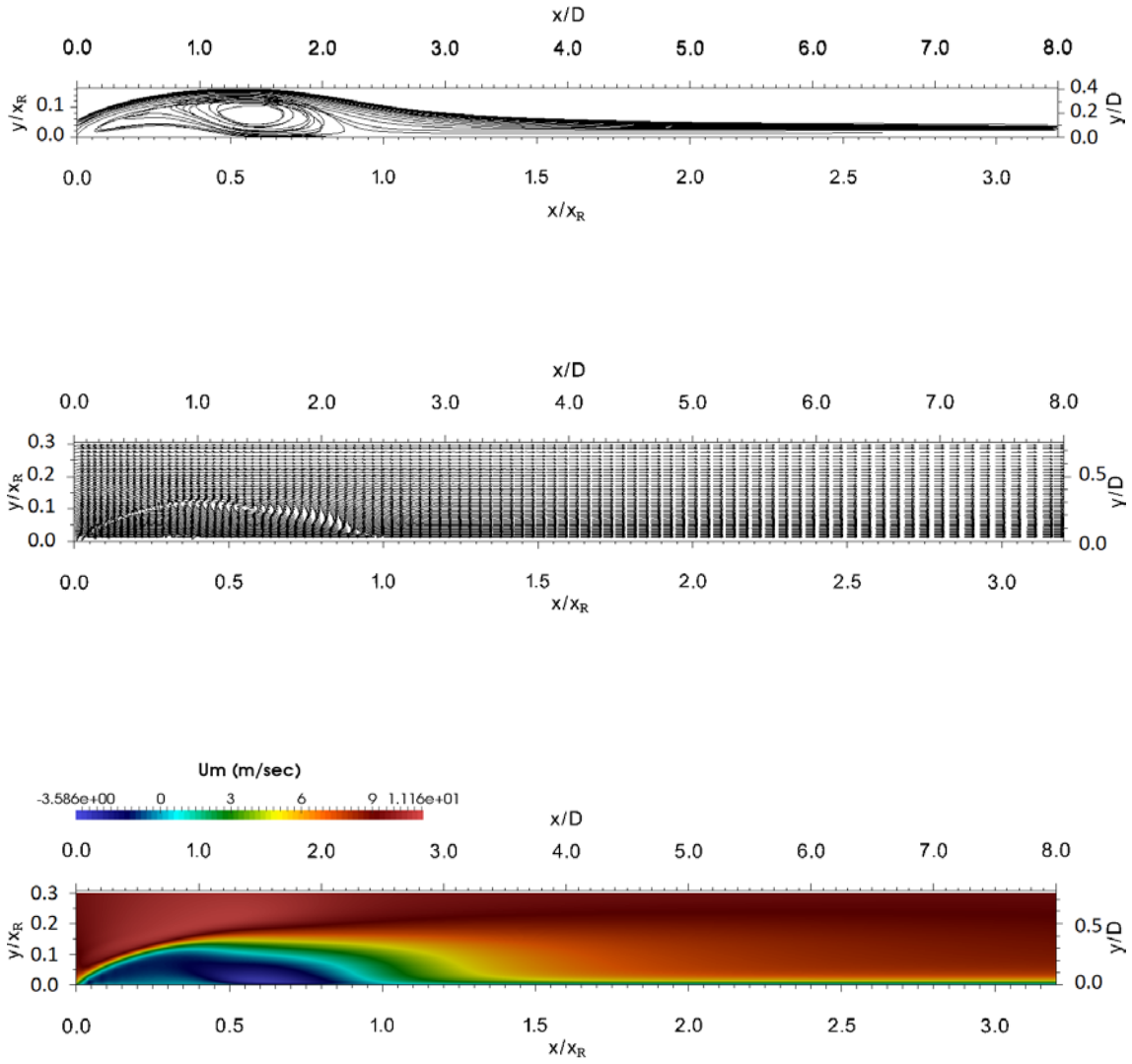

Fig. 4-73. Mean velocity streamlines, velocity vectors, and streamwise velocity contours for 3D_case1 with FST

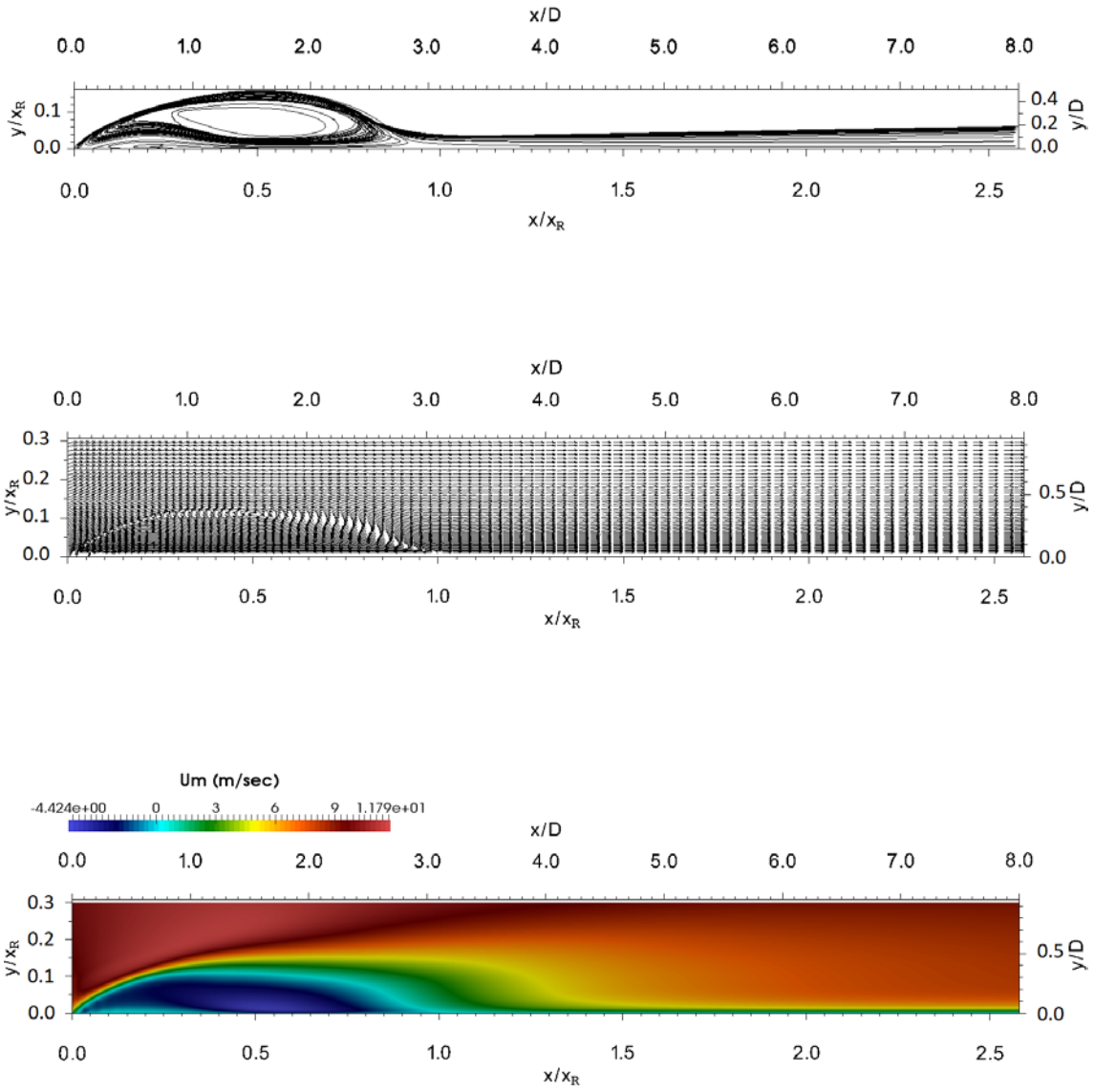

Fig. 4-74. Mean velocity streamlines, velocity vectors, and streamwise velocity contours for 3D_case2 with FST

4.3.2 Transition process

For all geometries in the current study, the transition process is presented by an *x*-*y* plane of instantaneous spanwise vorticity at the mid-spanwise direction when taken at three arbitrary times as shown in Fig. 4-75 for the flat plate, Fig. 4-76 for 3D_case1, and Fig. 4-77 for 3D_case2.

Comparing with the transition processes for the NFST case in Section 4.2.2, it can be observed that an elevated intensity of free stream turbulence leads to the early breakdown

of the free shear layer. In addition, the flow unsteadiness occurs earlier, speeding up the transition. This was also shown by Yang and Abdalla (2009) and Langari and Yang (2013).

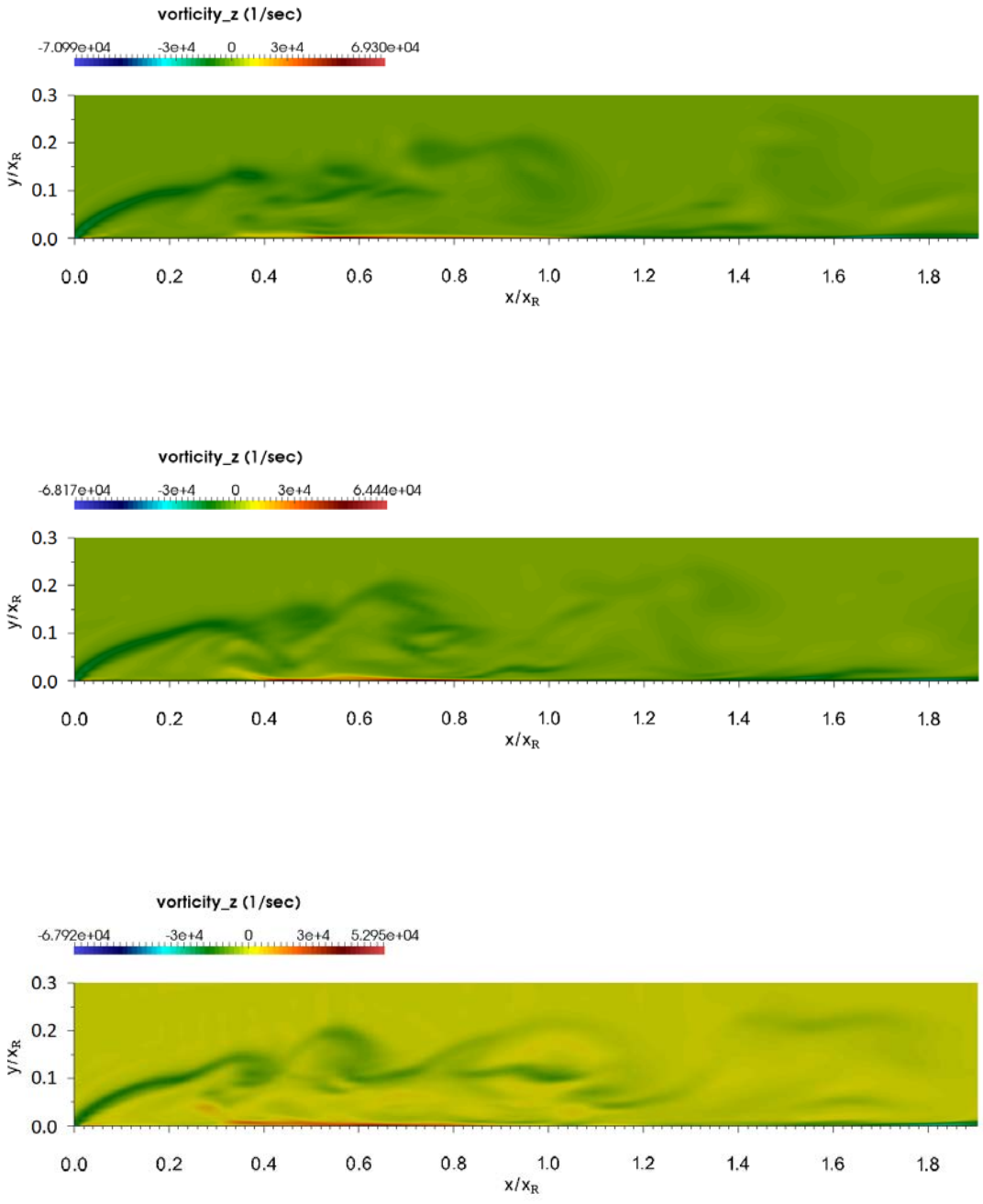

Fig. 4-75. The *x-y* plane of instantaneous spanwise vorticity at three arbitrary times for the flat plate with FST

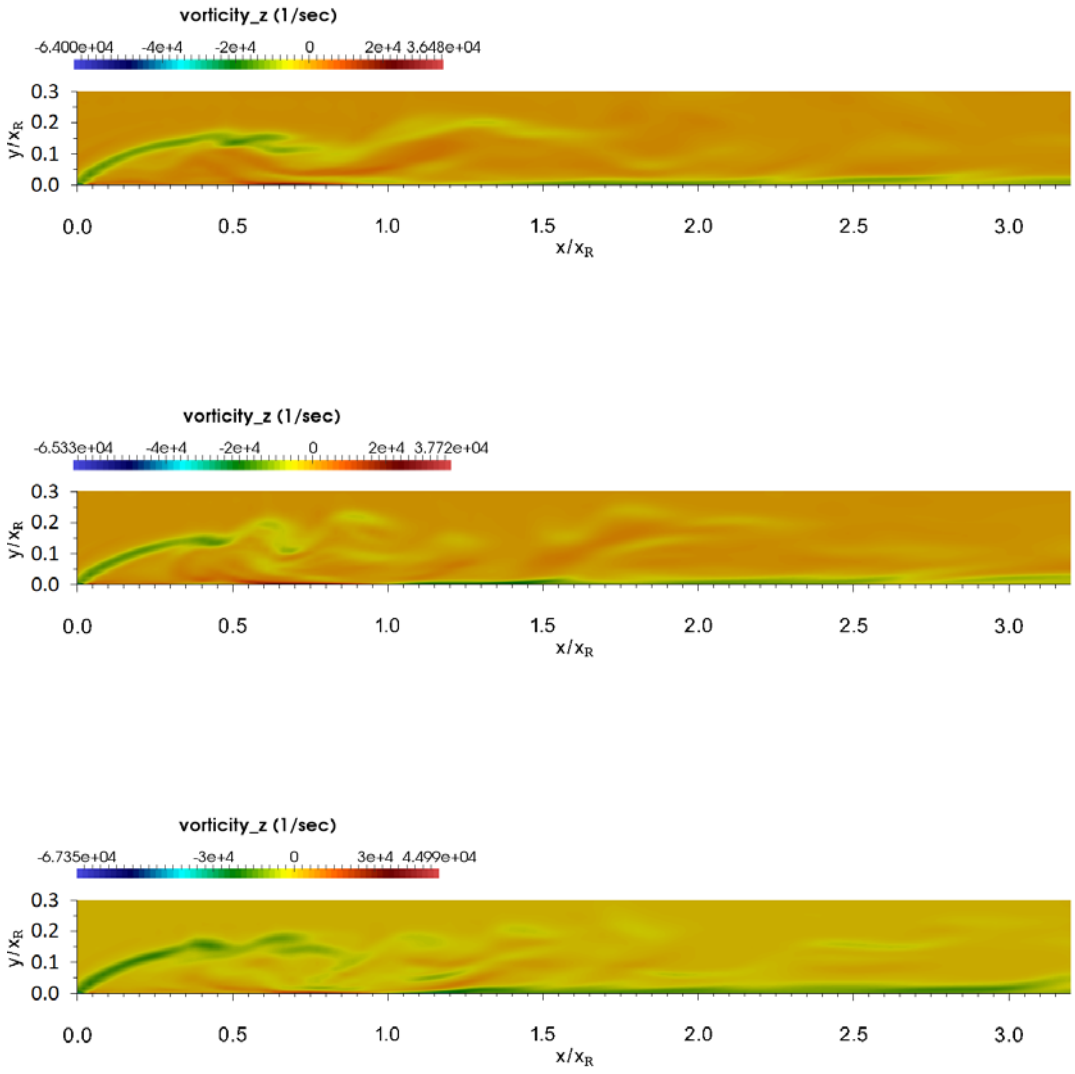

Fig. 4-76. The *x*-*y* plane of instantaneous spanwise vorticity at three arbitrary times for 3D_case1 with FST

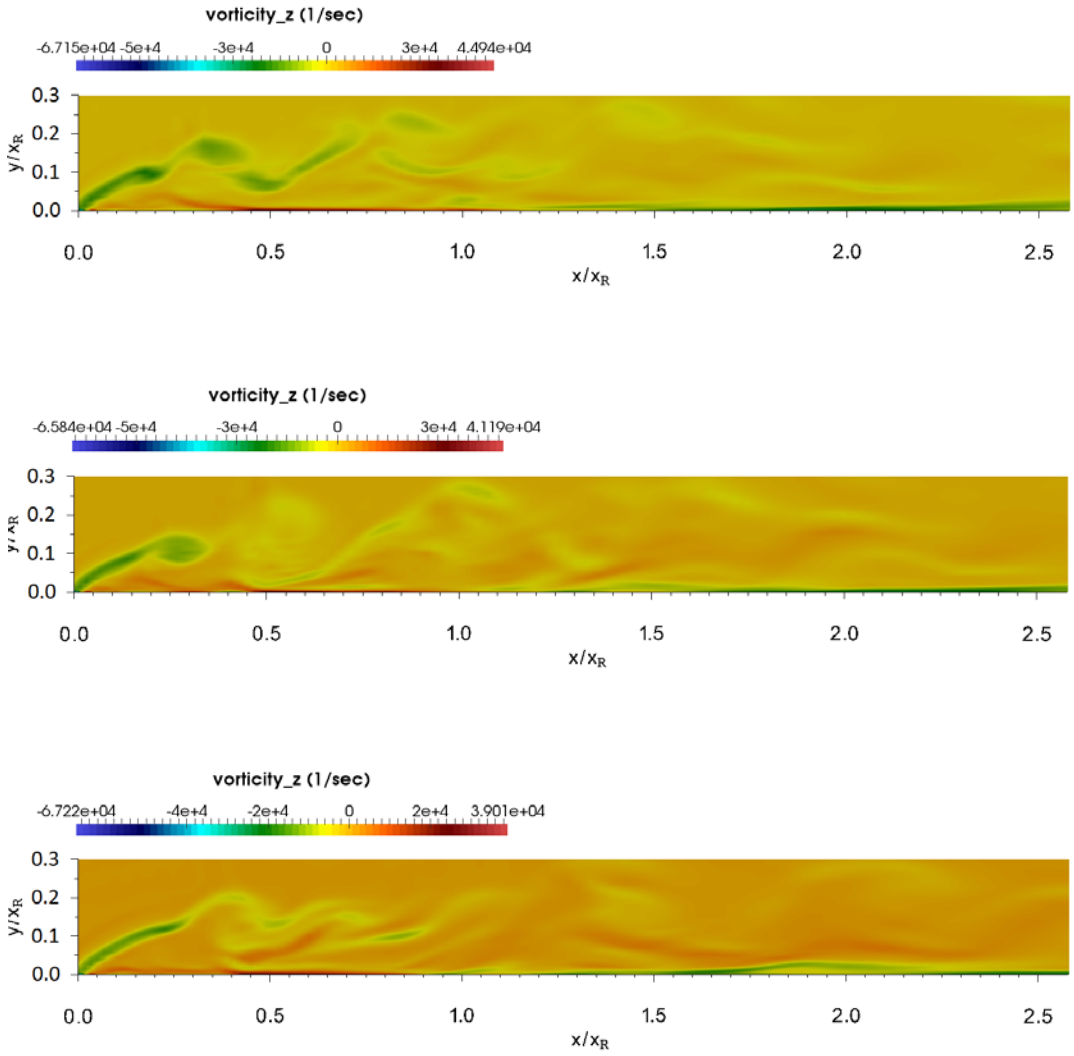

Fig. 4-77. The *x-y* plane of instantaneous spanwise vorticity at three arbitrary times for 3D_case2 with FST

For both three-dimensional geometries, the instantaneous magnitude vorticity isosurface with FST is employed to present the transition process on the top and side surfaces of the geometry as exhibited in Fig. 4-78 for 3D_case1 and Fig. 4-79 for 3D_case2. As shown in these figures, there is no a considerable difference in locations of the flow development stages on either surface of these two three-dimensional geometries, i.e., streamwise locations of the transition start, three-dimensional flow development and reattachment are essentially identical.

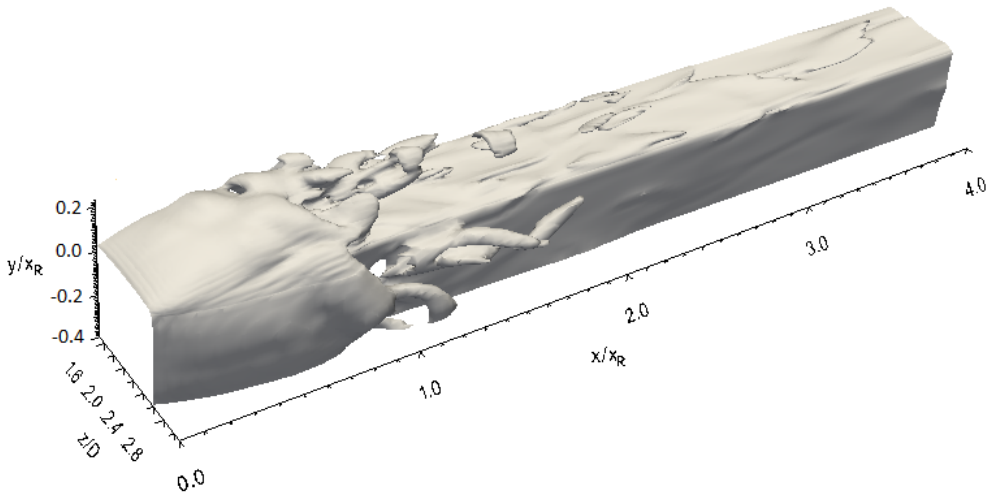

Fig. 4-78. Vorticity magnitude isosurface on the top and side surfaces of 3D_case1 with FST

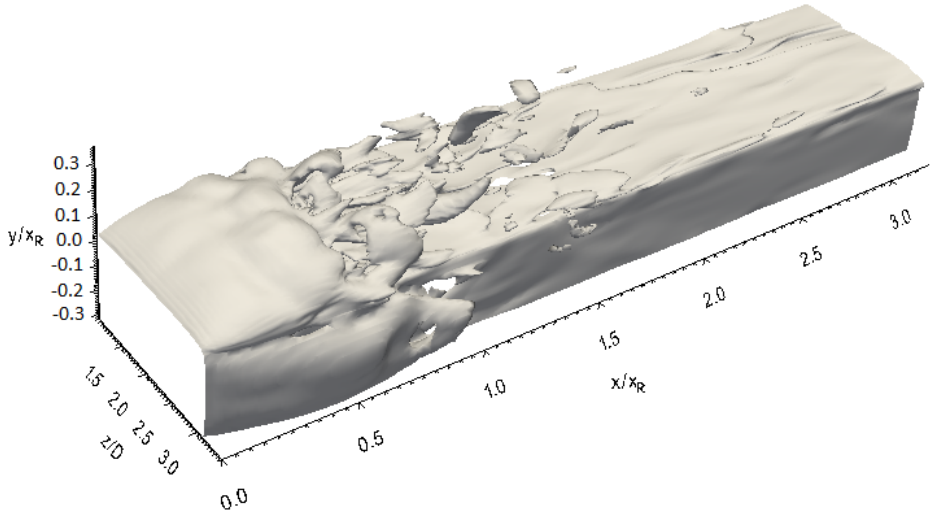

Fig. 4-79. Vorticity magnitude isosurface on the top and side surfaces of 3D_case2 with FST

4.3.3 Instantaneous reattachment length

For all geometries, an instantaneous reattachment length with an elevated free stream turbulence intensity is plotted by instantaneous streamwise velocity contours in the *x-y* plane at $z/D = 2$ taken at three arbitrary times as shown in Fig. 4-80 for the flat plate, Fig. 4-81 for 3D_case1, and Fig. 4-82 for 3D_case2. In a comparison with the results for NFST that are presented in Section 4.2.3, it is clear shown that the instantaneous size of the

separation bubble for the FST case is smaller, and the instantaneous reattachment length is highly unsteady around the mean reattachment line.

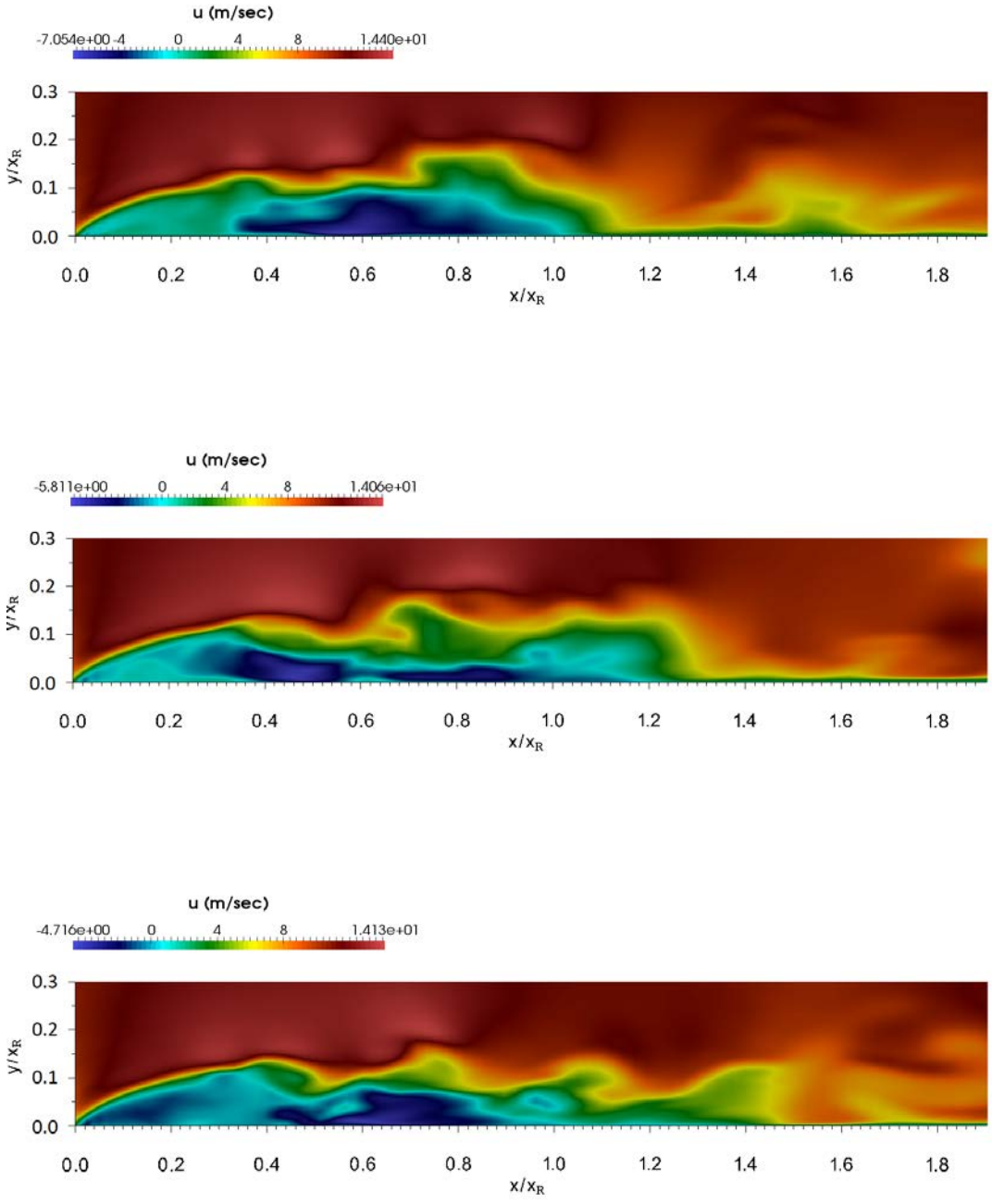

Fig. 4-80. Instantaneous streamwise velocity contours at three arbitrary times for the flat plate with FST

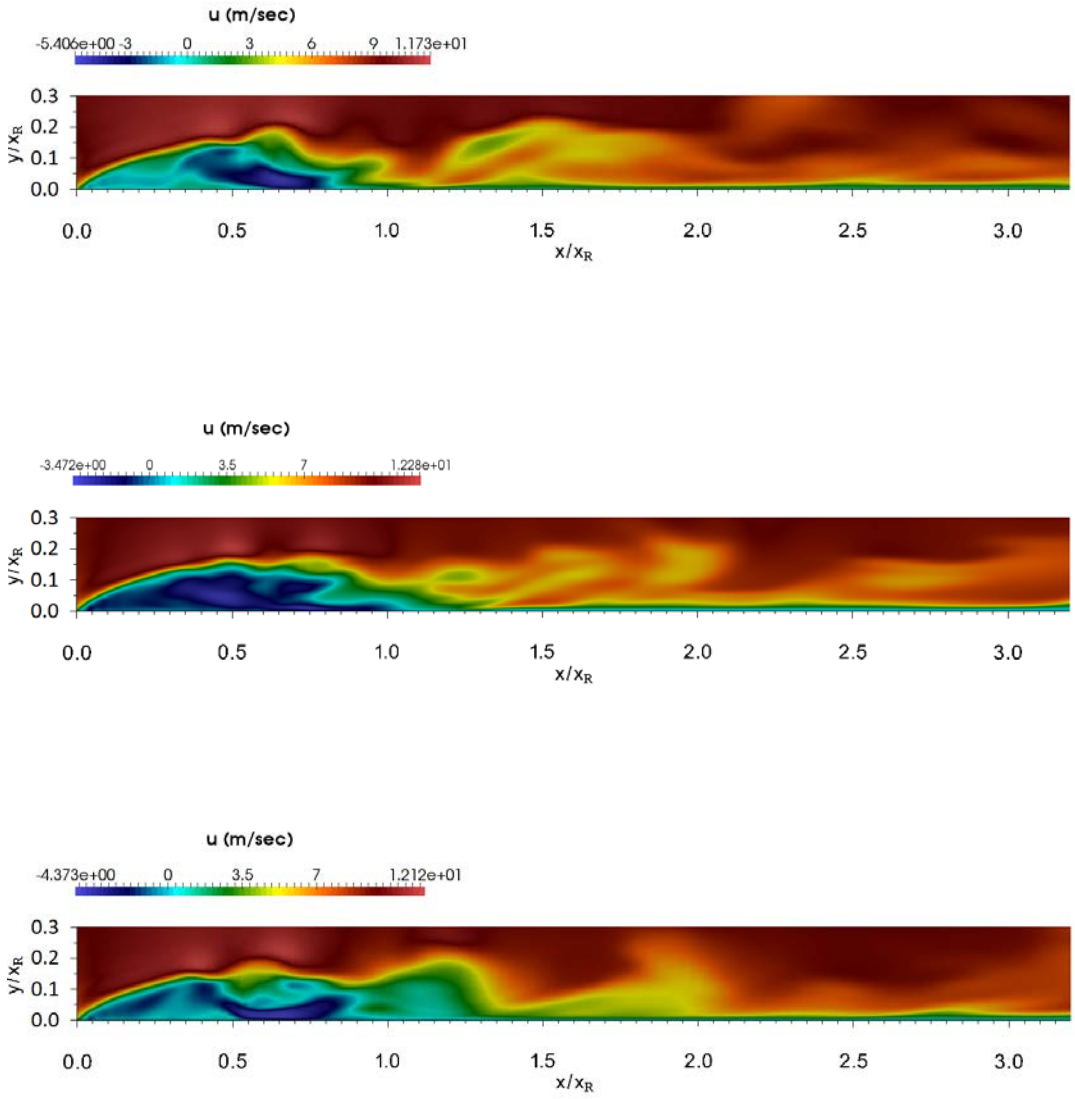

Fig. 4-81. Instantaneous streamwise velocity contours at three arbitrary times for 3D_case1 with FST

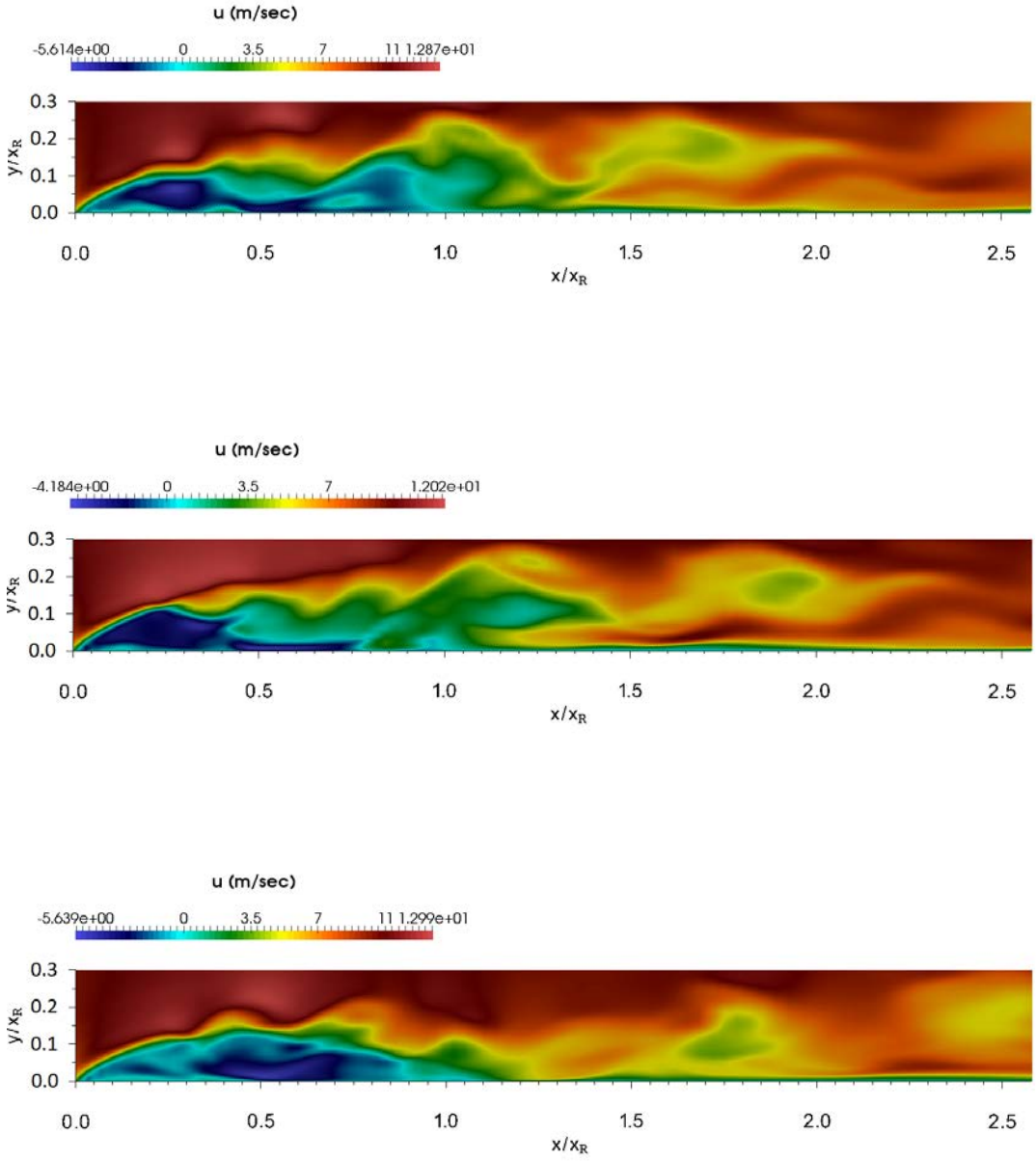

Fig. 4-82. Instantaneous streamwise velocity contours at three arbitrary times for 3D_case2 with FST

The variation in the instantaneous reattachment length (x_i) normalised by the mean reattachment length (x_R) is shown in Fig. 4-83 for the flat plate, Fig. 4-84 for 3D_case1, and Fig. 4-85 for 3D_case2. The maximum and minimum instantaneous reattachment lengths are about $x_{imax.} = 1.4x_R$ and $x_{imin.} = 0.76x_R$ for the flat plate, $x_{imax.} = 1.28x_R$ and $x_{imin} = 0.84x_R$ for 3D_case1, and $x_{imax.} = 1.35x_R$ and $x_{imin} = 0.8x_R$ for 3D_case2. Therefore, the differences between the maximum and minimum instantaneous reattachment lengths are

$0.64x_R$ (64% of the mean reattachment length) for the flat plate, $0.44x_R$ (44% of the mean reattachment length) for 3D_case1, and $0.55x_R$ (55% of the mean reattachment length) for 3D_case2.

It can be seen that the unsteadiness in the instantaneous reattachment length for both three-dimensional geometries with FST is in good agreement with Gartshore and Savill (1982) while for the flat plate, this parameter is overpredicted compared to that presented in the literature. It is worth pointing out that there was no elevated intensity of free stream turbulence in the study of Gartshore and Savill (1982). Therefore, it is fair to predict that the unsteadiness in the instantaneous reattachment length in the flat plate is larger than that in Gartshore and Savill (1982).

As shown in Section 4.2.3, the unsteadiness in the instantaneous reattachment length with NFST is $0.52x_R$ for the flat plate, $0.36x_R$ for 3D_case1, and $0.47x_R$ for 3D_case2. It can be seen that the differences between the maximum and minimum instantaneous reattachment lengths with FST are higher than that for NFST. Therefore, it can be concluded that the randomness in instantaneous reattachment length with a high intensity of free stream turbulence is larger.

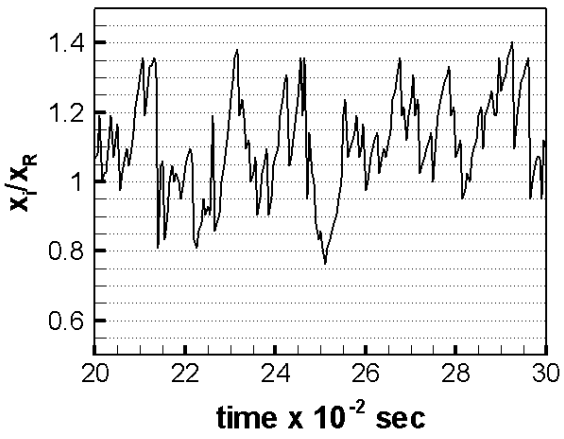

Fig. 4-83. Variation of the instantaneous reattachment length for the flat plate with FST

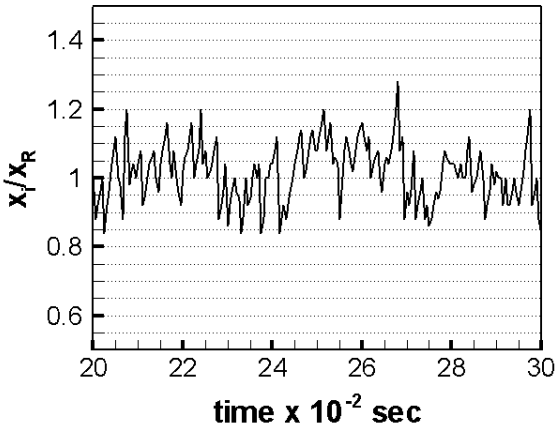

Fig. 4-84. Variation of the instantaneous reattachment length for 3D_case1 with FST

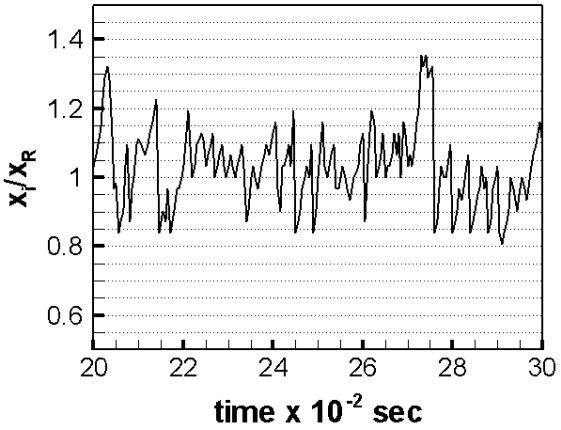

Fig. 4-85. Variation of the instantaneous reattachment length for 3D_case2 with FST

4.4 Summary

Current time-averaged variables of transitional separated-reattached flow over a blunt flat plate with NFST (< 0.2% intensity of free stream turbulence) and FST (3.7% intensity of free stream turbulence) are presented and compared in a reasonable fashion with available experimental and simulated data. The good agreements between the current results and the results of other studies are obtained from the comparisons described in this chapter, this is encouraging, as this gives us confidence in extending these studies to simulate such flows on three-dimensional geometries characterized by different aspect ratios (the width to thickness ratio of the geometry): 1 (3D_case1) and 2 (3D_case2).

It is believed that no similar or analogous results have been presented in the literature for any separated-reattached flow on a three-dimensional geometry. Hence, the current study is the first to examine the properties of transitional separated-reattached flow generated on a three-dimensional geometry with two levels of intensity of free stream turbulence (< 0.2% and 3.7%). In addition, a comparison of the flow properties between the two-dimensional flat plate and the two three-dimensional geometries is carried out.

It is observed that the mean reattachment length for the flat plate is longer than that for both three-dimensional geometries when the flow is with NFST or FST. It has been shown that with FST, the reduction in the mean reattachment length is about 30% for the flat plate, 26.47% for 3D_case1 and 21.5% for 3D_case2.

It is found that the minimum mean streamwise velocity for the flat plate is slightly lower than that for 3D_case1 and 3D_case2 for both disturbance levels. The maximum Reynolds stresses in the flat plate are higher than those for both three-dimensional geometries by about 20% - 25% for NFST, and 25%-35% for FST. However, peaks in the Reynolds stresses profiles for 3D_case2 are slightly higher than those for 3D_case1.

Transition stages for all geometries have been illustrated using instantaneous spanwise vorticity contours at $z/D = 2$. For the flat plate with NFST, the transition stages are similar to those reported in Yang and Voke (2001) and Abdalla and Yang (2005). The separated laminar flow becomes unstable and spanwise vortices are formed due to an inviscid Kelvin-Helmholtz instability mechanism. Further downstream, the separated layer rolls up, and the Kelvin-Helmholtz rolls shed and travel downstream. These rolls develop to form three-dimensional streamwise vortices around the reattachment location. A breakdown of three-dimensional structures into relatively smaller structures then occurs within the turbulent reattached boundary layer.

The transition stages for 3D_case1 and 3D_case2 are found to be similar to the above transition stages. In addition, there is no difference between locations of the flow development stages on the top and side surfaces of these geometries.

Transition stages with FST for geometries used in the current study are similar to those presented for NFST, where it may be noticed that due to the presence of elevated intensity

of free stream turbulence, the flow unsteadiness occurred earlier, speeding up the transition and leading to the early breakdown of the separated shear layer.

Unsteadiness in the instantaneous reattachment length relative to the mean reattachment length for NFST in the instances of the flat plate and 3D_case2 is in good agreement with that presented in various studies of different geometries, while in 3D_case1, the instantaneous reattachment length is underpredicted. Unsteadiness in the instantaneous reattachment length for FST for 3D_case1 and 3D_case2 is in good agreement with results presented in the literature, while the movement in the instantaneous length for the flat plate is overpredicted. For all geometries, the difference between the maximum and minimum instantaneous reattachment lengths with FST is higher than that with NFST, indicating that the randomness in the instantaneous reattachment length with a high intensity of free stream turbulence is greater.

Chapter Five

Primary Instability Mechanism

5.1 Absolute and convective instability for NFST

To investigate if any absolute instability region exists in the separation bubble in any geometry of the current study, instantaneous streamwise velocity profiles at four streamwise locations are taken at three arbitrary times as presented in Figs. 5-1, 5-2 and 5-3 for the flat plate, 3D_case1 and 3D_case2, respectively. The instantaneous streamwise velocity is normalized against the inlet free stream velocity and plotted at x/x_R = 0.2, 0.4, 0.6 and 0.8 to cover the separation bubble mean length.

Alam and Sandham (2000) reported that the absolute instability is present when reverse flow amount in the instantaneous velocity profile exceeds 20%. As shown in Figs. 5-1, 5-2 and 5-3, the reverse flow is lower than 20% and hence there is no absolute instability region in the separation bubble in any geometry of the current study, where all separation bubbles are properly classified as convectively unstable.

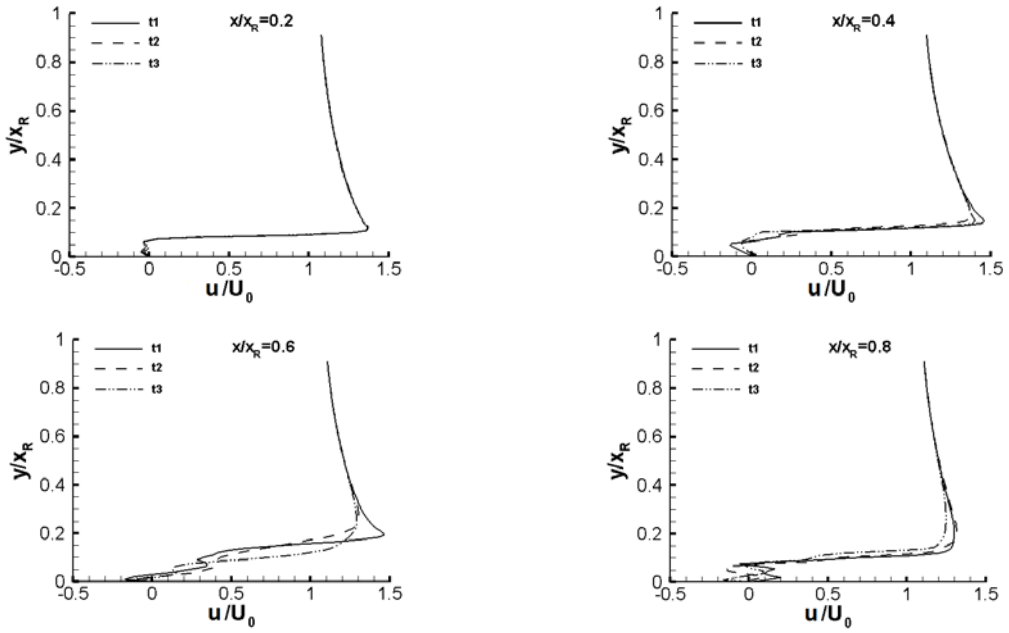

Fig. 5-1. Instantaneous streamwise velocity profiles at three arbitrary times for the flat plate with NFST

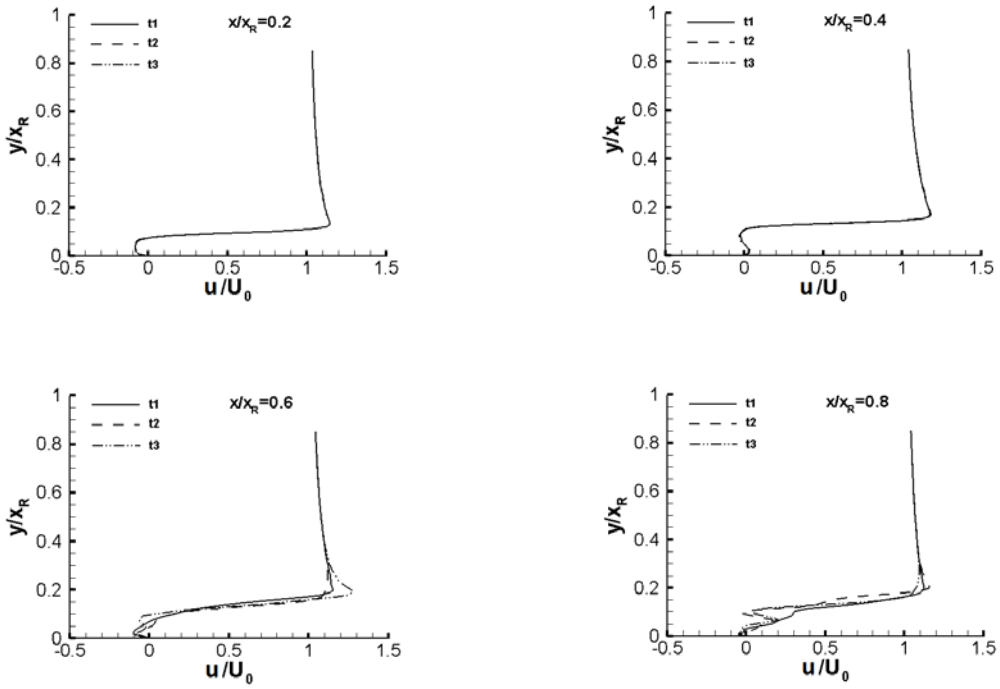

Fig. 5-2. Instantaneous streamwise velocity profiles at three arbitrary times for 3D_case1 with NFST

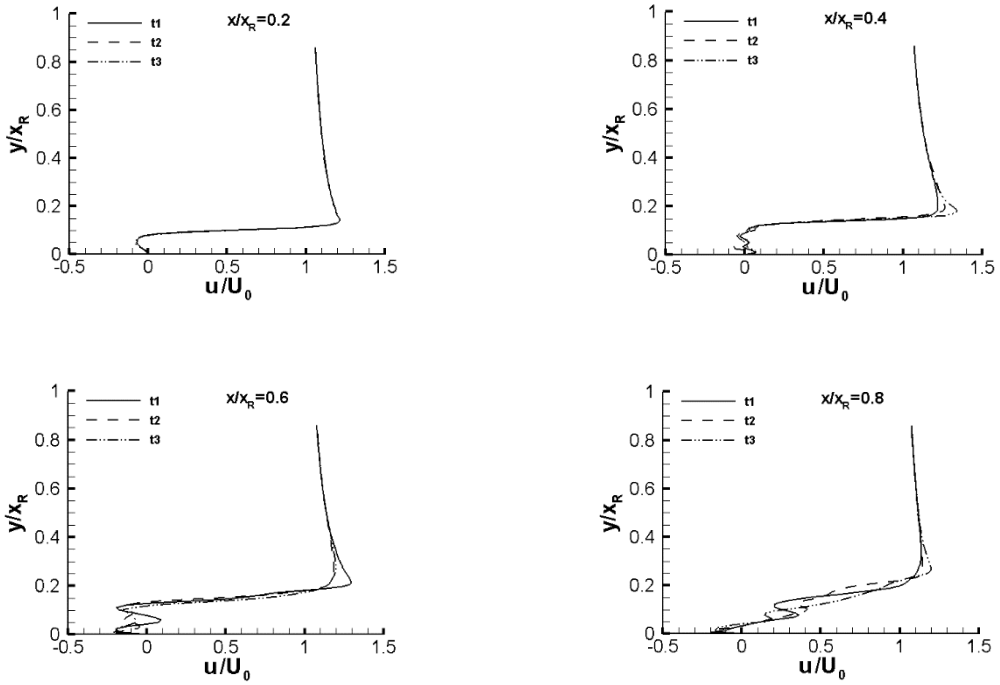

Fig. 5-3. Instantaneous streamwise velocity profiles at three arbitrary times for 3D_case2 with NFST

5.2 Unsteadiness location for NFST

Before the separation line, and indeed even after this location in one specific region, the flow is laminar and two-dimensional for all geometries. This is clearly shown in Fig. 5-4 for the flat plate, Fig. 5-5 for 3D_case1 and Fig. 5-6 for 3D_case2, which show isosurfaces of the instantaneous velocity components at two arbitrary times.

For the flat plate, it can be seen that the flow is two-dimensional, where the spanwise velocity is zero until $x/x_R = 0.2$ (corresponding to $x/D = 1.2$) as shown in Fig. 5-4. Further downstream the spanwise velocity appears, indicating the beginning of the initial unsteadiness in the free shear layer. Over the distance between $x/x_R = 0.2$ and 0.45 (x/D = 1.2 - 2.7), the unsteadiness develops slowly implying the low amplitude growth of disturbances. From $x/x_R = 0.45$ onward, the growth of the disturbances becomes violent and the unsteadiness develops rapidly.

The instantaneous velocity components for 3D_case1 plotted in Fig. 5-5 show that the flow is two-dimensional up to $x/x_R = 0.4$ (corresponding to $x/D = 1.36$). Further downstream, there is an appearance of the spanwise velocity, which is an indication of the unsteadiness beginning in the free shear layer. It can be seen that the flow development becomes violent at $x/x_R = 0.6$ onward where before this location, in the region that is bounded between $x/x_R = 0.4$ and 0.6 (x/D = 1.36 - 2.04), the flow is relatively quiet, indicting linear development of the flow in this region.

After the separation, the free shear layer in 3D_case2 retains a two-dimensionality nature without any distortion up to $x/x_R = 0.31$ (corresponding to $x/D = 1.2245$) as shown in Fig. 5-6. At this location onward, the unsteadiness starts with an appearance of the spanwise velocity indicating the beginning of the transition. It can be seen in Fig. 5-6 that the flow development keeps slowly between two streamwise positions of $x/x_R = 0.31$ and x/x_R = 0.55 (x/D = 1.2245 and 2.1725). Further downstream, a strong three-dimensional motion with a high distortion of the shear layer takes place.

It is worth pointing out that for all geometries, various isosurfaces for the instantaneous velocity components at different times are investigated, and similar observations to the above description can be made.

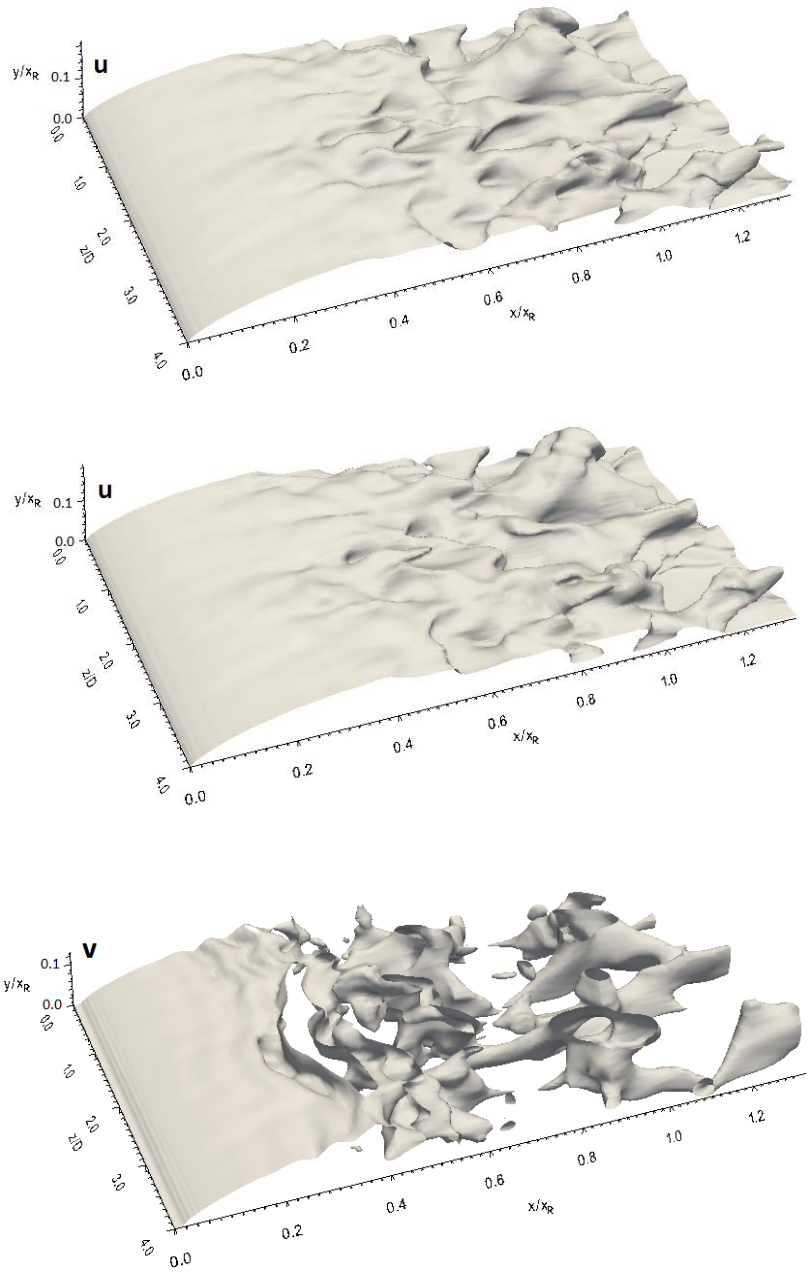

Caption for these figures is on the following page

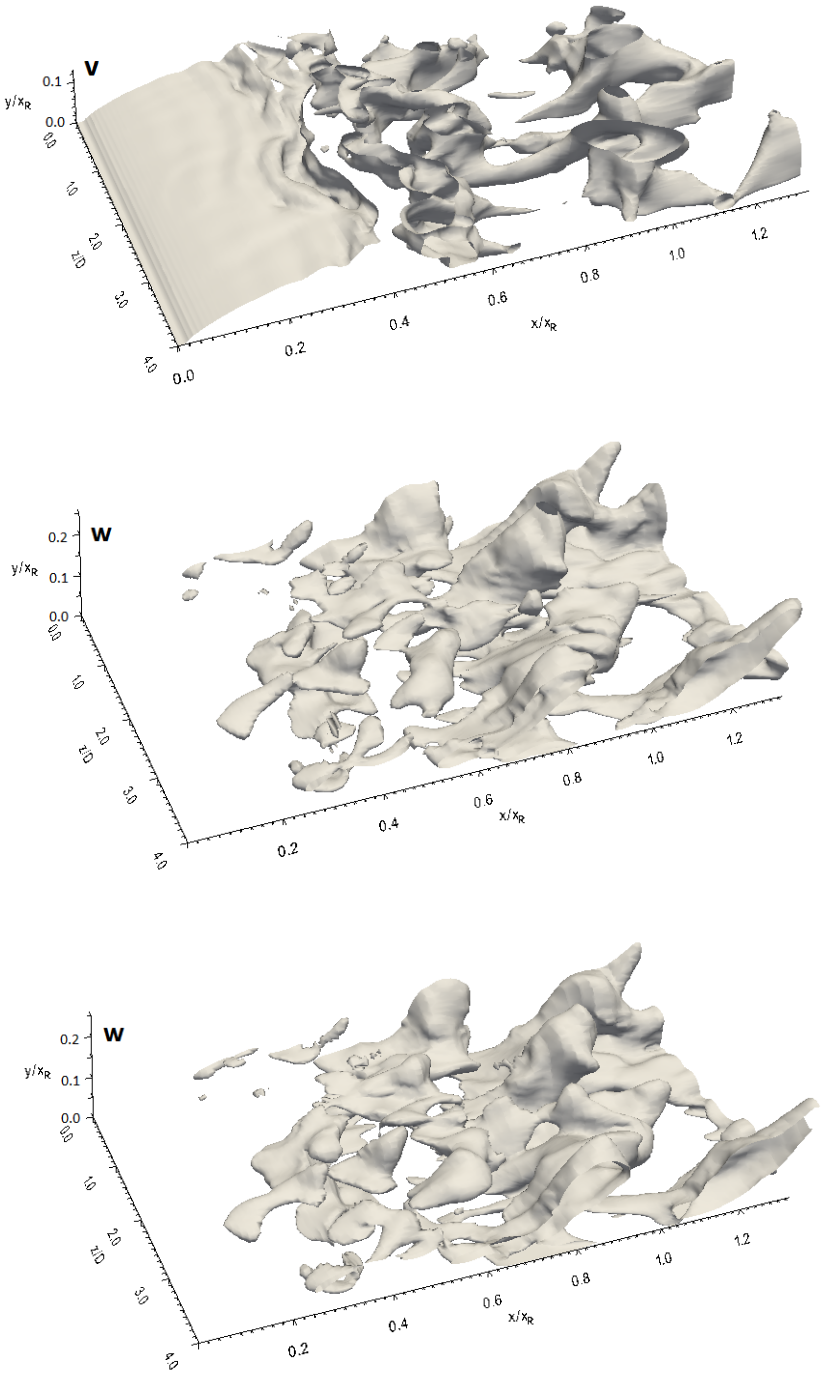

Fig. 5-4. Isosurfaces for the instantaneous velocity components at two arbitrary times for the flat plate with NFST

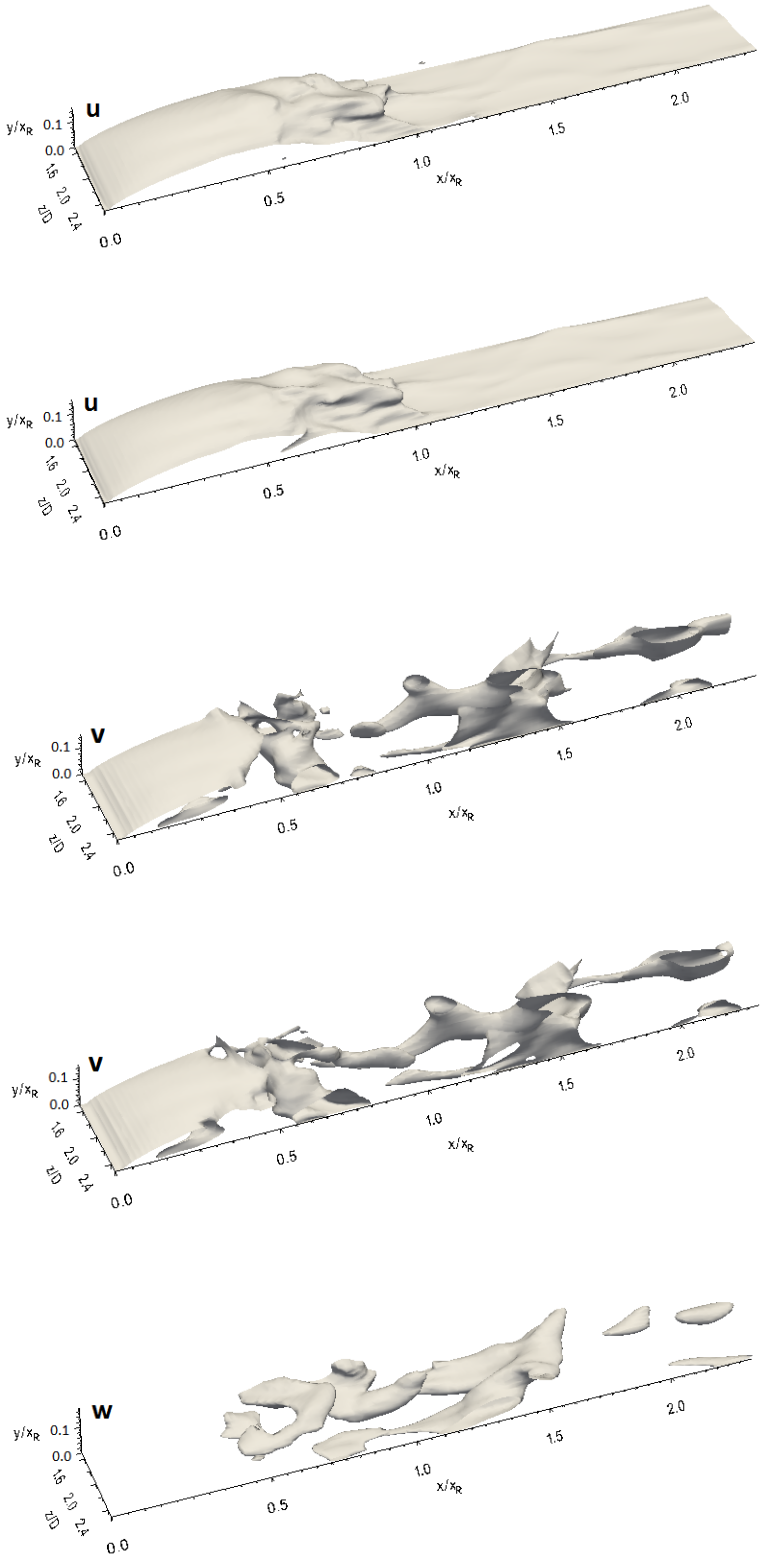

Caption for these figures is on the following page

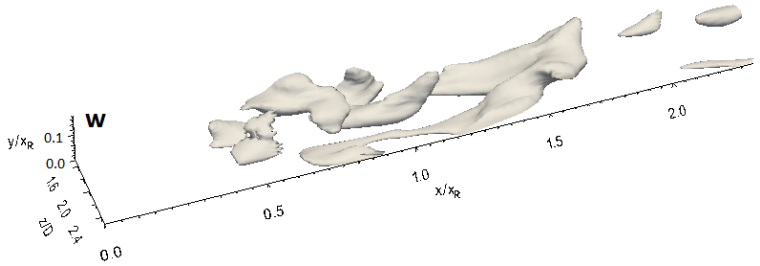

Fig. 5-5. Isosurfaces for the instantaneous velocity components at two arbitrary times for 3D_case1 with NFST

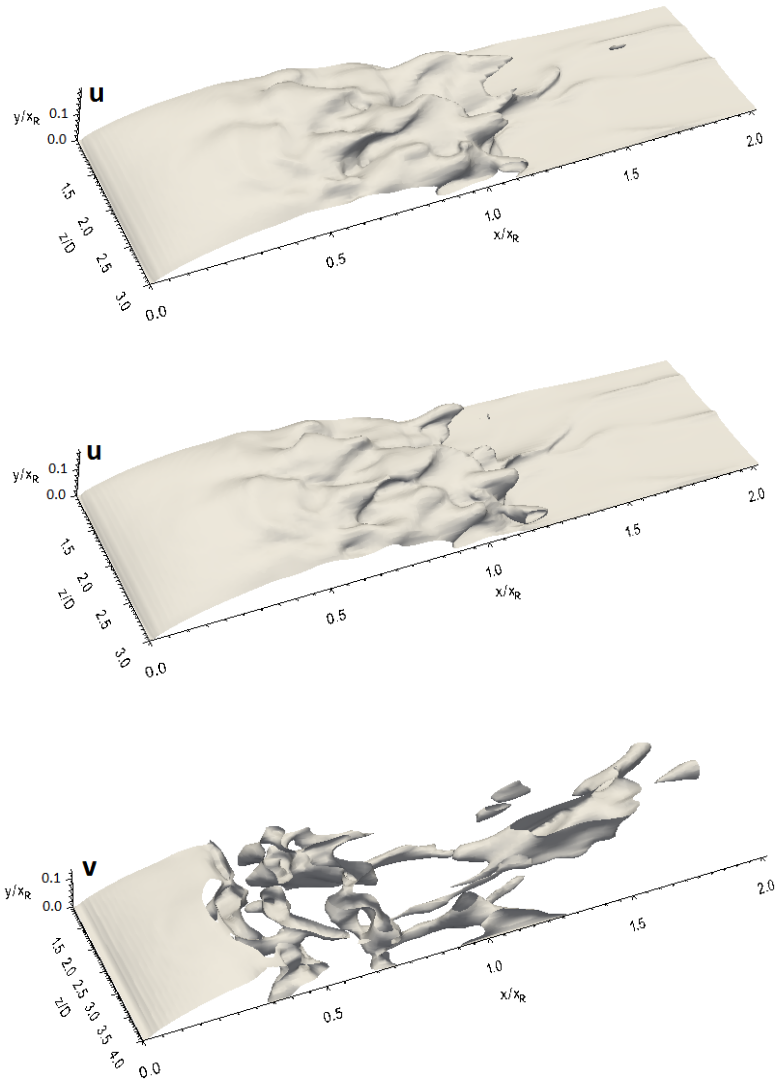

Caption for these figures is on the following page

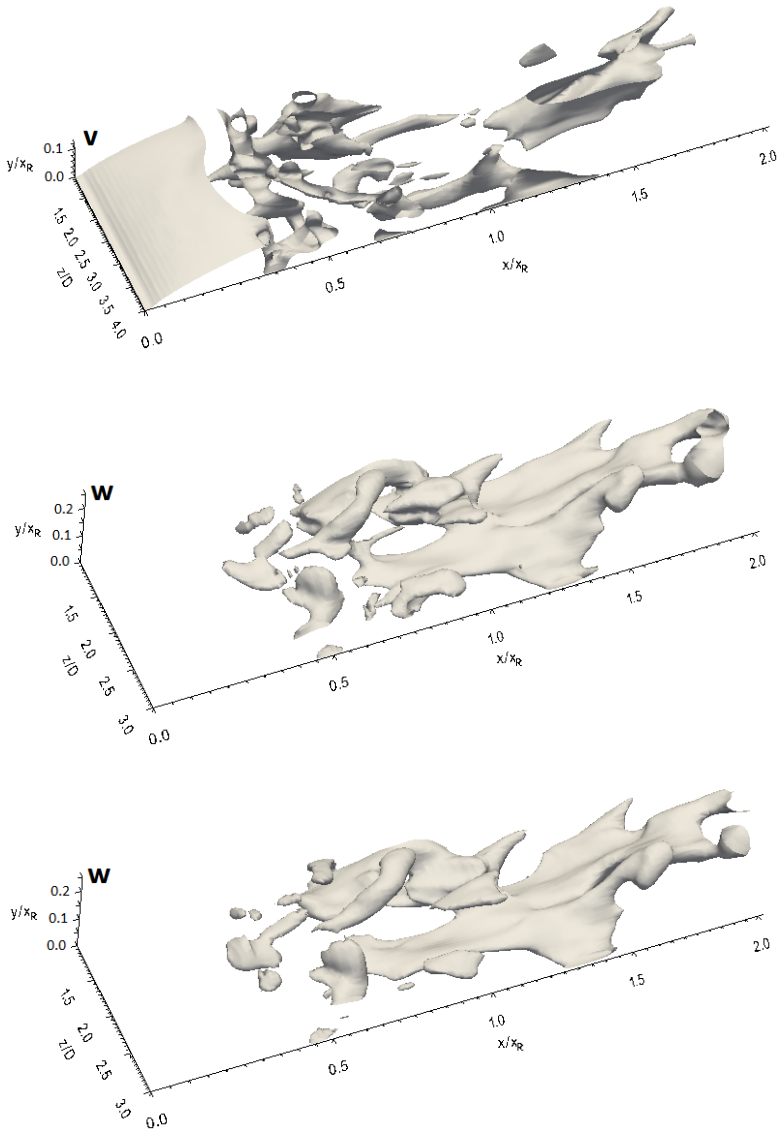

Fig. 5-6. Isosurfaces for the instantaneous velocity components at two arbitrary times for 3D_case2 with NFST

It is interesting to note that the laminar two-dimensional separated layer in 3D_case1 is slightly longer than that in 3D_case2. The current LES results demonstrate that the distance of the separated two-dimensional flow is 1.2*D* for the flat plate, 1.36*D* for 3D_case1 and 1.2245*D* for 3D_case2. This indicates that the transition takes place earlier in the flat plate flow. In addition, it seems that there is an effect (no matter how small) due to the aspect ratio of the three-dimensional geometry on the beginning of the

transition location. However, the beginning of the transition location in 3D_case2 is close to that of the flat plate.

It is noticeable that there is a difference in the distance of the instability low amplitude development region depending on the nature of the geometry. For the flat plate, this distance is 1.5*D*, 0.68*D* for 3D case_1 and 0.948*D* for 3D_case2, indicating that this region is longer in the flat plate than that in the other geometries. Moreover, the distance of this region increases with the increasing aspect ratio of the three-dimensional geometries.

The location at which the initial unsteadiness appears, and the unsteadiness low amplitude development region can be also shown by contours of the instantaneous streamwise velocity in the *y*-*z* plane at several streamwise locations for all geometries.

For the flat plate, it can be seen that the flow is steady at $x/x_R = 0.1$ as shown in Fig. 5-7. Further downstream, a low unsteadiness appears in the separated layer, where low amplitude waves can be seen in this layer as shown at $x/x_R = 0.2$. The unsteadiness remains relatively low up to $x/x_R = 0.45$, where a violent distortion in the free shear layer can be observed at this location onward. At $x/x_R = 0.8$, a total breakdown of the separated layer symmetry, which is associated with violent three-dimensional motions of the flow, occurs.

In order to show the flow development on the top and side surfaces of both three-dimensional geometries, the instantaneous streamwise velocity are plotted in *y*-*z* planes.

For 3D_case1, the instantaneous streamwise velocity contours in the *y*-*z* plane shown in Fig. 5-8 illustrate that the flow on the top and side surfaces is laminar, steady and two-dimensional up to $x/x_R = 0.4$. Further downstream, the flow becomes three-dimensional with the linear development of a relatively low unsteadiness up to $x/x_R = 0.6$. Then, violent non-linear motions are superimposed on the flow due to the increase in the amplitude of the disturbances, leading to a complete distortion of the symmetry of the separated layer as shown at $x/x_R = 0.7$ and 0.8 in Fig. 5-8.

For 3D_case2, the instantaneous streamwise velocity contours in the *y*-*z* plane shown in Fig. 5-9 illustrate that the shear layer symmetry on the top and side surfaces is uniform up to $x/x_R = 0.3$. Flow unsteadiness is present at a location greater than $x/x_R = 0.3$. A

relatively low distortion in the free shear layer takes place up to the midpoint of the separation bubble due to the linear development of the unsteadiness, as shown at x/x_R = 0.4 and x/x_R = 0.5 in Fig. 5-9. Further downstream, a violent distortion in the free shear layer, which is associated with the non-linear development of the unsteadiness and three-dimensional motions of the flow, can be observed.

Further evidence showing the locations of the start and development of the unsteadiness in the free shear layer is presented in the instantaneous streamwise velocity profiles taken at three arbitrary times.

For the flat plate, the instantaneous streamwise velocity profiles are approximately similar at x/x_R = 0.2, as shown in Fig. 5-1. Further downstream at x/x_R = 0.4, the difference in instantaneous streamwise velocity profiles is clear but is not as significant. At the other two locations (x/x_R = 0.6 and 0.8), instantaneous streamwise velocity profiles are quite different. This indicates violent disturbances in the flow.

For 3D_case1, the instantaneous streamwise velocity profiles that are shown in Fig. 5-2 illustrate that the flow is steady at x/x_R = 0.2. The difference in these profiles is barely apparent at x/x_R = 0.4. Further downstream, the difference in the streamwise velocity profiles is clear due to the violent unsteadiness in the flow.

The instantaneous streamline velocity profiles for 3D_case2 presented in Fig. 5-3 show that these profiles are similar at x/x_R = 0.2, demonstrating that the flow is two-dimensional and steady. The flow unsteadiness appears in the instantaneous streamwise velocity profiles at x/x_R = 0.4 onward, where different profiles at different times can be seen.

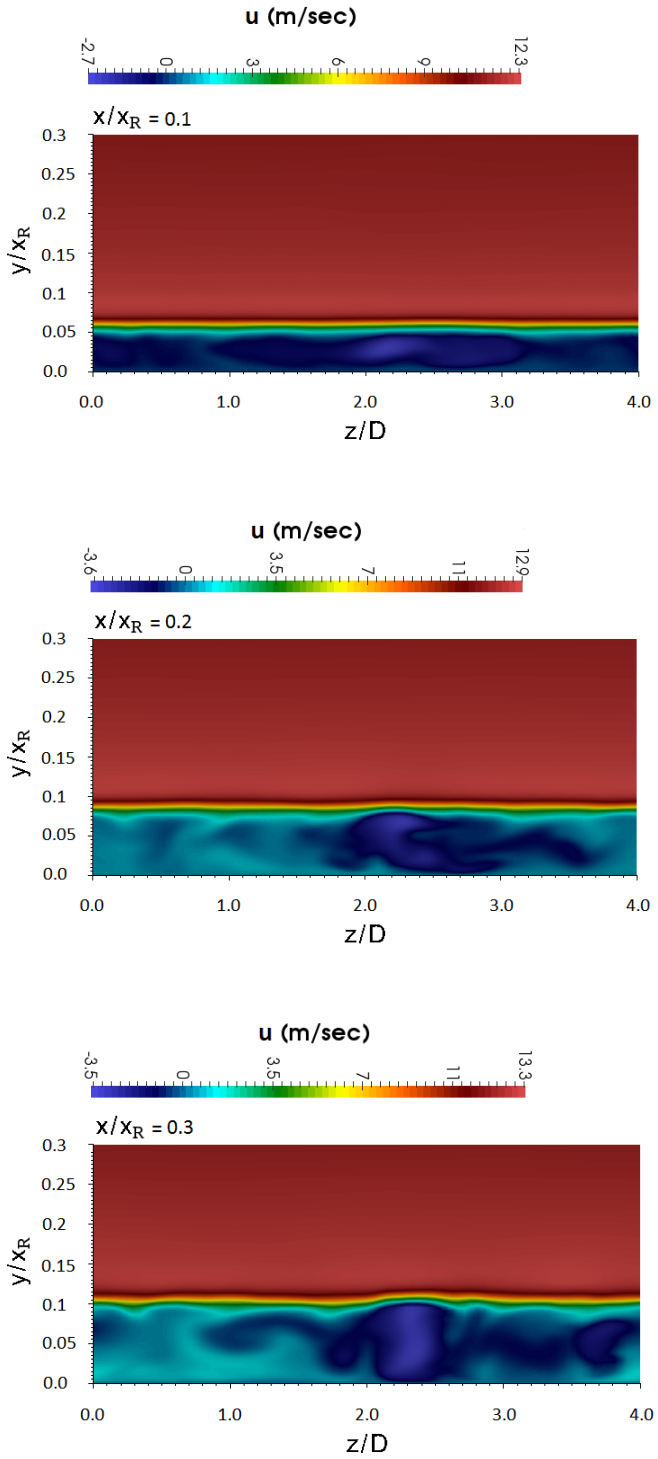

Caption for these figures is on the following page

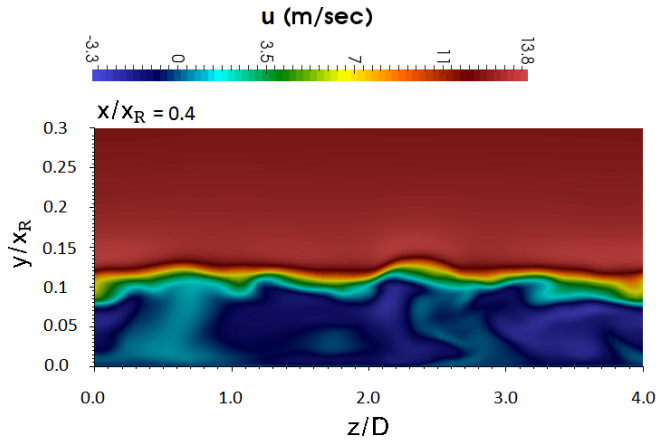
u (m/sec)
-3.3
0
3.5
7
11
13.8
x/xR = 0.4
y/xR
0.3
0.25
0.2
0.15
0.1
0.05
0.0
0.0
1.0
2.0
3.0
4.0
z/D

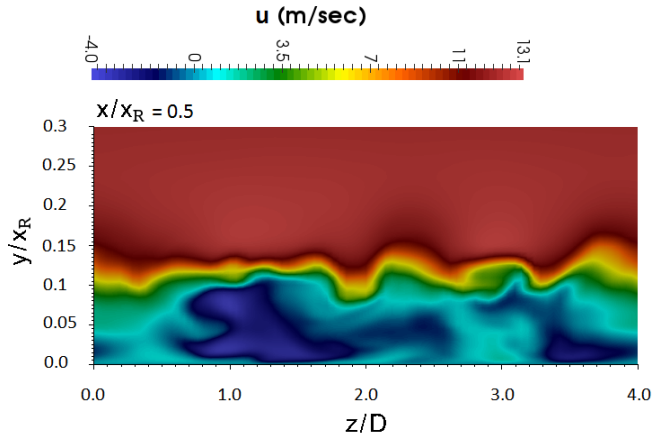
u (m/sec)
-4.0
0
3.5
7
11
13.1
x/xR = 0.5
y/xR
0.3
0.25
0.2
0.15
0.1
0.05
0.0
0.0
1.0
2.0
3.0
4.0
z/D

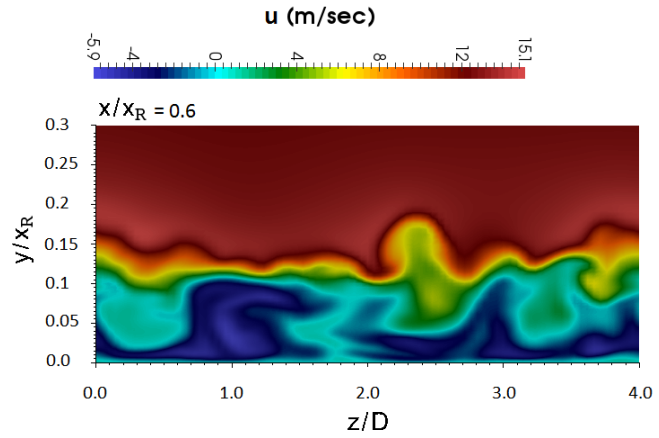
u (m/sec)
-5.9
-4
0
4
8
12
15.1
x/xR = 0.6
y/xR
0.3
0.25
0.2
0.15
0.1
0.05
0.0
0.0
1.0
2.0
3.0
4.0
z/D

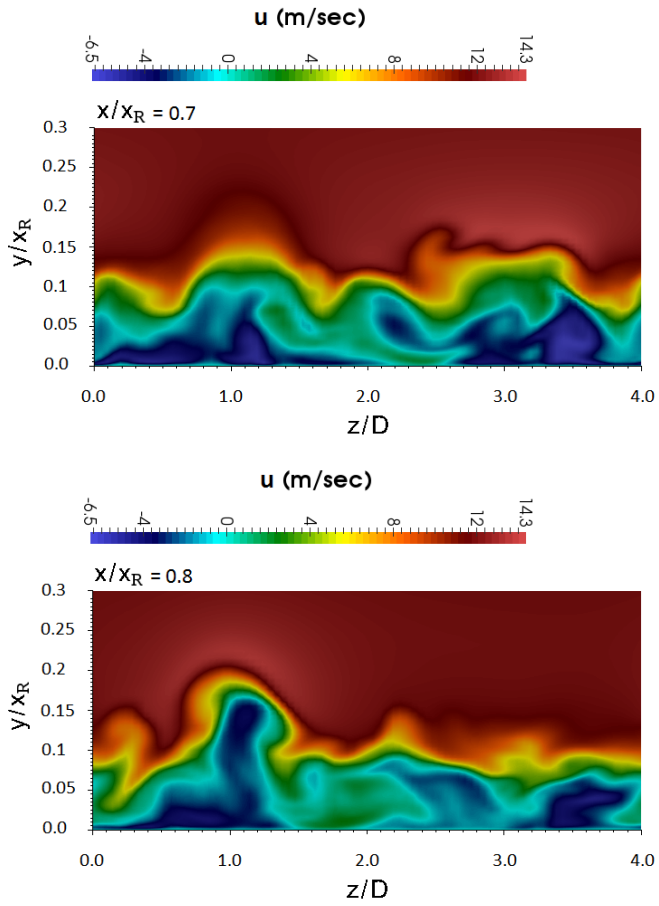

Fig. 5-7. Instantaneous streamwise velocity contours in the *y*-*z* plane at different streamwise locations for the flat plate with NFST

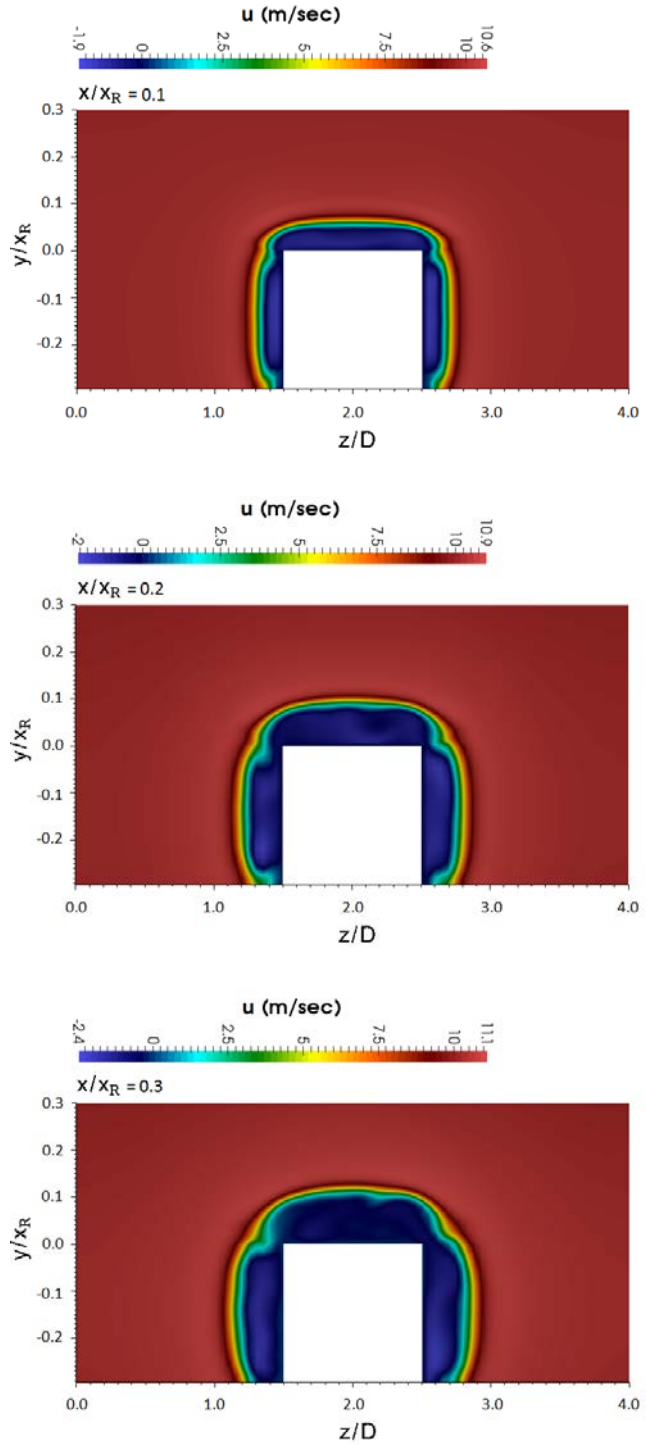

Caption for these figures is on the following page

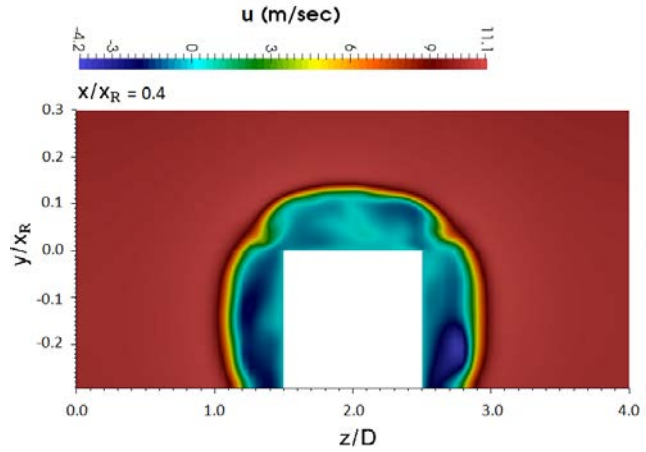
u (m/sec)
-4.2
-3
0
3
6
9
11.1
x/x_R = 0.4
0.3
0.2
0.1
0.0
-0.1
-0.2
y/x_R
0.0
1.0
2.0
3.0
4.0
z/D

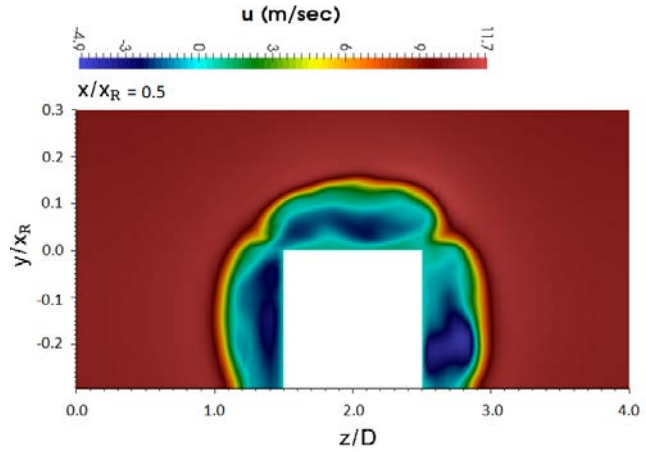
u (m/sec)
-4.9
-3
0
3
6
9
11.7
x/x_R = 0.5
0.3
0.2
0.1
0.0
-0.1
-0.2
y/x_R
0.0
1.0
2.0
3.0
4.0
z/D

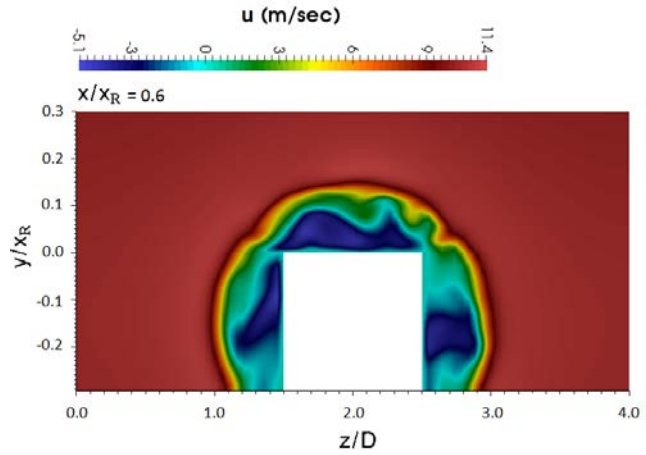
u (m/sec)
-5.1
-3
0
3
6
9
11.4
x/x_R = 0.6
0.3
0.2
0.1
0.0
-0.1
-0.2
y/x_R
0.0
1.0
2.0
3.0
4.0
z/D

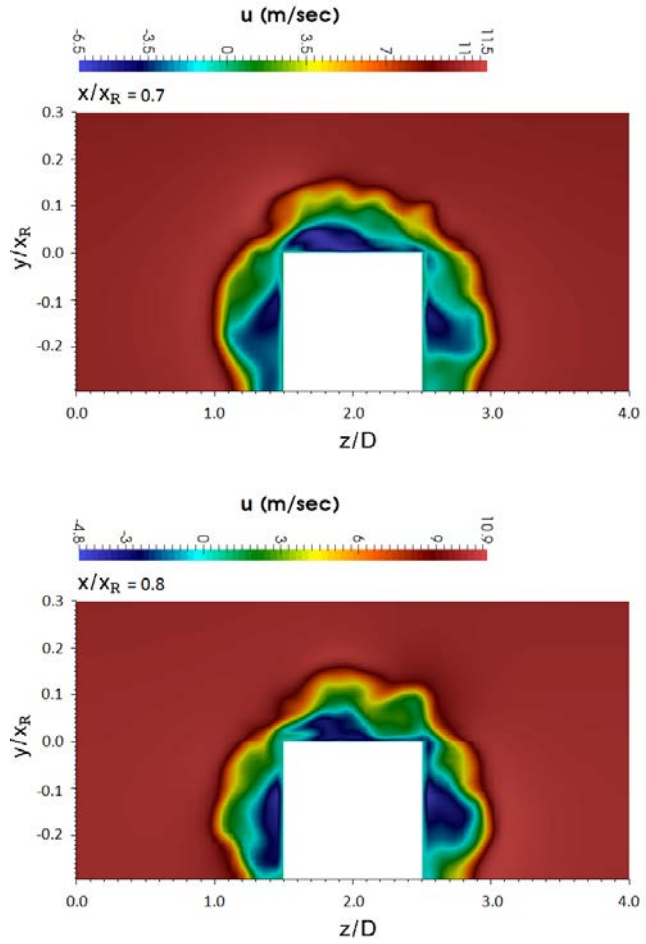

Fig. 5-8. Instantaneous streamwise velocity contours in the *y*-*z* plane at different streamwise locations for 3D_case1 with NFST

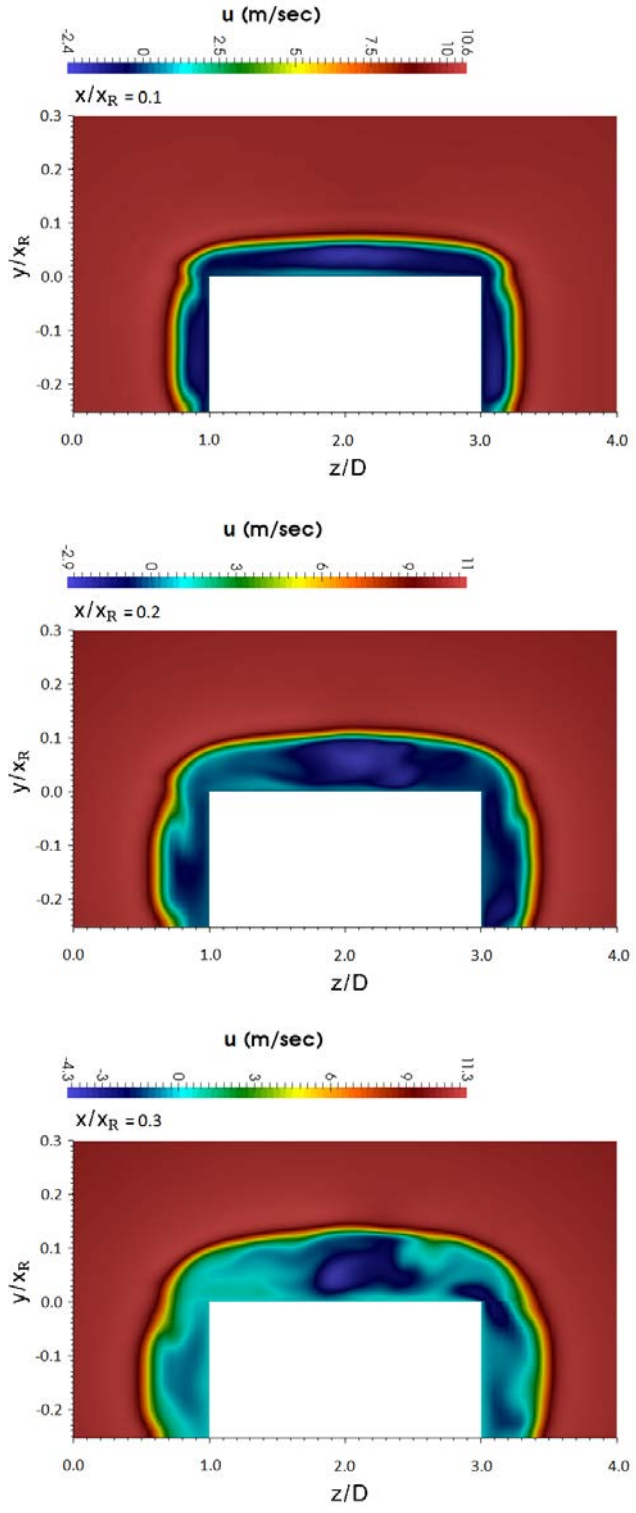

Caption for these figures is on the following page

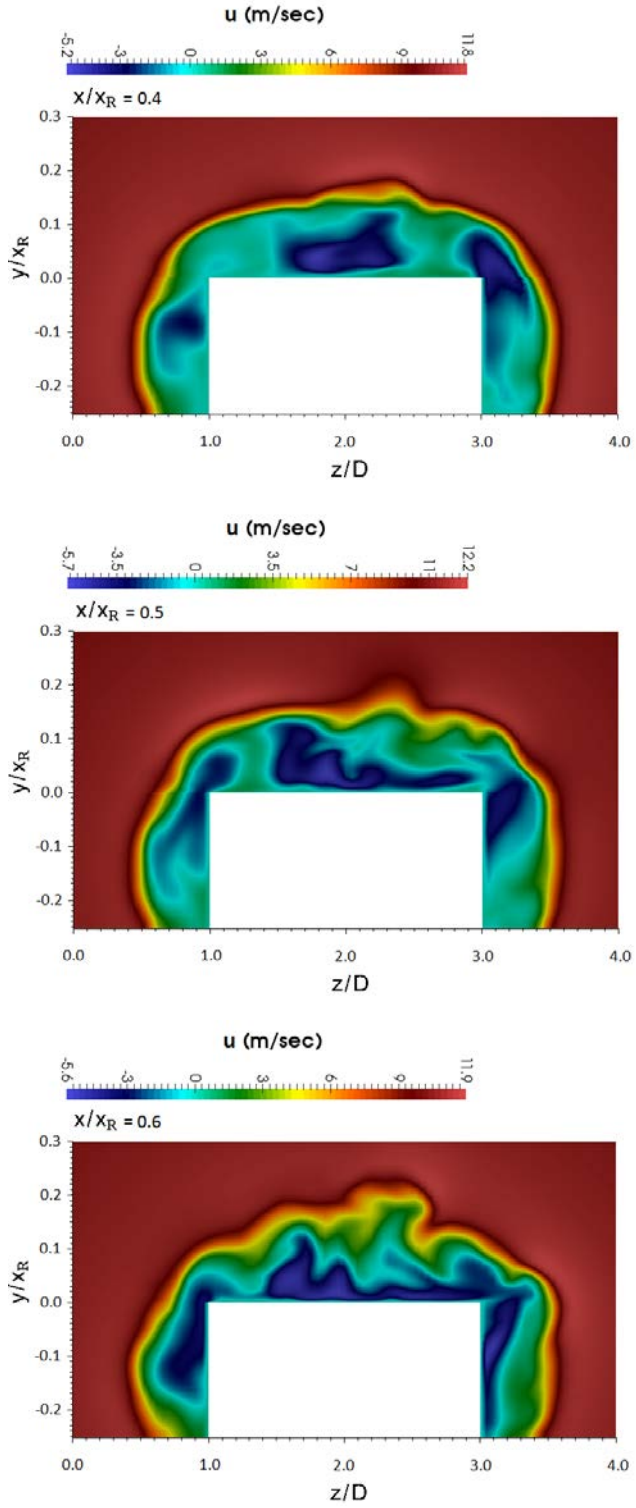
u (m/sec)
-5.2
-3
0
3
6
9
11.8
x/x_R = 0.4
y/x_R
z/D
u (m/sec)
-5.7
-3.5
0
3.5
7
11
12.2
x/x_R = 0.5
y/x_R
z/D
u (m/sec)
-5.6
-3
0
3
6
9
11.9
x/x_R = 0.6
y/x_R
z/D

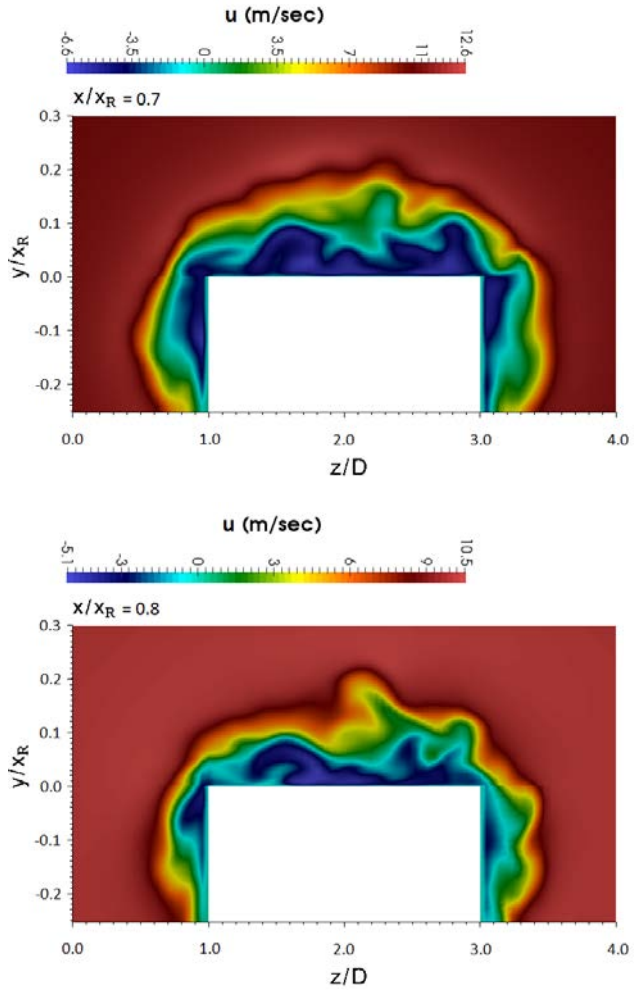

Fig. 5-9. Instantaneous streamwise velocity contours in the *y*-*z* plane at different streamwise locations for 3D_case2 with NFST

5.3 Primary instability mechanism for NFST

As shown for all geometries in the current study, streamwise velocity profiles have an inflection point, which is defined as a point where a graph changes between concave upward and concave downward, and is basically the location where the second derivative of the streamwise velocity is zero, i.e., $\frac{\partial^2 U}{\partial y^2} = 0$. The inflection point is a necessary condition for inviscid instability to small disturbances of the flow (Versteeg and Malalasekera, 2007). Therefore, the flow is inviscidly unstable for all geometries.

To identify whether the instability of the present free shear layer is the inviscid Kelvin-Helmholtz instability, the Kelvin-Helmholtz instability will be considered in more detail following Yang and Yoke (2001). Consider the case of two uniform, incompressible, and

inviscid fluids of densities ρ_1 and ρ_2 and velocities U_1 and U_2 separated by a horizontal boundary. Let the density ρ_2 of the upper fluid be less than the density ρ_1 of the lower fluid, so the arrangement is stable in the absence of streaming, i.e., $U_1 = U_2 = 0$. For any difference U_1-U_2, no matter how small it is, instability occurs for all wavenumbers greater than a minimum value, which can be defined as:

$$k_{min} = \frac{g(\propto_1 - \propto_2)}{\propto_1 \propto_2 (U_1 - U_2)^2} \tag{5-1}$$

where $\propto_1 = \frac{\rho_1}{\rho_1+\rho_1}$ and $\propto_2 = \frac{\rho_2}{\rho_1+\rho_1}$. The static arrangement stability in the absence of streaming is unable to restrain the instability of disturbances of sufficiently small wavelengths in the presence of streaming. This is the Kelvin-Helmholtz instability, as documented by Chandrasekhar (1981). To further clarify whether the independence of the Kelvin-Helmholtz instability on $|U_1$-$U_2|$ is due to the sharp discontinuities in ρ and U which have been assumed in its derivation, Chandrasekhar (1981) considered the case of continuous variation of U and a certain distribution of ρ (characterized by the Richardson number) and concluded from inviscid linear stability analysis that for any value of Richardson number, there are always bands of wavelengths for which the Kelvin-Helmholtz instability occurs. When the Richardson number is zero, i.e., for constant density, the condition for the Kelvin-Helmholtz instability is $0 < Kh < 1.2785$ where K is the wavenumber and h is the free shear layer thickness. This condition was considered by Yang and Voke (2001) to identify the instability mechanism of the transition.

The wavenumber K is given by:

$$K = 2\pi f / c \tag{5-2}$$

where f is the characteristic frequency and c is the wave speed which is the velocity at the critical layer, i.e., the streamwise velocity at the inflection point (the shear layer centre) (Kiya and Sasaki, 1983; Yang and Voke, 2001; Simoni et al., 2012).

In the current study, the centre of the shear layer is defined as the wall-normal location where the root mean square fluctuating streamwise velocity u'_{rms} attains its maximum value, which is consistent with the definition given by Kiya and Sasaki (1983). The edge of the shear layer is defined as the locus where $u'_{rms}/U_0 = 2.5\%$, similar to the definition given by Djilali and Gartshore (1991).

For the flat plate, the calculated centres and edges of the free shear layer are plotted together with the centres and edges of a turbulent separated layer on a blunt flat plate with a Reynolds number of 26×10^3 that were presented in the experiment of Kiya and Sasaki (1983) as shown in Fig. 5-10. Despite the separated flow nature and Reynolds number that were used in Kiya and Sasaki (1983) being different from those used in the current study, there is a good agreement between the distribution of the locations of centres and edges of the free shear layer in both studies as shown in Fig. 5-10.

Simulated centres and edges of the free shear layer for 3D_case1 and 3D_case are shown in Fig. 5-11 and Fig. 5-12, respectively.

To investigate if the current LES results satisfy the condition of the Kelvin-Helmholtz instability ($0 < Kh < 1.2785$) for all geometries in the present study, the following calculations are carried out.

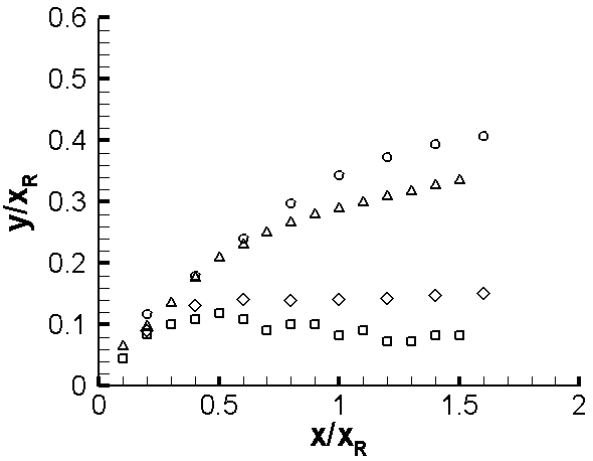

Fig. 5-10. Variation of the current centre of the shear layer (squares) and the current edge of the shear layer (triangles) with streamwise distance compared with experimental centre of the shear layer in Kiya and Sasaki (1983) (diamonds) and experimental edge of the shear layer in Kiya and Sasaki (1983) (circles) for the flat plate with NFST

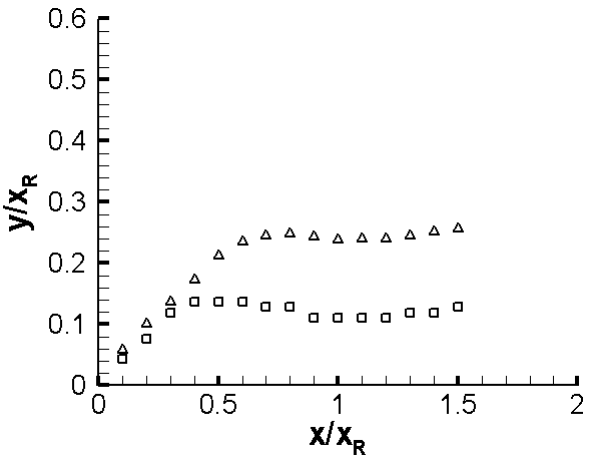

Fig. 5-11. Variation of centre of the shear layer (squares) and edge of the shear layer (triangles) with streamwise distance for 3D_case1 with NFST

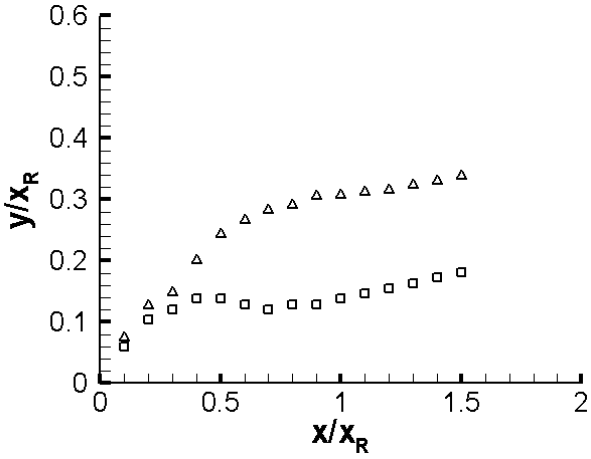

Fig. 5-12. Variation of centre of the shear layer (squares) and edge of the shear layer (triangles) with streamwise distance for 3D_case2 with NFST

For the flat plate, the shear layer thickness at the beginning of the unsteadiness at x/x_R = 0.2 is $0.0982x_R$ as shown in Fig. 5-10. Hence, the unstable region for the wavenumbers can be represented as $0 < K < 13.0193/x_R$. Therefore, the Kelvin-Helmholtz instability will not exist in the current study when the wavenumbers are higher than $13.0193/x_R$ or wavelengths are smaller than $0.4828x_R$, (where the wavelength is defined as $2\pi/K$).

The wave speed at x/x_R = 0.2 is $0.5032U_0$. The characteristic frequency varies between 120 Hz and 140 Hz or $0.7639U_0/x_R$ - $0.8912U_0/x_R$, as will be shown in Chapter 6. Hence, the maximum wavenumber ($K_{max} = 2\pi f_{max}/c$) at the unsteadiness starting location is $11.1324/x_R$ corresponding to the wavelength of $0.5646x_R$.

The maximum wave numbers at several streamwise positions up to $x/x_R = 0.4$ are shown in Table 5-1. All wavenumbers are within the Kelvin-Helmholtz instability conditions. Therefore, it can be concluded that the free shear layer for the flat plate is inviscidly unstable due to the Kelvin-Helmholtz instability mode.

x/x_R	0.2	0.25	0.3	0.35	0.4
K_{max}	$11.1324/x_R$	$9.2608/x_R$	$11.261/x_R$	$8.0229/x_R$	$10.5995/x_R$

Table 5-1. Maximum wavenumber values at several streamwise positions for the flat plate with NFST

For 3D_case1, the shear layer thickness at the position where the unsteadiness first appears at $x/x_R = 0.4$ is $0.1735x_R$ as shown in Fig. 5-11. Thus, the unstable region for the wavenumbers becomes $0 < K < 7.3688/x_R$. Hence, the Kelvin-Helmholtz instability mechanism will not occur in the current study for wavenumbers higher than $7.3688/x_R$ or wavelengths smaller than $0.853x_R$.

The wave speed at $x/x_R = 0.4$ is $0.6948U_0$. The characteristic frequency varies between 150 Hz and 180 Hz or $0.5411U_0/x_R$ - $0.6493U_0/x_R$, as will be shown in Chapter 6. Therefore, the maximum wavenumber at the unsteadiness starting point is $K_{max} = 2\pi f_{max}/c = 5.874/x_R$ corresponding to a wavelength of $1.07x_R$.

Table 5-2 presents the maximum wavenumbers at several streamwise locations, and clearly shows that the primary instability mechanism for 3D_case1 is the inviscid Kelvin-Helmholtz instability mechanism.

x/x_R	0.4	0.45	0.5	0.55
K_{max}	$5.874/x_R$	$6.927/x_R$	$6.2539/x_R$	$6.251/x_R$

Table 5-2. Maximum wavenumber values at several streamwise positions for 3D_case1 with NFST

For 3D_case2, the thickness of the shear layer at the unsteadiness starting position ($x/x_R = 0.31$) is $0.1501x_R$. The unstable region for the wavenumbers can be represented as $0 < K < 8.5176/x_R$. Therefore, the Kelvin-Helmholtz instability mechanism will not exist in

the current study when wavenumbers are higher than $8.5176/x_R$ or wavelengths are smaller than $0.738x_R$.

The wave speed at $x/x_R = 0.31$ is $0.599U_0$ and the characteristic frequency varies within the range of 150 Hz - 180 Hz or $0.6286U_0/x_R$ - $0.7543U_0/x_R$. Therefore, the maximum wavenumber at the unsteadiness start position is $K_{max} = 2\pi f_{max}/c = 7.9153/x_R$ corresponding to a wavelength of $0.794x_R$. The primary instability mechanism in the free shear layer for 3D_case2 is the inviscid Kelvin-Helmholtz instability mechanism because all values of K_{max} at the selected locations in the free shear layer are within the conditions required for the Kelvin-Helmholtz instability as shown in Table 5-3.

x/x_R	0.31	0.35	0.4	0.45	0.5
K_{max}	$7.9153/x_R$	$6.5092/x_R$	$7.6187/x_R$	$7.8455/x_R$	$8.2393/x_R$

Table 5-3. Maximum wavenumber values at several streamwise positions for 3D_case2 with NFST

Roberts and Yaras (2006) illustrated that the condition of the Kelvin-Helmholtz instability mechanism, depending on the above conclusion of Chandrasekhar (1981), is associated with the velocity profile at the unsteadiness start location, which is well represented by a hyperbolic tangent function. They reported that the frequency range of the Kelvin-Helmholtz instability corresponds to $0 < Kd < 1$, where K is the wavenumber of the dominant disturbance frequency and d is a length scale determined by the hyperbolic tangent curve fit to the velocity distribution, which is roughly about 0.25 of the shear layer thickness.

In the current study, $K_{max}\, d$ at the unsteadiness start location is 0.2733 for the flat plate, 0.2547 for 3D_case1 and 0.297 for 3D_case2. These values satisfy the Kelvin- Helmholtz instability condition ($0 < Kd < 1$) that is presented in Roberts and Yaras (2006). Therefore, the primary instability mechanism that drives the transition is indeed the Kelvin-Helmholtz instability mechanism in all geometries for the current study.

5.4 Absolute and convective instability for FST

Instantaneous streamwise velocity profiles in the presence of elevated intensities of free stream turbulence are plotted in Fig. 5-13 for the flat plate, Fig. 5-14 for 3D_case1 and Fig. 5-15 for 3D_case2. In these figures, four streamwise locations are chosen to present the magnitude of the reverse flow at three arbitrary times. Streamwise positions are distributed within the separation bubble to cover the region extending from a point close to the separation to one close to the reattachment. These positions are x/x_R = 0.2, 0.4, 0.6 and 0.8.

The magnitude of the reverse flow in the instantaneous streamwise velocity is presented to reveal the existence of the absolute instability in the separation bubble. The absolute instability takes place if the amount of the reverse flow is more than 20% of the maximum local velocity (Alam and Sandham, 2000). In the current study, the reverse flow amount is lower than 20% for all geometries as shown in Figs. 5-13, 5-14 and 5-15, which demonstrates that even with elevated intensities of free stream turbulence, the separation bubble is classified as convectively unstable where there is no sign of absolute instability in the flow in the current study.

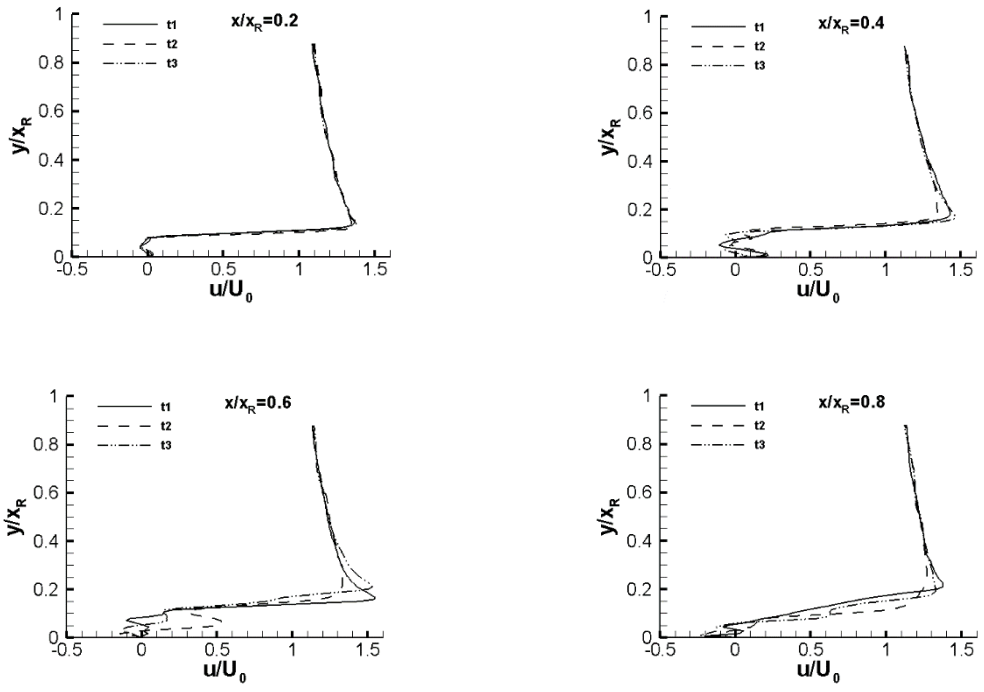

Fig. 5-13. Instantaneous streamwise velocity profiles at three arbitrary times for the flat plate with FST

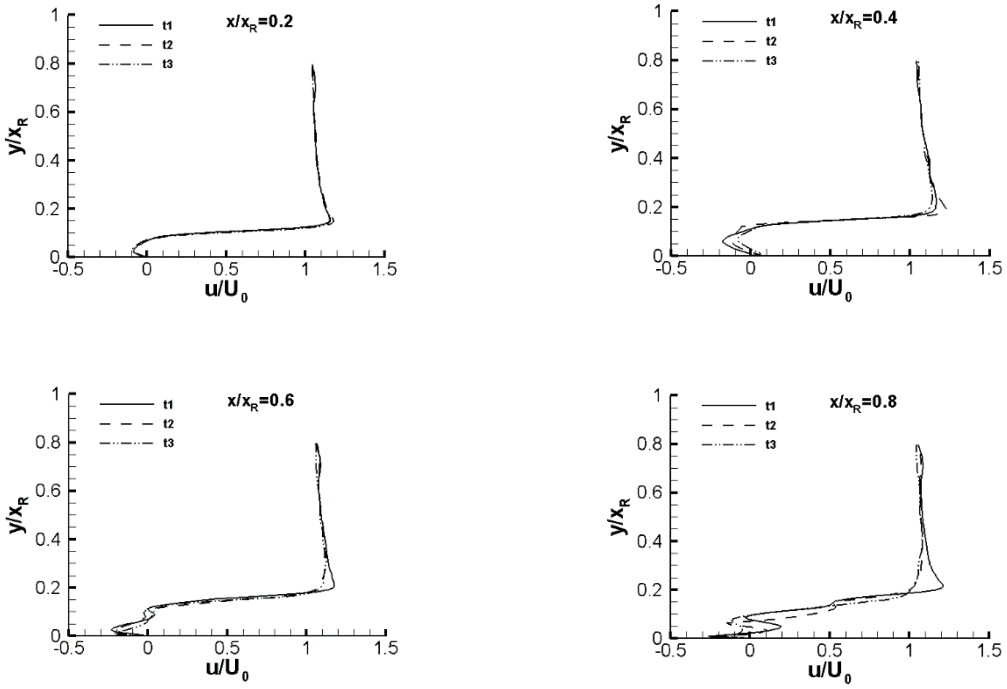

Fig. 5-14. Instantaneous streamwise velocity profiles at three arbitrary times for 3D_case1 with FST

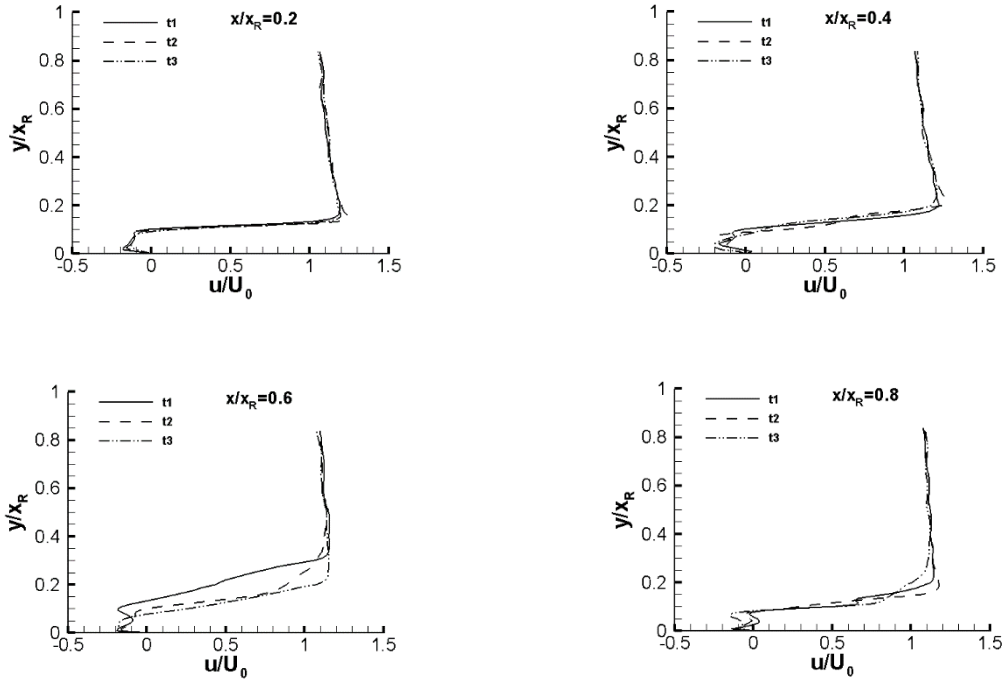

Fig. 5-15. Instantaneous streamwise velocity profiles at three arbitrary times for 3D_case2 with FST

5.5 Unsteadiness location for FST

With an elevated intensity of free stream turbulence, the unsteadiness start location and region of low amplitude growth of the unsteadiness for all geometries can be identified by inspection of the instantaneous velocity components isosurfaces. Instantaneous velocity components isosurfaces with FST at two arbitrary times are plotted in Fig. 5-16 for the flat plate, Fig. 5-17 for 3D_case1 and Fig. 5-18 for 3D_case2.

For the flat plate, the instantaneous velocity components clearly show that the unsteadiness of the free shear layer starts at x/x_R = 0.1 (corresponding to x/D = 0.42), where the initial appearance of the spanwise velocity can be seen in Fig. 5-16. Before this location, the flow is laminar, two-dimensional and steady. Therefore, it can be seen that the unsteadiness in the free shear layer moves upstream from x/D = 1.2 with NFST to x/D = 0.42 with FST.

Unsteadiness in the separated shear layer with FST grows with low amplitude from x/x_R = 0.1 to x/x_R = 0.3, where the separated shear layer, in a relative sense, maintains its symmetry in this region. Further downstream, there is a breakdown in the symmetry of the separated shear layer indicating the strong and rapid growth of the disturbances in the flow.

For 3D_case1, the free shear layer is still two-dimensional, steady and laminar up to x/x_R = 0.3 (corresponding to x/D = 0.75), where at this location and onward, the spanwise velocity can be clearly seen, as shown in Fig. 5-17. Hence, due to high disturbances in the incoming flow, the laminar flow distance in the free shear layer reduces from 1.36D with NFST to 0.75D with FST.

Free shear layer with FST develops with a relatively low level of disturbances within the distance starting from x/x_R = 0.3 and ending at x/x_R = 0.5. Further downstream, non-linear growth of disturbances takes place as shown in Fig. 5-17.

For 3D_case2, the steady laminar part of the free shear layer decreases from x/D = 1.2245 with NFST to x/D = 0.62 using FST as shown in Fig. 5-18. It is clear seen that the position of the unsteadiness that begins in the free shear layer is at x/x_R = 0.2 (corresponding to

x/D = 0.62). In addition, the low amplitude development region of the unsteadiness extends from x/x_R = 0.2 to x/x_R = 0.4.

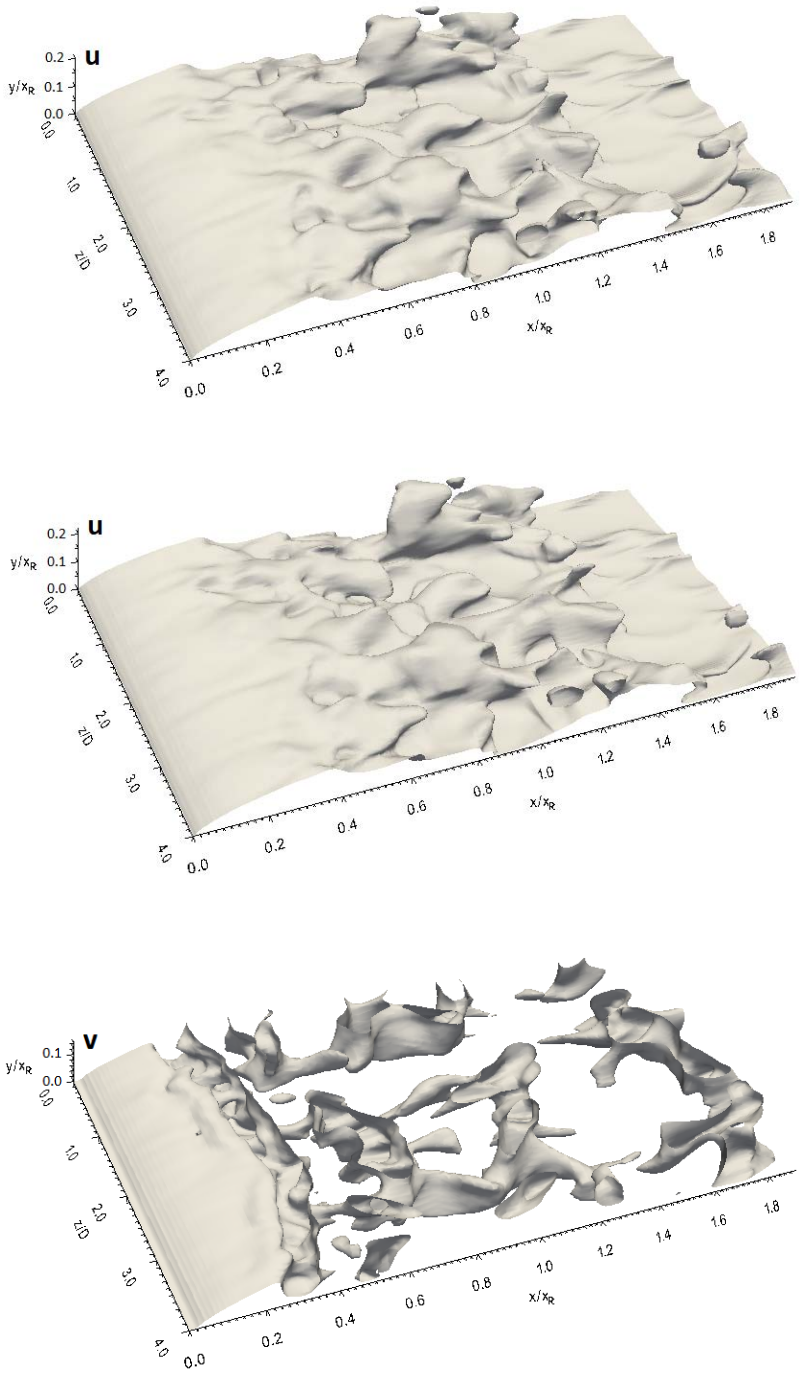

Caption for these figures is on the following page

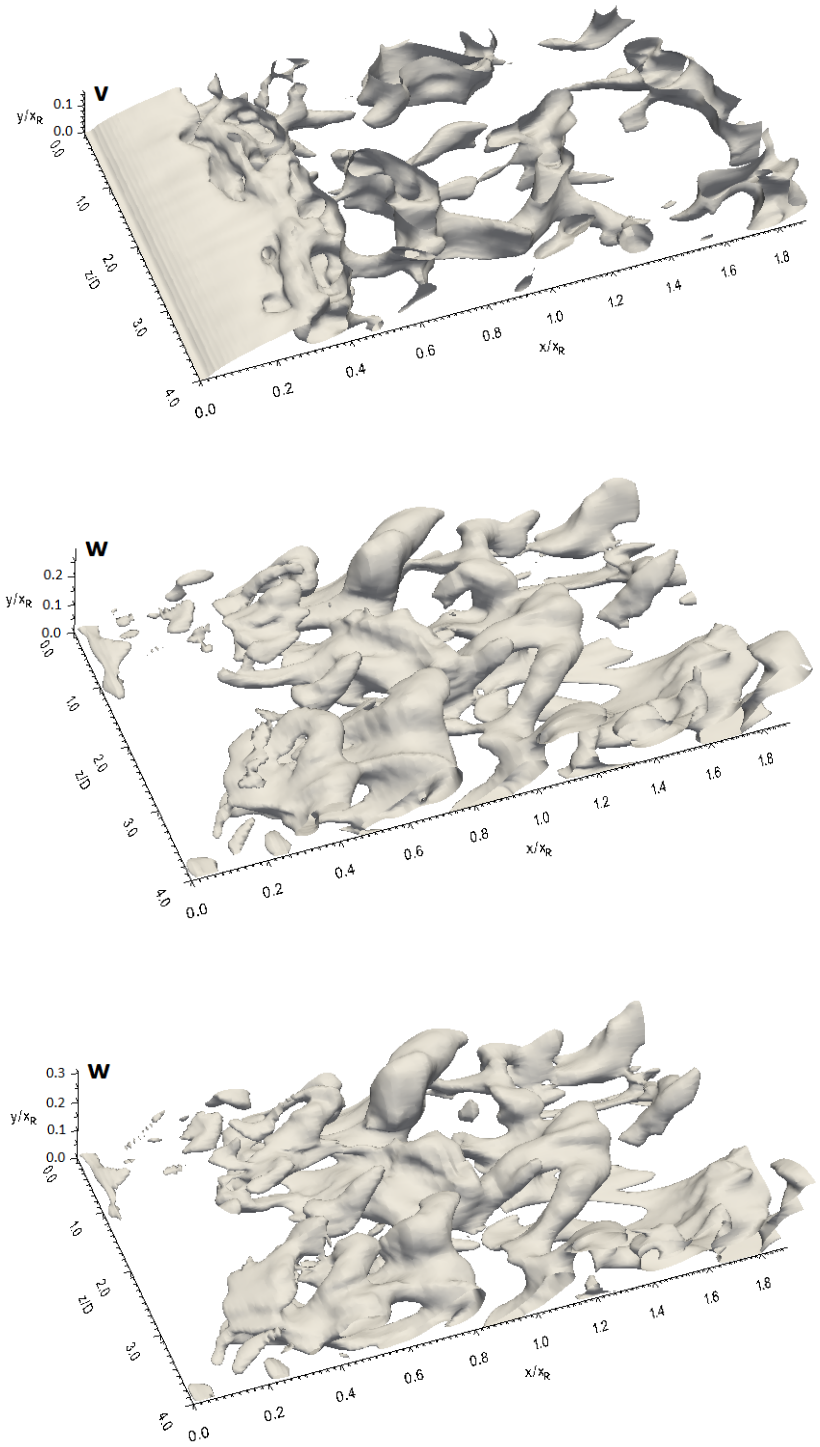

Fig. 5-16. Isosurfaces for the instantaneous velocity components at two arbitrary times for the flat plate with FST

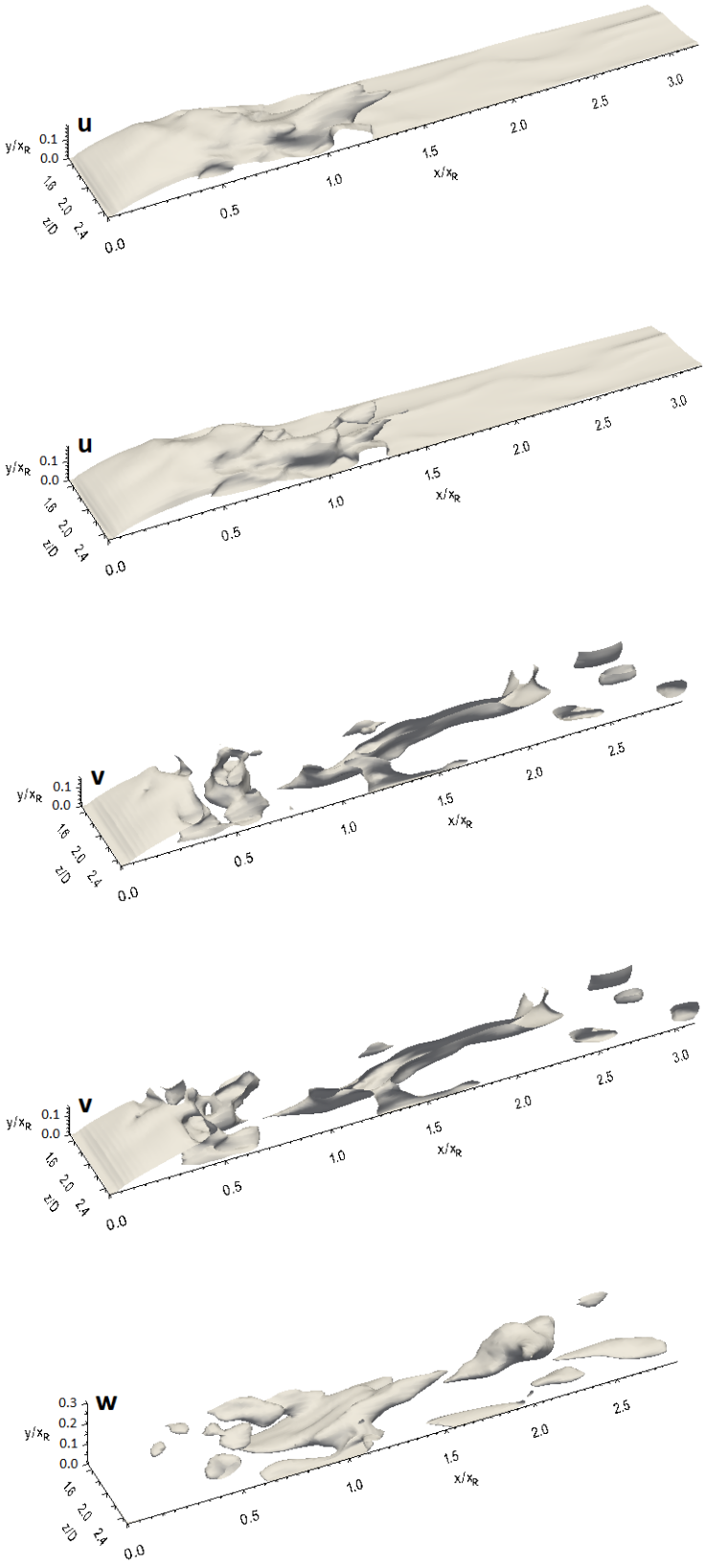

Caption for these figures is on the following page

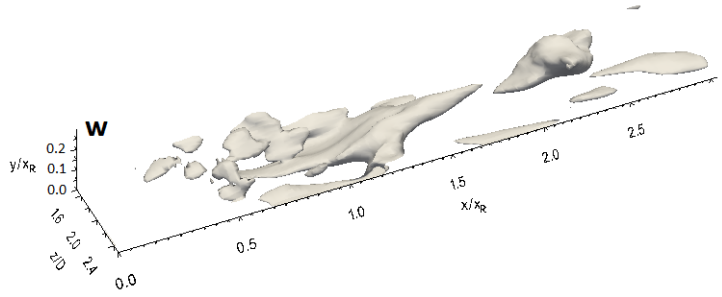

Fig. 5-17. Isosurfaces for the instantaneous velocity components at two arbitrary times for 3D_case1 with FST

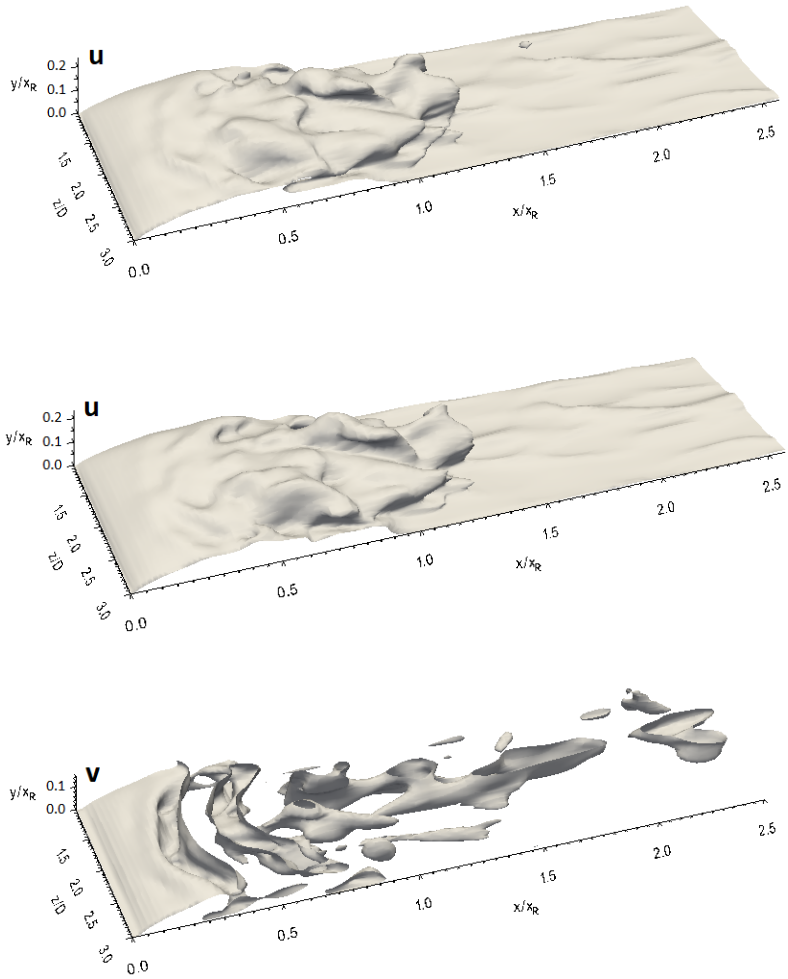

Caption for these figures is on the following page

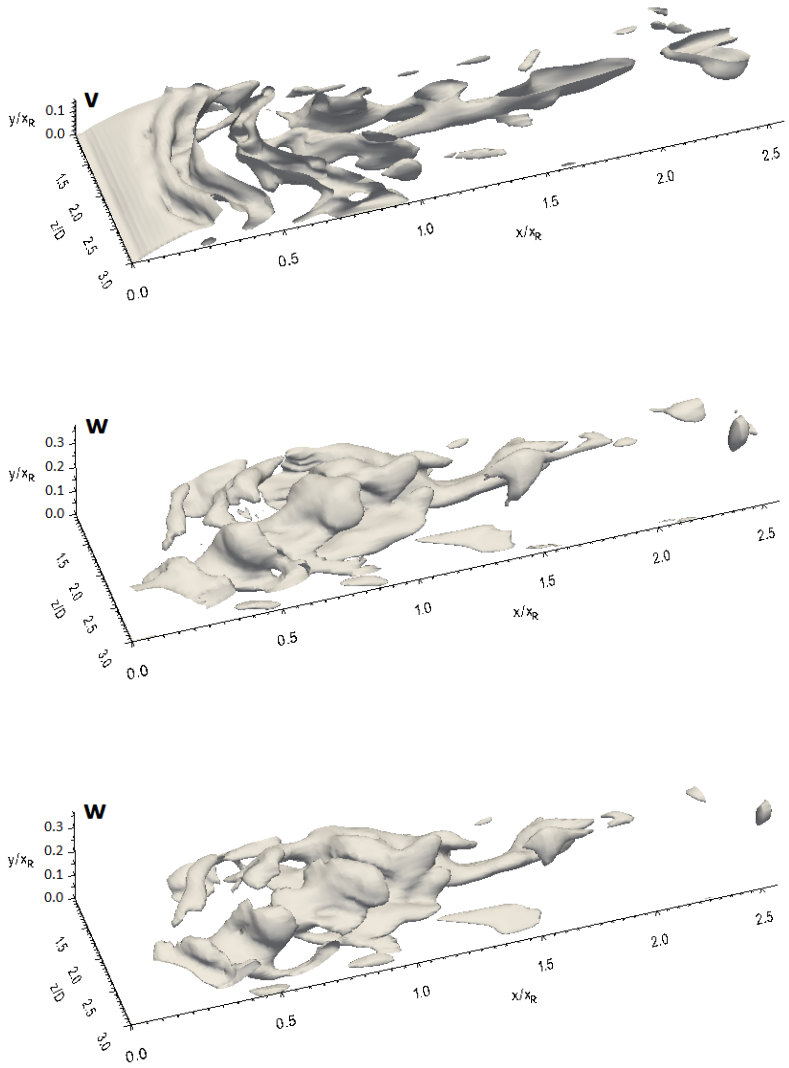

Fig. 5-18. Isosurfaces for the instantaneous velocity components at two arbitrary times for 3D_case2 with FST

In general, it can be seen from the instantaneous velocity components isosurfaces for all geometries in the current study that the unsteadiness starting location in the free shear layer moves upstream with FST leading to an early transition. This is consistent with the results presented by Yang and Abdalla (2009) and Langari and Yang (2013).

The first appearance and development stages of the unsteadiness in the separated shear layer for all geometries are also presented by employing *y*-*z* contours of the instantaneous streamwise velocity at different streamwise locations in the separation bubble. The first streamwise location is close to the separation line (x/x_R = 0.1) and the last streamwise

location is near to the mean reattachment (x/x_R =0.8), as shown in Fig. 5-19 for the flat plate, Fig. 5-20 for 3D_case1 and Fig. 5-21 for 3D_case2.

For the flat plate, the separated shear layer is approximately quiet at x/x_R = 0.1, where a low waviness can just be seen in the separated shear layer indicating the start of the unsteadiness as shown in Fig. 5-19. At x/x_R = 0.2, the waviness becomes stronger, but the separated layer essentially maintains its symmetry. Breakdown of the separated shear layer symmetry takes place at x/x_R = 0.3, where the non-linear growth of the disturbances is in the free shear layer. Further downstream, the unsteadiness becomes violent referring strong three-dimensional motions of the flow. Then, a total distortion of the separated shear layer can be clearly observed at x/x_R = 0.8 as shown in Fig. 5-19.

For 3D_case1, the instantaneous streamwise velocity contours in the *y*-*z* plane presented in Fig. 5-20 show that the flows on the top and side surfaces of this geometry are still laminar up to x/x_R = 0.3. At x/x_R = 0.3, there is a low amplitude waving in the separated shear layer, indicating the start of flow unsteadiness. In the region between x/x_R = 0.3 and x/x_R = 0.5, the unsteadiness grows linearly with a slight distortion in the separated layer. Further downstream, the symmetry of the free shear layer breaks down, indicating the existence of violent motions of the flow as shown at x/x_R = 0.8 in Fig. 5-20.

For 3D_case2, the unsteadiness beginning in the separated shear layer on the top and side surfaces of this geometry is clearly seen at x/x_R = 0.2 as presented in Fig. 5-21. At x/x_R = 0.2, a low-amplitude distortion in the free shear layer begins. Upstream of x/x_R = 0.2, the free shear layer is completely quiet, indicating the flow in the region which starts from the leading edge of the geometry and ends at x/x_R = 0.2 is laminar, two-dimensional and steady. The region of the linear development of the unsteadiness in the free shear layer extents from x/x_R = 0.2 to x/x_R = 0.4 as shown in Fig. 5-21. In this region, there is a slight development in the unsteadiness. Further downstream, violent three-dimensional motions associated with the non-linear growth of the flow unsteadiness occur. Close to the mean reattachment line, high amplitude of the disturbances leads to a complete distortion of symmetry of the separated shear layer as shown at x/x_R = 0.8 in Fig. 5-21.

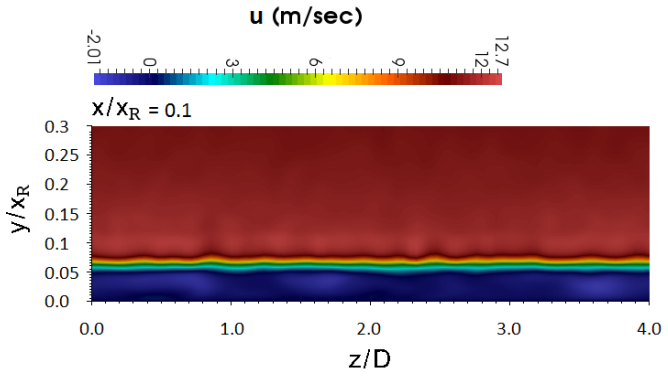

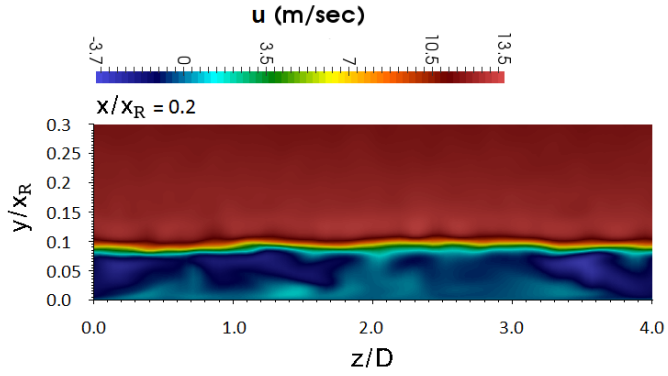

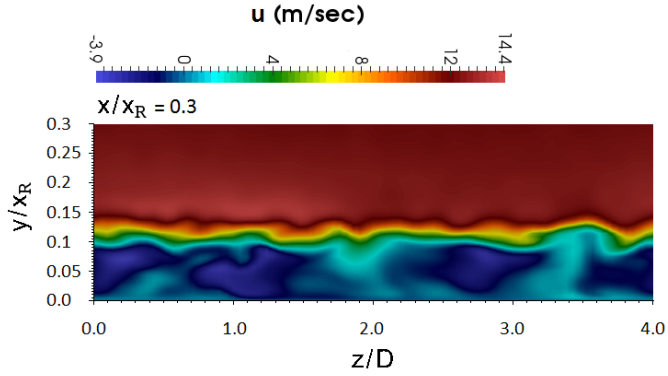

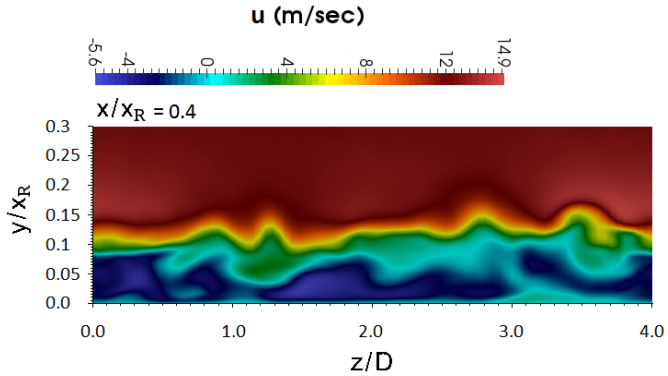

Caption for these figures is on the following page

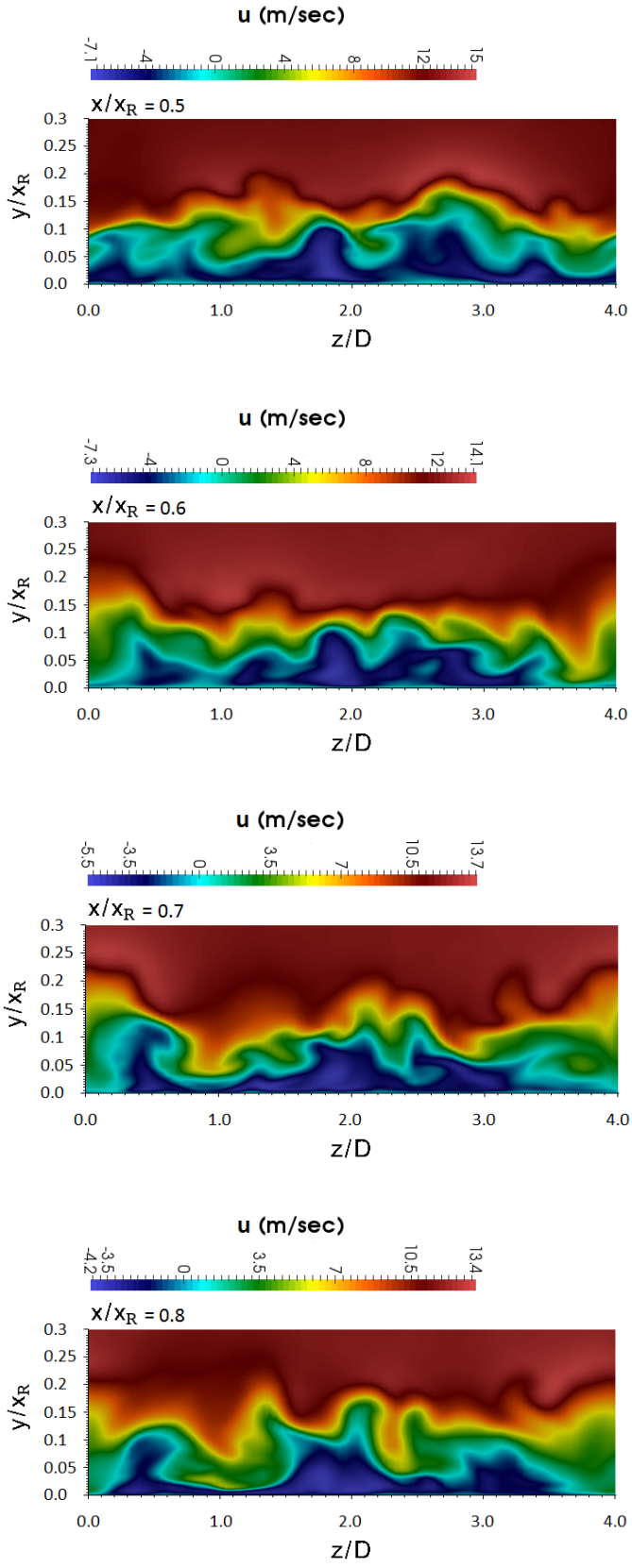

Fig. 5-19. Instantaneous streamwise velocity contours in the *y-z* plane at different streamwise locations for the flat plate with FST

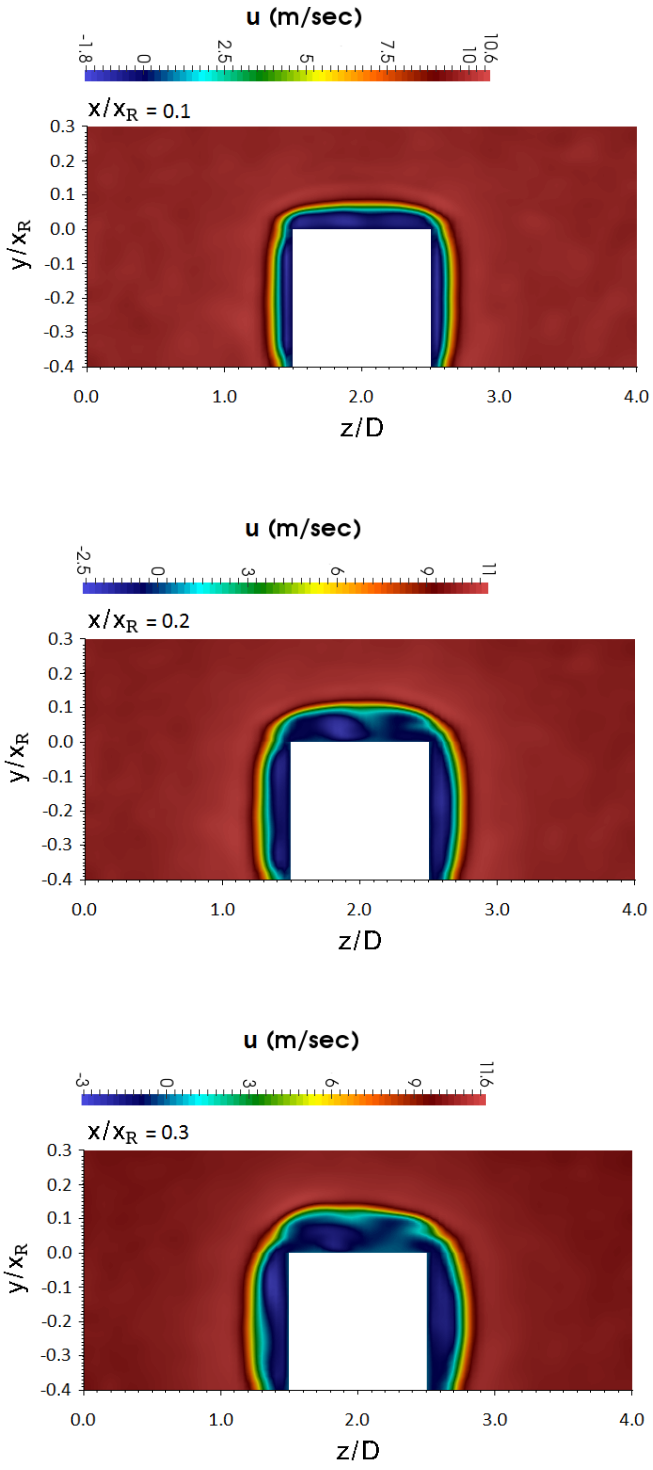

Caption for these figures is on the following page

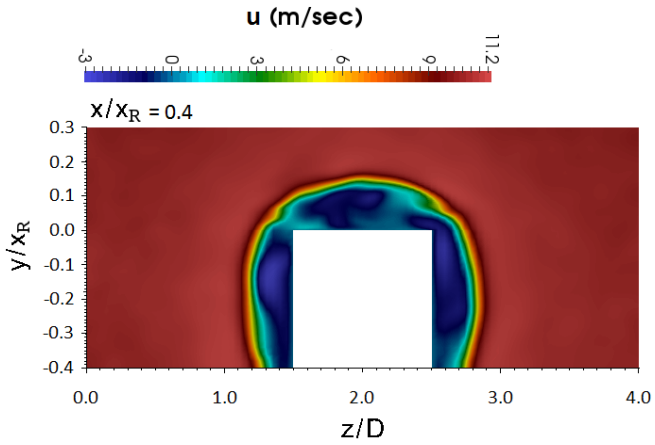
u (m/sec)
-3
0
3
6
9
11.2
x/x_R = 0.4
0.3
0.2
0.1
0.0
-0.1
-0.2
-0.3
-0.4
y/x_R
0.0
1.0
2.0
3.0
4.0
z/D

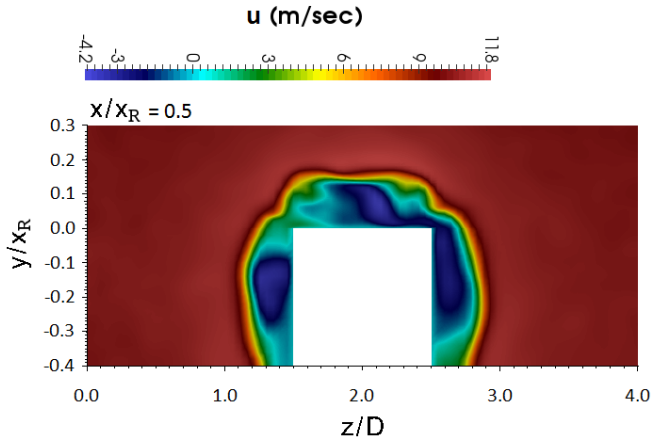
u (m/sec)
-4.2
-3
0
3
6
9
11.8
x/x_R = 0.5
0.3
0.2
0.1
0.0
-0.1
-0.2
-0.3
-0.4
y/x_R
0.0
1.0
2.0
3.0
4.0
z/D

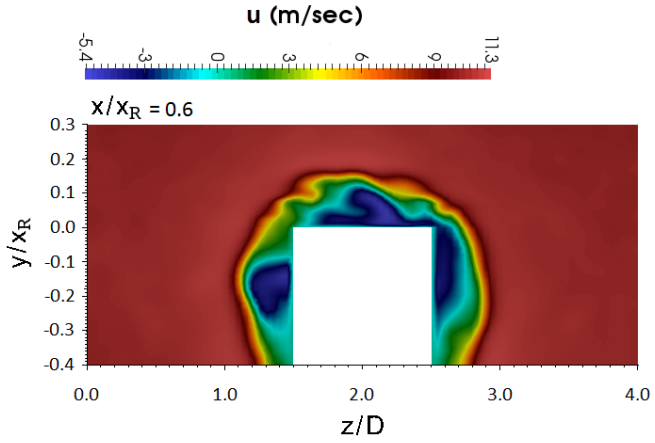
u (m/sec)
-5.4
-3
0
3
6
9
11.3
x/x_R = 0.6
0.3
0.2
0.1
0.0
-0.1
-0.2
-0.3
-0.4
y/x_R
0.0
1.0
2.0
3.0
4.0
z/D

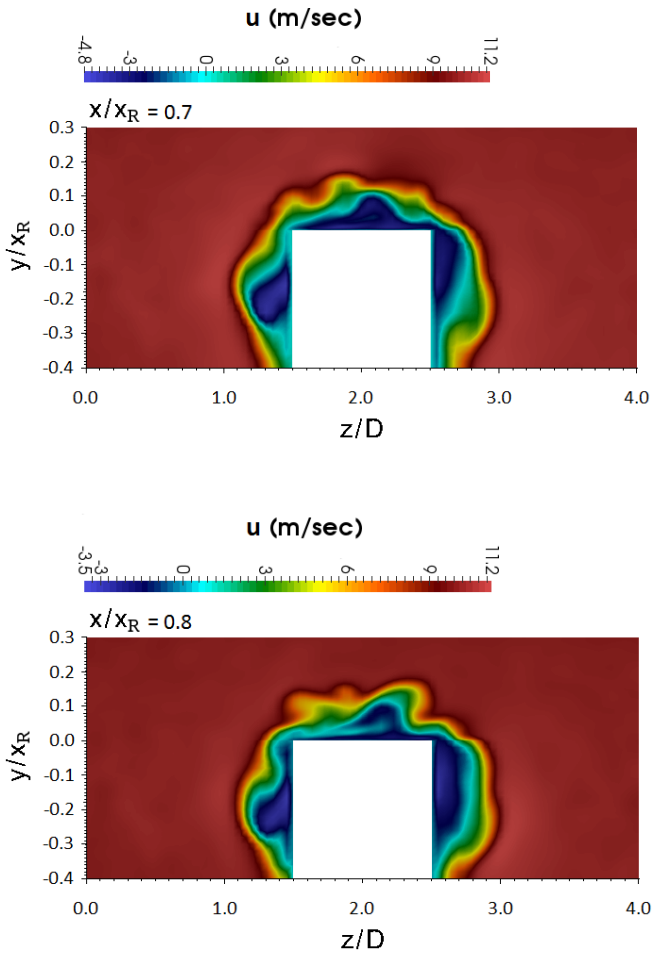

Fig. 5-20. Instantaneous streamwise velocity contours in the *y-z* plane at different streamwise locations for 3D_case1 with FST

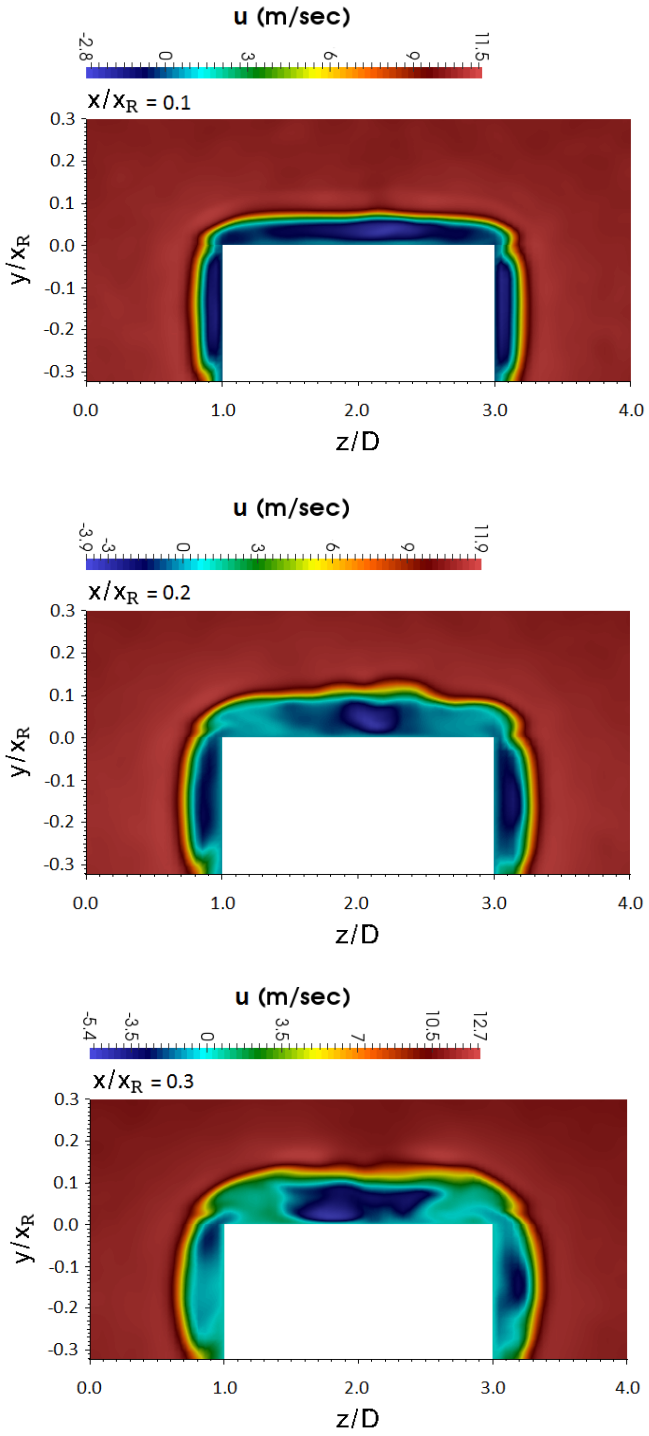

Caption for these figures is on the following page

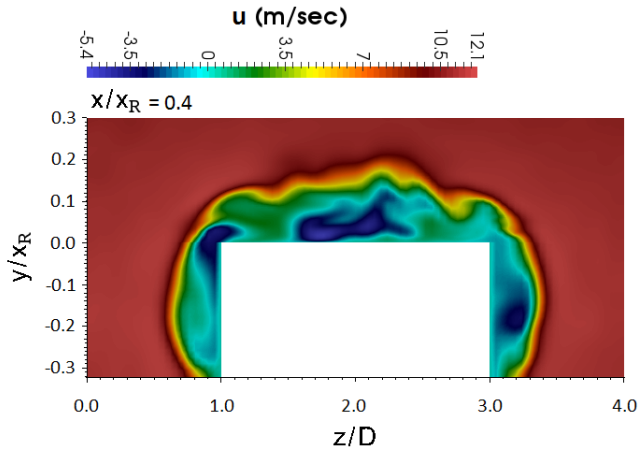
u (m/sec)
-5.4
-3.5
0
3.5
7
10.5
12.1
x/x_R = 0.4
y/x_R
z/D

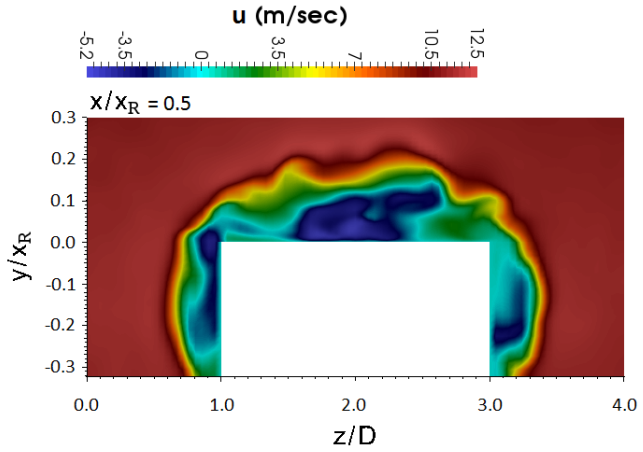
u (m/sec)
-5.2
-3.5
0
3.5
7
10.5
12.5
x/x_R = 0.5
y/x_R
z/D

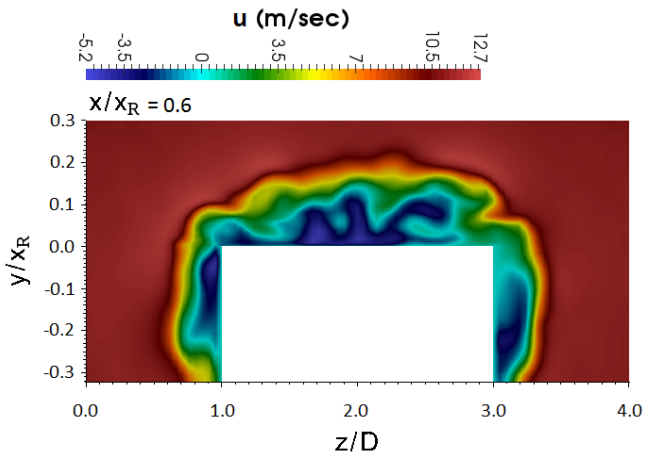
u (m/sec)
-5.2
-3.5
0
3.5
7
10.5
12.7
x/x_R = 0.6
y/x_R
z/D

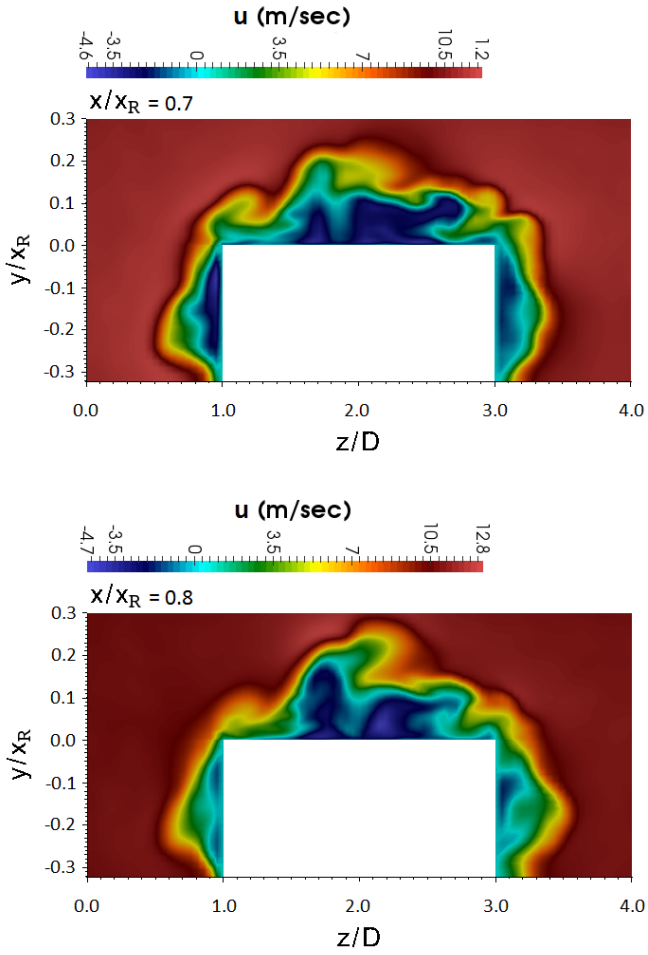

Fig. 5-21. Instantaneous streamwise velocity contours in the *y-z* plane at different streamwise locations for 3D_case2 with FST

Instantaneous streamwise velocity profiles taken at three arbitrary times confirmed the appearance of the flow unsteadiness and development locations as shown in Figs. 5-13, 5-14, and 5-15 for the flat plate, 3D_case1 and 3D_case2, respectively.

Despite the instantaneous streamwise velocity profiles at x/x_R = 0.2 for the flat plate seeming similar, there is a slight difference in these profiles as shown in Fig. 5-13. This indicates that there is a low unsteadiness in the flow at this location. At x/x_R = 0.4 onward, the difference in the instantaneous streamwise velocity profiles becomes clearly apparent, and indeed becomes stronger at x/x_R = 0.6 and x/x_R = 0.8 as shown in Fig. 5-13. This demonstrates the violent three-dimension motions that are associated with the rapid growth of the disturbances in the free shear layer.

For 3D_case1, there is no difference in the instantaneous streamwise velocity profiles at x/x_R = 0.2, this means that the flow is laminar and two-dimensional at this position as shown in Fig. 5-14. The flow unsteadiness can be seen at x/x_R = 0.4 because the similarity in the velocity profiles disappears. Close to the mean reattachment line at x/x_R = 0.8, different instantaneous streamwise velocity profiles can also be seen. This refers violent three-dimensional motions of the flow as shown in Fig. 5-14.

The slight differences that are seen in the instantaneous streamwise velocity profiles for 3D_case2 at x/x_R = 0.2 and x/x_R = 0.4 show that the level of the flow unsteadiness at these positions is low as shown in Fig. 5-15. This low unsteadiness indicates the low amplitude development of the disturbances in the separated shear layer. However, the large difference in the streamwise velocity profile is clearly apparent at x/x_R = 0.6 and x/x_R = 0.8. This indicates the flow at these positions, which is associated with the rapid development of the disturbances in the separated shear layer, is strongly disturbed.

Generally speaking, the presence of a 3.7% intensity of free stream turbulence changes the locations of the start, and subsequent development, of the unsteadiness in the free shear layer, and leads to an early transition for the current geometries as follows:

- The distance of the laminar part of the separation bubble with FST is 0.42*D* for the flat plate, 0.75*D* for 3D_caes1 and 0.62*D* for 3D_case2.
- The reduction in the distance of the laminar part of the separation bubble when the flow changes from NFST to FST is 0.78*D* for the flat plate, 0.61*D* for 3D_caes1 and 0.6045*D* for 3D_case2.
- The distance of the low amplitude development of the instability with FST is 0.84*D* for the flat plate, 0.5*D* for 3D_caes1 and 0.62*D* for 3D_case2.
- The reduction in the distance of the low amplitude development of the instability when the flow changes from NFST to FST is 0.66*D* for the flat plate, 0.18*D* for 3D_caes1 and 0.328*D* for 3D_case2.

Therefore, it can be concluded that with FST, the transition location in the flat plate moves upstream by a distance that is longer than that considered in both three-dimensional geometries. In addition, the distance of the instability low amplitude development in the flat plate is longer than that in both three-dimensional geometries. This can be considered

to be due to differences in the transitional separated-reattached flow between two- and three-dimensional geometries.

In a compression between 3D_case1 and 3D_case2 based on the above data with FST, it can be seen that there is no significant effect of the aspect ratio of the three-dimensional geometries on the distance by which the early transition moves upstream, while the reduction in the distance of the instability linear development when the flow changes from NFST to FST in 3D_case1 is lower. In other words, the increase of the aspect ratio of the three-dimensional geometries from 1 to 2 with FST leads to a reduction in the distance of the instability linear development, while the transition in both geometries moves upstream by a similar distance.

5.6 Primary instability mechanism for FST

It is of great interest to investigate the effect of a 3.7% intensity of free stream turbulence on the primary instability mechanism in transitional separated-reattached flow. Two studies were performed at different intensity levels of the free stream turbulence to investigate the effects on the primary instability mechanism of such flow. Yang and Abdalla (2009) used a 2% intensity of free stream turbulence with flow separated over a blunt flat plate at the Reynolds number of 6.5×10^3. They reported that the Kelvin-Helmholtz instability is still the primary instability mechanism driving the transition. On the other hand, Langari and Yang (2013) applied a 5.6% intensity of the free stream turbulence on a separated shear layer formed on a semi-circular leading edge flat plate with a Reynolds number of 3450. A bypassed transition was reported in Langari and Yang (2013), where there was no sign of the Kelvin-Helmholtz instability in this study.

If the effects of different leading-edges of the flat plate and Reynolds numbers are neglected in the above two studies, it can be concluded that the bypassed transitions occur within a range of intensity of free stream turbulence between 2% and 5.6%. The current intensity of the free stream turbulence is between the two levels used in the above two studies. Hence, the current elevated intensity of free stream turbulence (3.7%) reduces the range of possibility of the bypassed transition occurrence in a flat plate. In other words, if the bypassed transition exists with a 3.7% intensity of free stream turbulence, the range of intensity of free stream turbulence that leads to the bypassed transition will

be bounded by 2% and 3.7%, or if the bypassed transition does not exist with a 3.7% intensity of free stream turbulence, the range of intensity of free stream turbulence that leads to the bypassed transition will be bounded by 3.7% and 5.6%.

Therefore, the target of the current study is to reveal that when the transitional separated-reattached flow forms on a blunt flat plate with a 3.7% intensity of free stream turbulence, will the Kelvin-Helmholtz instability remain responsible for starting the transition? Or will it be bypassed? In addition, the current study is the first to investigate the effects of high intensities of free stream turbulence on the primary instability mechanism in transitional separated-reattached flow formed over three-dimensional geometries with two different aspect ratios.

Edges and centres of the free shear layer with FST are presented in Fig. 5-22 for the flat plate, Fig. 5-23 for 3D_case1 and Fig. 5-24 for 3D_case2. In a comparison between FST and NTSF for all geometries, it can be seen that the values at the edges and centres of the separated shear layer at the same locations of x/x_R in NFST are higher than those in FST.

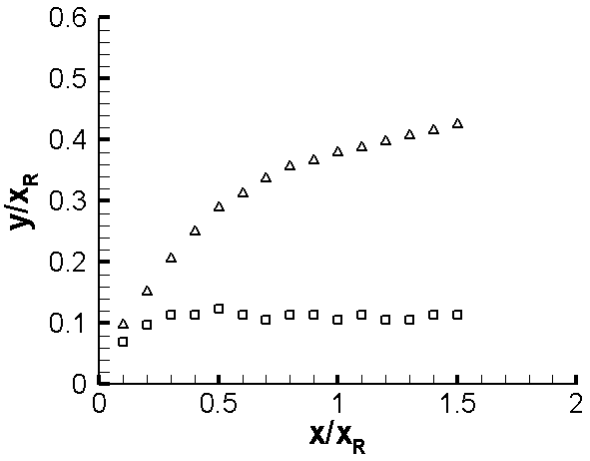

Fig. 5-22. Variation of centre of the shear layer (squares) and edge of the shear layer (triangles) with streamwise distance for the flat plate with FST

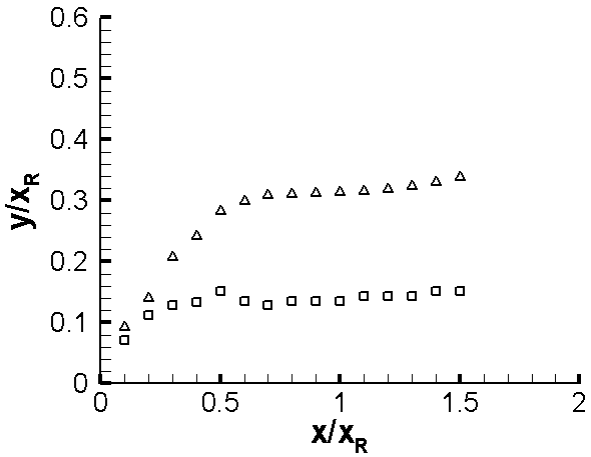

Fig. 5-23. Variation of centre of the shear layer (squares) and edge of the shear layer (triangles) with streamwise distance for 3D_case1 with FST

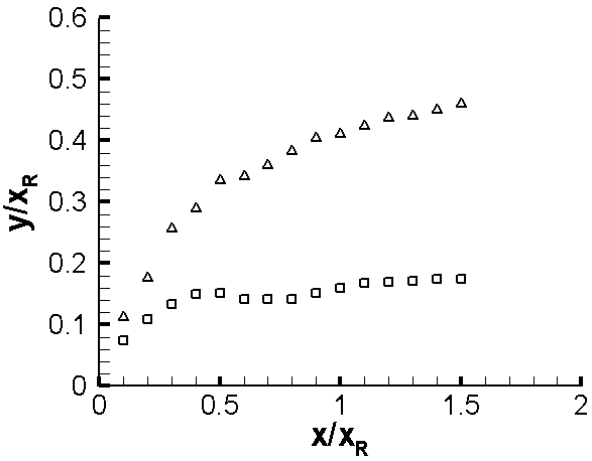

Fig. 5-24. Variation of centre of the shear layer (squares) and edge of the shear layer (triangles) with streamwise distance for 3D_case2 with FST

The condition for the presence of a Kelvin-Helmholtz instability ($0 < Kh < 1.2785$) as the primary instability mechanism in the separated shear layer for all geometries studied in the current study is considered here. Similar calculation procedures to these presented in Section 5-3 are also applied here.

For the flat plate, the separated shear layer thickness at the location where the unsteadiness first appears ($x/x_R = 0.1$) is $0.0971x_R$ as shown in Fig. 5-22. So, the unstable region for the wavenumbers can be represented by $0 < K < 13.166/x_R$, i.e., the Kelvin-Helmholtz instability will not exist in the shear layer for the flat plate when wavenumbers are higher than $13.166/x_R$ or wavelengths are smaller than $0.477x_R$.

The wave speed at $x/x_R = 0.1$ is $0.864U_0$ and the characteristic frequency, as will be shown in Chapter 6, varies between 145 Hz and 170 Hz or $0.646U_0/x_R - 0.757U_0/x_R$. Hence, the maximum wavenumber ($K_{max} = 2\pi f_{max}/c$) at the unsteadiness start point is $5.507/x_R$ corresponding to a wavelength of $1.14x_R$.

It is worth pointing out that many points, where the region extends from the position of the unsteadiness starting to the point of $x/x_R = 0.25$, are selected to investigate the existence of the Kelvin-Helmholtz instability. Wavenumbers at these points are below $13.166/x_R$ as shown in Table 5-4. This indicates that the Kelvin-Helmholtz instability mechanism is still the primary instability mechanism in the free shear layer with a 3.7% intensity of free stream turbulence.

x/x_R	0.1	0.15	0.2	0.25
K_{max}	$5.505/x_R$	$5.277/x_R$	$6.994/x_R$	$7.652/x_R$

Table 5-4. Maximum wavenumber values at several streamwise positions for the flat plate with FST

The shear layer thickness at the start of the unsteadiness beginning at $x/x_R = 0.3$ for 3D_case1 is $0.2077x_R$ as shown in Fig. 5-23. Based on this value, the condition for the presence of a Kelvin-Helmholtz instability for 3D_case1 is $0 < K < 6.155/x_R$. So, for wavenumbers greater than $6.155/x_R$ or wavelengths less than $1.021x_R$, the Kelvin-Helmholtz instability will not occur in the separated shear layer.

The wave speed at $x/x_R = 0.3$ is $0.611U_0$ and the characteristic frequency varies between 150 Hz and 190 Hz or $0.397U_0/x_R$ - $0.503U_0/x_R$. Therefore, the maximum wavenumber at the unsteadiness start point (K_{max}) is $5.167/x_R$ corresponding to a wavelength of $1.216x_R$.

To be more confident that the Kelvin-Helmholtz instability is the dominant primary instability mechanism in the separated shear layer, other points within the low amplitude growth region of the unsteadiness are also considered. The wavenumbers at these points show that the transition is indeed driven by the Kelvin-Helmholtz instability in 3D_case1 as shown in Table 5-5.

x/x_R	0.3	0.35	0.4	0.45
K_{max}	$5.167/x_R$	$5.155/x_R$	$5.264/x_R$	$4.957/x_R$

Table 5-5. Maximum wavenumber values at several streamwise positions for 3D_case1 with FST

The Kelvin-Helmholtz instability condition for 3D_case2 is $0 < K < 7.26/x_R$. This is calculated based on the value of $0.1761x_R$, which is the shear layer thickness at the unsteadiness start location ($x/x_R = 0.2$) as shown in Fig. 5-24. The Kelvin-Helmholtz instability does not appear in the free shear layer for 3D_case2 when wavenumber exceeds $7.26/x_R$ or wavelength is below $0.865x_R$.

The wave speed at $x/x_R = 0.2$ is $0.585U_0$ and the characteristic frequency varies from 150 Hz to 190 Hz or $0.493U_0/x_R$ - $0.624U_0/x_R$. Hence, the maximum wave number at the unsteadiness start point (K_{max}) is $6.698/x_R$ corresponding to a wavelength of $0.938x_R$.

Wavenumbers at different points within the region between $x/x_R = 0.2$ and $x/x_R = 0.35$ are shown in Table 5-6. Based on these values, the Kelvin-Helmholtz instability is still responsible for starting the transition in the separated shear layer in 3D_case2.

x/x_R	0.2	0.25	0.3	0.35
K_{max}	$6.698/x_R$	$5.809/x_R$	$6.383/x_R$	$6.313/x_R$

Table 5-6. Maximum wavenumber values at several streamwise positions for 3D_case2 with FST

Using the Kelvin-Helmholtz instability condition ($0 < Kd < 1$) reported in Roberts and Yaras (2006) shows that with FST, $K_{max}\ d$ is 0.133 for the flat plate, 0.268 for 3D_case1 and 0.294 for 3D_case2. Therefore, the transition in the free shear layer for all geometries studied here is indeed driven by the Kelvin-Helmholtz instability.

5.7 Summary

For all geometries used in the current study with NFST and FST, the possibility of the presence of an absolute instability throughout the separation bubble is investigated in this chapter. It is clearly shown that there is no any trace of the absolute instability, where the separation bubble is classified as convectively unstable.

With NFST, the streamwise location of the initial unsteadiness beginning in the separated shear layer in the flat plate is found to be closer to the separation line than for either of the three-dimensional geometries. In 3D_case2, the unsteadiness in the free shear layer takes place earlier than that in 3D_case1. The first appearance of the unsteadiness is at 1.2245*D* for 3D_case2, while it is at x/D = 1.36 for 3D_case1.

Movement of the unsteadiness location in the separated shear layer toward to the separation line is observed with the application of a high intensity of free stream turbulence for all geometries. The reduction in the distance of the separated laminar flow is 0.78*D* for the flat plate, 0.61*D* for 3D_caes1, and 0.6045*D* for 3D_case2. In addition, with FST, the reduction in the distance of the instability linear development is 0.66*D* for the flat plate, 0.18*D* for 3D_case1 and 0.328*D* for 3D_case2. Hence, for the three-dimensional geometries with FST, there is no considerable effect due to geometry aspect ratio on reduction in the distance of the laminar flow in the separation bubble, while it is observed that the reduction in the distance of the instability linear development for 3D_case1 is lower than that for 3D_case2.

For all geometries in the current study with NFST and FST, the transition in the separated shear layer is driven by the inviscid Kelvin-Helmholtz instability mechanism, which is the dominant instability mechanism in the separation bubble.

The contours of the instantaneous streamwise velocity with NFST and FST in the *y*-*z* plane for both 3D_case1 and 3D_case2 show that there is no difference in the locations of the flow development on the top and side surfaces of the geometries. This means that the beginning of the unsteadiness and its low amplitude growth region, and violent three-dimensional motions in the free shear layers on the top and side surfaces of the geometries take place at the similar streamwise locations.

Chapter Six

Spectral Analysis

6.1 Background

In order to elucidate the frequency modes that may exist in each geometry in the current study, extensive data for instantaneous pressure and velocity components are calculated at specific inspection points. These points are distributed within the separation bubble, at the mean reattachment point, and within the developed turbulent boundary layer as shown in the next section.

For all geometries studied here, there are 40,000 samples at each inspection point taken every 10 time steps (time step = 2×10^{-6} s) corresponding to 0.8 s, which is the total time of the simulation. Hence, the sampling frequency is 50 kHz.

The traditional Fourier transform method is employed here to extract the local frequency magnitude from the time series signals as the velocity components. The maximum frequency which can be resolved is about 25 kHz and the minimum frequency is about 1.25 Hz for all geometers in the current study.

In spite of the Fourier transform method showing the time series frequency information, this method is inefficient and inaccurate when the time series involves a wide range of high and low frequencies out of the dominant frequencies range, where these high and low frequencies may be eliminated from the spectra by the Fourier transform (Kaiser, 1994). Spectra of transitional and turbulent flows usually involves a wide range of frequencies due to vortex shedding and vortex development. So, the predetermined scaling method, such as the Fourier transform, is not appropriate as a spectral analyses method (Kaiser, 1994). Therefore, to present more details based on the time series signals of the velocity components, the wavelet transform method is used in the present study. Wavelet transform analyses, which is a time frequency localization and scale independent method, may be more successful.

Wavelet transform analyses show a two-dimensional picture illustrating wavelet power concentration in time (*x*-axis) *vs.* scales (*y*-axis). Scales *are equivalent to the period and present an approximate measure of the Fourier period of the signal* (Torrence and Compo, 1998). The wavelet transform method can be used to analyse time series that contains non-stationary power at many different frequencies (Daubechies, 1990). For a time series, x_n, with equal time spacing, δt, and $n = 0, \ldots, N\text{-}1$ (where N is the total number of time steps), consider a wavelet function $\Psi_0(\eta)$ which depends on a non-dimensional 'time' parameter η. *To be admissible as a wavelet, this function must have zero mean and be localized in both time and frequency space* (Farge, 1992). The Morlet wavelet function, which is employed here, is an example of a wavelet function and is defined as:

$$\Psi_0(\eta) = \pi^{-1/4} e^{i\omega_0 \eta} e^{-\eta^2/2} \tag{6-1}$$

where ω_0 is the non-dimensional frequency, which is taken to be 6 to satisfy the admissibility condition (Farge, 1992).

Wavelet function usually refers to either *orthogonal* or *non-orthogonal* wavelets. The use of an *orthogonal* basis implies the use of the *discrete wavelet transform*, while a *non-orthogonal* wavelet function can be used with either the *discrete* or the *continuous wavelet transform* (Farge, 1992).

The *continuous wavelet* transform of a discrete sequence x_n is defined as the convolution of x_n with a scaled and translated version of $\Psi_0(\eta)$ (Torrence and Compo, 1998):

$$W_n(s) = \sum_{n'=0}^{N-1} x_{n'} \Psi^* \left[\frac{(n'-n)\delta t}{s}\right] \tag{6-2}$$

where the (*) indicates the complex conjugate, and the transform is divided into real (amplitude) $|W_n(s)|$ and imaginary (phase) parts. The *wavelet power spectrum* is defined as the absolute value of the wavelet transform squared ($|W_n(s)|^2$) and gives a measure of the time series variance at each scale (period) and time (Torrence and Compo, 1998). So, variation of the wavelet scale (s) and translating along a localized time index (n) leads to a picture that illustrates both the amplitude of any features versus the scale (period), and the variation of this amplitude with time. For more details about the Morlet wavelet, the reader is referred to Torrence and Compo (1998).

The Morlet wavelet used in the present study to produce a wavelet picture (based on the code developed by Torrence and Compo (1998)) employs the continuous transform, although all of the results for significance testing, smoothing in time and scale, and cross-wavelets are similarly applicable to the discrete wavelet transform. A modification is carried out for this code to analyse the current LES time series signals.

To identify the set of scales (s) to use in the wavelet transform described in equation (6-2) for *non-orthogonal* wavelet analyses, an arbitrary set of scales can be used. Torrence and Compo (1998) recommended scales expanded in fractional powers of two, as follows:

$$s_j = s_0 2^{j\delta j}, \qquad j = 0, 1, \ldots\ldots, J \tag{6-3}$$

$$J = \delta j^{-1} log_2(N\delta t / s_0) \tag{6-4}$$

where s_0 is the smallest resolvable scale and J determines the largest scale. Torrence and Compo (1998) reported that the smallest scale (s_0) should be chosen so that the equivalent Fourier period is approximately $2\delta t$. They recommended that the choice of a sufficient small δj depends on the width in spectral space of the wavelet function and smaller values of δj give finer resolution. They showed that the largest value of δj, which still gives adequate sampling in scale, must not be exceed 0.5.

For all geometries, the samples are stored every 10 time steps (2×10^{-5}) so the smallest scale $s_0 = 2\delta t = 4 \times 10^{-5}$ and $N = 4 \times 10^4$. Abdalla et al. (2007) recommended that 0.25, as a value for δj, is sufficient for transitional separated-reattached flow over a surface-mounted obstacle. Hence, the value of δj selected for the current study is 0.25. Therefore, J is taken as 57 based on equation (6-4), and the largest scale $s_J = 0.779$ s. Torrence and Compo (1998) reported that no interesting events occur over a long period and they recommended that the largest scale should be less than half of the total time, which is 0.8 s in the current study. So, 51 is considered here as a value for J providing 52 scales ranging from 4×10^{-5} to 0.327 s. These selected variables produce a smooth picture of the wavelet power spectrum in the current study.

Analysis of the time signal employing wavelet spectra leads to control different events that involved with the span of the time signal by exciting or damping them. This was recommended by Abdalla et al. (2009), where they reported that wavelet spectra give a

clear picture of the extent of the event (amplitude) and any smaller events associated with it. This information could be useful in controlling such events (damping or exciting as required for specific applications). Moreover, the wavelet power spectrum can be used to identify the occurrence time and reoccurrence period of such events.

However, it is worth pointing out that there is a disadvantage to use wavelet transform for spectral analysis. This method provides only qualitative results, and is a particular criticism of using this method of power spectrum analysis. (Torrence and Compo, 1998). Regarding this point, the Fourier transform method is better if the frequency within the time series signal is needed.

6.2 Spectral analysis locations for NFST

For all geometries, the instantaneous pressure and velocity components are stored at specific points to act as inspection stations for existing frequency modes.

For the flat plate, there are 108 points that are distributed across nine streamwise, four wall-normal, and three spanwise locations. Streamwise locations include a point just after the separation at x/x_R = 0.0416; five points are distributed within the mean separation bubble length at x/x_R = 0.1666, 0.3333, 0.5, 0.6666, and 0.8333; at the reattachment x/x_R = 1; and in the developed boundary layer after the reattachment at x/x_R = 1.0833 and 3. These locations correspond to x/D = 0.25, 1, 2, 3, 4, 5, 6, 6.5, and 18, respectively.

For 3D_case1, time traces for the instantaneous pressure and velocity components are stored at 96 locations that include eight streamwise, four wall-normal, and three spanwise positions. Locations of streamwise points are at x/x_R = 0.0735 as a point is just after the separation; x/x_R = 0.2941, 0.5882, 0.7352, and 0.8823 as points distributed within the mean length of the separation bubble; at the reattachment x/x_R = 1; and in the developed boundary layer after the reattachment at x/x_R = 1.1764 and 5.2941. These locations correspond to x/D = 0.25, 1, 2, 2.5, 3, 3.4, 4, 18, respectively.

For 3D_case2, eight streamwise, four wall-normal, and three spanwise locations are selected as stations for spectral analysis. Streamwise locations are x/x_R = 0.0632, 0.2531, 0.5063, 0.6329, 0.7594, 1, 1.2658, and 4.5569 which correspond to x/D = 0.25, 1, 2, 2.5, 3, 3.95, 5, 18, respectively. These locations cover a point just after the separation position,

four points that are distributed within the separation bubble, the mean reattachment point, and two points within the turbulent boundary layer.

For all geometries in the current study, the instantaneous pressure and velocity components are also stored at four wall-normal locations for each streamwise location. These locations with shifting the origin point of the wall-normal axis to the geometry surface are y/D = 0.05, 0.3, 0.5, and 1. These locations correspond to y/x_R = 0.0083, 0.05, 0.0833, 0.1666, respectively for the flat plate and y/x_R = 0.0147, 0.0882, 0.147, 0.2941, respectively for 3D_case1 and y/x_R = 0.0126, 0.0759, 0.1265, 0.2531, respectively for 3D_case2. For all geometries, these wall-normal stations are chosen to be close the wall, shear layer centre, and the edge of the shear layer.

All the above streamwise and wall-normal positions are located at three spanwise points, z/D = 1, 2, 3 for the flat plate and z/D = 1.6, 2, 2.4 for 3D_case1, and z/D = 1.2, 2, 2.8 for 3D_case2. Spectral analysis inspection point locations are detailed, respectively, in Table 6-1 for the flat plate, Table 6-2 for 3D_case1, and Table 6-3 for 3D_case2.

It is worth pointing out that the inspection of Fourier spectra for the instantaneous pressure and velocity components shows similar behaviour at each selected point for all geometries. Therefore, there are only the spectral analyses for the instantaneous streamwise and wall-normal velocities to be presented in the current study.

It should be noted here that for all geometries, the Fourier spectra for the instantaneous velocity components at any spanwise position for the same streamwise and wall-normal locations show very similar results. Hence, the following Fourier spectra figures are plotted at the spanwise position at the centre of the computational domain, z/D = 2. The wavelet spectra figures are presented and described here based on only these selected Fourier spectra points.

It is interesting to show that due to the large number of inspection points used in the current study, the frequency and wavelet spectra are not presented for all wall-normal locations at each streamwise position in this chapter.

		x/x_R								
		0.0416	0.1666	0.3333	0.5	0.6666	0.8333	1	1.0833	3
y/x_R	0.0083	1	2	3	4	5	6	7	8	9
	0.05	10	11	12	13	14	15	16	17	18
	0.0833	19	20	21	22	23	24	25	26	27
	0.1666	28	29	30	31	32	33	34	35	36

Table 6-1. Locations of spectral analysis inspection points at *z/D* = 2 for the flat plate with NFST

		x/x_R							
		0.0735	0.2941	0.5882	0.7352	0.8823	1	1.1764	5.2941
y/x_R	0.0147	1	2	3	4	5	6	7	8
	0.0882	9	10	11	12	13	14	15	16
	0.147	17	18	19	20	21	22	23	24
	0.2941	25	26	27	28	29	30	31	32

Table 6-2. Locations of spectral analysis inspection points at *z/D* = 2 for 3D_case1 with NFST

		x/x$_R$							
		0.0632	0.2531	0.5063	0.6329	0.7594	1	1.2658	4.5569
y/x$_R$	0.0126	1	2	3	4	5	6	7	8
	0.0759	9	10	11	12	13	14	15	16
	0.1265	17	18	19	20	21	22	23	24
	0.2531	25	26	27	28	29	30	31	32

Table 6-3. Locations of spectral analysis inspection points at z/D = 2 for 3D_case2 with NFST

6.3 Spectral analysis for the flat plate for NFST

For the flat plat, frequency and wavelet spectra for the instantaneous streamwise velocity at a point close to the separation line and very close to the plate surface, x/x_R = 0.0416 and y/x_R = 0.0083, are shown in Fig. 6-1. It is noted that there is no spectacular high or low frequency peaks can be distinguished in the frequency spectrum for the instantaneous streamwise velocity at this position as shown in Fig. 6-1a. Fig. 6-1b presents the wavelet spectrum for the instantaneous streamwise velocity at the same location. Clearly, there are no interesting events to be observed from this picture.

At the same streamwise position and at the second wall-normal location, y/x_R = 0.05, the instantaneous wall-normal velocity frequency spectrum is similar to that presented in Fig. 6-1a with no recognised high or low frequency peaks as shown in Fig. 6-2a. At this position, the frequency spectrum for the instantaneous streamwise velocity also does not show any high or low frequency peaks. At the same streamwise station and at other two wall-normal locations, y/x_R = 0.0833 and y/x_R = 0.1666, the appearance of high or low frequencies cannot be distinguished in the frequency spectra for the instantaneous velocity components.

The wavelet spectrum for the instantaneous wall-normal velocity at y/x_R = 0.05 is presented in Fig. 6-2b. It can be seen that there are not any interesting events generated

by this wavelet picture. There are no interesting events evident in any of the other wavelet spectra at x/x_R = 0.0416 for wall-normal locations.

Wavelet power spectra at all wall-normal locations at the first streamwise point close to the separation point indicate that the flow in this region of the separation bubble is quiet, and without any considerable power concentration.

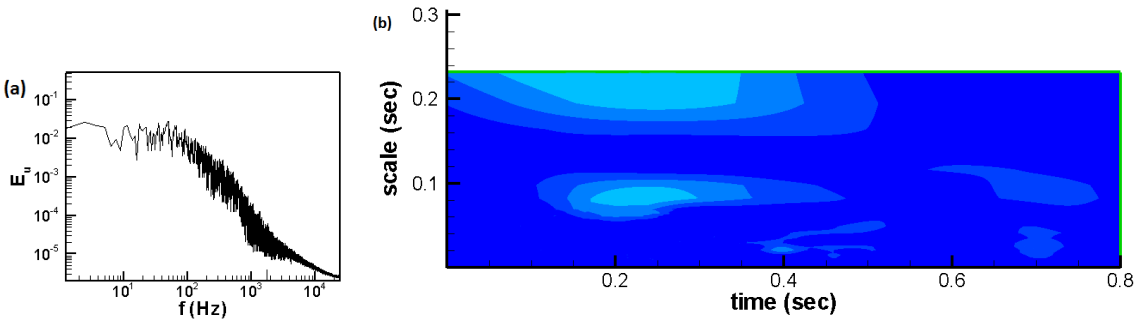

Fig. 6-1. Frequency and wavelet spectra for u at x/x_R = 0.0416 and y/x_R = 0.0083: (a) frequency spectrum, (b) wavelet spectrum for the flat plate with NFST

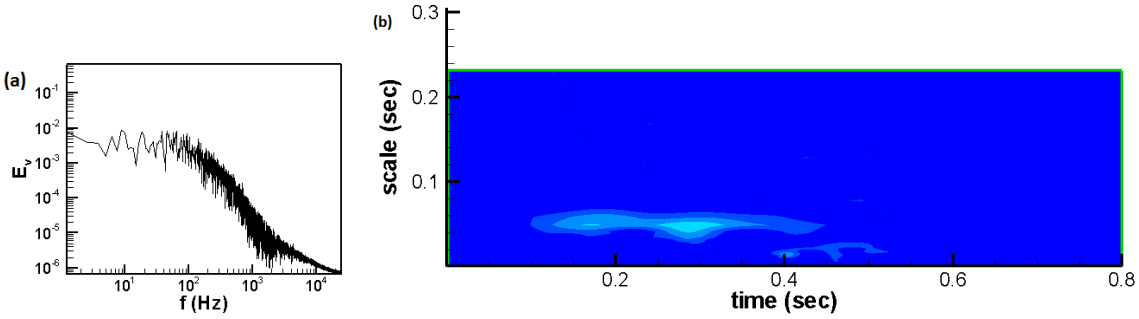

Fig. 6-2. Frequency and wavelet spectrum for v at x/x_R = 0.0416 and y/x_R = 0.05: (a) frequency spectrum, (b) wavelet spectrum for the flat plate with NFST

At the second streamwise position, x/x_R = 0.1666, and for all wall-normal locations, frequency spectra for the instantaneous streamwise and wall-normal velocities do not present any high or low frequency peaks at any of the wall-normal stations. For example, this is shown in Figs. 6-3a and 6-3c, which present Fourier transforms for the instantaneous streamwise and wall-normal velocities at y/x_R = 0.05, respectively.

At this location, wavelet transforms for the instantaneous streamwise and wall-normal velocities are presented in Figs. 6-3b and 6-3d, respectively. The instantaneous streamwise velocity spectrum shows two narrow and low amplitude power concentrations. The first of these extends from the beginning of the time signal to 0.18 s whilst the other is located between 0.32 s and 0.62 s as shown in Fig. 6-3b. Both power regions are of low amplitude and at a band between $0.04 \leq \text{scale} \leq 0.08$. At the same location, the wavelet power spectrum for the instantaneous wall-normal velocity shown in Fig. 6-3d displays narrow and low-amplitude power concentrations that are centred at 0.3, 0.4, and 0.6 s.

At all wall-normal points at the second streamwise station, $x/x_R = 0.1666$, wavelet power spectra for the instantaneous velocity components show different narrow and low-amplitude power concentration regions distributed through the time span of the signal, while frequency spectra for the instantaneous velocity components still do not show any high or low frequency peaks.

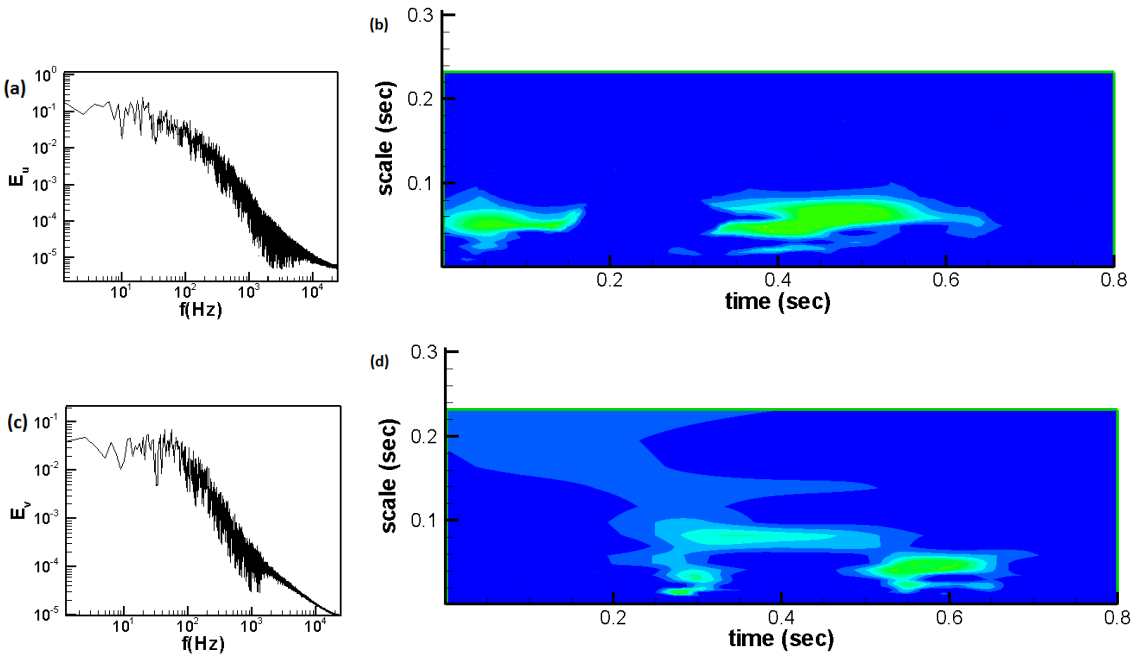

Fig. 6-3. Fourier and wavelet transforms at $x/x_R = 0.1666$ and $y/x_R = 0.05$: (a) Fourier transform for u, (b) wavelet transform for u, (c) Fourier transform for v, (d) wavelet transform for v for the flat plate with NFST

However, at the first and second streamwise positions, Fourier transform spectra do not show any peak in the frequency, while the wavelet power spectra show low-amplitude power concentration regions in the time span of the signal. This is an indication of the ability of the wavelet power spectra to extract the smaller power contents and details of the time signals. The appearance of the power concentration regions in the wavelet spectra at the laminar part of the separation bubble may refer to influence of the unsteadiness of the separated shear layer, especially, at the second streamwise location which is close to the start of the unsteadiness region (x/x_R = 0.2). Another possible explanation for the appearance of the power concentration regions at the first and second streamwise locations is due to the effect of the shedding of vortical structures from the separated shear layer that occurs downstream.

Moving downstream to the location x/x_R = 0.3333, frequency spectra for the instantaneous streamwise and wall-normal velocities at a point very close to the wall, y/x_R = 0.0083, are shown in Figs. 6-4a and 6-4c, respectively. In these figures, a peak with the frequency band 120 Hz - 140 Hz is clearly apparent, which is equivalent to 0.76 U_0/x_R - 0.89 U_0/x_R in the current study. At this streamwise location and for all wall-normal positions, a similar peak to that of the high frequency band, 0.76 U_0/x_R - 0.89 U_0/x_R, is shown by frequency spectra for the instantaneous velocity components. This frequency is the characteristic (regular) shedding frequency that is attributed to the shedding of large-scale structures from the separation bubble.

The current value of the characteristic shedding frequency is in a good agreement with values documented in the literature. For a blunt flat plate with a turbulent separated-reattached flow, the regular shedding frequency reported in the experimental work of Kiya and Sasaki (1983) was 0.6 U_0/x_R - 0.8 U_0/x_R. Cherry et al. (1984) observed 0.7 U_0/x_R as a regular shedding frequency. For a similar geometry but with a transitional separated-reattached flow, 0.7 U_0/x_R - 0.875 U_0/x_R was obtained as a regular shedding frequency by Abdalla and Yang (2005). For such flow on a flat plate with a semi-circular leading edge, Yang and Voke (2001) found 0.77 U_0/x_R as the value of the regular shedding frequency.

In a turbulent separated-reattached flow on different geometries, the regular shedding frequency for a backward-facing step was documented as 0.5 U_0/x_R - 0.8 U_0/x_R in Mabey (1972), 0.6 U_0/x_R in Driver et al., (1987), 0.5 U_0/x_R in Lee and Sung (2001) and 1 U_0/x_R

in Spazzini et al. (2001) and Heenan and Morrison (1996). In a separation bubble formed behind a normal flat plate mounted in the front of a long splitter plate, the value of the regular shedding frequency was found as 0.6 U_0/x_R - 0.9 U_0/x_R in the experimental work of Hudy et al. (2003).

Wavelet spectra for the selected velocities at x/x_R = 0.3333 and y/x_R = 0.0083 are shown in Figs. 6-4b and 6-4d. It can be observed in Fig. 6-4b that the wavelet power contours for the instantaneous streamwise velocity clearly shows a power concentration corresponding to the frequency peak shown in Fig. 6-4a. Furthermore, this wavelet power picture shows that most of the power is concentrated within a period of 0.25 s – 0.5 s ($0.02 \leq$ scale ≤ 0.1). This power region is associated with two lower amplitude power regions. The first one is within a band of $0.02 \leq$ scale ≤ 0.06 at a shorter period of 0.1 s – 0.15 s, whilst the other one is within a band of $0.08 \leq$ scale ≤ 0.16 at a longer period of 0.5 s – 0.8 s. The wavelet spectrum for the instantaneous streamwise velocity that shown in Fig. 6-4b presents a variation in the frequency of occurrence and the associated amplitudes within the time signal of the instantaneous streamwise velocity. It shows three amplified frequencies, while the frequency spectrum for this velocity shows just one peak of a band of frequencies and smooths out the others.

At the same streamwise and wall-normal locations, the wavelet power spectrum for the instantaneous wall-normal velocity shown in Fig. 6-4d displays three main power regions centred at a similar time in the power regions of the wavelet spectrum for the instantaneous streamwise velocity. It can be seen that most of the power is concentrated within a period of 0.1 s - 0.2 s which corresponds to the frequency peak shown in Fig. 6-4c. Different events with different power concentration regions that take place over different times and scales are displayed by wavelet spectra at the other wall-normal positions of x/x_R = 0.3333. These power regions refer to the shedding frequency of the vortical structures as captured by the frequency spectra. In addition, these wavelet pictures present various other power concentration regions related to frequencies that are rolled out by the Fourier frequency spectrum.

However, with the clear picture provided by the wavelet spectrum about the included events and the time of their occurrence, results of the wavelet spectra are qualitative where the magnitude of the frequency peak can just be identified by the frequency spectra

analyses, consistent with the conclusions in Abdalla et al. (2009) for a transitional separated-reattached flow over a forward-facing step and a cubic obstacle.

At the centre of the separation bubble length, $x/x_R = 0.5$, and at wall-normal locations $y/x_R = 0.0083$, $y/x_R = 0.05$, and $y/x_R = 0.1666$, the spectra for the instantaneous velocity components reveal the regular shedding frequency band 0.76 U_0/x_R - 0.89 U_0/x_R. This frequency is clearly presented in the instantaneous streamwise velocity frequency spectrum at the same streamwise position for $y/x_R = 0.0833$, as shown in Fig. 6-5a. In return, the corresponding wavelet power spectrum presents a power concentration which indicates the time of occurrence of the frequency peak at 0.2 s ≤ time ≤ 0.3 s as shown in Fig. 6-5b. In addition, there are other events with lower amplitudes surrounding the peak frequency power concentration that are distributed along the time span of the signal. These power concentration regions indicate event occurrence times rolled out by the frequency spectra.

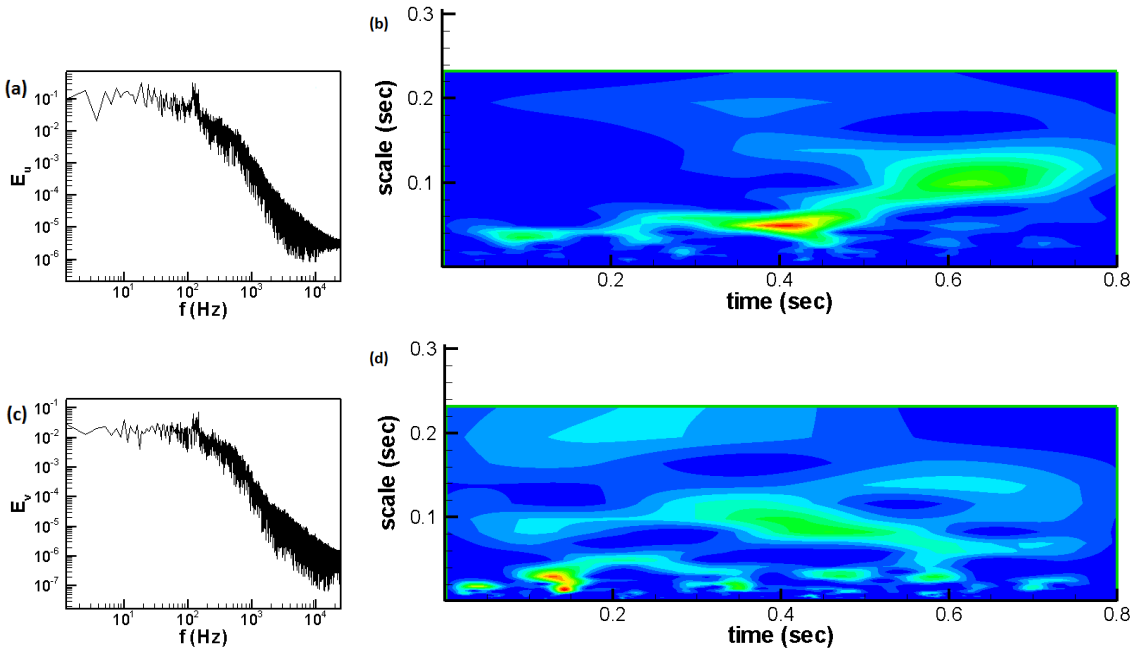

Fig. 6-4. Frequency and wavelet spectra at $x/x_R = 0.3333$ and $y/x_R = 0.0083$: (a) frequency spectrum for u, (b) wavelet spectrum for u, (c) frequency spectrum for v, (d) wavelet spectrum for v for the flat plate with NFST

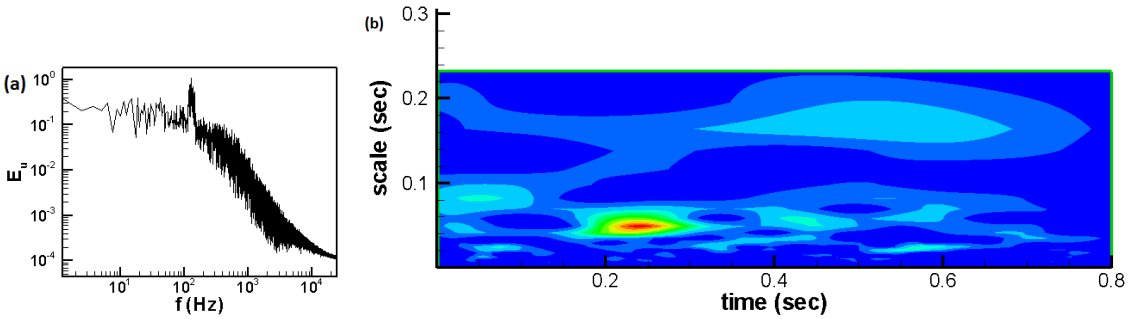

Fig. 6-5. Frequency and wavelet spectra at x/x_R = 0.5 and y/x_R = 0.0833 for u: (a) frequency spectrum, (b) wavelet spectrum for the flat plate with NFST

Moving downstream to the location x/x_R = 0.6666, the frequency spectrum for the instantaneous wall-normal velocity that is very close to the solid surface at y/x_R = 0.0083 is shown in Fig. 6-6a. In this frequency spectrum, and in the instantaneous streamwise velocity frequency spectrum, the regular shedding frequency band 0.76 U_0/x_R - 0.89 U_0/x_R is not observed and no high or low frequency peaks can be seen.

At the same streamwise station, moving upward to all other wall-normal locations, frequency spectra for the instantaneous velocity components do not show any high or low frequency peaks. It is worth pointing out that this streamwise position of the separation bubble is located within the recirculation zone, as expected, a high frequency will be seen in the associated frequency spectra.

However, at this streamwise location the wavelet transform still presents the presence of various events, as shown in Fig. 6-6b. This figure shows the wavelet spectrum for the instantaneous wall-normal velocity at y/x_R = 0.0083. It is clearly seen that there is a main power concentration within a long period of 0.2 s ≤ time ≤ 0.8 s within a band of 0.12 ≤ scale ≤ 0.22.

In this region of the separation bubble, it is useful to understand that the wavelet spectrum offers an indication of the dynamics of the coherent structures after being shed from the separated layer, such as their pairing (merging) or evolution (as will be shown in Chapter 7), while the frequency spectra do not show any peak frequencies indicative of these events. Wavelet transforms for the instantaneous velocity components at all other wall-

normal stations at this streamwise position give evidence for the occurrence of specific events that indicate the development of coherent structures.

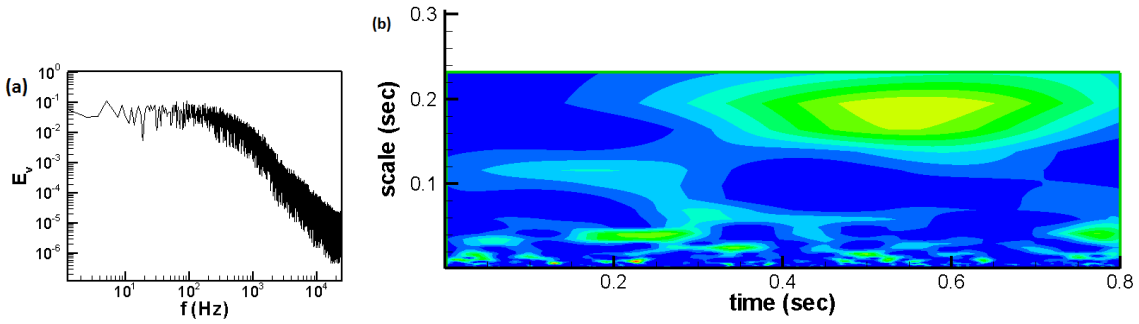

Fig. 6-6. Fourier and wavelet transforms for v at x/x_R = 0.6666 and y/x_R = 0.0083: (a) Fourier transform, (b) wavelet transform for the flat plate with NFST

A similar scenario for the frequency and wavelet spectra behaviour can be seen when moving downstream to the streamwise position x/x_R = 0.8333, which is also located within the recirculation zone. There are no high or low frequency peaks in the frequency spectra for the instantaneous velocity components at all wall-normal locations, while the wavelet power spectra for the instantaneous velocity components show various power concentrations within different bands of scales and periods of time. As an example, the frequency and wavelet spectra for the instantaneous streamwise velocity at x/x_R = 0.8333 and y/x_R = 0.05 that shown in Figs. 6-7a and 6-7b respectively. The wavelet power spectrum shows a number of power concentrations that are connected with each other and extend throughout the entire life span of the signal. These amplified powers may indicate a significant change in the coherent structure shape from two-dimensional Kilven-Helmholtz rolls to three-dimensional hairpin structures by direct breakdown (as will be shown in Chapter 7). This process may produce different power concentrations as shown in Fig. 6-7b. A narrow scales band of amplified power concentration can be seen in this figure that occurs within 0.3 s ≤ time ≤ 0.4 s. This power concentration is between lower scale and shorter time bands power region and higher scale and longer time bands power region.

Again, it can be concluded that the wavelet power spectra provide more details of the time signal more than the frequency spectra where in the later spectra analysis, many of the flow events cannot be traced.

There is a possible explanation for the absence of any amplified frequency within the frequency spectra downstream of x/x_R = 0.5, as shown in the previous figures. This could possibly be due to the current transitional separated-reattached flow not being characterized by a strong shedding process, where the rapidly becomes turbulent. This will be discussed further in Chapter 7. A similar conclusion was also made by Abdalla et al. (2007) for a transitional separation on a surface-mounted obstacle.

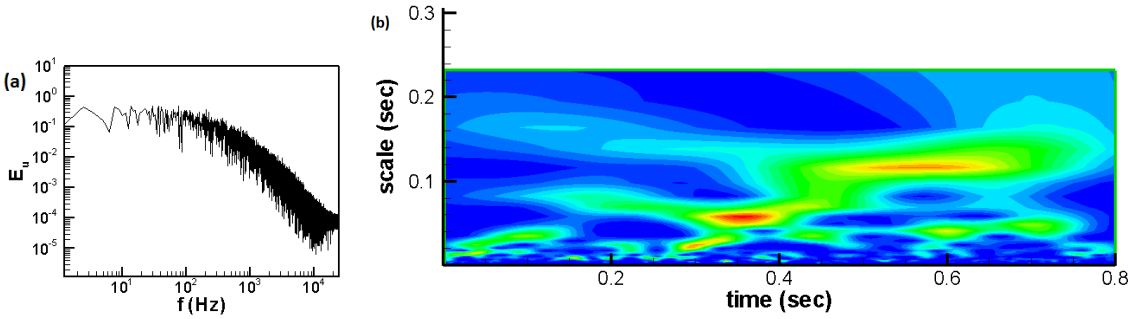

Fig. 6-7. Fourier and wavelet spectra for u at x/x_R = 0.8333 and y/x_R = 0.05: (a) Fourier spectrum, (b) wavelet spectrum for the flat plate with NFST

At the reattachment point, x/x_R = 1, and further downstream at the two points within the turbulent boundary layer, x/x_R = 1.0833 and 3, frequency and wavelet spectra for the instantaneous streamwise and wall-normal velocities at different wall-normal locations are shown in Figs. 6-8, 6-9, and 6-10. It is found that at all wall-normal positions and at these three streamwise locations, the Fourier frequency spectra for the instantaneous velocity components are quiet, and also no high or low frequency peaks can be detected. This is clearly seen in Figs. 6-8a and 6-9a, which present frequency spectra for the instantaneous streamwise velocity at points (x/x_R = 1, y/x_R = 0.0083) and (x/x_R = 1.0833, y/x_R = 0.05) and in Fig. 6-10a for the instantaneous wall-normal velocity frequency spectrum at the point (x/x_R = 3, y/x_R = 0.0833).

Wavelet spectra for the instantaneous velocity components at similar locations are shown in Figs. 6-8b, 6-9b, 6-10b. The wavelet spectrum for the instantaneous streamwise velocity at the point (x/x_R = 1, y/x_R = 0.0083) is shown in Fig. 6-8b. In spite of the absence of any frequency peak in the Fourier transform at this location, the wavelet transform

shows that there is a significant power concentration centred at 0.4 s. This power may indicate the event associated with the coherent structures shedding from the separation bubble to the reattached turbulent boundary layer.

Further downstream in the reattached turbulent boundary layer at a location located close to the reattachment point, $x/x_R = 1.0833$, the wavelet power spectrum for the instantaneous streamwise velocity at $y/x_R = 0.05$ is presented in Fig. 6-9b. It is clear that a power concentration is present which is associated with a continuous breakdown of the coherent structures to smaller structures, indicating that the reattached turbulent boundary layer has not yet reached the recovery state. This is discussed in detail in Chapter 8.

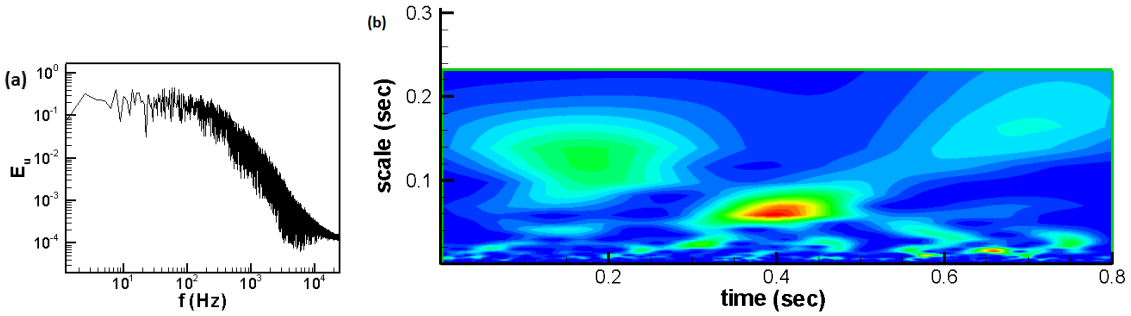

Fig. 6-8. Frequency and wavelet spectra for u at $x/x_R = 1$ and $y/x_R = 0.0083$: (a) frequency spectrum, (b) wavelet spectrum for the flat plate with NFST

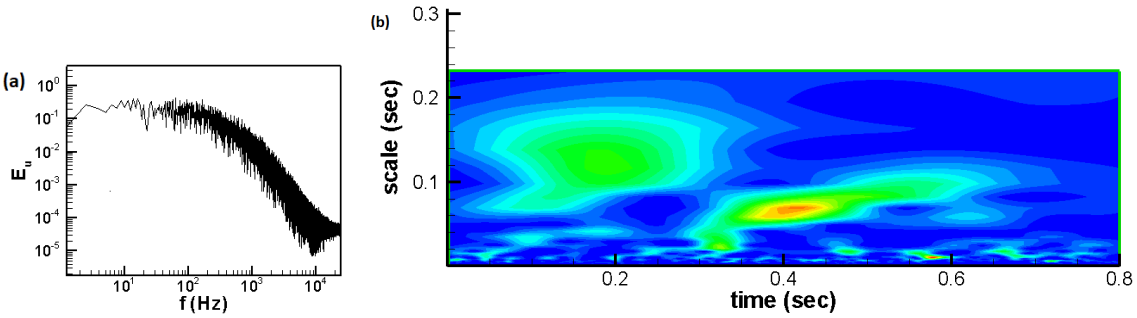

Fig. 6-9. Frequency and wavelet spectra for u at $x/x_R = 1.0833$ and $y/x_R = 0.05$: (a) frequency spectrum, (b) wavelet spectrum for the flat plate with NFST

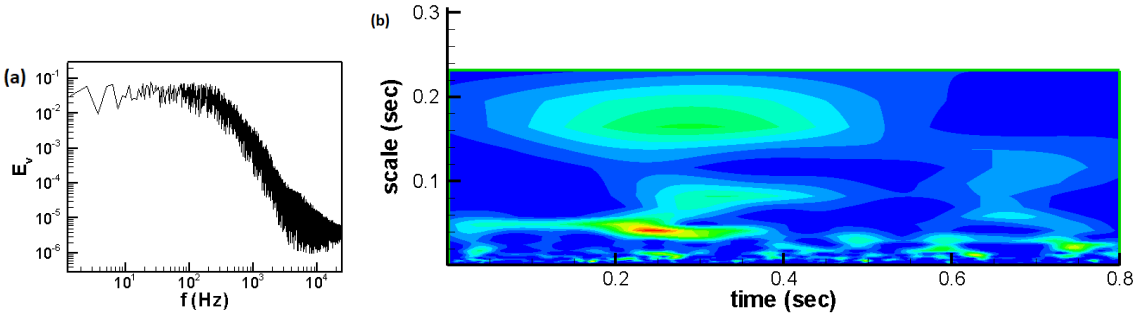

Fig. 6-10. Frequency and wavelet spectra for v at $x/x_R = 3$ and $y/x_R = 0.0833$: (a) frequency spectrum, (b) wavelet spectrum for the flat plate with NFST

At the last streamwise point, $x/x_R = 3$, within the turbulent boundary layer, the wavelet power transform for the instantaneous wall-normal velocity at $y/x_R = 0.0833$ is shown in Fig. 6-10b. The power content in this figure seems to be associated with continuous development of the turbulent boundary layer after the reattachment. Despite this streamwise location approaching the end of the computational box, the wavelet power spectrum still provides evidence of the occurrence of certain events which may indicate the delay in the turbulent boundary layer reaching its equilibrium state. This is shown in detail in Chapter 8.

6.4 Spectral analysis for 3D_case1 for NFST

In this section, the spectra analysis is applied to 3D_case1 with NFST. At the streamwise station $x/x_R = 0.0735$, where is close to the separation line, the instantaneous wall-normal velocity frequency and wavelet spectra at $y/x_R = 0.0147$ and the instantaneous streamwise velocity frequency and wavelet spectra at $y/x_R = 0.0882$ are shown in Fig. 6-11.

There are no distinguished high or low frequency peaks that can be observed in the frequency spectra for either instantaneous velocity components. At the same streamwise position and at other wall-normal locations, the instantaneous velocity components spectra do not have any indication of existing high or low frequency peaks.

There are no interesting events that can be seen in the wavelet spectra for the instantaneous velocity components at all wall-normal locations at the same streamwise position. This is clearly shown in wavelet transforms for the instantaneous streamwise velocity at $y/x_R = 0.0147$ and the instantaneous wall-normal velocity at $y/x_R = 0.0882$, as

can be seen in Figs. 6-11b and 6-11d, respectively. It can be seen that there is a short scale and period bands of low amplitude power regions distributed in the wavelet pictures in these two figures. It is similar, indeed, for other wavelet pictures for the instantaneous velocity components at other wall-normal positions for $x/x_R = 0.0735$.

No considerable power regions are observed in the wavelet contours at $x/x_R = 0.0735$ for all wall-normal positions. This indicates that the flow close to the separation point is quiet and without any activity due to development of coherent structures or disturbances created by elevated levels of intensity of free stream turbulence. This is also found to be the case in the flat plate, as shown in Section 6-3. As shown previously, the current spectral analysis is carried out under the effects of low intensity of free stream turbulence (< 0.2%).

Moving downstream to the location $x/x_R = 0.2941$, the frequency spectra for the instantaneous streamwise and wall-normal velocities at $y/x_R = 0.0882$ are shown in Figs. 6-12a and 6-12c, respectively. In these spectra, and the frequency spectra for the instantaneous velocity components at other wall-normal positions at this streamwise station, no obvious high or low frequency peaks could be identified.

At the same streamwise and wall-normal stations ($x/x_R = 0.2941$, $y/x_R = 0.0882$), it can be seen that relatively considerable power regions appear in the wavelet spectra for the instantaneous velocity components as shown in Fig. 6-12b for the instantaneous streamwise velocity and Fig. 6-12d for the instantaneous wall-normal velocity. The wavelet spectrum in Fig. 6-12b clearly shows a power concentration region centred around a time of 0.3 s and connected with other low scale band power regions. The power region that is presented in Fig. 6-12d extends across a period of $0.35 \leq \text{time} \leq 0.7$ with a scale band of $0.02 \leq \text{scale} \leq 0.08$. At the same streamwise location and indeed for other wall-normal positions, wavelet spectra for the velocity components show different, moderate power regions distributed within the time signals.

As well as showing for the flat plate, the reason of low amplitude power regions in the wavelet spectra at $x/x_R = 0.2941$ is due to influence of the unsteadiness of the separated shear layer or shedding of vortical structures from the separated shear layer located downstream.

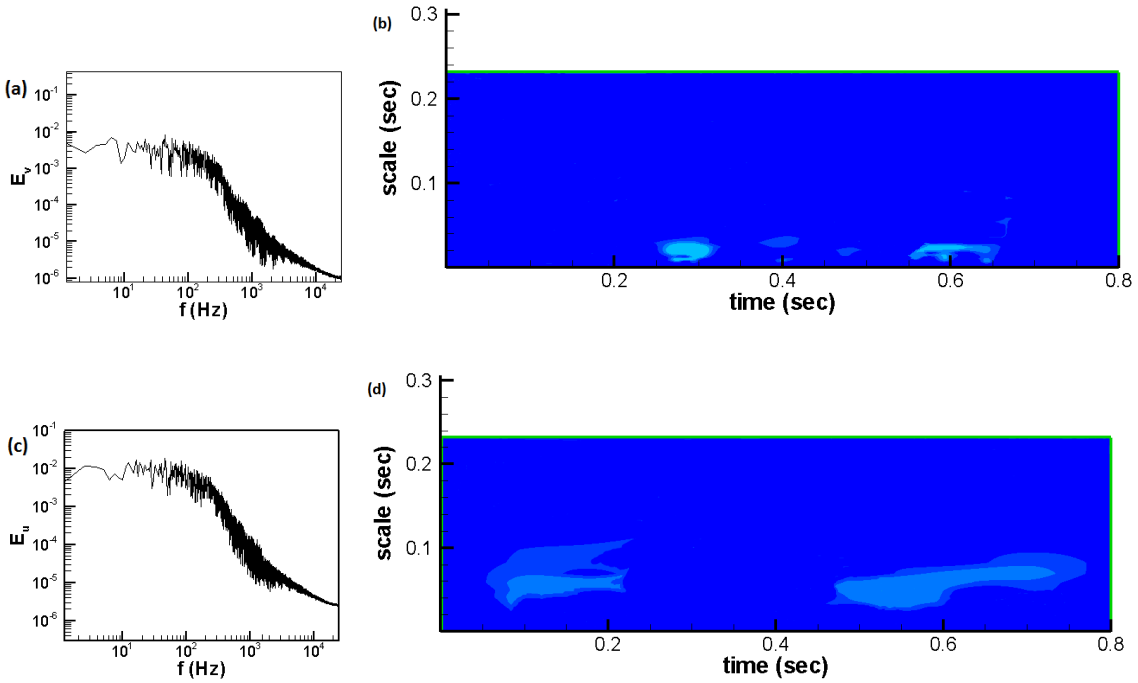

Fig. 6-11. Frequency and wavelet spectra at x/x_R = 0.0735: (a) frequency spectrum for v at y/x_R = 0.0147, (b) wavelet spectrum for v at y/x_R = 0.0147, (c) frequency spectrum for u at y/x_R = 0.0882, (d) wavelet spectrum for u at y/x_R = 0.0882 for 3D_case1 with NFST

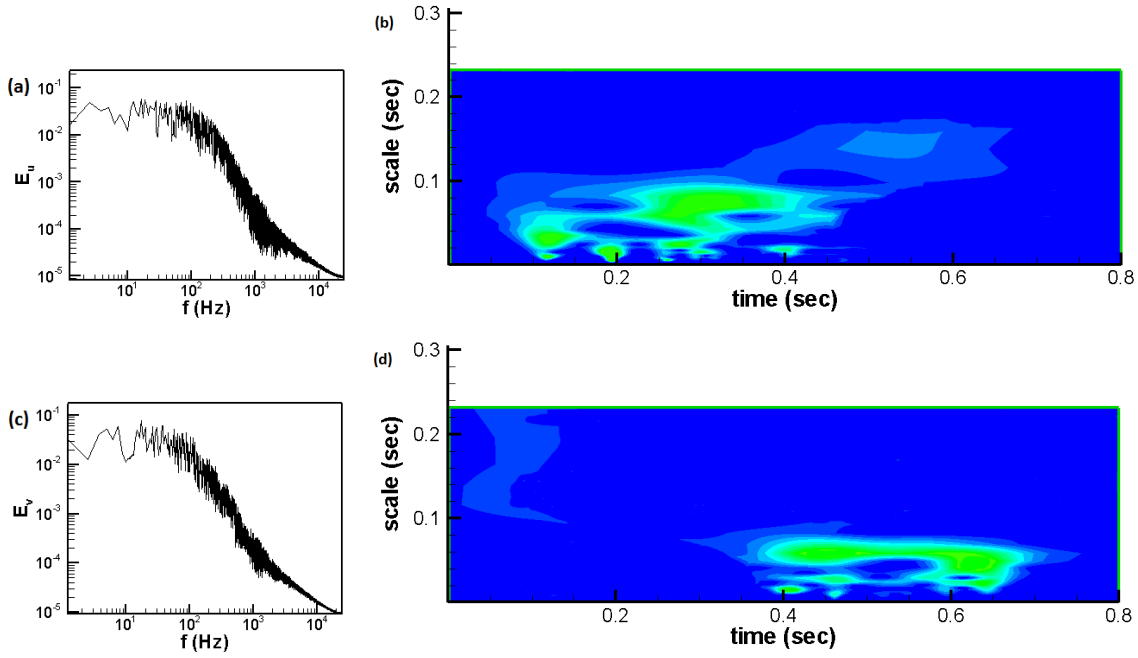

Fig. 6-12. Frequency and wavelet spectra at x/x_R = 0.2941 and y/x_R = 0.0882: (a) frequency spectrum for u, (b) wavelet spectrum for u, (c) frequency spectrum for v, (d) wavelet spectrum for v for 3D_case1 with NFST

At the streamwise station, x/x_R = 0.5882, and for all wall-normal locations, the instantaneous velocity components frequency spectra present clearly a band of peak frequencies at about 150 Hz - 180 Hz as shown in Fig. 6-13a for the instantaneous wall-normal velocity at y/x_R = 0.0882 and Fig. 6-13c for the instantaneous streamwise velocity at y/x_R = 0.147. In the current study, this is equivalent to 0.54 U_0/x_R - 0.65 U_0/x_R. This frequency band is the characteristic (regular) shedding frequency that indicates the shedding of large scale structures from the separation bubble.

For 3D_case1 or any three-dimensional geometry flow, it is believed that the current study is the first to report on spectral analysis for transitional separated-reattached flow over such a geometry. Therefore, there is no a comparison between the value of the regular shedding frequency in 3D_case1 and other studies.

The value of the regular shedding frequency for 3D_case1 is different from that identified from the flat plate. However, the regular shedding frequency magnitude for 3D_case1 is in a good agreement with that reported in the literature for different two-dimensional geometries in Section 6.3.

The wavelet transform for each set of the instantaneous velocity components shows various interesting events located at the same streamwise station, x/x_R = 0.5882, along the wall-normal direction. At y/x_R = 0.0882, the wavelet picture for the instantaneous wall-normal velocity shown in Fig. 6-13b presents numerous high amplitude power regions, one of which is indicative of the characteristic shedding frequency captured in the frequency spectrum shown in Fig. 6-13a. Other power regions indicate other involved frequencies, though these are not apparent in the frequency spectrum.

At the same streamwise station and the wall-normal position, y/x_R = 0.147, the wavelet transform for the instantaneous streamwise velocity illustrates a high amplitude power concentration extending from the beginning of the time signal to 0.2 s, as shown in Fig. 6-13d. This power region may indicate the regular shedding frequency shown in Fig. 6-13b. In addition, it can be seen that another power region connects with the first power region with similar bands of scales, where it may be considered a repetition of the event shown by the first power concentration region.

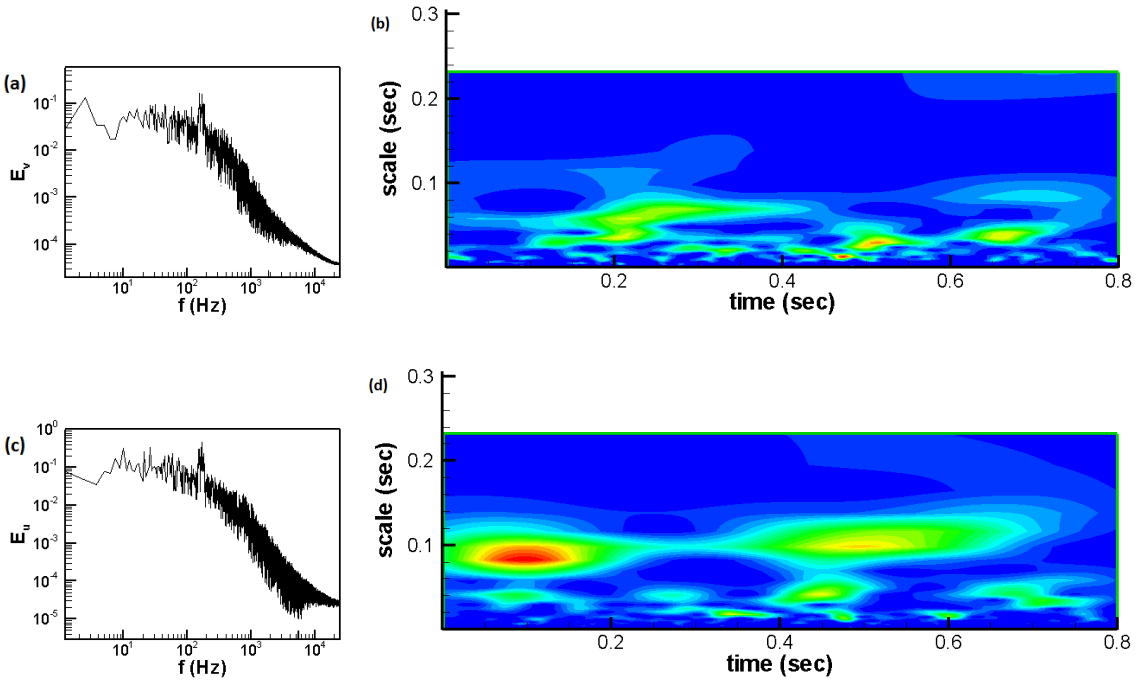

Fig. 6-13. Frequency and wavelet spectra at x/x_R = 0.5882: (a) frequency spectrum for v at y/x_R = 0.0882, (b) wavelet spectrum for v at y/x_R = 0.0882, (c) frequency spectrum for u at y/x_R = 0.147, (d) wavelet spectrum for u at y/x_R = 0.147 for 3D_case1 with NFST

All other frequency spectra for the instantaneous velocity components at the same streamwise station, x/x_R = 0.5882, and for all other wall-normal locations show a similar magnitude of the regular shedding frequency band. In this streamwise position, wavelet spectra show power concentration regions associated with the current shedding frequency in addition to the other power contents, which are not otherwise apparent in the frequency spectra.

For all wall-normal locations at the streamwise position, x/x_R = 0.7352, frequency spectra for the selected velocity components clearly show the existing regular shedding frequency band, 0.54 U_0/x_R - 0.65 U_0/x_R. This is shown in Fig. 6-14a for the instantaneous streamwise velocity frequency spectrum at the wall-normal position, y/x_R = 0.0882. Similarly, other frequency spectra for the instantaneous velocity components for other wall-normal positions show this frequency band.

Wavelet spectra for each of the selected velocities at this streamwise position show a concentration of power at different times with different scales. This is shown in Fig. 6-14b for the instantaneous streamwise velocity wavelet spectrum at y/x_R = 0.0882. In this

figure, there is a wide power region corresponding to the regular shedding frequency that extends from 0.3 s to the end of the time signal, in addition to the narrow power region bounded by 0.6 s ≤ time ≤ 0.75 s and 0.02 s ≤ scale ≤ 0.06 s that may indicate other frequency content that is not apparent in the frequency spectrum presented in Fig. 6-14a.

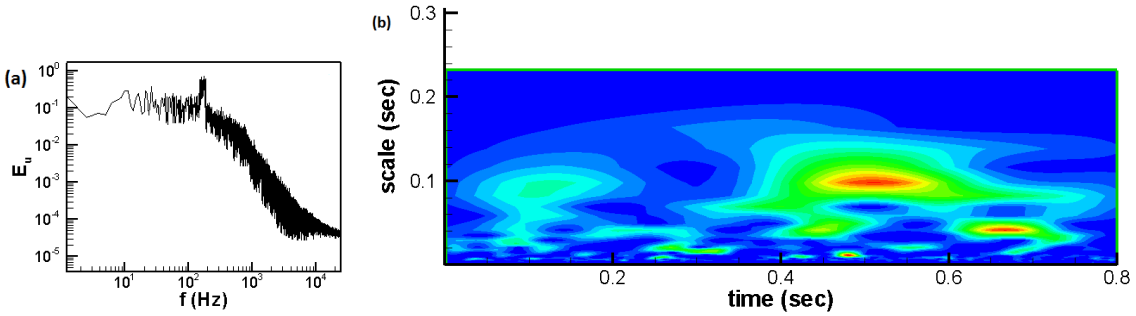

Fig. 6-14. Fourier and wavelet transforms for u at x/x_R = 0.7352 and y/x_R = 0.0882: (a) Fourier transform, (b) wavelet transform for 3D_case1 with NFST

Going further downstream to x/x_R = 0.8823, the regular shedding frequency band 0.54 - 0.65 U_0/x_R can barely be identified in the instantaneous velocity components at the first and second wall-normal positions, y/x_R = 0.0147 and 0.0882, where there is no appearance of this frequency peak at the other two wall-normal locations. This is clearly shown in the frequency spectrum in Fig. 6-15a for the instantaneous wall-normal velocity at the second wall-normal position, y/x_R = 0.0882, and Fig. 6-15c for the instantaneous streamwise velocity at the third wall-normal position, y/x_R = 0.147.

A large number of events are still apparent in the wavelet transforms for the selected velocity components at this streamwise position. As can be seen in Fig. 6-15b, which shows the instantaneous wall-normal velocity wavelet spectrum at y/x_R = 0.0882, there is a very narrow scale band power region starting from the beginning of the time signal and ending at 0.1 s. This power concentration indicates the frequency peak in the frequency spectrum for this velocity. In addition, the low amplitude power regions can be seen centred at 0.4 s and 0.8 s which indicate the occurrence of events with lower frequencies.

At the same streamwise station, x/x_R = 0.8823, and at y/x_R = 0.147, the wavelet spectrum for the instantaneous streamwise velocity shows a power concentration region with

similar time and scale bands to those shown in the wavelet spectrum for the instantaneous wall-normal velocity at y/x_R = 0.0882 as shown in Fig. 6-15d. This power region may be indicative of the shedding frequency peak, though this peak is not apparent in the frequency spectrum in Fig. 6-15c. The power spectrum shown in Fig. 6-15d shows the presence of additional low amplitude power regions that indicate other events that can be associated with the development of coherent structures in this part of the separation bubble.

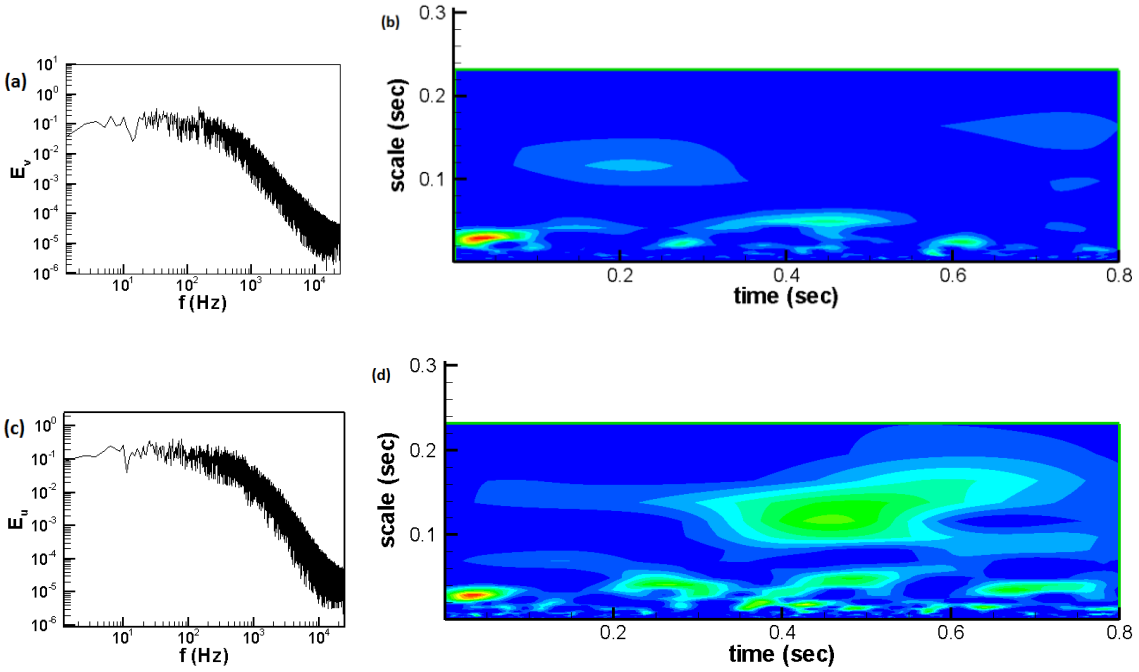

Fig. 6-15. Frequency and wavelet spectra at x/x_R = 0.8823: (a) frequency spectrum for v at y/x_R = 0.0882, (b) wavelet spectrum for v at y/x_R = 0.0882, (c) frequency spectrum for u at y/x_R = 0.147, (d) wavelet spectrum for u at y/x_R = 0.147 for 3D_case1 with NFST

For all wall-normal locations at the mean reattachment point, x/x_R = 1, and two turbulent boundary layer locations, x/x_R =1.1764 and 5.2941, there are no high or low frequency peaks apparent in either of the selected velocity components frequency spectra. This is shown in Figs. 6-16a, 6-17a, and 6-18a, which present the Fourier transforms for the instantaneous wall-normal velocity at (x/x_R = 1, y/x_R = 0.0882), the instantaneous streamwise velocity at (x/x_R = 1.1764, y/x_R = 0.147) and the instantaneous streamwise

velocity at (x/x_R = 5.2941, y/x_R = 0.0882). From these figures, it can be clearly seen that there are no frequency peaks that can be distinguished in the frequency spectra.

However, for all geometrises studied here, flow structures are shed from the separation bubble to the reattached turbulent flow which still develop further downstream, as will be demonstrated in Chapter 8. Although the frequency spectra do not show the powers released by these processes, the wavelet transform method clearly illustrates these powers as shown in Figs. 6-16, 6-17 and 6-18.

The wavelet transform for the instantaneous wall-normal velocity at the mean reattachment point and close to the shear layer centre at y/x_R = 0.0882 shows two low amplitude power regions. The first is close to beginning the time signal, whilst the other region extends from 0.4 s to a time close to the end of the time signal as shown in Fig. 6-16b. These two power regions, and indeed other narrow power regions, indicate that there are events still taking place at this streamwise station regardless of the fact that these powers do not appear in the frequency spectra. Further downstream, similar behaviour can be seen in terms of the power regions in the wavelet spectra at the two streamwise positions located in the turbulent boundary layer as shown in Fig. 6-17b for x/x_R = 1.1764 and Fig. 6-18b for x/x_R = 5.2941.

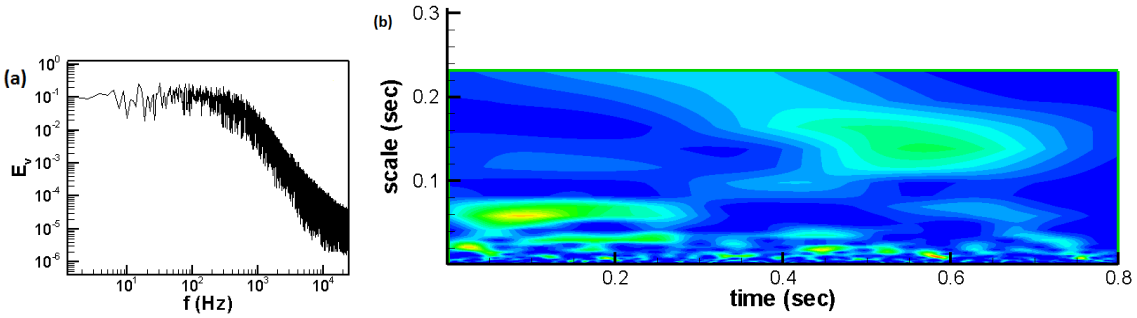

Fig. 6-16. Frequency and wavelet spectra for v at x x_R = 1 and y/x_R = 0.0882: (a) frequency spectrum, (b) wavelet spectrum for 3D_case1 with NFST

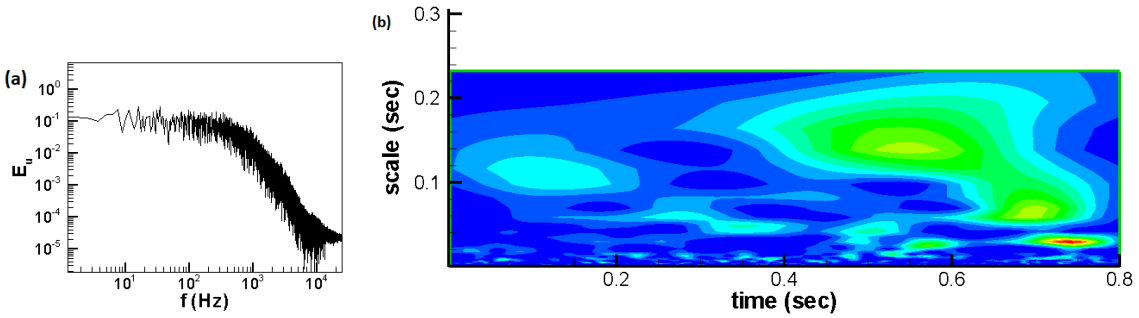

Fig. 6-17. Frequency and wavelet spectra for u at x/x_R = 1.1764 and y/x_R = 0.147: (a) frequency spectrum, (b) wavelet spectrum for 3D_case1 with NFST

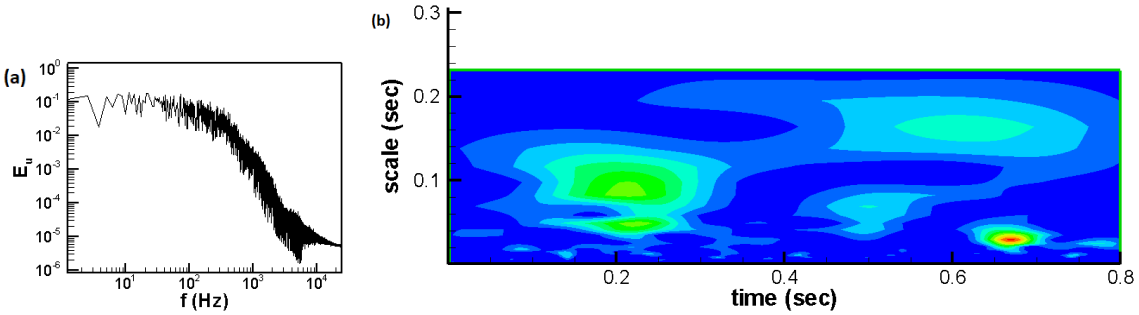

Fig. 6-18. Frequency and wavelet spectra for u at x/x_R = 5.2941 and y/x_R = 0.0882: (a) frequency spectrum, (b) wavelet spectrum for 3D_case1 with NFST

6.5 Spectral analysis for 3D_case2 for NFST

For 3D_case2, spectral analysis employing the frequency and wavelet transform methods is carried out using the inspection stations detailed in Table 6-3. At the streamwise position, which is close to the separation point x/x_R = 0.0632, frequency and wavelet spectra for the instantaneous streamwise velocity at a position close to the solid surface, y/x_R = 0.0126, are shown in Figs. 6-19a and 6-19b, respectively. It can be found that no any frequency peaks are identified in the frequency spectrum, while the wavelet spectrum presents a number of very low amplitude power regions with narrow bands of scales.

At y/x_R = 0.1265, frequency and wavelet spectra of the instantaneous wall-normal velocity present similar behaviour, where there is no frequency peak in the frequency spectrum and the wavelet transform shows a narrow and low amplitude power region, as can be seen in Figs. 6-19c and 6-19d respectively. All frequency and wavelet spectra for the

instantaneous velocity components at the other wall-normal locations at this streamwise station present a similar situation.

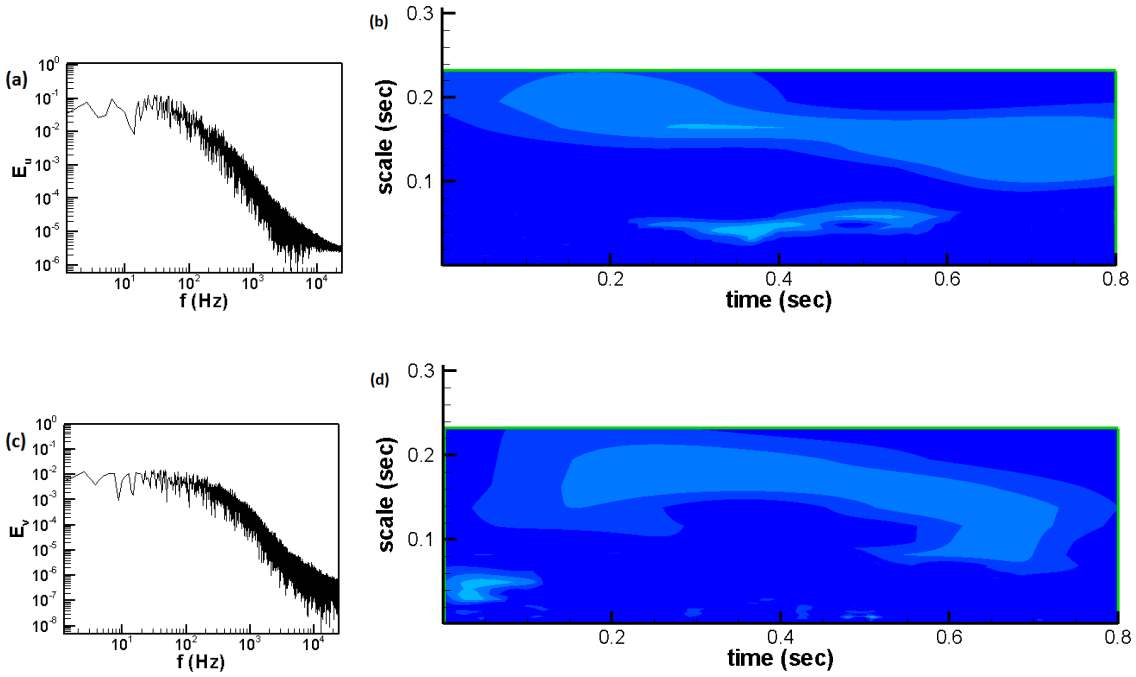

Fig. 6-19. Frequency and wavelet spectra at x/x_R = 0.0632: (a) frequency spectrum for u at y/x_R = 0.0126, (b) wavelet spectrum for u at y/x_R = 0.0126, (c) frequency spectrum for v at y/x_R = 0.1265, (d) wavelet spectrum for v at y/x_R = 0.1265 for 3D_case2 with NFST

For the second streamwise station at x/x_R = 0.2531, the frequency spectra for the instantaneous velocity components at all wall-normal locations have not got any frequency peaks. This is shown in frequency spectrum for the instantaneous streamwise velocity at y/x_R = 0.0126 in Fig. 6-20a, and for the instantaneous wall-normal velocity at y/x_R = 0.2531 in Fig. 6-20c. Frequency spectra for the instantaneous velocity components at the other wall-normal locations are also failed to capture any high or low peaks in the frequency.

At this streamwise point and for all wall-normal stations, low amplitude power regions can be seen in the wavelet transform as shown in Fig. 6-20b for the instantaneous streamwise velocity at y/x_R = 0.0126, and Fig. 6-20d for the instantaneous wall-normal

velocity at y/x_R = 0.2531. All other wavelet spectra at all other wall-normal positions at x/x_R = 0.2531 exhibit low amplitude power regions with different time and scale bands.

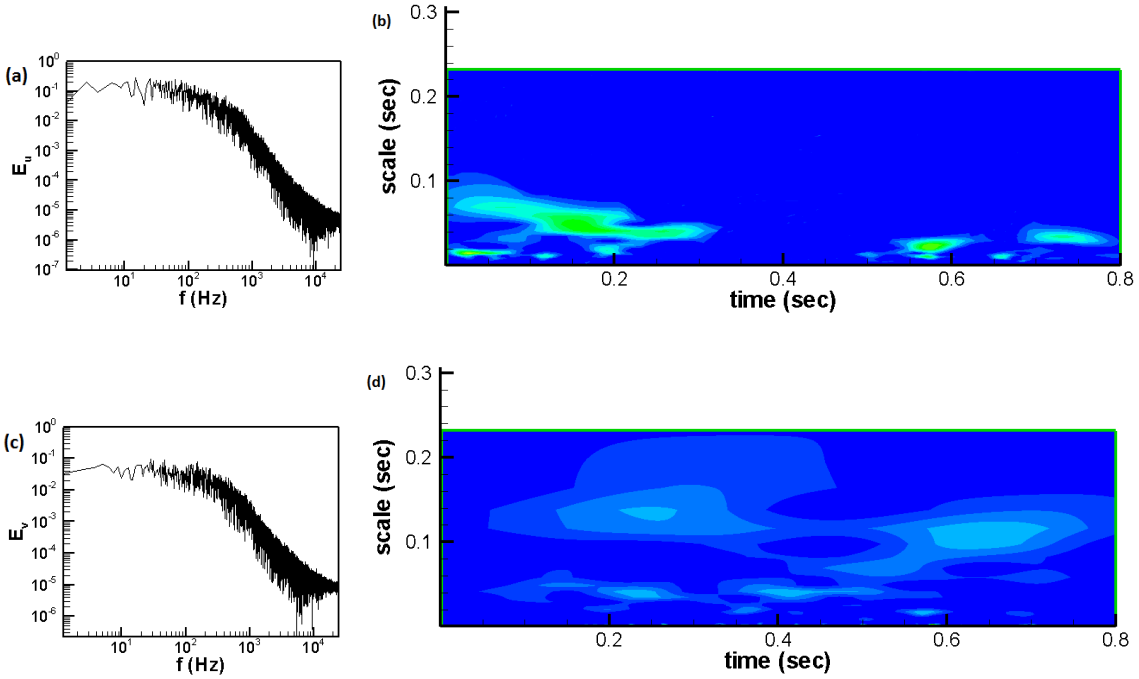

Fig. 6-20. Frequency and wavelet spectra at x/x_R = 0.2531: (a) frequency spectrum for u at y/x_R = 0.0126, (b) wavelet spectrum for u at y/x_R = 0.0126, (c) frequency spectrum for v at y/x_R = 0.2531, (d) wavelet spectrum for v at y/x_R = 0.2531 for 3D_case2 with NFST

With their relatively low levels of intensity of free stream turbulence, the figures for the wavelet spectra are similar for all geometries. The wavelet spectra show no considerable power regions at the location just after the separation line, and low amplitude power concentrations in a position just upstream of the start of the unsteadiness in the free shear layer. A similar reason for this behaviour as that discussed for the flat plate (in Section 6.3) and 3D_case1 (in Section 6.4) is likely.

Close to the mid-distance of the separation bubble at x/x_R = 0.5063, frequency spectra for the instantaneous velocity components at all wall-normal positions show a frequency peak band bounded between 150 Hz and 180 Hz. This is clearly observed in Fig. 6-21a, which shows the instantaneous streamwise velocity frequency spectrum at y/x_R = 0.0759, and Fig. 6-21c, which shows the instantaneous wall-normal velocity frequency spectrum

at y/x_R = 0.1265. In addition, the peak in the high frequency region is also shown in the frequency spectra for the velocity components at other wall-normal locations.

This frequency band corresponds to that identified in 3D_case1, and is equivalent to 0.62 U_0/x_R - 0.75 U_0/x_R for 3D_case2. This band of frequencies is the characteristic (regular) shedding frequency of vortical structures from the separated layer and is in a good agreement with such frequencies reported in the literature for different two-dimensional geometries.

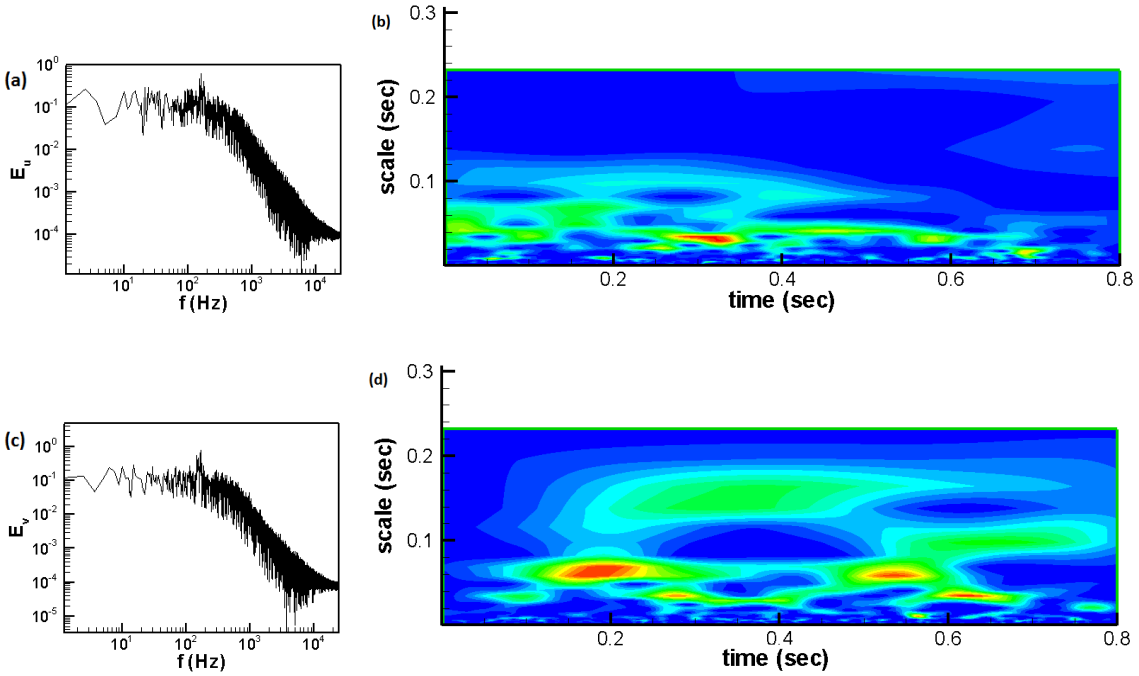

Fig. 6-21. Frequency and wavelet spectra at x/x_R = 0.5063: (a) frequency spectrum for u at y/x_R = 0.0759, (b) wavelet spectrum for u at y/x_R = 0.0759, (c) frequency spectrum for v at y/x_R = 0.1265, (d) wavelet spectrum for v at y/x_R = 0.1265 for 3D_case2 with NFST

At x/x_R = 0.5063, the wavelet spectra for each of the velocity components show high amplitude power regions that relate to the characteristic shedding frequency. For example, the wavelet spectrum for the instantaneous wall-normal velocity at y/x_R = 0.1265 is shown in Fig. 6-21d. This wavelet picture presents two repeated high-power concentration regions, one of which is relatively large whilst the other is somewhat smaller. The large power region is bounded by a range of scales of 0.04 ≤ scale ≤ 0.08,

whilst the smaller one is characterized by a narrow scales band of $0.02 \leq \text{scale} \leq 0.04$. The time between centres of each of the repeated power regions is 0.35 s. The large power region is associated with the regular shedding frequency, whilst the small power region indicates an event frequency that is smoothed out by the frequency spectra.

The wavelet transforms for each of the instantaneous velocity components at x/x_R = 0.5063 and all wall-normal points exhibit different power concentration regions that are characterised by different time and scale bands. Some of these regions indicate the structure shedding frequency apparent in the frequency spectra for each of the instantaneous velocity components.

Further downstream at x/x_R = 0.6329, frequency spectra for the instantaneous velocity components present a frequency peak at all wall-normal positions except the fourth (y/x_R = 0.2531). This is clearly seen in Fig. 6-22. It can be clearly shown that the frequency spectra for the wall-normal velocity at y/x_R = 0.0759 present the frequency peak with the band of values of 0.62 U_0/x_R - 0.75 U_0/x_R as shown in Fig. 6-22a. This frequency peak indicates the regular shedding frequency of the coherent structures that shed from the separated shear layer. No frequency peaks can be recognized in the frequency spectra for the instantaneous streamwise velocity at y/x_R = 0.2531, which is the fourth wall- normal location, as shown in Fig. 6-22c. However, the characteristic shedding frequency that is shown in Fig. 6-22a refers that the separated shear layer at the streamwise position of x/x_R = 0.6329 is still affected by the shedding process of the flow structures.

The reason of disappearance of a frequency peak in the frequency spectra for the instantaneous streamwise velocity at the fourth wall-normal location (y/x_R = 0.2531) shown in Fig. 6-22c is due to that this location is close to the edge of the separated shear layer, i.e., the distance between this location and the centre of the separated shear layer is longer than the distance between other wall-normal locations and the centre of the separated shear layer.

It is worth pointing out that the most important events, such as vortex shedding, take place close to the centre of the separated shear layer. Therefore, the effect of these events is clearly shown in the frequency spectra for the instantaneous flow variables at inspection locations that are located close to the centre of the separated shear layer rather than those

away from the centre of the separated shear layer. So, it is usual to present a frequency peak in the frequency spectra of the instantaneous velocity at $y/x_R = 0.0759$ (as shown in Fig. 6-22a) and disappear a frequency peak in the frequency spectra of the instantaneous velocity at $y/x_R = 0.2531$ (as shown in Fig. 6-22c).

At the same streamwise location ($x/x_R = 0.6329$), the wavelet spectra for the instantaneous wall-normal velocity at $y/x_R = 0.0759$ are shown in Fig. 6-22b. It can be seen that there is major power region is centred around 0.4 s with a band of $0.1 \leq$ scale ≤ 0.2. Linked to this event, there is another event which is characterised by lower band of scale compared the major event ($0.02 \leq$ scale ≤ 0.04). These two events are thought to be associated with the frequency peak noticed in the frequency spectra for the instantaneous wall-normal velocity at same streamwise and wall-normal position shown in Fig. 6-22a. The wavelet spectra shown in Fig. 6-22b also indicate that there are two events with much narrower band of scale compared the major event. One of these events has taken place at $0.4 \leq$ time ≤ 0.7 and the other, which is with lower power concentration, has taken place at $0.7 \leq$ time ≤ 0.8.

Comparing the events presented by the frequency spectra with the events presented by wavelet spectra shown in Figs. 6-22a and 6-22b respectively, it is clearly observed that the frequency spectra and wavelet spectra present the event that associates with the vortex shedding with the regular shedding frequency. This event is indicated by the sharp frequency peak band ($0.62\ U_0/x_R$ - $0.75\ U_0/x_R$) that is shown in the frequency spectra and the major power region that is shown in the wavelet spectra. In addition, the wavelet spectra capture up other two power concentration regions that refer to other events at the time when they happened. These two events may indicate to the coherent structures development process or vortex shedding with frequency is lower than the regular shedding frequency. These two events are ruled out by the frequency spectra, where in the frequency spectra there is just one frequency peak that clearly indicates to the magnitude of the regular shedding frequency.

The difference between the frequency spectra and wavelet spectra that shown above is associated with the fact that the wavelet spectra can provide only qualitative results and give a better picture of the extent of the event and any smaller events associated with it and the time of occurrence of these events compared with the frequency spectra.

Move upward to the fourth wall-normal position (y/x_R = 0.2531) at the same streamwise location (x/x_R = 0.6329), the wavelet spectra for the instantaneous streamwise velocity is shown in Fig. 6-22d. Although the frequency spectra for the instantaneous streamwise velocity at this location do not show any peak of frequencies as shown in Fig 6-22c, the wavelet spectra present different power concentration regions. Absence of frequency peak in the frequency spectra at this location is because this location is far from the centre of the separated shear layer. However, the superiority of the wavelet transform method over its Fourier transform counterpart is presented here, where the wavelet spectra present occurrence of events as shown in Fig. 6-22d.

In Fig. 6-22d, the wavelet spectra present a significant power region. This power region indicates an event that is taken place over a period of $0 \leq \text{time} \leq 0.5$. With narrower scale band, shorter period and lower amplitude than that for the main event, there are two power concentration regions presented in the wavelet spectra indicative of the occurrence of different events. The events that presented by the wavelet spectra are thought to be associated with the development of the large structures that shed from the separated shear layer. Unfortunately, these events are ruled out by the frequency spectra that are shown in Fig. 6-22c. Therefore, the current simulated results show that the wavelet spectra can present different power regions which indicate different events that are not presented by the frequency spectra. Similar observation was reported by Abdalla et al. (2009) where they performed the wavelet transform and Fourier transform methods for the spectral analyses. Abdalla et al. (2009) showed that while the frequency spectra do not show any frequency peak, the wavelet spectra present different power concentration regions indicating different events.

At x/x_R = 0.7594, which is just before the mean reattachment point, there is no sign of any recognized frequency peak in the frequency spectra for the instantaneous velocity components at all wall-normal positions as shown in Figs. 6-23. On the other hand, the associated wavelet spectra still show the power regions indicative of development of the flow structures.

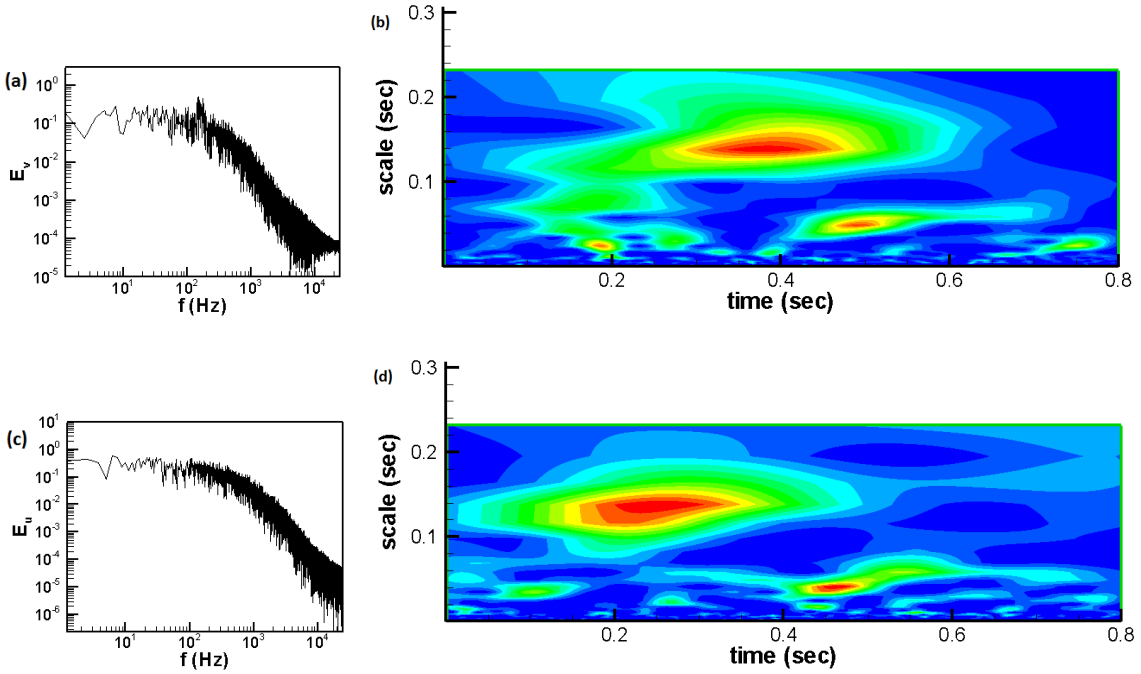

Fig. 6-22. Frequency and wavelet spectra at x/x_R = 0.6329: (a) frequency spectrum for v at y/x_R = 0.0759, (b) wavelet spectrum for v at y/x_R = 0.0759, (c) frequency spectrum for u at y/x_R = 0.2531, (d) wavelet spectrum for u at y/x_R = 0.2531 for 3D_case2 with NFST

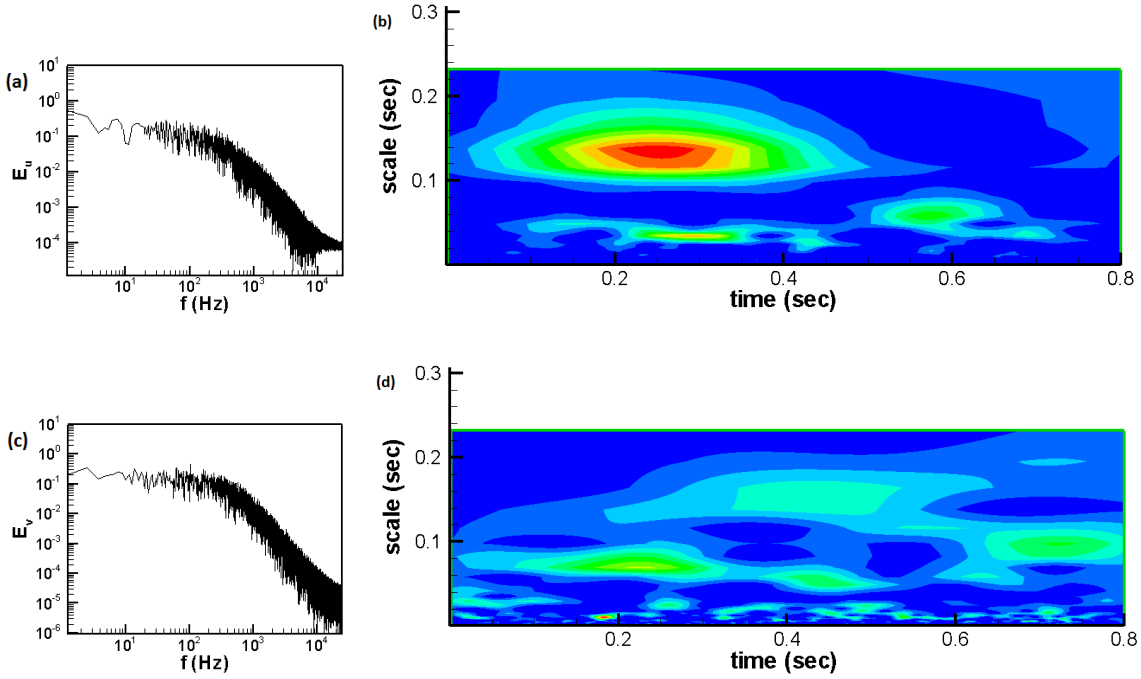

Fig. 6-23. Frequency and wavelet spectra at x/x_R = 0.7594: (a) frequency spectrum for u at y/x_R = 0.0126, (b) wavelet spectrum for u at y/x_R = 0.0126, (c) frequency spectrum for v at y/x_R = 0.1265, (d) wavelet spectrum for v at y/x_R = 0.1265 for 3D_case2 with NFST

Like the flow in the flat plate and 3D_case1, similar behaviour mentioned above is seen in the frequency and wavelet spectra at the streamwise station located just before the mean reattachment line as presented in Sections 6.3 and 6.4 respectively. At this location, there is no frequency peak in the frequency spectra, while the wavelet transforms indicate strong regions of power. This is considered quite normal because this location is within the region where coherent structures are expected to develop. Development of coherent structures, such as breakdown or topological development, as will be shown in Chapter 7, releases kinetic energy that manifests as power regions in the wavelet figures.

At the mean reattachment point and at locations further downstream, similar behaviour of in the frequency and wavelet spectra to that shown in Section 6.3 for the flat plate and Section 6.4 for 3D_case1 can be observed here. No frequency peak can be detected in the frequency spectra, while wavelet spectra still show high amplitude power regions at the mean reattachment point, x/x_R = 1.2658 and x/x_R = 4.5569. Figs. 6-24, 6-25, 6-26 give examples of frequency and wavelet spectra for the instantaneous velocity components at different wall-normal locations for these three streamwise stations. It can be seen that there are no peaks in the frequency spectra, but wavelet spectra still show different amplitude power regions.

At the mean reattachment point, the wavelet spectrum for the instantaneous streamwise velocity shown in Fig. 6-24b displays an elevated amplitude power region that extends from the beginning of the time signal to approximately 0.5 s and is bounded within $0.08 \leq$ scale $\leq$ end of available scales. This power region is indicative of the shedding of flow structures from the separation bubble to the reattached turbulent flow which normally takes place at such a position of the flow.

Further downstream, a large number of power regions with the lower amplitudes associated with flow development of a non-recovered turbulent boundary layer are illustrated by the wavelet spectra in Fig. 6-25b, which presents the wavelet transform for the instantaneous wall-normal velocity at x/x_R = 1.2658, and Fig. 6-26b, which presents wavelet transform for the instantaneous streamwise velocity at x/x_R = 4.5569.

As will be discussed in Chapter 8, after the reattachment the turbulent boundary layer still develops due to the existence of flow structures and their development. This may explain

the appearance of power concentration regions that are displayed by the wavelet spectra within this part of the transitional separated-reattached for all geometries studied here.

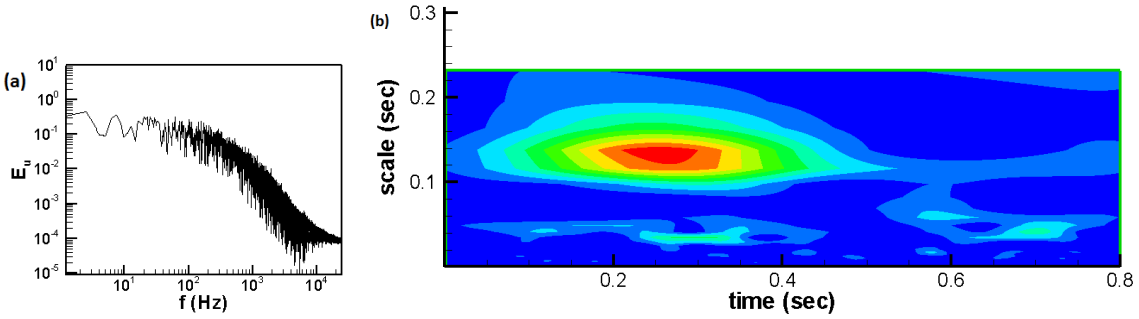

Fig. 6-24. Frequency and wavelet spectra for u at x x_R = 1 and y/x_R = 0.0126: (a) frequency spectrum, (b) wavelet spectrum for 3D_case2 with NFST

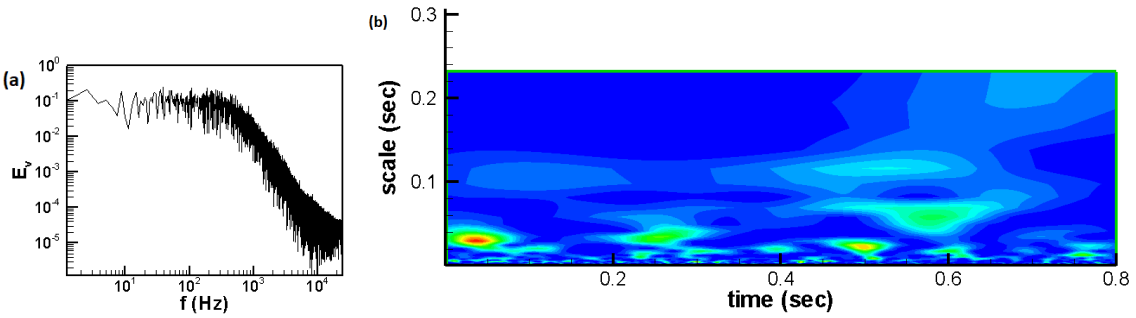

Fig. 6-25. Frequency and wavelet spectra for v at x/x_R = 1.2658 and y/x_R = 0.1265: (a) frequency spectrum, (b) wavelet spectrum for 3D_case2 with NFST

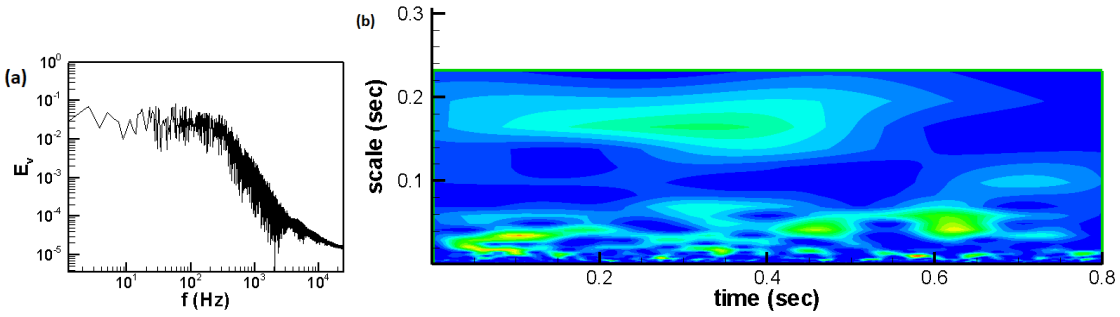

Fig. 6-26. Frequency and wavelet spectra for v at x/x_R = 4.5569 and y/x_R = 0.2531: (a) frequency spectrum, (b) wavelet spectrum for 3D_case2 with NFST

6.6 Spectral analysis locations for FST

A similar procedure to that performed in Section 6.2 is used here to investigate frequency modes in the presence of a 3.7% of intensity of free stream turbulence for all geometries. There are specific inspection points used to store 40,000 symbols for the instantaneous pressure and velocity components taken every 10 time steps, corresponding to 0.8 s total simulation time with a sampling frequency of 50 kHz. For all geometries, seven streamwise, four wall-normal and three spanwise locations were chosen as inspection points.

For the flat plate, the streamwise locations are x/D = 0.25, 1, 2, 3, 4.2, 5, and 18, corresponding to x/x_R = 0.059, 0.238, 0.476, 0.714, 1, 1.19, and 4.285, respectively. Spanwise positions are z/D = 1, 2, and 3.

For 3D_case1, the streamwise locations are x/D = 0.25, 1, 1.5, 2, 2.5, 3.5, and 18, corresponding to x/x_R = 0.1, 0.4, 0.6, 0.8, 1, 1.4, and 7.2, respectively. Spanwise positions are z/D = 1.6, 2, 2.4.

For 3D_case2, the streamwise locations are x/D = 0.25, 1, 2, 2.5, 3.1, 4, and 18, corresponding to x/x_R = 0.08, 0.322, 0.645, 0.806, 1, 1.29, 5.806, respectively. Spanwise positions are z/D = 1.2, 2, 2.8.

Wall-normal locations for all geometries when shifting the origin point of the wall-normal axis to the geometry surface are y/D = 0.05, 0.3, 0.5, and 1. These locations correspond to y/x_R = 0.012, 0.071, 0.119, 0.238 for the flat plate, y/x_R = 0.02, 0.12, 0.2, 0.4 for 3D_case1 and y/x_R = 0.016, 0.096, 0.161, 0.322 for 3D_case2, respectively. Spectral analysis inspection points are detailed in Table 6-4 for the flat plate, Table 6-5 for 3D_case1, and Table 6-6 for 3D_case2.

It is worth pointing out that inspection of Fourier spectra for the instantaneous pressure and velocity components for all geometries shows similar behaviour at each selected point. So, the spectral analysis for just the instantaneous streamwise and wall-normal velocities will be presented here, as well as those carried out for NFST. In addition, Fourier transform spectra for the instantaneous velocity components at all spanwise positions for the same streamwise and wall-normal locations show very similar results. Therefore, all of the following Fourier transform spectra figures corresponding to data at

the spanwise position are located at the centre of the computational domain, *z/D* = 2. Accordingly, wavelet spectra figures are presented and described here for just these selected Fourier transform spectral points.

		x/x_R						
		0.059	0.238	0.476	0.714	1	1.19	4.285
y/x_R	0.012	1	2	3	4	5	6	7
	0.071	8	9	10	11	12	13	14
	0.119	15	16	17	18	19	20	21
	0.238	22	23	24	25	26	27	28

Table 6-4. Locations of spectral analysis inspection points at *z/D* = 2 for the flat plate with FST

		x/x_R						
		0.1	0.4	0.6	0.8	1	1.4	7.2
y/x_R	0.02	1	2	3	4	5	6	7
	0.12	8	9	10	11	12	13	14
	0.2	15	16	17	18	19	20	21
	0.4	22	23	24	25	26	27	28

Table 6-5. Locations of spectral analysis inspection points at *z/D* = 2 for 3D_case1 with FST

		x/x_R						
		0.08	0.322	0.645	0.806	1	1.29	5.806
y/x_R	0.016	1	2	3	4	5	6	7
	0.096	8	9	10	11	12	13	14
	0.161	15	16	17	18	19	20	21
	0.322	22	23	24	25	26	27	28

Table 6-6. Locations of spectral analysis inspection points at z/D = 2 for 3D_case2 with FST

To the best of the author's knowledge, there is only one study in the literature that has used the wavelet transform to analyse the time signal for a transitional separated-reattached flow over a two-dimensional cubic obstacle and forward-facing step. This study was carried out by Abdalla et al. (2009). However, they did not consider a high level of intensity of free stream turbulence in their study.

If the wavelet transform is performed in a presence of a high intensity of free stream turbulence, the obvious question is that whether there any similarities or differences between this case and that of NFST. The current study will discover that.

6.7 Spectral analysis for the flat plate for FST

Frequency spectra for the time signals stored in the streamwise position just after the separation line (x/x_R = 0.059) do not show high or low peaks in frequency at any wall-normal location. This can be confirmed by the frequency spectrum presented in Fig. 6-27a for the instantaneous streamwise velocity at y/x_R = 0.012 and Fig. 6-27c for the instantaneous wall normal velocity at y/x_R = 0.071. Wavelet spectra at the same streamwise position and all wall-normal locations show the presence of high amplitude power regions distributed along the span of the time signal as presented for the instantaneous streamwise velocity at y/x_R = 0.012 in Fig. 6-27b and the instantaneous wall normal velocity at y/x_R = 0.071 in Fig. 6-27d.

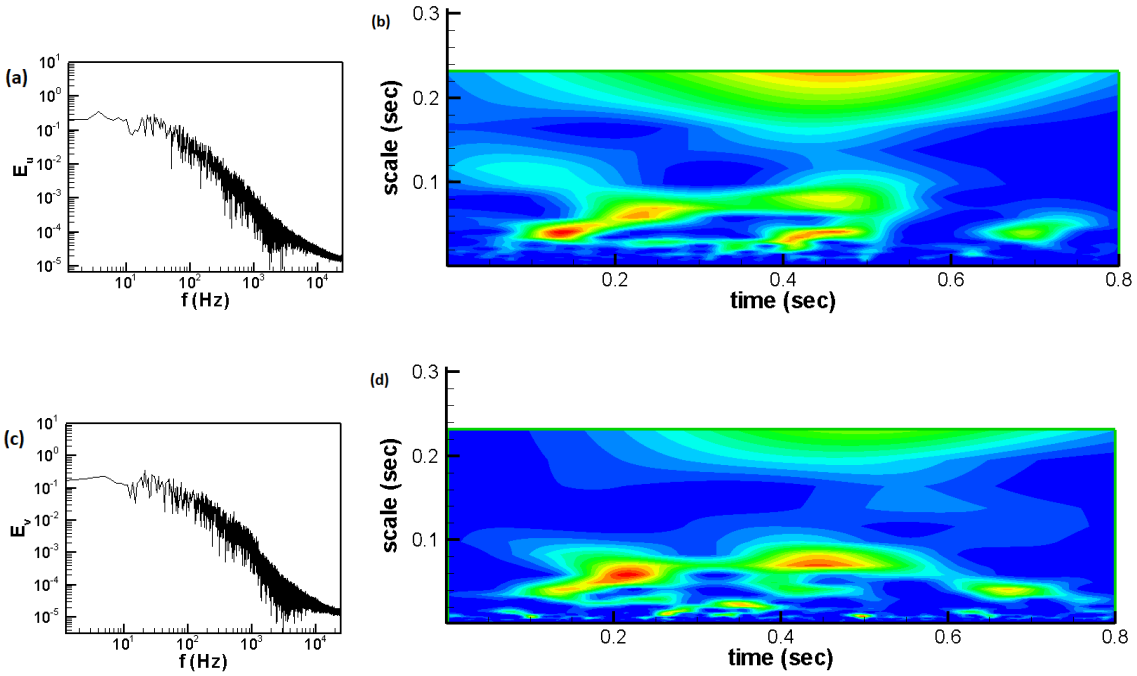

Fig. 6-27. Frequency and wavelet spectra at x/x_R = 0.059: (a) frequency spectrum for u at y/x_R = 0.012, (b) wavelet spectrum for u at y/x_R = 0.012, (c) frequency spectrum for v at y/x_R = 0.071, (d) wavelet spectrum for v at y/x_R = 0.071 for the flat plate with FST

In spite of the flow in this location still being laminar, the wavelet transform indicates the existence of power concentration regions. It is shown in the previous sections that power concentration regions are associated with the energy released from the development stages of coherent strictures. In the present case, namely that of elevated intensity of free stream turbulence, there are no large structures formed yet and the flow is still laminar at x/x_R = 0.059. So, it can be concluded that the power concentration regions apparent in the wavelet spectra in the laminar flow region of the separated layer indicate the presence of elevated intensity of free stream turbulence and its effects on the incoming flow.

Moving downstream to x/x_R = 0.238, there is a peak of high frequency with a band ranging over 145 Hz - 170 Hz that can be seen in the frequency spectra at all wall-normal locations as shown in Fig. 6-28a for frequency spectrum for u at y/x_R = 0.071 and Fig. 6-28c for frequency spectrum for v at y/x_R = 0.119. This frequency band is equivalent to 0.646 U_0/x_R – 0.757 U_0/x_R. So, the characteristic (regular) shedding frequency for the flat plate with FST is 0.646 U_0/x_R – 0.757 U_0/x_R. This value of high frequency is close to that found with NFST for the same geometry (0.76 U_0/x_R - 0.89 U_0/x_R). This indicates that the Kelvin-

Helmholtz instability is still the primary instability mechanism in the free shear layer. It is worth pointing out that the value of characteristic shedding frequency is in a good agreement with that reported in the literature in Section 6.3.

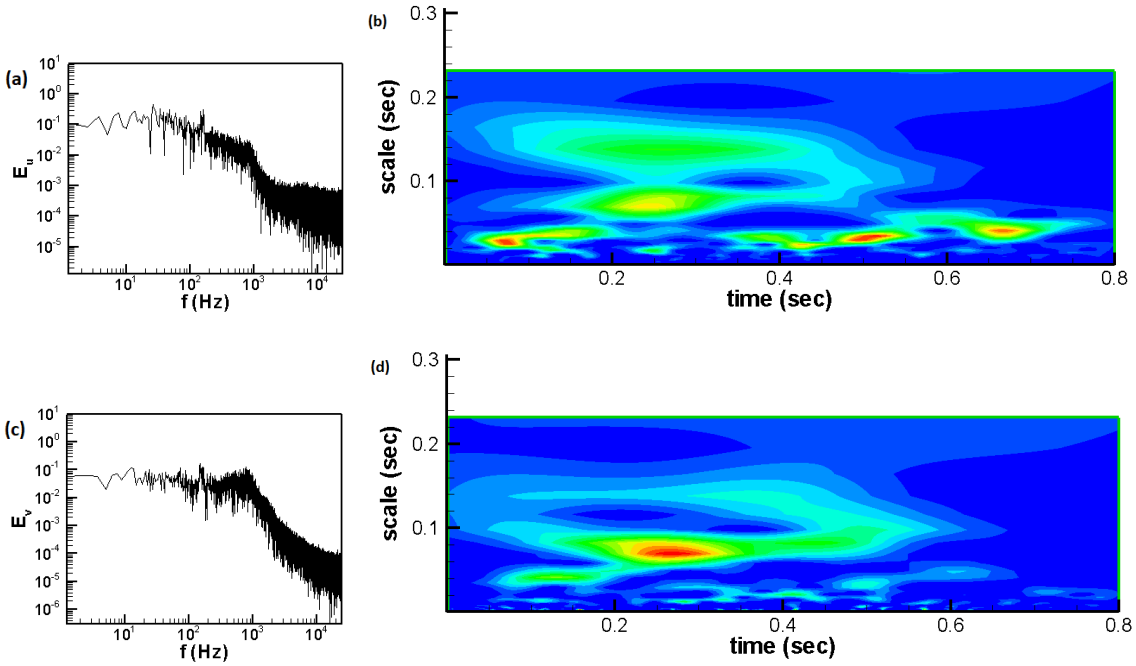

Fig. 6-28. Frequency and wavelet spectra at x/x_R = 0.238: (a) frequency spectrum for u at y/x_R = 0.071, (b) wavelet spectrum for u at y/x_R = 0.071, (c) frequency spectrum for v at y/x_R = 0.119, (d) wavelet spectrum for v at y/x_R = 0.119 for the flat plate with FST

It is worth noting that the frequency spectra at x/x_R = 0.238 show not only a peak for the characteristic shedding frequency, but also there is another peak with a higher frequency centred around 1000 Hz (equivalent to 4.456 U_0/x_R) as shown in Fig. 2-28c, that illustrates the frequency spectra for the instantaneous wall-normal velocity at y/x_R = 0.119. The high frequency does not manifest clearly in the position close to the solid surface while it is clearly apparent in other wall-normal positions as shown in Figs. 6-28a and 6-28c.

The high frequency value is approximately seven times that of the characteristic shedding frequency. The selective high shedding frequency mode was detected in Tafti and Vanka (1991) for a turbulent separated-reattached flow and in Abdalla and Yang (2005) for a transitional separated-reattached flow over a blunt flat plate. In these studies, the value of such a high shedding frequency was estimated to be seven times the magnitude of the

regular shedding frequency. Thus, the current selective high shedding frequency value is in a good agreement with the values presented in Tafti and Vanka (1991) and Abdalla and Yang (2005).

Wavelet spectra at x/x_R = 0.238 continue to show power concentration regions that correspond to the regular and selective high shedding frequencies. These regions, with their different time and scale bands, are nevertheless similar to those found for NFST as shown in Figs. 6-28b and 6-28d.

Further downstream at x/x_R = 0.476 and, indeed, at all wall-normal locations, there are no any high or low frequency peaks apparent in the frequency spectra as shown in Figs. 6-29a, 6-29c. Furthermore, at this streamwise location, the associated wavelet spectra exhibit high amplitude power regions consistent with the development of large structures in this region of the separation bubble as shown in Figs. 6-29b, 6-29d.

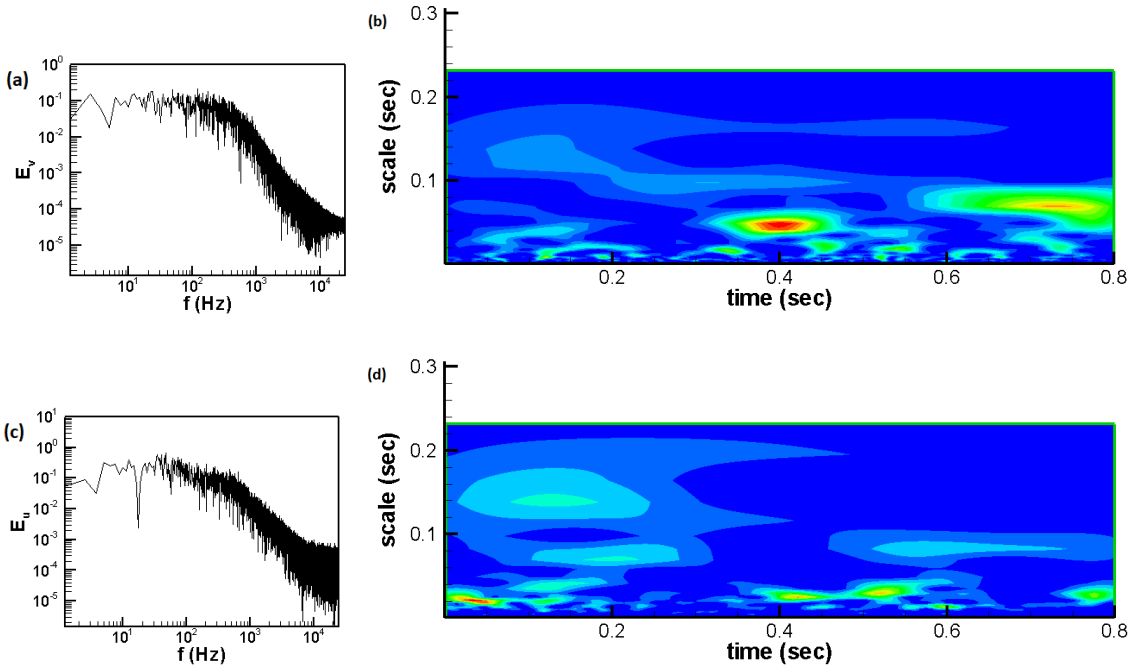

Fig. 6-29. Frequency and wavelet spectra at x/x_R = 0.476: (a) frequency spectrum for v at y/x_R = 0.071, (b) wavelet spectrum for v at y/x_R = 0.071, (c) frequency spectrum for u at y/x_R = 0.119, (d) wavelet spectrum for u at y/x_R = 0.119 for the flat plate with FST

At a location just prior to the mean reattachment (x/x_R = 0.714) and for all wall-normal locations, frequency spectra for the instantaneous velocity components do not show any high or low frequency peaks. Wavelet spectra at this streamwise location still present power concentration regions indicating energy released from the development of coherent structures. This behaviour is shown in Figs. 6-30a and 6-30b, where the frequency and wavelet spectra, respectively, are plotted for the instantaneous streamwise velocity at y/x_R = 0.071.

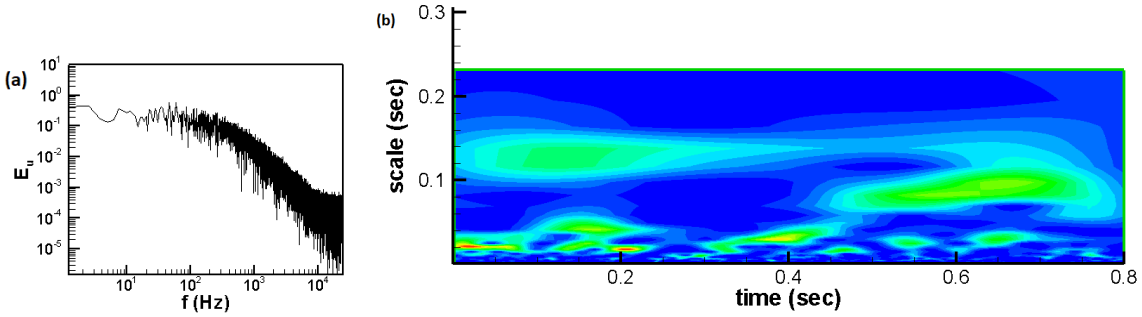

Fig. 6-30. Frequency and wavelet spectra for u at x/x_R = 0.714 and y/x_R = 0.071: (a) frequency spectrum, (b) wavelet spectrum for the flat plate with FST

At the mean reattachment point and two further streamwise points in the reattached turbulent boundary layer (x/x_R = 1.19 and x/x_R = 4.285) and for all wall-normal positions, no high or low frequency peaks can be observed in the frequency spectra for the instantaneous velocity components as shown in Fig. 6-31a for x/x_R = 1, Fig. 6-32a for x/x_R = 1.19 and Fig. 6-33a for x/x_R = 4.285.

At x/x_R = 1, the wavelet transform spectra still show power concentration regions corresponding to energy released from shedding structures from the separation bubble as shown in Fig. 6-31b.

Power regions shown in the wavelet transforms at x/x_R = 1.19 and x/x_R = 4.285 indicate the development of turbulent boundary layers after the reattachment associate with the energy generated from the breakdown of large structures to smaller turbulent structures, as will be presented in Chapter 7. This is clearly shown in Fig. 6-32b for x/x_R = 1.19 and Fig. 6-33b for x/x_R = 4.285.

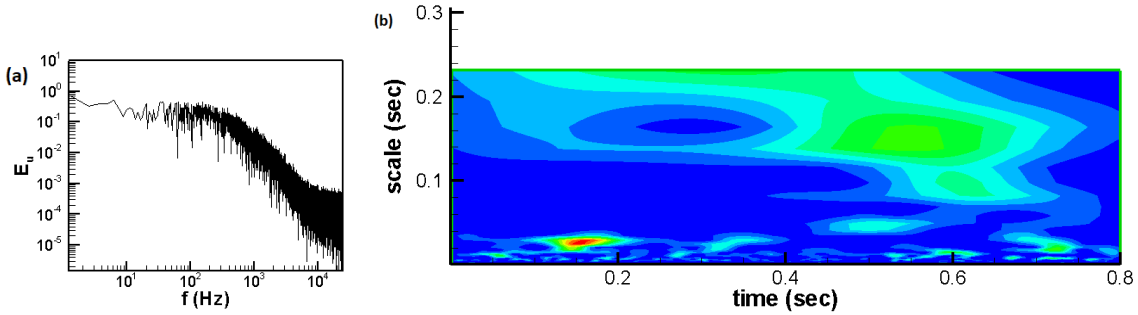

Fig. 6-31. Frequency and wavelet spectra for u at x/x_R = 1 and y/x_R = 0.119: (a) frequency spectrum, (b) wavelet spectrum for the flat plate with FST

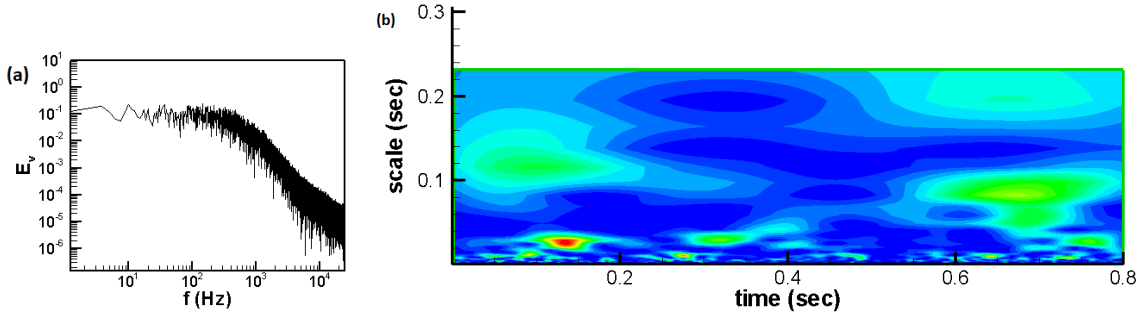

Fig. 6-32. Frequency and wavelet spectra for v at x/x_R = 1.19 and y/x_R = 0.071: (a) frequency spectrum, (b) wavelet spectrum for the flat plate with FST

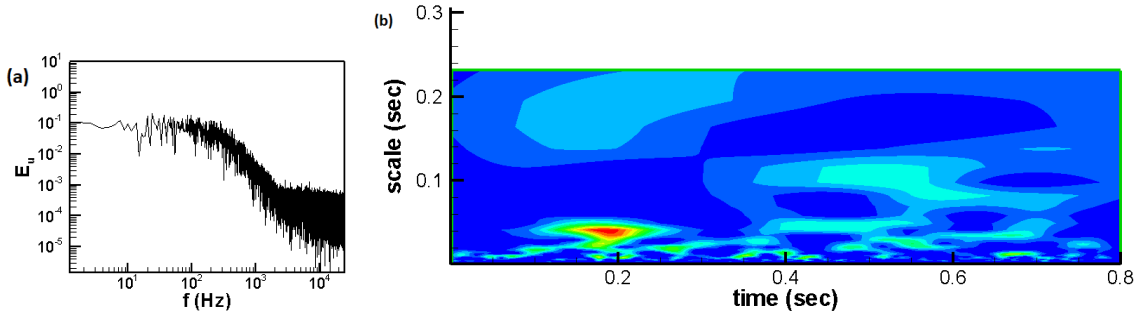

Fig. 6-33. Frequency and wavelet spectra for u at x/x_R = 4.285 and y/x_R = 0.238: (a) frequency spectrum, (b) wavelet spectrum for the flat plate with FST

6.8 Spectral analysis for 3D_case1 for FST

Close to the separation line at a streamwise location of x/x_R = 0.1, the frequency spectra for the instantaneous velocity components at all wall-normal stations seem to be quiet, and are without any high or low frequency peaks. This is clearly shown in Figs. 6-34a and 6-34c.

An inspection of the wavelet spectra recorded at same streamwise position reveals that these spectra are non-uniform and involve numerous power concentration regions, as shown in Figs. 6-34b and 6-34d. The non-uniformity arises due to the effects of elevated intensity of free stream turbulence within the incoming flow. A similar observation can be made for the investigation of wavelet spectra contours at a streamwise position close to the separation line for the flat plate. An abnormal distribution of power concentration regions in the wavelet spectra is also observed, indicative of the effects of high intensity of free stream turbulence in this region of the separation bubble.

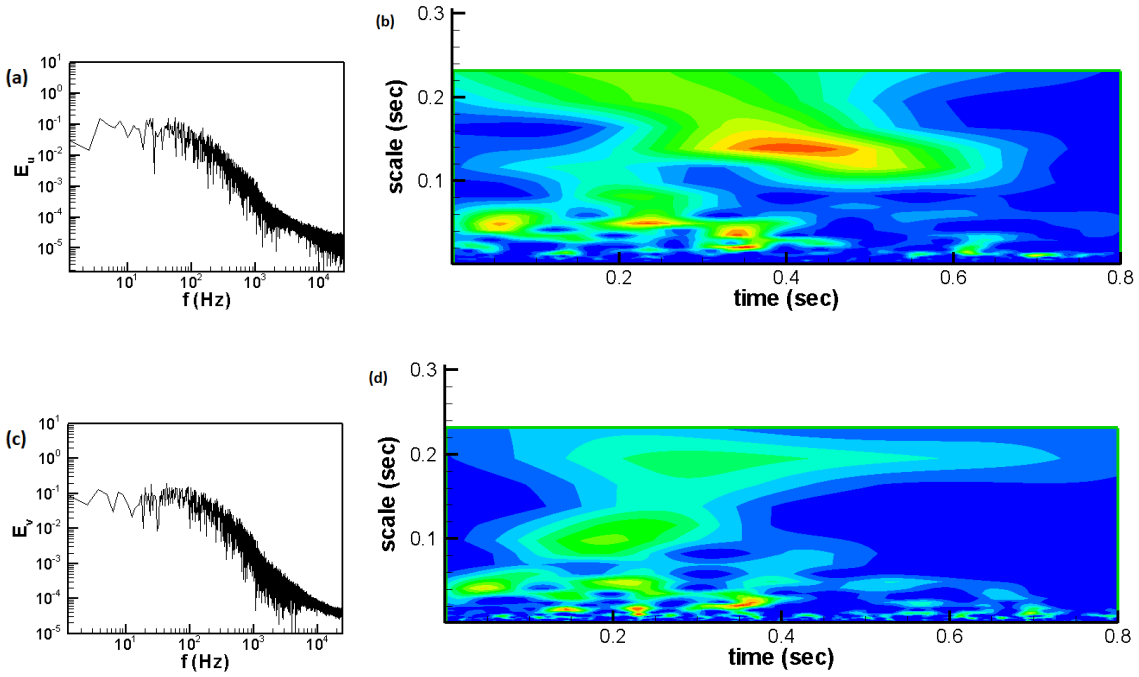

Fig. 6-34. Frequency and wavelet spectra at x/x_R = 0.1: (a) frequency spectrum for u at y/x_R = 0.02, (b) wavelet spectrum for u at y/x_R = 0.02, (c) frequency spectrum for v at y/x_R = 0.12, (d) wavelet spectrum for v at y/x_R = 0.12 for 3D_case1 with FST

Moving downstream to x/x_R = 0.4, a peak associated with a high frequency band between 150 Hz and 190 Hz is clearly shown in the frequency spectra at just the first and second wall-normal stations, where frequency spectra at the third and fourth wall-normal stations do not show this high frequency band, as can be seen from Figs. 6-35a, 6-35c and 6-35e. The high frequency band is clearly apparent in frequency spectrum for the instantaneous streamwise velocity at the second wall-normal location (y/x_R = 0.12) as presented in Fig.

6-35a, while the frequency spectrum for the instantaneous wall-normal velocity at the third wall-normal location (y/x_R = 0.2) does not show a frequency peak as can be seen from Fig. 6-35c. However, the high frequency band for 3D_case1 is equivalent to 0.397 U_0/x_R - 0.503 U_0/x_R. This high frequency band is indicative of the characteristic shedding frequency for this geometry with FST. Clearly, this is a good agreement between the characteristic shedding frequency for 3D_case1 with FST and NFST (0.54 U_0/x_R - 0.65 U_0/x_R). Thus, the Kelvin-Helmholtz instability remains the primary instability mechanism in the free shear layer for this geometry, whether the flow has a high intensity of free stream turbulence or otherwise, as presented in Chapter 5.

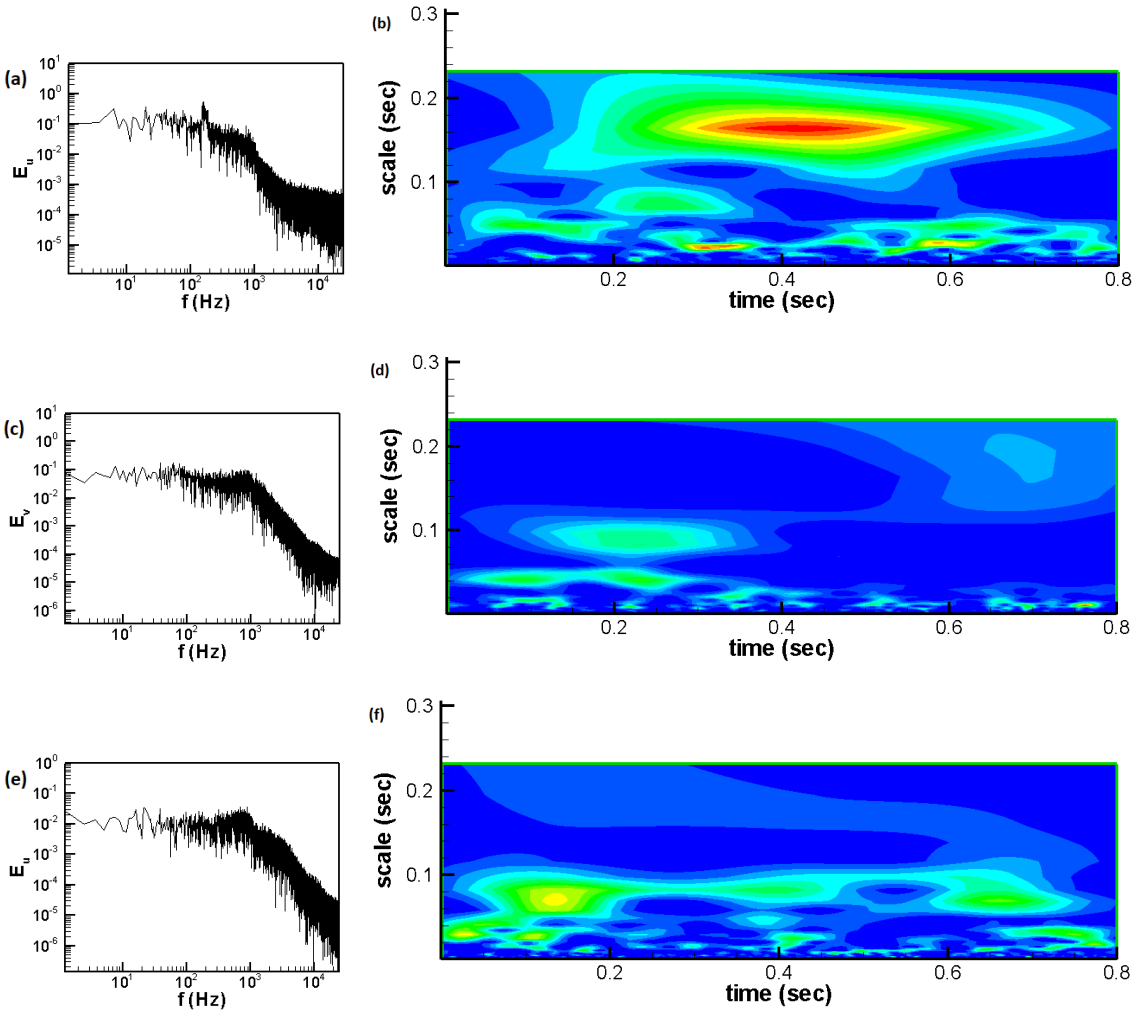

Fig. 6-35. Frequency and wavelet spectra at x/x_R = 0.4: (a) frequency spectrum for u at y/x_R = 0.12, (b) wavelet spectrum for u at y/x_R = 0.12, (c) frequency spectrum for v at y/x_R = 0.2, (d) wavelet spectrum for v at y/x_R = 0.2, (e) frequency spectrum for u at y/x_R = 0.4, (f) wavelet spectrum for u at y/x_R = 0.4 for 3D_case1 with FST

Another interesting high-frequency peak can be seen at the fourth wall-normal location only as shown in Fig. 6-35e, as can be seen in the frequency spectrum for the instantaneous streamwise velocity at y/x_R = 0.4. This high frequency peak is centred around approximately 1000 Hz and has a value equivalent to 2.652 U_0/x_R for 3D_case1. As observed for the flat plate, this high frequency peak is the result of the selective high shedding frequency and is approximately seven times the value of the characteristic shedding frequency for 3D_case1.

Due to the characteristic shedding frequency being present at just the first and second wall-normal positions close to the geometry surface, the wavelet spectrum for the instantaneous streamwise velocity demonstrates amplitude power concentration region at y/x_R = 0.12 as shown in Fig. 6-35b. This region indeed corresponds to the value of the characteristic shedding frequency. The wavelet spectrum for the instantaneous wall-normal velocity at y/x_R = 0.2 shown in Fig. 6-35d indicates lower amplitude power regions. At this location, the characteristic shedding frequency is not present in the frequency spectrum as shown in Fig. 6-35c.

Going further downstream to x/x_R = 0.6, the characteristic and selective high frequencies have disappeared in the frequency spectra for the instantaneous velocity components at all wall-normal positions as shown in Figs. 3-36a and 3-36c.

Development of large structures is still apparent in the wavelet spectra at x/x_R = 0.6. This is clearly shown by power regions in the wavelet transforms in Figs. 3-36b and 3-36d. Similar behaviour for the frequency and wavelet spectra can be seen at x/x_R = 0.8 in Fig. 6-37.

At the mean reattachment point, no high or low peak frequency can be observed in frequency spectra, while wavelet spectra still present different power concentration regions indicating a process whereby structures are shed from the separation bubble as shown in Fig. 6-38.

Within the region of the development of the reattached turbulent boundary layer, the frequency spectra at the two selected points (x/x_R = 1.4 and x/x_R = 7.2) do not show any high or low frequency peaks at all wall-normal locations, as can be seen in Fig. 6-39 for x/x_R = 1.4 and Fig. 6-40 for x/x_R = 7.2. In these figures, the energy released from the

breakdown of large structures into smaller turbulent structures is represented the power concentration regions that can be seen in the wavelet spectrum contours.

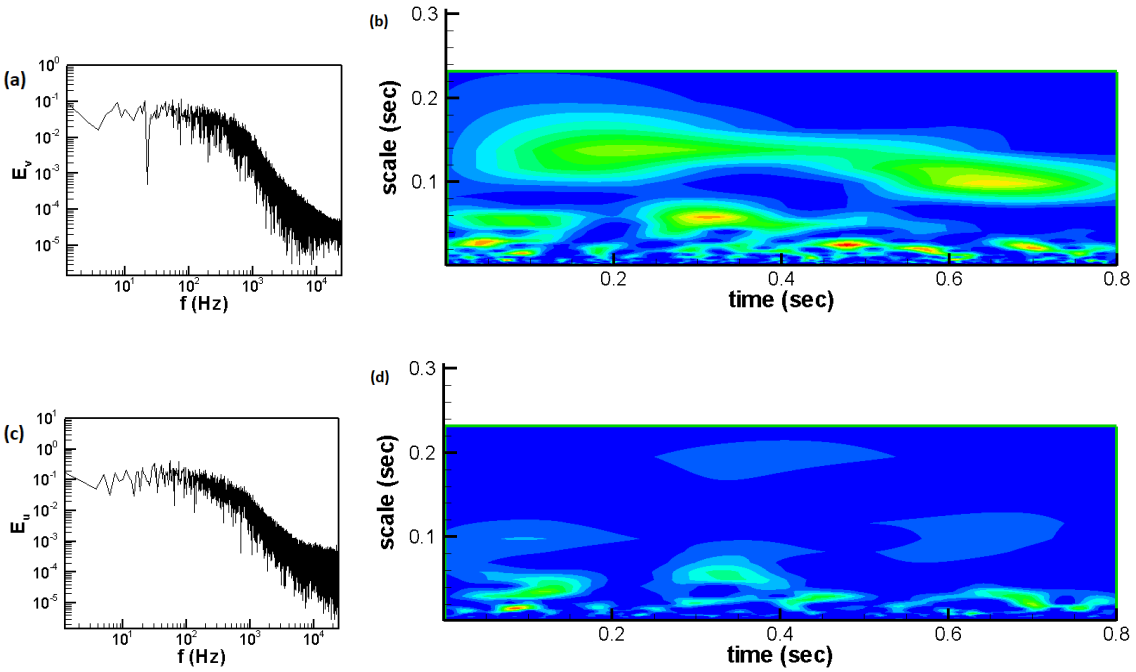

Fig. 6-36. Frequency and wavelet spectra at x/x_R = 0.6: (a) frequency spectrum for v at y/x_R = 0.02, (b) wavelet spectrum for v at y/x_R = 0.02, (c) frequency spectrum for u at y/x_R = 0.12, (d) wavelet spectrum for u at y/x_R = 0.12 for 3D_case1 with FST

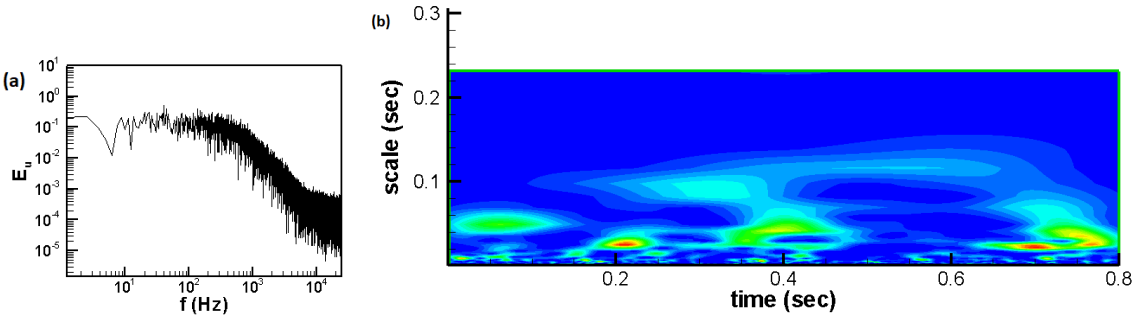

Fig. 6-37. Frequency and wavelet spectra for u at x/x_R = 0.8 and y/x_R = 0.2: (a) frequency spectrum, (b) wavelet spectrum for 3D_case1 with FST

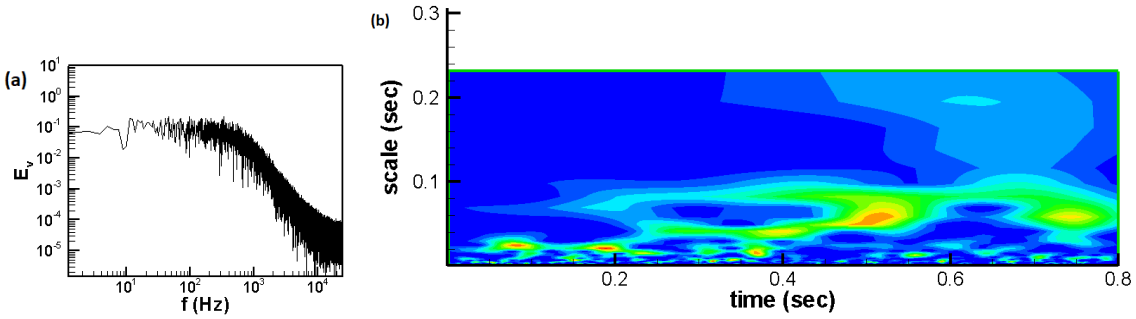

Fig. 6-38. Frequency and wavelet spectra for v at x/x_R = 1 and y/x_R = 0.12: (a) frequency spectrum, (b) wavelet spectrum for 3D_case1 with FST

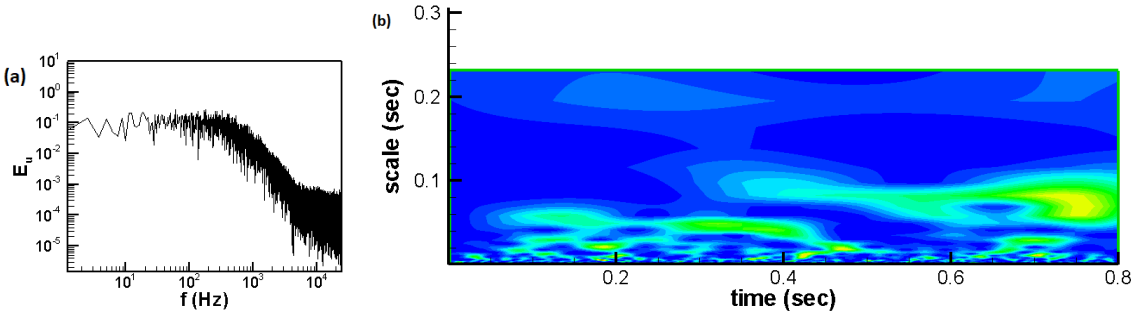

Fig. 6-39. Frequency and wavelet spectra for u at x/x_R = 1.4 and y/x_R = 0.2: (a) frequency spectrum, (b) wavelet spectrum for 3D_case1 with FST

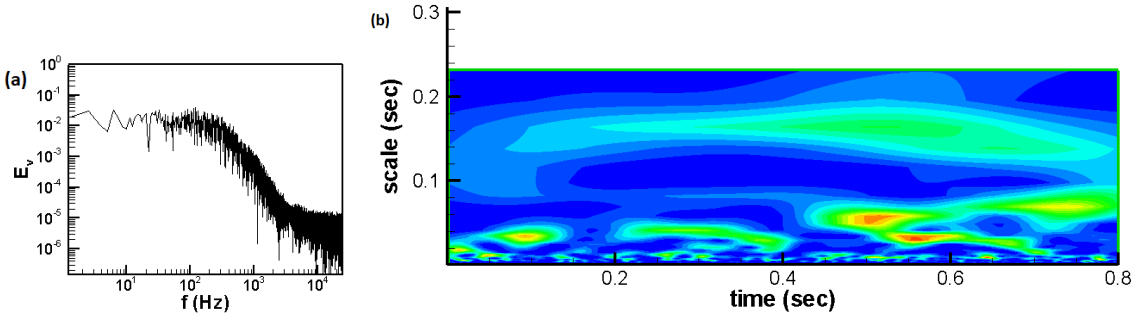

Fig. 6-40. Frequency and wavelet spectra for v at x/x_R = 7.2 and y/x_R = 0.4: (a) frequency spectrum, (b) wavelet spectrum for 3D_case1 with FST

6.9 Spectral analysis for 3D_case2 for FST

Inspection of the frequency spectra for the instantaneous velocity components at a position just after the separation line (x/x_R = 0.08) shows that there are no high or low frequency peaks at any of the wall-normal locations as shown in Figs. 6-41a and 6-41c. Due to effects of the elevated intensity of free stream turbulence, as shown in the flat plat

and 3D_case1, wavelet spectra at this location show many power regions distributed throughout the time signal as can be seen in Figs. 6-41b and 6-41d.

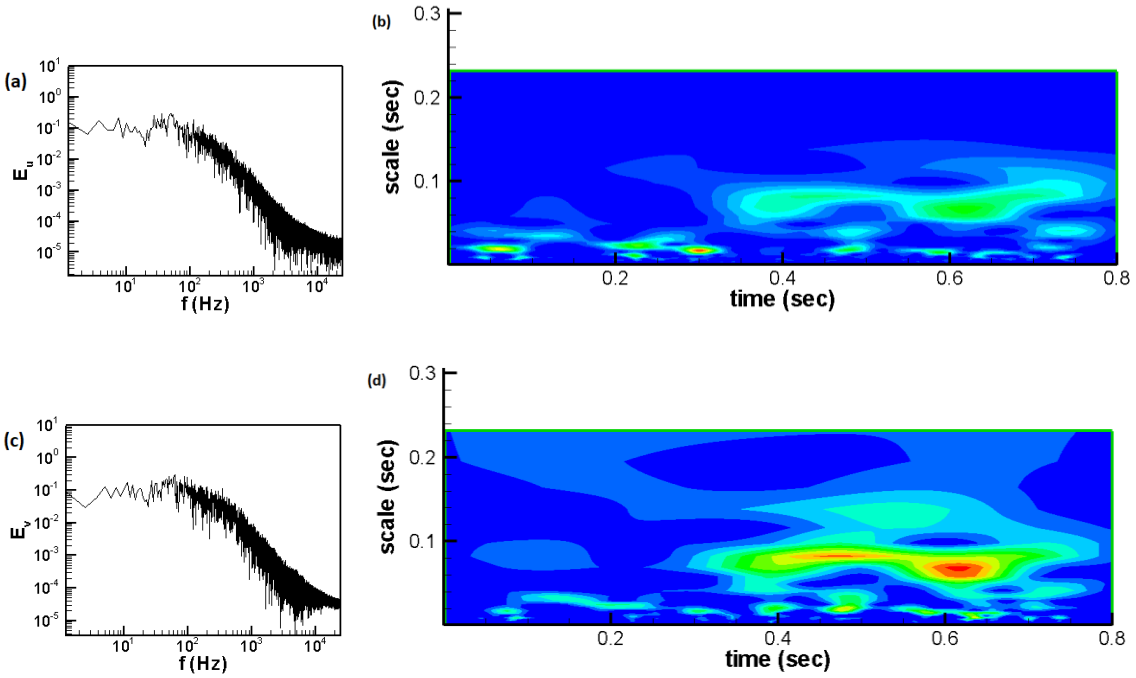

Fig. 6-41. Frequency and wavelet spectra at x/x_R = 0.08: (a) frequency spectrum for u at y/x_R = 0.016, (b) wavelet spectrum for u at y/x_R = 0.016, (c) frequency spectrum for v at y/x_R = 0.096, (d) wavelet spectrum for v at y/x_R = 0.096 for 3D_case2 with FST

At the second streamwise position (x/x_R = 0.322), and with the exception of the fourth wall-normal location, the characteristic shedding frequency appears to be represented by a high frequency peak band extending from 150 Hz to 190 Hz as shown in Figs. 6-42a, 6-42c, and 6-42e. For 3D_case2 with FST, the characteristic shedding frequency is equivalent to 0.493 U_0/x_R – 0.624 U_0/x_R. It can be seen that there is a good agreement between the current characteristic shedding frequency and one with NFST (0.62 U_0/x_R - 0.75 U_0/x_R). In addition to the characteristic shedding frequency, frequency spectra at x/x_R = 0.322 and the fourth wall-normal location (y/x_R = 0.322) indicate a high selective shedding frequency with a value centred at around 1000 Hz as shown in Fig. 6-42e. For 3D_case2, the high selective shedding frequency is equivalent to 3.29 U_0/x_R. As presented for the flat plate and 3D_case1, the value of the high selective shedding frequency for 3D_case2 is close to seven times that of the characteristic shedding frequency. This is

considered to be in a good agreement with the equivalent results reported by Tafti and Vanka (1991) and Abdalla and Yang (2005).

The wavelet spectra presented in Figs. 6-42b, 6-42d and 6-42f show a number of power concentration regions related to the high frequencies captured in the frequency spectra at same streamwise location.

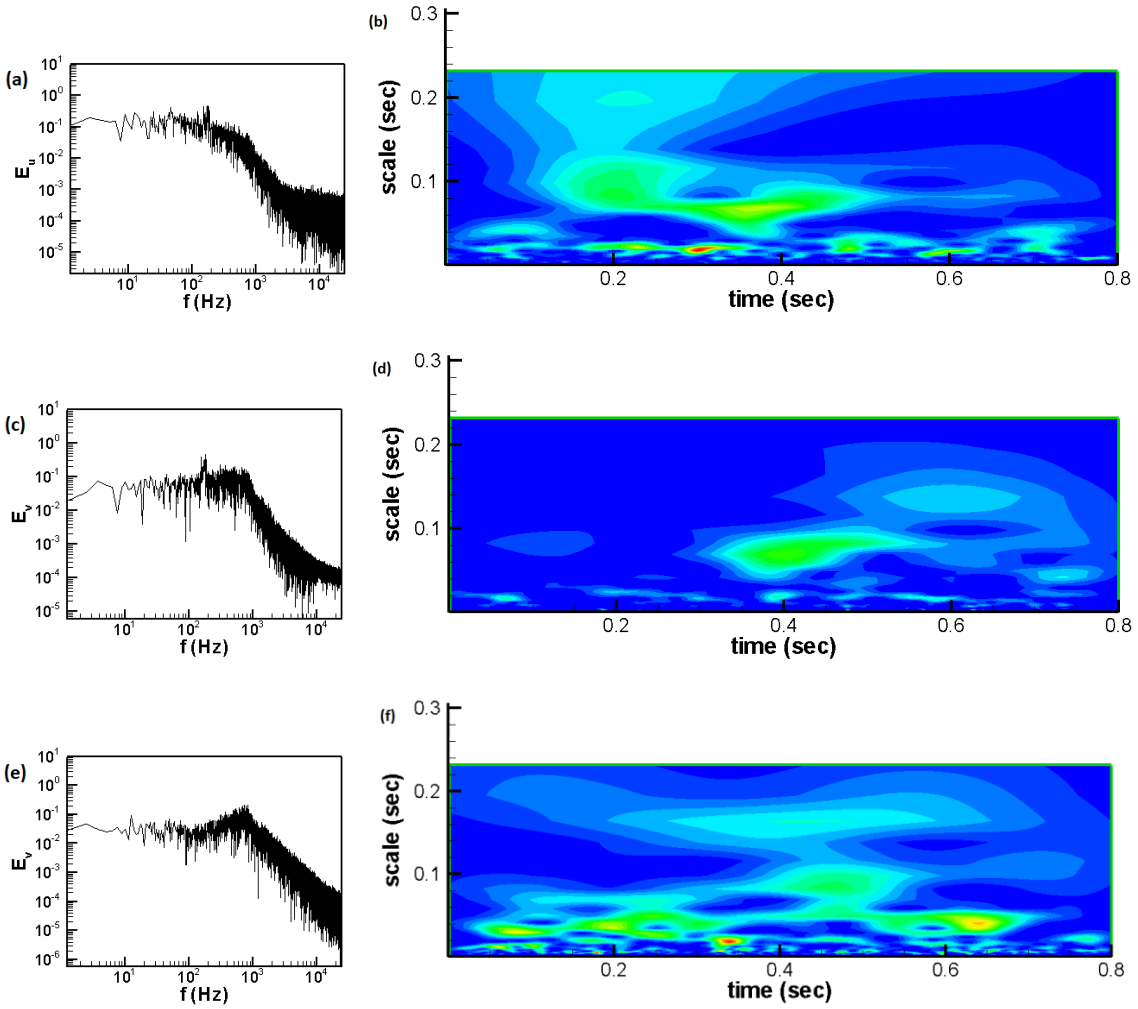

Fig. 6-42. Frequency and wavelet spectra at x/x_R = 0.322: (a) frequency spectrum for u at y/x_R = 0.096, (b) wavelet spectrum for u at y/x_R = 0.096, (c) frequency spectrum for v at y/x_R = 0.161, (d) wavelet spectrum for v at y/x_R = 0.161, (e) frequency spectrum for v at y/x_R = 0.322, (f) wavelet spectrum for v at y/x_R = 0.322 for 3D_case2 with FST

Moving further downstream to the streamwise points located within the separation bubble, at the mean reattachment point and within the reattached turbulent boundary

layer, frequency spectra do not display any high or low frequency peaks whilst wavelet spectra still indicate power regions that correspond to various events taking place at these points, such as development of coherent structures, their breakdown, and their shedding to the reattached turbulent boundary layer. These are shown in Fig. 6-43 for x/x_R = 0.645, Fig. 6-44 for x/x_R = 0.806, Fig. 6-45 for x/x_R = 1, Fig. 6-46 for x/x_R = 1.29 and Fig. 6-47 for x/x_R = 5.806.

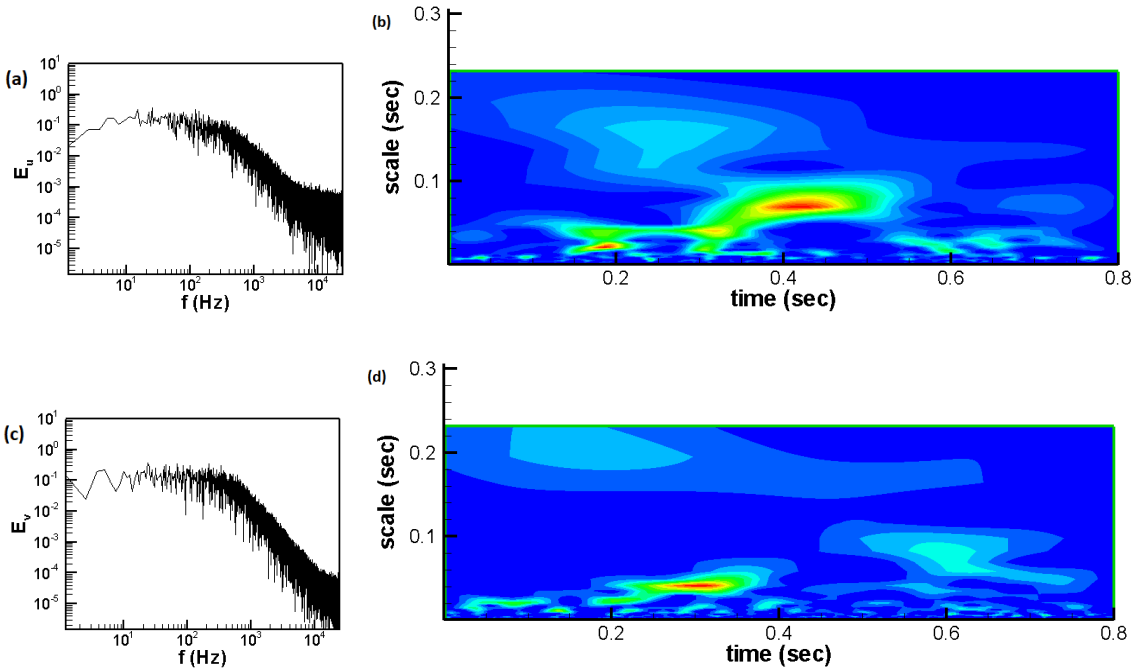

Fig. 6-43. Frequency and wavelet spectra at x/x_R = 0.645: (a) frequency spectrum for u at y/x_R = 0.016, (b) wavelet spectrum for u at y/x_R = 0.016, (c) frequency spectrum for v at y/x_R = 0.161, (d) wavelet spectrum for v at y/x_R = 0.161 for 3D_case2 with FST

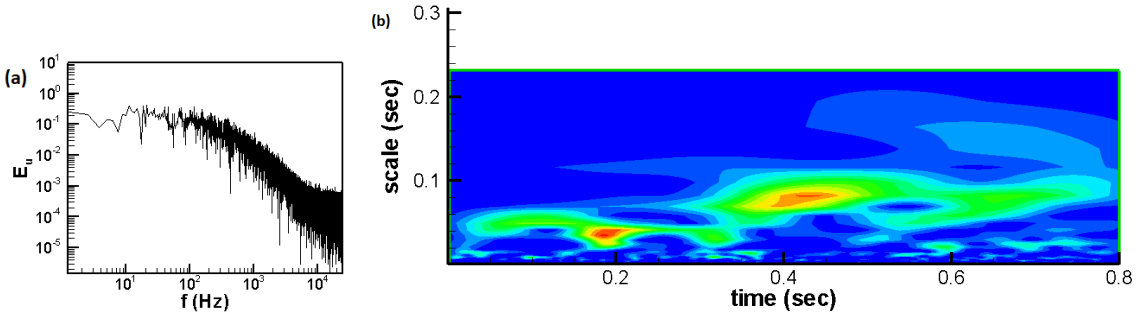

Fig. 6-44. Frequency and wavelet spectra for u at x/x_R = 0.806 and y/x_R = 0.096: (a) frequency spectrum, (b) wavelet spectrum for 3D_case2 with FST

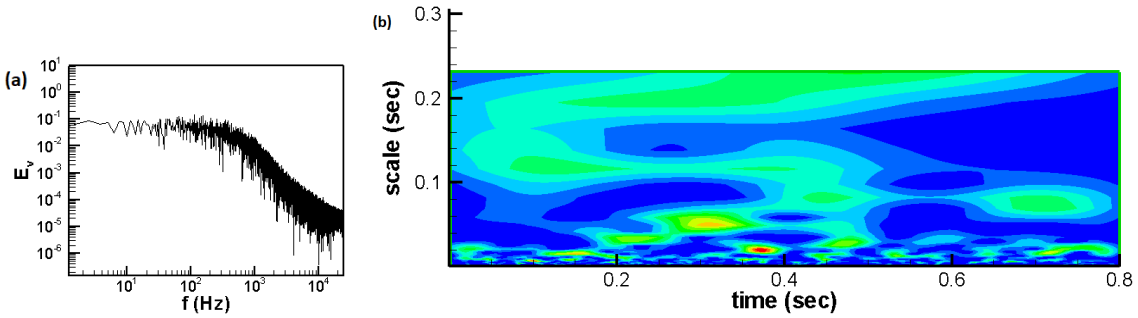

Fig. 6-45. Frequency and wavelet spectra for v at x/x_R = 1 and y/x_R = 0.016: (a) frequency spectrum, (b) wavelet spectrum for 3D_case2 with FST

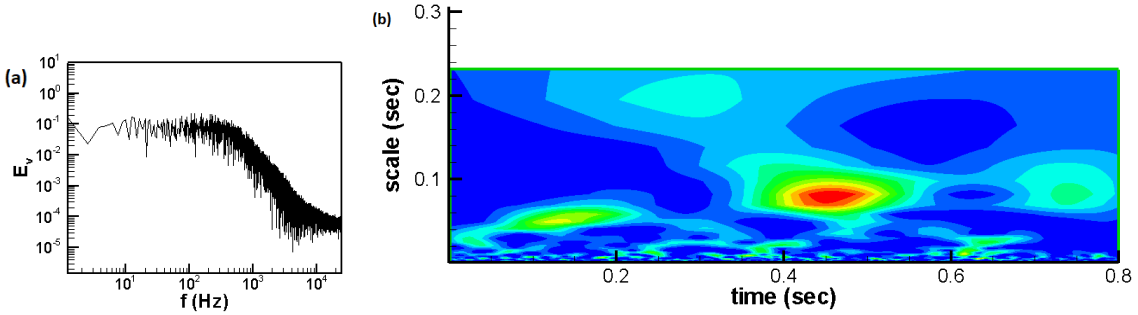

Fig. 6-46. Frequency and wavelet spectra for v at x/x_R = 1.29 and y/x_R = 0.161: (a) frequency spectrum, (b) wavelet spectrum for 3D_case2 with FST

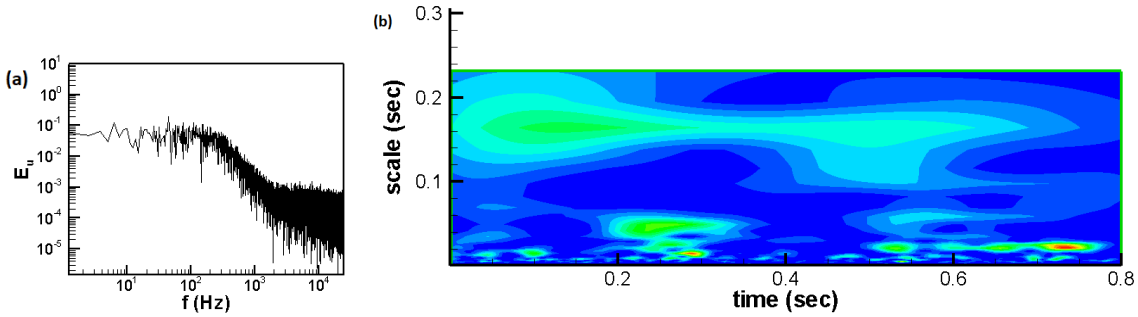

Fig. 6-47. Frequency and wavelet spectra for u at x/x_R = 5.806 and y/x_R = 0.322: (a) frequency spectrum, (b) wavelet spectrum for 3D_case2 with FST

6.10 Existing frequency modes

From the above spectral analysis, the investigation of existence of any frequency mode (low shear layer flapping frequency, characteristic shedding frequency, and selective high shedding frequency) in each case study in the current thesis is carried out.

For NFST, the characteristic shedding frequency is found to lie within a band of frequencies. For the flat plate this band is 120 Hz - 140 Hz which is equivalent to 0.76 U_0/x_R - 0.89 U_0/x_R. For 3D_case1 and 3D_case2 this band is 150 Hz - 180 Hz, which is equivalent 0.54 U_0/x_R - 0.65 U_0/x_R for 3D_case1 and 0.62 U_0/x_R - 0.75 U_0/x_R for 3D_case2.

For FST, the characteristic shedding frequency is also found within a band of frequencies. In the flat plate this band is 145 Hz - 170 Hz, which is equivalent 0.646 U_0/x_R - 0.757 U_0/x_R, while it is found as 150 Hz - 190 Hz for both three-dimensional geometries, equivalent to 0.397 U_0/x_R - 0.503 U_0/x_R for 3D_case1 and 0.493 U_0/x_R - 0.624 U_0/x_R for 3D_case2.

For all geometries, there is no existence of selective high shedding frequency mode with NFST, while there is a sign for this mode in the frequency spectra with FST. The magnitude of this high frequency is approximately seven times that of the value of the characteristic shedding frequency.

It is important to mention that the selective high shedding frequency mode was detected in Tafti and Vanka (1991) for a turbulent separated-reattached flow, and in Abdalla and Yang (2005) for a transitional separated-reattached flow over a blunt flat plate. In these studies, the value of this high shedding frequency was estimated to be seven times that of the magnitude of the regular shedding frequency. The high frequency mode has also been reported in experimental work into turbulent separation conducted by Kiya and Sasaki (1983) for a blunt flat plate, and by Lee and Sung (2001) for a backward-facing step.

The low frequency mode (low frequency flapping), which is believed to be due to the free shear layer flapping, has identified in various turbulent separation studies and the transitional separated-reattached flow in Yang and Voke (2001) for a flat plate with a semi-circular leading edge. For turbulent separation flows, Hillier and Cherry (1981), Kiya and Sasaki (1983), and Cherry et al. (1984) found this low frequency mode to have a value of $0.12U_0/x_R$.

Based on the data with NFST, $0.12U_0/x_R$ is equivalent to 18.85 Hz for the flat plate, 33.26 Hz for 3D_case1 and 28.63 Hz for 3D_case2. So, the low frequency flapping would occur every 0.05 s for the flat plate, 0.03 s for 3D_case1, and 0.035 s for 3D_case2 where it exits. In the current study, the sampling process was carried out over 0.8 s for all

geometries. So, the current samples were able to cover 16, 27 and 23 low frequency cycles in the flat plate, 3D_case1, and 3D_case2, respectively, again if this mode exists.

With FST, $0.12U_0/x_R$ is equivalent to 26.92 Hz for the flat plate, 45.24 Hz for 3D_case1, and 36.48 Hz for 3D_case2. Thus, if the low frequency shear layer flapping exists, it would take place every 0.037 s for the flat plate, 0.022 s for 3D_case1 and 0.027 s for 3D_case2. Therefore, the total simulation time (0.8 s) could cover 22, 36 and 30 low frequency modes in the flat plate, 3D_case1 and 3D_case2, respectively, if it exists.

It is worth pointing out that the sampling time in Tafti and Vanka (1991) was equivalent to just three low frequency cycles and this phenomenon was straightforwardly captured in their study. So, we can say with some confidence that the low shear layer flapping really is absent in the current study.

It was believed that the reason for the disappearance of the low frequency shear layer flapping in transitional separated-reattached flows was due to the action of the laminar part of the separation bubble, which works as a 'filter' for the low frequency motion in the shear layer (Abdalla and Yang, 2005). In addition, this phenomenon only appears in turbulent separated-reattached flows, as was suggested by Cherry et al. (1984). Moreover, Castro (2005) reported that if the ratio of the backflow velocity to the free stream velocity is less than 20%, low frequency shear layer flapping is generally absent. As shown in Chapter 5, the maximum backflow velocity is smaller than 20% of the local free stream velocity for all geometries. Therefore, the current study is consistent with the above studies, where the low amplitude power concentration regions apparent in the wavelet power spectra close to the separation line in the current study do not represent the low frequency shear layer flapping, but are rather related to either the start of the unsteadiness or structure-shedding process that occurs downstream.

6.11 Summary

Within transitional separated-reattached flow over all geometries used in the current study, specific inspection points are selected to collect the instantaneous pressure and velocity components at every 10 time steps during the time period (0.8 s). This is carried out for two cases of disturbances of the flow: a low intensity of free stream turbulence (< 0.2%) and an elevated intensity of free stream turbulence (3.7%).

Fourier transform and wavelet power transform are used to analyse the spectra of the time signal. The wavelet power spectra clearly show the extent of events (amplitudes) and the time at which they occurred (and indeed their reoccurrence period if this happened). In addition, any associated smaller events, as characterised by narrow scales (periods) and shorter times, are apparent in the wavelet figures. These smaller events are smoothed out by Fourier transform spectra.

Close to the separation line, different intensities in the power regions of wavelet spectra are observed depending on whether the flow case is NFST or FST. With NFST, wavelet spectra are uniform, and contain very low amplitude power regions. However, with FST, wavelet spectrum contours seem to be non-uniform with many amplified power concentration regions, indicating the influence of a high level of disturbances in the incoming flow on the free shear layer.

Fourier transform spectra show that the regular shedding frequency of vortical structures from the separated shear layer for all geometries is in a good agreement with that documented in the literature. Furthermore, it is observed that for all geometries studied here, there is a good agreement between the characteristic shedding frequencies, whether the flow has a high or low intensity of free stream turbulence. In addition, there is no apparent effect due to the aspect ratio of the three-dimensional geometry on the magnitude of the characteristic shedding frequency. It is also observed that for a specific distance downstream from the mid-distance of the separation bubble, frequency spectra do not show the frequency peak of the regular shedding frequency. A possible explanation for this observation could be due to the current transitional separated-reattached flow not being characterized by a strong shedding process and thus that there is a rapid transformation to turbulent flow.

For all geometries, the selective high shedding frequency mode is absent with NFST. With FST, this frequency mode appears in the frequency spectra recorded for all geometries. The magnitude of this high frequency is approximately seven times that of the value of the characteristic shedding frequency.

For all geometries with NFST and FST, inspection of Fourier transform spectra shows that there is no trace any low frequency modes (shear layer flapping) in the thorough

spectra analysis conducted for the selected instantaneous velocity components in the current study.

Low amplitude power content in the wavelet spectra for the first and second streamwise locations, which are in the laminar shear layer and close to the separation point, for all geometries might indicate the presence of the low frequency shear layer flapping phenomenon, although the frequency spectra at these locations do not show any low frequency peak. However, the appearance of the low amplitude power concentration regions in the wavelet spectra in the laminar part of the separation bubble is believed due to the influence of the unsteadiness in the separated shear layer, especially on the second streamwise location which is close to the start of the unsteadiness region. Another possible explanation for these low power concentration regions was due to the effects of the shedding of vortical structures from the separated shear layer that takes place downstream.

Chapter Seven

Development of Coherent Structures

7.1 Two-dimensional flow visualization for NFST

In order to have an initial conception for forming and development of coherent structures, the *x-y* plane of instantaneous pressure contours and the corresponding instantaneous velocity vectors at the mid-distance of the spanwise direction, $z/D = 2$, with the sequential times (every 250 time steps) are considered in this chapter.

For the flat plate, the formation of a weak vortex can be observed at a region between $x/x_R = 0.25$ and $x/x_R = 0.3$ as shown in Fig. 7-1a, where four structures *A*, *B*, *C*, and *D* can be seen. Structure *A* is the smallest structure, and is formed in the early stage of the separation bubble. Structures *B* and *C* move downstream along the separated shear layer and they become larger and larger. Structure *C* becomes the largest one and moves further from the separation line. The distance between structures *B* and *C* becomes shorter compared with the distance between structures *C* and *D* as shown in Fig. 7-1b, where it is believed that the structure *C* moves slowly due to its larger size. It is clear seen that structure *B* tries to 'catch up' with structure *C* in a region between $x/x_R = 0.4$ and $x/x_R = 0.6$, where considerable three-dimensional motions of the flow take place. At the same time, structure *A* grows when moving downstream as shown in Fig. 7-1b.

Gradually, structures *B* and *C* merge with each other to form a new and strong structure *E* as shown in Fig. 7-1c. The structure *E* moves a short distance downstream as shown in Figs. 7-1d and 7-1e and then breaks down into smaller structures around the mean reattachment line as shown in Figs. 7-1f, 7-1g, and 7-1h. Structure *D* is considered to be a precursor structure to the structure *E*, and breaks down into smaller structures around the mean reattachment line, this is also shown in Figs. 7-1c and 7-1d.

At the same time, another structure upstream of structure *A* begins to form as shown in Fig. 7-1e. This new structure moves downstream and it is believed that it merges with structure *A* to form a new large structure *F* as shown in Fig. 7-1f. When structure *F* moves

downstream, another structure is formed at upstream of structure *F* as shown in Figs. 7-1f, 7-1g and 7-1h, indicating that the there is a repetition of the above process.

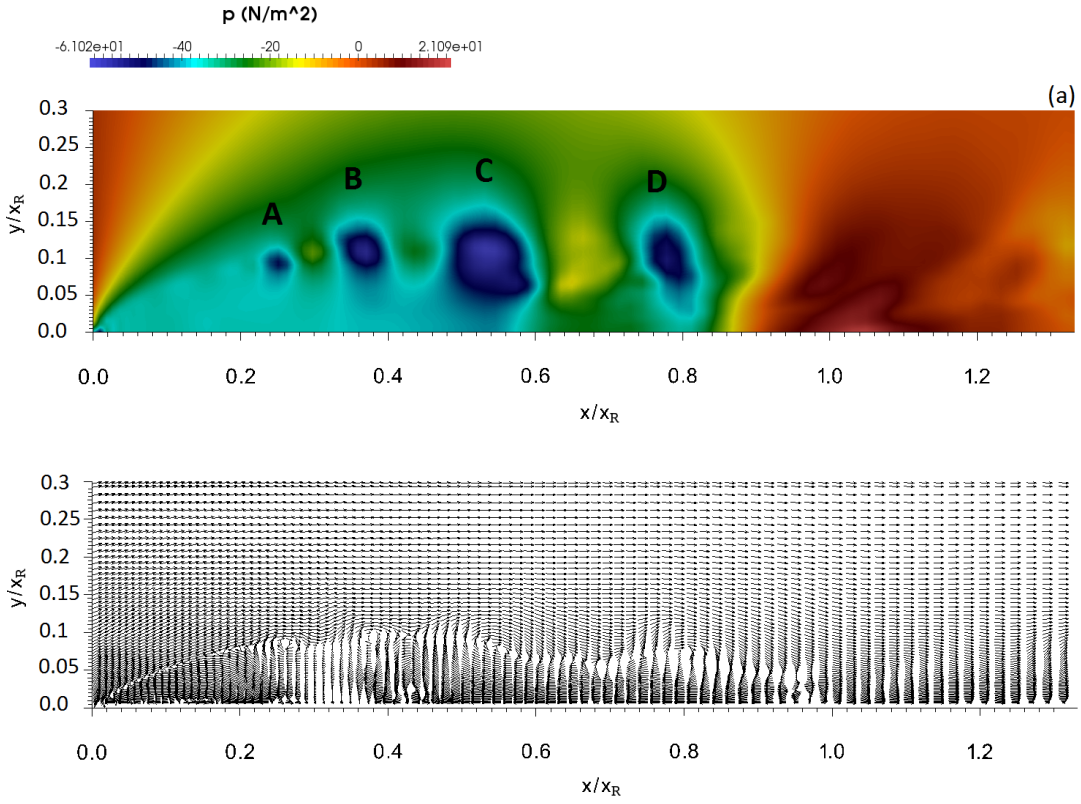

Caption for these figures is on the following page

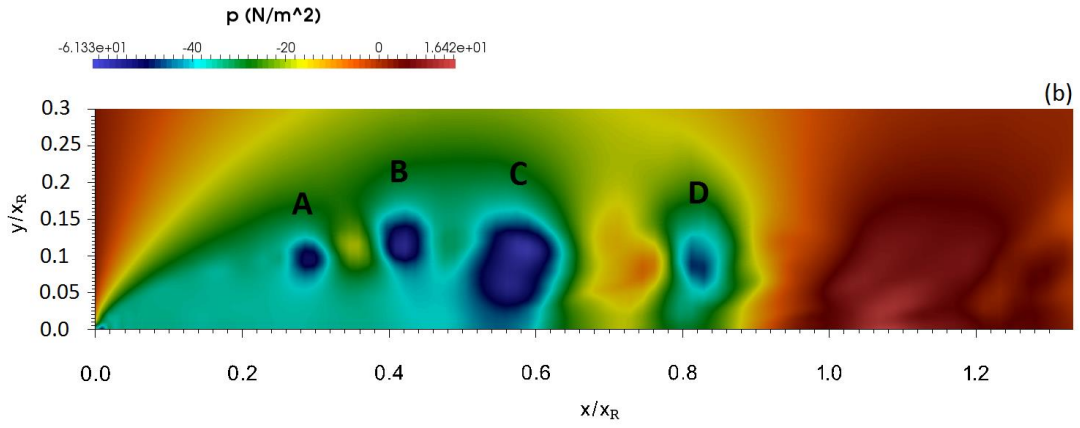
p (N/m^2)
-6.133e+01
-40
-20
0
1.642e+01
(b)
A
B
C
D
y/x_R
x/x_R
0.0
0.05
0.1
0.15
0.2
0.25
0.3
0.0
0.2
0.4
0.6
0.8
1.0
1.2

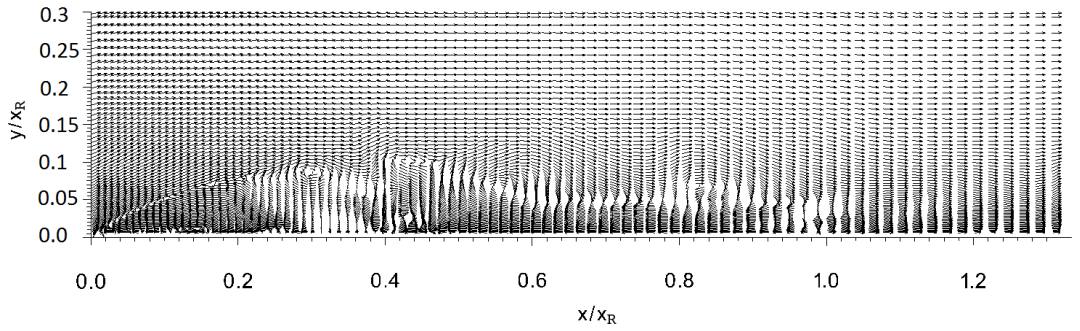
y/x_R
x/x_R
0.0
0.05
0.1
0.15
0.2
0.25
0.3
0.0
0.2
0.4
0.6
0.8
1.0
1.2

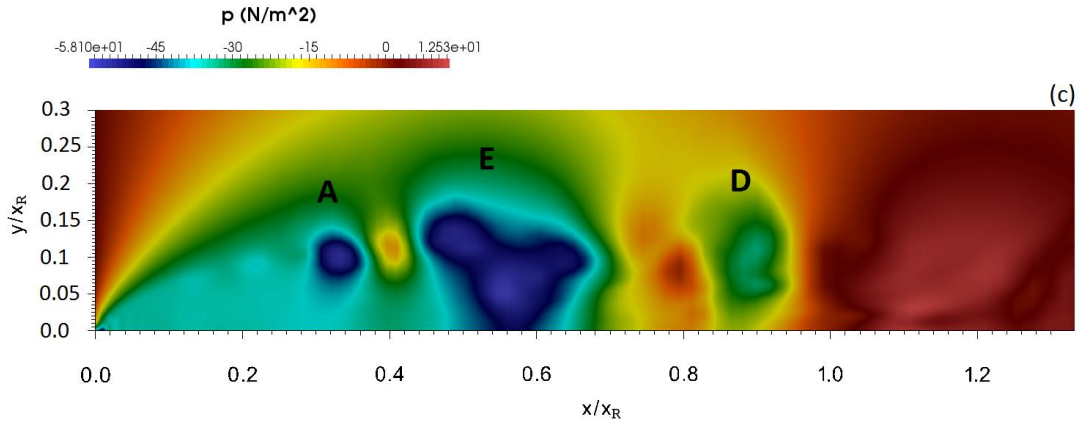
p (N/m^2)
-5.810e+01
-45
-30
-15
0
1.253e+01
(c)
A
E
D
y/x_R
x/x_R
0.0
0.05
0.1
0.15
0.2
0.25
0.3
0.0
0.2
0.4
0.6
0.8
1.0
1.2

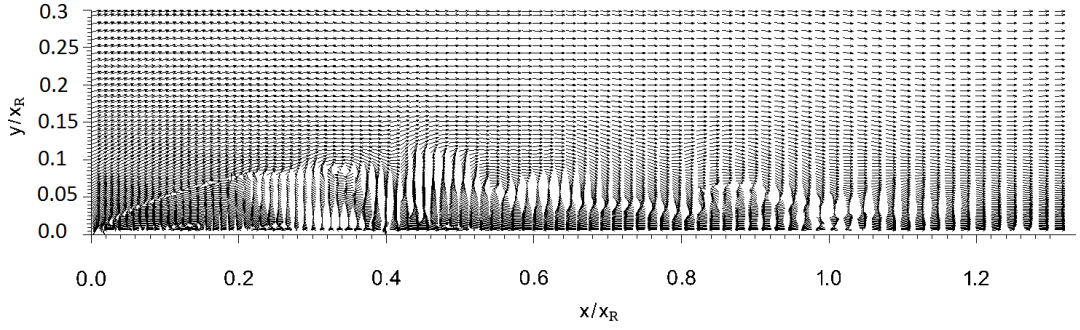
y/x_R
x/x_R
0.0
0.05
0.1
0.15
0.2
0.25
0.3
0.0
0.2
0.4
0.6
0.8
1.0
1.2

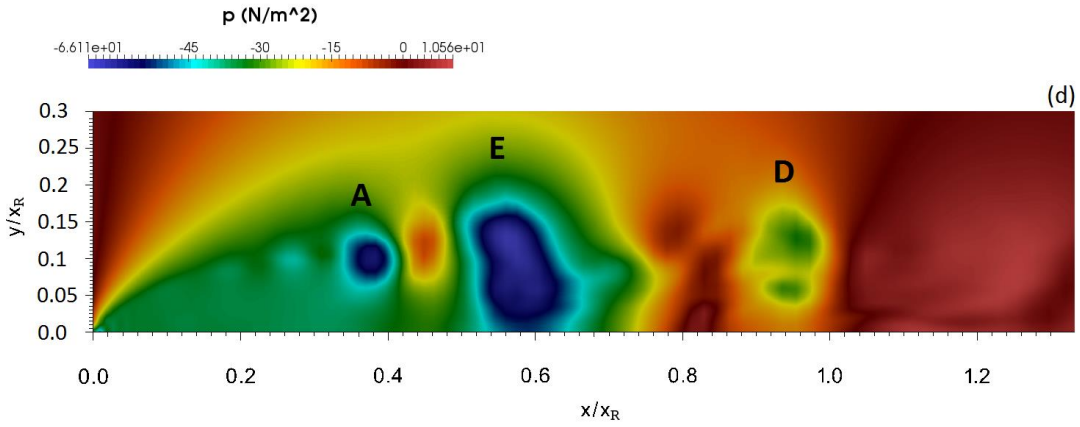
p (N/m^2)
-6.611e+01
-45
-30
-15
0
1.056e+01
(d)
A
E
D
y/x_R
x/x_R

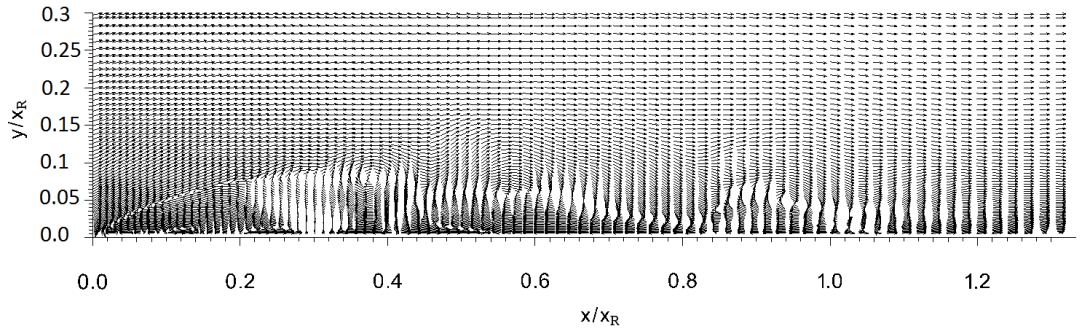
y/x_R
x/x_R

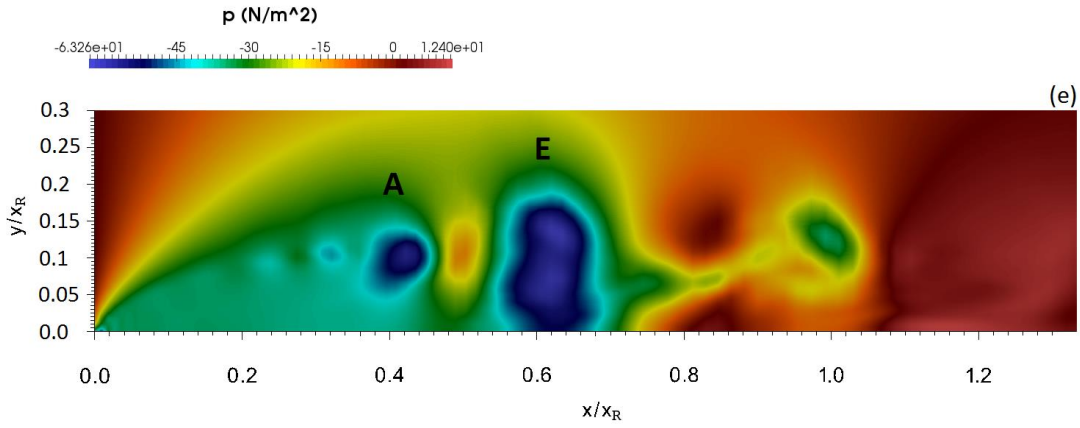
p (N/m^2)
-6.326e+01
-45
-30
-15
0
1.240e+01
(e)
A
E
y/x_R
x/x_R

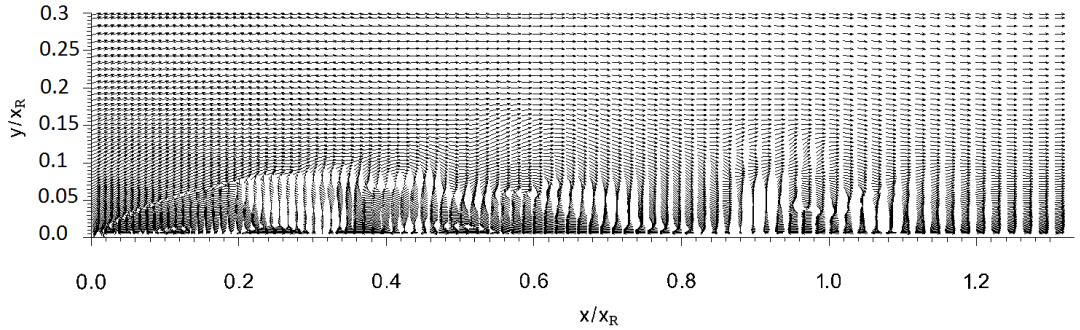
y/x_R
x/x_R

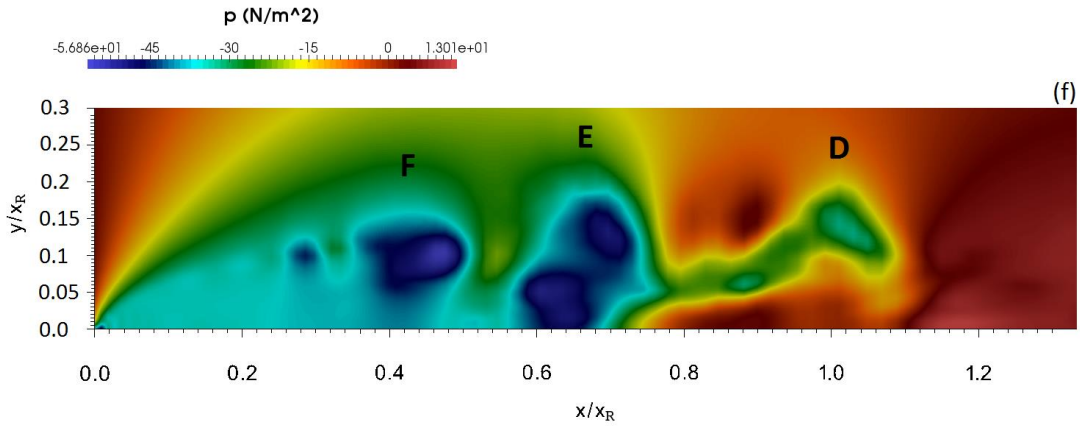
p (N/m^2)
-5.686e+01 -45 -30 -15 0 1.301e+01
(f)
F
E
D
y/x_R
x/x_R
0.0 0.05 0.1 0.15 0.2 0.25 0.3
0.0 0.2 0.4 0.6 0.8 1.0 1.2

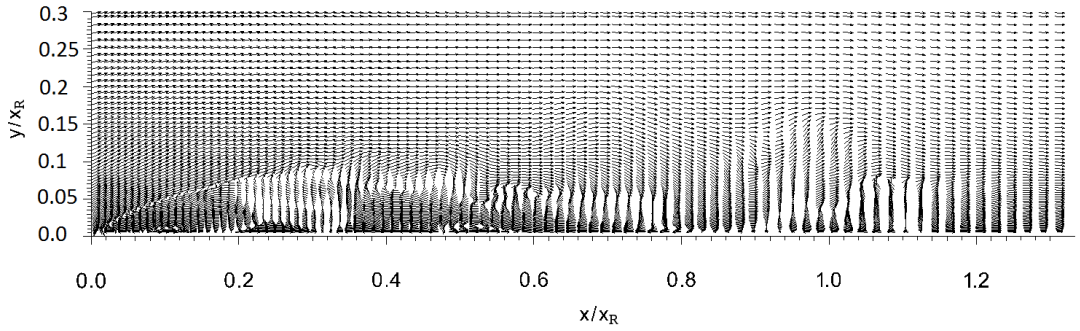
y/x_R
x/x_R
0.0 0.05 0.1 0.15 0.2 0.25 0.3
0.0 0.2 0.4 0.6 0.8 1.0 1.2

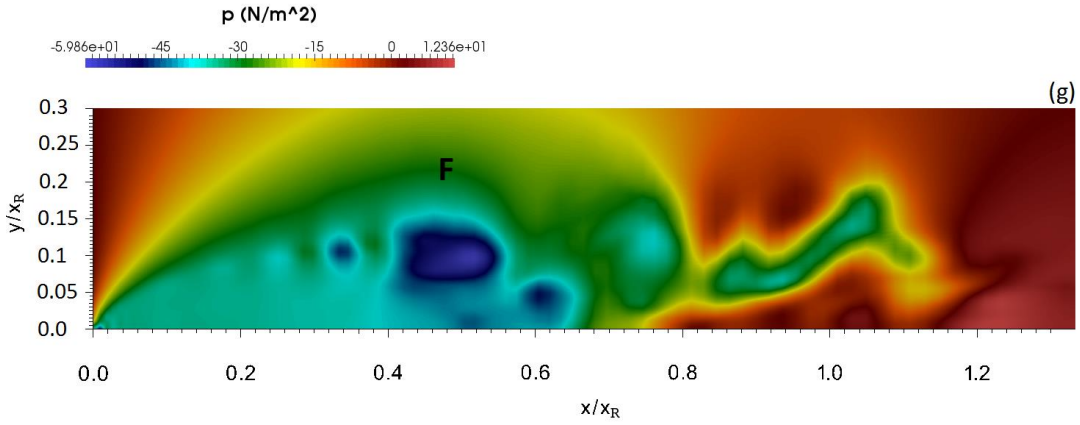
p (N/m^2)
-5.986e+01 -45 -30 -15 0 1.236e+01
(g)
F
y/x_R
x/x_R
0.0 0.05 0.1 0.15 0.2 0.25 0.3
0.0 0.2 0.4 0.6 0.8 1.0 1.2

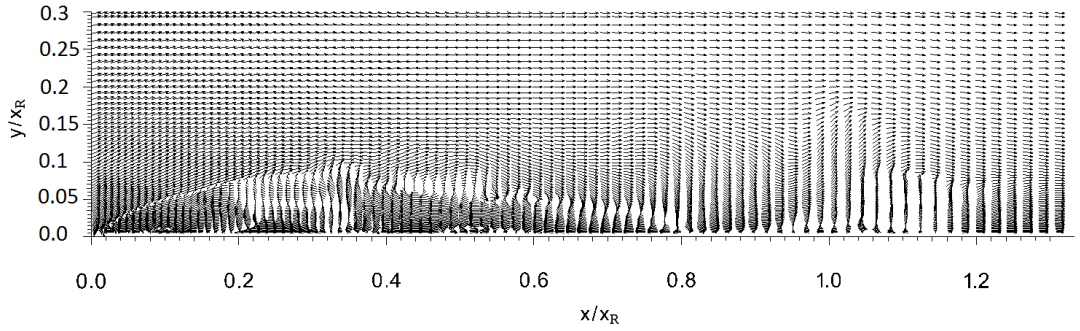
y/x_R
x/x_R
0.0 0.05 0.1 0.15 0.2 0.25 0.3
0.0 0.2 0.4 0.6 0.8 1.0 1.2

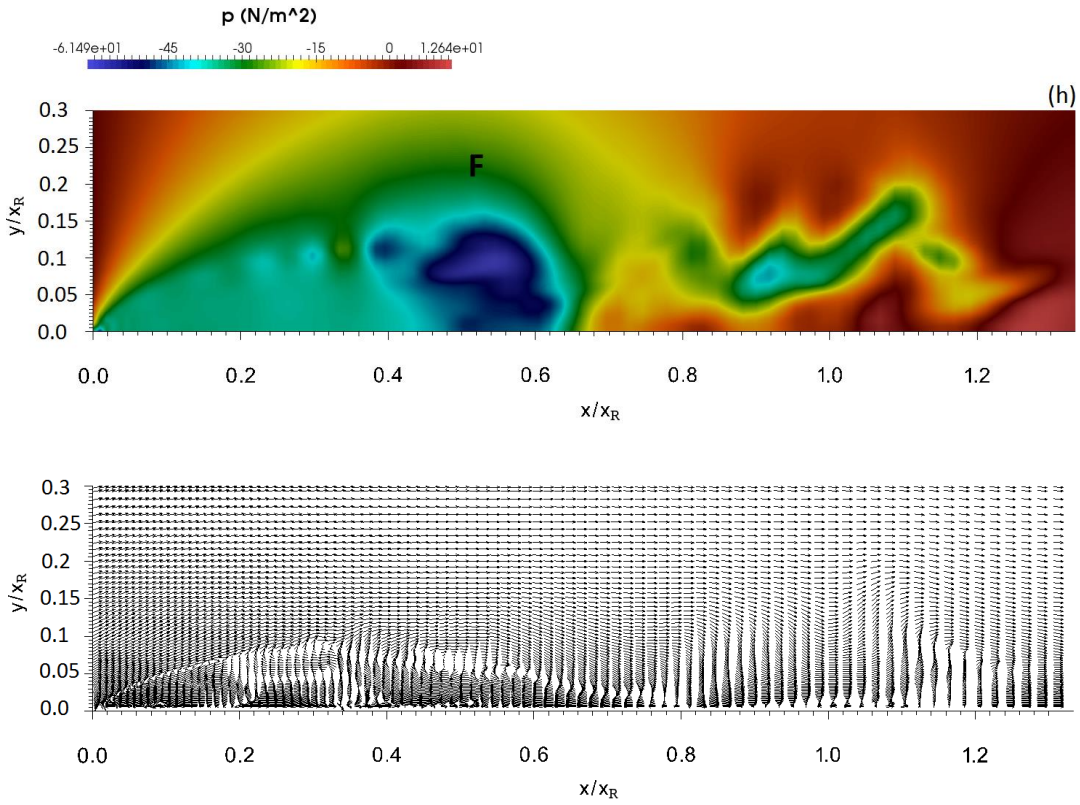

Fig. 7-1. Instantaneous pressure contours and the corresponding instantaneous velocity vectors for the flat plate displaying vortex formation and shedding at sequential times (every 250 time steps) with NFST

In transitional separated-reattached flow for 3D_case1, it can be seen that the Kelvin-Helmholtz rolls are formed at about x/x_R = 4.5 as shown for structure *A* in Fig. 7-2a. In this figure, the structure previously named *B* becomes larger as it moves downstream. In a further location, at x/x_R = 6, structure *B* develops a distortion to its shape. This development takes a certain distance and ends around the mean reattachment line as shown in Figs 7-2b, 7-2c, and 7-2d. Further downstream, structure *B* decays, where it is observed with some difficulty as shown in Figs. 7-2e and 7-2f.

A similar situation to the above scenario can be seen for structure *A* as shown in Figs 7-2d, 7-2e, and 7-2f. Generally, this scenario repeats itself with every newly formed structure as shown in Fig. 7-2.

It can be seen that there is no vortex merging stage for this geometry, where it is believed that this stage is unlikely to happen in 3D_case1. This is an interesting difference in the

transition stages presented in the current study between 3D_case1 and the flat plate, where in the latter geometry the vortex merging stage can be clearly seen, as per Fig. 7-1.

Fig. 7-3 shows stations of coherent structure motion in 3D_case2 from their shedding from the separated layer to their decay in the reattached turbulent boundary layer. It is clearly seen that there is no appearance of the structures merging along the separation bubble for this geometry, which is similar to that observed for 3D_case1. Hence, it can be concluded that the vortex merging process, as one of coherent structure development stages, may not occur in a transitional separated-reattached flow on a three-dimensional geometry.

Coherent structure development for 3D_case2 that is exhibited in Fig. 7-3 shows the formation of Kelvin-Helmholtz rolls at about x/x_R = 3.5 as shown in Fig. 7-3a. In this figure, it can be seen that there are three structures: *A*, which is at the early stage of the transition; *B*, which is larger than *A* and located at about x/x_R = 5.5; and *C*, which is close to the mean reattachment line. Structure *A* travels downstream and becomes larger while structure *B* seems to be smaller due to its breakdown into smaller structures as shown in Fig. 7-3b. In this figure, there is a reduction in size of structure *C* that is interpreted as a breakdown in this structure.

Structure *A* still grows when moving downstream as shown in Figs. 7-3c, d, and e. In Fig. 7-3f, there is another structure that forms in the first half of the separation bubble while structure *A* passes to the second half of the separation bubble. At the same time, structure *B* sheds to the reattached turbulent boundary layer as shown in Fig. 7-3f. The new structure then grows and moves downstream and structure *A* seems to be smaller compared to its nominal size in Fig. 7-3f, this is shown in Fig. 7-3g. Finally, the new structure becomes larger and structure *A* disappears as shown in Fig. 7-3h.

For all geometries, it can be clearly observed that there is a periodic process of formation, movement, shedding and disintegration of the structures as shown in Fig. 7-1 for the flat plate, Fig. 7-2 for 3D_case1 and Fig. 7-3 for 3D_case2.

The fact that there are no vortices merging in both 3D_case1 and 3D_case2 is most likely due to the twisting nature of the Kelvin-Helmholtz structure in the first half of the separation bubble. This may lead to early breakdown of this rectangular ring vortex into

four Kelvin-Helmholtz structures on each surface. This event may reduce the ability of Kelvin-Helmholtz structures to merge with each other. Thus, it can be concluded that the transition stages in the three-dimensional geometries are shorter in the space and time than the transition stages for the flat plate. The transition to turbulence in three-dimensional geometries takes place quickly to form a smaller separation bubble compared with the separation bubble that is constructed on the flat plate.

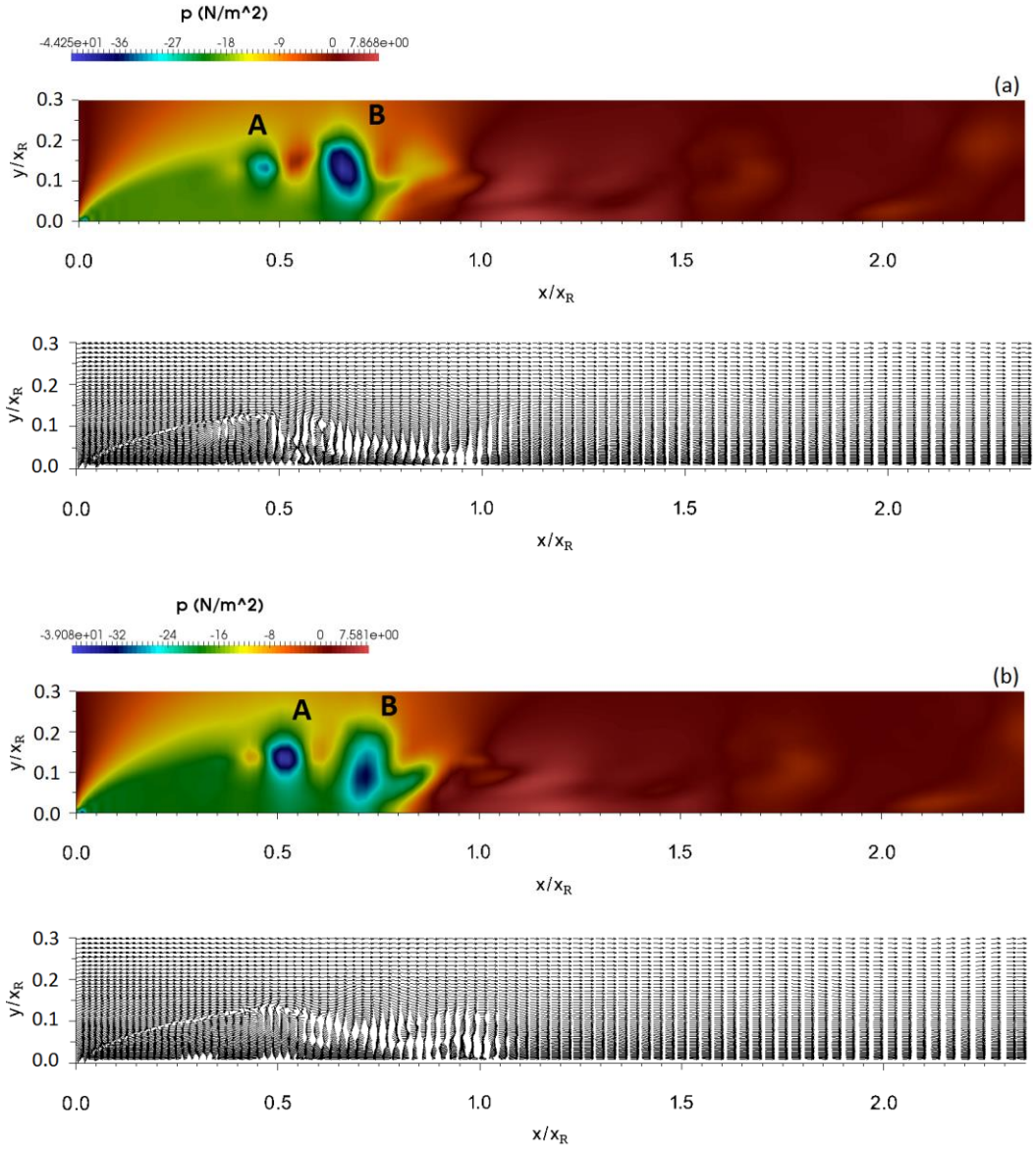

Caption for these figures is on the following page

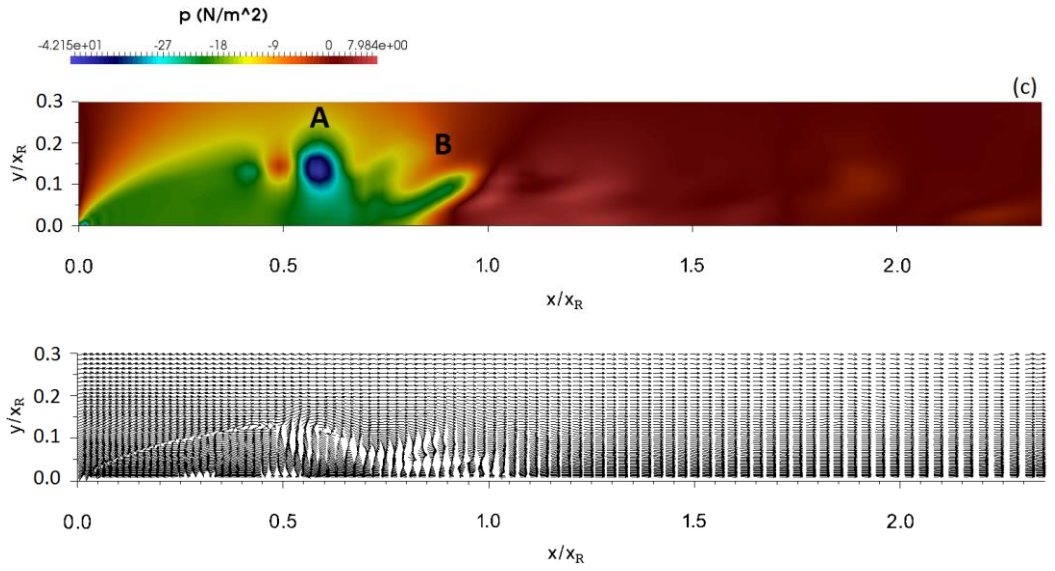
p (N/m^2)
-4.215e+01 -27 -18 -9 0 7.984e+00
(c)
A
B
y/x_R
x/x_R
0.0
0.1
0.2
0.3
0.5
1.0
1.5
2.0

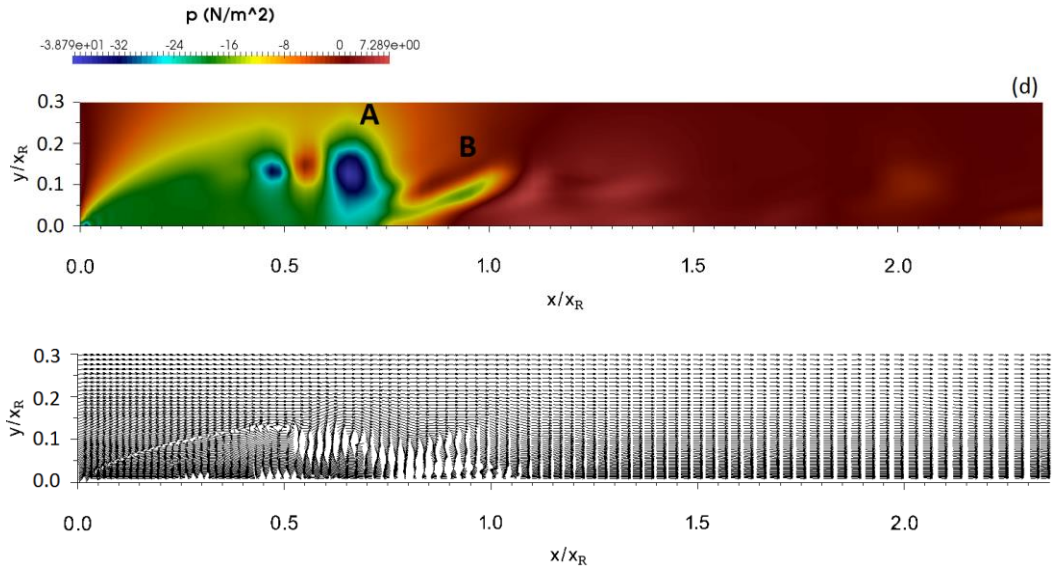
p (N/m^2)
-3.879e+01 -32 -24 -16 -8 0 7.289e+00
(d)
A
B
y/x_R
x/x_R
0.0
0.1
0.2
0.3
0.5
1.0
1.5
2.0

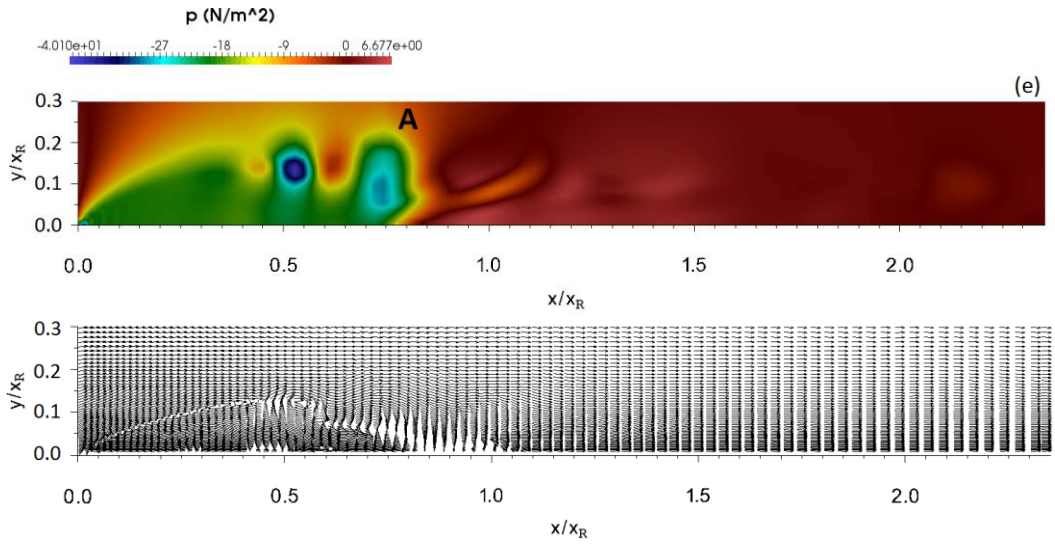
p (N/m^2)
-4.010e+01 -27 -18 -9 0 6.677e+00
(e)
A
y/x_R
x/x_R
0.0
0.1
0.2
0.3
0.5
1.0
1.5
2.0

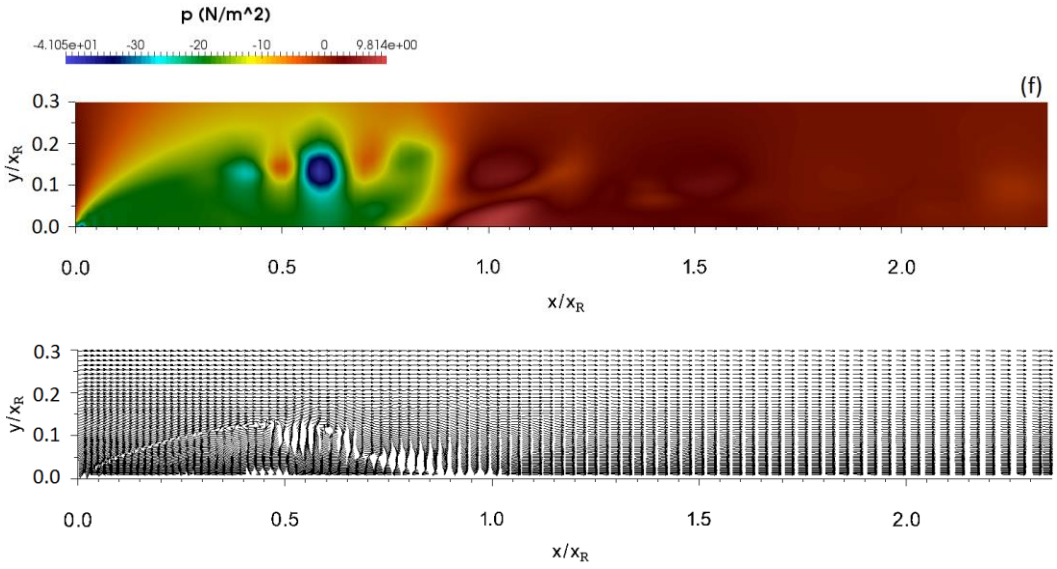
p (N/m^2)
-4.105e+01 -30 -20 -10 0 9.814e+00
(f)
y/x_R
x/x_R
0.0 0.1 0.2 0.3
0.0 0.5 1.0 1.5 2.0

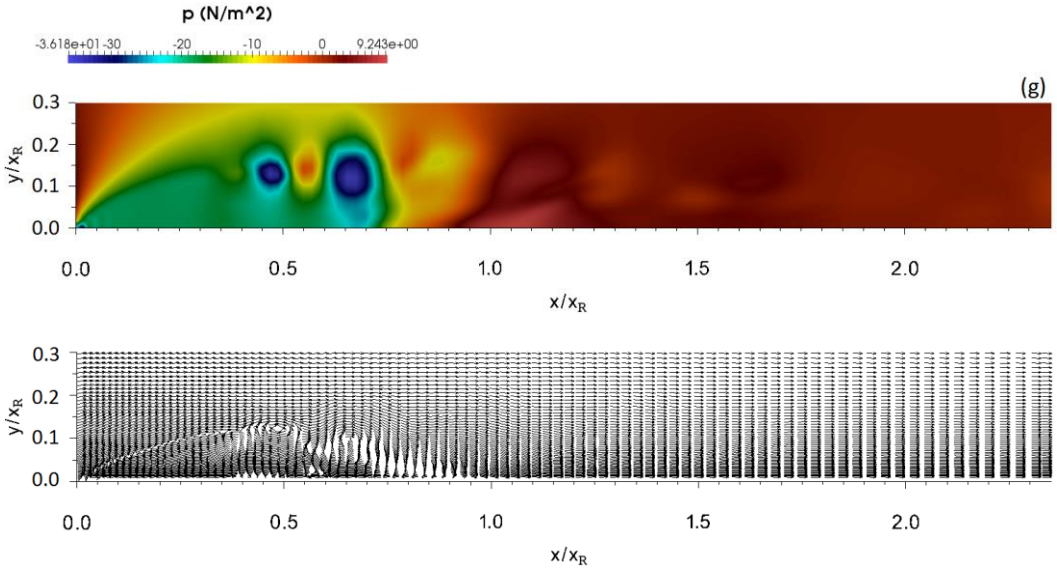
p (N/m^2)
-3.618e+01 -30 -20 -10 0 9.243e+00
(g)
y/x_R
x/x_R
0.0 0.1 0.2 0.3
0.0 0.5 1.0 1.5 2.0

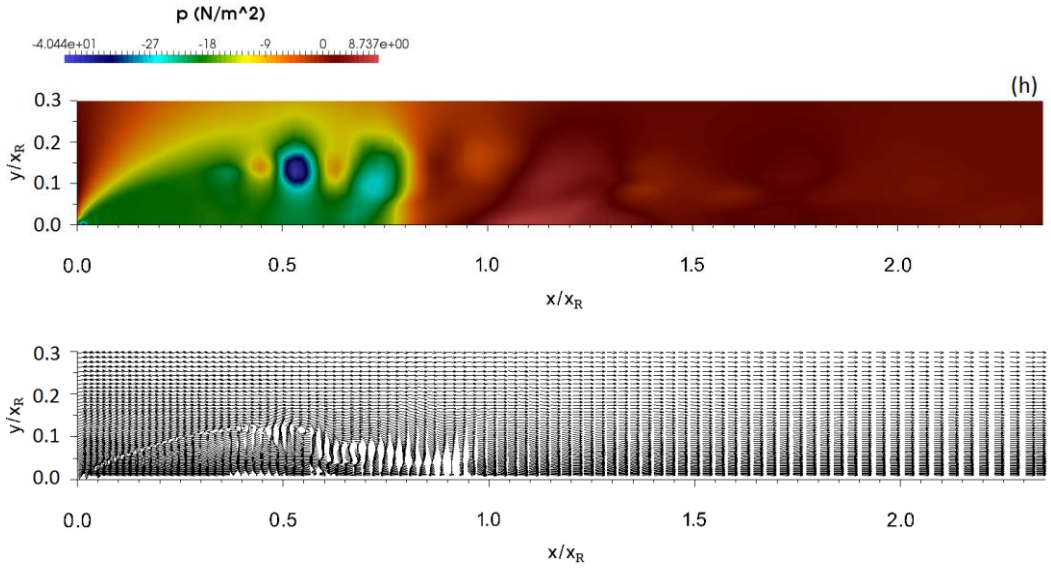

Fig. 7-2. Instantaneous pressure contours and the corresponding instantaneous velocity vectors for 3D_case1 displaying vortex formation and shedding at sequential times (every 250 time steps) with NFST

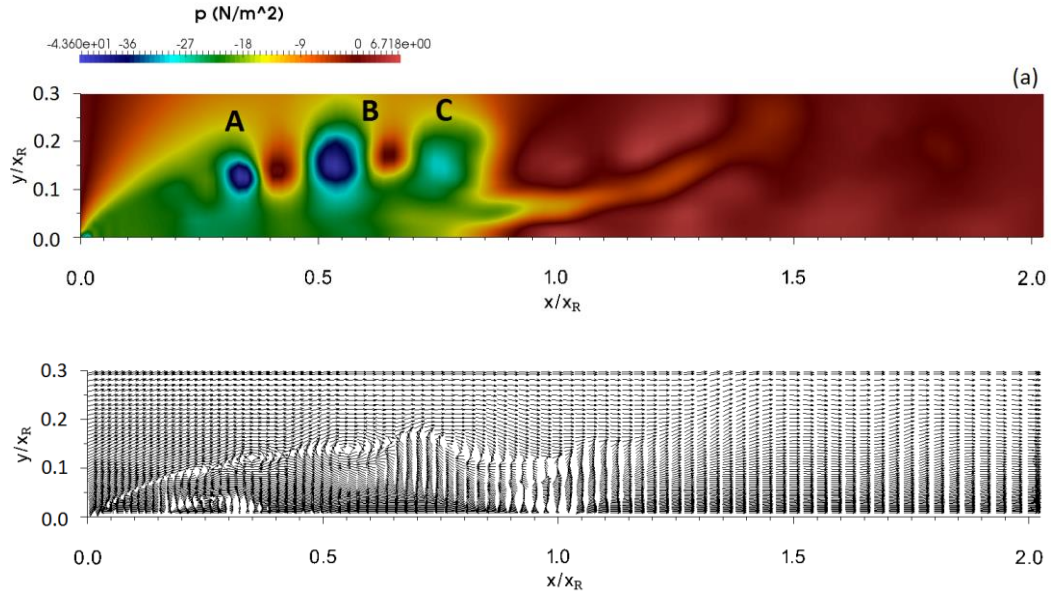

Caption for these figures is on the following page

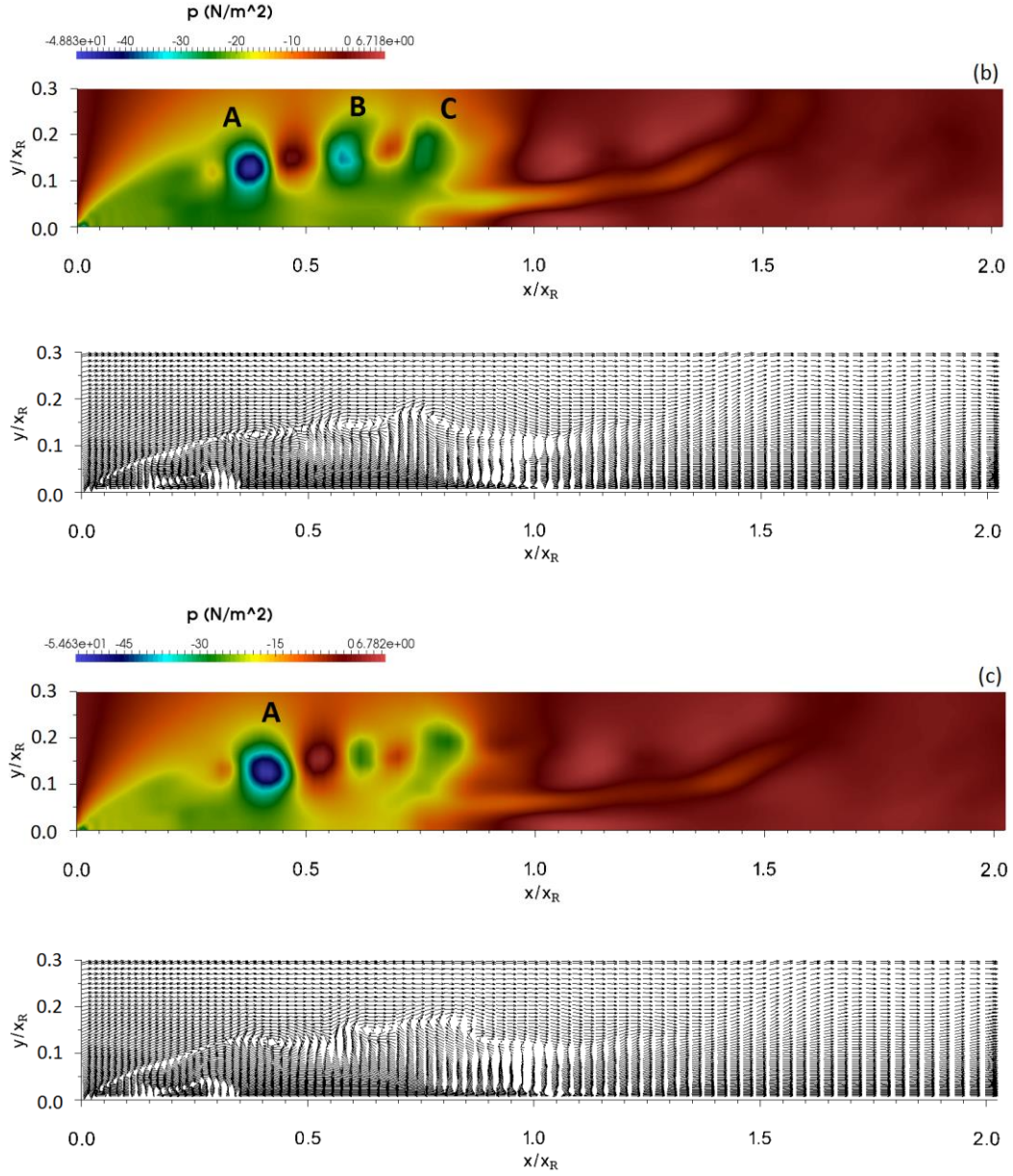
p (N/m^2)
-4.883e+01 -40 -30 -20 -10 0 6.718e+00
(b)
A
B
C
y/x_R
x/x_R
0.0
0.1
0.2
0.3
0.5
1.0
1.5
2.0
p (N/m^2)
-5.463e+01 -45 -30 -15 0 6.782e+00
(c)
A

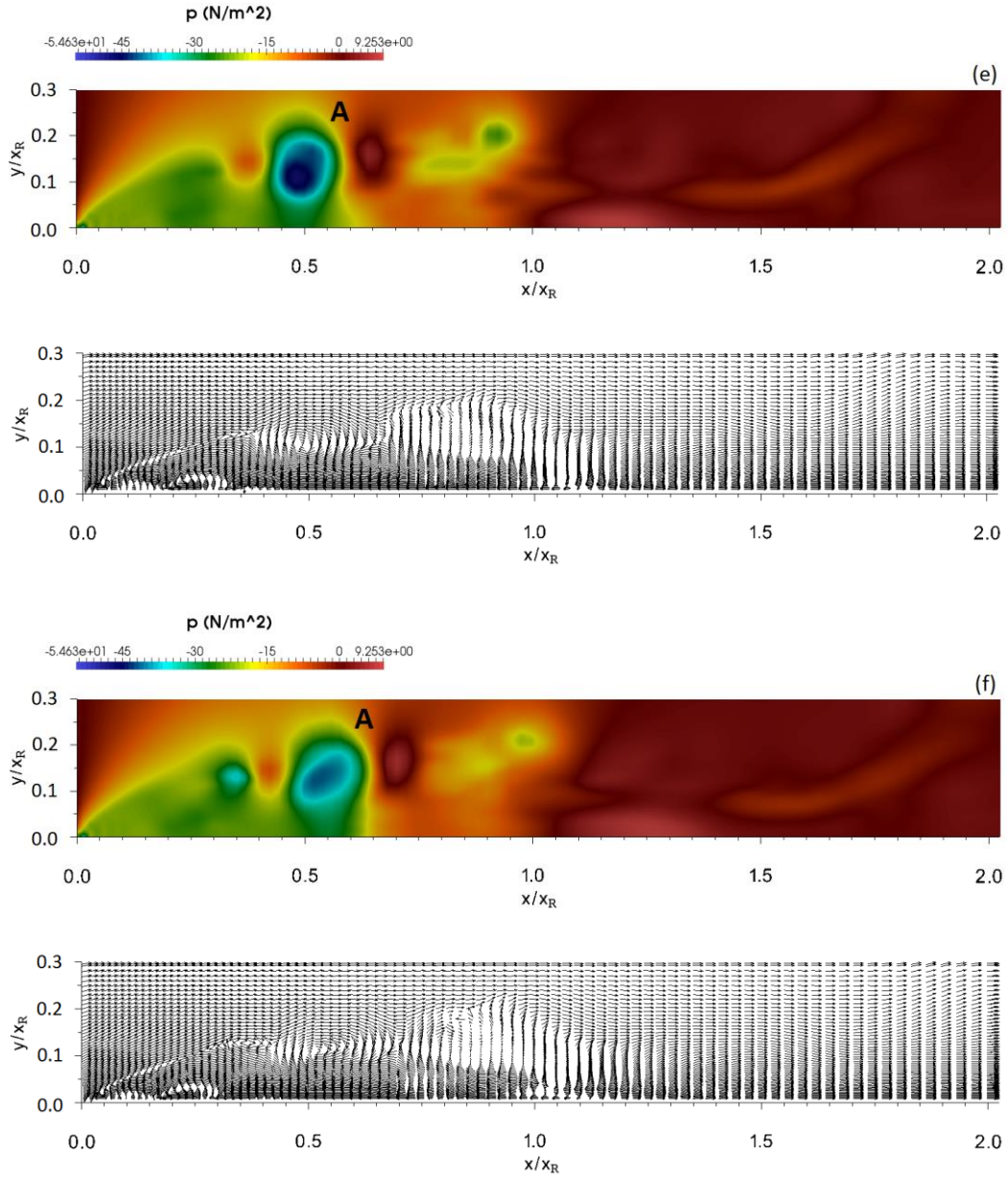
p (N/m^2)
-5.463e+01 -45 -30 -15 0 9.253e+00
(e)
A
y/x_R
x/x_R
0.0
0.1
0.2
0.3
0.5
1.0
1.5
2.0
p (N/m^2)
-5.463e+01 -45 -30 -15 0 9.253e+00
(f)
A
y/x_R
x/x_R

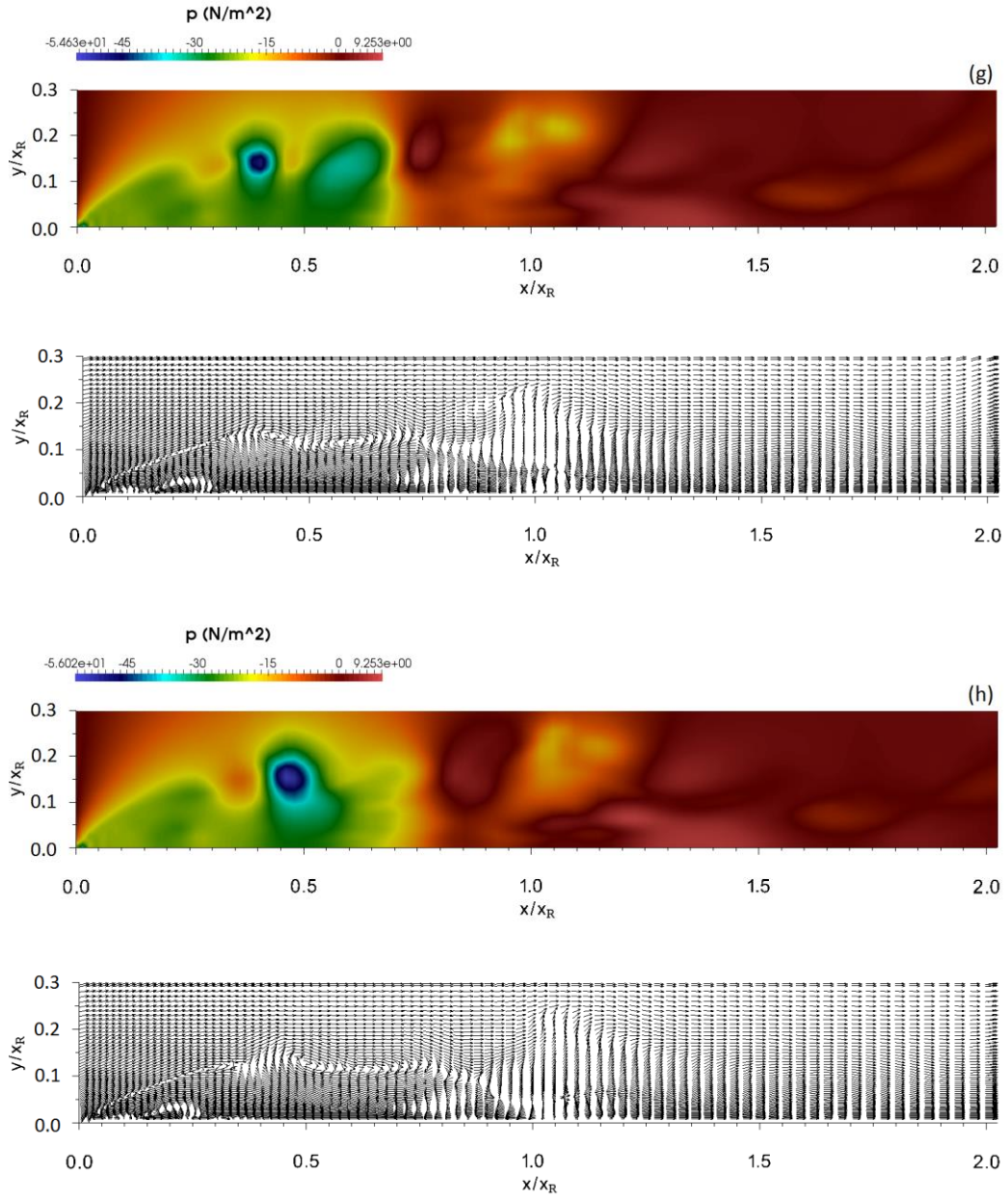

Fig. 7-3. Instantaneous pressure contours and the corresponding instantaneous velocity vectors for 3D_case2 displaying vortex formation and shedding at sequential times (every 250 time steps) with NFST

7.2 Three-dimensional flow visualization for NFST

For a more accurate realization of the formation of coherent structures and their subsequent development, a three-dimensional flow visualization of coherent structures is employed here. Basically, there are three flow visualization techniques described in the literature: low-pressure isosurface, vorticity field isosurface, and Q-criterion isosurface.

Robinson (1991a) employed low-pressure isosurfaces to investigate the development of coherent structures in a turbulent boundary layer. Streamwise vorticity isosurfaces were used by Comte et al. (1998) to reveal coherent structures in a turbulent mixing layer flow. They compared these schemes and showed that the low-pressure isosurface is more accurate than the vorticity field isosurface in illustrating coherent structures in the flow in the a presence of a solid surface due to a high mean shear created by the no-slip condition compared to the typical vortical intensity of the vortices located close to the solid surface.

However, Abdalla and Yang (2004b) speculated that employing a low-pressure isosurface requires that the threshold which is strongly dependent on the pressure surrounding the vortical structure needs to be adjusted. They reported that in the regions with a high concentration of vortices, this technique may fail to capture the details of the vortical organization. Abdalla and Yang (2004b) showed that a positive Q-criterion isosurface isolates areas where the strength of the rotation exceeds the strain, leading to coherent structures that can be identified as vortex envelops.

For the present study, the low pressure, vorticity field and Q-criterion isosurfaces are adopted as the flow visualization schemes to examine coherent structures and their development.

7.2.1 Low pressure isosurface

For the flat plate, four low fluctuating pressure isosurfaces are taken at sequential times (every 250 time steps), which are shown in Fig. 7-4. The flow topology shows the shedding of two-dimensional Kelvin-Helmholtz rolls downstream of the plate's leading edge. These rolls grow in size when they move downstream as shown in Fig. 7-4a. It is clear that around $x/x_R = 0.6$, the Kelvin–Helmholtz structures are subjected to a 'waviness' motion along the spanwise direction, these keep their two-dimensionality nature due to their axis remaining perpendicular to the flow direction as shown in Fig. 7-4b. It can be seen that the growth of Kelvin–Helmholtz structures is due to the merging between two rolls as shown in Fig. 7-4c, where there are two Kelvin-Helmholtz structures catch up with each other and merge to form one large structure. This large vortex keeps its coherency and two-dimensional nature where its axis is still perpendicular to the flow

direction. It is worth pointing out that the vortex merging process is captured clearly in the current study as shown in Fig. 7-4c. It is possible that the vortex merging process takes place over a very short time period, and 250 time steps might not be sufficient to present many vortex merging processes.

Further downstream, the new two-dimensional structure breaks down into small three-dimensional hairpin structures around the mean reattachment line. These streamwise structures move a certain distance within the reattached turbulent boundary layer before their own breakdown into smaller turbulent structures.

For transitional separated-reattached flow on a blunt flat plate, Abdalla and Yang (2004b) reported the stages of coherent structure development. They showed that Kelvin–Helmholtz rolls that shed downstream of the plate leading edge subsequently pair with each other and grow in size as they move downstream. The Kelvin–Helmholtz structures are subjected to what can loosely be described as sinusoidal undulation (waviness) along the spanwise direction, maintaining their coherency and two-dimensional nature where their axis remains perpendicular to the flow direction. Further downstream, Kelvin–Helmholtz structures become more distorted leading to the appearance of a well-organized array of hairpin streamwise vortices originating from the initially shed vortical roll.

It was concluded in Abdalla and Yang (2004b) that these streamwise three-dimensional structures develop and evolve as a topological consequence of the spanwise oscillation of the Kelvin–Helmholtz rolls, where these rolls transform into lambda-shaped (hairpin) vortices. The heads of these three-dimensional vortices lie on the original Kelvin–Helmholtz rolls while the legs connect the following rolls. These streamwise vortices become part of the core of the spanwise vortices, as resulting from the pairing of two Kelvin–Helmholtz rolls.

In addition to the lambda-shaped vortices, Abdalla and Yang (2004b) observed the formation of streamwise rib vortices as a sequence of evolving Kelvin–Helmholtz rolls. It was assumed that these ribs actually originated from the lambda-shaped vortices which were subjected to greater amounts of stretching along the axial direction leading to the disintegration of their legs.

Abdalla and Yang (2004b) concluded that the formation of the new structure, formed due to the pairing of two Kelvin-Helmholtz rolls, was due to a helical-pairing instability which is a secondary instability mechanism of the transition. This instability mechanism is believed to be responsible of the formation of the large structure in the current study due to the similarity between the current study and that of Abdalla and Yang (2004b) about the new large structure formation.

Despite the similarity between coherent structure development in the current study and Abdalla and Yang's (2004b) study involving the waviness action and formation of large structures from the merging of two Kelvin-Helmholtz rolls and their transformation into hairpin structures, there is a difference in the later stages of the coherent structure development between these two studies. In the present study, Kelvin–Helmholtz rolls break down directly into hairpin structures, while Yang and Abdalla (2008) showed that the three-dimensional structures were the result of a topological evolution of the large two-dimensional structures. Abdalla and Yang (2004b) reported that hairpin structures were connected between two Kelvin–Helmholtz rolls, where their heads lay on the original Kelvin-Helmholtz roll while their legs connected the following roll. In addition, it should be noted that rib-like structures are not formed here, though they were clearly apparent in Abdalla and Yang (2004b).

Rapid disintegration of the large structure, which is observed in the current study, was also reported for numerous transitional separated-reattached flows over different geometries. For a surface-mounted obstacle and forward-facing step, Abdalla et al. (2009) observed a rapid breakdown of the large structure into hairpin structures, but, rib-like structures were not observed in their study.

Ba et al. (2014) observed the rapid formation of hairpin vortices, which evolved from transverse Kelvin-Helmholtz structures shedding from the free shear layer over a two-dimensional bump. It was shown in Ba et al. (2014) that during the early stages of the transition, which constitute the location of the initial stage of coherent structure formation, transverse vortices with evident two-dimensionality were formed. These vortices lines extend directly along the spanwise direction. Due to the increased disturbance downstream, these vortices lose their two-dimensional nature and rapidly transform into hairpin structures.

McAuliffe and Yaras (2010) employed the low pressure isosurface to present the development of coherent structures in transitional separated-reattached flow that were induced by an adverse pressure gradient on a flat plate. They demonstrated that Kelvin-Helmholtz rolls rapidly transform into hairpin-like structures in the reattachment region. For a separation bubble that formed on a flat plate, Spalart and Strelets (2000) observed that Kelvin-Helmholtz vortices instantly become three-dimensional structures. They reported that there was a sudden transition and a rapid breakdown to turbulence.

In the later stages of the transition in a separation bubble formed on a NACA 0018 aerofoil, Kurelek et al. (2016) and Kirk and Yarusevych (2017) reported that spanwise coherent structures underwent significant and rapid breakdown into smaller-scale structures.

At relatively low Reynolds numbers of separated-reattached flow over a blunt flat plate, Sasaki and Kiya (1991) carried out experimental work to visualise coherent structures. They reported that new structures are formed from the amalgamation of two or three spanwise rolled-up vortices that were shed from the separated shear layer. Downstream of the mean reattachment line, hairpin structures were directly formed without any stretching of the spanwise rolls in the streamwise direction.

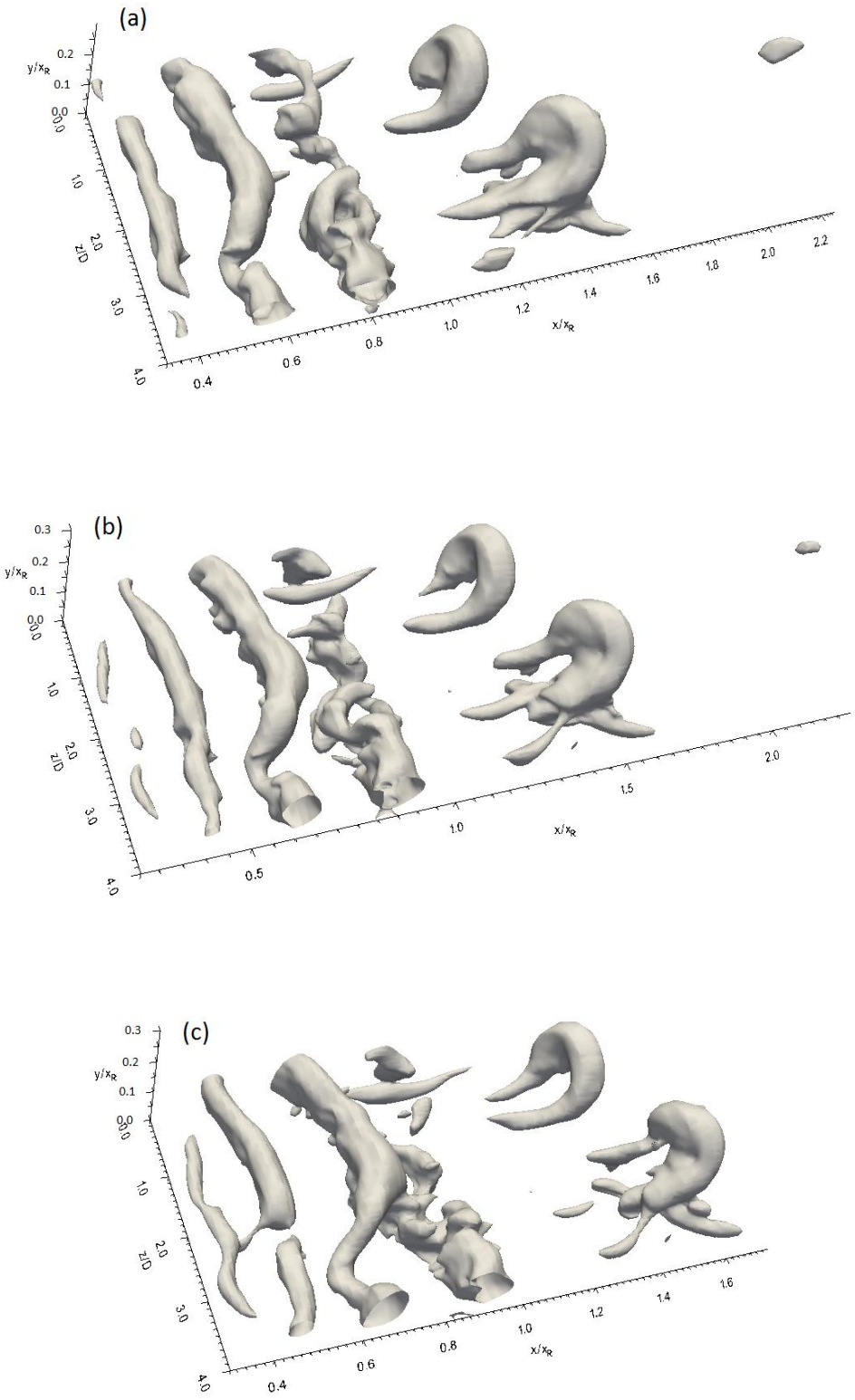

Caption for these figures is on the following page

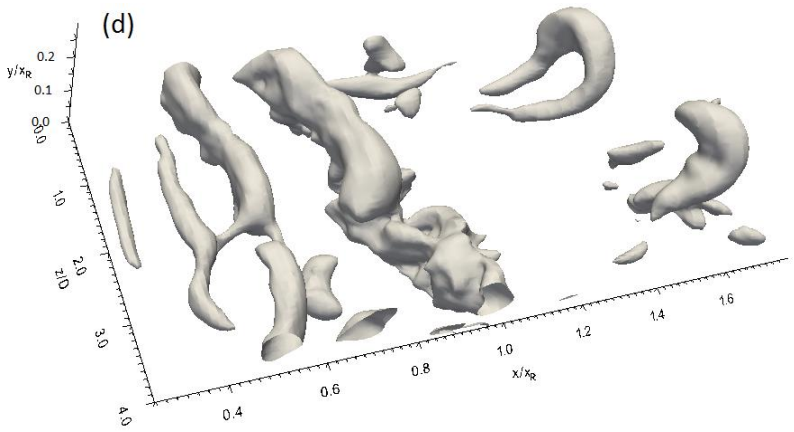

Fig. 7-4. Low pressure isosurface at sequential times (every 250 time steps) for the flat plate with NFST

Low fluctuating pressure isosurfaces for 3D_case1 taken every 250 time steps are shown in Fig. 7-5. It can be seen that Kelvin-Helmholtz roll formation occurs at about $x/x_R = 4.5$. These structures move and become larger when convecting downstream. The large Kelvin-Helmholtz structure develops topologically to become a hairpin structure around the mean reattachment line. Further downstream, it is apparent that the hairpin structures that are shed to the turbulent reattached flow are disintegrating into smaller structures.

As mentioned in the *x-y* plane of pressure contours that are shown in Fig. 7-2, there is no merging of the vortices in this geometrical shape. The low pressure isosurface for 3D_case1 that is shown in Fig. 7-5 confirms that, as can be clearly seen, there are no vortex-merging processes as one of the transition events in this geometry, where the formation of the hairpin structures is due to a topological evolution of the Kelvin-Helmholtz rolls.

It is believed that the difference in the stages of coherent structure development within the transitional separated flow is a consequence of the nature of the different geometrical shapes, i.e., with the property of two-dimensionality, there is an additional stage that is represented by the merging of vortices which is completely absent over the three-dimensional geometry. So, it can be concluded that due to this additional stage, the spatial and temporal evolution of the transition to turbulence is longer for the flat plate than that for 3D_case1. For this reason, the separation bubble that formed in the flat plate is longer than that formed in 3D_case1 by about 2.6*D* as shown in Chapter 4. In Chapter 5, it is

shown that the lengths of the laminar part of the separation bubble in the flat plate and 3D_case1 are very much the same. So, the difference in the length of the separation bubble between the flat plate and 3D_case1 arises from the transition start location onward, where this part of the separation bubble involves the formation and development of the coherent structures, of which the vortex pairing process is just one, for the flat plate.

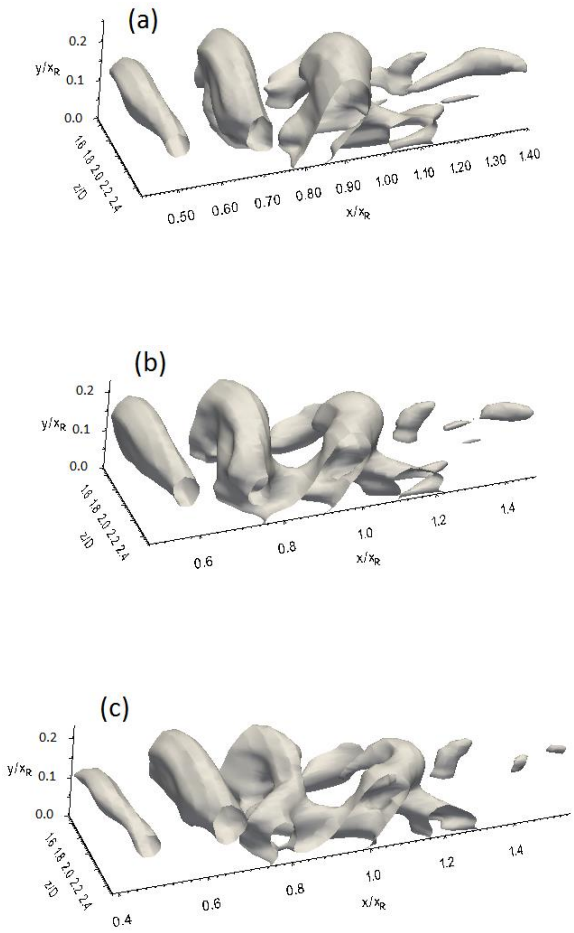

Caption for these figures is on the following page

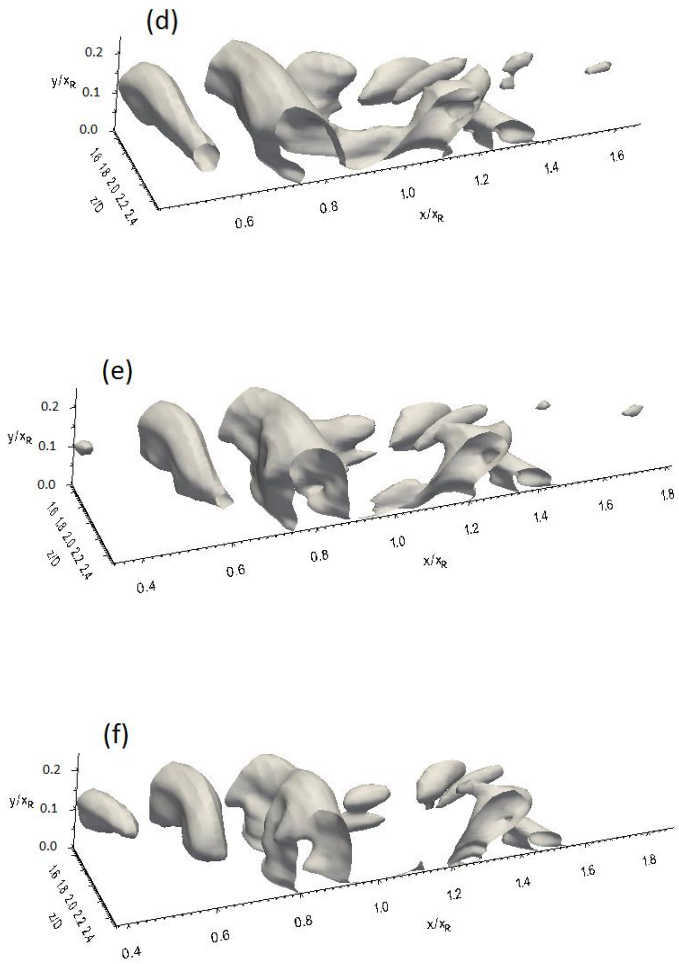

Fig. 7-5. Low pressure isosurface at sequential times (every 250 time steps) for 3D_case1 with NFST

For 3D_case2, the sequential low fluctuating pressure isosurfaces taken every 250 time steps are shown in Fig. 7-6. Fig. 7-6a shows four structures in different situations. The second and third structures that are located around x/x_R = 1 and 0.7, respectively, seem to be within a breakdown state into hairpin structures, while the fourth Kelvin-Helmholtz roll maintains its two-dimensional nature. Moreover, the first hairpin structure that is shed downstream of the mean reattachment line maintains its shape up to x/x_R = 1.2.

The following snapshot of a low fluctuating pressure isosurface that is shown in Fig. 7-6b illustrates that the Kelvin-Helmholtz roll, which is close to the separation line, becomes larger when convecting downstream, other structures in the similar circumstances can be observed in the previous time snapshot. Fig. 7-6c presents the shedding of one Kelvin-Helmholtz roll while the previous one continues to enlarge in

size. Many hairpin structures are formed by the breakdown of the Kelvin-Helmholtz roll in the region between x/x_R = 1.2 and 1.4, which can be seen in Figs. 7-6e and 7-6f. The hairpin structures that are presented at previous times disintegrate to smaller structures around x/x_R = 1.5 as shown in Fig. 7-6f. In this figure, there is another disintegration of a Kelvin-Helmholtz roll into smaller structures at x/x_R = 0.7.

As shown in Fig. 7-6, there is no vortex pairing process captured in the transition flow of 3D_case2. In this geometry, coherent structure development involves the shedding of Kelvin-Helmholtz rolls from the separated layer at about x/x_R = 0.4; the size of these structures increases when they are moving downstream; distortion of these rolls takes place downstream of x/x_R = 0.6 where, around the mean reattachment line, there is a breakdown of these rolls into hairpin structures; these then move downstream and disintegrate into smaller structures within the turbulent reattached flow.

It is believed that the formation of a smaller separation bubble in 3D_case2 than that in the flat plate is due to the transition to turbulence in the flat plate being longer due to a presence of the vortex merging process in the flat plate. It is clearly observed in Chapter 5 that the difference between the lengths of the laminar part of the separation bubble in the flat plate and 3D_case2 is small. Hence, the shorter transition to turbulence in 3D_case2 indeed leads to a smaller separation bubble compared with that on the flat plate.

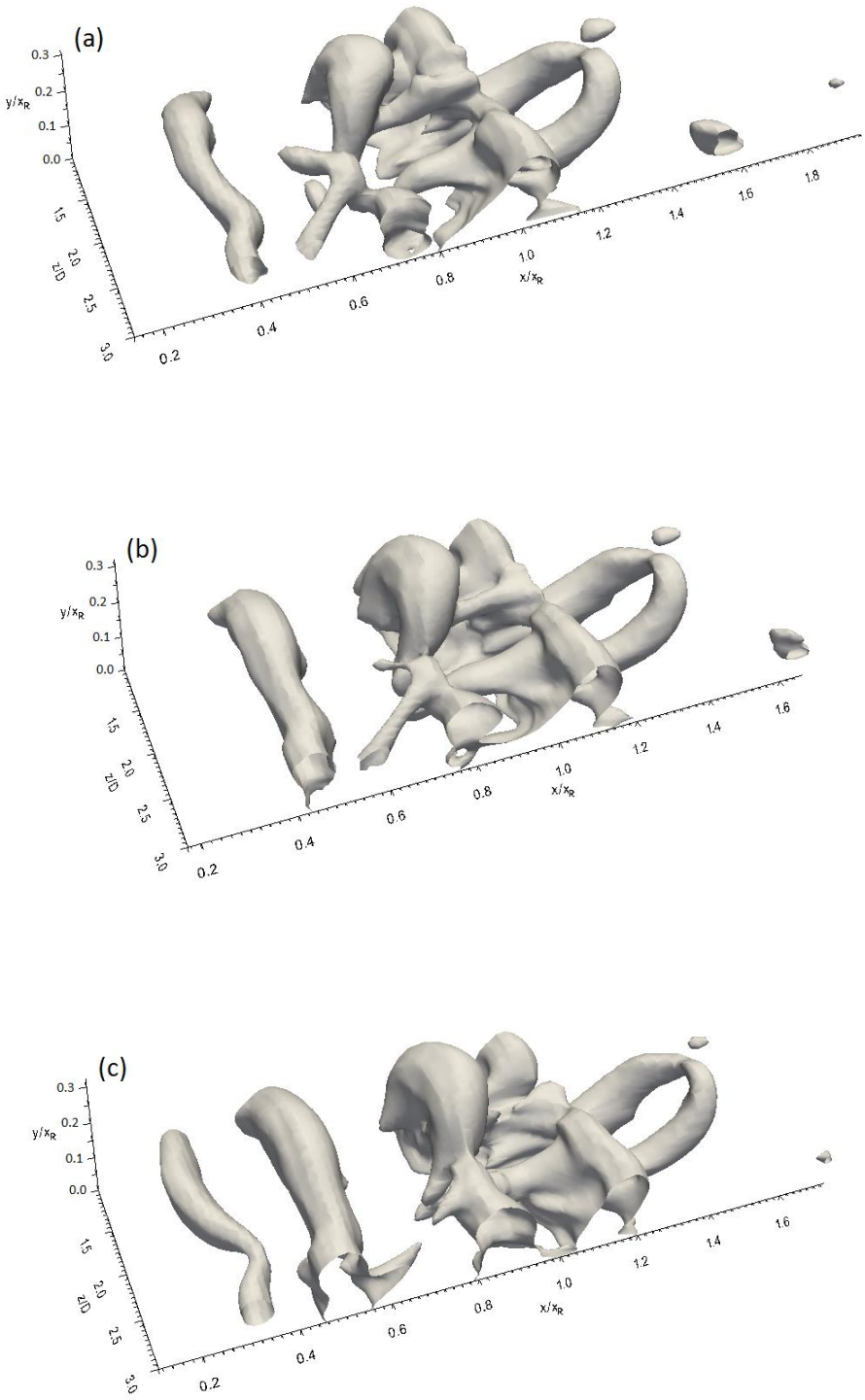

Caption for these figures is on the following page

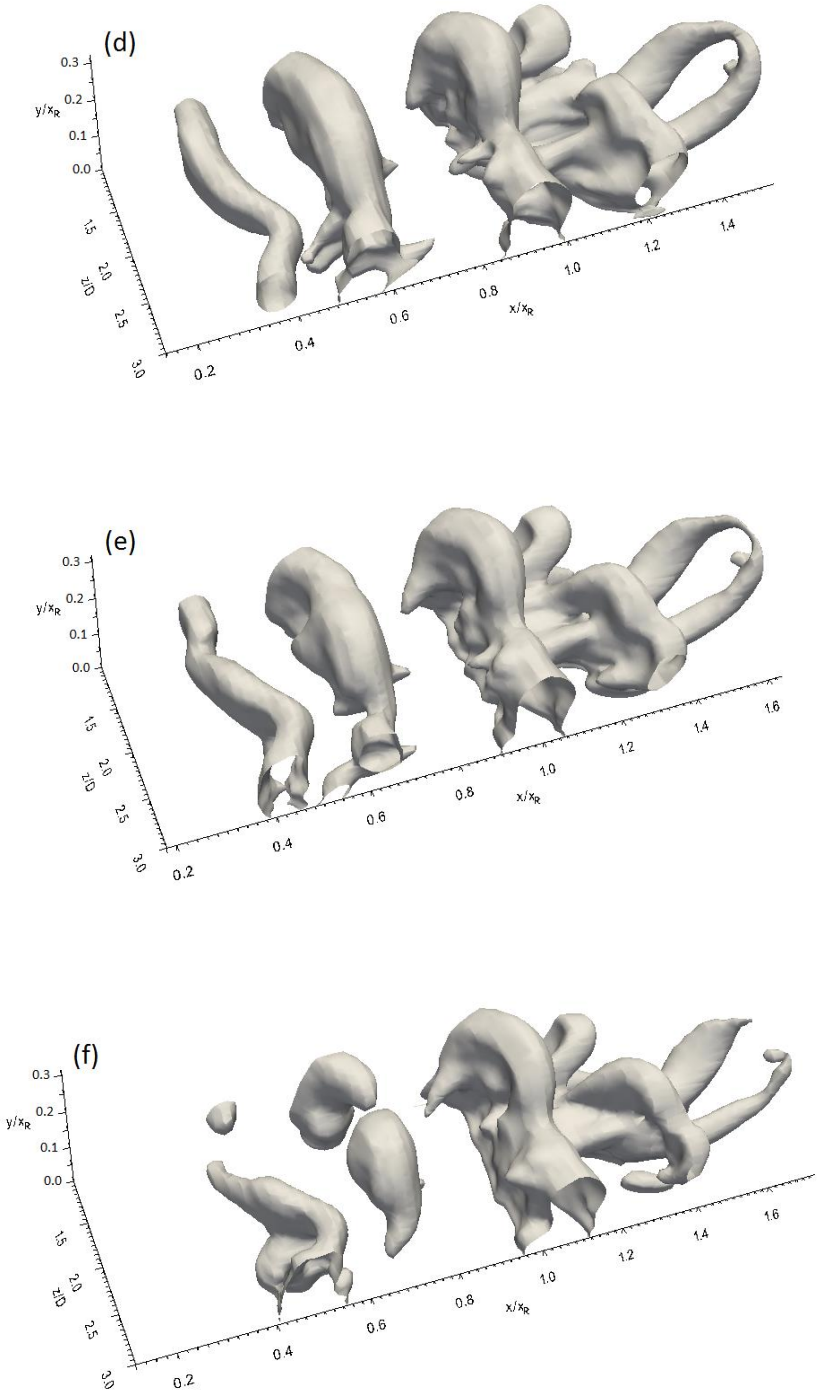

Fig. 7-6. Low pressure isosurface at sequential times taken every 250 time steps for 3D_case2 with NFST

Similarities and differences between coherent structure development between the geometries used in the current study can be summarized as follows:

- The vortex merging process is only observed for the flat plate, where there is no any sign of this action in other two geometries.
- Due to there being no structure merging process in either of the three-dimensional geometries, the time and distance for the transition to turbulence in the flat plate is longer, leading to a longer separating bubble.
- The formation of hairpin structures occurred through a breakdown of Kelvin-Helmholtz rolls in the flat plate and 3D_case2, while this same formation takes place through a topological development of the Kelvin-Helmholtz roll in 3D_case1.

For all geometries in the current study, it can be clearly seen that the hairpin structures which shed into the turbulent boundary layer after the reattachment disintegrate into smaller structures. This process takes place in 3D_case1 faster than that for other two geometries. The structure disintegration distance in 3D_case1 is located between x/x_R = 1 and 1.4, while the hairpin structures still survive up to x/x_R = 1.6 for the flat plate and 1.5 for 3D_case2. This may indicate that the recovery and development of the reattached turbulent boundary layer occur faster and over a shorter distance in 3D_case1. This will be discussed in Chapter 8.

7.2.2 Vorticity fields isosurface

7.2.2.1 Vorticity magnitude isosurface

Vorticity magnitude is one of many flow variables which is conventionally used to visualize the flow field. Vorticity magnitude isosurfaces for the flat plate taken at sequential times (every 250 time steps) are shown in Fig. 7-7. It can be seen that there is a plane sheet of the vorticity in the laminar region of the flow between the leading edge and the onset of the flow unsteadiness at about x/x_R = 0.2. Further downstream, this sheet is subjected to a small distortion up to x/x_R = 4.5, where significant three-dimensional motions of the flow appear. Three-dimensional hairpin structures are formed associated with the three-dimensional nature of the flow around the mean reattachment region. These structures shed to the turbulent boundary layer and move a certain distance before their breakdown into smaller turbulent structures as shown in Fig. 7-7.

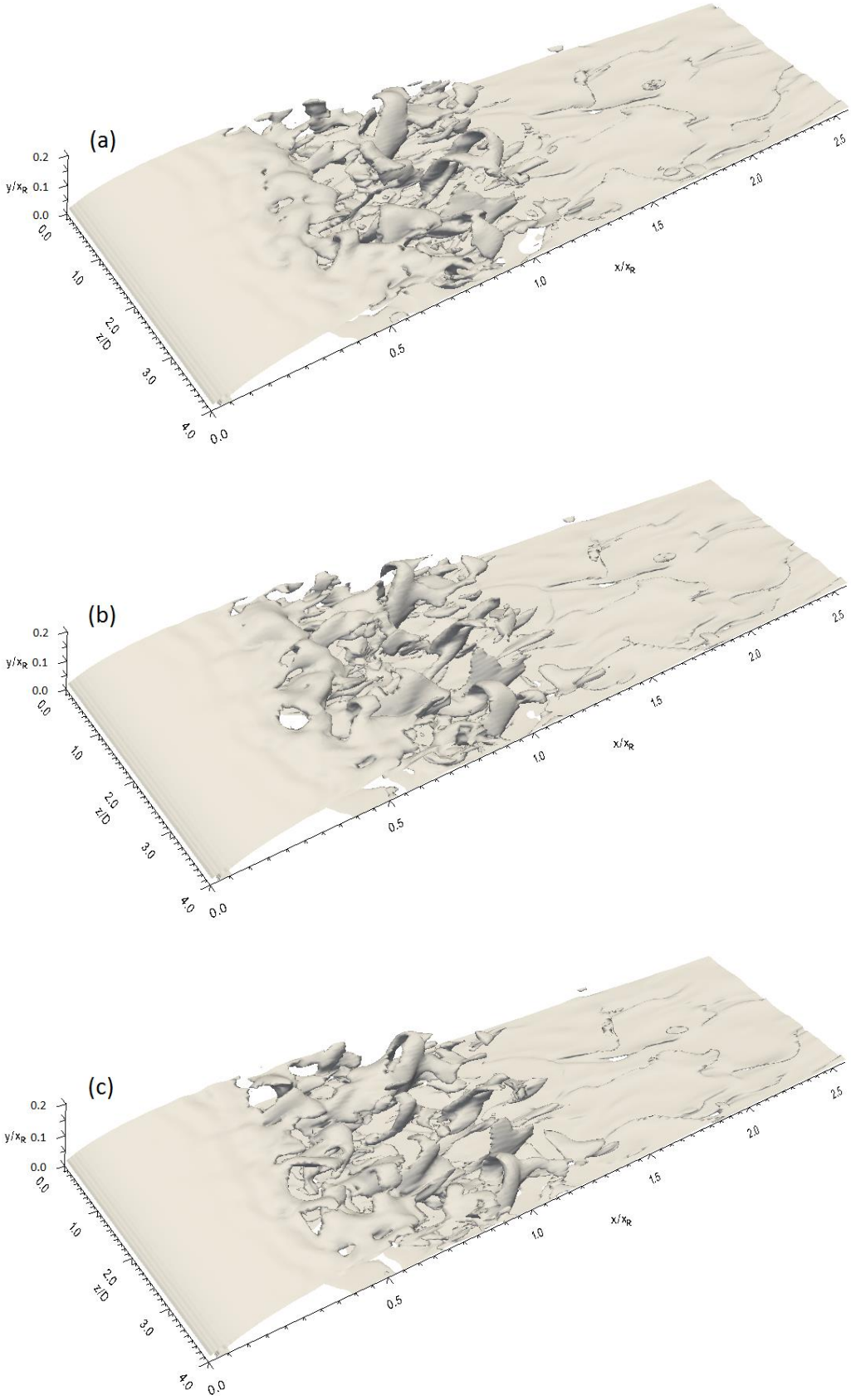

Caption for these figures is on the following page

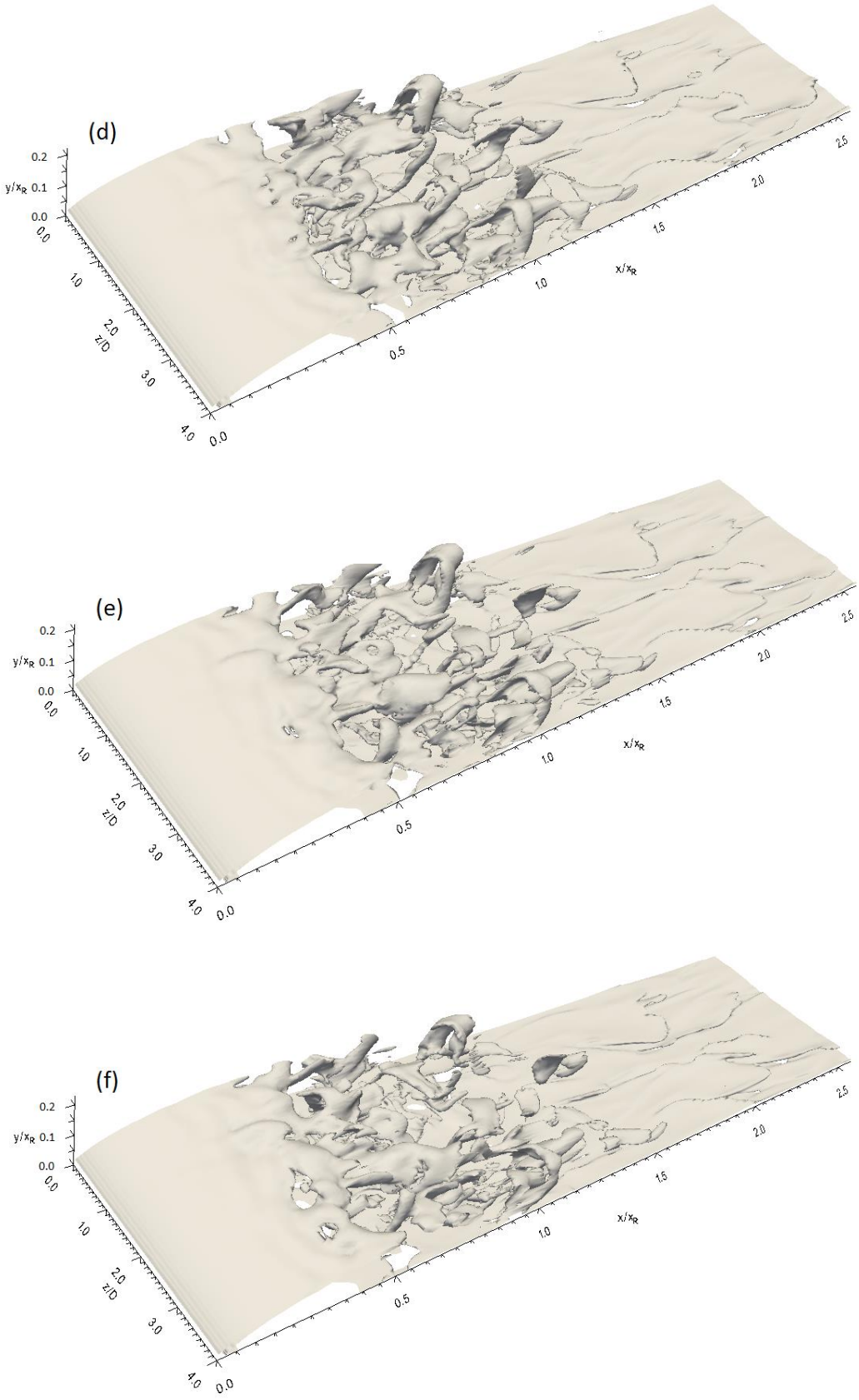

Fig. 7-7. Vorticity magnitude isosurface at sequential times (every 250 time steps) for the flat plate with NFST

In 3D_case1, the vorticity magnitude isosurfaces taken at sequential times (every 250 time steps) present a similar behaviour to that for the flat plate as shown in Fig. 7-8. There is a presence in the vorticity sheet which extends into the laminar region of the separation bubble from the leading edge of the geometry to x/x_R = 0.4, where the start of the unsteadiness is located. Further downstream, there is a sign of a small distortion in the vorticity sheet up to x/x_R = 0.6, where the symmetry of this sheet is broken. Further downstream, there is a significant three-dimensional flow that leads to the formation of hairpin structures around the mean reattachment line. It can be clearly seen that the breakdown process of the hairpin structures within the turbulent boundary layer is complete at about x/x_R = 1.4 as shown in Fig. 7-8.

Vorticity magnitude isosurfaces at the top and side surfaces of 3D_case1 taken at the same times as Fig. 7-8 are shown in Fig. 7-9. It can be seen that there is no difference in the vorticity development on either surface. There are two plane sheets of the vorticity on each surface that develop to form hairpin structures around the mean reattachment line. These hairpin structures then break down into smaller structures within the turbulent boundary layer after the reattachment.

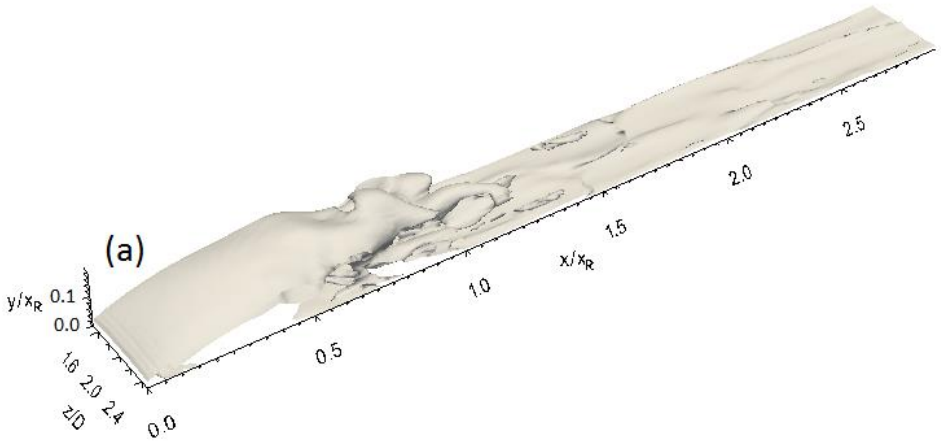

Caption for this figure is on the following page

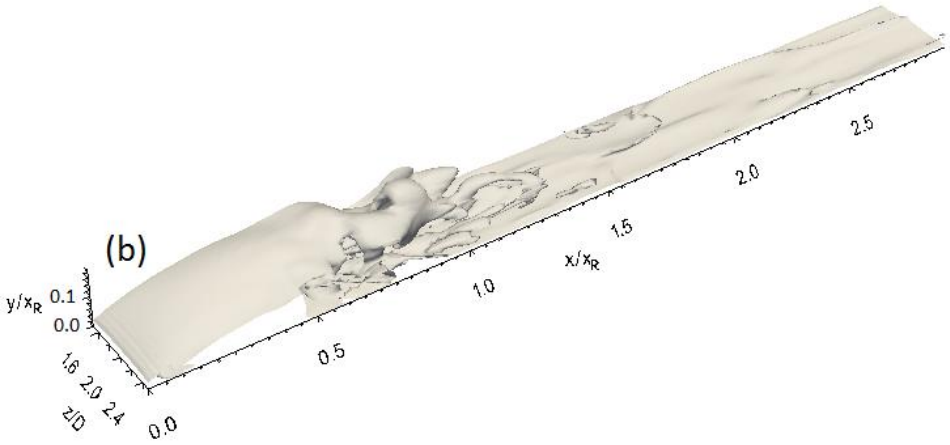
(b)
y/x_R
0.1
0.0
1.6
2.0
2.4
z/D
0.0
0.5
1.0
1.5
2.0
2.5
x/x_R

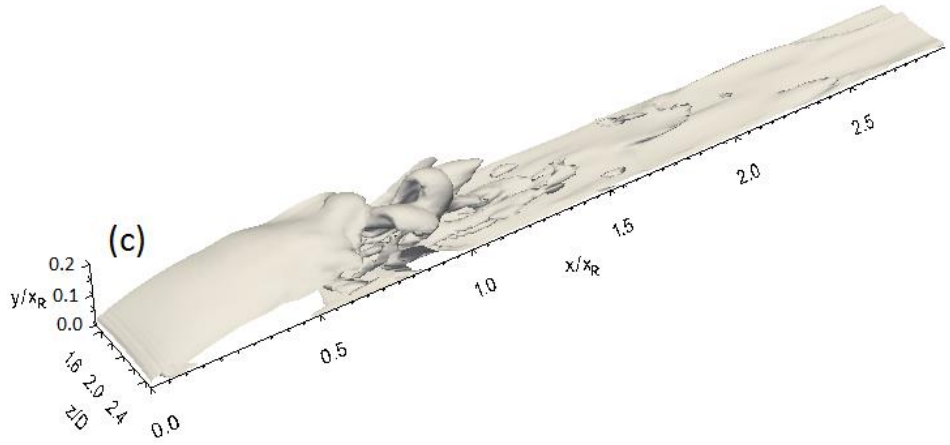
(c)
0.2
y/x_R
0.1
0.0
1.6
2.0
2.4
z/D
0.0
0.5
1.0
1.5
2.0
2.5
x/x_R

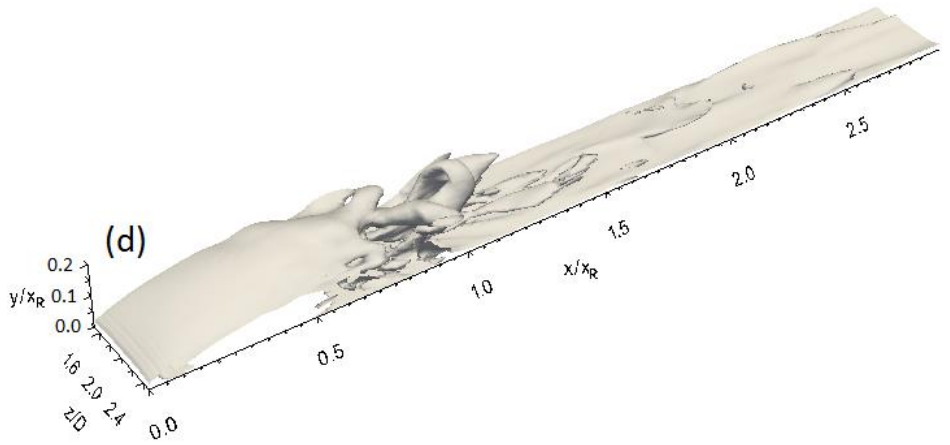
(d)
0.2
y/x_R
0.1
0.0
1.6
2.0
2.4
z/D
0.0
0.5
1.0
1.5
2.0
2.5
x/x_R

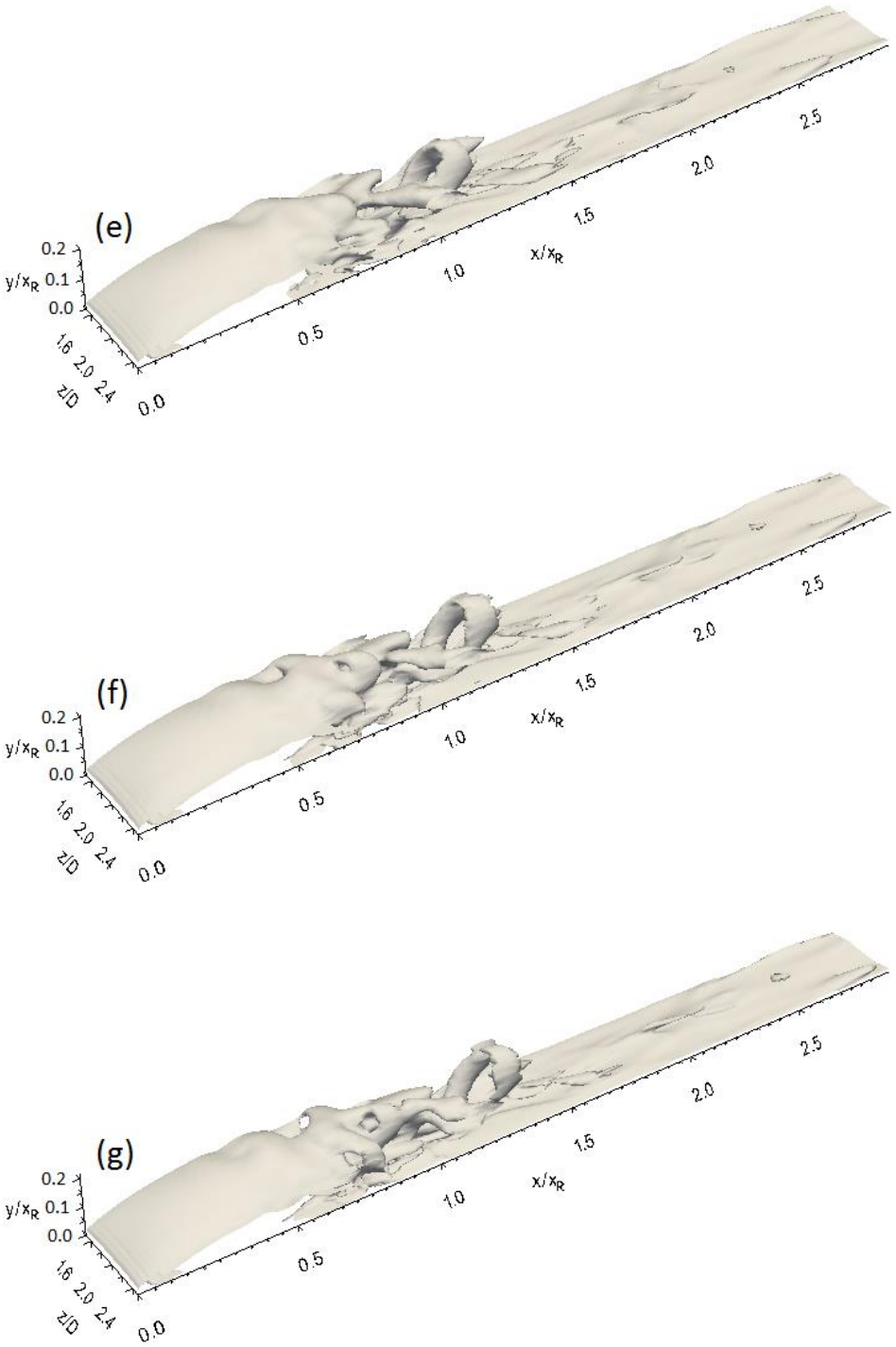
(e)
(f)
(g)
0.2
0.1
0.0
y/x_R
1.6
2.0
2.4
z/D
0.0
0.5
1.0
1.5
2.0
2.5
x/x_R

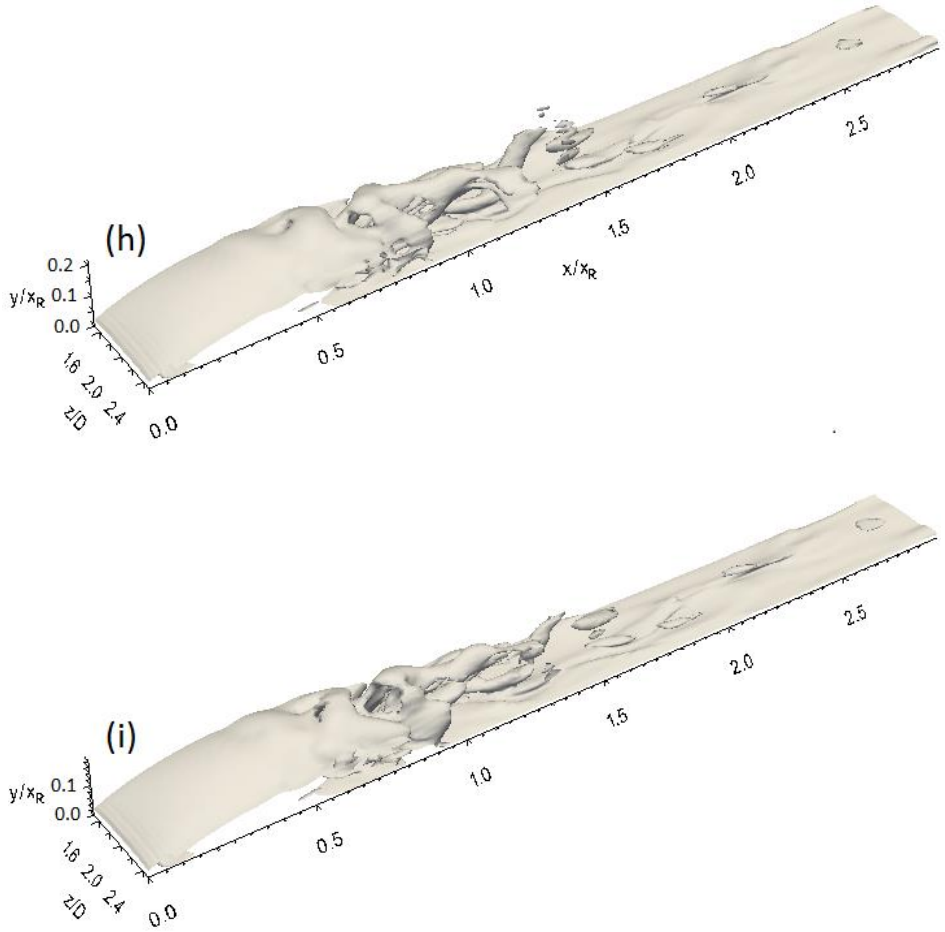

Fig. 7-8. Vorticity magnitude isosurface at sequential times (every 250 time steps) for 3D_case1 with NFST

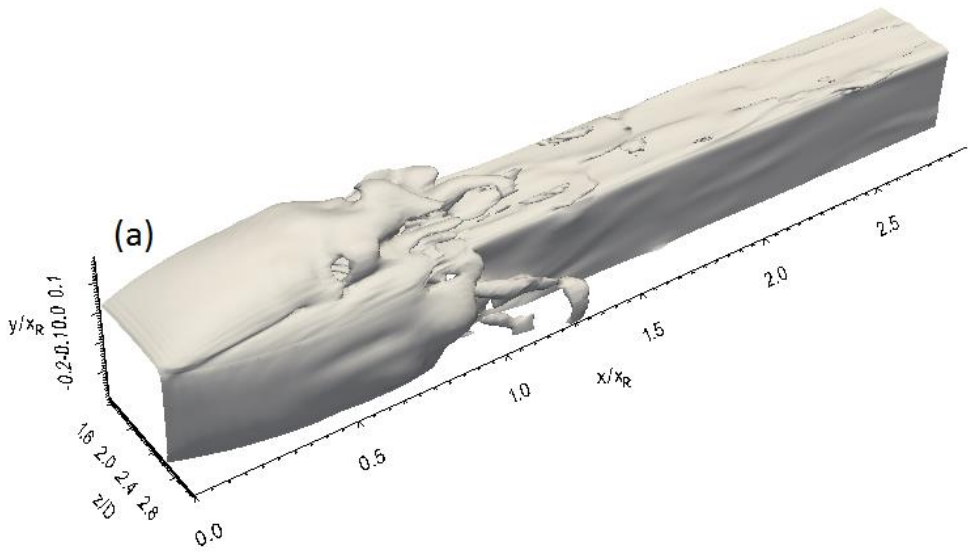

Caption for this figure is on the following page

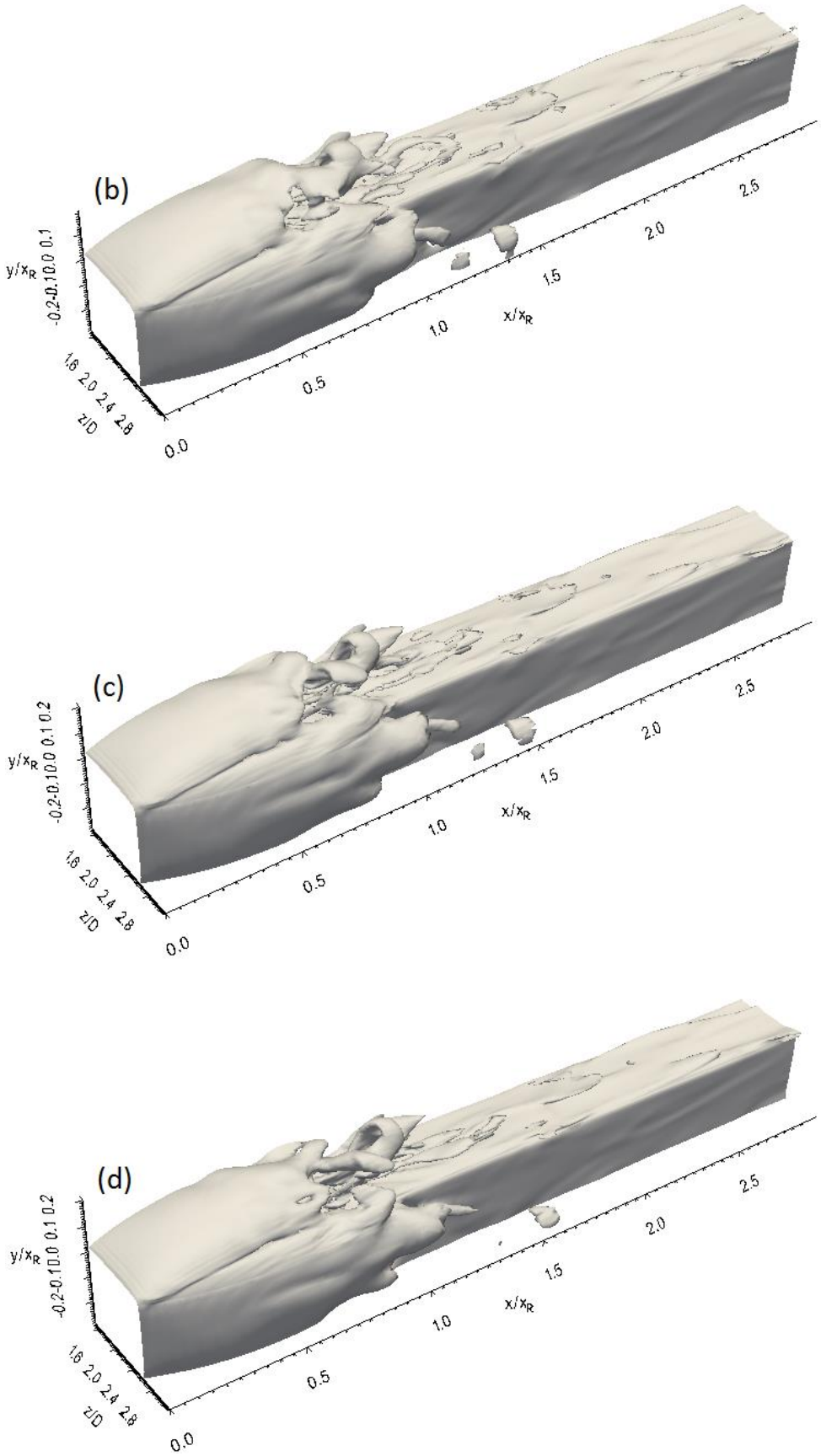
(b)
(c)
(d)
y/x_R
-0.2 -0.1 0.0 0.1 0.2
x/x_R
0.0 0.5 1.0 1.5 2.0 2.5
z/D
1.6 2.0 2.4 2.8

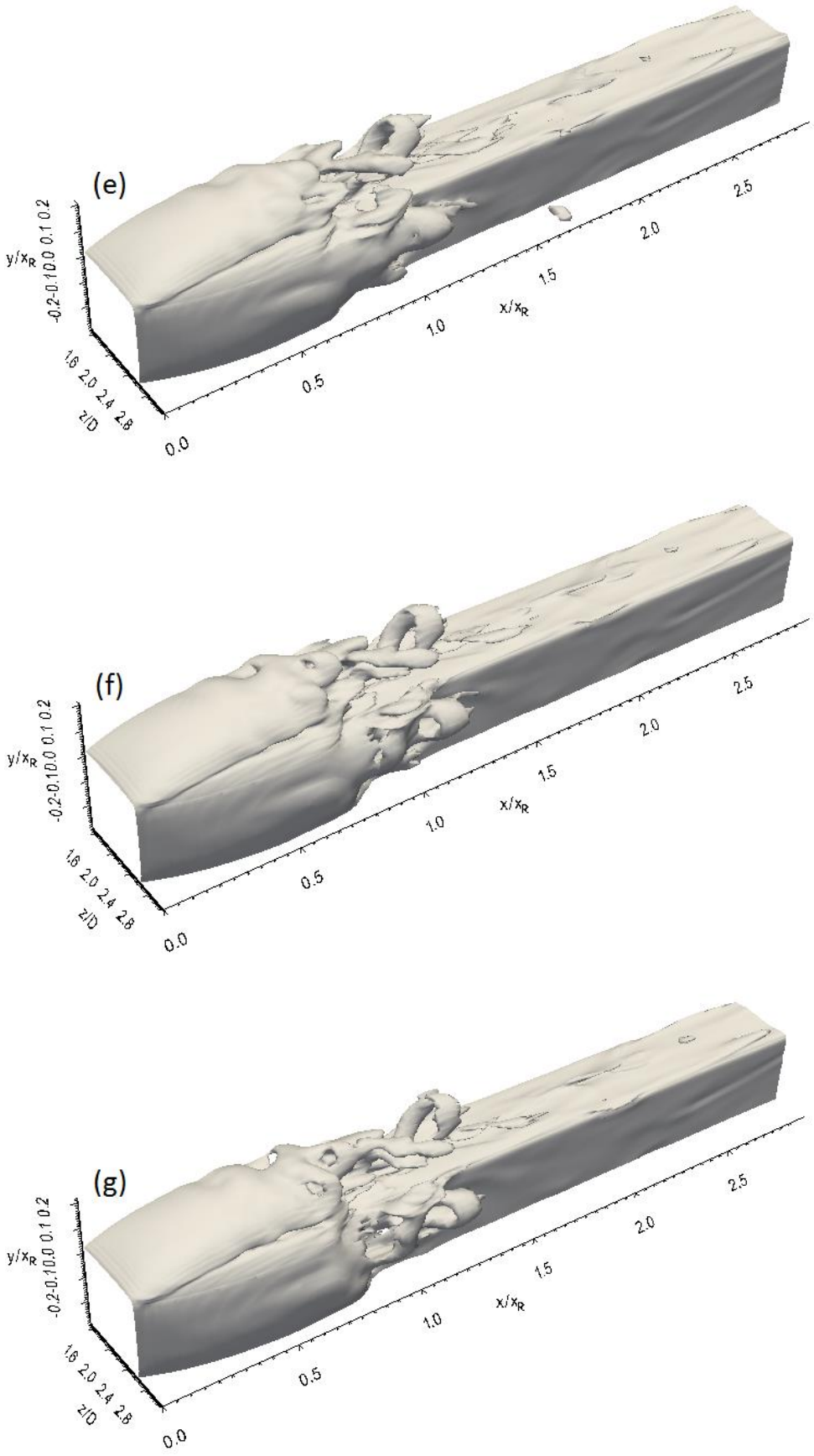
(e)
(f)
(g)
y/x_R
-0.2 -0.1 0.0 0.1 0.2
z/D
1.6 2.0 2.4 2.8
x/x_R
0.0 0.5 1.0 1.5 2.0 2.5

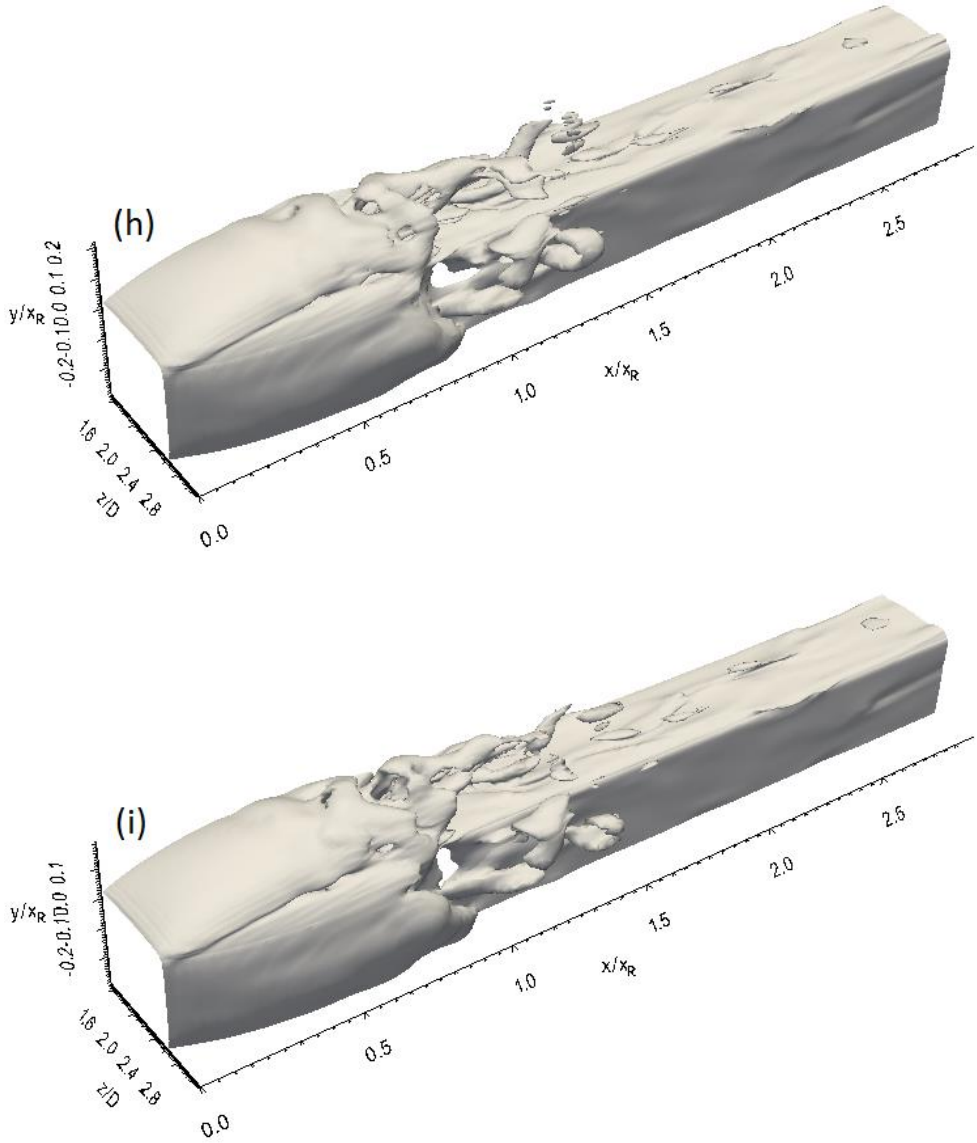

Fig. 7-9. Vorticity magnitude isosurface on the top and side surfaces at sequential times (every 250 time steps) for 3D_case1 with NFST

Vorticity magnitude isosurfaces taken at sequential times (every 250 time steps) for 3D_case2 are exhibited in Fig. 7-10. There is no difference in the associated variables behaviours among all geometries of the current study apart from the unsteadiness location. In 3D_case2, the vorticity magnitude sheet that formed on the leading edge remains smooth up to $x/x_R = 0.31$ as shown in Fig. 7-10, indicating that the flow is laminar and two-dimensional within this region. Further downstream, the vorticity sheet undergoes a small distortion up to $x/x_R = 0.55$. At about $x/x_R = 0.6$, there is a breakdown

of the vorticity sheet regularity associated with significant three-dimensional motions of the flow, leading to the formation of hairpin structures around the mean reattachment line. Further downstream, hairpin structures still appeared over a short distance before their disintegration into smaller turbulent structures.

Vorticity magnitude development on the top and side surfaces for 3D_case2 are shown in Fig. 7-11, where snapshots are taken at similar times to those in Fig. 7-10. It is clearly seen that there are two plane sheets of the vorticity on each surface subject to the unsteadiness at the same streamwise location. The regularity of these sheets then has been distorted, leading to turbulent reattached flow as shown in Fig. 7-11.

In spite of the comparable behaviour of the flow presented by employing the low pressure and the vorticity magnitude isosurfaces, the latter technique presents clearly only small hairpin structures in the flow, while the transition events such as construction of Kelvin-Helmholtz rolls and their pairing process in the flat plate or Kelvin-Helmholtz rolls evolution in all geometries cannot be represented by the vorticity magnitude isosurfaces. Hence, this technique cannot display all types of existing coherent structures.

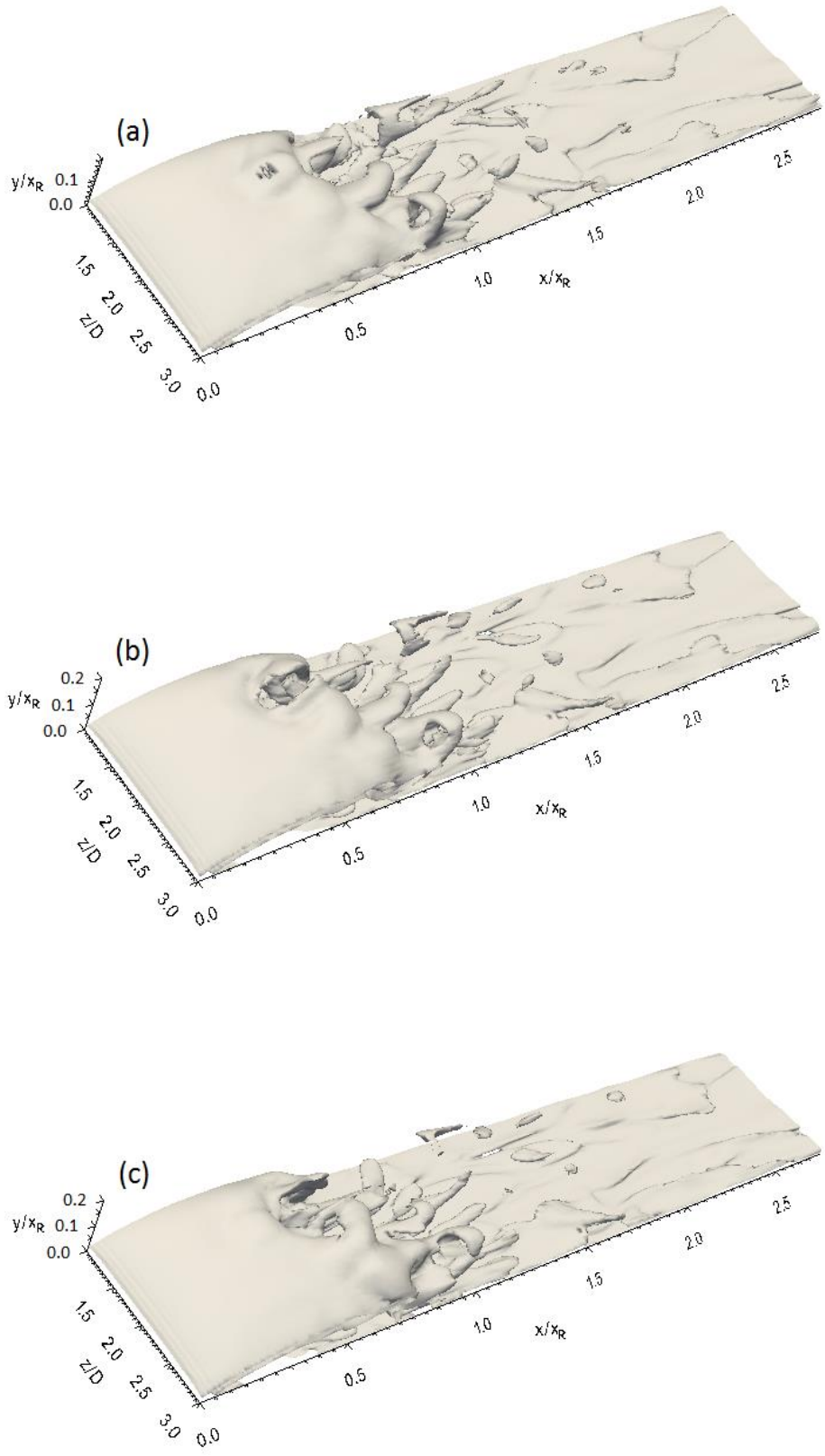

Caption for these figures is on the following page

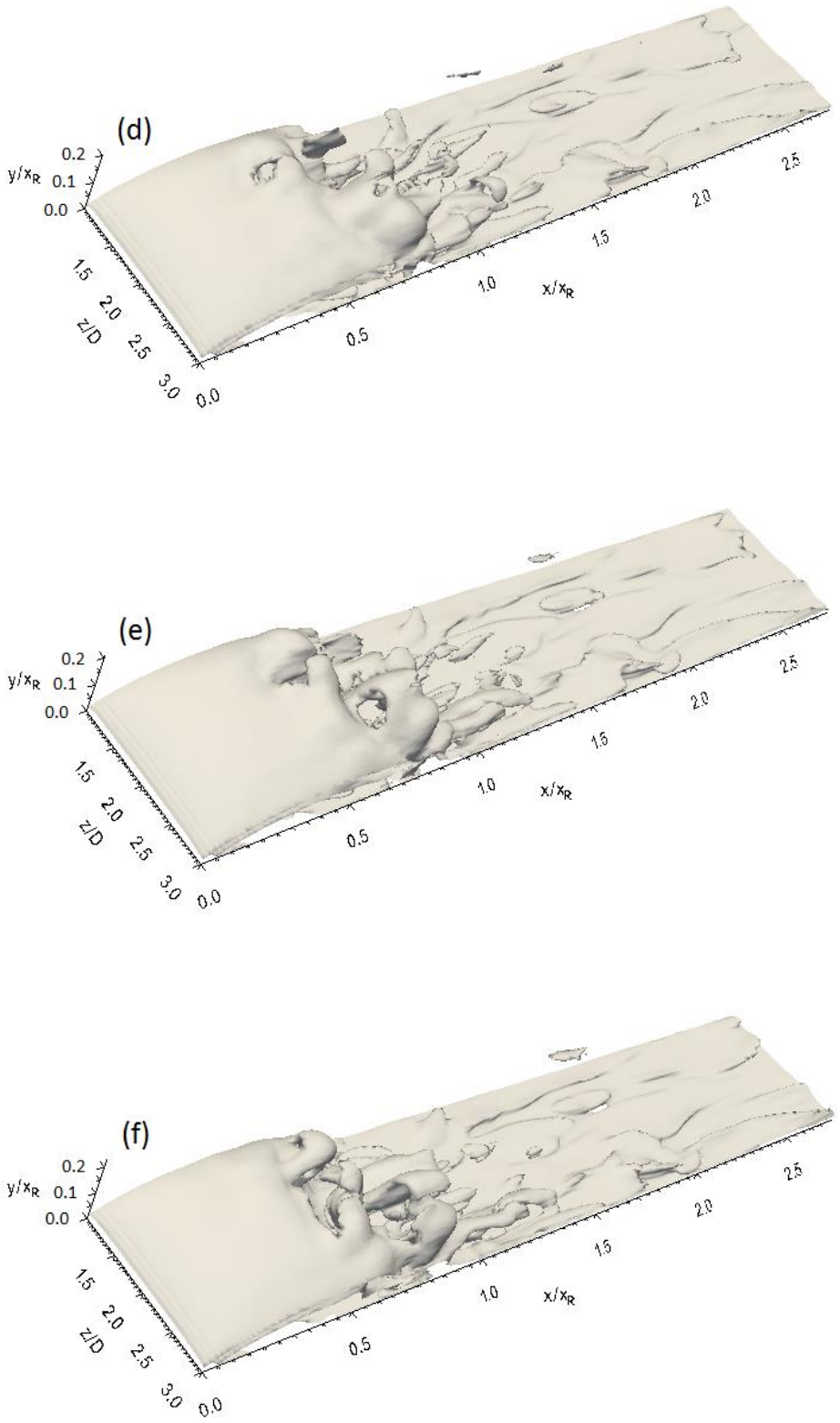

Fig. 7-10. Vorticity magnitude isosurface at sequential times (every 250 time steps) for 3D_case2 with NFST

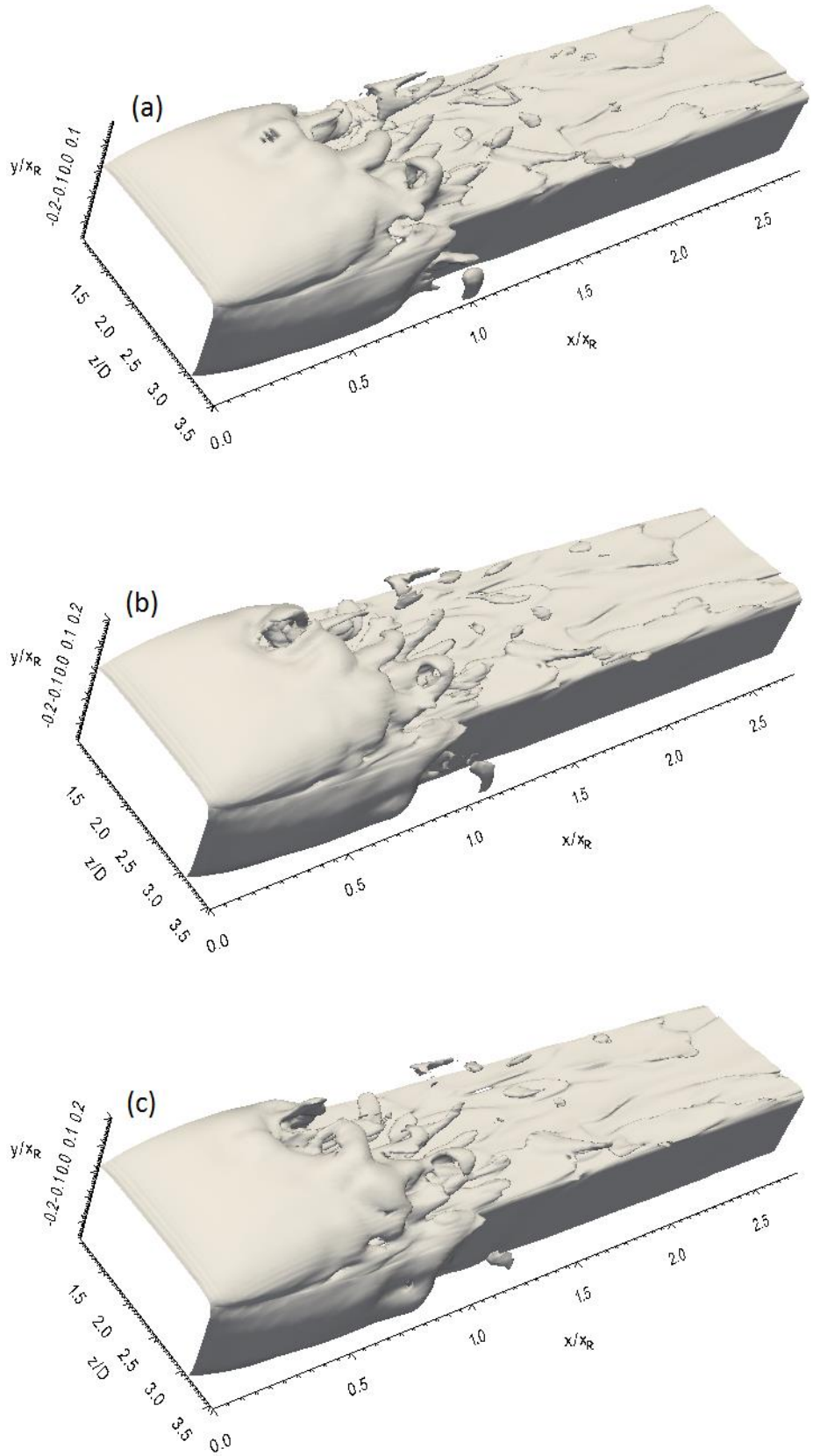

Caption for these figures is on the following page

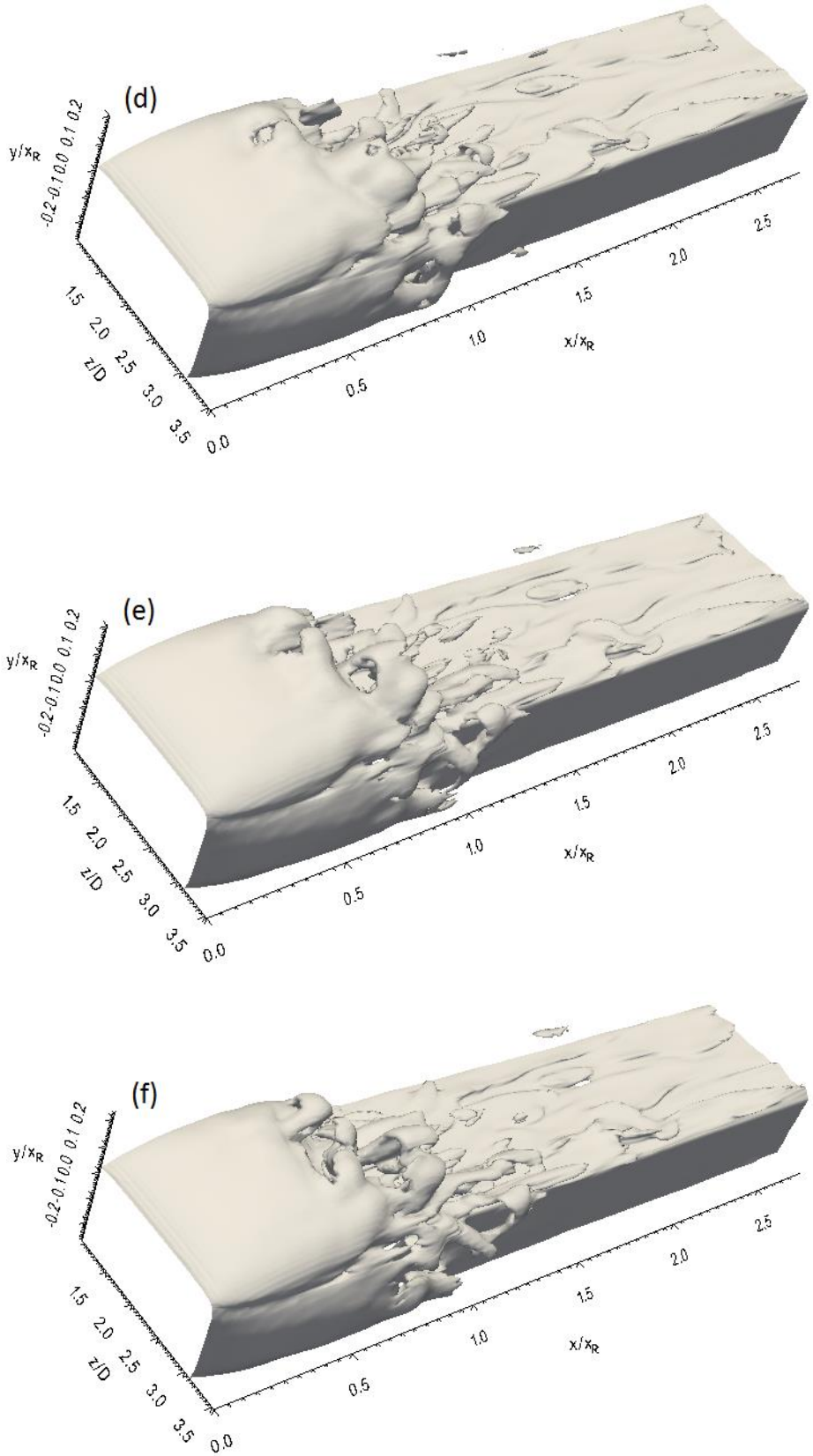

Fig. 7-11. Vorticity magnitude isosurface on the top and side surfaces at sequential times (every 250 time steps) for 3D_case2 with NFST

7.2.2.2 Streamwise vorticity isosurface

The streamwise vorticity isosurface for the flat plate is shown in Fig. 7-12, where six streamwise vorticity isosurfaces, taken every 250 time steps, are presented. There is no trace of the streamwise vorticity before $x/x_R = 0.2$, indicating that the flow is laminar up to this point. Further downstream, the streamwise vorticity develops and the appearance of vortical structures can be seen in the region from $x/x_R = 0.45$ to $x/x_R = 1$. After the reattachment, disintegration of the streamwise vortical structures in the turbulent boundary layer can be seen, where these structures move a distance of up to $x/x_R = 1.7$ before breaking down into very small structures as shown in Fig. 7-12. It is clear noted that the streamwise vortical structures form angles with the solid wall (lifted up) and these angles may be the reason for the existence of these structures after the reattachment line. From $x/x_R = 1$ to $x/x_R = 1.7$, these structures gradually become parallel to the plate wall and the angles between the streamwise structures and the solid wall disappear after the breakdown of these structures into smaller structures further downstream. A similar observation was reported by Abdalla and Yang (2004b) for a transitional separation flow on a blunt flat plate.

Fig. 7-13 shows streamwise vorticity isosurfaces taken at sequential times (every 250 time steps) for 3D_case1. The streamwise vorticity starts appearing at $x/x_R = 0.4$ and develops further downstream. In the region between $x/x_R = 0.6$ and the mean reattachment location the existence of streamwise vortical structures, which are inclined at acute angles to the solid surface of the geometry, can be clearly seen. With faster disintegration than that observed for the flat plate, the streamwise vortical structures for 3D_case1 break down into smaller structures in the turbulent boundary layer. At $x/x_R = 1.5$ onward, the inclined streamwise vorticity structures completely disappear.

The streamwise vorticity isosurfaces (taken every 250 time steps) for 3D_case2 plotted in Fig. 7-14 show a similar scenario to the above. It is clearly seen that there is no appearance of streamwise vorticity up to $x/x_R = 0.31$, indicating that the flow is laminar before this location. A significant amount of streamwise vorticity can be seen to appear in the region from $x/x_R = 0.6$ to $x/x_R = 1$. Streamwise vorticity structures make angles with the wall. These structures pass the mean reattachment line and survive up to $x/x_R = 1.5$. Further downstream, these structures vanish as shown in Fig. 7-14.

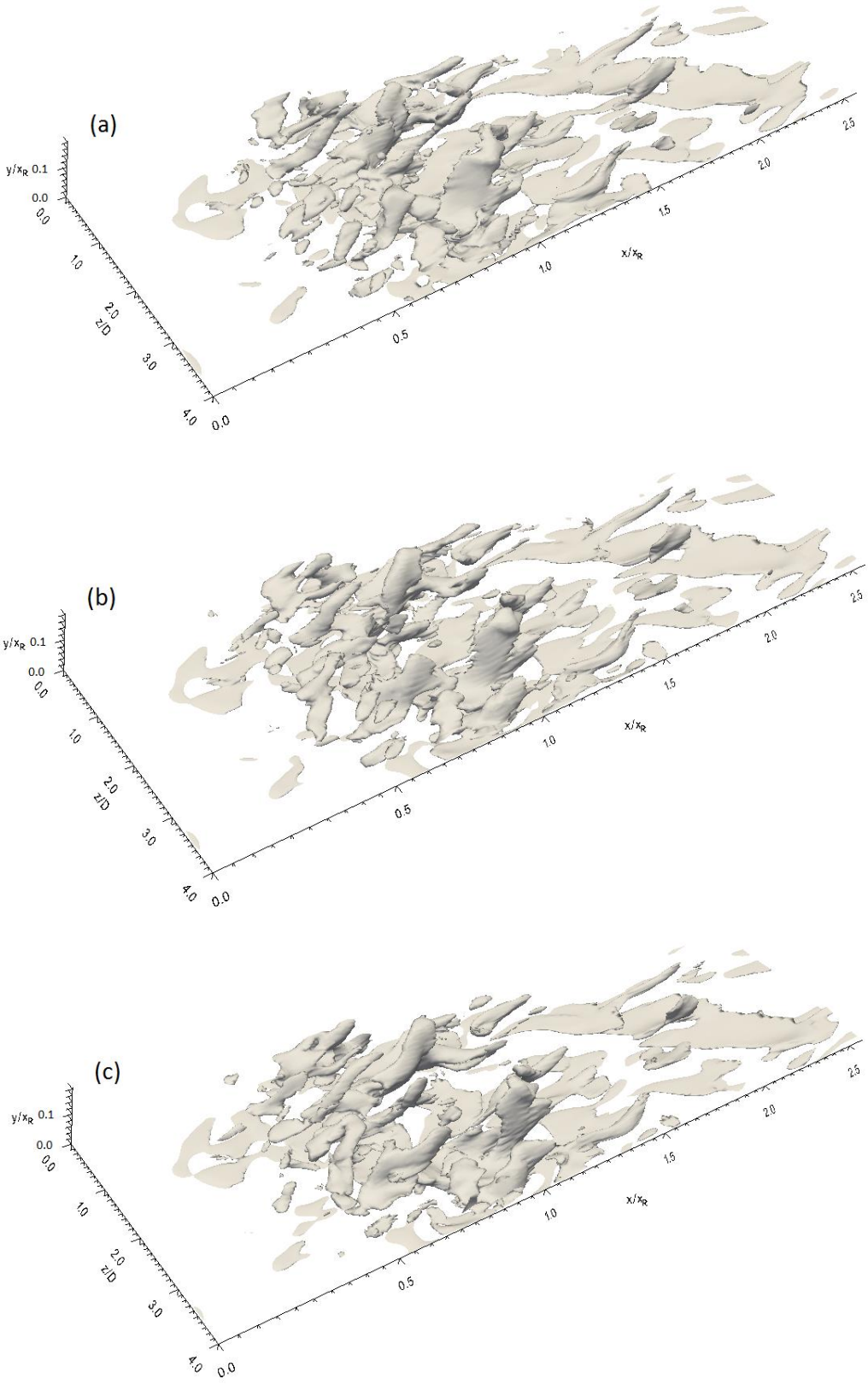

Caption for these figures is on the following page

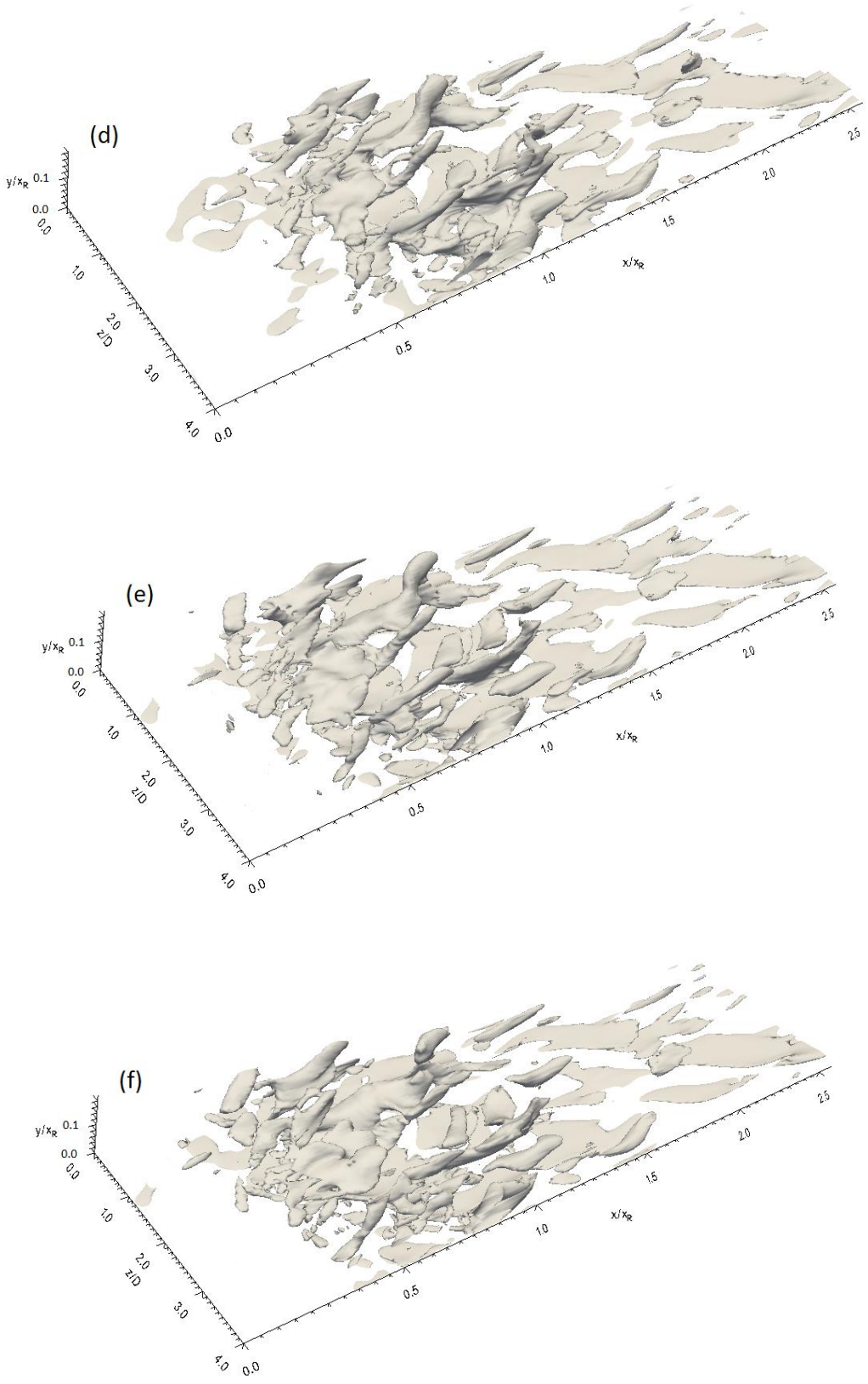

Fig. 7-12. Streamwise vorticity isosurface at sequential times (every 250 time steps) for the flat plate with NFST

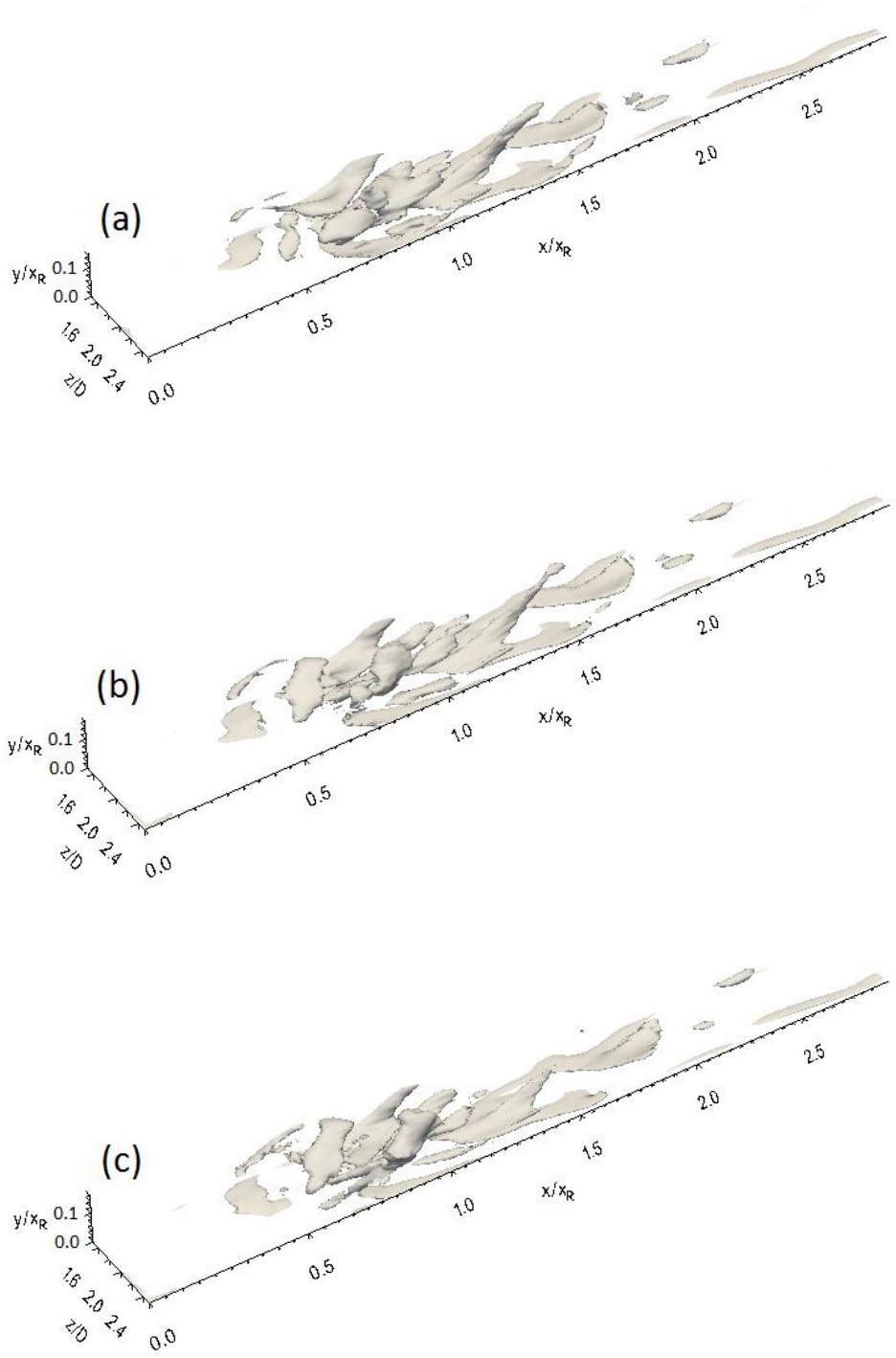

Caption for these figures is on the following page

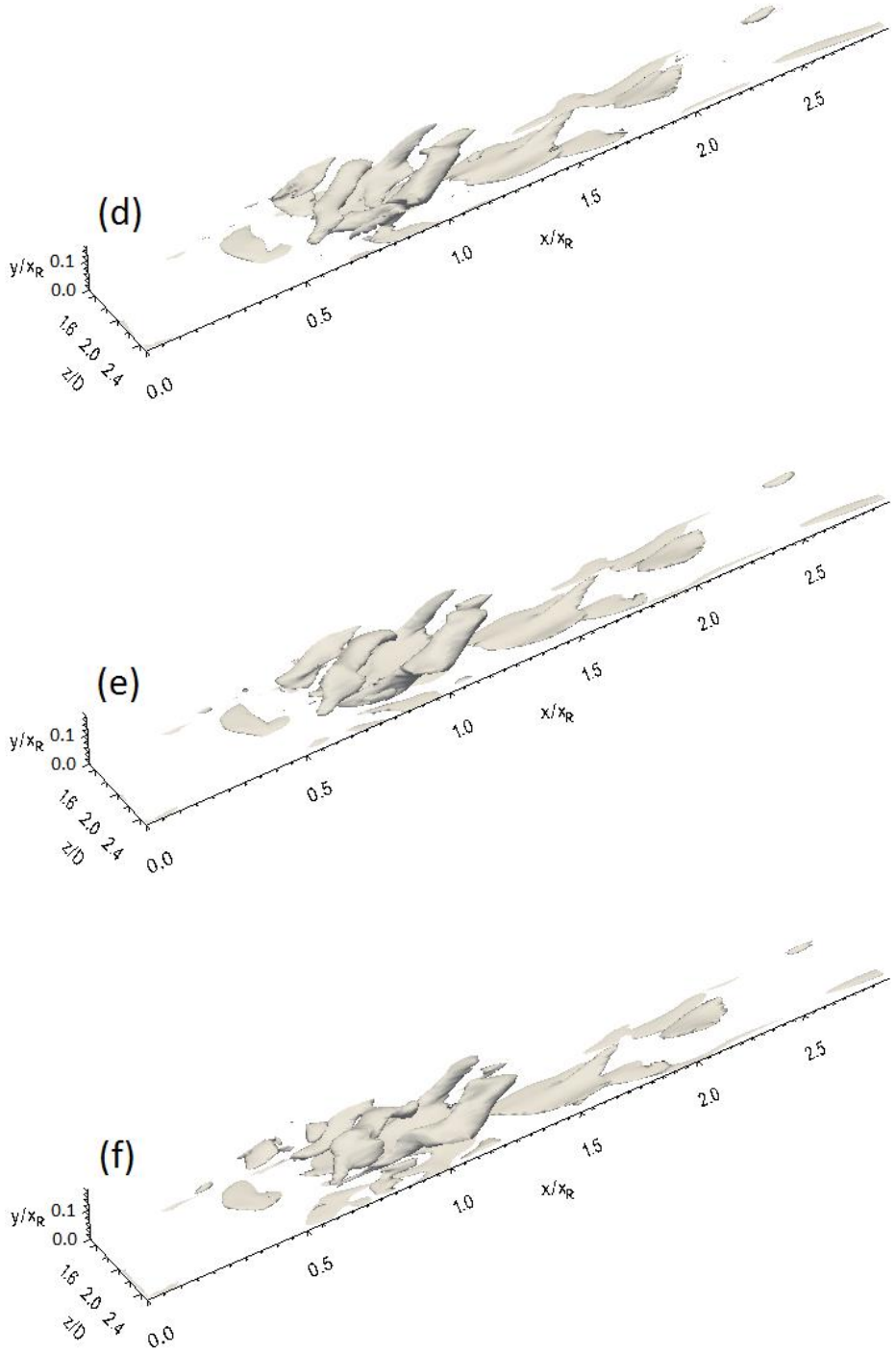

Fig. 7-13. Streamwise vorticity isosurface at sequential times (every 250 time steps) for 3D_case1 with NFST

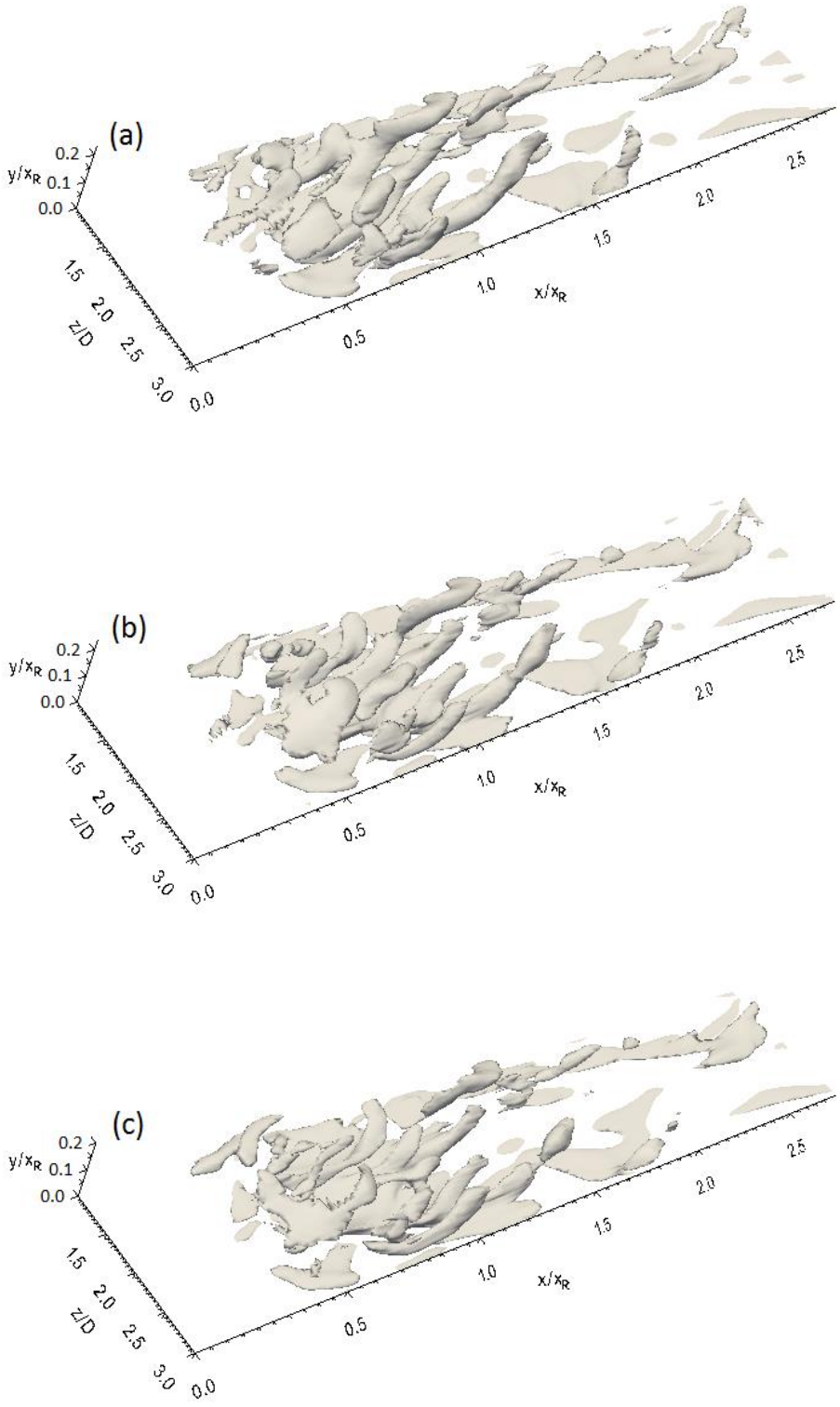

Caption for these figures is on the following page

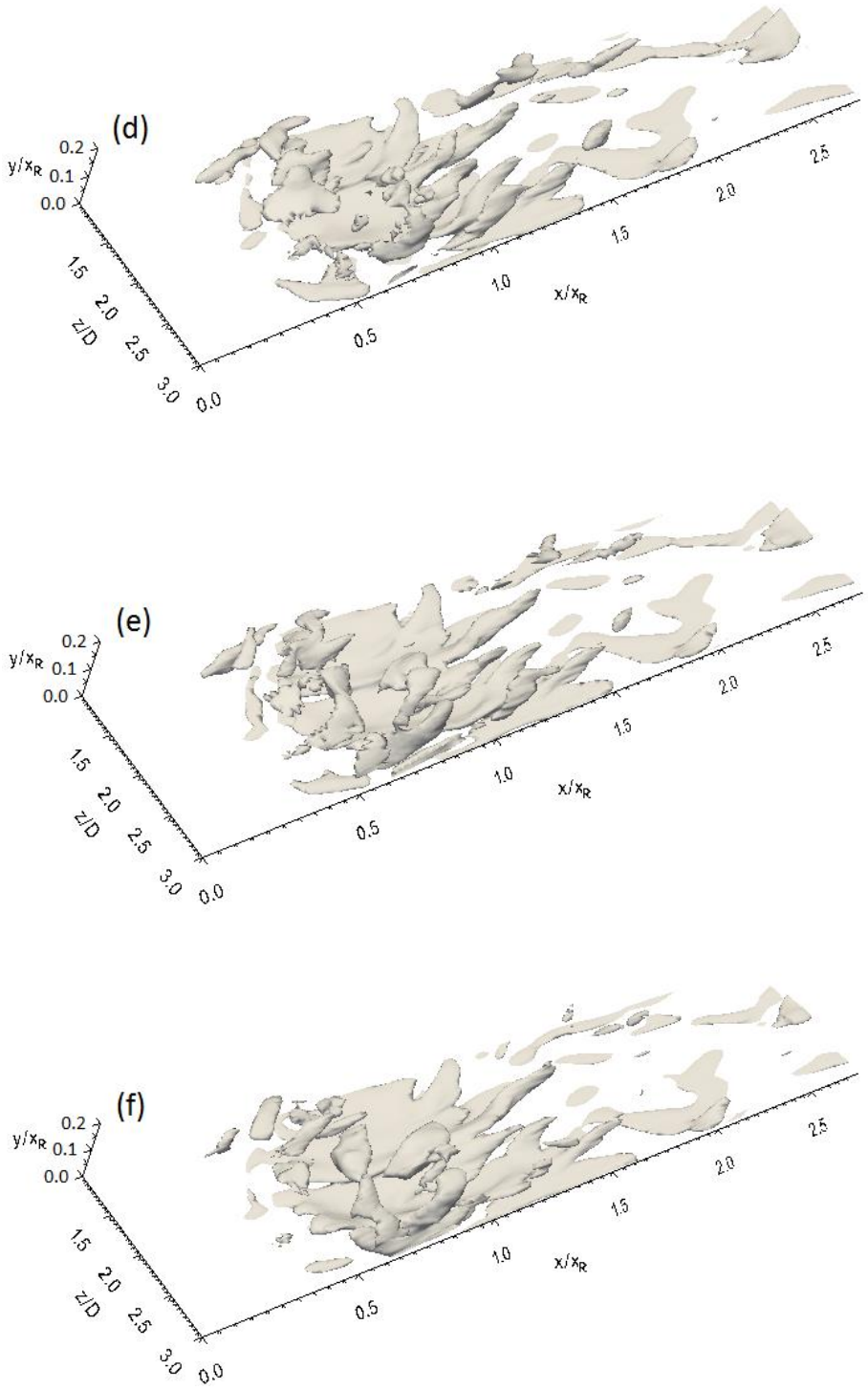

Fig. 7-14. Streamwise vorticity isosurface at sequential times (every 250 time steps) for 3D_case2 with NFST

For all geometries in the current study, the streamwise vorticity isosurfaces clearly show that the main concentration of the streamwise vorticity occurs in the second half of the separation bubble. This indicates that in this region most events relating to the transition to full turbulence take place.

Tafti and Vanka (1991) presented a relationship between the appearance of the streamwise vorticity and correlation coefficient between the root mean square fluctuating streamwise and wall-normal velocities $(-\overline{u'v'}/u'_{rms}v'_{rms})$ for a turbulent separated-reattached flow. They showed that the correlation coefficient profile is non-uniform at a location where streamwise vorticity is significant. Further downstream at the mean reattachment line and further within the reattached flow, the wall-normal distribution of the correlation coefficient trends to be more uniform due to spread of the streamwise vorticity throughout the shear layer.

Figs. 7-15, 7-16, and 7-17 present profiles for the correlation coefficient between the root mean square fluctuating streamwise and wall-normal velocities at different streamwise locations for the flat plate, 3D_case1, and 3D_case2, respectively. For all geometries, three streamwise locations are chosen at the significant appearance of the streamwise vorticity, the reattachment point, and a further location in the turbulent boundary layer.

The correlation coefficient profile at $x/x_R = 0.6$ for the flat plate shown in Fig. 7-15 is non-uniform, indicating the existence of large streamwise vortical structures. The correlation is very small close to the wall and increases to a value of about 0.3 at the shear layer centre ($y/x_R = 0.109$). The maximum value of the correlation is 0.346 at $y/x_R = 0.137$, coinciding with significant streamwise vorticity. At the mean reattachment ($x/x_R = 1$), distribution of the correlation coefficient through the shear layer is roughly uniform, with a nearly constant value of 0.34. Further downstream, distribution of the correlation coefficient remains roughly uniform as shown at $x/x_R = 2$ in Fig. 7-15.

For 3D_case1, the correlation coefficient at the shear layer centre ($y/x_R = 0.136$) and at the location of the significant streamwise vorticity ($x/x_R = 0.6$) is about 0.32 as shown in Fig. 7-16. At this streamwise location, the maximum value of the correlation coefficient is 0.377 at $y/x_R = 0.153$, indicative of the appearance of significant streamwise vorticity. The wall-normal distribution of the correlation coefficient at the mean reattachment line

trends to be uniform in the shear layer. Further downstream at x/x_R = 2, a uniform distribution of the correlation coefficient with a value of around 0.35 can be seen in Fig. 7-16.

At x/x_R = 0.6 for 3D_case2, the correlation coefficient profile seems to be more regular than that for the other two geometries as seen in Fig. 7-17. The maximum value of the correlation coefficient is 0.37 at y/x_R = 0.163. At the mean reattachment point and further downstream, the uniformity of the correlation coefficient profile matches that of other two geometries much more closely. This may indicate that the recovery of the turbulent reattached boundary layer is faster for 3D_case2 than that for other two geometries because of the good uniformity of the correlation coefficient profile indicating a better spread of the streamwise vorticity throughout the shear layer (Tafti and Vanka, 1991). This subject is addressed further in Chapter 8.

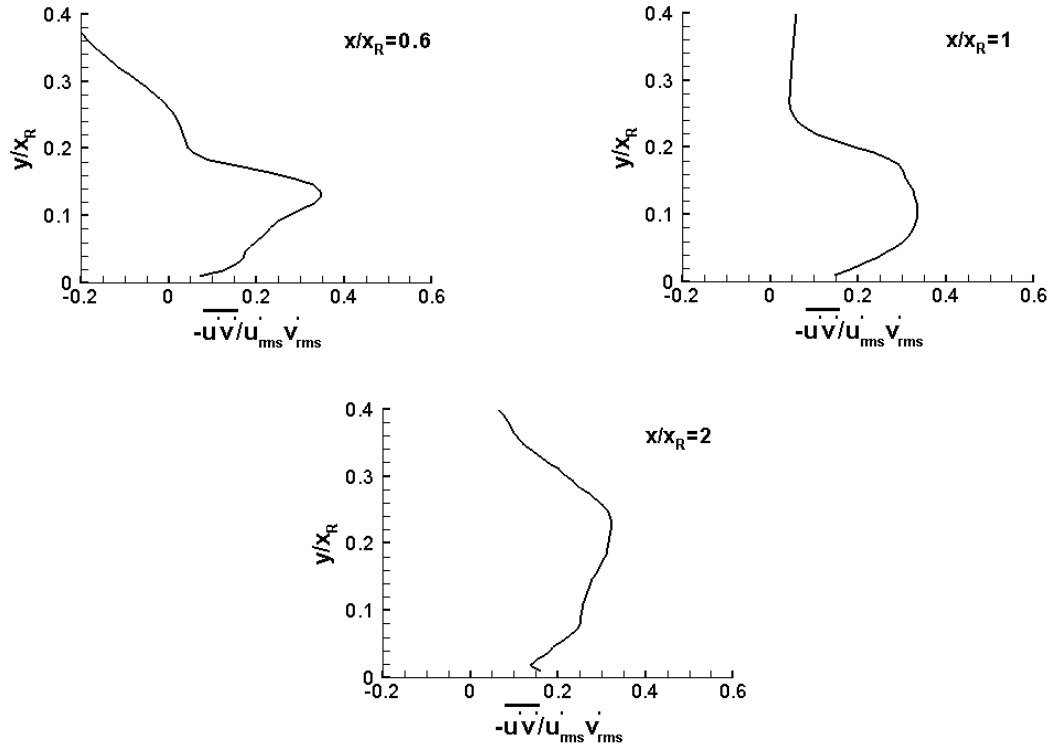

Fig. 7-15. Wall-normal distribution of the correlation coefficient between u'_{rms} and v'_{rms} at three streamwise positions for the flat plate with NFST

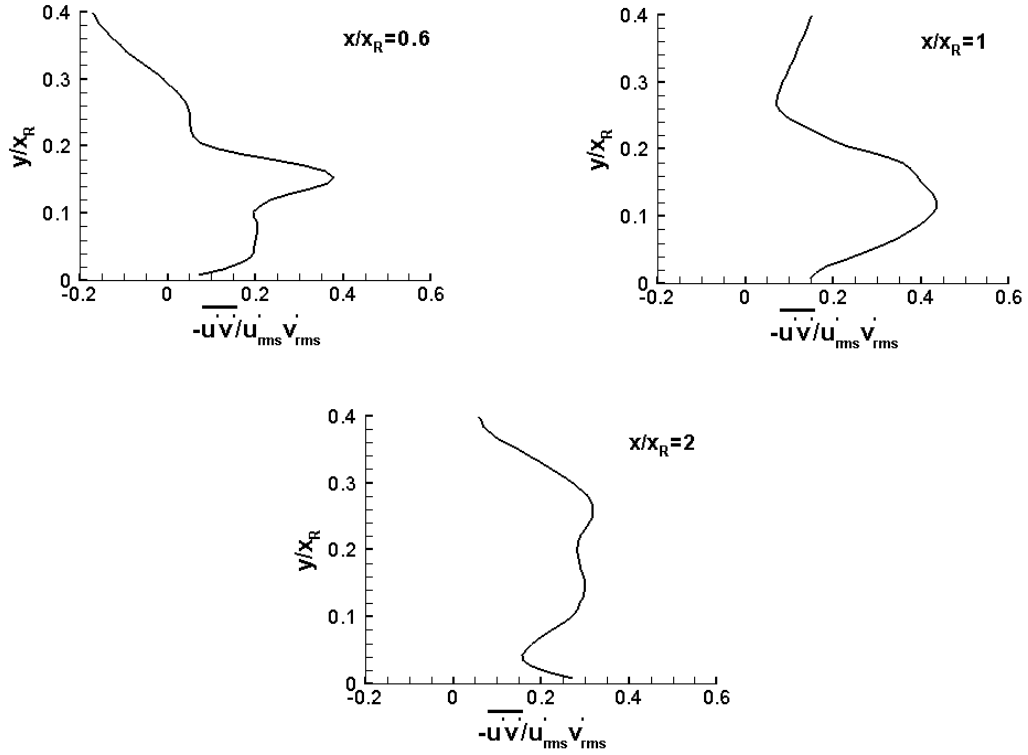

Fig. 7-16. Wall-normal distribution of the correlation coefficient between u'_{rms} and v'_{rms} at three streamwise positions for 3D_case1 with NFST

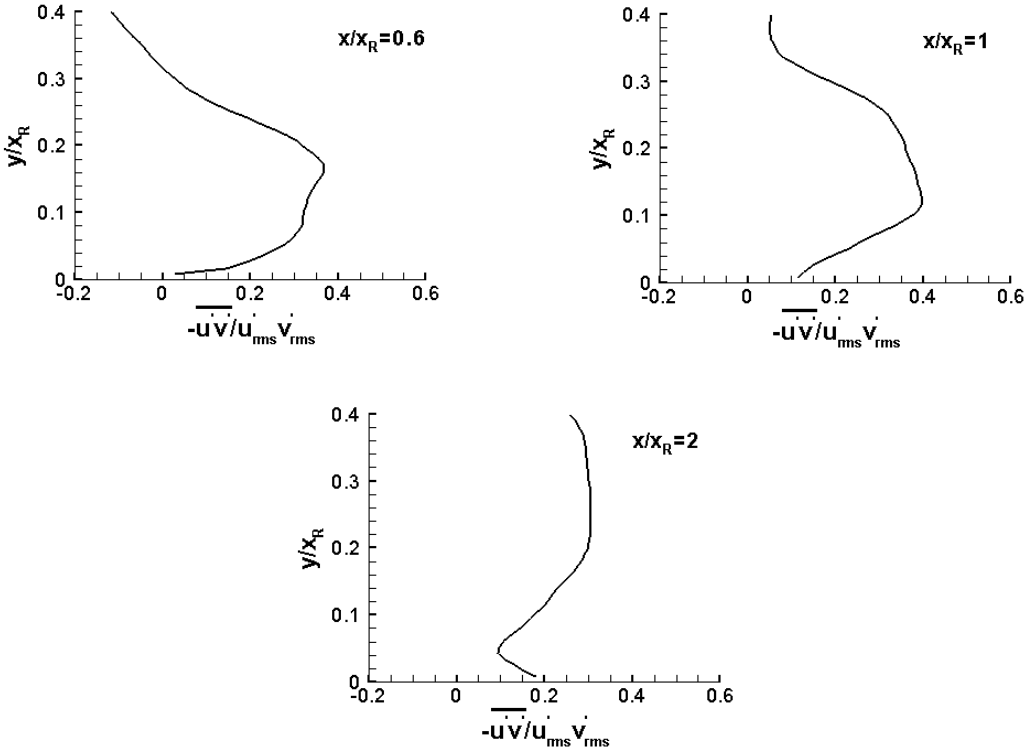

Fig. 7-17. Wall-normal distribution of the correlation coefficient between u'_{rms} and v'_{rms} at three streamwise positions for 3D_case2 with NFST

As shown above, the current LES results for all geometries predict an accurate distribution of the correlation coefficients indicating good agreement with the description of Tafti and Vanka (1991) as regards this topic.

7.2.2.3 Wall-normal vorticity isosurface

Inspection of wall-normal vorticity isosurface presents similar inclined structures that are identified by a streamwise vorticity isosurface as shown in Fig. 7-18 for the flat plate, Fig. 7-19 for 3D_case1 and Fig. 7-20 for 3D_case2, where each presents six wall-normal vorticity isosurfaces taken every 250 time steps.

For the flat plate, significant vortical wall-normal structures appear at x/x_R = 0.45 and become larger when moving toward the mean reattachment line. Finally, these structures break down into smaller turbulent structures further downstream in the turbulent boundary layer as shown in Fig. 7-18

For 3D_case1, it is clear seen that the large wall-normal vortical structures that appear at x/x_R = 0.6 travel downstream and disintegrate into smaller structures at x/x_R = 1.2 as shown in Fig. 7-19. It is also clearly seen that the distance at which the vortical structures in 3D_case1 disintegrate is shorter than that for the flat plate. Similar behaviour is observed for the streamwise vorticity isosurfaces for both geometries. This may indicate that the recovery of the turbulent boundary layer happens much faster in 3D_case1.

The wall-normal vorticity isosurface for 3D_case2 shown in Fig. 7-20 exhibits similar behaviour for the vortical wall-normal structures shown for other two geometries apart from location of the first appearance of these structures. It can be seen that the first appearance of the wall-normal vorticity for 3D_case2 is at about x/x_R = 0.31. These vorticities grow when they are moving downstream. Their growth is associated with the significant three-dimensional motions of the flow. Downstream of the reattachment, the large structures disintegrate into smaller structures but whose sizes are larger than that for 3D_case1.

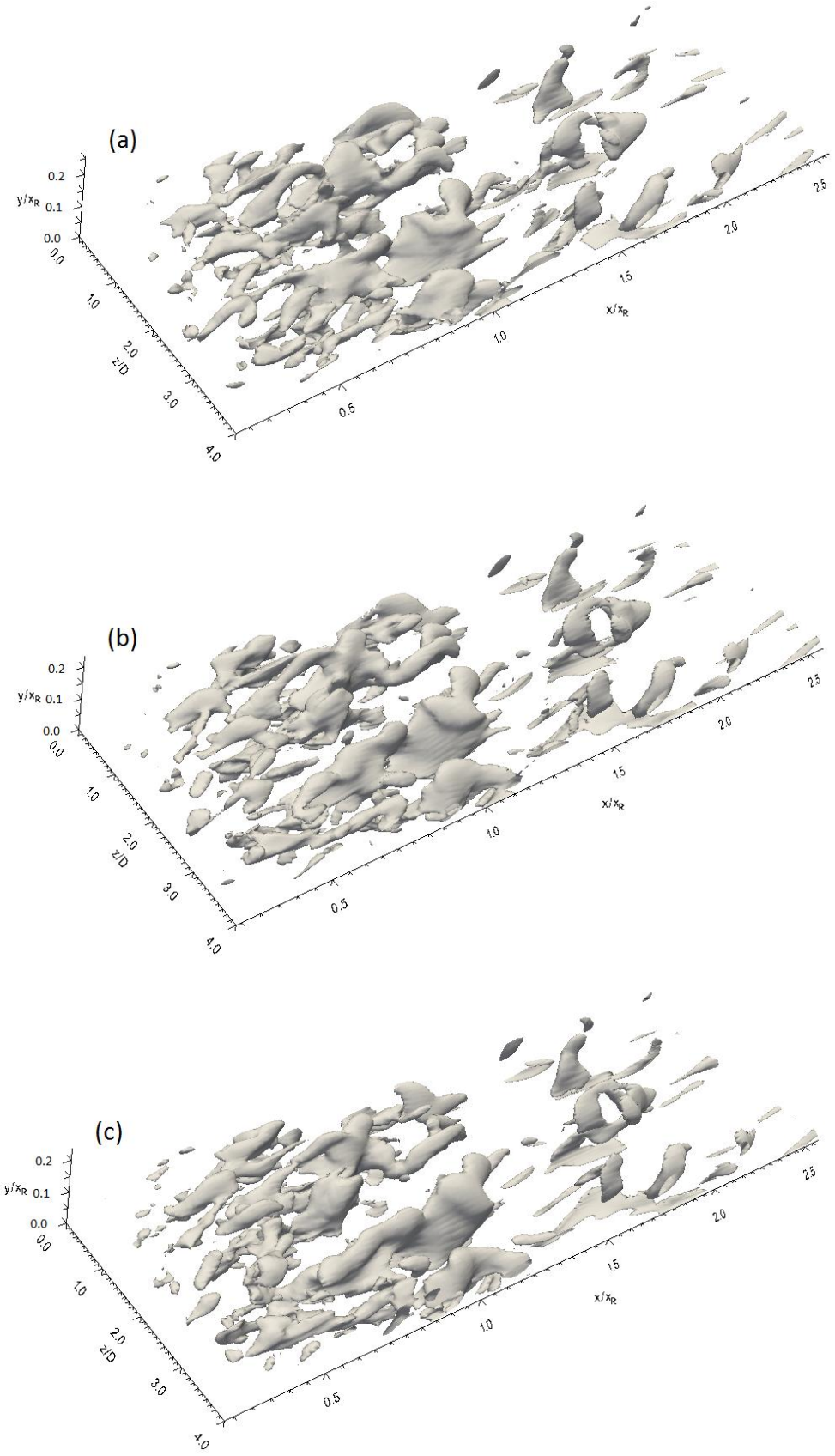

Caption for these figures is on the following page

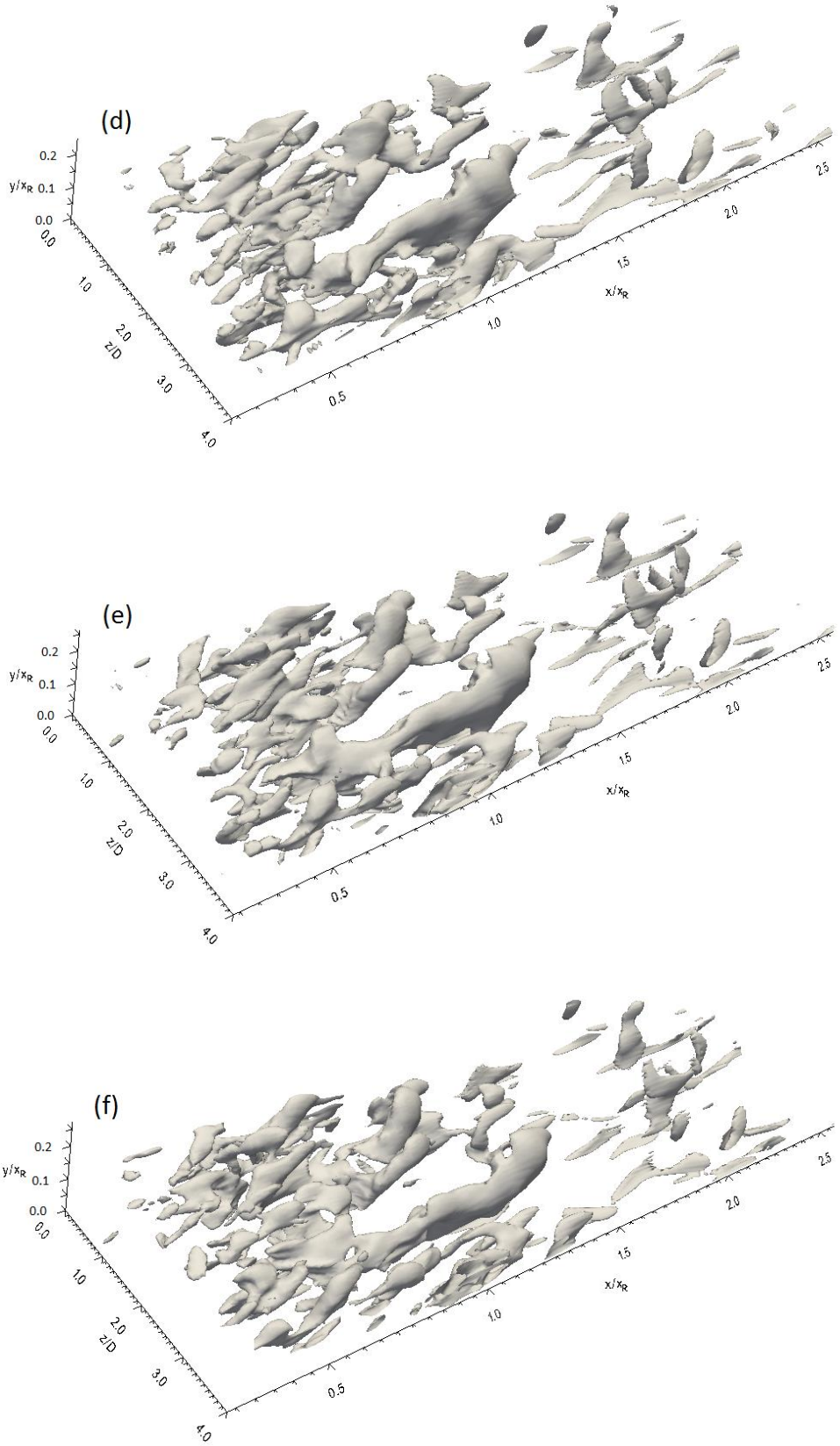

Fig. 7-18. Wall-normal vorticity isosurface at sequential times (every 250 time steps) for the flat plate with NFST

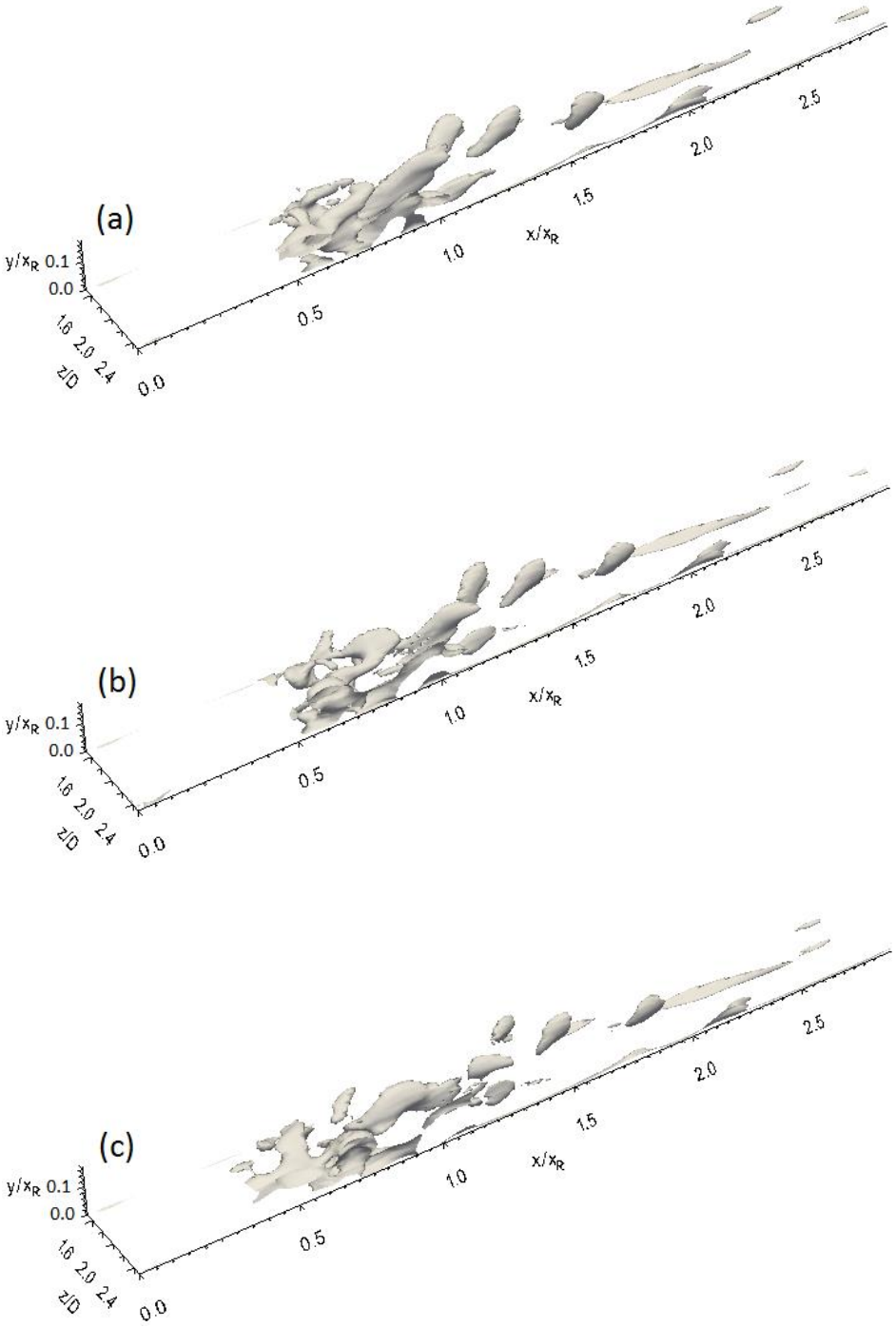

Caption for these figures is on the following page

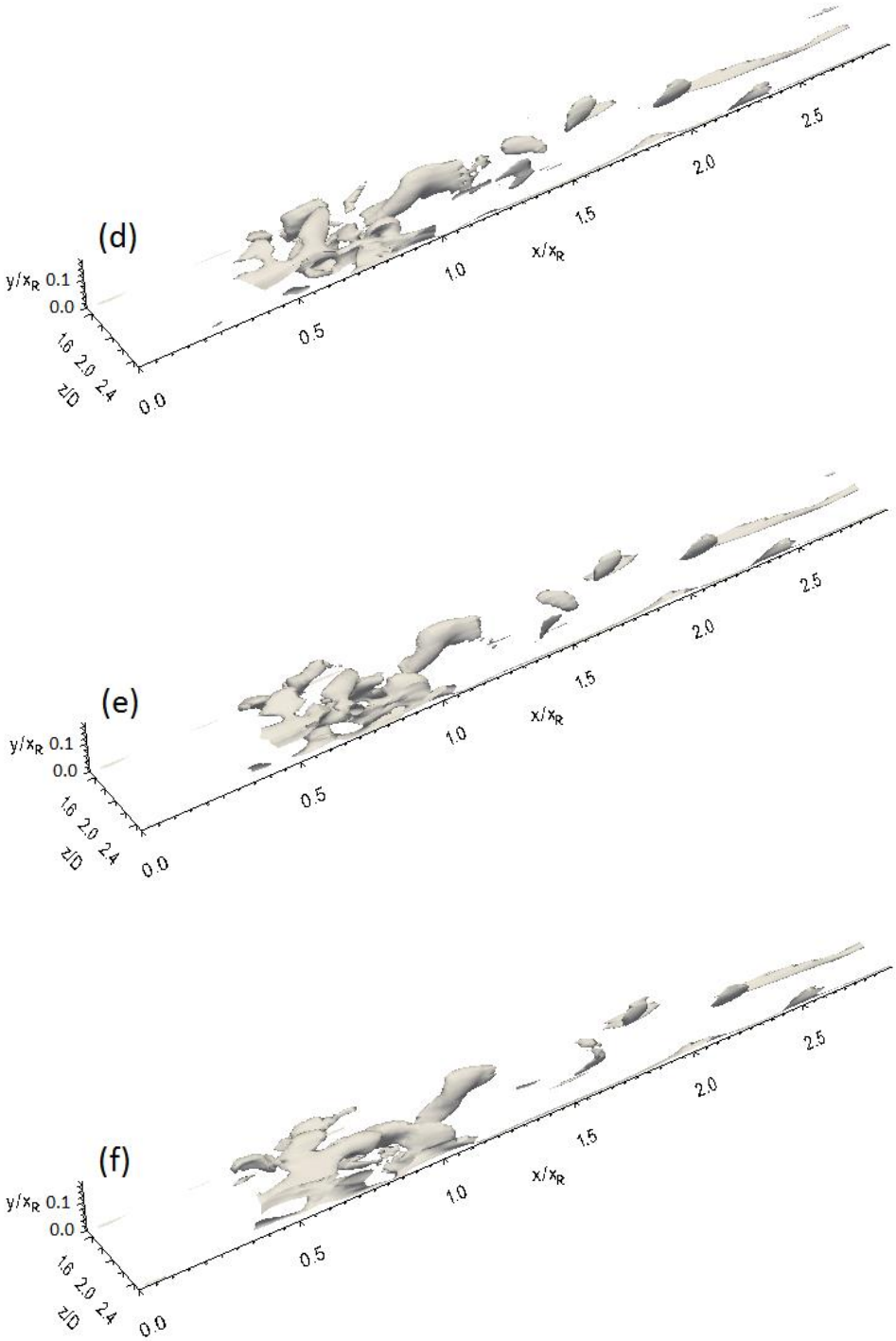

Fig. 7-19. Wall-normal vorticity isosurface at sequential times (every 250 time steps) for 3D_case1 with NFST

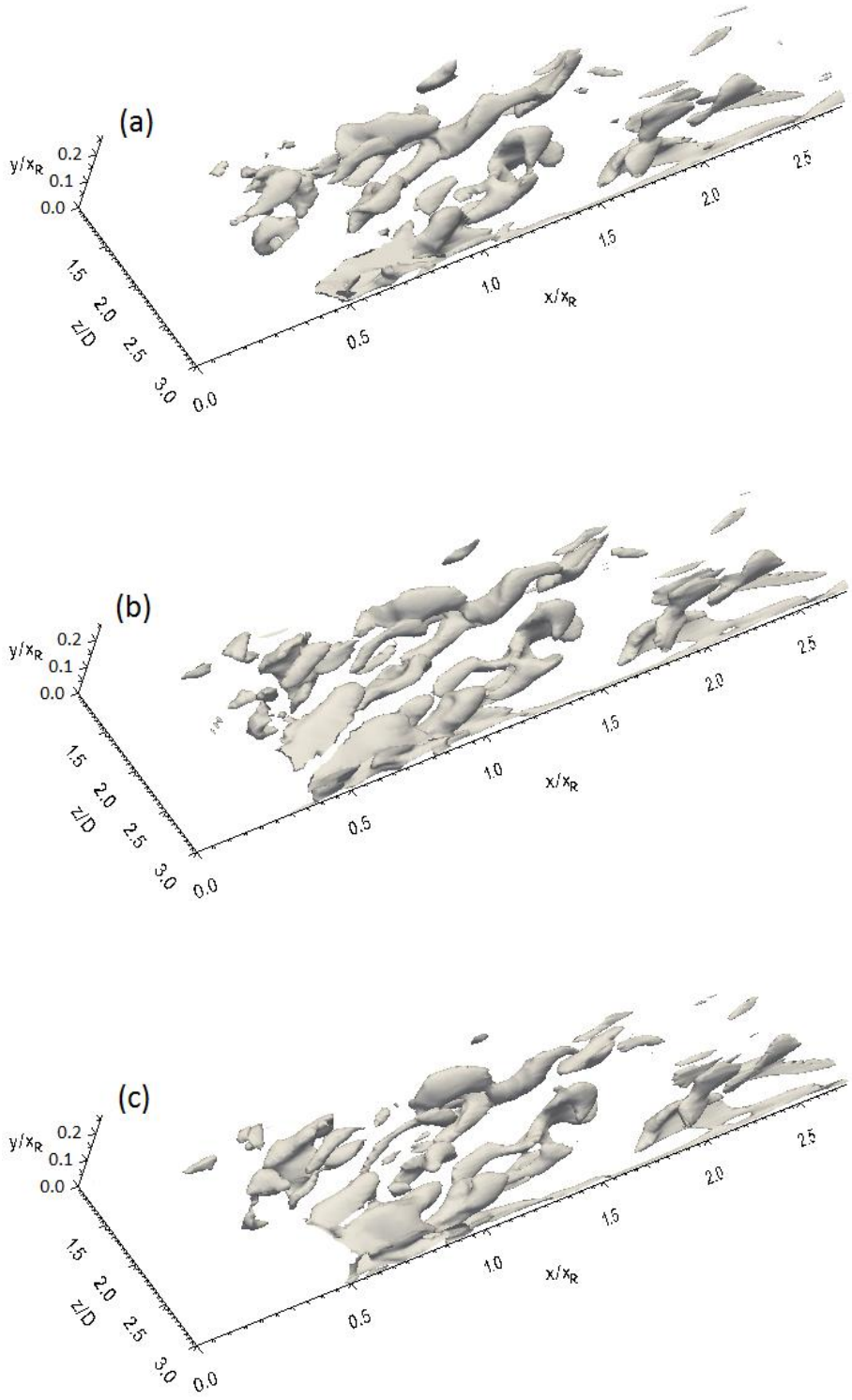

Caption for these figures is on the following page

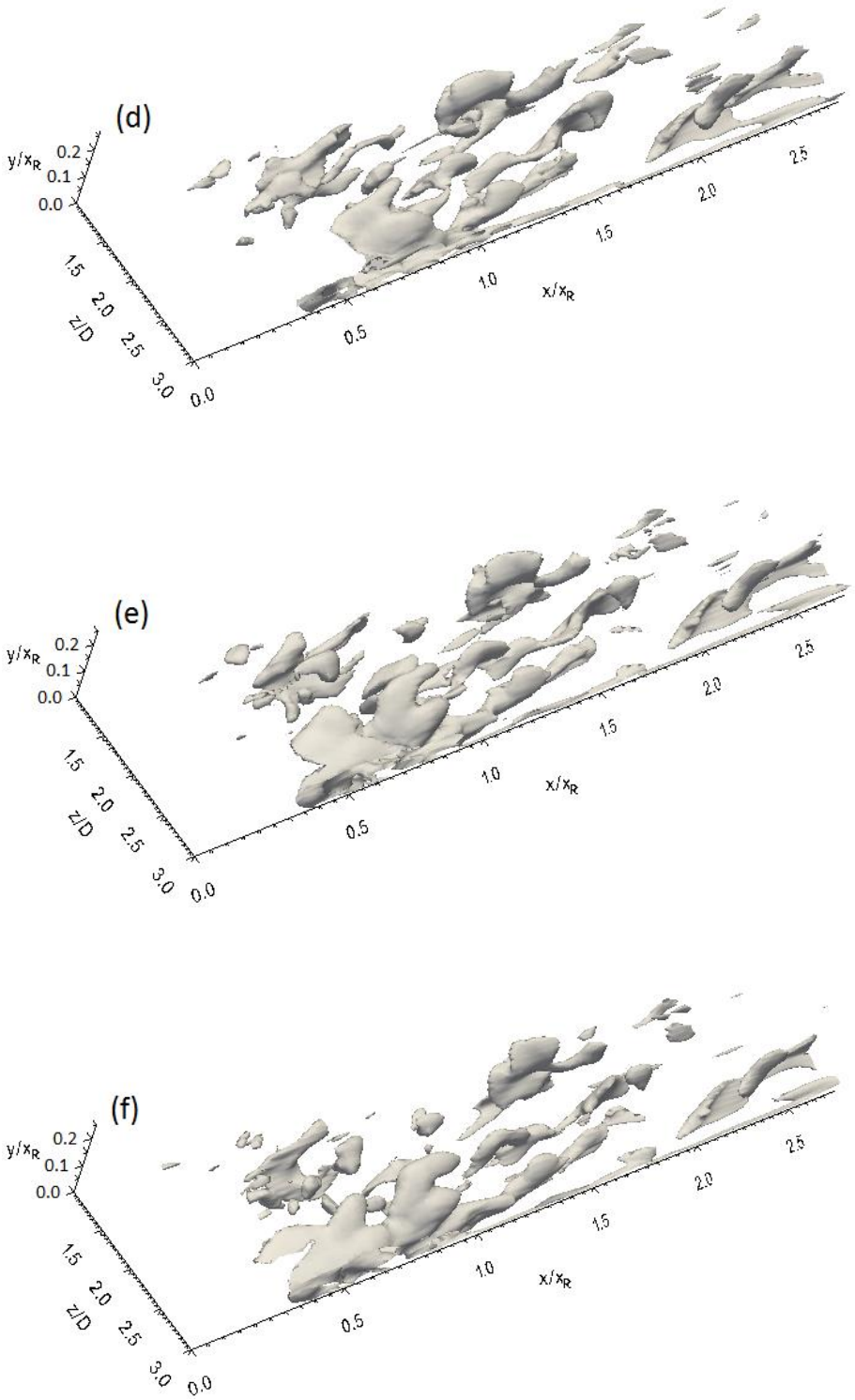

Fig. 7-20. Wall-normal vorticity isosurface at sequential times (every 250 time steps) for 3D_case2 with NFST

7.2.2.4 Spanwise vorticity isosurface

In this section, the spanwise vorticity isosurfaces show the similar conduct to that observed for the streamwise and wall-normal vorticity isosurfaces regarding the locations at which structures appear and subsequently disintegrate.

Sequential spanwise vorticity isosurfaces for the flat plate taken every 250 time steps are shown in Fig. 7-21. It can be clearly seen that the formation of a plane sheet of vorticity starts from the leading edge up to the beginning of unsteadiness position, where the vorticity sheet is uniform up to x/x_R = 0.2. Further downstream, up to x/x_R = 0.45, this sheet shows wrinkling as a result of an increase in disturbance. Further downstream, significant spanwise vorticity structures appear that are associated with violent three-dimensional motions of the flow. Downstream of the mean reattachment line and up to x/x_R = 1.5, the breakdown of large structures into smaller structures is completed.

For 3D_case1, Fig. 7-22 shows the spanwise vorticity isosurface at six sequential times (every 250 time steps). It can be seen that a plane vorticity sheet extends from the leading edge of the geometry to x/x_R = 0.4. Further downstream and up to x/x_R = 0.6, the vorticity sheet develops smoothly with very little distortion. From x/x_R = 0.6 to x/x_R = 1.2, the presence of spanwise vorticity structures can be observed. Beyond x/x_R = 1.2, these structures vanish due to their breakdown into smaller structures within the turbulent boundary layer.

The plane spanwise vorticity sheet appears to be smooth and uniform in the region between the geometry leading edge and the location at which unsteadiness starts (x/x_R = 0 to 0.31) for 3D_case2 as shown in Fig. 7.23, which shows six spanwise vorticity isosurfaces taken every 250 time steps. The symmetry of the vorticity sheet breaks down at about x/x_R = 0.6, indicating the start of violent three-dimensional motions of the flow. Further downstream, large vorticity structures that appear around the mean reattachment line can be barely observed beyond x/x_R = 1.5 indicating their disintegration into smaller turbulent structures.

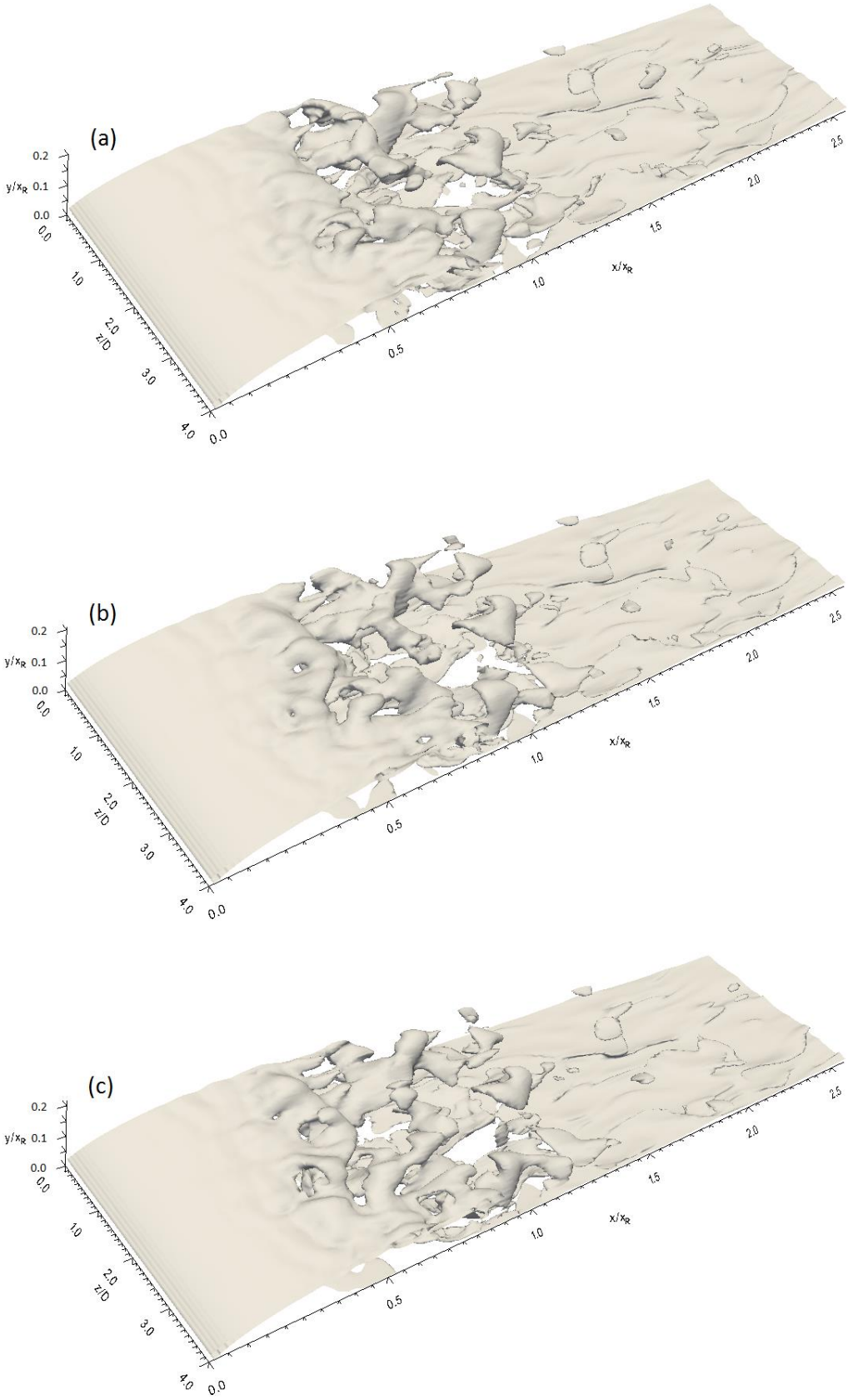

Caption for these figures is on the following page

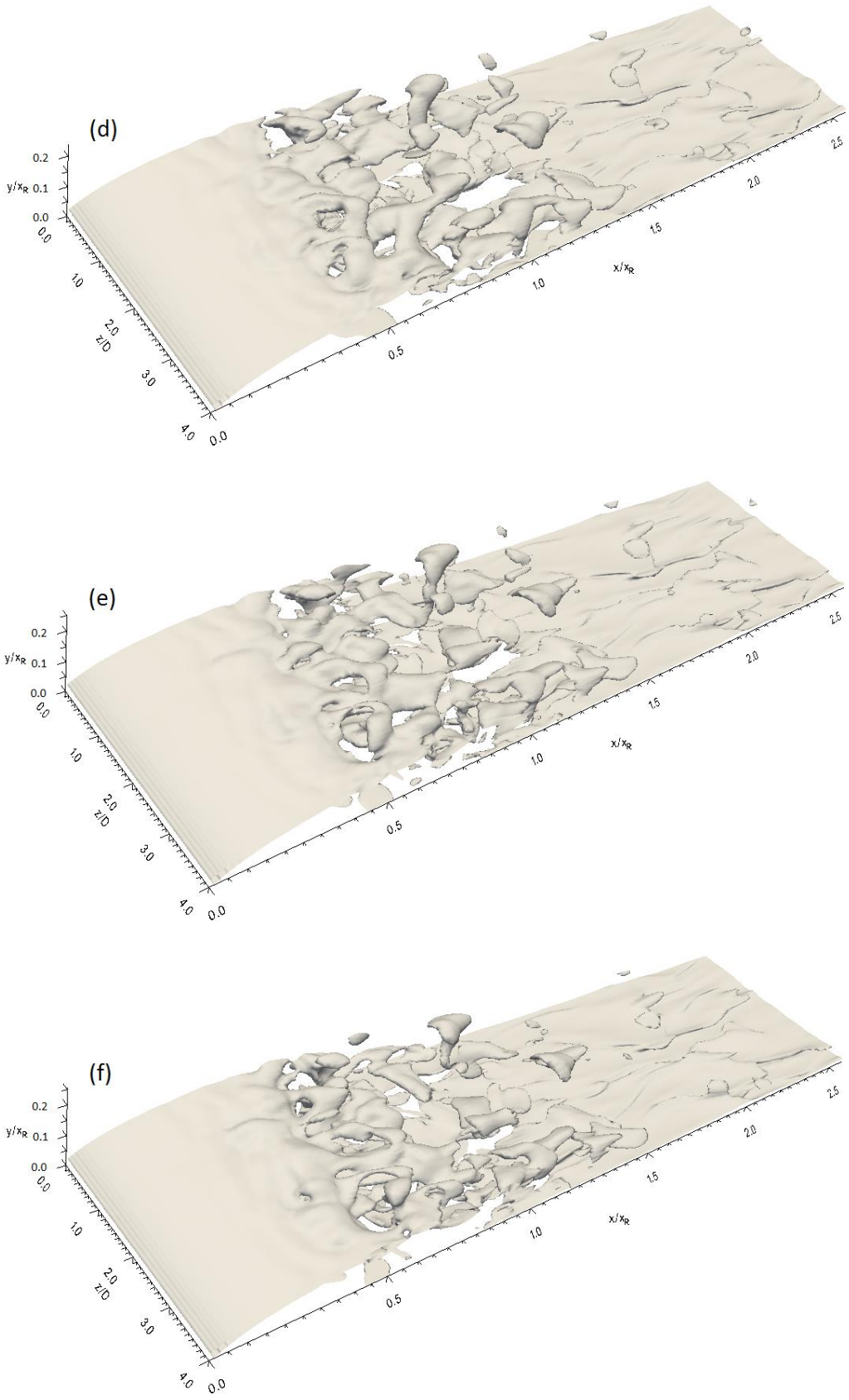

Fig. 7-21. Spanwise vorticity isosurface at sequential times (every 250 time steps) for the flat plate with NFST

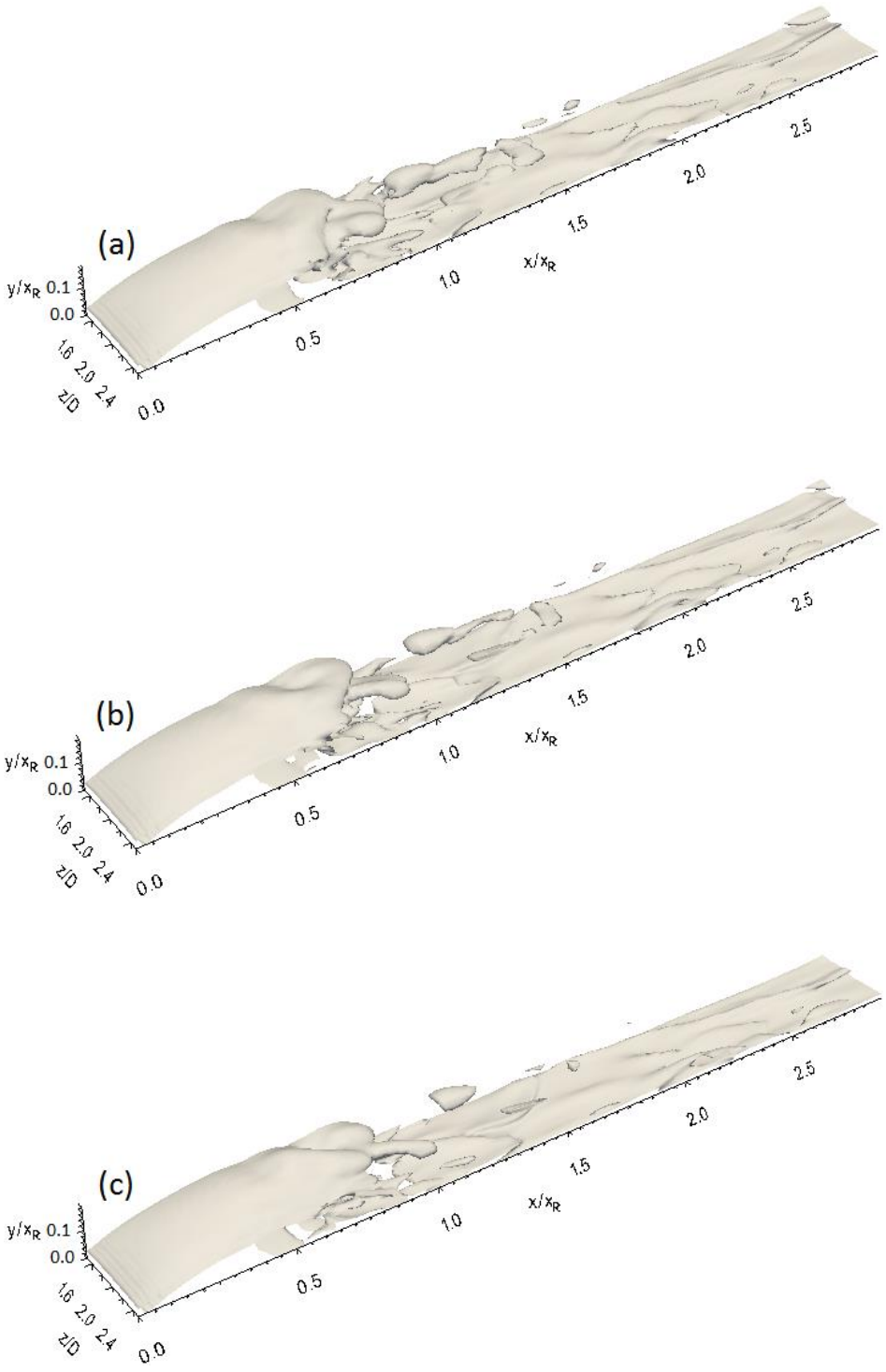

Caption for these figures is on the following page

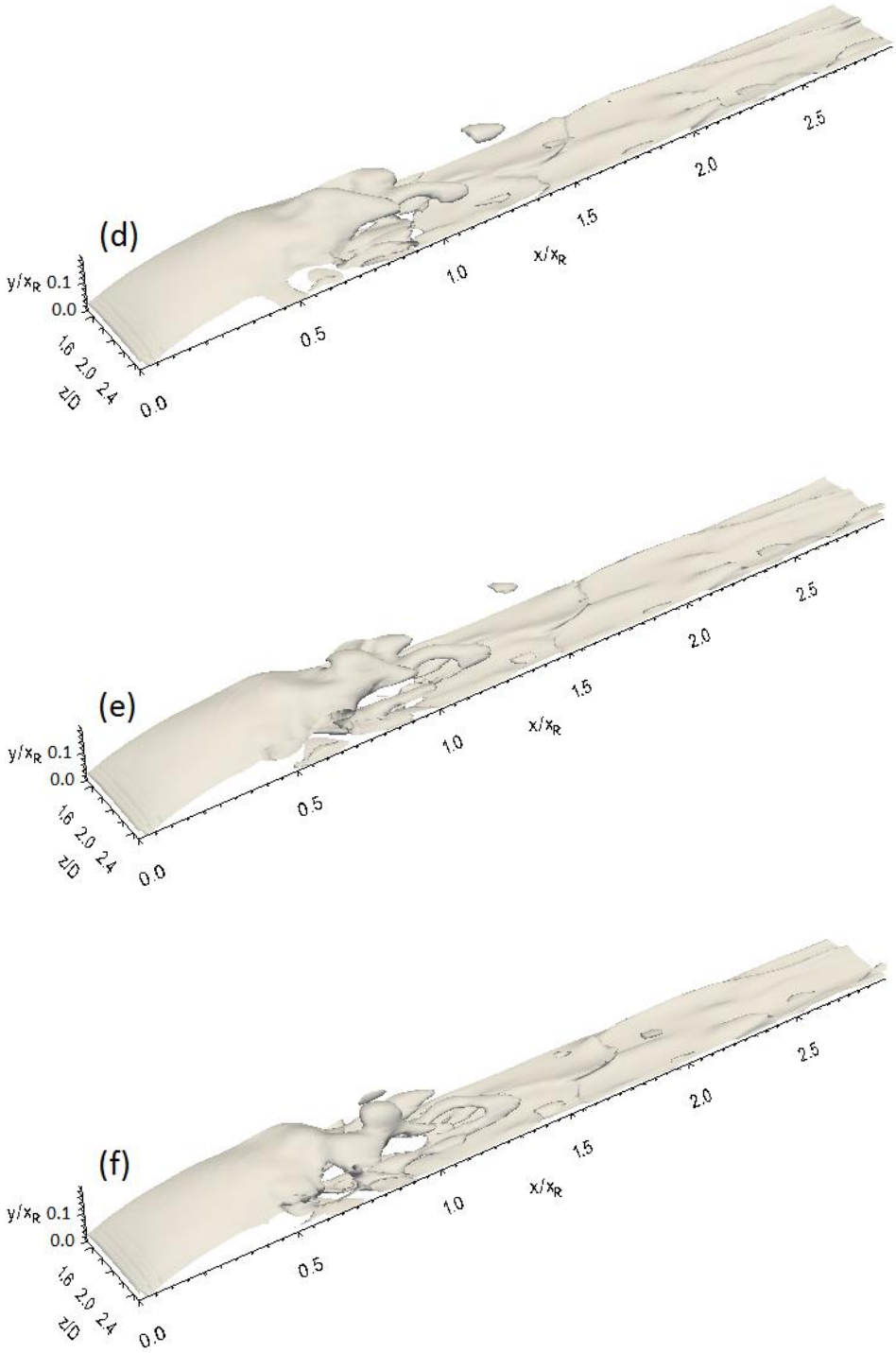

Fig. 7-22. Spanwise vorticity isosurface at sequential times (every 250 time steps) for 3D_case1 with NFST

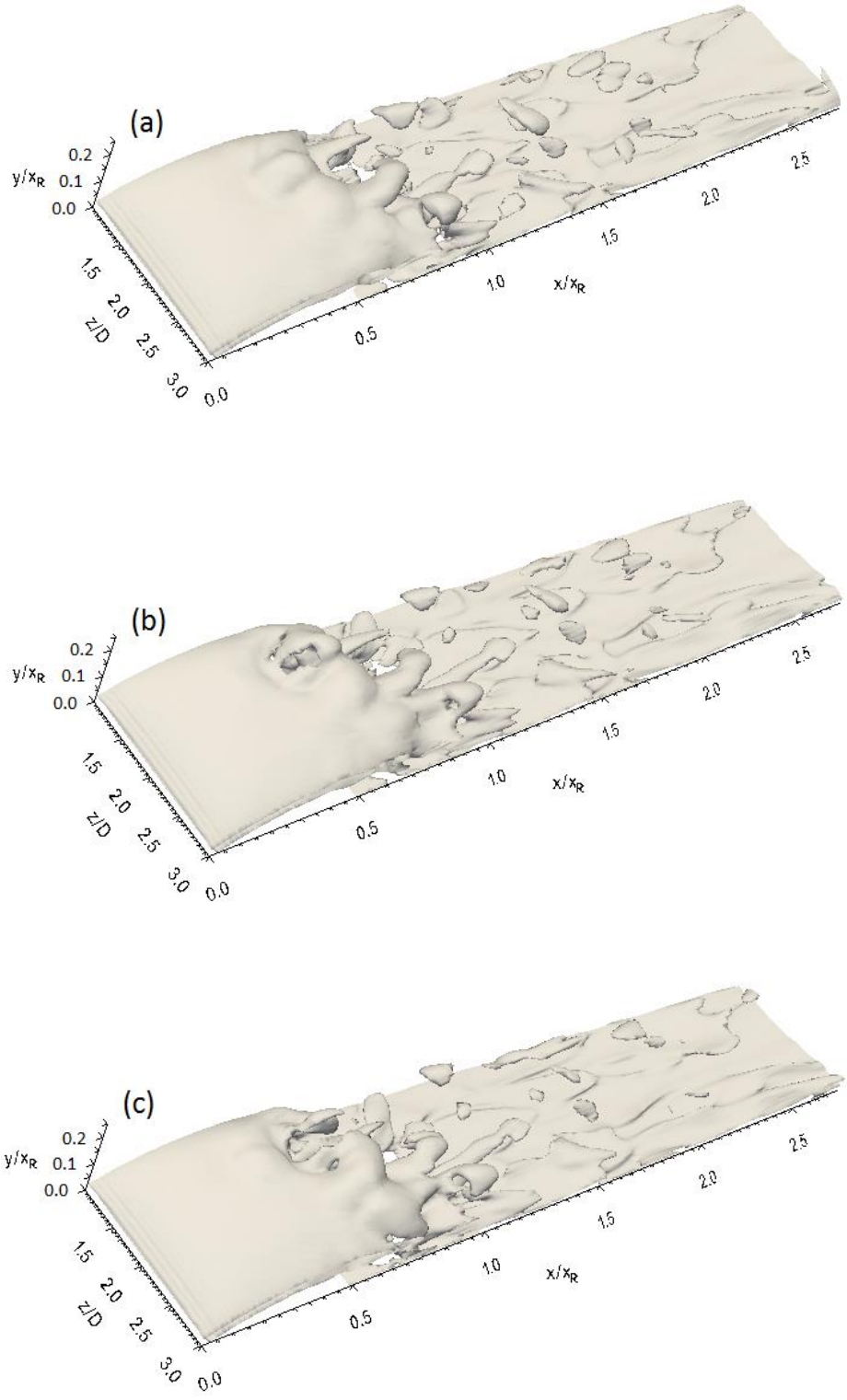

Caption for these figures is on the following page

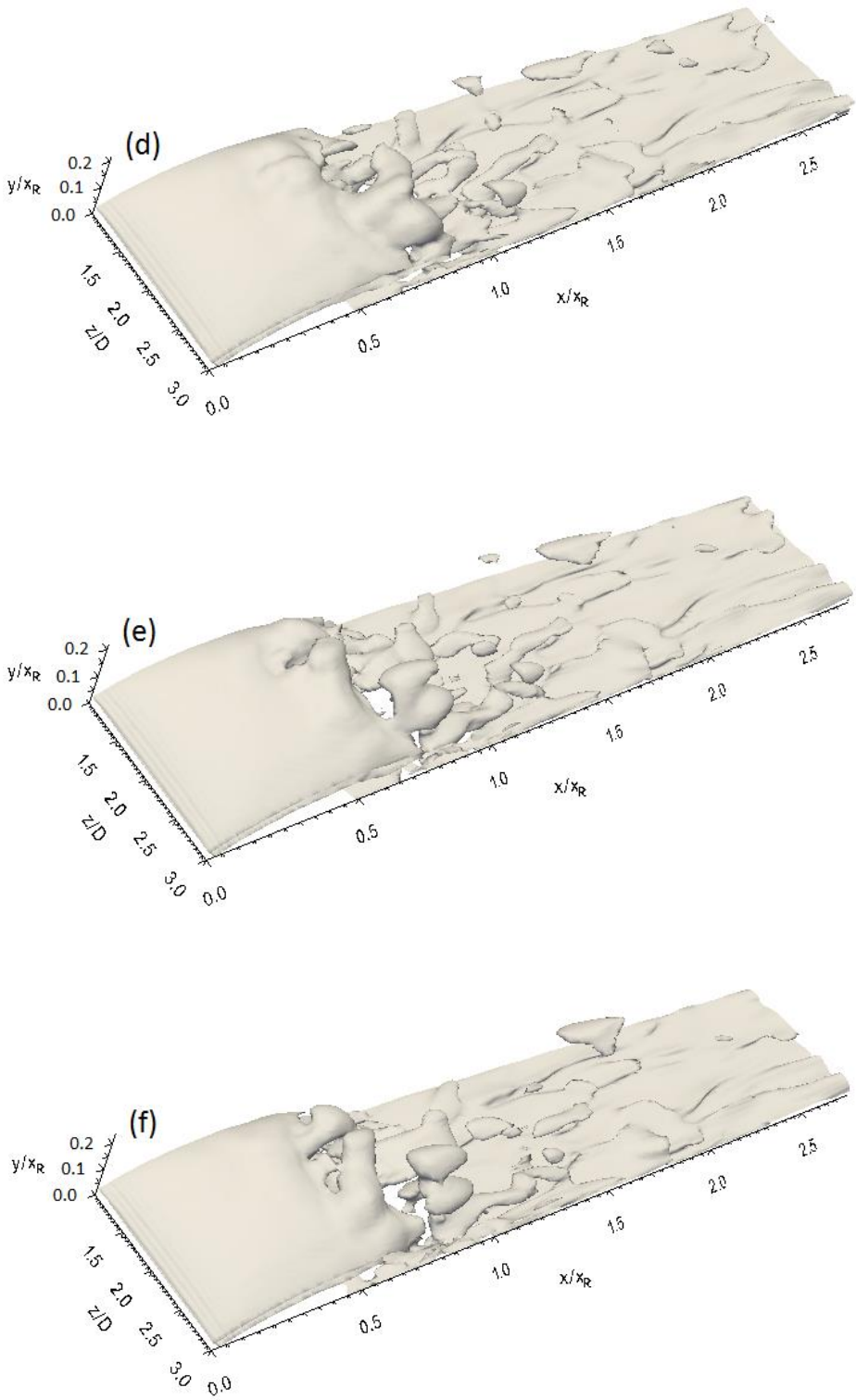

Fig. 7-23. Spanwise vorticity isosurface at sequential times (every 250 time steps) for 3D_case2 with NFST

It is worth pointing out that the flow visualizations performed by employing vorticity field isosurfaces studied here show significant appearance of vortical streamwise, wall-normal and spanwise structures in the second half of the separation bubble. In addition, disintegration of these structures in the turbulent boundary layer can be also observed. Two-dimensional Kelvin-Helmholtz rolls and their development to three-dimensional hairpin structures are not illustrated in these isosurfaces, while all or some of these structures are clearly shown by the low pressure isosurface and vorticity magnitude isosurface, as previously demonstrated. However, the main purpose for using the vorticity field isosurface is to illustrate the disintegration of large structures within the turbulent flow and the distance to the turbulent boundary layer recovery associated with the breakdown of large coherent structures into small turbulent structures.

In general, the evolution of the coherent structures from being two-dimensional to three-dimensional in nature is not well represented by the vorticity magnitude and vorticity components isosurfaces. This is considered to be a shortcoming in these flow visualization schemes, which are thus not considered suitable to describe the evolution of the coherent structures.

7.2.3 Q-criterion isosurface

The flow visualization technique that shares some of the properties with the vorticity and pressure criterion is called the Q-criterion, or second invariant of velocity gradient tenser (Δu) (Hunt et al., 1988). The Q-criterion is defined as:

$$Q = \frac{1}{2}(\Omega_{ij}\Omega_{ij} - S_{ij}S_{ij}) \tag{7-1}$$

where ($\Omega_{ij}\Omega_{ij}$) is the rotation (vorticity) rate and ($S_{ij}S_{ij}$) is the strain rate, where the Q-criterion represents the balance between them.

The antisymmetric component (Ω_{ij}) of Δu is:

$$\Omega_{ij} = \frac{u_{i,j} - u_{j,i}}{2} \tag{7-2}$$

and the symmetric component (S_{ij}) of Δu is:

$$S_{ij} = \frac{u_{i,j} + u_{j,i}}{2} \quad (7\text{-}3)$$

Applying the Q-criterion technique in the instance of the flat plate is illustrated in Fig. 7-24, which shows six Q-criterion isosurfaces taken every 250 time steps. Two-dimensional Kelvin-Helmholtz rolls are apparent in the first half of the separation bubble, while the second half is characterized by the three-dimensional hairpin structures.

Despite the merging of two Kelvin-Helmholtz rolls only being captured with some difficulty when employing Q-criterion isosurfaces, this stage of coherent structure development is shown in Figs. 7-24a and 7-24e. The clarity of this process is lower than that presented via the low pressure isosurface. However, the new large two-dimensional structure that formed as a consequence of the merging process is clearly located close to $x/x_R = 0.5$ as shown in Fig. 7-24.

The hairpin structures formation is a result of a rapid breakdown of the Kelvin-Helmholtz structures as shown in Fig. 7-24. The direct breakdown of the Kelvin-Helmholtz rolls into numerous three-dimensional hairpin vortices at a location around $x/x_R = 0.6$ can be clearly seen in Figs. 7-24a and 7-24e, and also at further than $x/x_R = 0.6$, as shown in Fig. 7-24c, where a structure with an axis perpendicular to the flow direction is observed up to $x/x_R = 0.65$.

Hairpin structures move downstream and pass the mean reattachment line to shed to the turbulent boundary layer. Further downstream at $x/x_R = 1.5$, hairpin structures lose their shape and break down into smaller turbulent structures as shown in Figs. 7-24b and 7-24d. In addition, some of the hairpin structures break down into smaller structures within the separation bubble, indicating that the flow transforms to being turbulent in nature before the mean reattachment line.

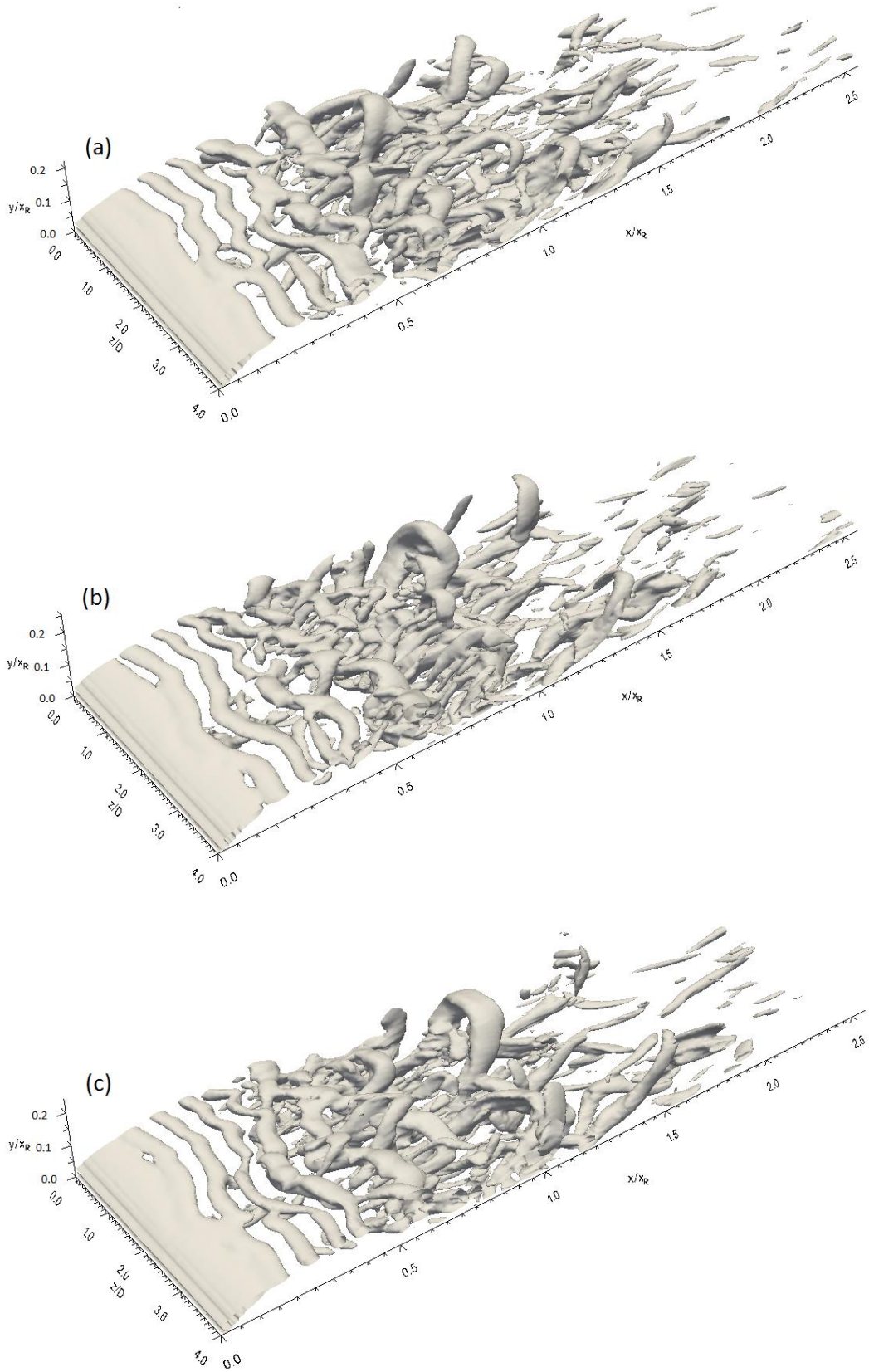

Caption for these figures is on the following page

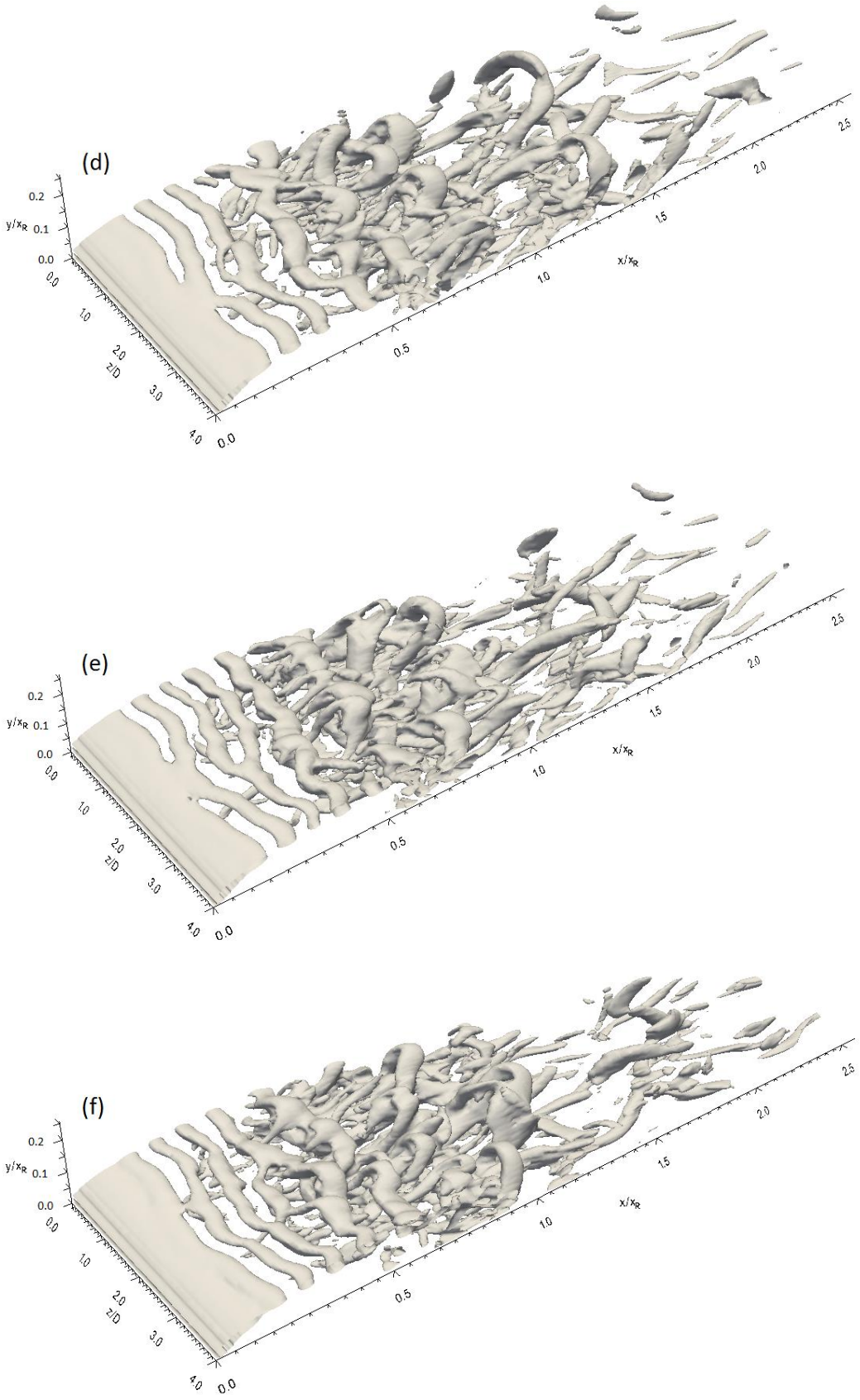

Fig. 7-24. Q-criterion isosurface at sequential times (every 250 time steps) for the flat plate with NFST

Q-criterion isosurfaces for 3D_case1 are presented every 250 time steps as shown in Fig. 7-25. Formation of the Kelvin-Helmholtz rolls and their shedding from the separated shear layer at around x/x_R = 0.45 is clearly seen. These rolls move downstream and improve topologically to become hairpin structures in the region between x/x_R = 0.7 and around the mean reattachment line. It can be seen that there is no merging or pairing of two Kelvin-Helmholtz rolls in 3D_case1. Once the Kelvin-Helmholtz roll has shed to the separated layer, it develops to form one hairpin structure while convicting downstream. Hairpin structures shed to the reattached turbulent boundary layer and travel a certain distance before their disintegration into smaller turbulent structures.

Some of the hairpin structures lose their coherency and break down before the mean reattachment line as shown for structure *A* in Figs. 7-25b and 7.25c. In Fig. 7-25b, structure *A* is a hairpin structure at about x/x_R = 0.8. This structure disintegrates into smaller turbulent structures at slightly downstream of x/x_R = 0.8 as shown in Fig. 7-25c, indicating that the flow becomes turbulent before the mean reattachment line.

Development of coherent structures of the transitional separated-reattached flow in the top and side surfaces of 3D_case1 can be seen in Fig. 7-26, which shows a number of Q-criterion isosurfaces taken every 250 time steps. The presence of a twisting structure around this geometrical shape can be seen just downstream of the laminar separated layer as shown in Fig. 7-26b. The rectangular ring structure breaks down into separated Kelvin-Helmholtz rolls on each surface as shown in Fig. 7-26d. These rolls develop topologically to form hairpin structures in the second half of the separation bubble. Further downstream, three-dimensional hairpin structures that shed to the turbulent reattached flow disintegrate into smaller structures. The above coherent structure development indicates that there is a similar development of coherent structures on each surface of 3D_case1.

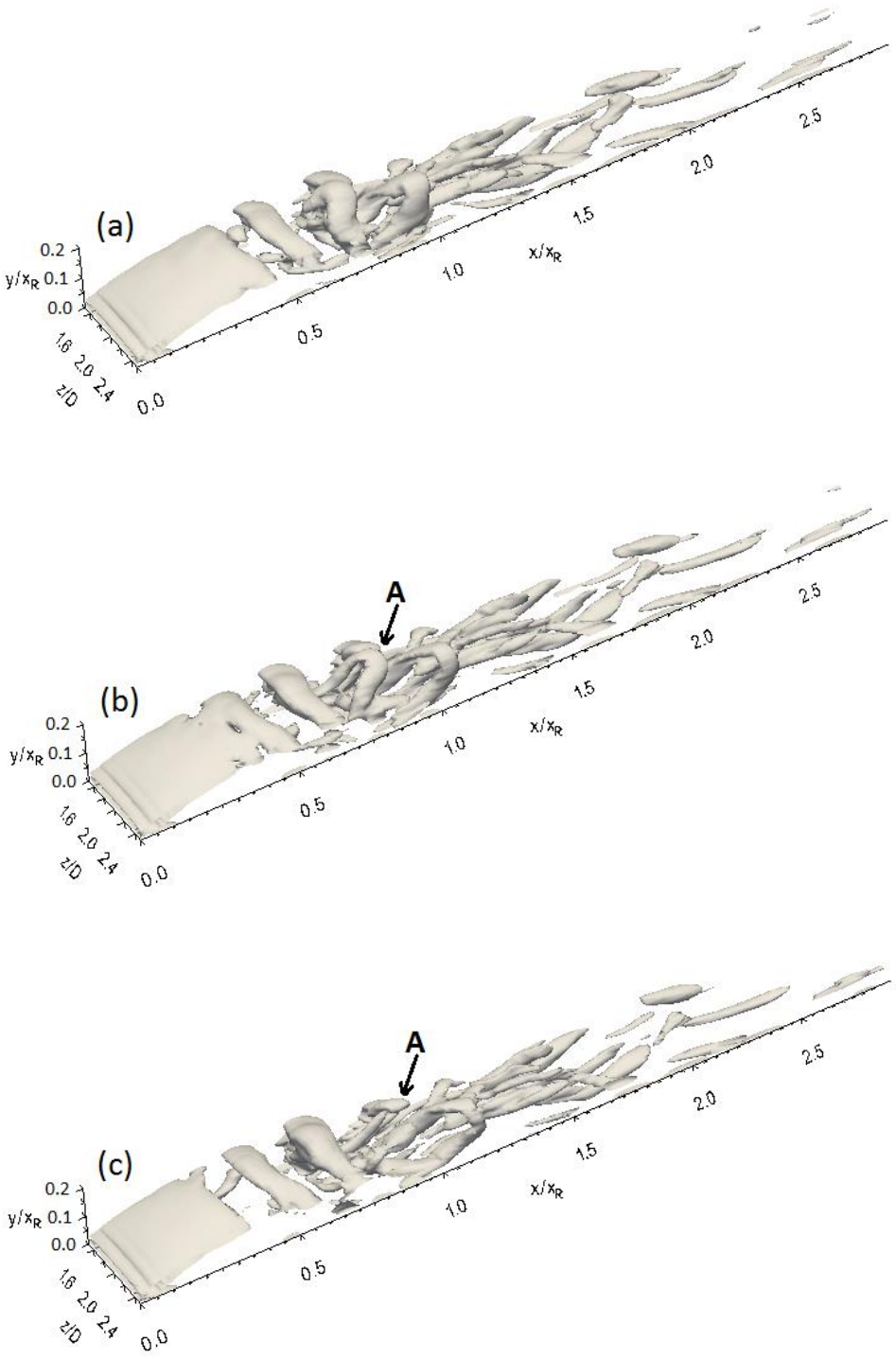

Caption for these figures is on the following page

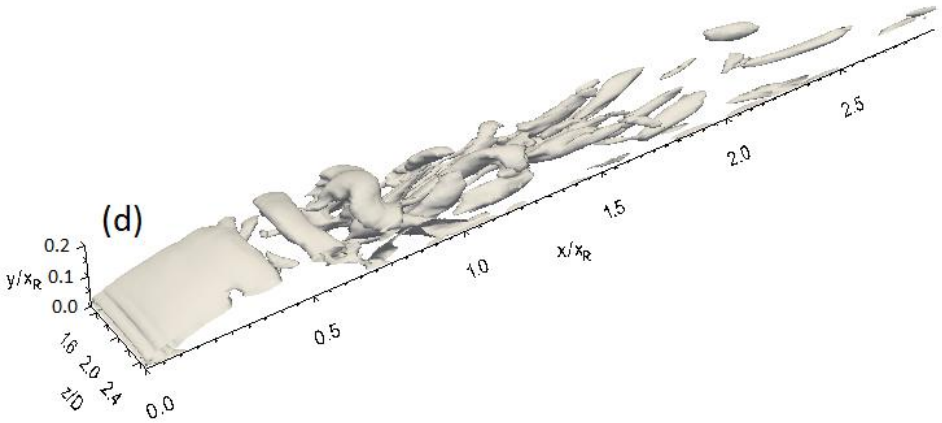
(d)
0.2
y/x_R 0.1
0.0
1.6 2.0 2.4
z/D
0.0
0.5
1.0
1.5
2.0
2.5
x/x_R

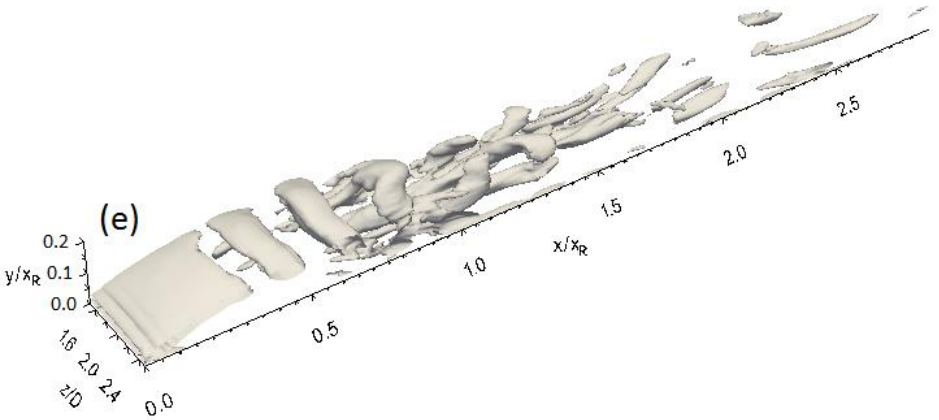
(e)
0.2
y/x_R 0.1
0.0
1.6 2.0 2.4
z/D
0.0
0.5
1.0
1.5
2.0
2.5
x/x_R

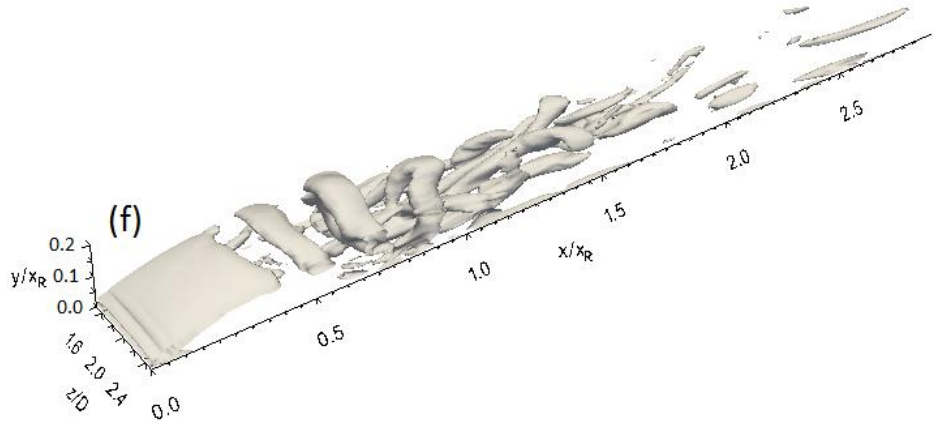
(f)
0.2
y/x_R 0.1
0.0
1.6 2.0 2.4
z/D
0.0
0.5
1.0
1.5
2.0
2.5
x/x_R

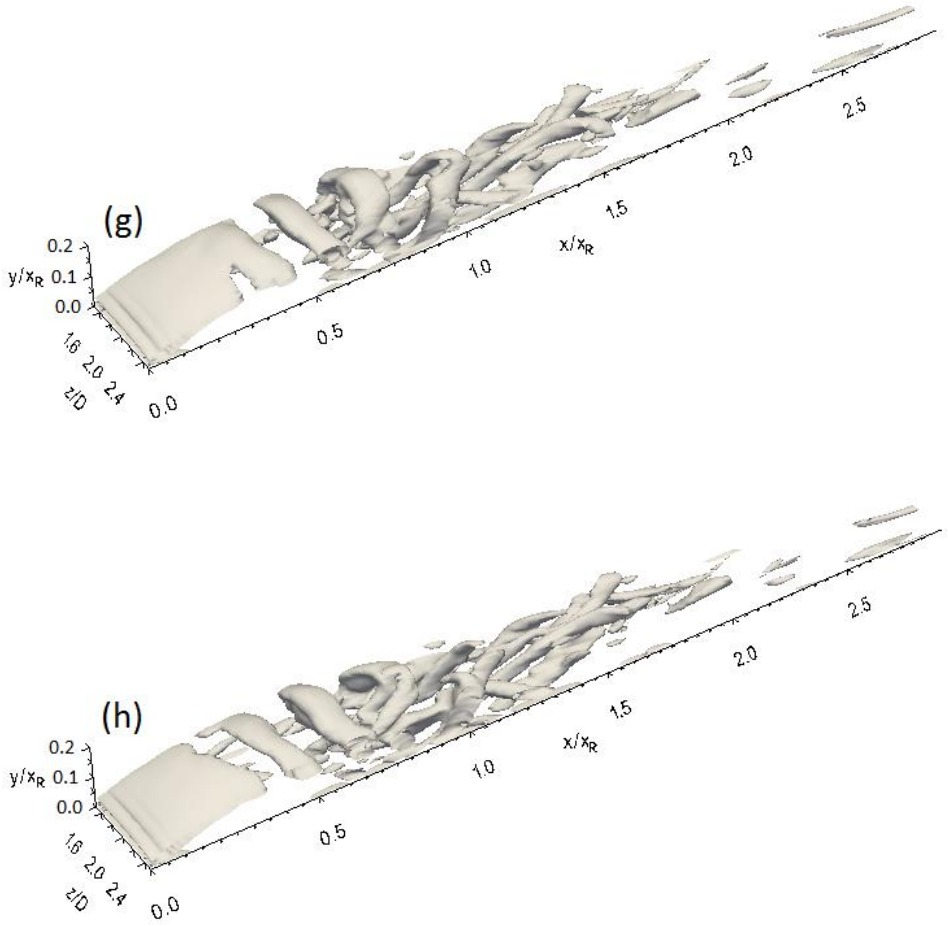

Fig. 7-25. Q-criterion isosurface at sequential times (every 250 time steps) for 3D_case1 with NFST

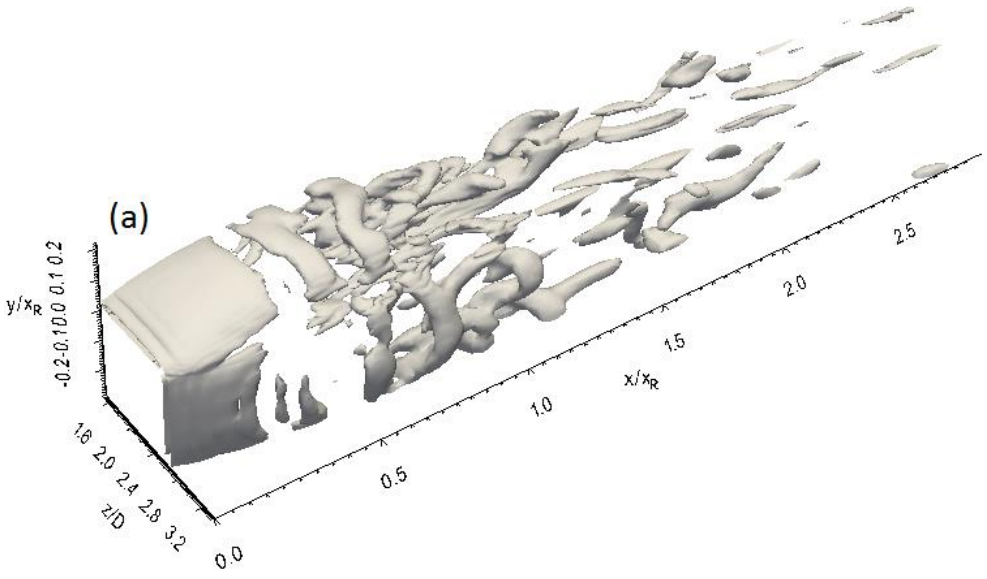

Caption for this figure is on the following page

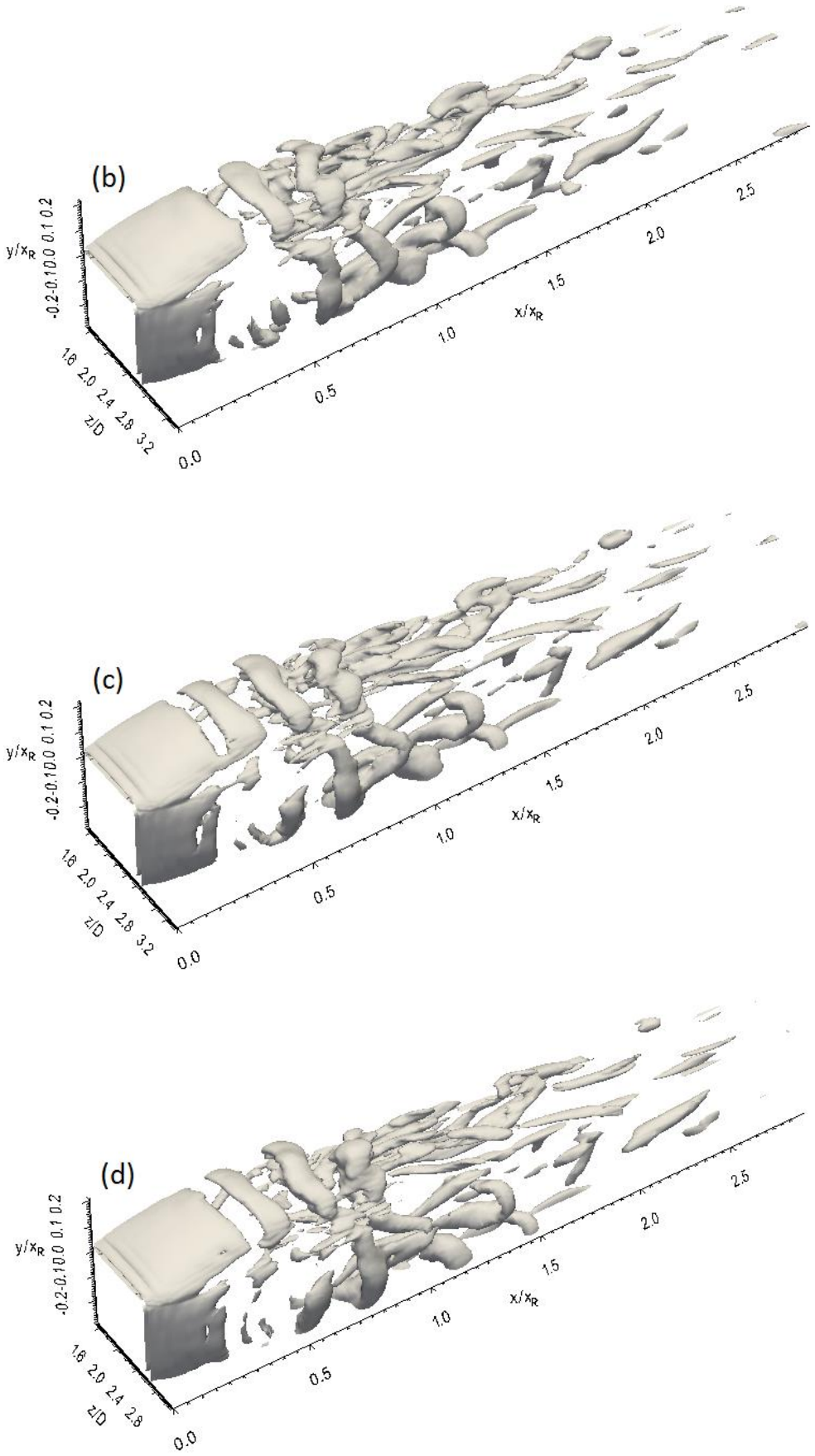
(b)
(c)
(d)
y/x_R
-0.2 -0.1 0.0 0.1 0.2
x/x_R
0.0 0.5 1.0 1.5 2.0 2.5
z/D
1.6 2.0 2.4 2.8 3.2

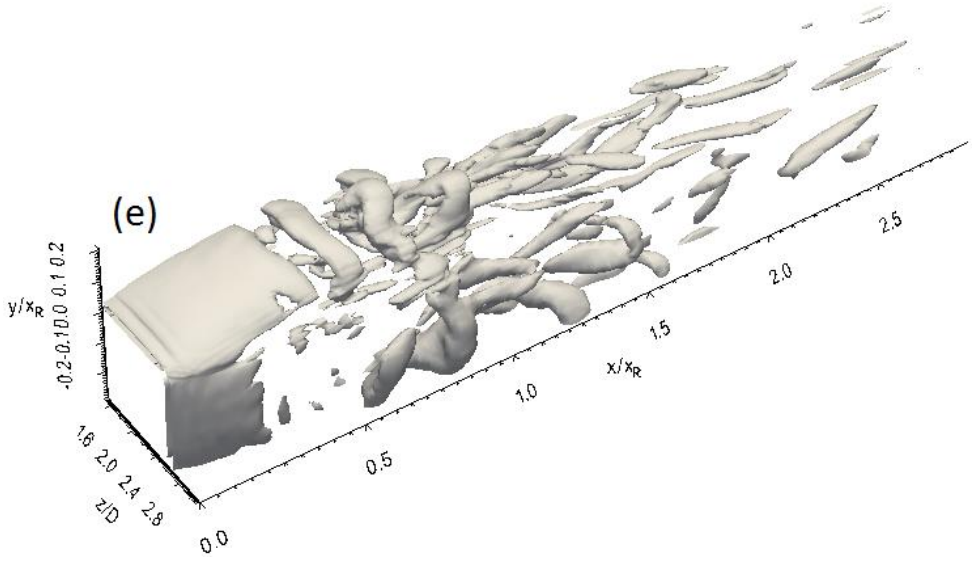
(e)
y/x_R
-0.2 -0.1 0.0 0.1 0.2
z/D
1.6 2.0 2.4 2.8
x/x_R
0.0 0.5 1.0 1.5 2.0 2.5

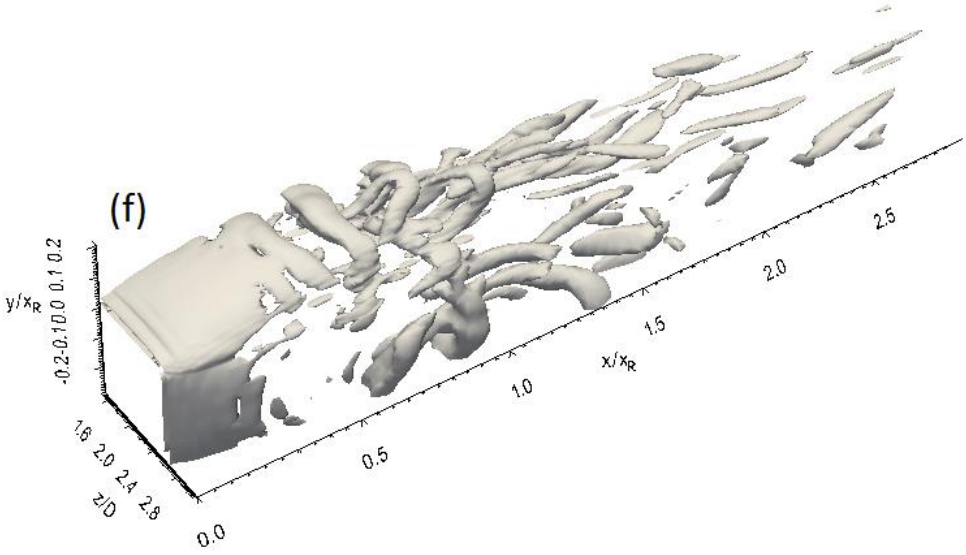
(f)
y/x_R
-0.2 -0.1 0.0 0.1 0.2
z/D
1.6 2.0 2.4 2.8
x/x_R
0.0 0.5 1.0 1.5 2.0 2.5

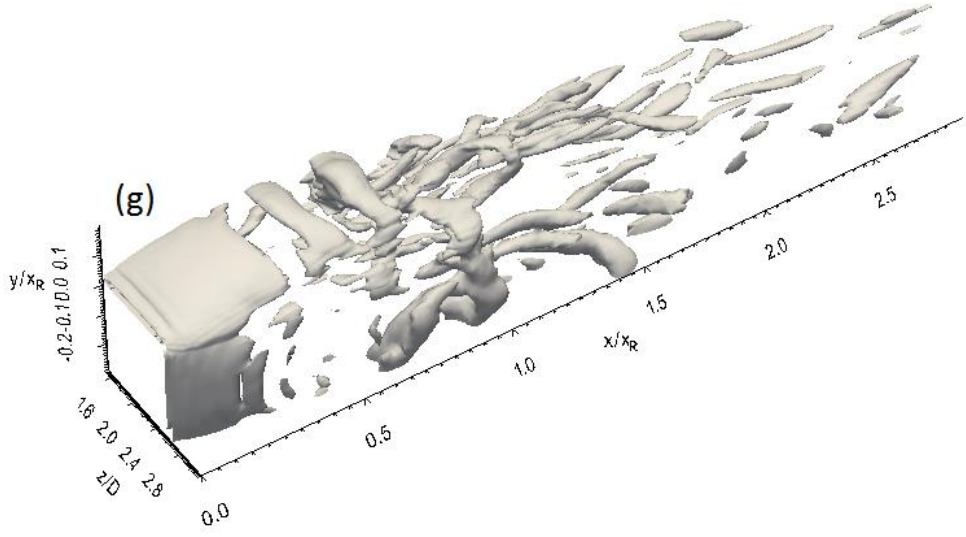
(g)
y/x_R
-0.2 -0.1 0.0 0.1
z/D
1.6 2.0 2.4 2.8
x/x_R
0.0 0.5 1.0 1.5 2.0 2.5

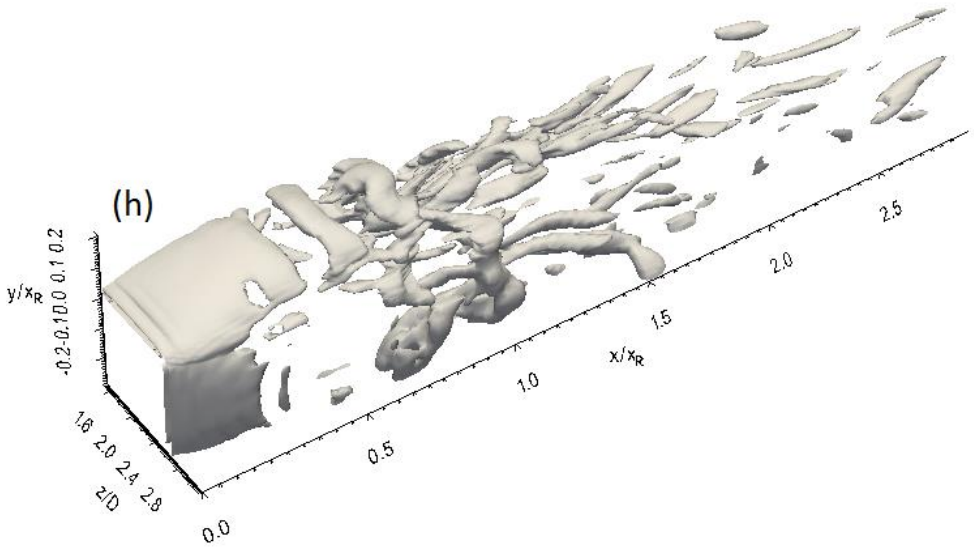

Fig. 7-26. Q-criterion isosurface on the top and side surfaces at sequential times (every 250 time steps) for 3D_case1 with NFST

Kelvin-Helmholtz rolls that shed downstream of x/x_R = 0.3 in 3D_case2 are clearly shown in Fig. 7-27, which shows sequential Q-criterion isosurfaces taken every 250 time steps. These rolls move downstream to the second half of the separation bubble and break down into streamwise hairpin structures around x/x_R = 0.8 as shown in Fig. 7-27e, where the breakdown of Kelvin-Helmholtz rolls is shown. Around the mean reattachment line and further downstream, hairpin structures break down into smaller turbulent structures. It is clearly shown in Fig. 7-27 that some of streamwise structures still maintain their coherency up to x/x_R = 1.5, indicating that recovery of the turbulent boundary layer may take a long distance to be achieved.

It is interesting to observe that in the Q-criterion snapshots presented in Fig. 7-27 for 3D_case2, there are no vortex merging processes that can be captured, unlike for the flat plate. In addition, topological improvement from the Kelvin-Helmholtz structure to hairpin structure, which clearly occurs for 3D_case1, is absent in 3D_case2, where hairpin vortices are formed by direct breakdown of Kelvin-Helmholtz rolls. Therefore, coherent structure development in transitional separated-reattached flow in 3D_case2 shares with some aspects of coherent structure development in the flat plat and 3D_case1. The similarity between the flat plate and 3D_case2 is the direct breakdown of Kelvin-

Helmholtz rolls into hairpin structures, while there are no structures merging through the transition for either 3D_case1 or 3D_case2.

Q-criterion isosurfaces, taken every 250 time steps, on the top and side surfaces of 3D_case2 are shown in Fig. 7-28. The twisting nature of the coherent structures in the early stages of the transition are clearly shown in Fig. 7-28a and 7-28b. Then, there are four Kelvin-Helmholtz rolls that move on each surface of 3D_case2. The Kelvin-Helmholtz structure on the top surface of 3D_case2 breaks down into hairpin structures as shown in Fig. 7-28. The Kelvin-Helmholtz rolls on the side surface of 3D_case2 seem to be within a topological development in transforming to hairpin structures, where there is no sign of breakdown of the Kelvin-Helmholtz structure into hairpin structures as shown in Fig. 7-28. However, on both the top and side surfaces of 3D_case2, there are evident hairpin structures that move up to x/x_R = 1.5. At this location onwards, these streamwise structures distort through its breakdown into smaller structures leading to the disintegration of its coherent hairpin shape as shown in Figs. 7-28e, f, and g.

It can be concluded from the above observation that the development of coherent structures on the top surface of 3D_case2 is different from that on the side surface of this geometry. This is considered to be another difference related to effect of the aspect ratio of the three-dimensional geometry on coherent structure development in transitional separated-reattached flow. Using the Q-criterion isosurface to identify coherent structures development on a three-dimensional geometry shows that this development is similar on both the top and side surfaces of 3D_case1, while the development of coherent structures on the top surface of 3D_case2 is different from that on the side surface of this geometry.

In general, it can be concluded in the current study that the low pressure isosurface illustrates large two-dimensional structures better than small three-dimensional structures. The pairing and merging of two Kelvin-Helmholtz rolls for the flat plate are clearly shown by using this technique. The Q-criterion isosurface is an ideal tool for illustrating the formation of the small hairpin structures and how the Kelvin-Helmholtz roll develops to the hairpin structure. Such a finding is consistent with conclusion of the studies by Dubief and Delcayre (2000) and Abdalla and Yang (2004b).

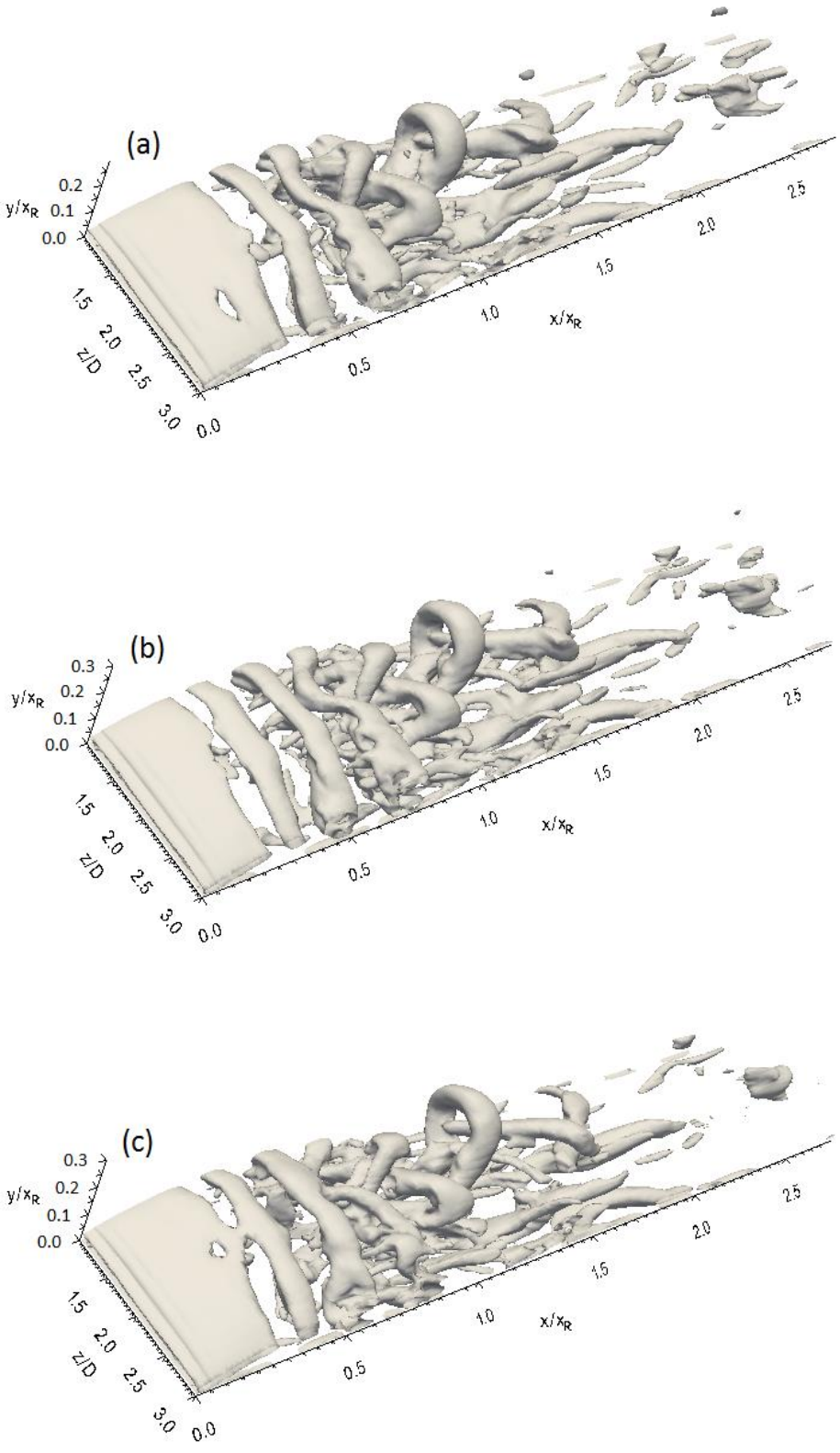

Caption for these figures is on the following page

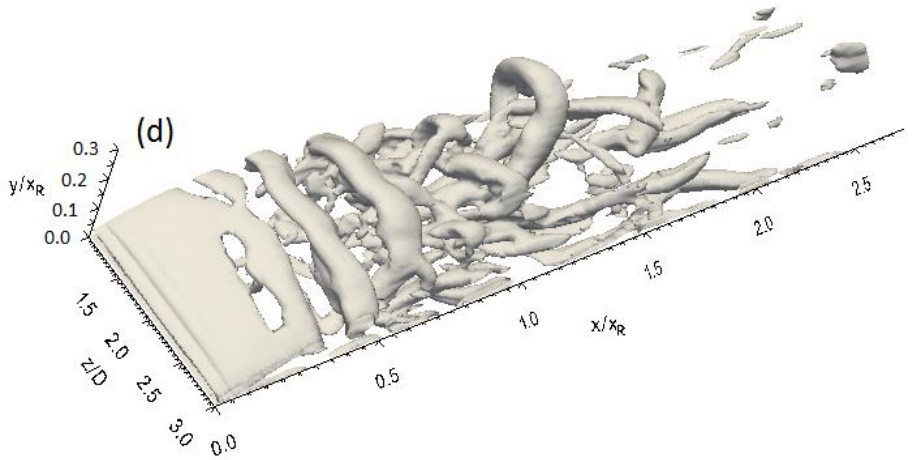
(d)
y/x_R
0.3
0.2
0.1
0.0
z/D
1.5
2.0
2.5
3.0
0.0
0.5
1.0
x/x_R
1.5
2.0
2.5

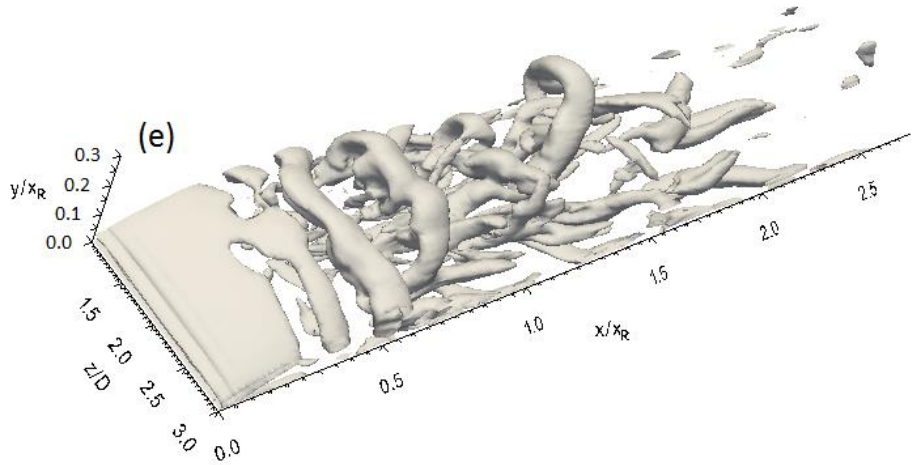
(e)
y/x_R
0.3
0.2
0.1
0.0
z/D
1.5
2.0
2.5
3.0
0.0
0.5
1.0
x/x_R
1.5
2.0
2.5

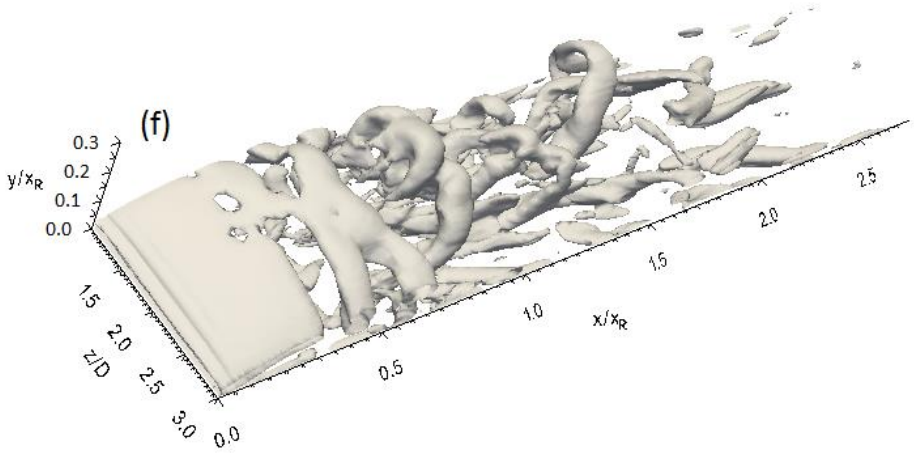
(f)
y/x_R
0.3
0.2
0.1
0.0
z/D
1.5
2.0
2.5
3.0
0.0
0.5
1.0
x/x_R
1.5
2.0
2.5

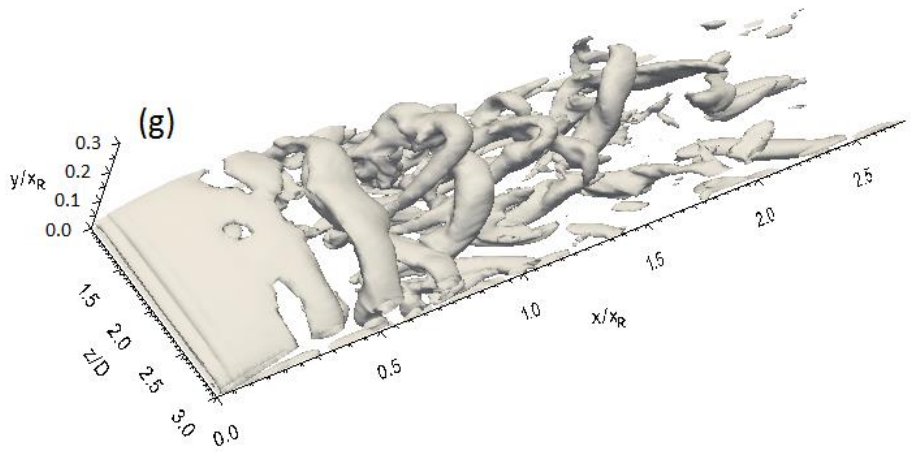

Fig. 7-27. Q-criterion isosurface at sequential times (every 250 time steps) for 3D_case2 with NFST

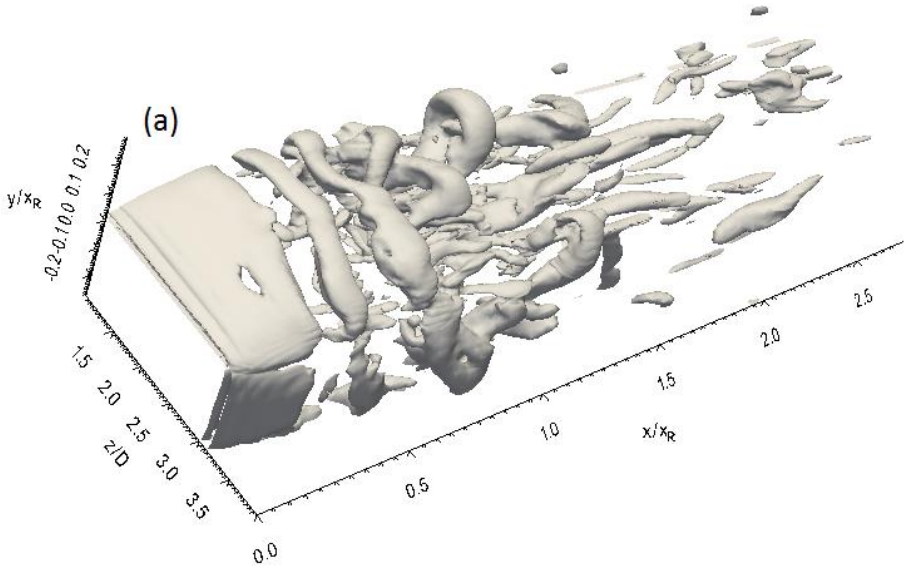

Caption for this figure is on the following page

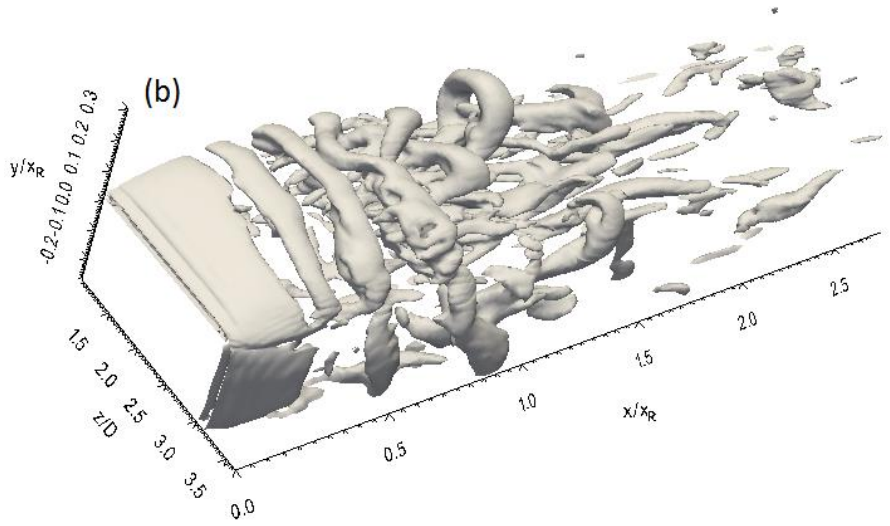
(b)
y/x_R
-0.2 -0.1 0.0 0.1 0.2 0.3
z/D
1.5 2.0 2.5 3.0 3.5
x/x_R
0.0 0.5 1.0 1.5 2.0 2.5

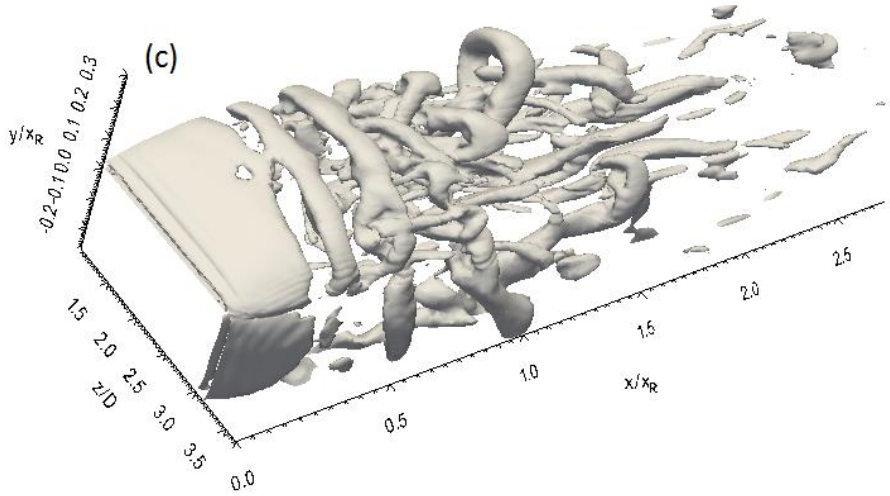
(c)
y/x_R
-0.2 -0.1 0.0 0.1 0.2 0.3
z/D
1.5 2.0 2.5 3.0 3.5
x/x_R
0.0 0.5 1.0 1.5 2.0 2.5

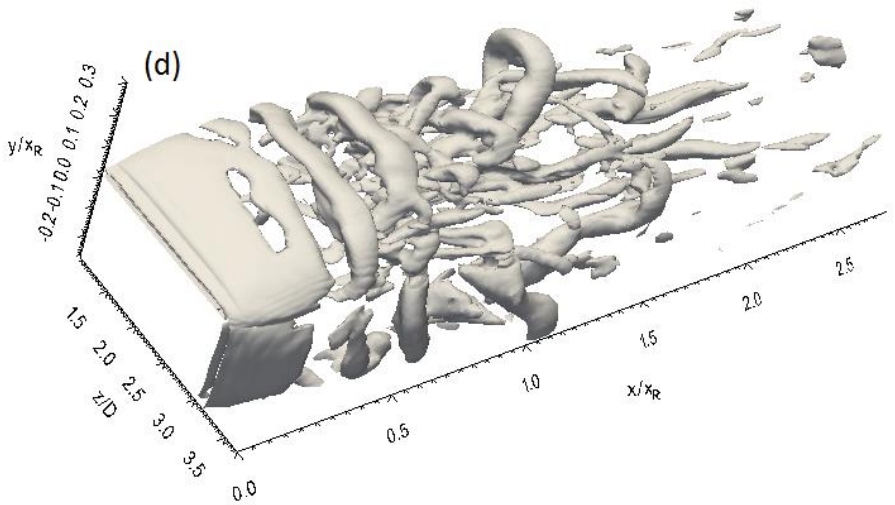
(d)
y/x_R
-0.2 -0.1 0.0 0.1 0.2 0.3
z/D
1.5 2.0 2.5 3.0 3.5
x/x_R
0.0 0.5 1.0 1.5 2.0 2.5

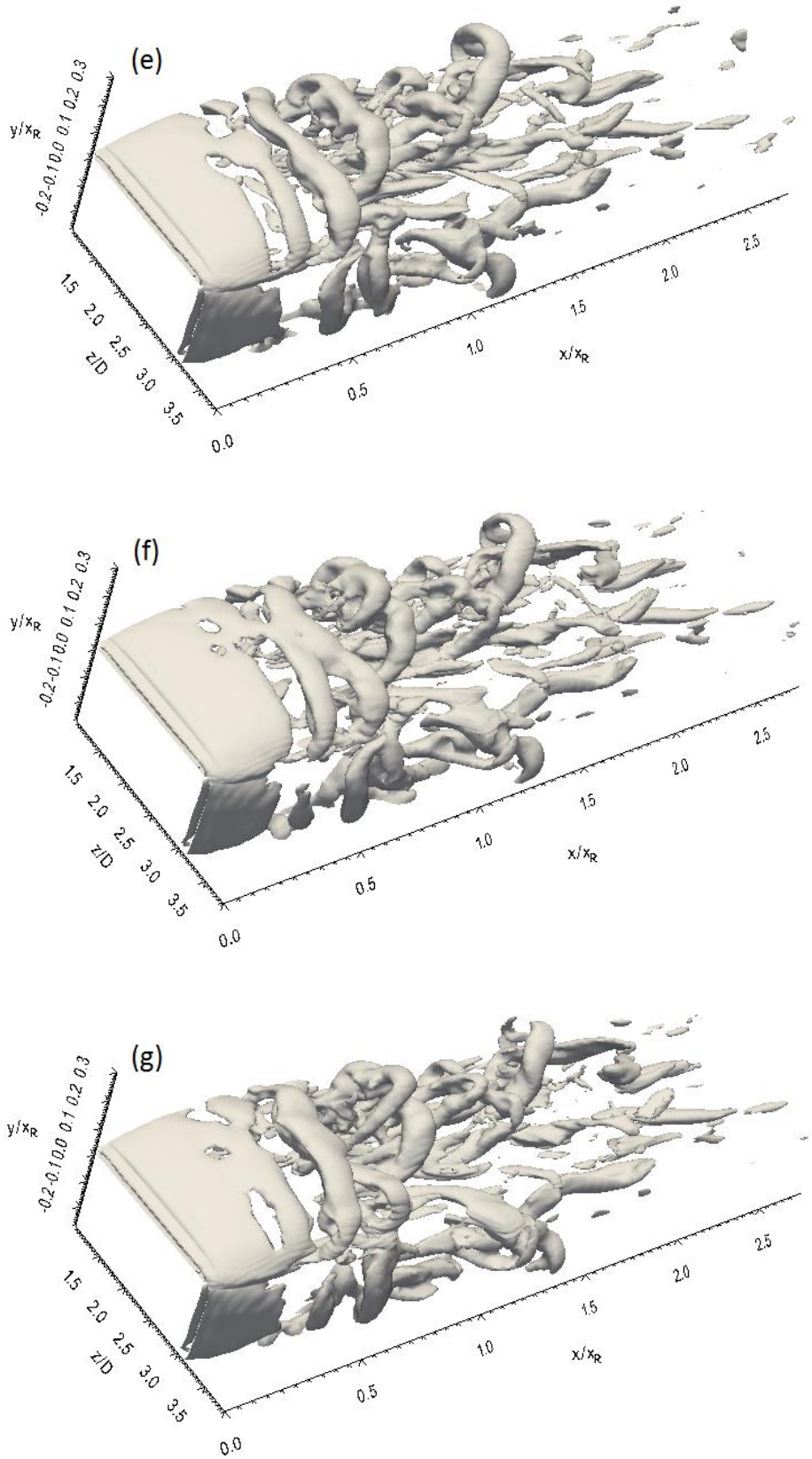

Fig. 7-28. Q-criterion isosurface on the top and side surfaces at sequential times (every 250 time steps) for 3D_case2 with NFST

7.3 Three-dimensional flow visualization for FST

In order to investigate the differences that may occur in coherent structures and their development due to the presence of a 3.7% intensity of free stream turbulence, the low pressure, vorticity field and Q-criterion isosurfaces are also considered here for all geometries in the current study.

7.3.1 Low pressure isosurface

A low fluctuating pressure isosurface taken at sequential times every 250 time steps for the flat plate is shown in Fig. 7-29. It can be seen that the coherent structures are distorted due to a presence of a high intensity of free stream turbulence. There is a spanwise motion in the Kelvin-Helmholtz rolls and hairpin structures that are not as clear as with NFST. However, Kelvin-Helmholtz rolls are still apparent, confirming that the Kelvin-Helmholtz instability is still the primary instability mechanism in the free shear layer, as presented in Chapter 5.

In addition to the distorted Kelvin-Helmholtz rolls, there is a set of hairpin structures in the region between x/x_R = 0.8 and x/x_R = 1, indicating the breakdown of the previous Kelvin-Helmholtz roll as shown in Fig 7-29a. However, it is not clear if there is a pairing of two Kelvin-Helmholtz rolls, such as with NFST, or whether the Kelvin-Helmholtz roll directly breaks down into hairpin structures.

It should be noted that the lack of clarity in the manner of development of coherent structures by employing the low pressure isosurface with FST is also reported in Yang and Abdalla (2005). They studied transitional separated-reattached flow with a 2% intensity of free stream turbulence on a blunt flat plate. They considered this to be a disadvantage of using this flow visualization technique to identify the coherent structures within the flow.

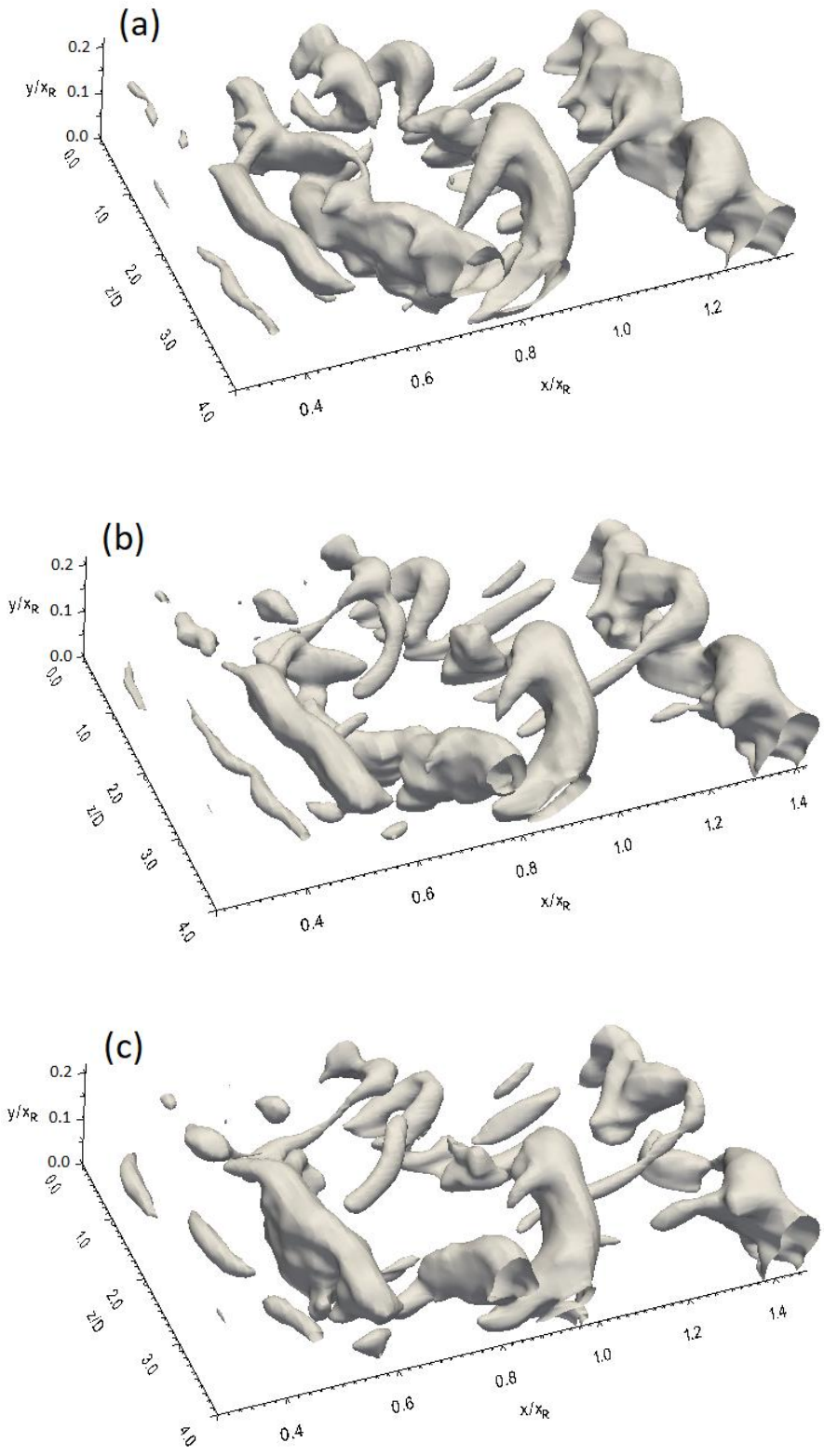

Caption for these figures is on the following page

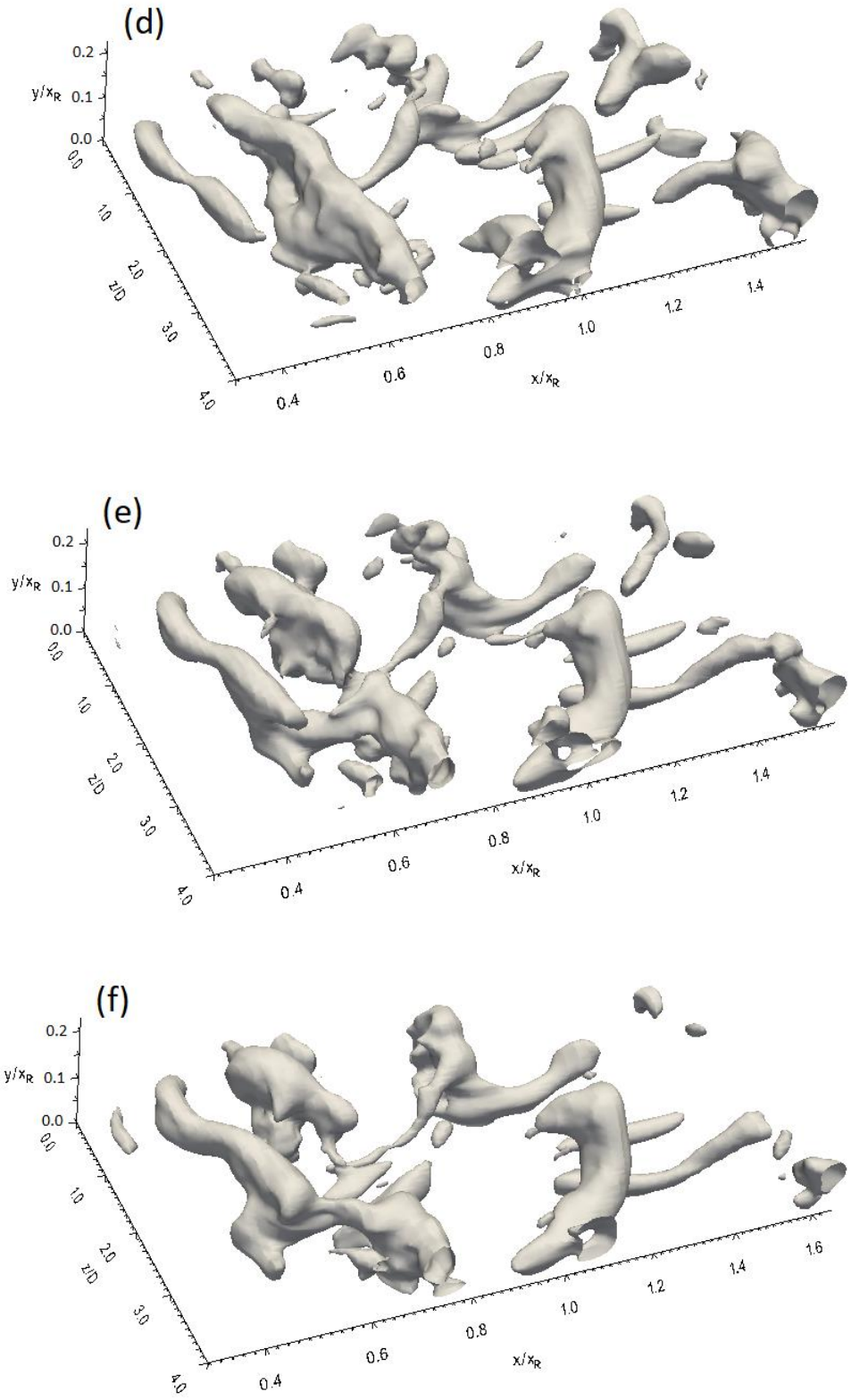

Fig. 7-29. Low pressure isosurface at sequential times (every 250 time steps) for the flat plate with FST

Deformed Kelvin-Helmholtz rolls, unclear hairpin structures and a degree of ambiguity as to the mechanism of their formation are also apparent in the low fluctuating pressure isosurfaces for other geometries as shown in Fig. 7-30 for 3D_case1 and Fig. 7-31 for 3D_case2.

However, for all geometries studied here, the low fluctuating pressure isosurfaces confirm the occurrence of the Kelvin-Helmholtz instability as the primary instability mechanism in the free shear layer through exhibiting Kelvin-Helmholtz rolls. Moreover, the low fluctuating pressure isosurfaces indicate the existence of hairpin structures as secondary coherent structures associated with the transition, and further their breakdown into smaller structures around the mean reattachment line and further downstream.

In the comparison between NFST and FST, the following can be concluded:

- In both cases, Kelvin-Helmholtz rolls exist, regardless of their clarity, after shedding from the separated layer.
- Secondary coherent structures in both cases are hairpin structures.
- Development of Kelvin-Helmholtz structures to form hairpin structures is clearly shown in NFST, while the existence of this process is ambiguous in FST.
- In both cases, hairpin structures are present around the mean reattachment line and move downstream within the reattached turbulent boundary layer.

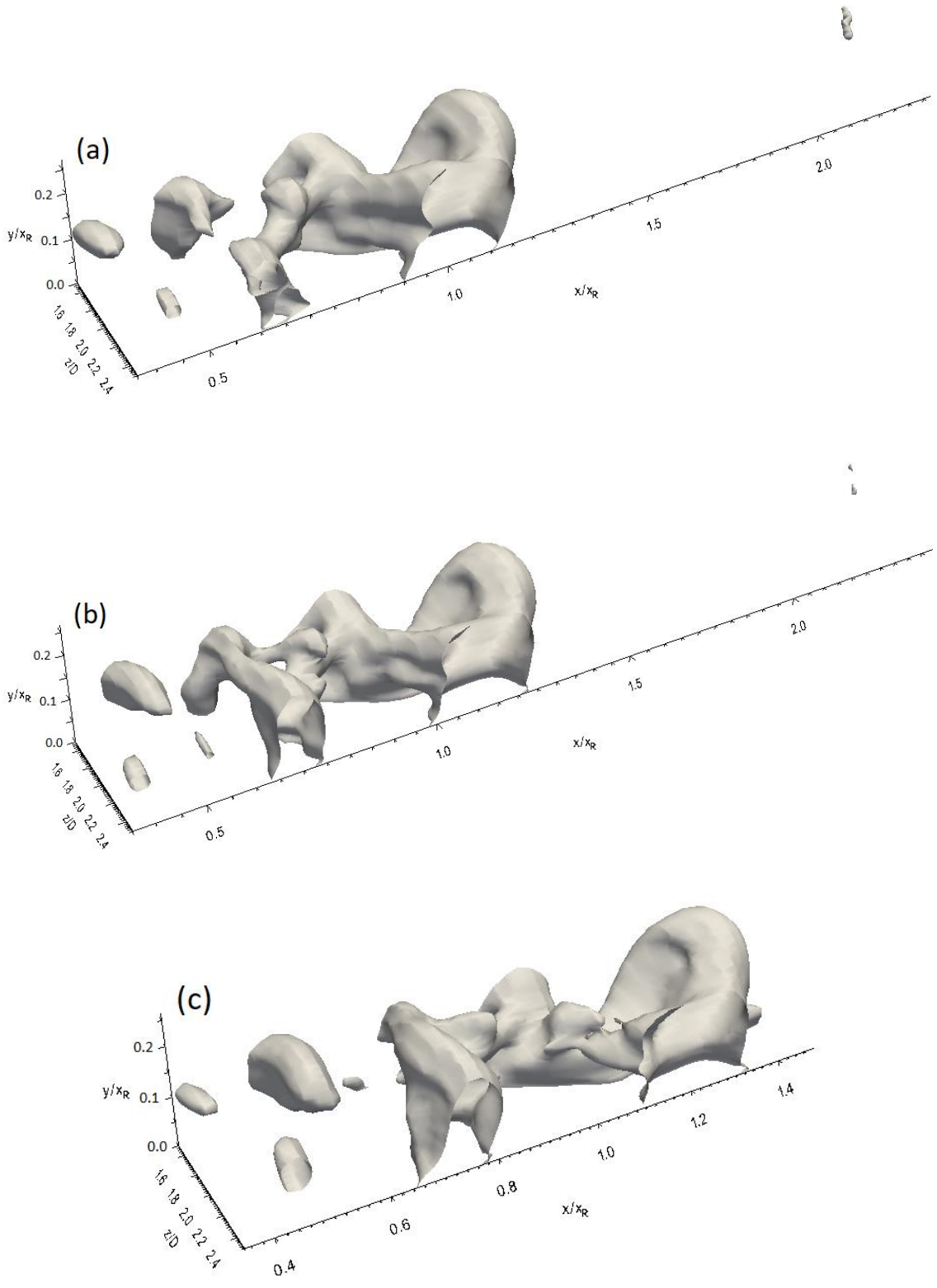

Caption for these figures is on the following page

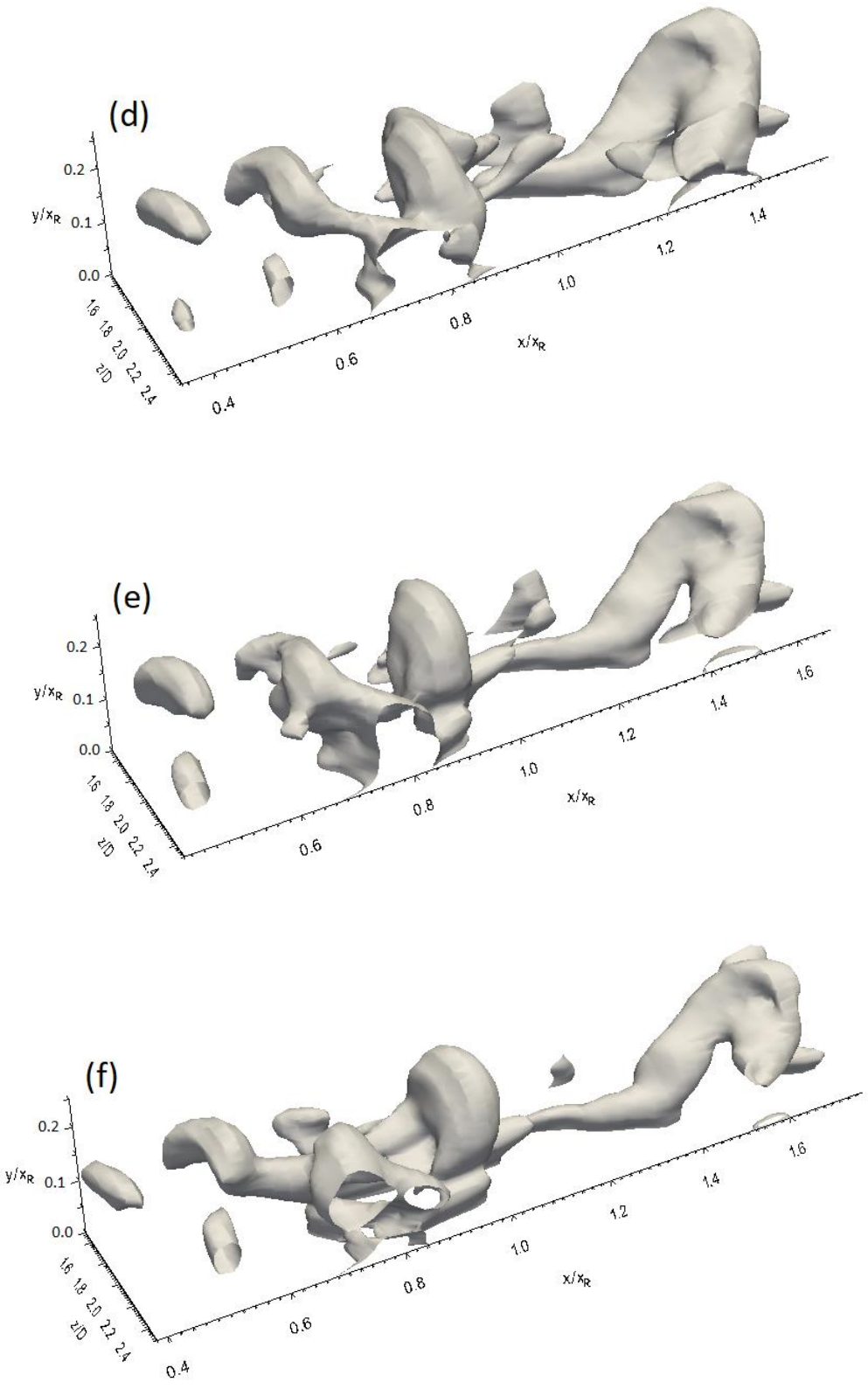

Fig. 7-30. Low pressure isosurface at sequential times (every 250 time steps) for 3D_case1 with FST

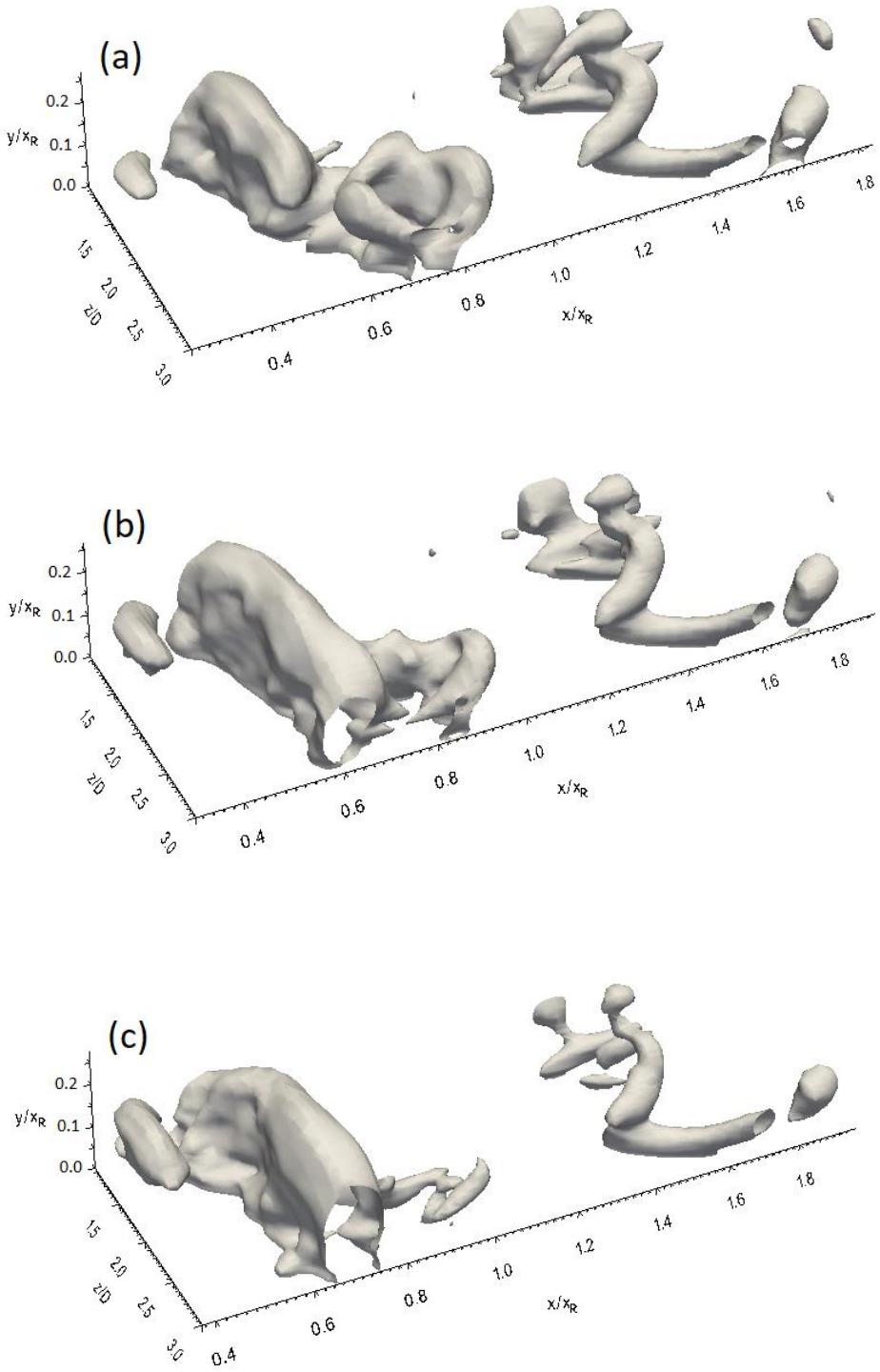

Caption for these figures is on the following page

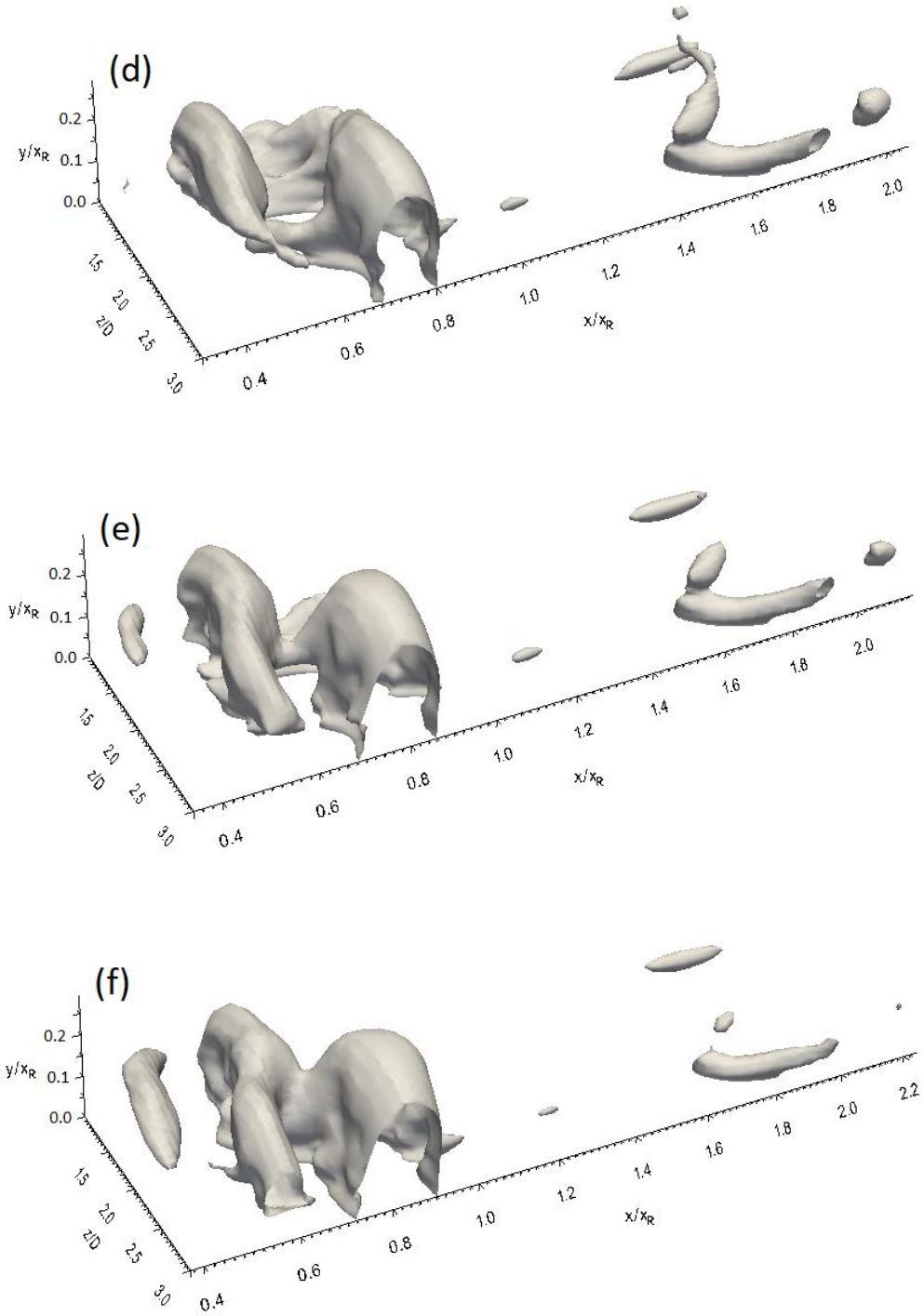

Fig. 7-31. Low pressure isosurface at sequential times taken every 250 time steps for 3D_case2 with FST

7.3.2 Vorticity fields isosurface

7.3.2.1 Vorticity magnitude isosurface

The vorticity magnitude isosurfaces taken every 250 time steps for the flat plate are shown in Fig. 7-32. It can be seen that with FST, the laminar part of the vorticity sheet is smaller than that in NFST. The location of the start of the unsteadiness moves upstream to x/x_R = 0.1. The unsteadiness has a relatively low amplitude up to x/x_R = 0.3. Further downstream, the formation of hairpin structures is clear; one such a structure, referred to as *A*, is shown in Fig. 7-32c.

Consideration of structure *A* shows that it is formed at about x/x_R = 0.5. It moves downstream up to x/x_R = 1, where it starts to break down into smaller structures. Further downstream, the coherency of structure *A* completely breaks down as shown in Fig. 7-32j.

The vorticity magnitude isosurfaces show that within the turbulent reattached boundary layer, large-scale structures still survive and they move a certain distance before they totally break down, indicating a delay in the recovery of the turbulent boundary layer. This will be shown in Chapter 8.

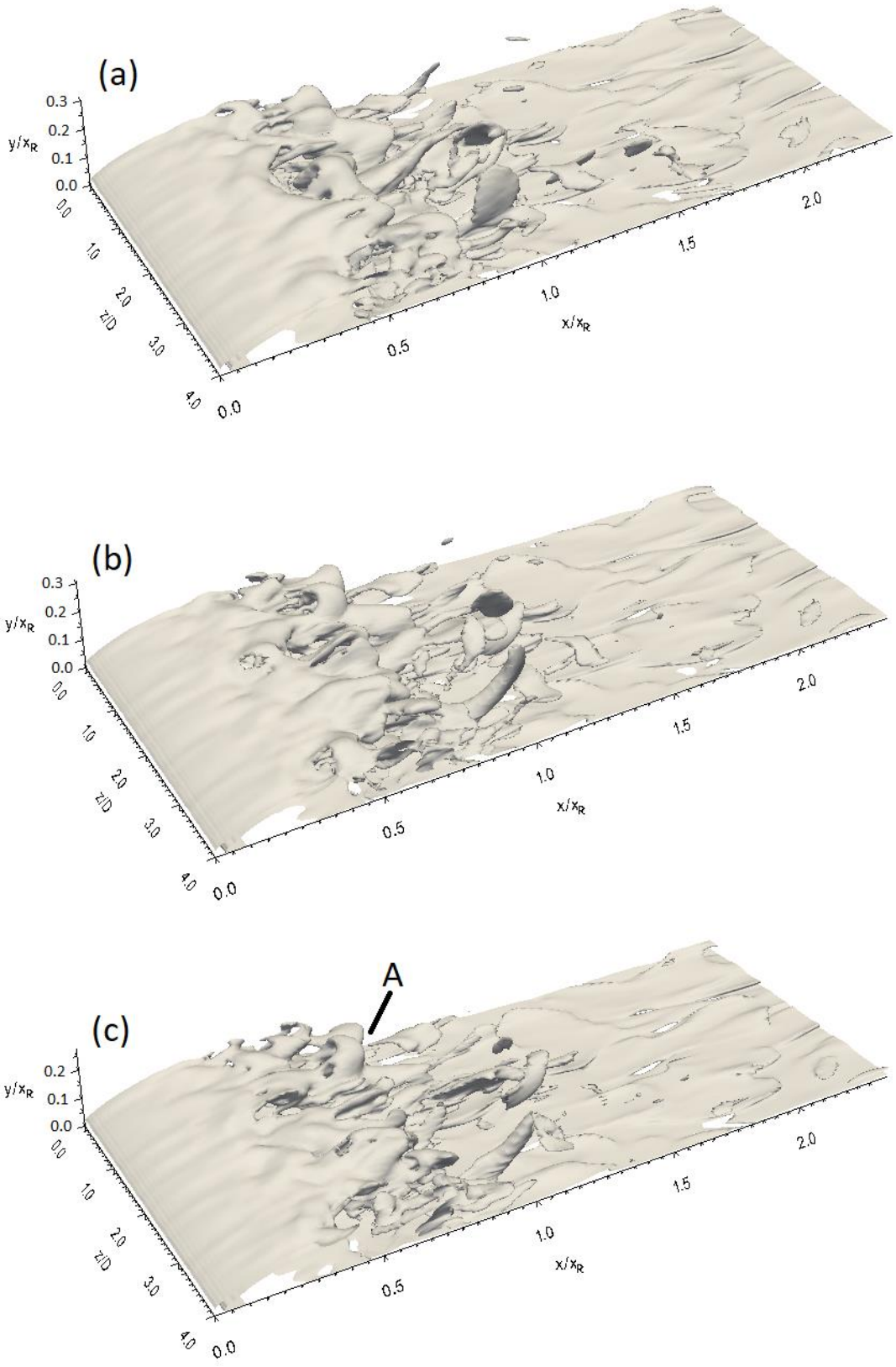

Caption for these figures is on the following page

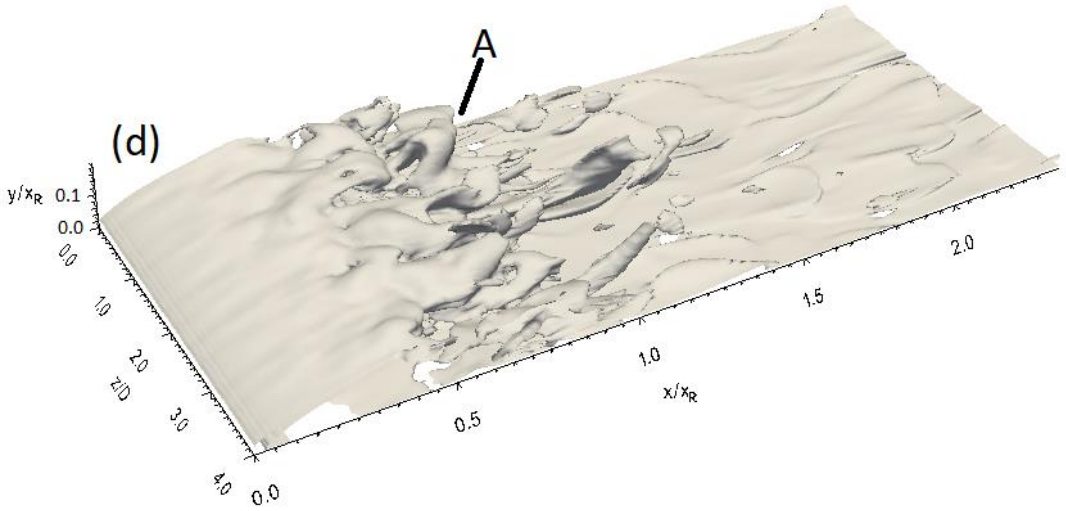
A
(d)
y/x_R
0.1
0.0
0.0
1.0
2.0
z/D
3.0
4.0
0.0
0.5
1.0
1.5
2.0
x/x_R

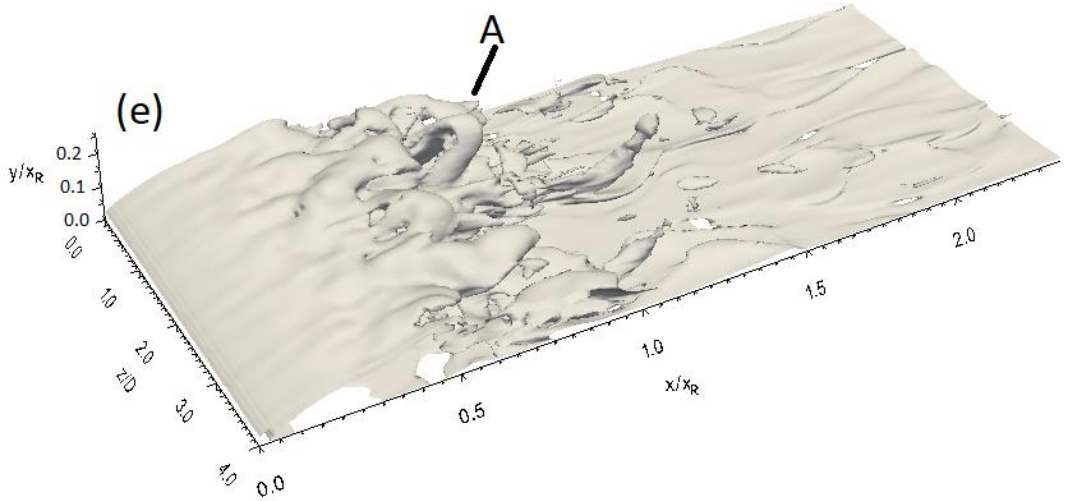
A
(e)
y/x_R
0.2
0.1
0.0
0.0
1.0
2.0
z/D
3.0
4.0
0.0
0.5
1.0
1.5
2.0
x/x_R

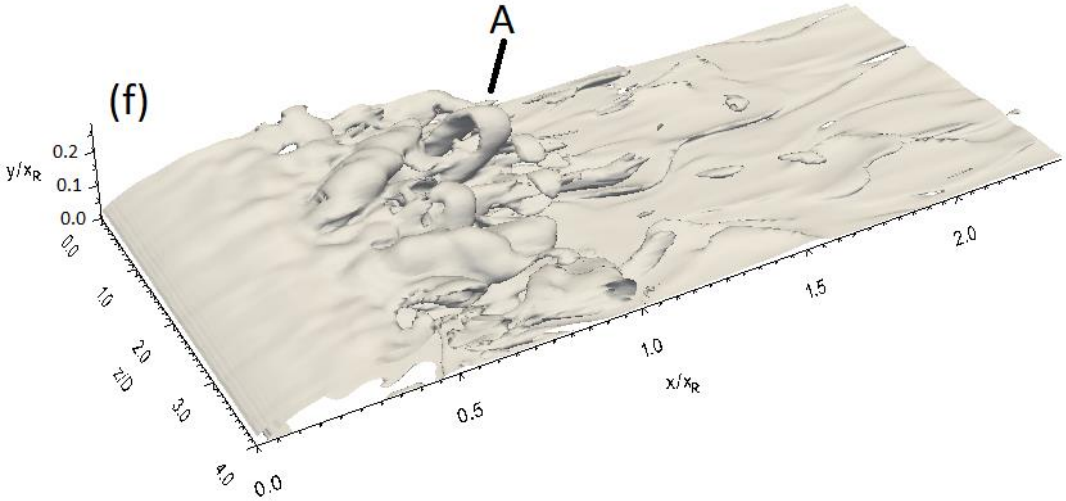
A
(f)
y/x_R
0.2
0.1
0.0
0.0
1.0
2.0
z/D
3.0
4.0
0.0
0.5
1.0
1.5
2.0
x/x_R

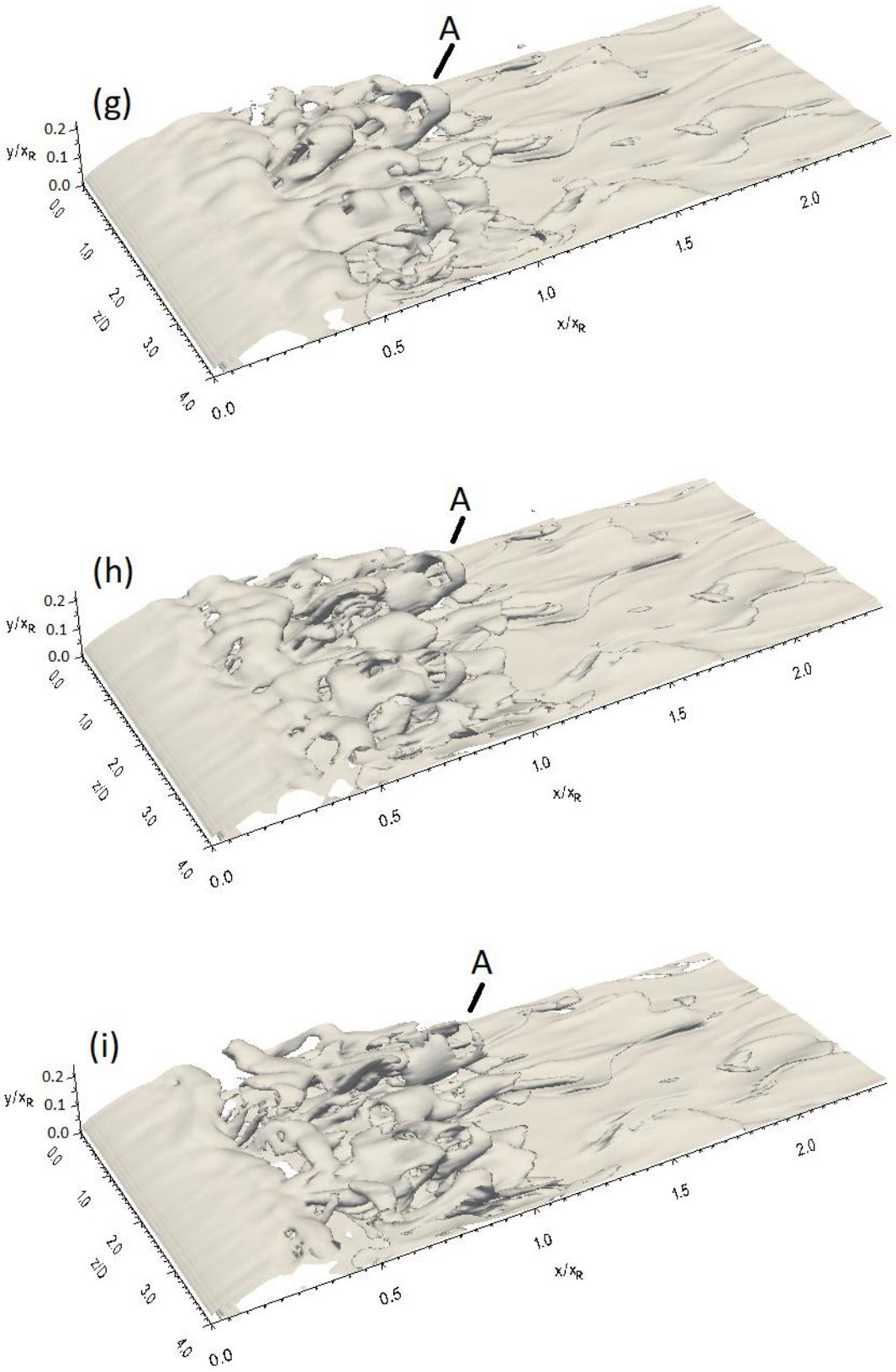
A
(g)
y/x_R
0.2
0.1
0.0
0.0
1.0
2.0
z/D
3.0
4.0
0.0
0.5
1.0
1.5
2.0
x/x_R
A
(h)
y/x_R
0.2
0.1
0.0
0.0
1.0
2.0
z/D
3.0
4.0
0.0
0.5
1.0
1.5
2.0
x/x_R
A
(i)
y/x_R
0.2
0.1
0.0
0.0
1.0
2.0
z/D
3.0
4.0
0.0
0.5
1.0
1.5
2.0
x/x_R

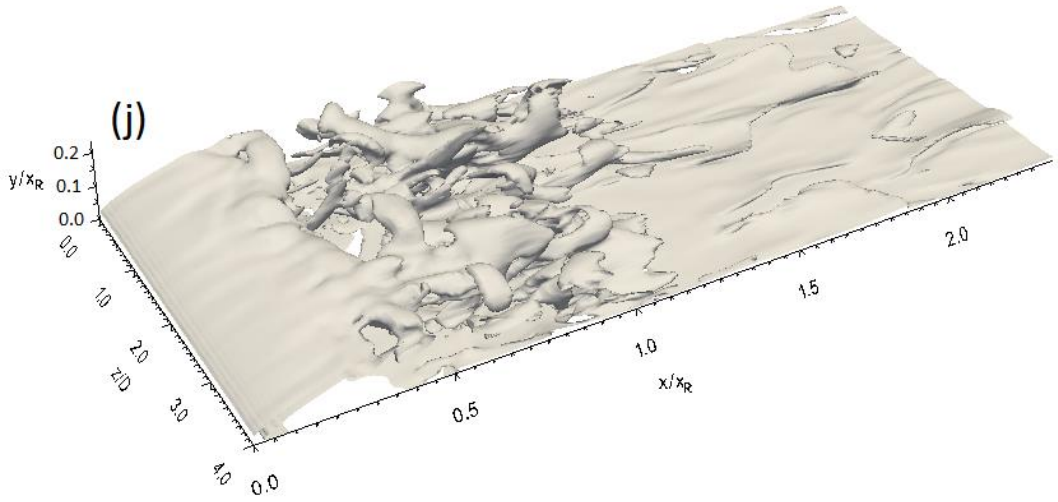

Fig. 7-32. Vorticity magnitude isosurface at sequential times (every 250 time steps) for the flat plate with FST

Similar behaviour to that of the vorticity magnitude isosurface presented for the flat plate is shown for 3D_case1 in Fig 7-33. There is also a reduction in the laminar part of the vorticity sheet and a more rapid occurrence of the transition. The linear development of the unsteadiness is in the region between $x/x_R = 0.3$ and $x/x_R = 0.5$. Further downstream, the formation of the hairpin structures that is associated with significant three-dimensional motions of the flow can be clearly shown in Fig. 7-33d, which represents the hairpin structure referred to as *A*. Structure *A* moves downstream and breaks down around the mean reattachment line as shown in Fig. 7-33g.

Large-scale structures are also present in the reattached turbulent boundary layer which completely disappear at a location further away from the mean reattachment line, implying a slowness in the reestablishment of the turbulent boundary layer. This will be further discussed in Chapter 8.

To show the development of the vorticity magnitude on both the top and side surfaces of 3D_case1, the isosurfaces for the vorticity magnitude on the top and side surfaces of 3D_case1 are presented in Fig. 7-34. It can be seen that there is no difference in the top and side vorticity sheets as regards the locations of the beginning of the unsteadiness, the appearance of the hairpin structures, and the breakdown of large-scale structures.

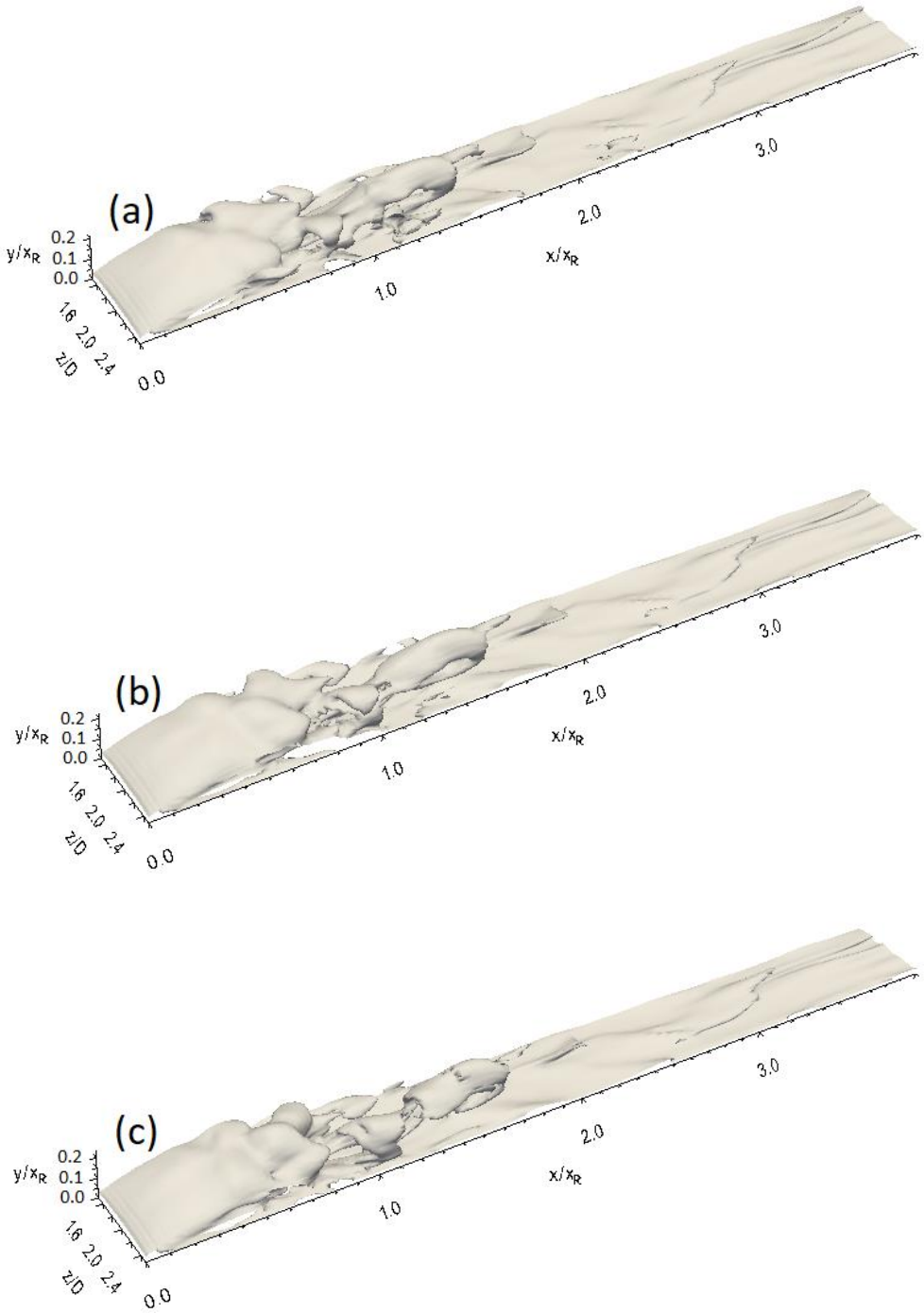

Caption for these figures is on the following page

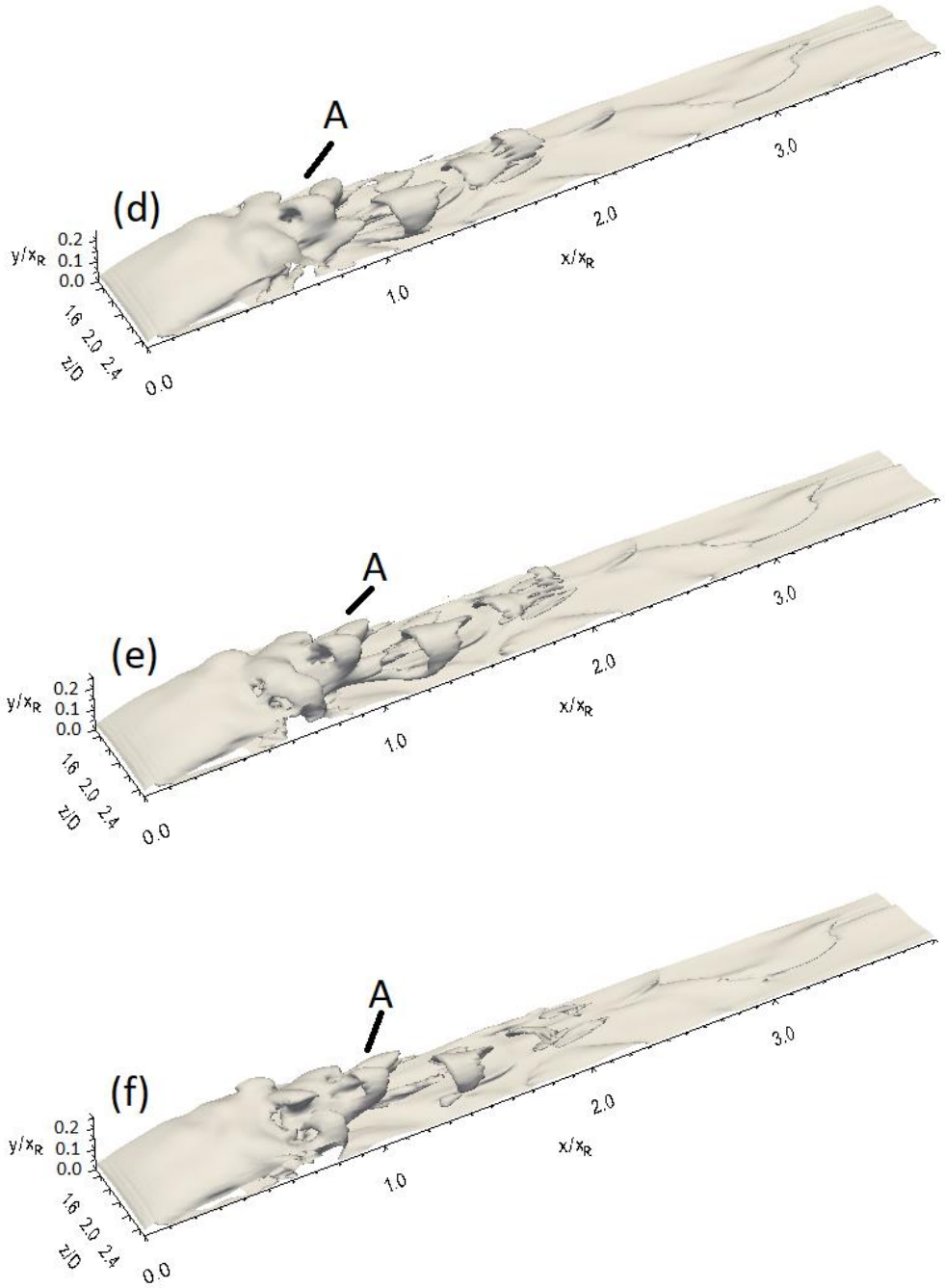
A
(d)
y/x_R
0.2
0.1
0.0
1.6
2.0
2.4
z/D
0.0
1.0
2.0
3.0
x/x_R
A
(e)
y/x_R
0.2
0.1
0.0
1.6
2.0
2.4
z/D
0.0
1.0
2.0
3.0
x/x_R
A
(f)
y/x_R
0.2
0.1
0.0
1.6
2.0
2.4
z/D
0.0
1.0
2.0
3.0
x/x_R

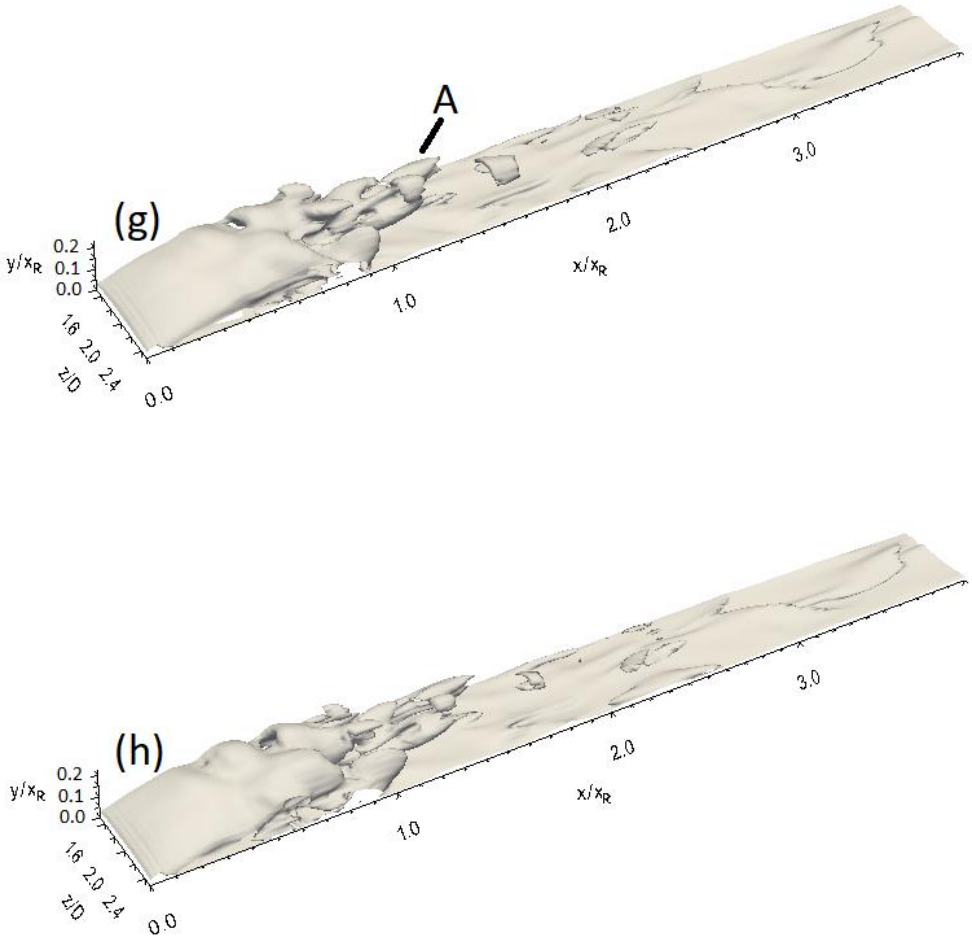

Fig. 7-33. Vorticity magnitude isosurface at sequential times (every 250 time steps) for 3D_case1 with FST

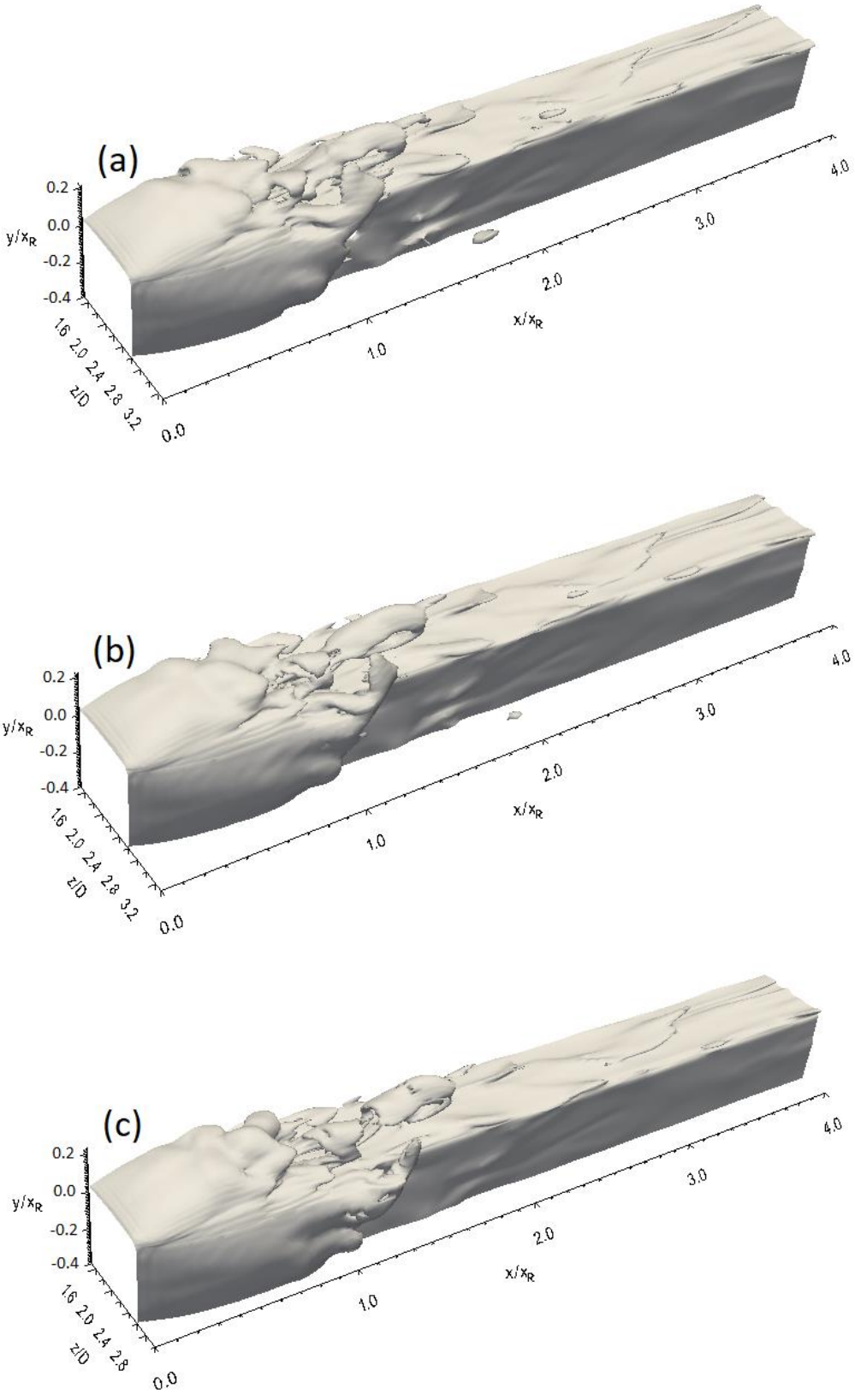

Caption for these figures is on the following page

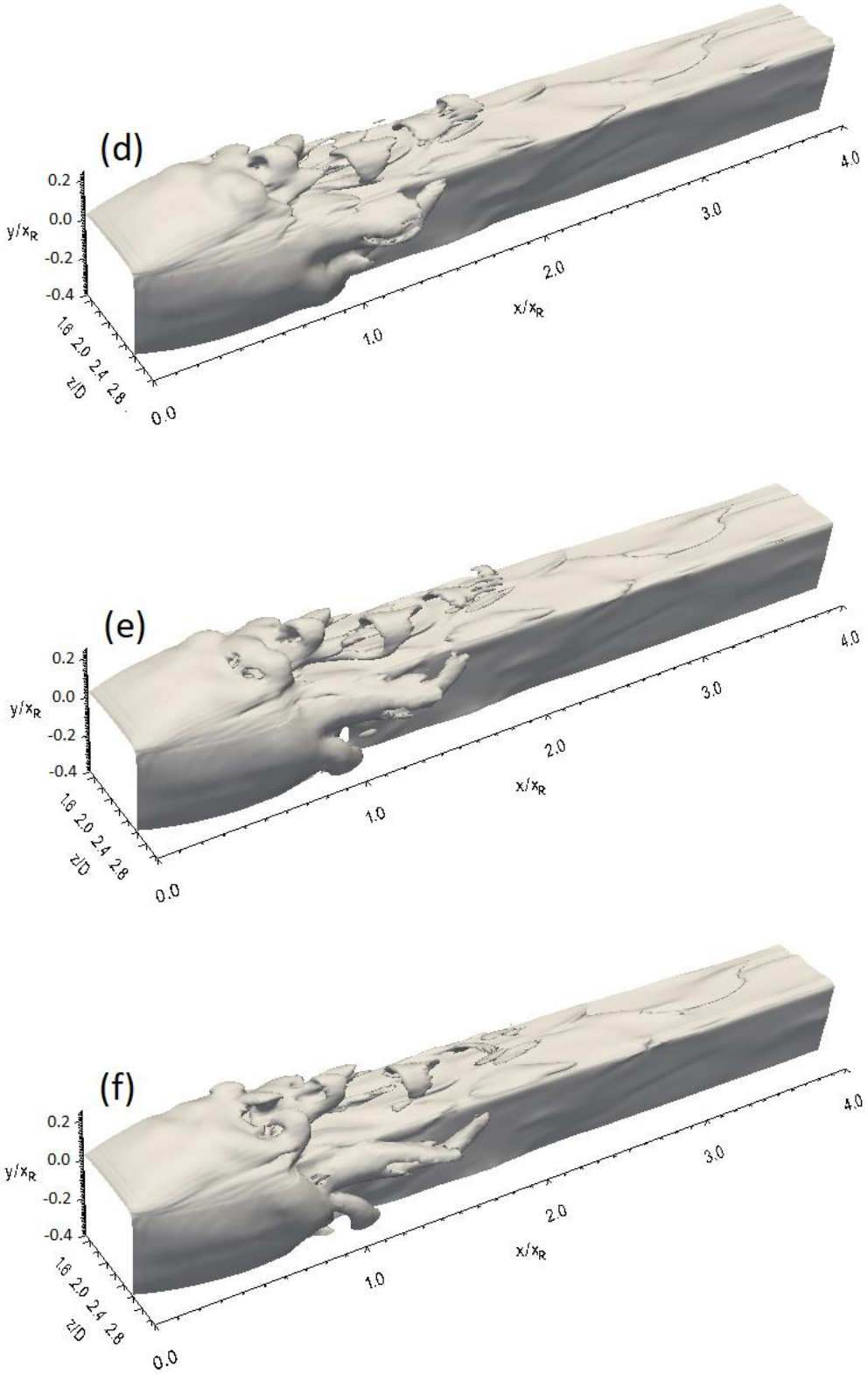
(d)
0.2
0.0
-0.2
-0.4
y/x_R
1.6 2.0 2.4 2.8
z/D
0.0
1.0
2.0
3.0
4.0
x/x_R
(e)
0.2
0.0
-0.2
-0.4
y/x_R
1.6 2.0 2.4 2.8
z/D
0.0
1.0
2.0
3.0
4.0
x/x_R
(f)
0.2
0.0
-0.2
-0.4
y/x_R
1.6 2.0 2.4 2.8
z/D
0.0
1.0
2.0
3.0
4.0
x/x_R

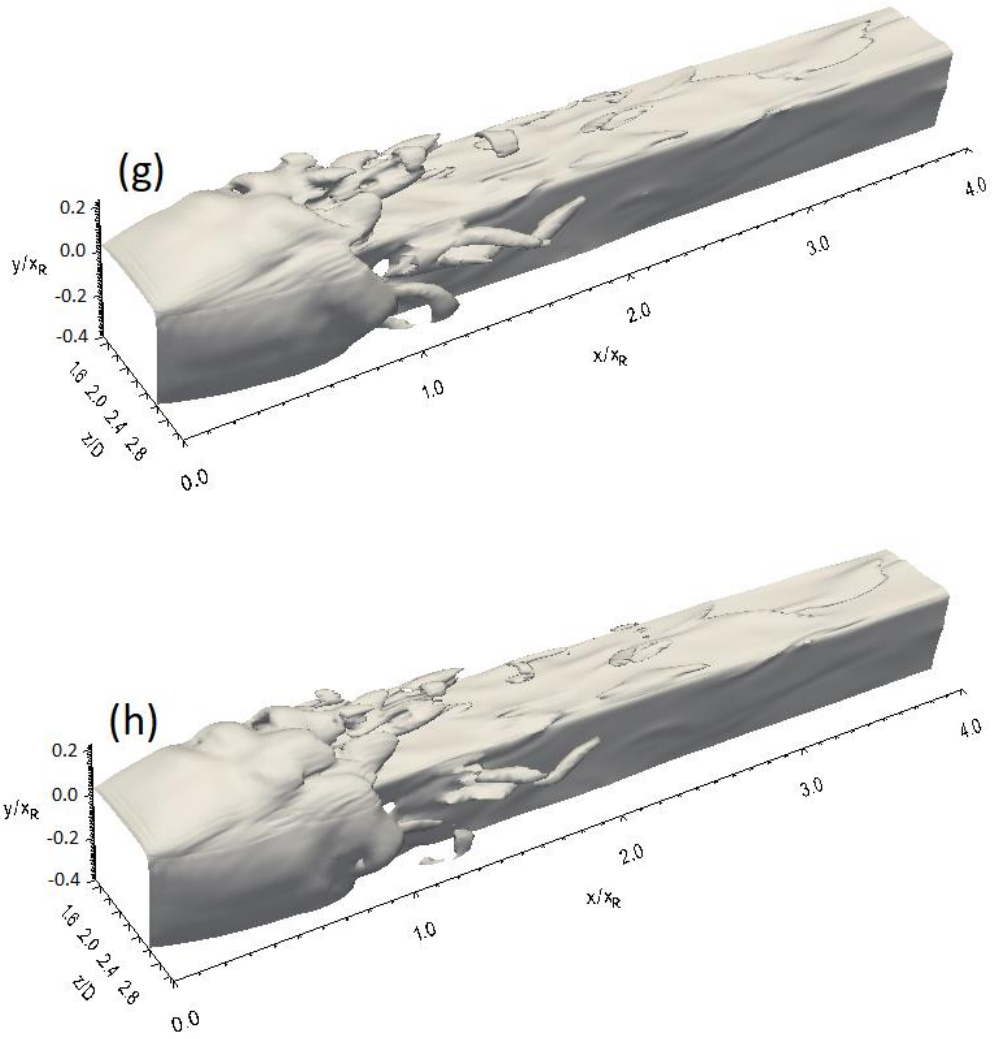

Fig. 7-34. Vorticity magnitude isosurface on the top and side surfaces at sequential times (every 250 time steps) for 3D_case1 with FST

The vorticity magnitude isosurfaces for 3D_case2 taken every 250 time steps show that the location of the appearance of the unsteadiness in the vorticity sheet is at about x/x_R = 0.2 as shown in Fig. 7-35. In addition, it is clearly seen that the unsteadiness is still low up to x/x_R = 0.4. Further downstream, hairpin structures are formed, and developed at the region that extends from x/x_R = 0.6 to a location that is further from the mean reattachment line as shown in the development of structures *A* and *B* in Figs. 7-35b and 7-35c. These structures shed to the reattached turbulent boundary layer and remain large-scale up to x/x_R = 1.5, leading to a delay in the turbulent boundary layer recovery after the reattachment, as it will be discussed in Chapter 8.

At similar times to the snapshots shown in Fig. 7-35, the vorticity magnitude isosurfaces for the top and side surfaces of 3D_case2 are taken as shown in Fig. 7-36. The vorticity magnitude development stages occur at the same streamwise locations on the top and side surfaces of 3D_case2 as shown in Fig. 7-36. However, the time period for the vorticity magnitude development shown in Fig. 7-36 does not clearly indicate the hairpin structures on the side surface of 3D_case2. Hence, another vorticity magnitude isosurface is exhibited with different time period to indicate the side surface hairpin structures as shown in Fig. 7-37. The hairpin structure referred to as *A* is indicated in Fig. 7-37a. It can be seen that structure *A* moves downstream and completely breaks down in the region between x/x_R = 1 and x/x_R = 1.5, which is similar to that presented for the top surface hairpin structures in Fig. 7-36.

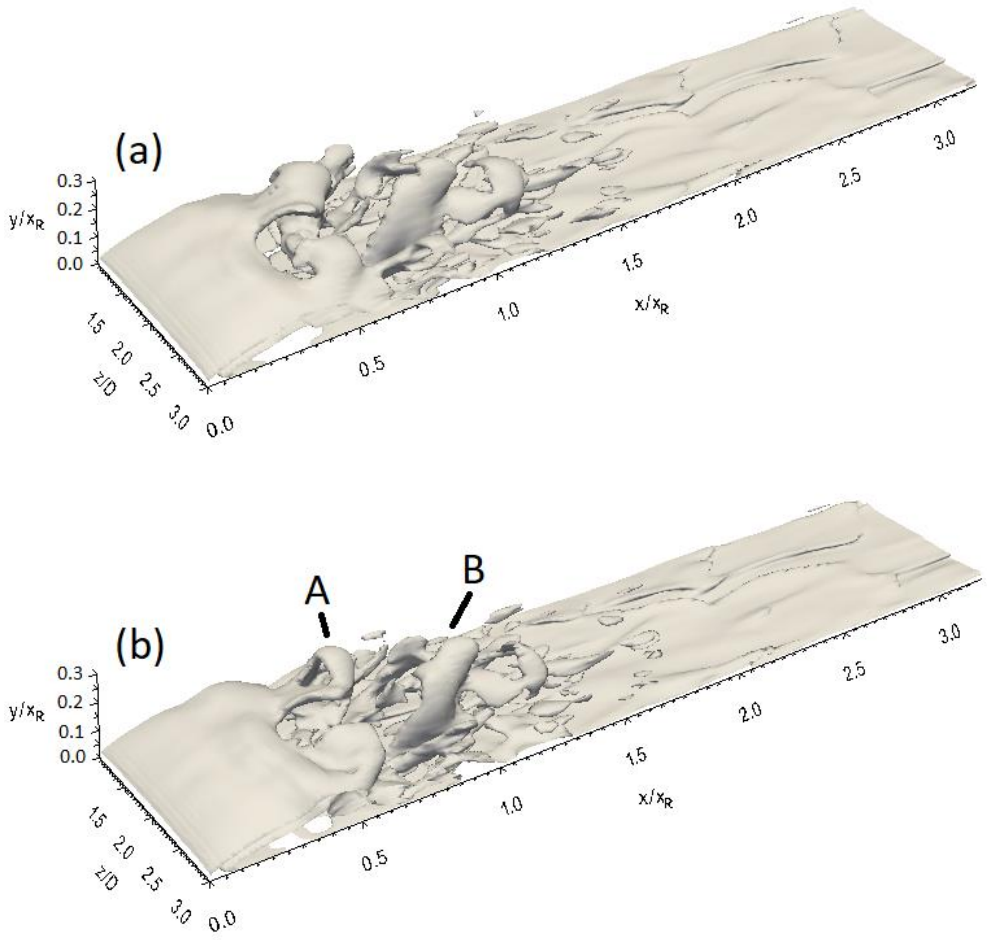

Caption for these figures is on the following page

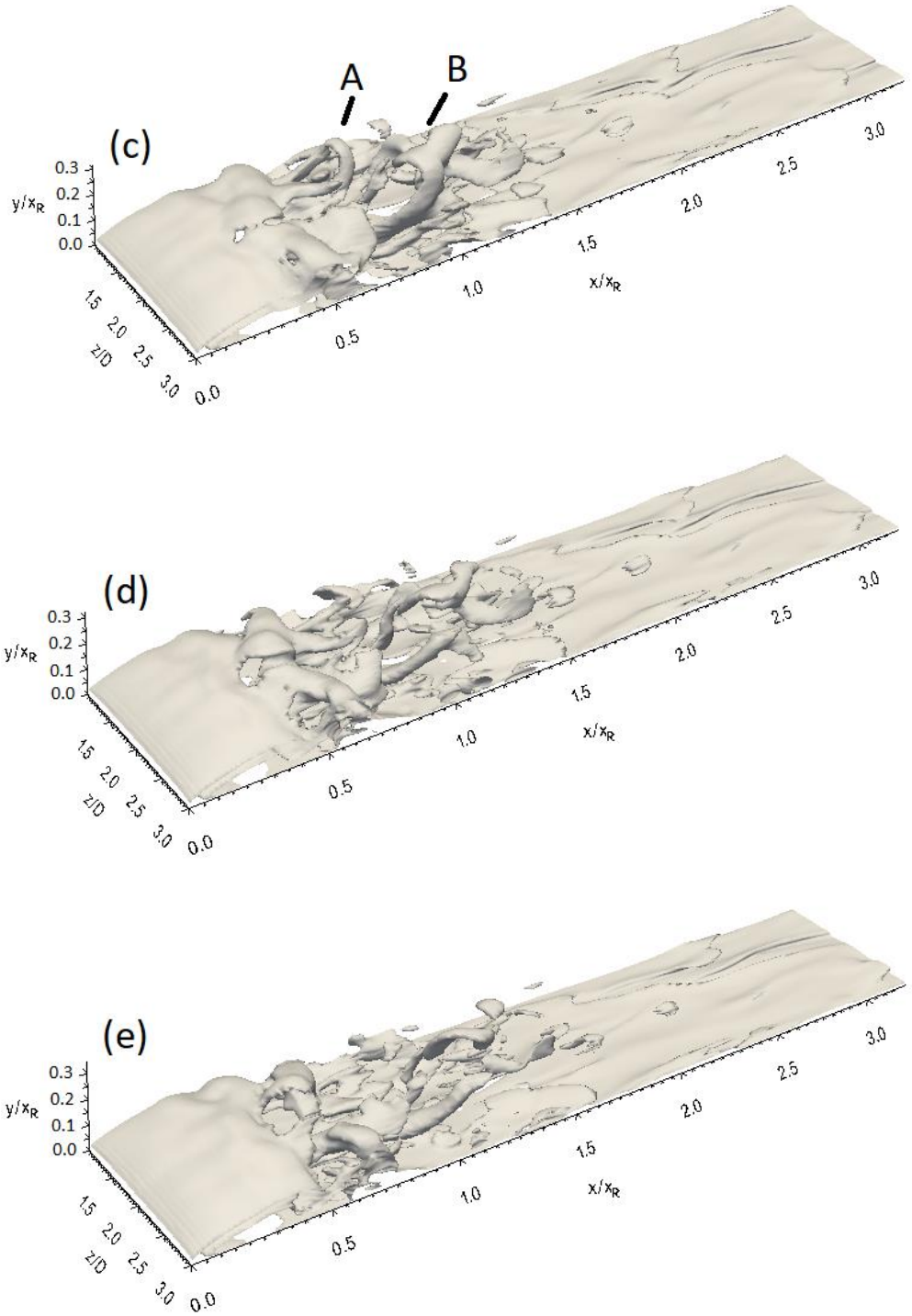
A
B
(c)
(d)
(e)
y/x_R
0.3
0.2
0.1
0.0
z/D
1.5
2.0
2.5
3.0
0.0
0.5
1.0
1.5
2.0
2.5
3.0
x/x_R

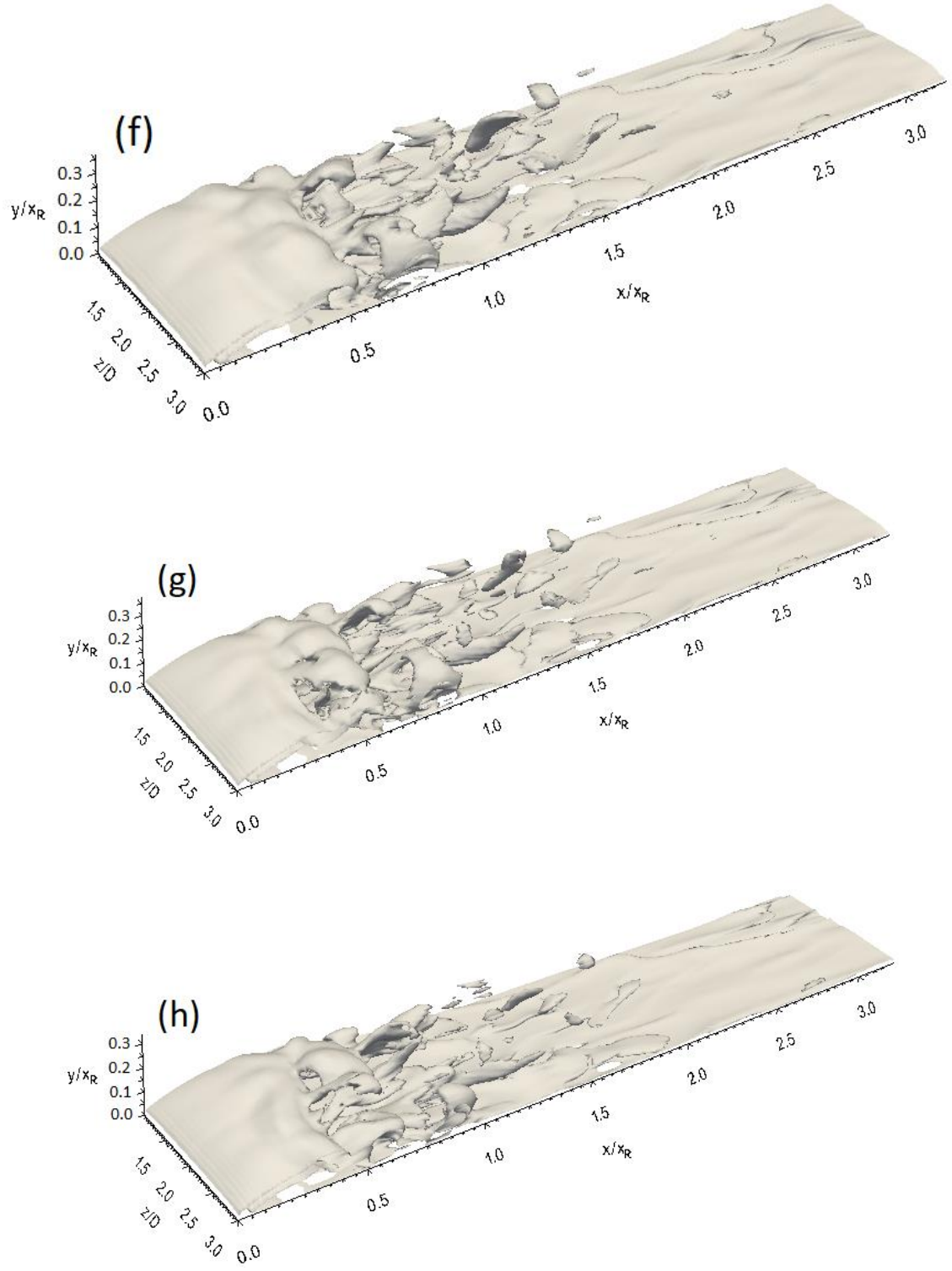

Fig. 7-35. Vorticity magnitude isosurface at sequential times (every 250 time steps) for 3D_case2 with FST

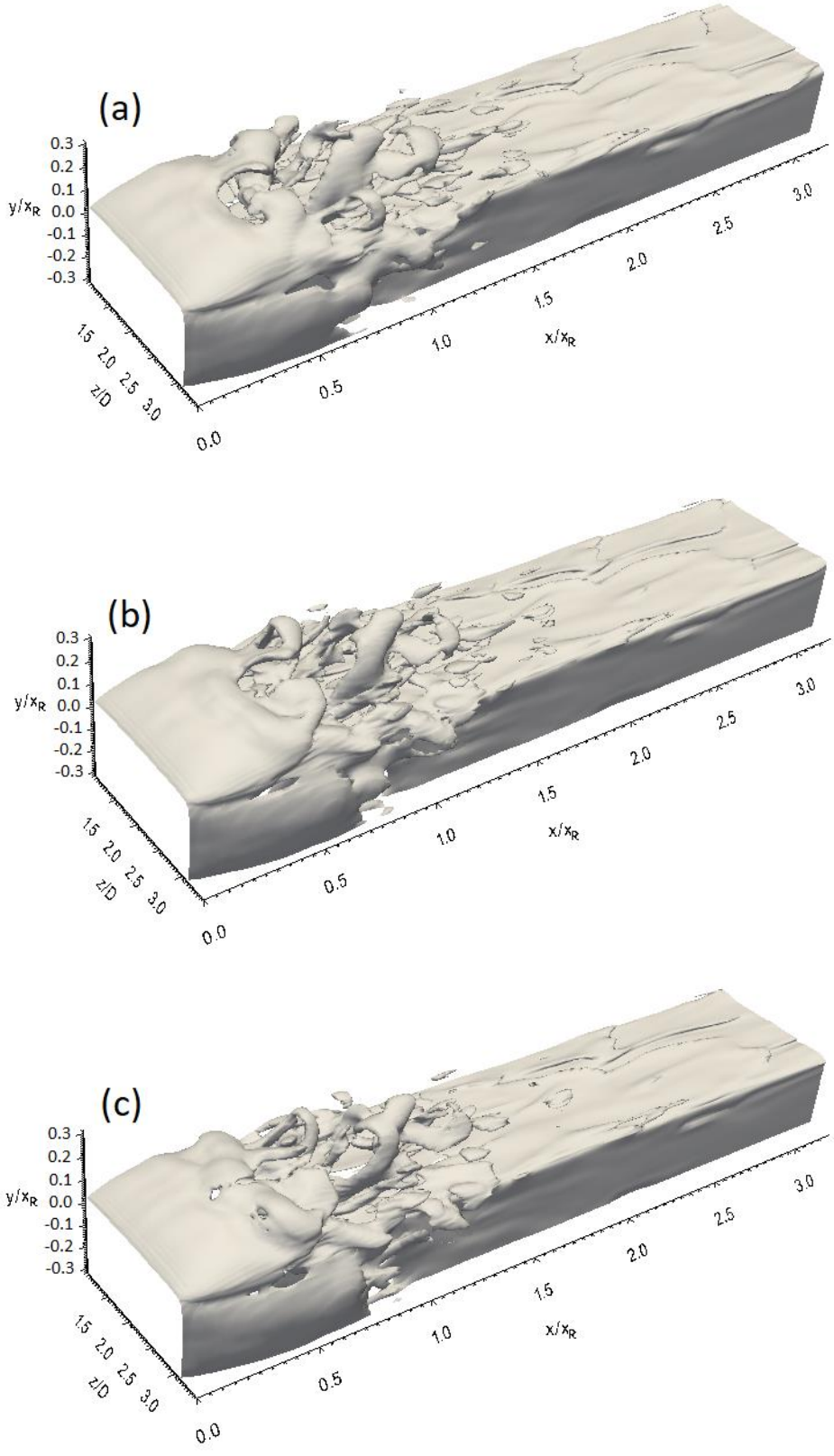

Caption for these figures is on the following page

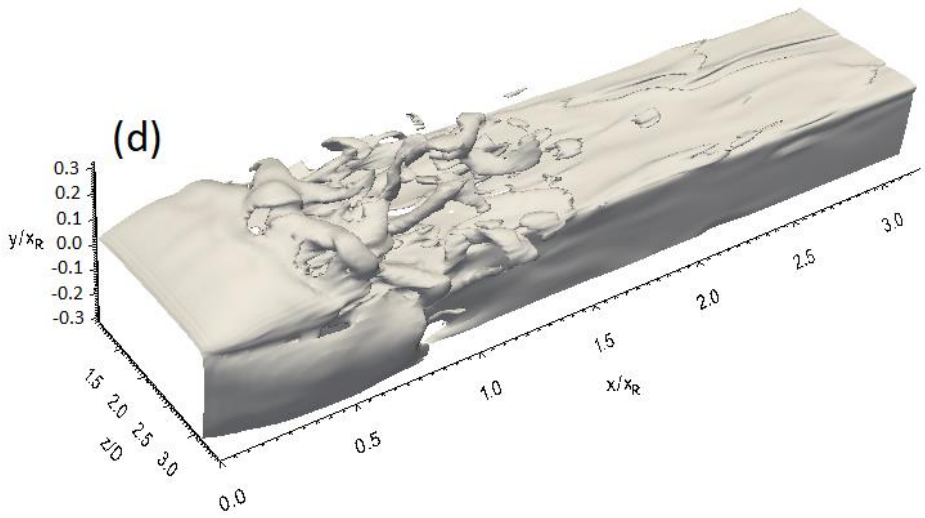
(d)
y/x_R
0.3
0.2
0.1
0.0
-0.1
-0.2
-0.3
z/D
1.5 2.0 2.5 3.0
x/x_R
0.0 0.5 1.0 1.5 2.0 2.5 3.0

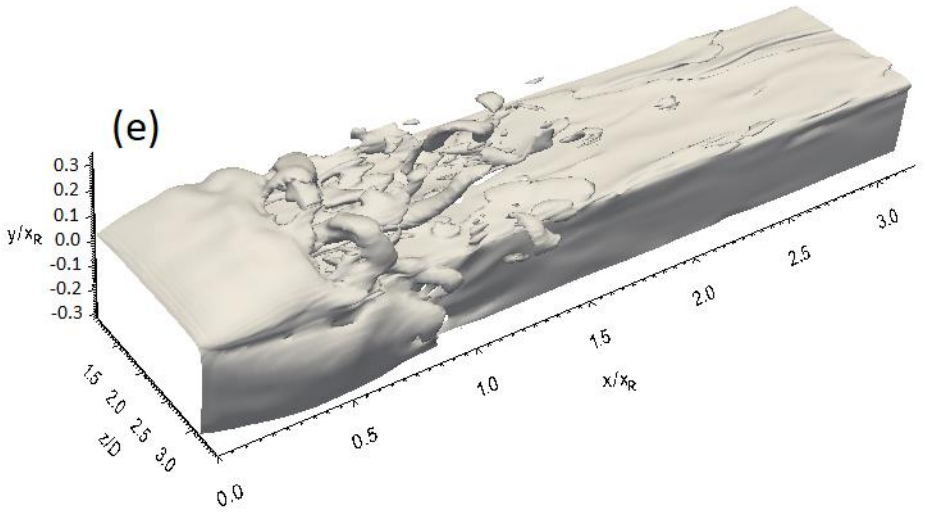
(e)
y/x_R
0.3
0.2
0.1
0.0
-0.1
-0.2
-0.3
z/D
1.5 2.0 2.5 3.0
x/x_R
0.0 0.5 1.0 1.5 2.0 2.5 3.0

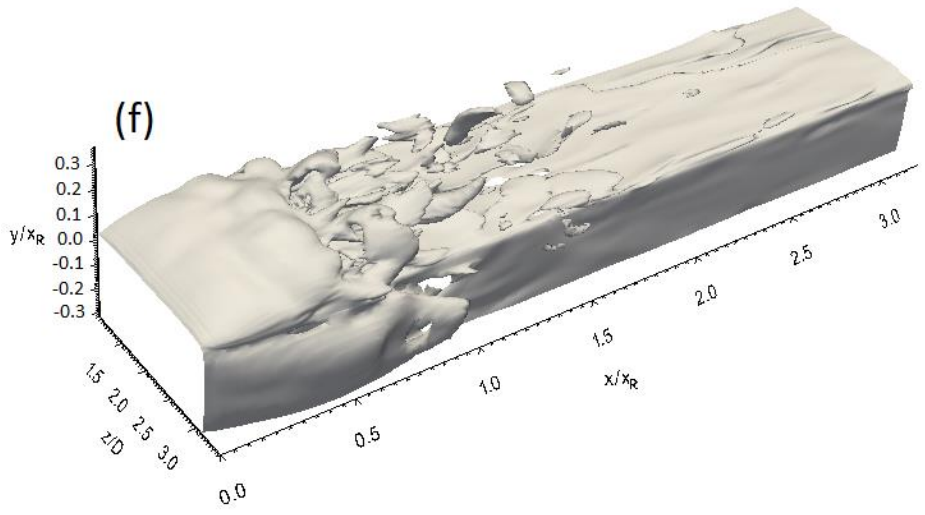
(f)
y/x_R
0.3
0.2
0.1
0.0
-0.1
-0.2
-0.3
z/D
1.5 2.0 2.5 3.0
x/x_R
0.0 0.5 1.0 1.5 2.0 2.5 3.0

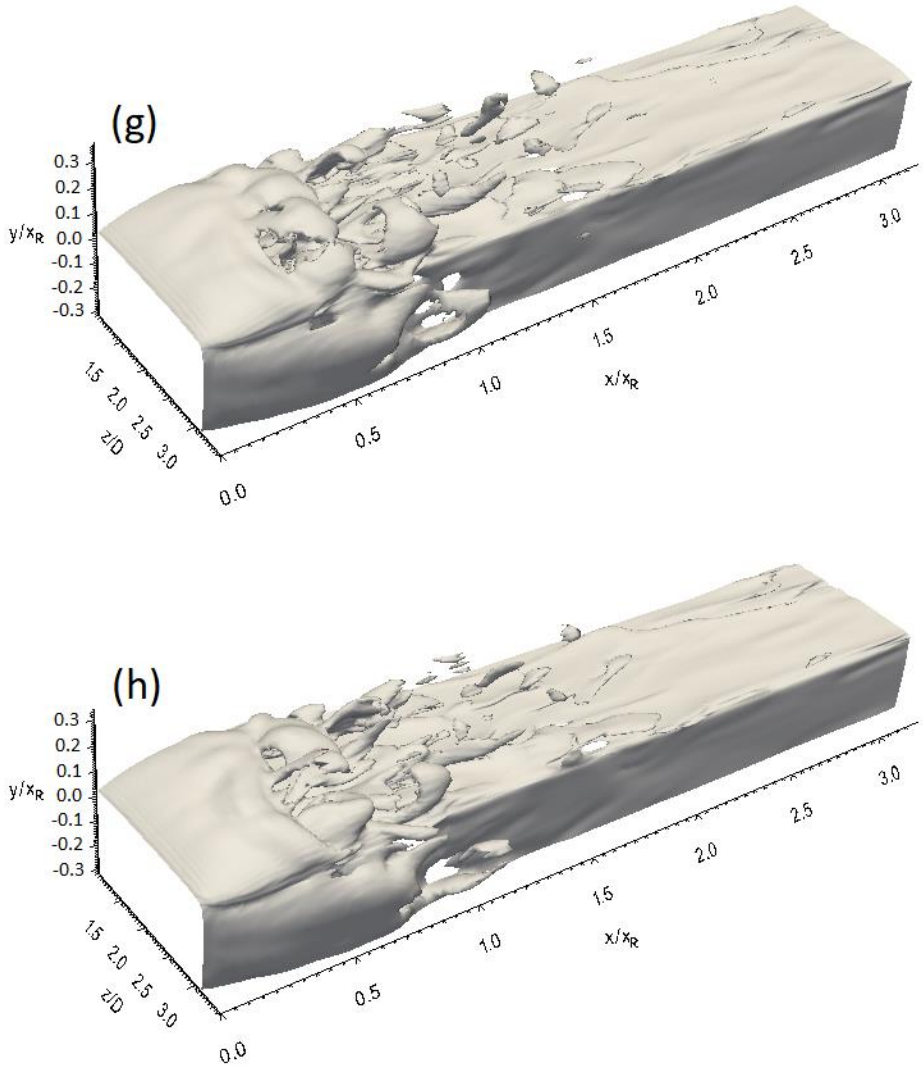

Fig. 7-36. Vorticity magnitude isosurface on the top and side surfaces at sequential times (every 250 time steps) for 3D_case2 with FST (period I)

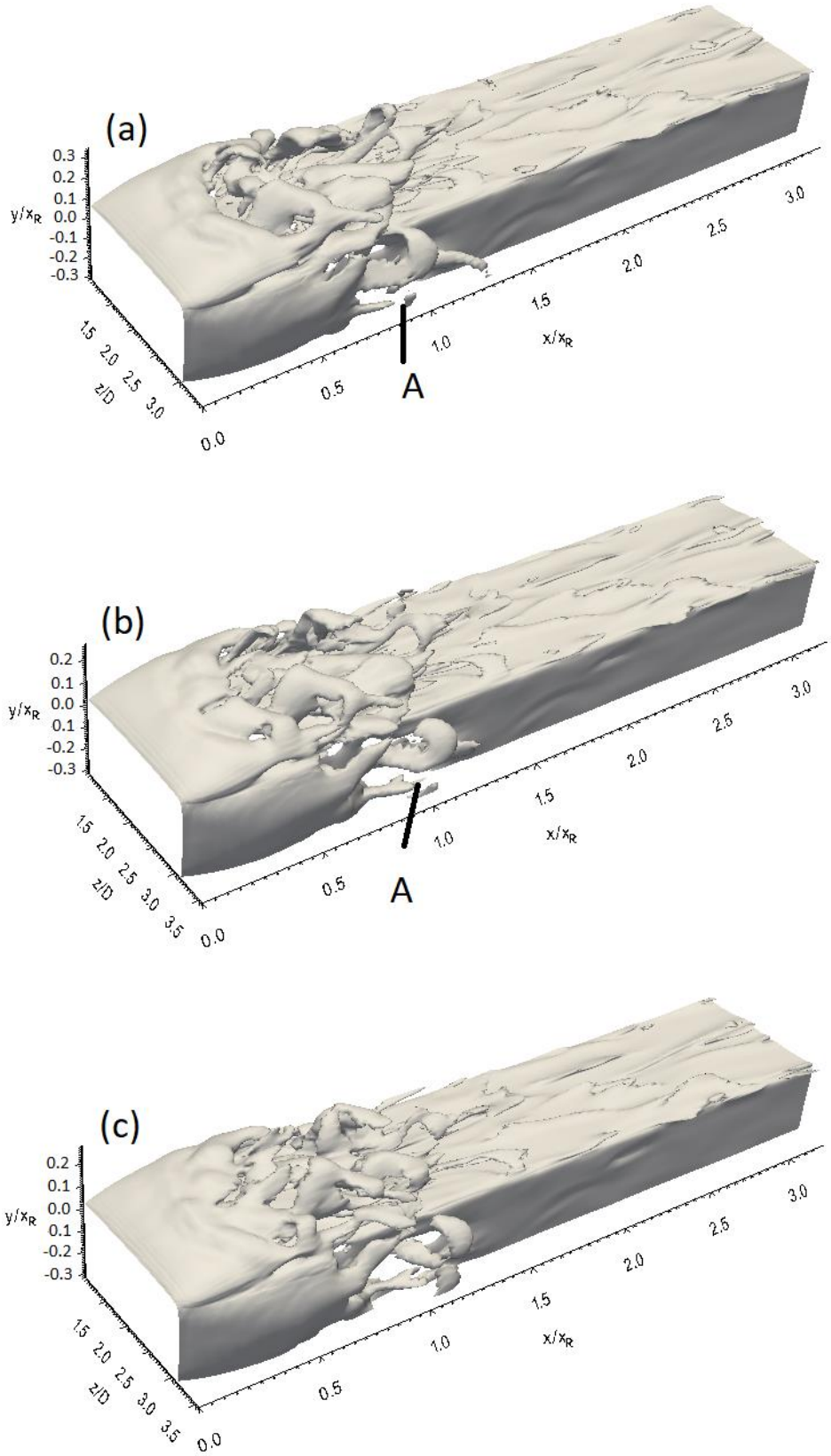

Caption for these figures is on the following page

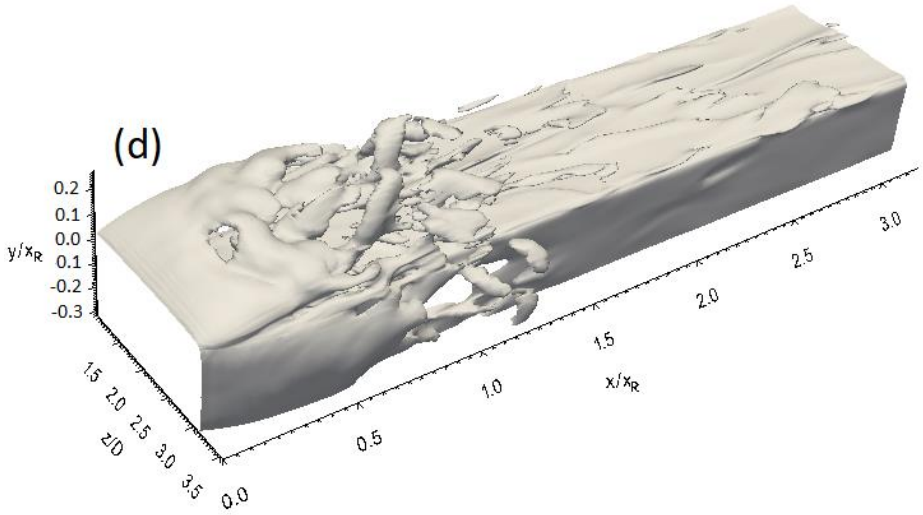

Fig. 7-37. Vorticity magnitude isosurface on the top and side surfaces at sequential times (every 250 time steps) for 3D_case2 with FST (period II)

7.3.2.2 Streamwise vorticity isosurface

For all geometries used in the current study, the difference identified in the streamwise vorticity behaviour due to the presence of a high intensity of free stream turbulence is merely related to the location at which this vorticity appears. This position becomes closer to the separation line compared to that presented for NFST. This is shown in Fig. 7-38 for the flat plate, Fig. 7-39 for 3D_case1, and Fig. 7-40 for 3D_case2. These figures show six streamwise vorticity isosurfaces taken every 250 time steps for each geometry.

For all geometries, a significant number of vortical structures can be seen to appear in the region between x/x_R = 0.5 and x/x_R = 1, indicating that in this region most events associated with the transition to full turbulence take place. Further downstream, streamwise vorticity structures that shed to the reattached turbulent boundary layer move a certain distance before disintegrating into small structures affecting the turbulent boundary layer development. Furthermore, it is clearly seen that the streamwise vorticity structures form an angle with the solid wall (lifted up), and it might be this angle that allows for the existence of these structures after the reattachment region.

The correlation coefficient between the root mean square fluctuating streamwise and wall-normal velocities $(-\overline{u'v'}/u'_{rms}v'_{rms})$ is plotted at x/x_R = 0.6, x/x_R = 1, and x/x_R = 2,

as shown in Fig. 7-41 for the flat plate, Fig. 7-42 for 3D_case1, and Fig. 7-43 for 3D_case2.

For all geometries, the profile of the correlation coefficient shows that at $x/x_R = 0.6$, there is a non-uniform distribution of the correlation coefficient in the wall-normal direction, indicating the existence of large streamwise vorticity structures. The correlation coefficient is very small when it is close to the wall, and increases to a maximum at the shear layer centre. At the mean reattachment ($x/x_R = 1$), the correlation coefficient distribution through the shear layer is roughly uniform. Further downstream, the distribution of the correlation coefficient remains essentially uniform for all geometries, as shown at the location of $x/x_R = 2$.

The above behaviour of the correlation coefficient profile for FST is similar to that found for NFST presented in Section 7.3.2.2. This indicates that there is no difference in the streamwise vorticity development for either of the flow cases.

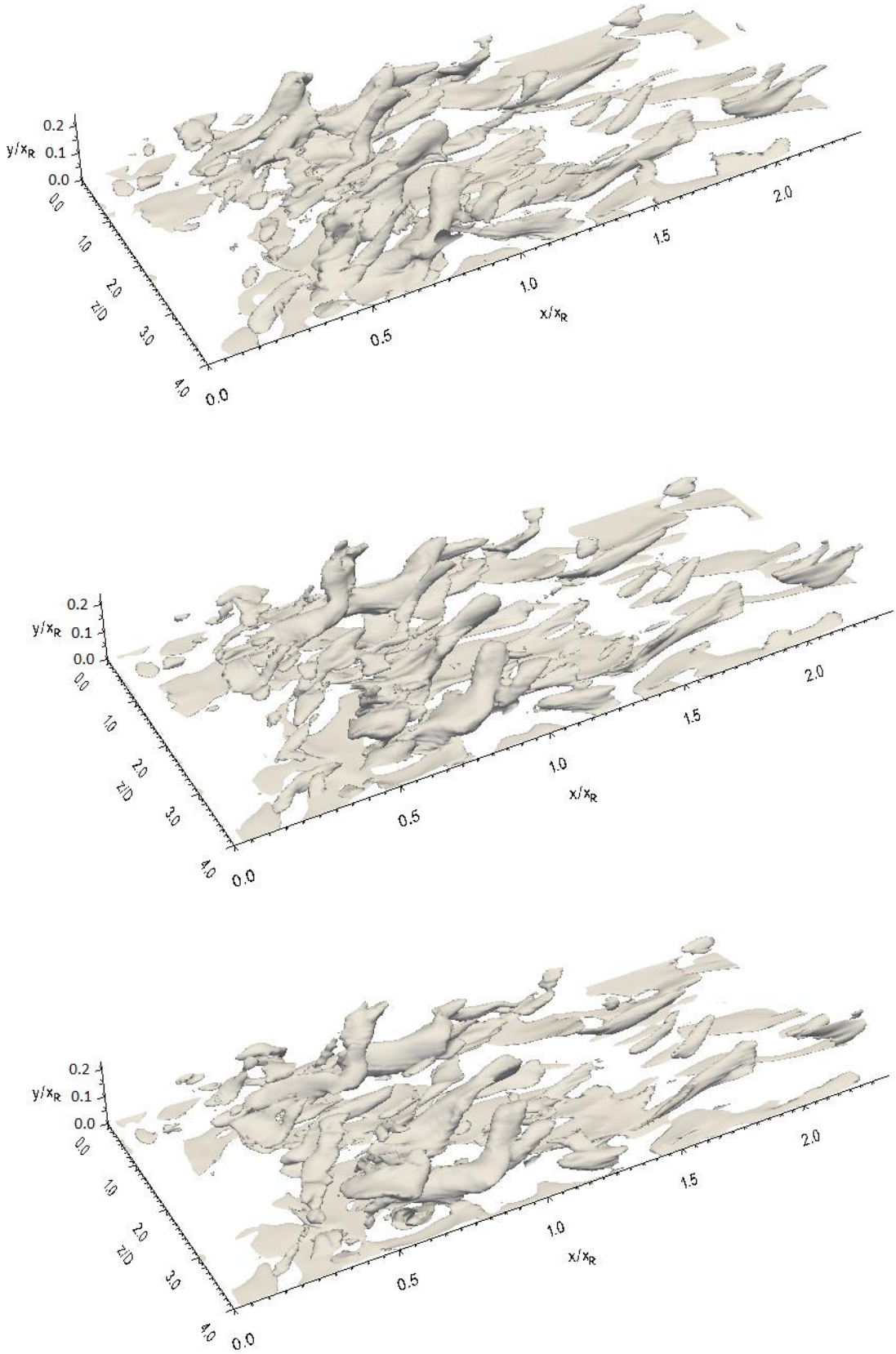

Caption for these figures is on the following page

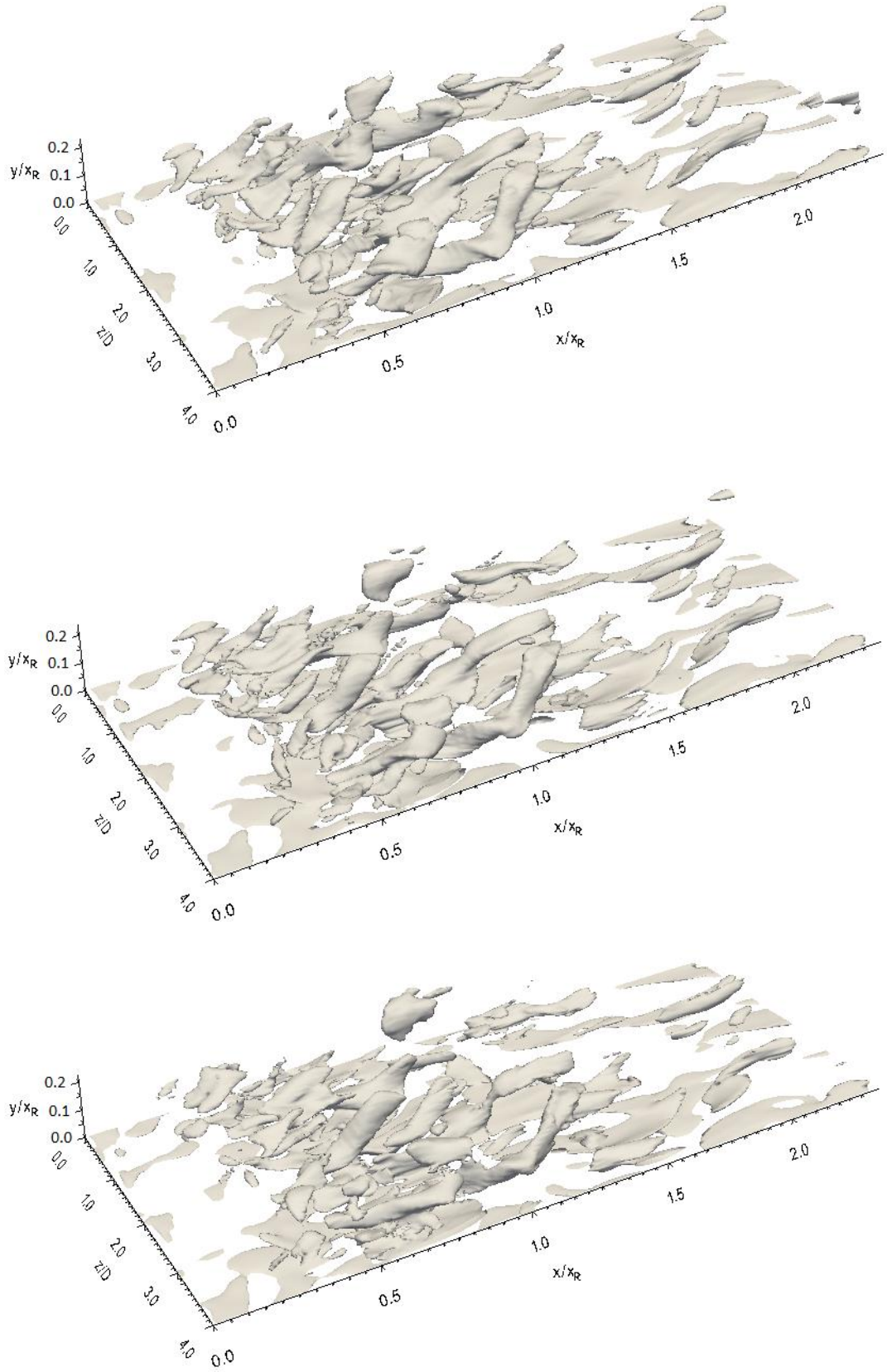

Fig. 7-38. Streamwise vorticity isosurface at sequential times (every 250 time steps) for the flat plate with FST

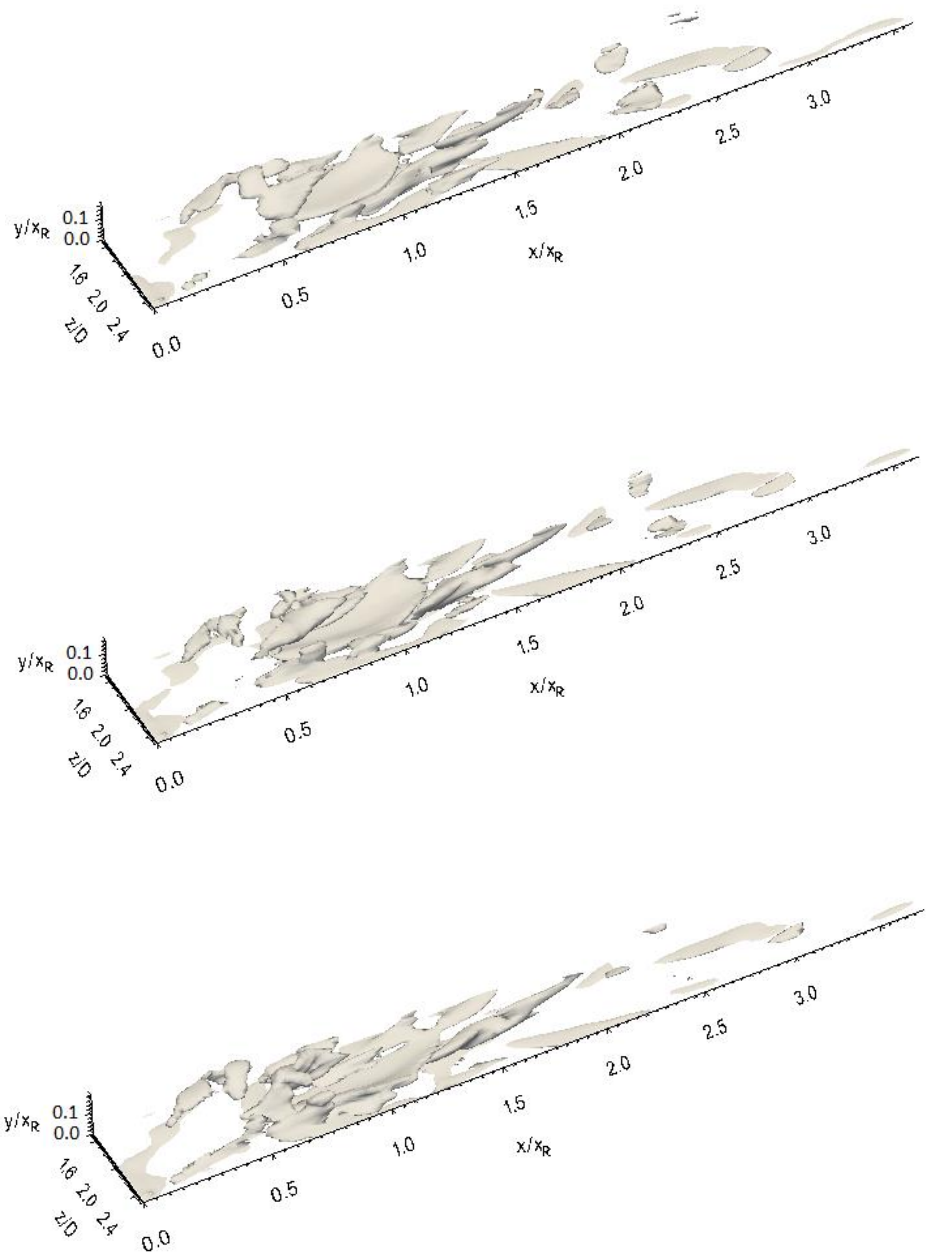

Caption for these figures is on the following page

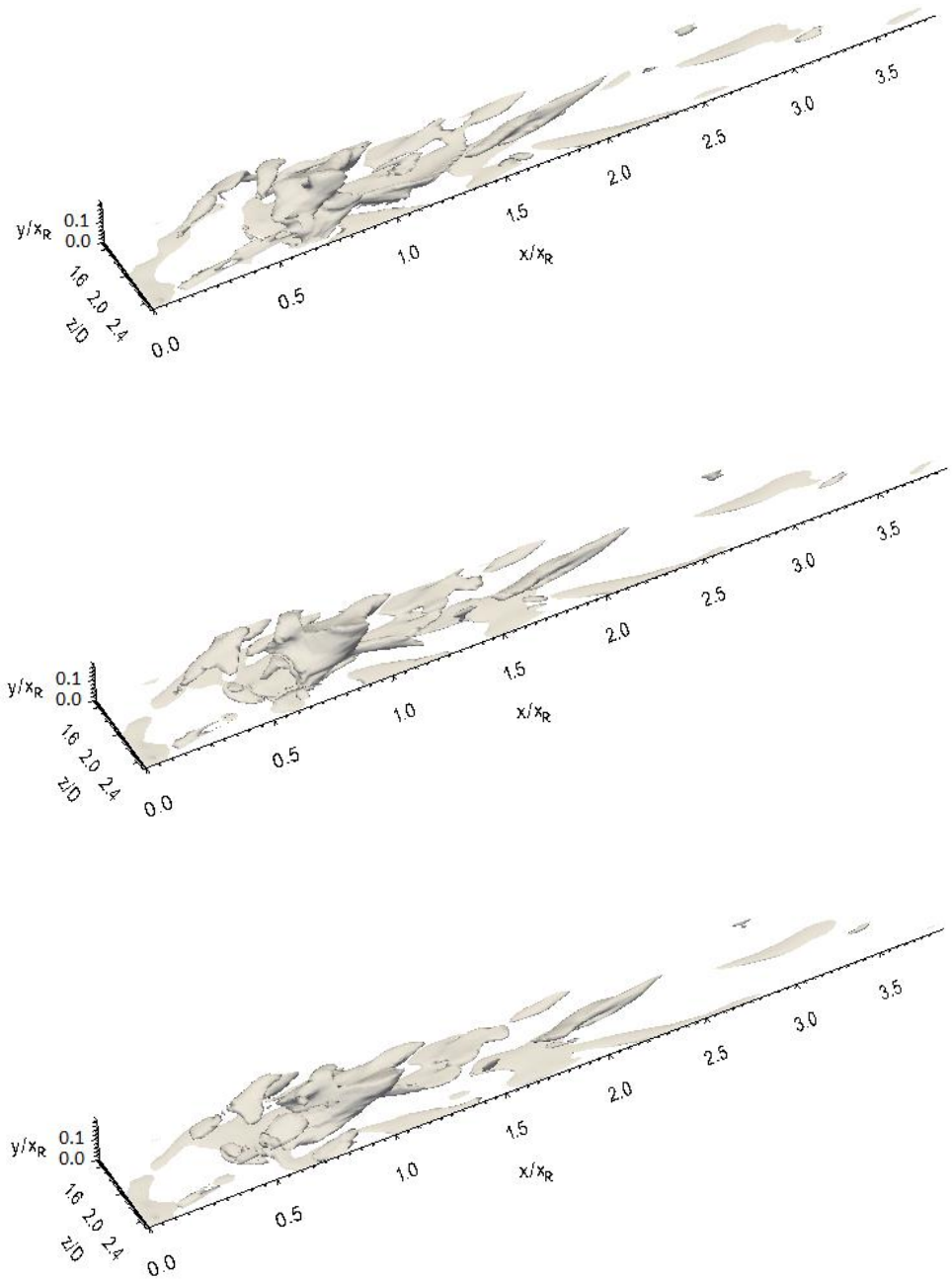

Fig. 7-39. Streamwise vorticity isosurface at sequential times (every 250 time steps) for 3D_case1 with FST

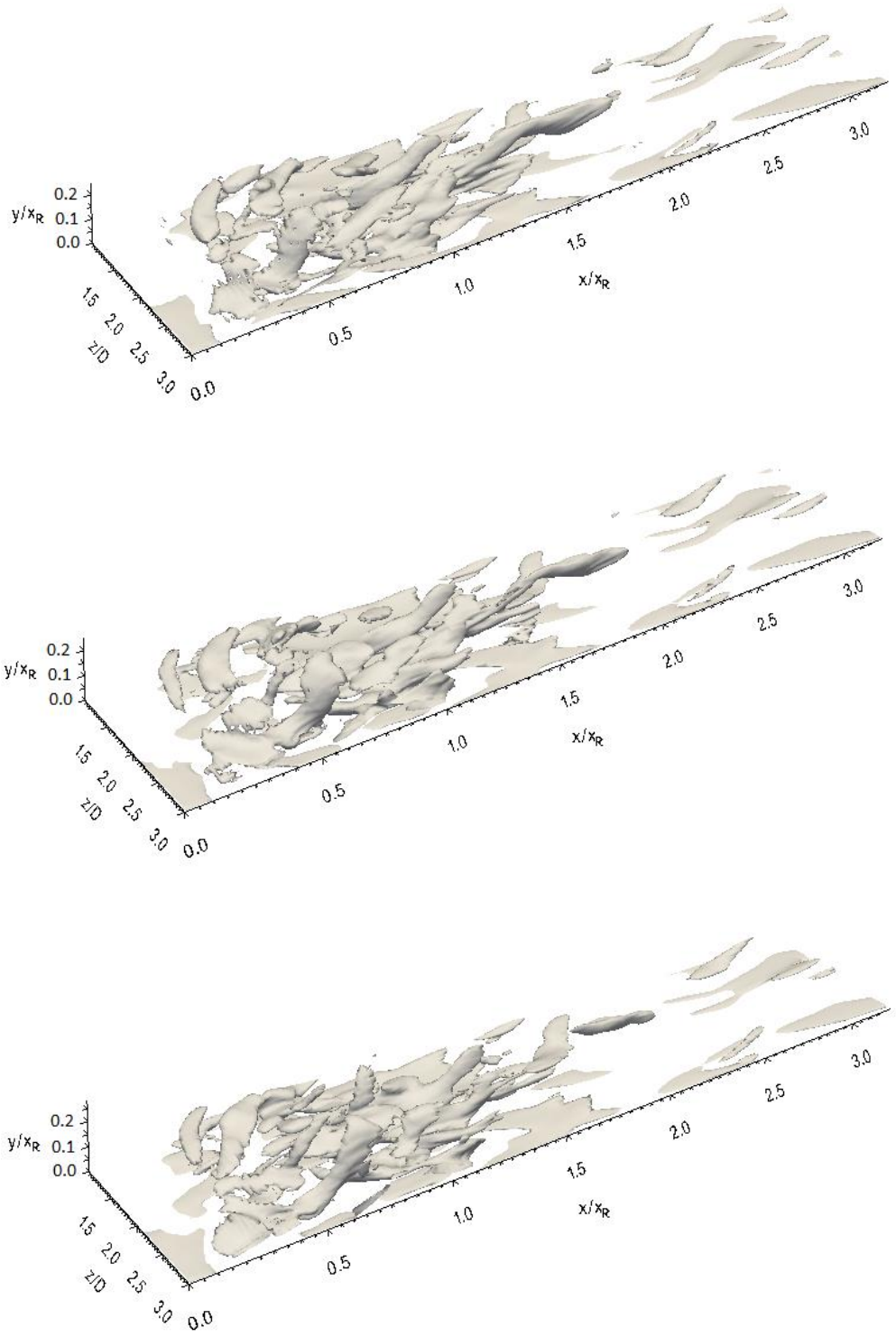

Caption for these figures is on the following page

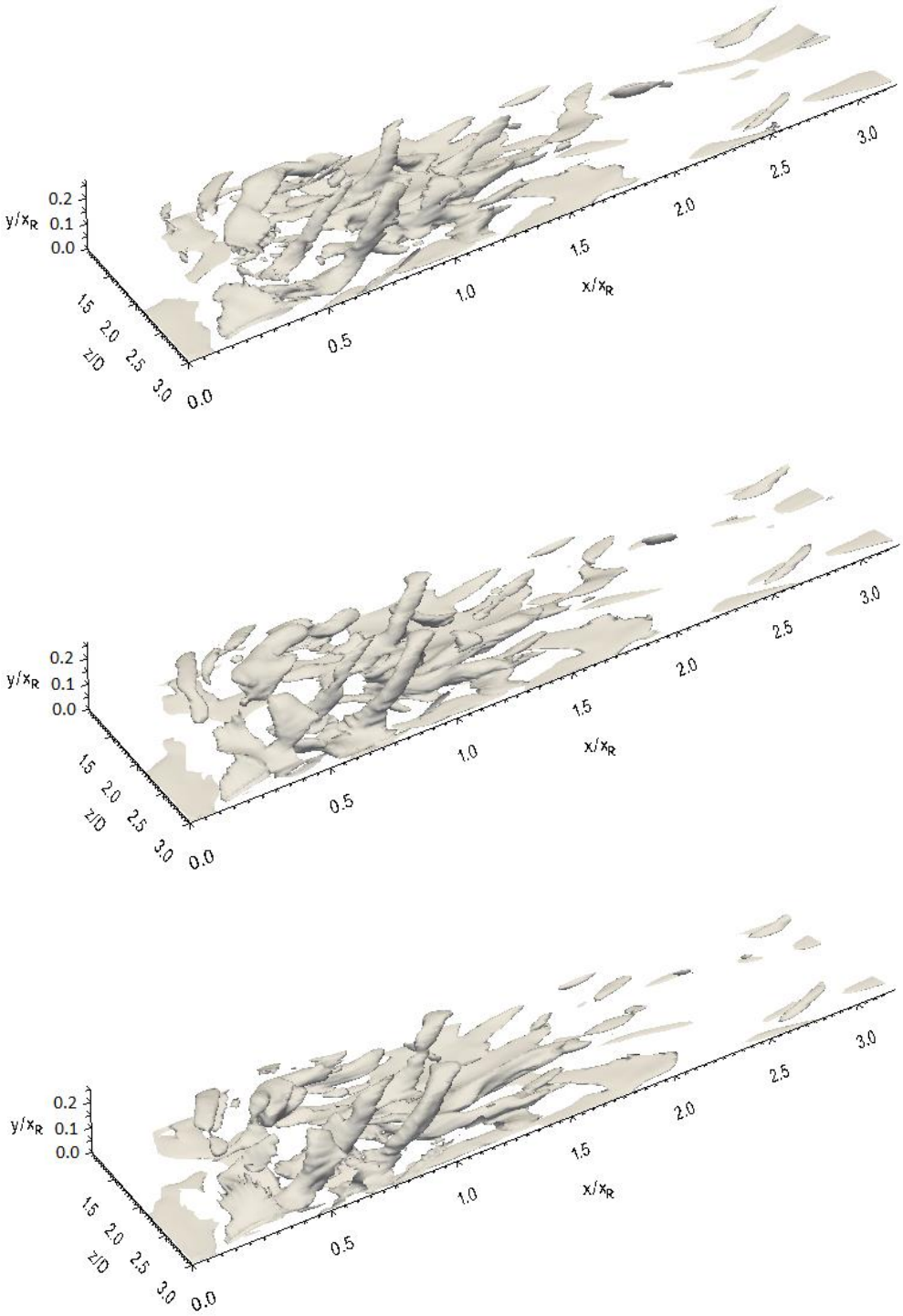

Fig. 7-40. Streamwise vorticity isosurface at sequential times (every 250 time steps) for 3D_case2 with FST

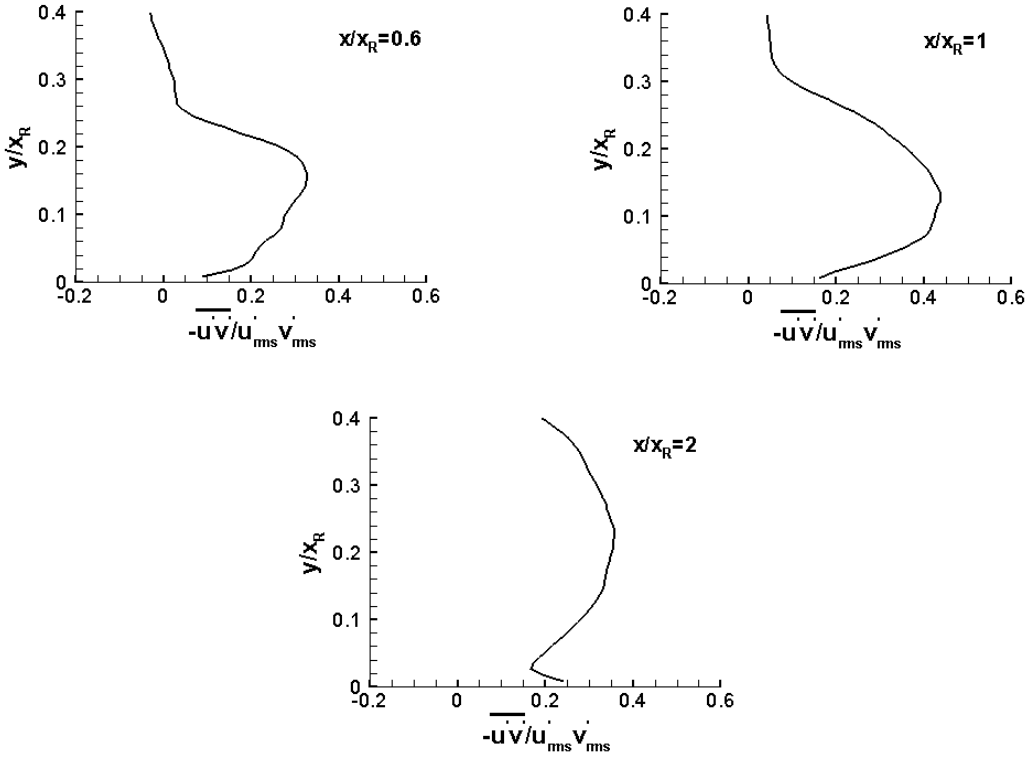

Fig. 7-41. Wall-normal distribution of the correlation coefficient between u'_{rms} and v'_{rms} at three streamwise positions for the flat plate with FST

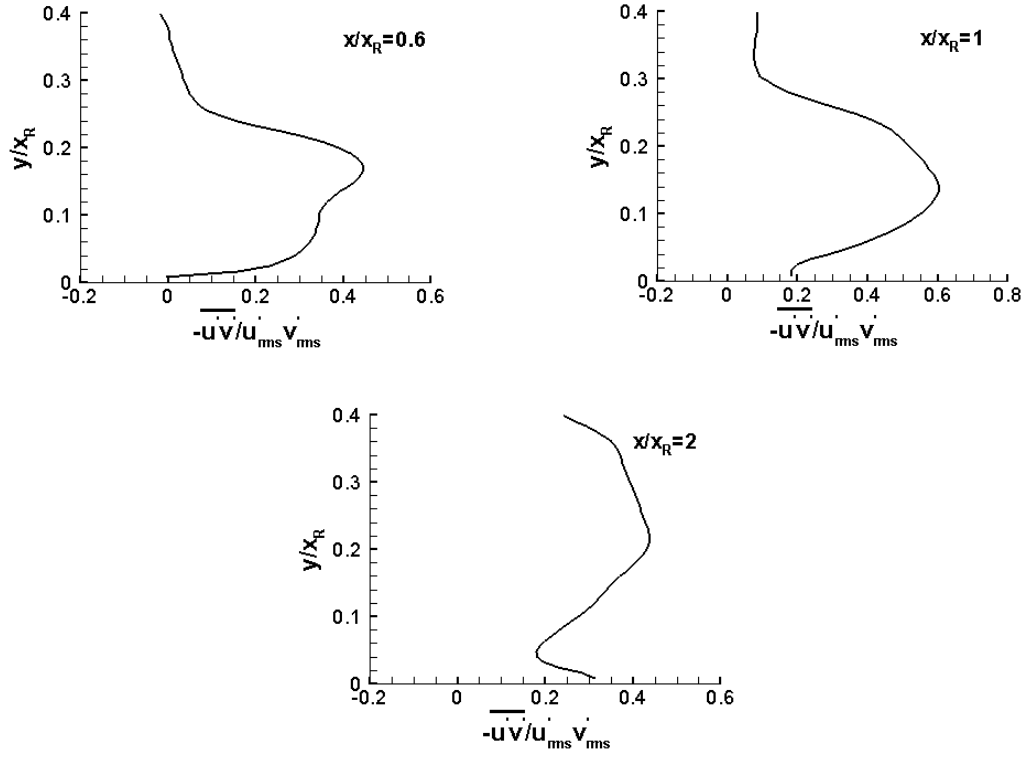

Fig. 7-42. Wall-normal distribution of the correlation coefficient between u'_{rms} and v'_{rms} at three streamwise positions for 3D_case1 with FST

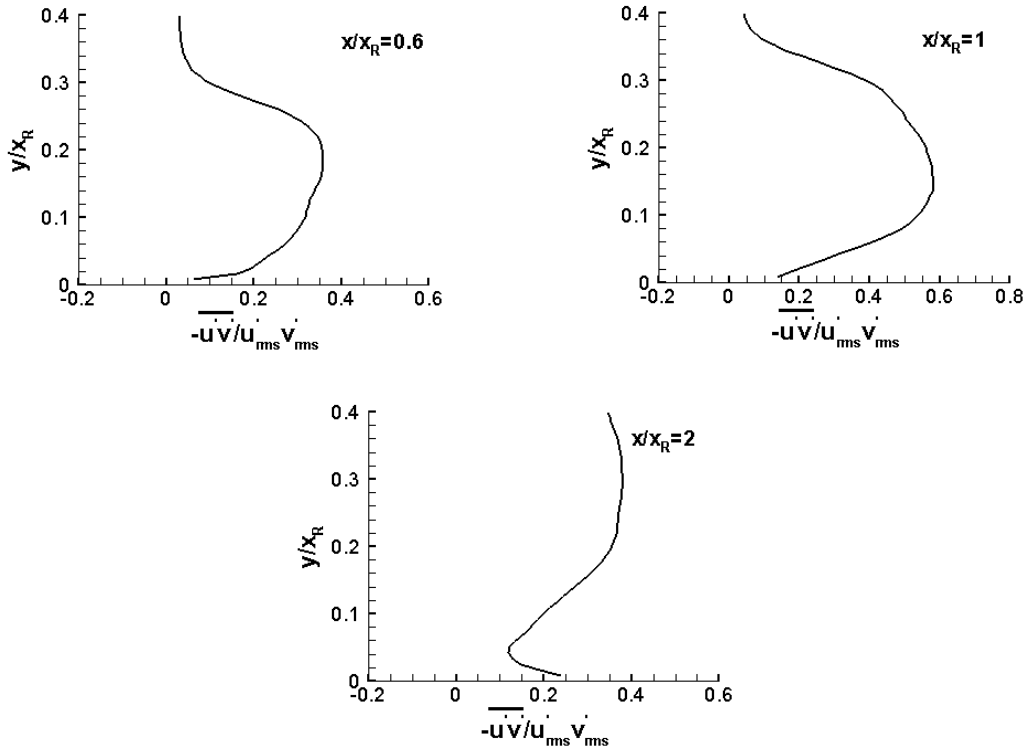

Fig. 7-43. Wall-normal distribution of the correlation coefficient between u'_{rms} and v'_{rms} at three streamwise positions for 3D_case2 with FST

7.3.2.3 Wall-normal vorticity isosurface

The wall-normal vorticity isosurfaces (taken every 250 time steps) are presented in Fig. 7-44 for the flat plate, Fig. 7-45 for 3D_case1 and Fig. 7-46 for 3D_case2, which show the similar inclined structures corresponding to that observed in the streamwise vorticity isosurfaces.

For all geometries, it is clearly seen that there are a considerable number of wall-normal vorticity structures in the region that extends from x/x_R = 0.5 to x/x_R = 1. Further downstream, the dominant process is the process of the breakdown, in which the large-scale structures break down into smaller turbulent structures in the reattached turbulent boundary layer.

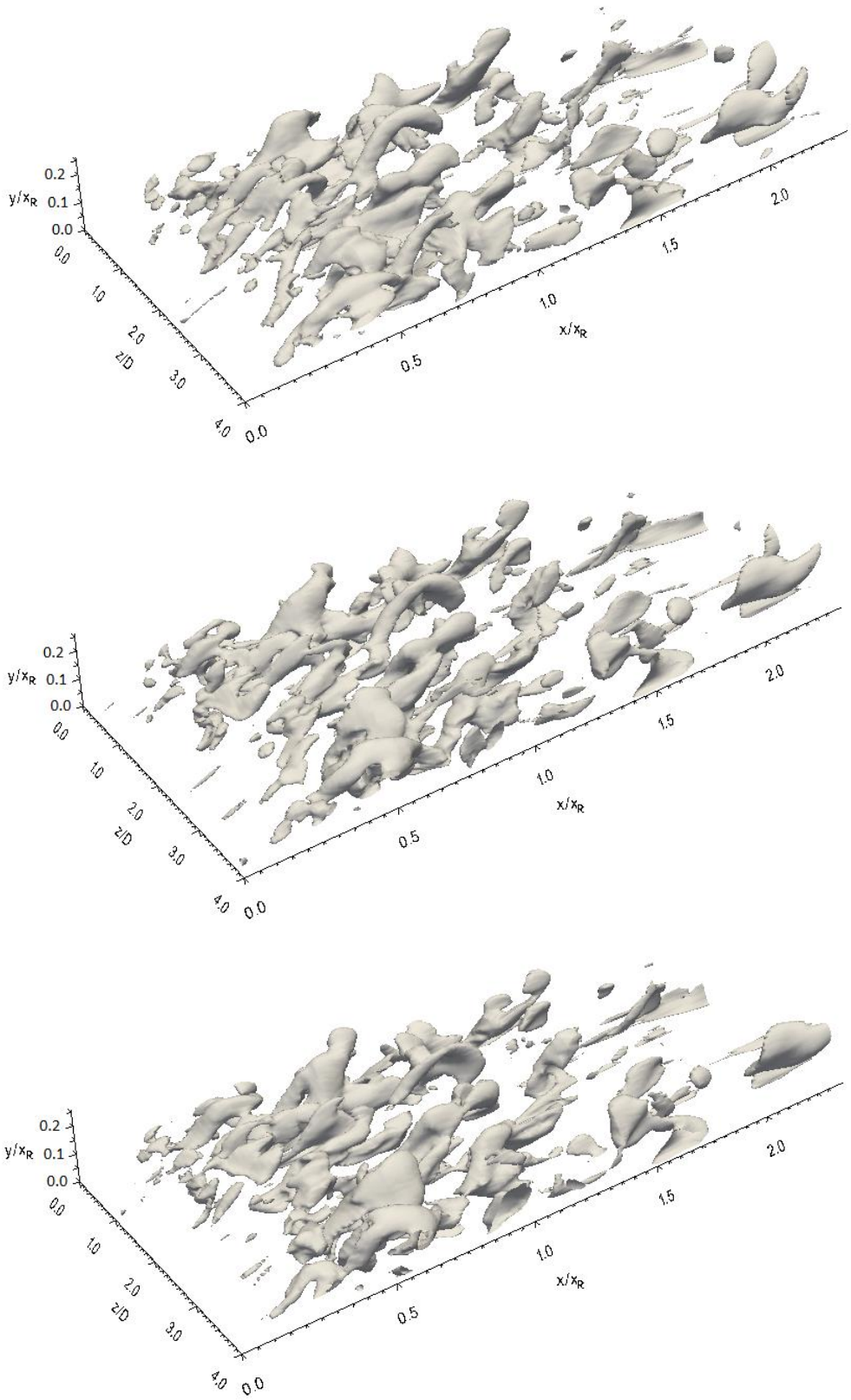

Caption for these figures is on the following page

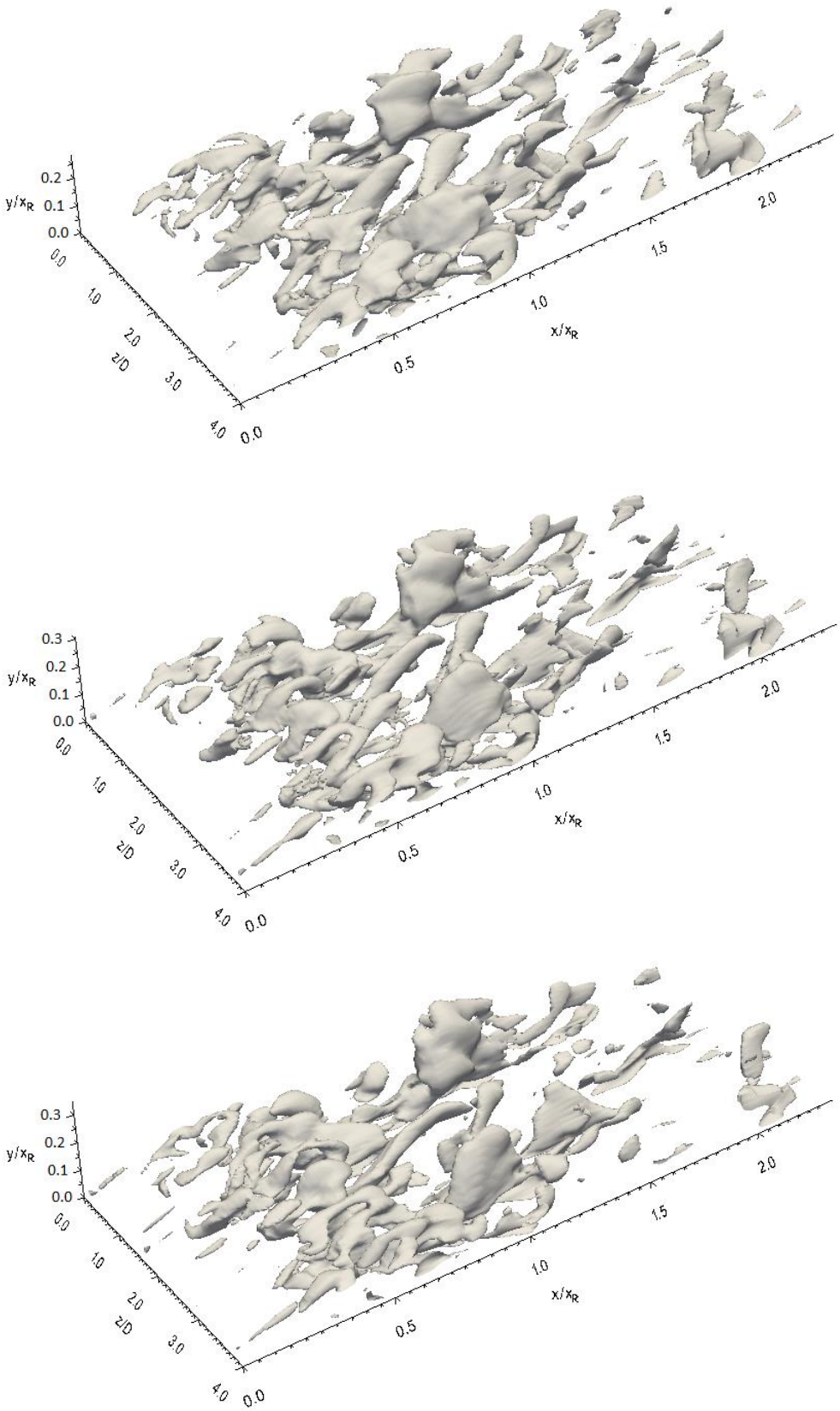

Fig. 7-44. Wall-normal vorticity isosurface at sequential times (every 250 time steps) for the flat plate with FST

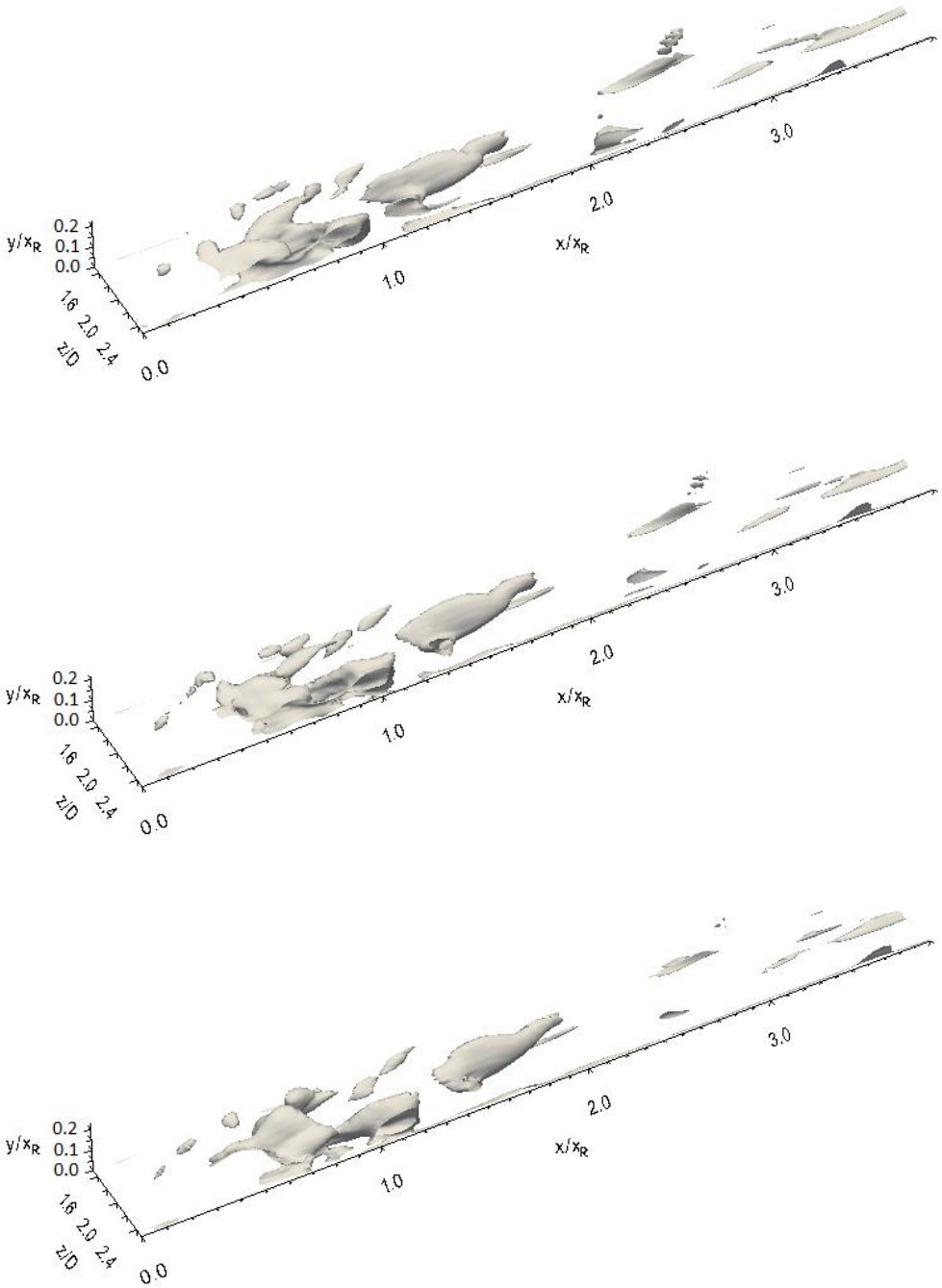

Caption for these figures is on the following page

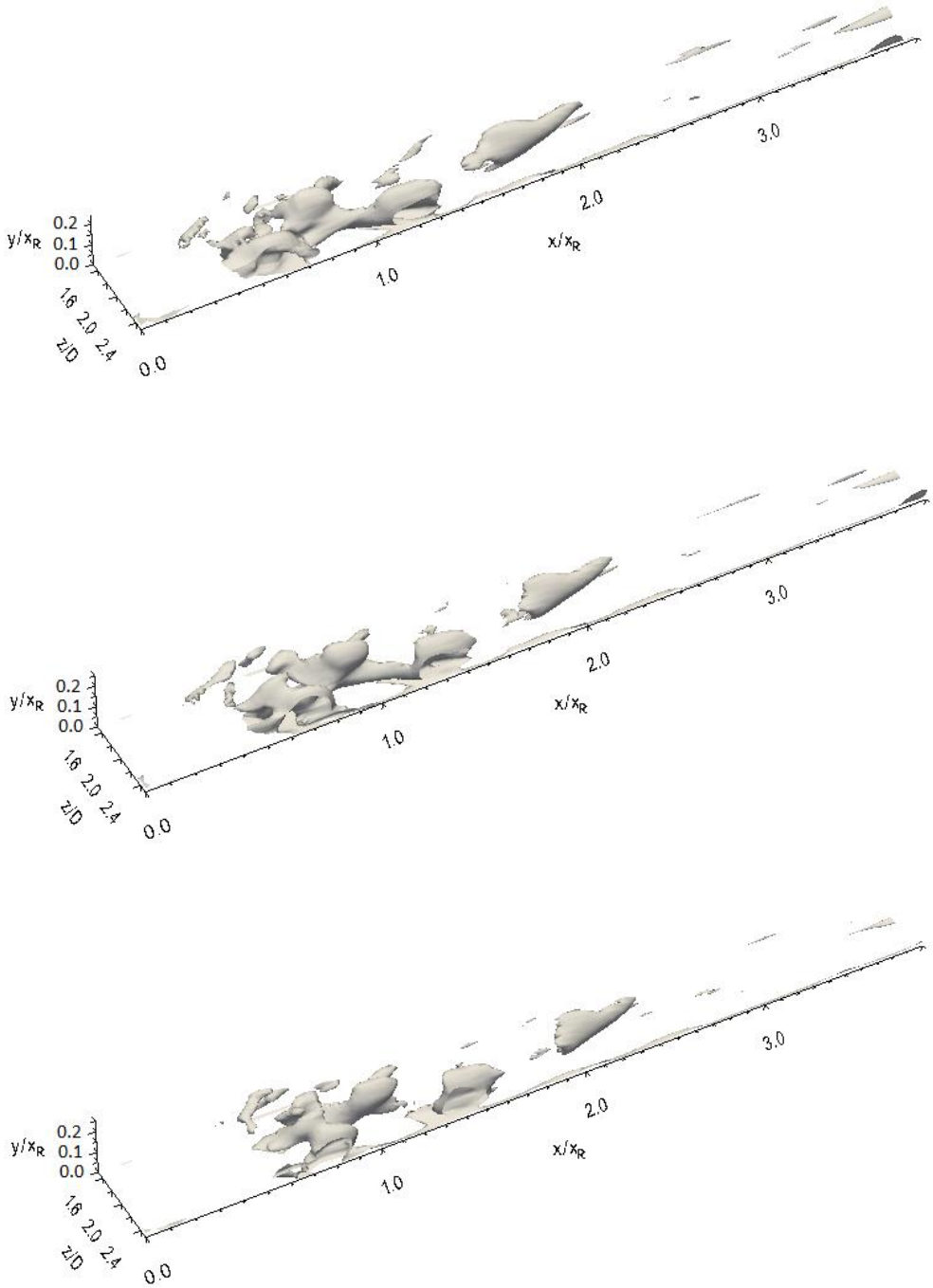

Fig. 7-45. Wall-normal vorticity isosurface at sequential times (every 250 time steps) for 3D_case1 with FST

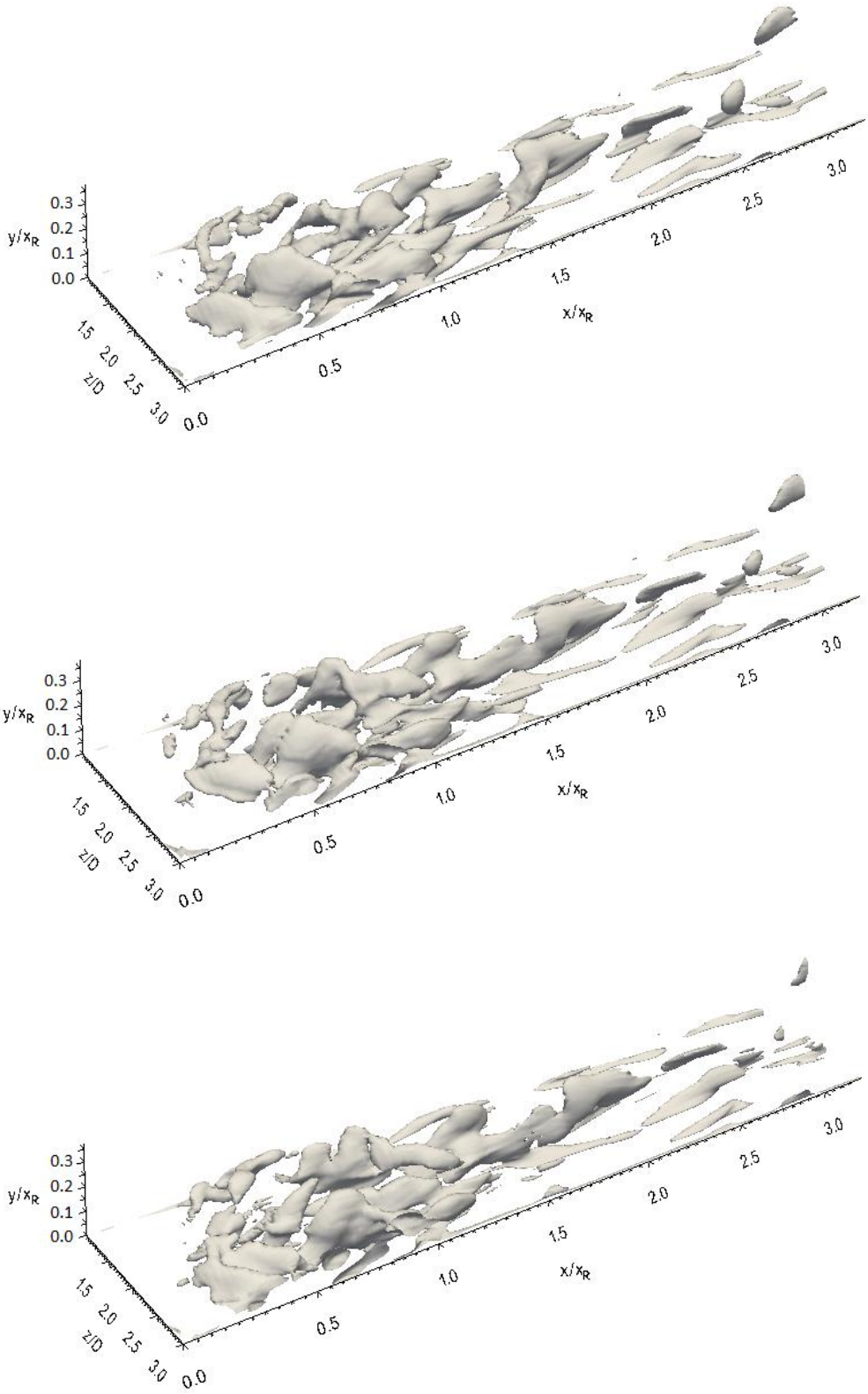

Caption for these figures is on the following page

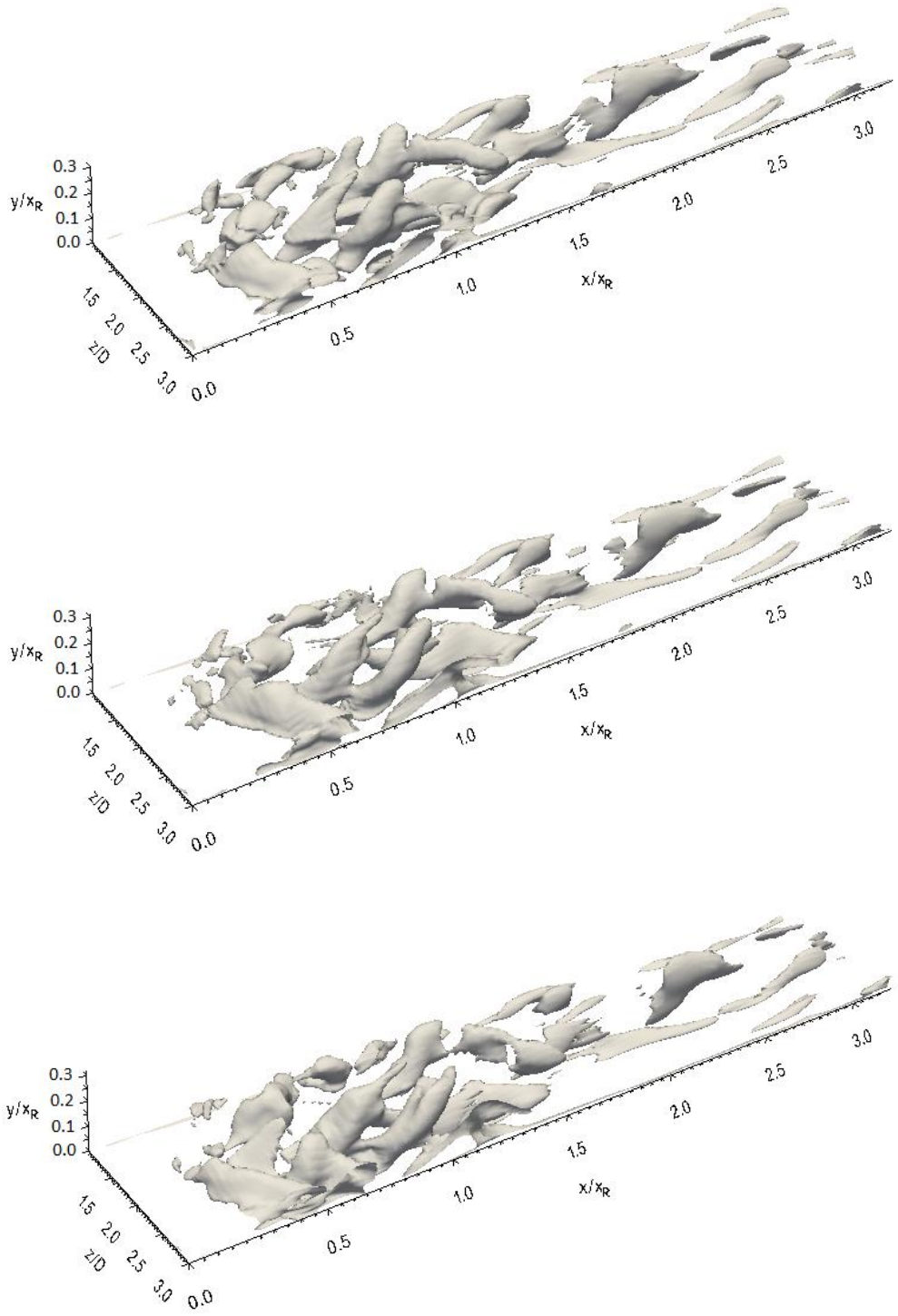

Fig. 7-46. Wall-normal vorticity isosurface at sequential times (every 250 time steps) for 3D_case2 with FST

7.3.2.4 Spanwise vorticity isosurface

The spanwise vorticity isosurfaces in the present study show similar behaviour to that presented by the streamwise and wall-normal vorticities isosurfaces with regards to the locations of the appearance of vortical structures and their breakdown.

The sequential spanwise vorticity isosurfaces for the flat plate taken every 250 time steps are shown in Fig. 7-47. It is clearly seen that the location of the beginning of the unsteadiness in a plane sheet of the vorticity is at $x/x_R = 0.1$. Further downstream and up to $x/x_R = 0.3$, this sheet shows the growth of low-amplitude disturbance. Further downstream, violent three-dimensional motions of the flow associated with the appearance of spanwise vorticity structures can be seen. Downstream of the mean reattachment line, the large-structures that shed to the reattached turbulent boundary layer move a certain distance before they are totally breakdown into smaller turbulent structures.

Six spanwise vorticity isosurfaces taken every 250 time steps for 3D_case1 are shown in Fig. 7-48. They illustrate a plane vorticity sheet that extends from the leading edge of the geometry up to $x/x_R = 0.3$. Further downstream, and up to $x/x_R = 0.5$, the vorticity sheet develops smoothly and shows only a small distortion. Spanwise vorticity structures are seen in the region from $x/x_R = 0.5$ to $x/x_R = 1$. Beyond the mean reattachment line, these structures vanish due to their breakdown into smaller structures within the reattached turbulent boundary layer.

For 3D_case2, a plane spanwise vorticity sheet appears which seems to be smooth and uniform in the region that extends from the geometry leading edge to $x/x_R = 0.2$, where the unsteadiness in the free shear layer starts as shown in Fig. 7.49. Violent three-dimensional motions of the flow occur at around $x/x_R = 0.4$. Further downstream and up to the mean reattachment line, large-scale vorticity structures begin to appear. Downstream from the mean reattachment line, spanwise vorticity structures disappear gradually up to $x/x_R = 1.5$, indicating their breakdown into smaller turbulent structures.

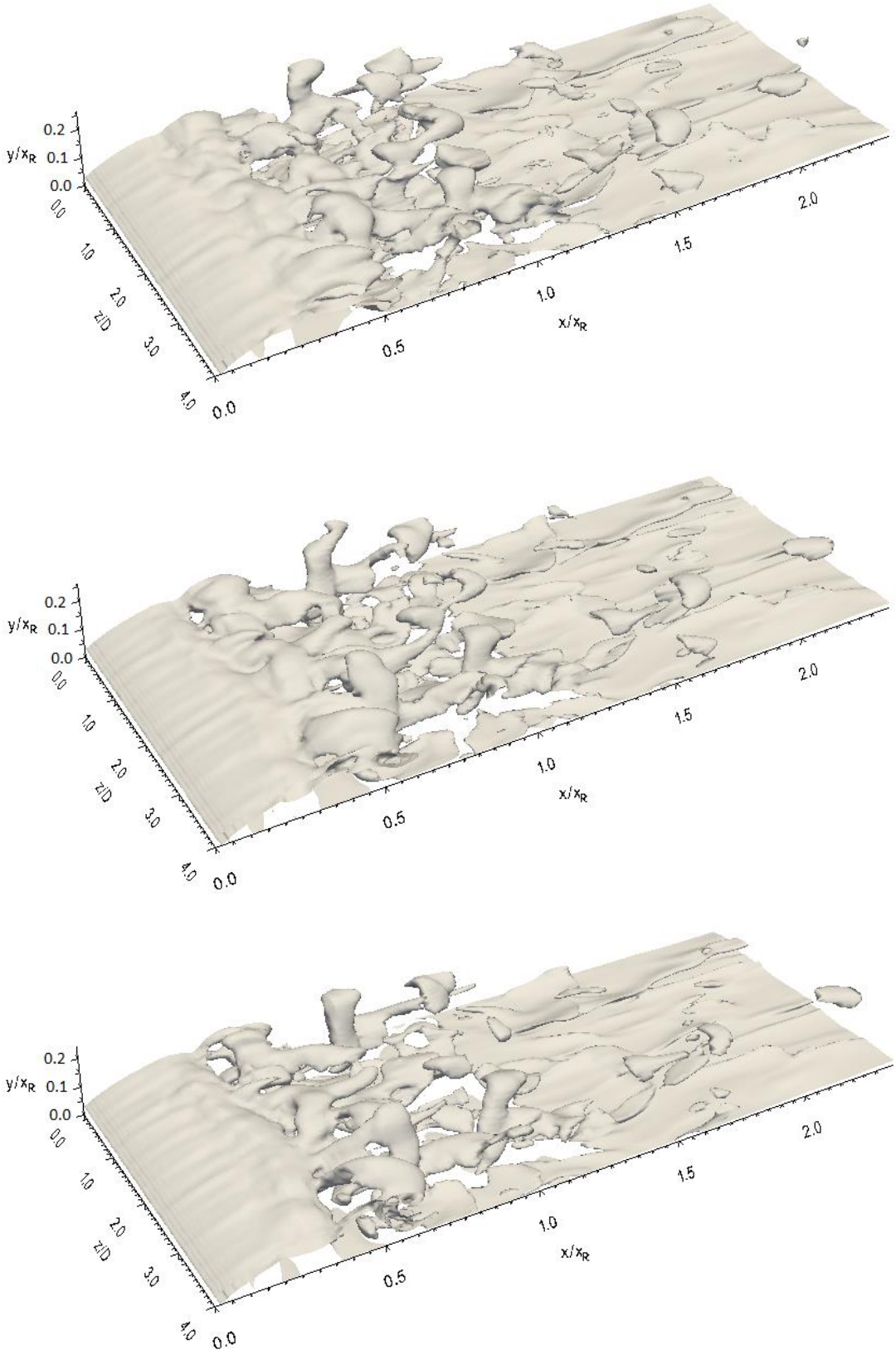

Caption for these figures is on the following page

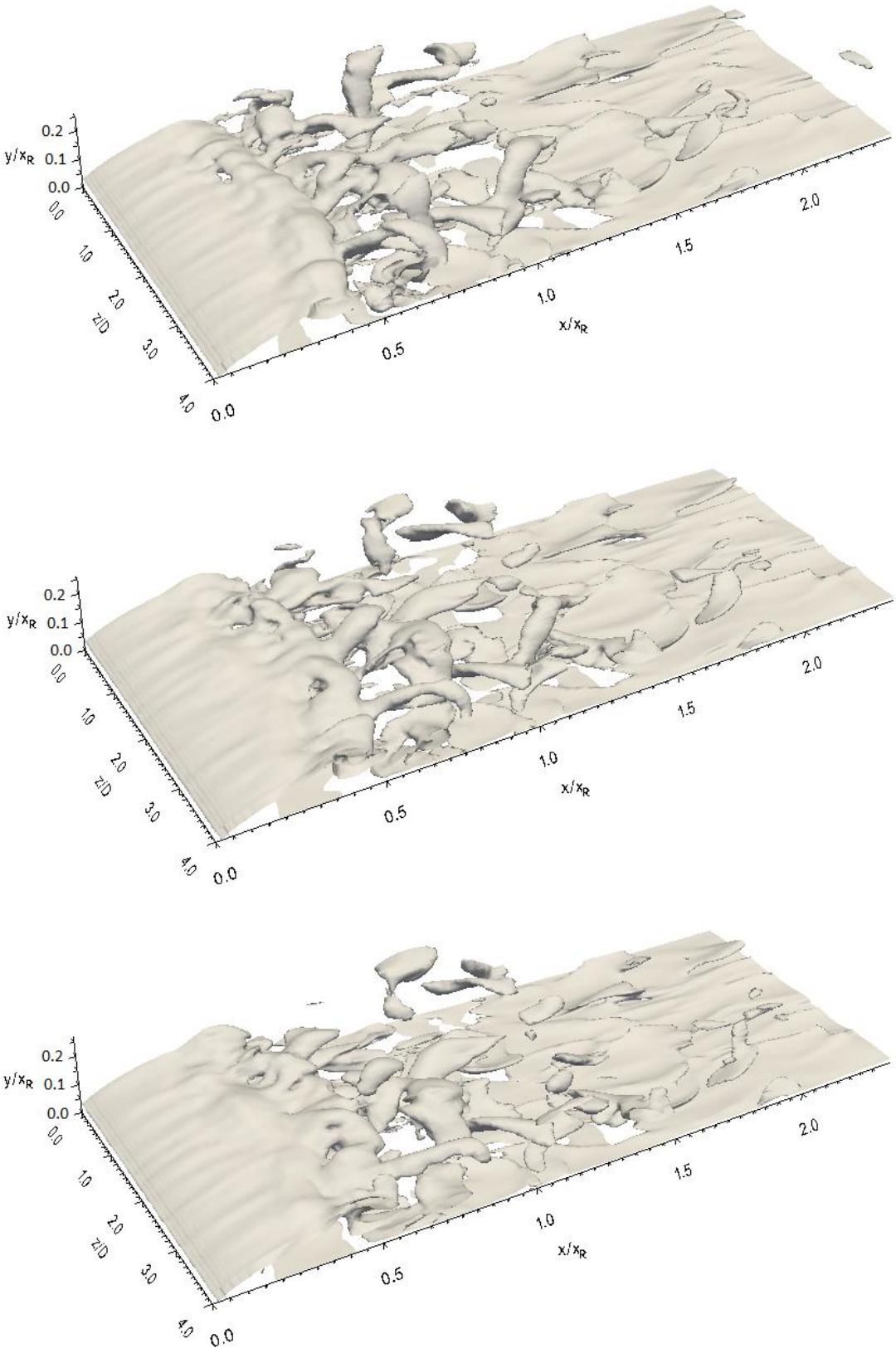

Fig. 7-47. Spanwise vorticity isosurface at sequential times (every 250 time steps) for the flat plate with FST

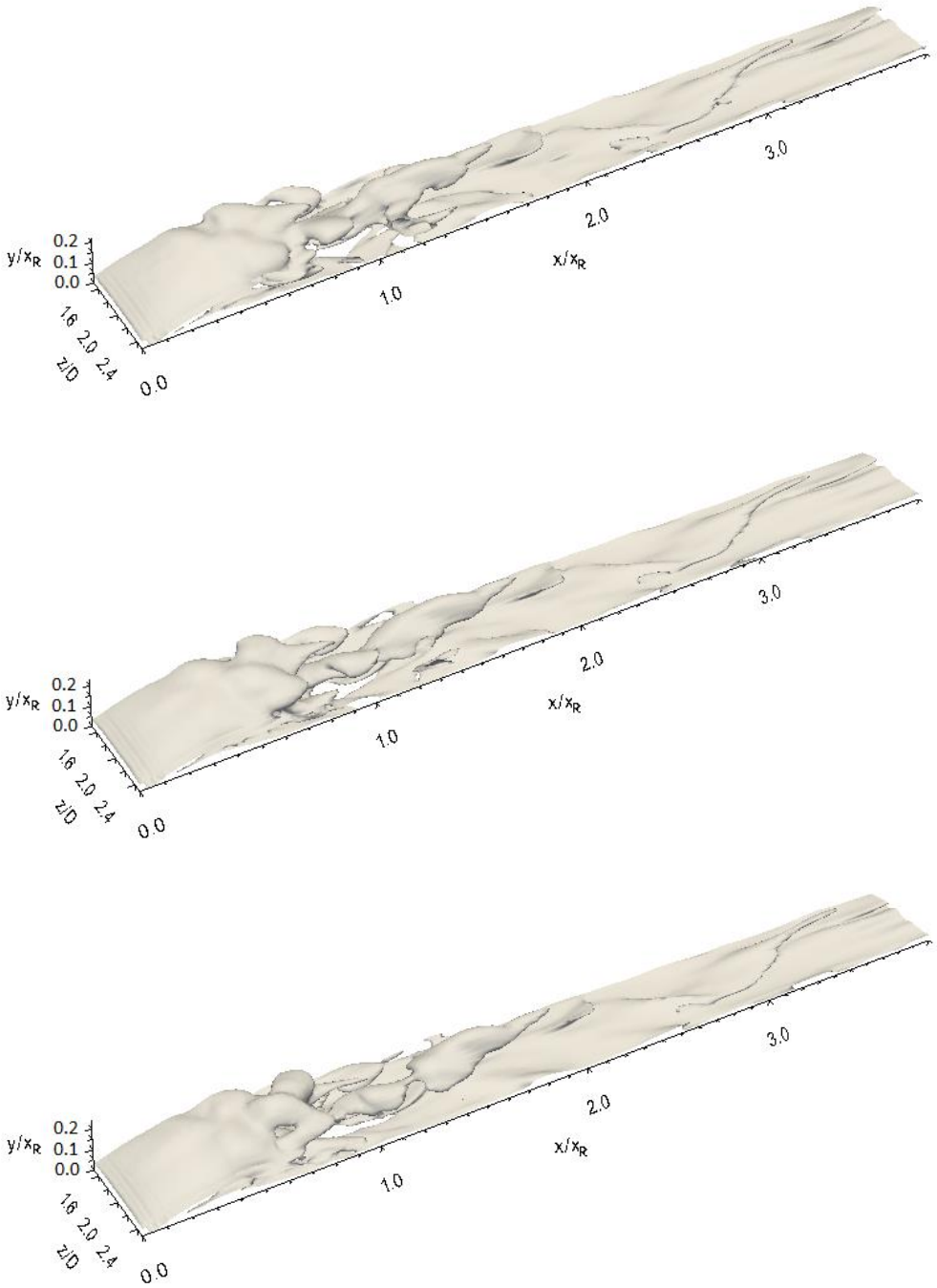

Caption for these figures is on the following page

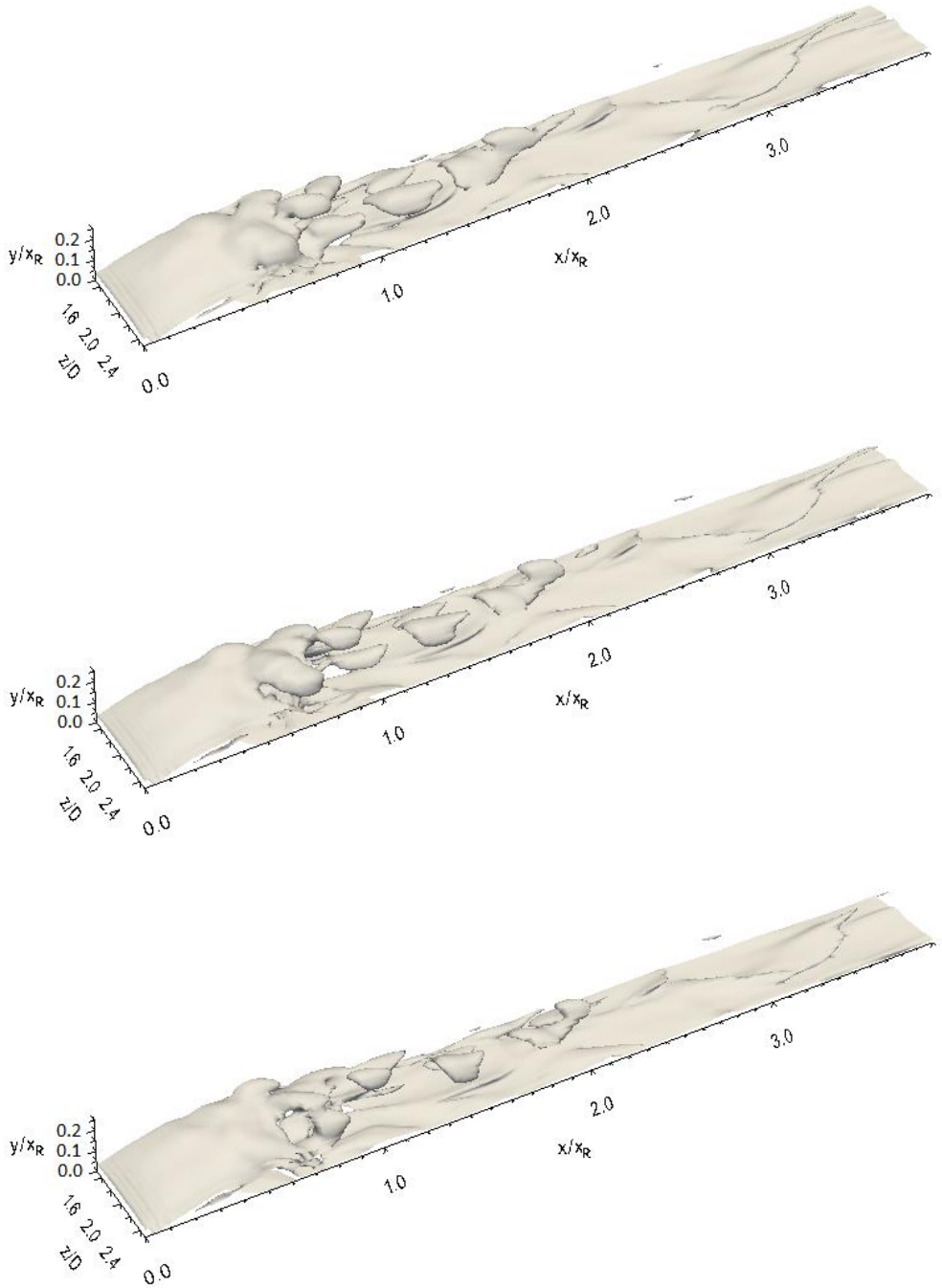

Fig. 7-48. Spanwise vorticity isosurface at sequential times (every 250 time steps) for 3D_case1 with FST

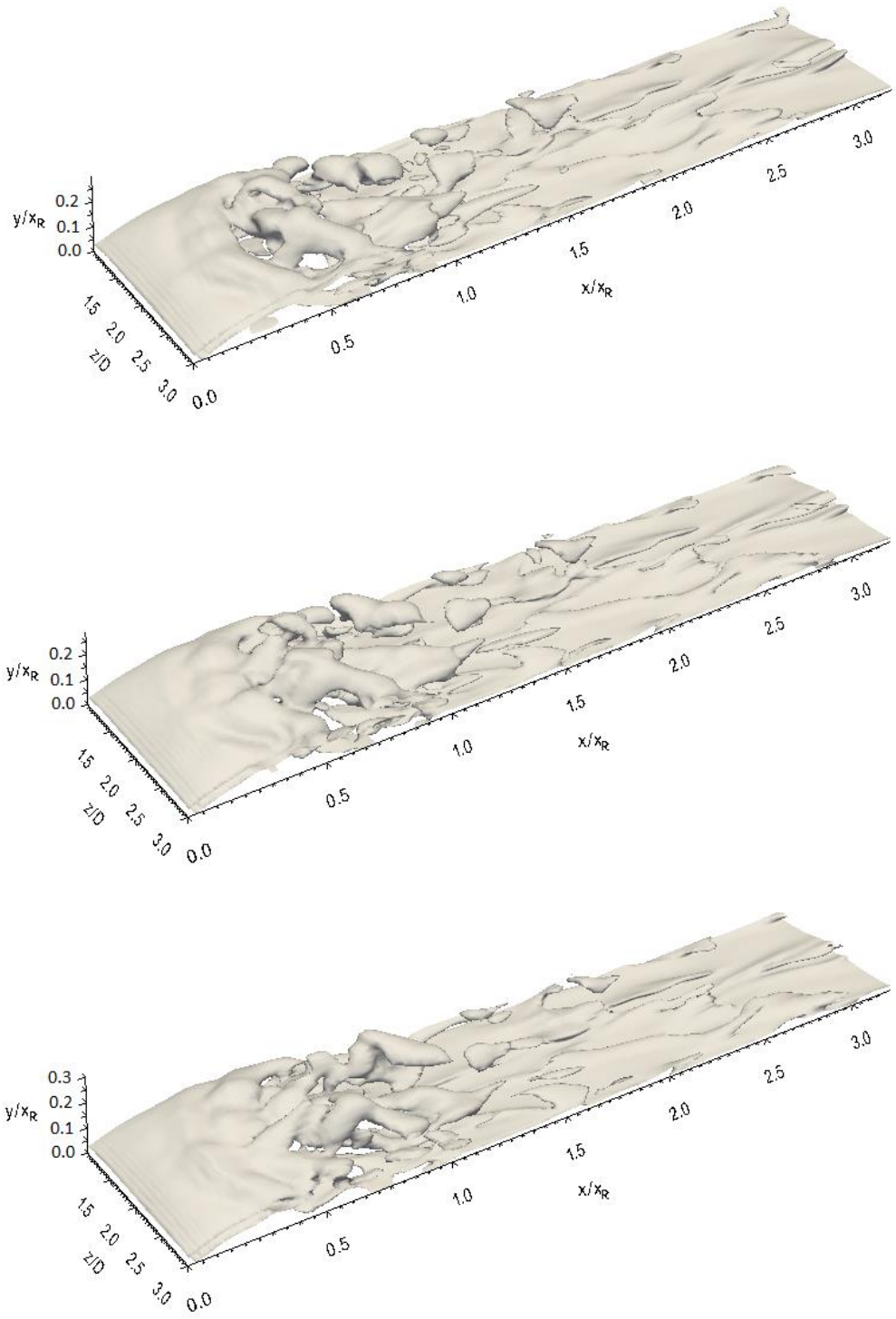

Caption for these figures is on the following page

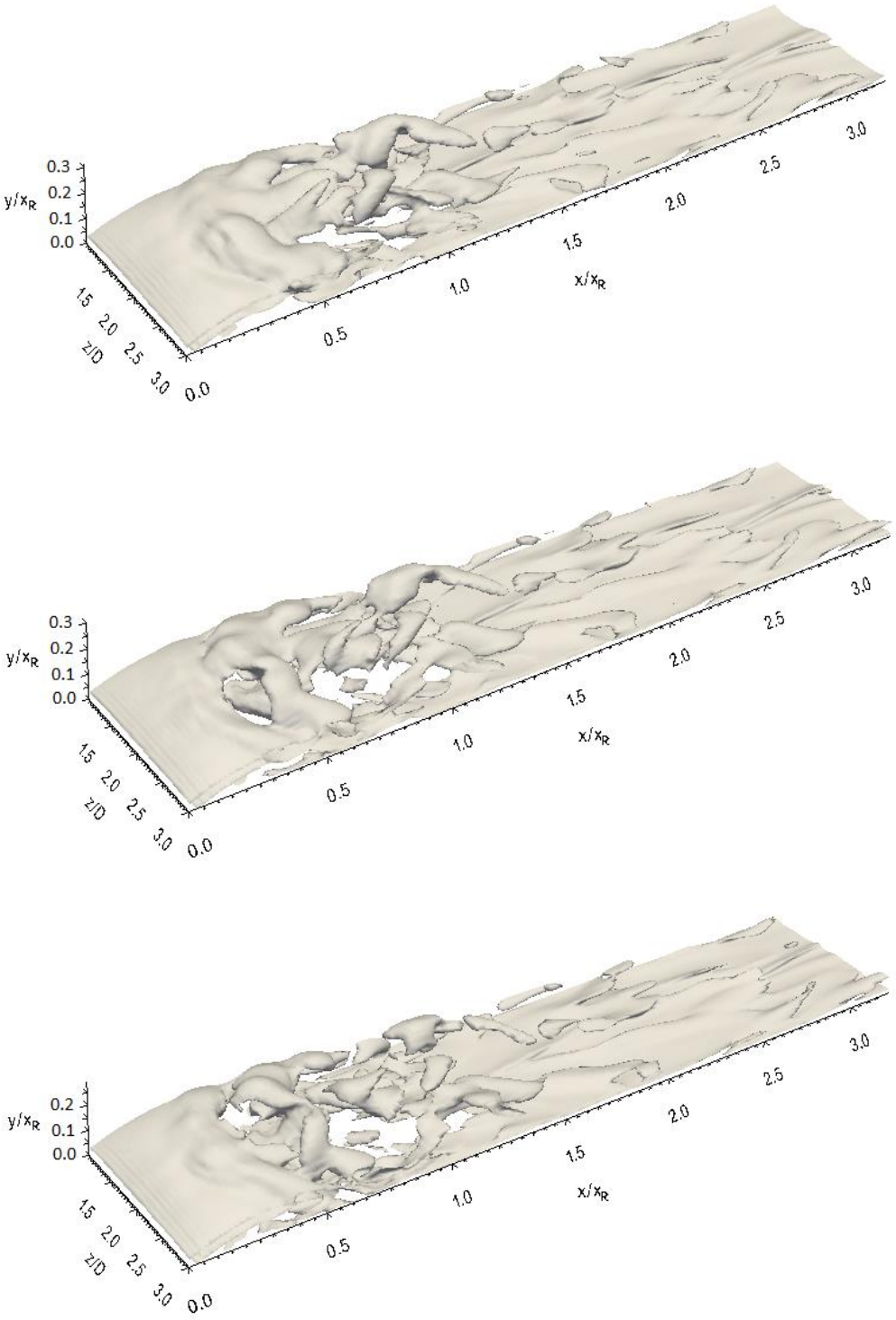

Fig. 7-49. Spanwise vorticity isosurface at sequential times (every 250 time steps) for 3D_case2 with FST

7.3.3 Q-criterion isosurface

In spite of the low pressure isosurface and vorticity field isosurface showing the existing coherent structures in the transitional separated-reattached flow with FST in this study, the clarity of the coherent structures is not well presented by these techniques. In the low pressure isosurface, in particular, there are only distorted Kelvin-Helmholtz rolls and hairpin structures, while in the vorticity magnitude isosurface, there are only hairpin structures and their breakdown are presented. Unfortunately, there is no any indication to formation and development of coherent structures by these two techniques with FST.

For the current geometries, the Q-criterion isosurface still represents the best flow visualization scheme of the current three schemes considered here, even with FST as shown below. In the Q-criterion isosurface, both Kelvin-Helmholtz rolls and hairpin structures are clearly represented, and the transfer process from a two-dimensional to three-dimensional nature is also clearly observed.

For the flat plate, a number of Q-criterion isosurfaces captured every 250 time steps are shown in Fig. 7-50. Kelvin-Helmholtz rolls are clearly seen in the first half of the separation bubble, where it may be noted that these rolls are not quite straight; they are subjected to a distortion arising from the high intensity of the free stream turbulence, unlike that presented with NFST. For NFST, Kelvin-Helmholtz rolls are completely parallel to the spanwise axis when they shed from the separated layer. However, the presence of Kelvin-Helmholtz rolls in the separation bubble with FST confirms the idea that the primary instability mechanism in the free shear layer is the Kelvin-Helmholtz instability as presented in Chapter 5.

Around $x/x_R = 0.5$, the direct breakdown of Kelvin-Helmholtz rolls into hairpin structures occurs as shown in Fig. 7-50. The hairpin structures move downstream and shed into the reattached turbulent boundary layer. It can be seen that some of hairpin structures are still present within the reattached turbulent boundary layer up to $x/x_R = 1.5$. Further downstream, the hairpin structures completely disappear due to their breakdown into smaller structures.

It can be concluded that with a 3.7% intensity of free stream turbulence for the flat plate, coherent structure development stages are as follows:

- Formation of Kelvin-Helmholtz rolls that shed from the separated layer.
- Direct breakdown of these rolls to form hairpin structures around $x/x_R = 0.5$.
- Shedding of hairpin structures into the reattached turbulent boundary layer.
- Hairpin structures move a certain distance up to $x/x_R = 1.5$ before their total disintegration.

There is no merging of Kelvin-Helmholtz rolls here, thus, it leads to reduce the transition stages, in terms of length and time, and enhancs the transformation to turbulence.

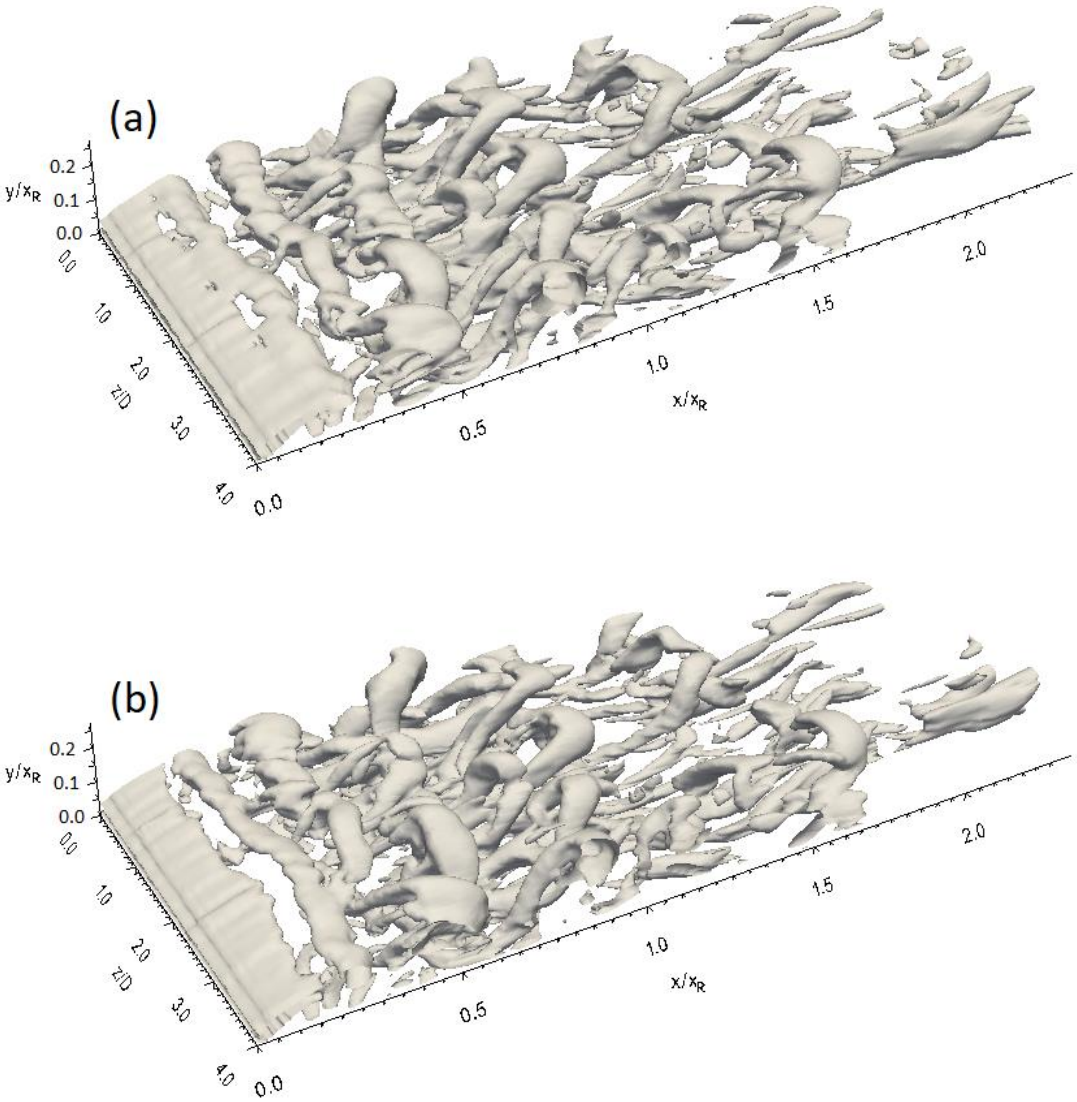

Caption for these figures is on the following page

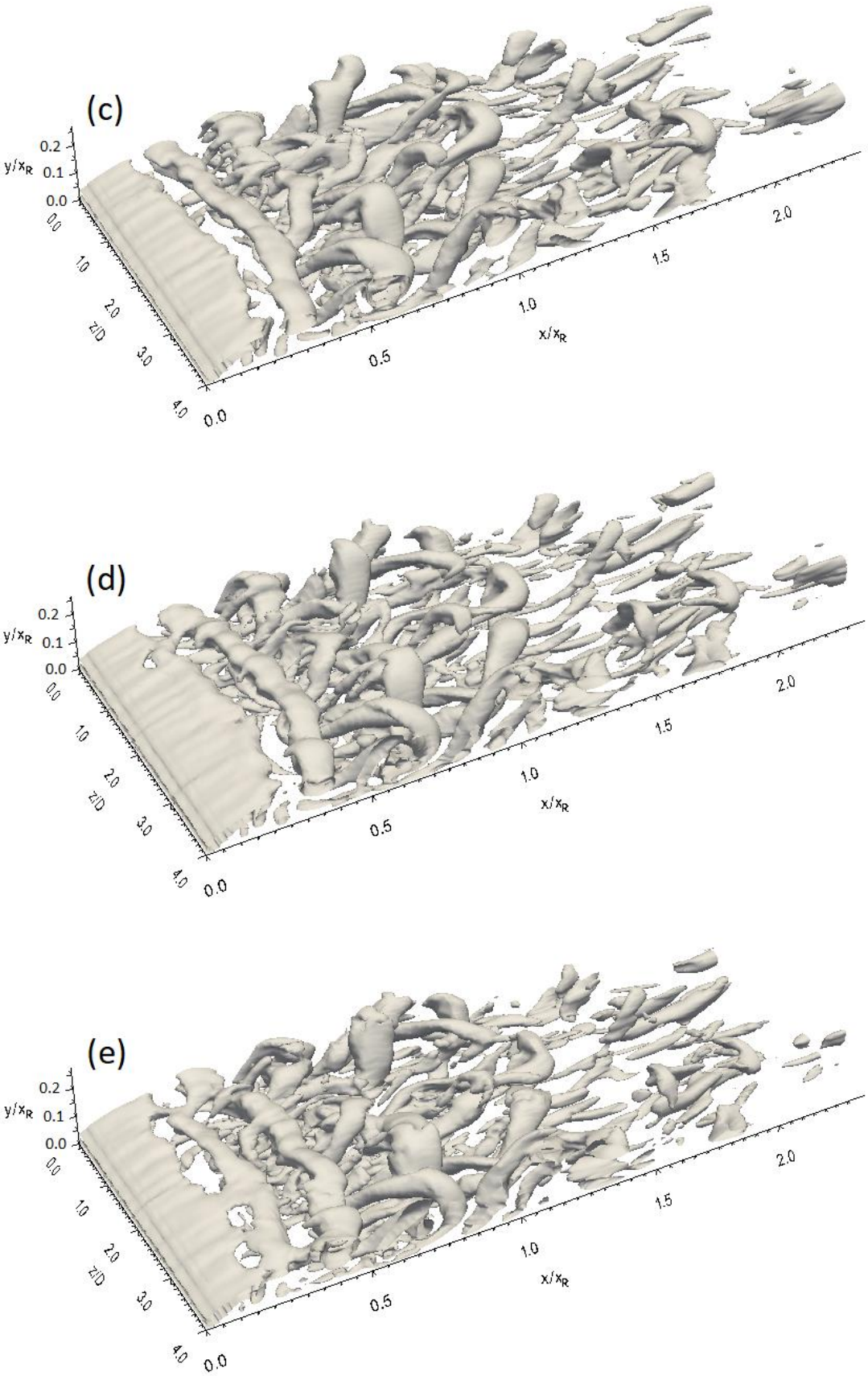
(c)
(d)
(e)
y/x_R
0.2
0.1
0.0
z/D
0.0
1.0
2.0
3.0
4.0
x/x_R
0.0
0.5
1.0
1.5
2.0

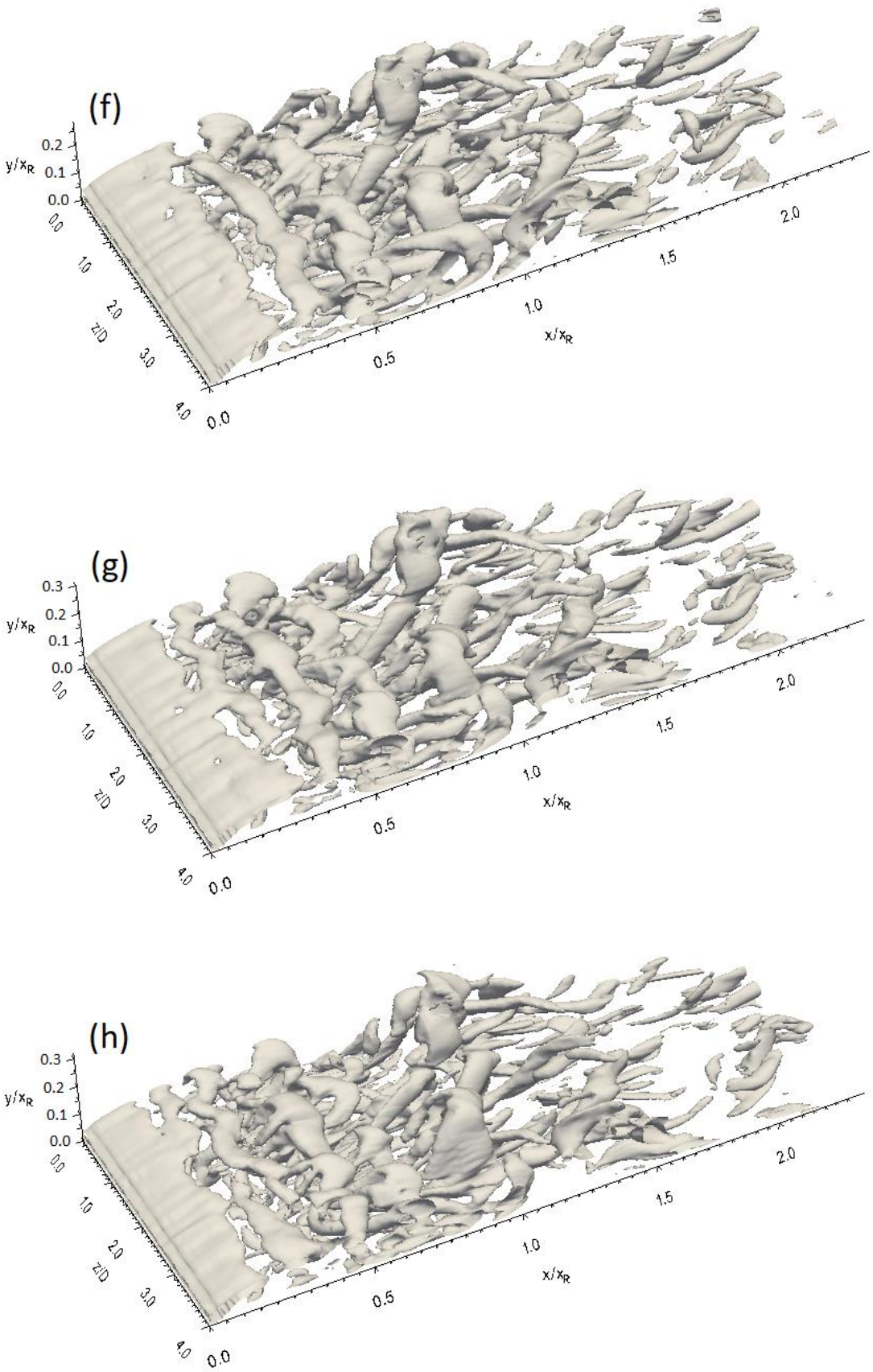
(f)
(g)
(h)
y/x_R
x/x_R
z/D
0.0
0.1
0.2
0.3
0.5
1.0
1.5
2.0
3.0
4.0

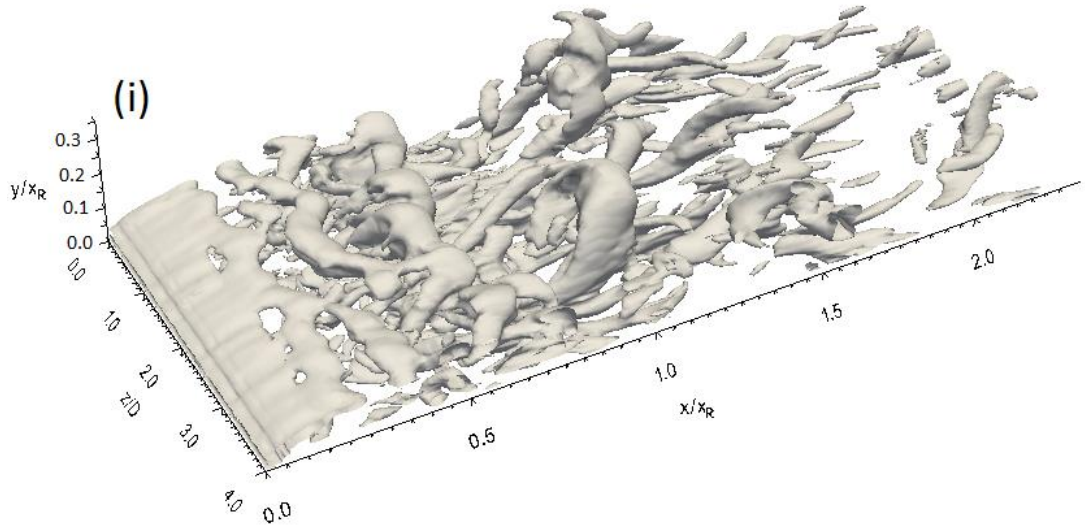
(i)
y/x_R
0.3
0.2
0.1
0.0
0.0
1.0
2.0
z/D
3.0
4.0
0.0
0.5
1.0
1.5
2.0
x/x_R

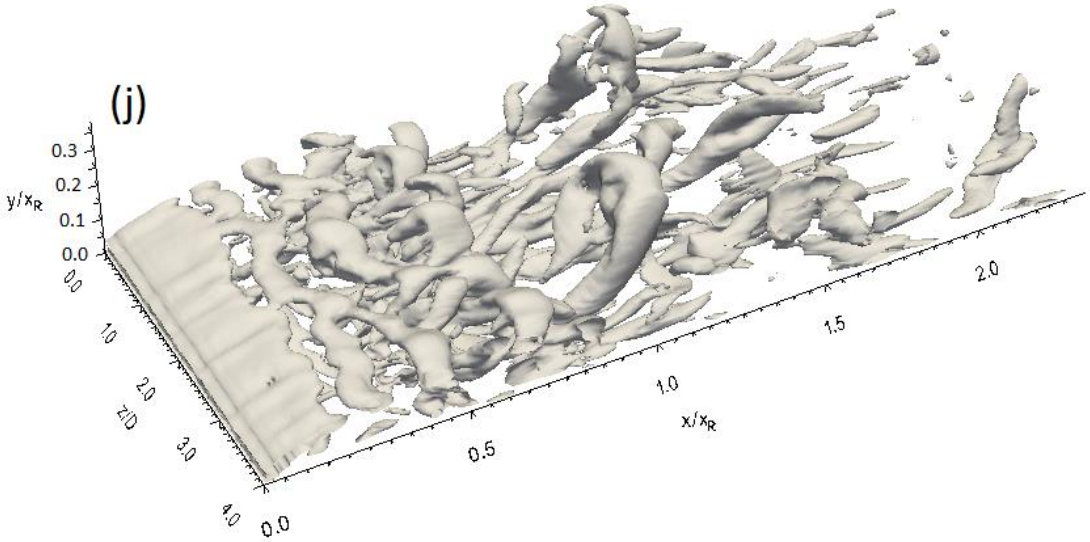
(j)
y/x_R
0.3
0.2
0.1
0.0
0.0
1.0
2.0
z/D
3.0
4.0
0.0
0.5
1.0
1.5
2.0
x/x_R

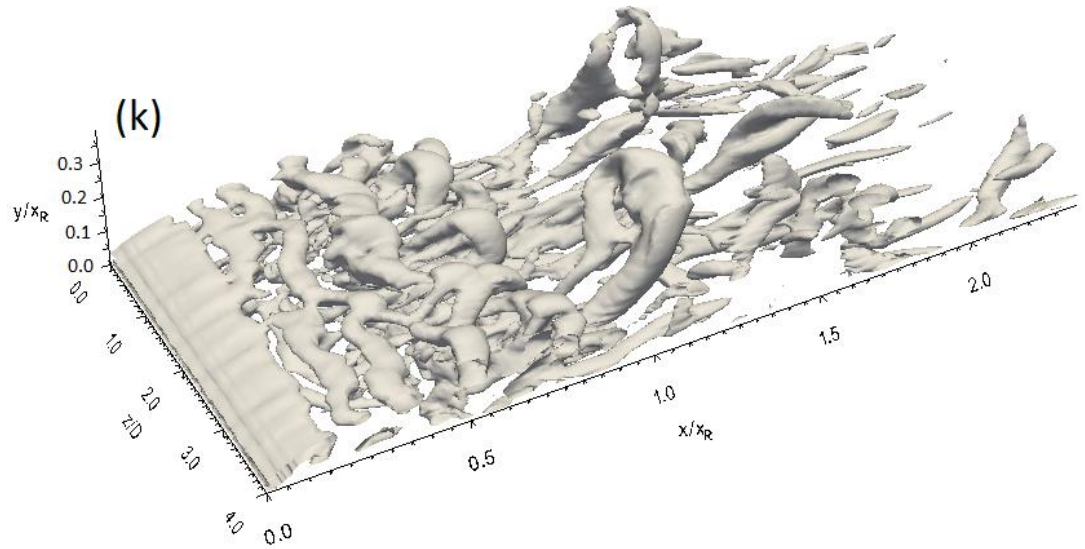
(k)
y/x_R
0.3
0.2
0.1
0.0
0.0
1.0
2.0
z/D
3.0
4.0
0.0
0.5
1.0
1.5
2.0
x/x_R

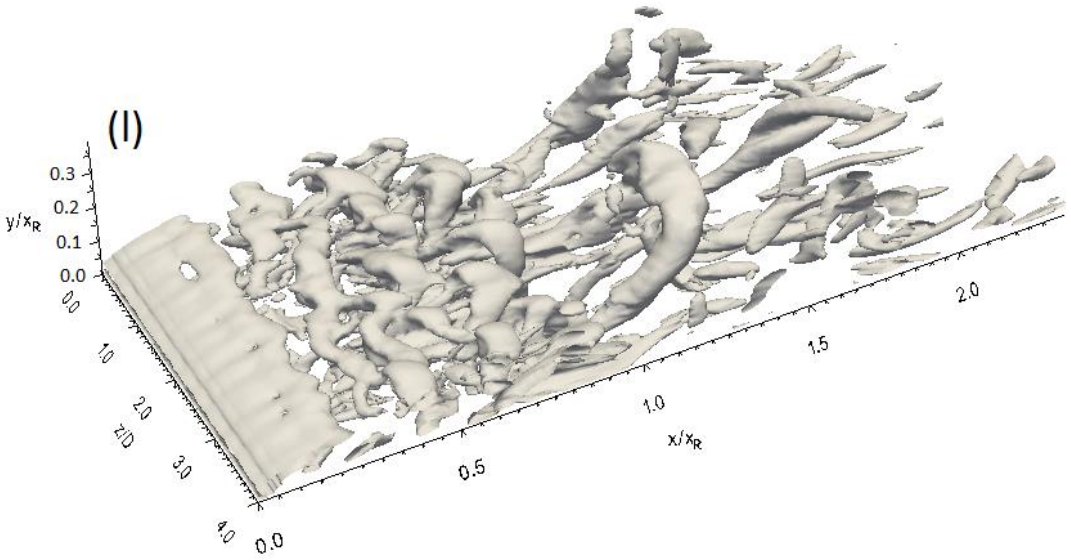
(l)
y/x_R
0.3
0.2
0.1
0.0
0.0
1.0
2.0
z/D
3.0
4.0
0.0
0.5
1.0
1.5
2.0
x/x_R

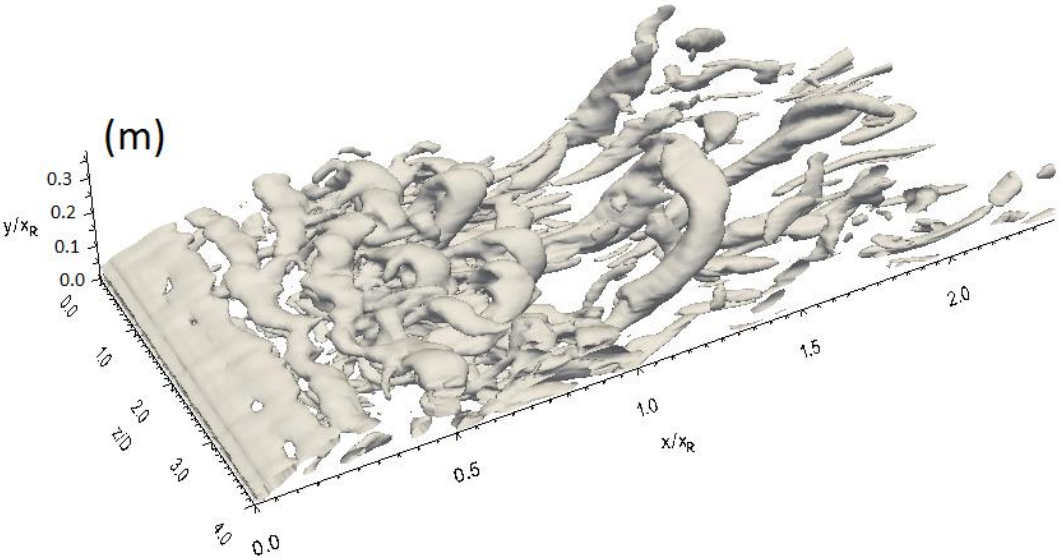
(m)
y/x_R
0.3
0.2
0.1
0.0
0.0
1.0
2.0
z/D
3.0
4.0
0.0
0.5
1.0
1.5
2.0
x/x_R

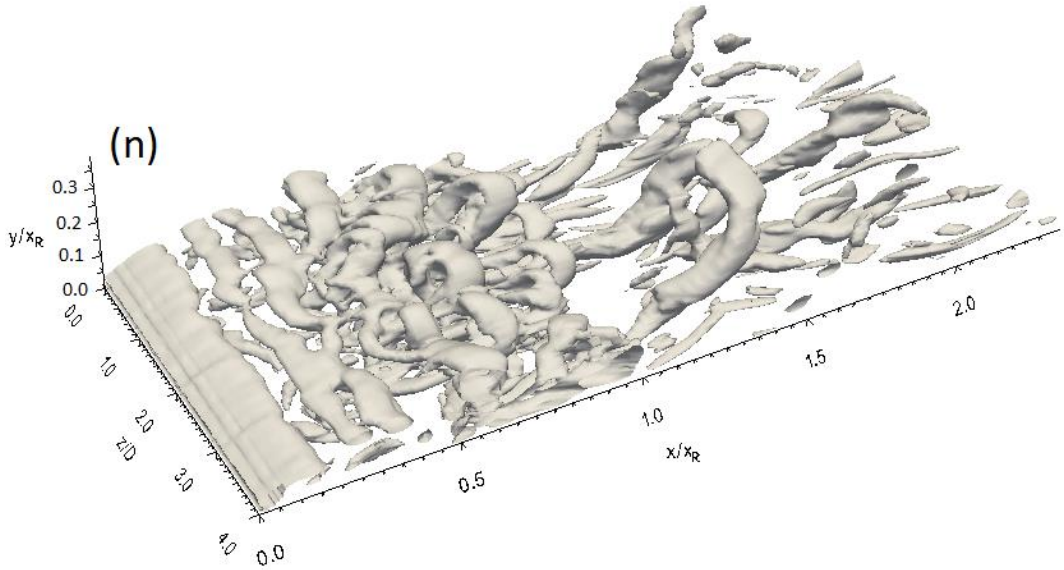
(n)
y/x_R
0.3
0.2
0.1
0.0
0.0
1.0
2.0
z/D
3.0
4.0
0.0
0.5
1.0
1.5
2.0
x/x_R

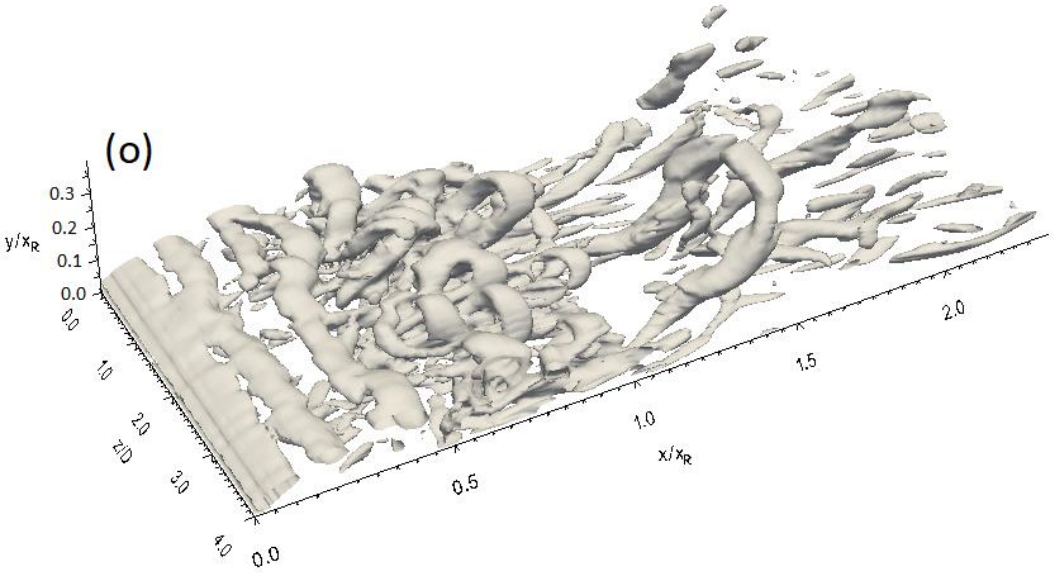
(o)
y/x_R
0.3
0.2
0.1
0.0
0.0
1.0
2.0
z/D
3.0
4.0
0.0
0.5
1.0
1.5
2.0
x/x_R

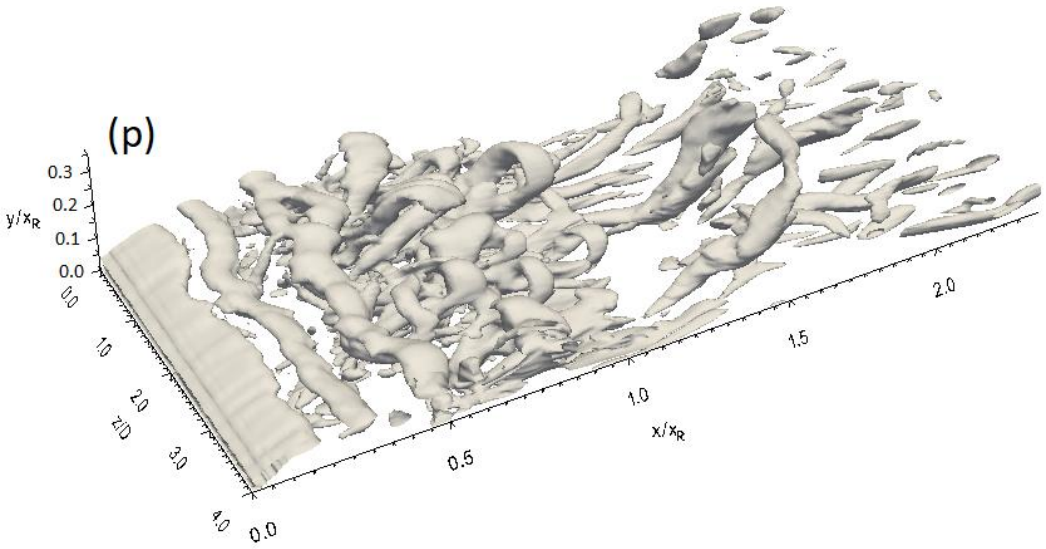
(p)
y/x_R
0.3
0.2
0.1
0.0
0.0
1.0
2.0
z/D
3.0
4.0
0.0
0.5
1.0
1.5
2.0
x/x_R

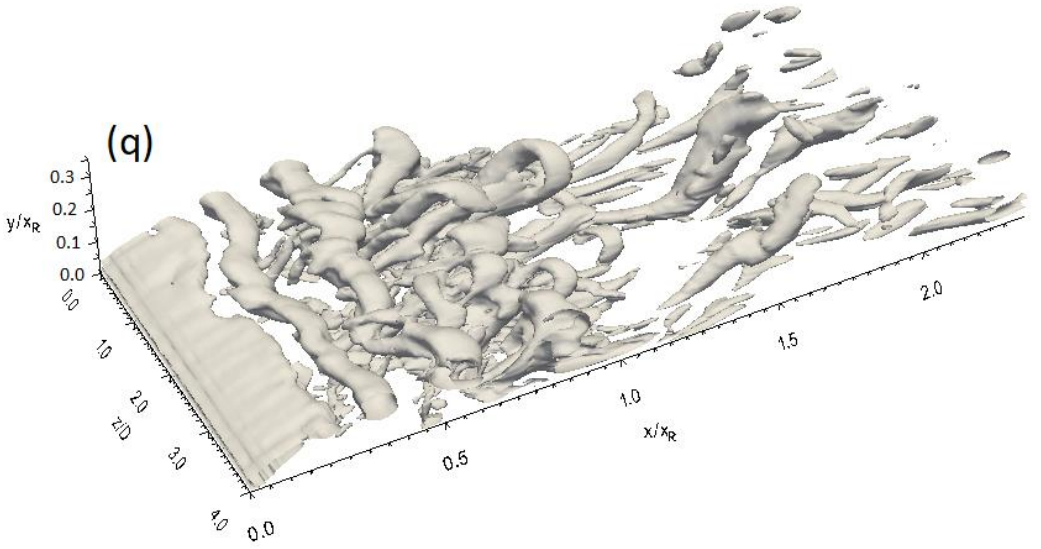
(q)
y/x_R
0.3
0.2
0.1
0.0
0.0
1.0
2.0
z/D
3.0
4.0
0.0
0.5
1.0
1.5
2.0
x/x_R

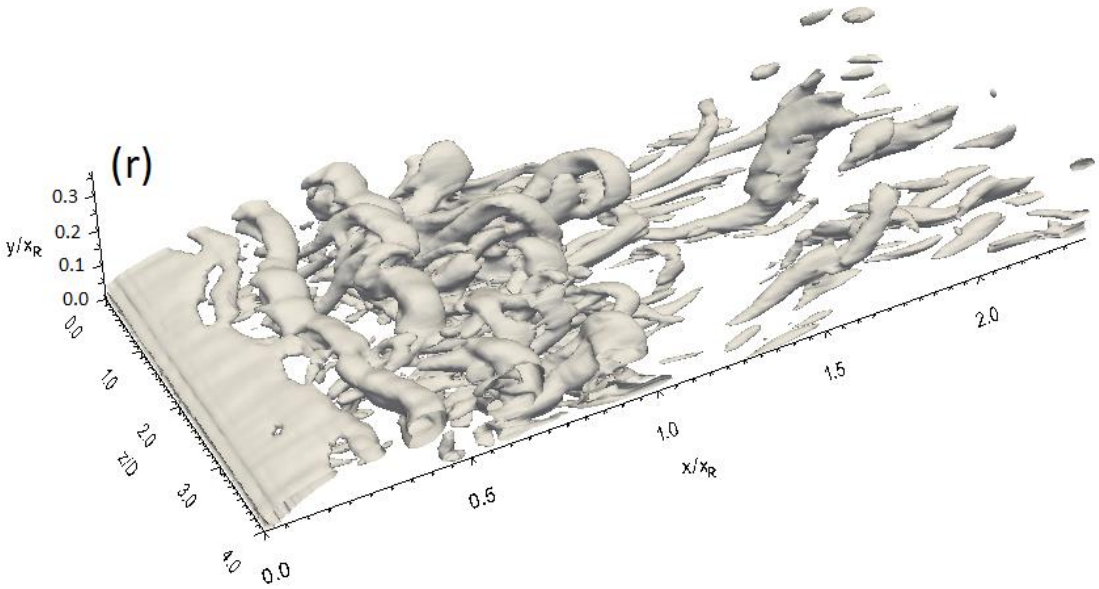

Fig. 7-50. Q-criterion isosurface at sequential times (every 250 time steps) for the flat plate with FST

It can be seen that the distortion intensity in the Kelvin-Helmholtz rolls that are shed from the separated layer in 3D_case1 is lower than that for the flat plate as shown in Fig. 7-51 which presents sequential Q-criterion isosurfaces taken every 250 time steps. However, the spanwise motion in the Kelvin-Helmholtz rolls for 3D_case1 can be still observed.

The existence of the Kelvin-Helmholtz rolls in 3D_case1 indicates that under the influence of a 3.7% intensity of free stream turbulence, the primary instability mechanism in the separation bubble for this geometry is the Kelvin-Helmholtz mechanism as discussed in Chapter 5.

In 3D_case1, the Kelvin-Helmholtz rolls move downstream, after which it seems that they develop topologically to form hairpin structures in the second half of the separation bubble as shown in Fig. 7-51. However, the clarity of this development process is lower than that presented in Section 7.2.3 for NFST. Despite the low clarity of the development of the coherent structures, inspection of Q-criterion isosurfaces presented in Figs. 7-51f - 7-51i can confirm the topological evolution of the coherent structures from Kelvin-Helmholtz rolls to hairpin structures.

The last stage of coherent structure development occurs after their shedding into reattached turbulent boundary layer in the region between $x/x_R = 1$ and $x/x_R = 2$. In this region, the hairpin structures lose their coherency by breaking down into smaller turbulent structures as shown in Fig. 7-51.

In general, despite the coherent structures and the clarity of their development with NFST being smoother than that presented here, the stages of development of the transition structures with NFST and FST are similar, i.e., the topological evolution of Kelvin-Helmholtz rolls into hairpin structures.

The development of coherent structures from the formation of Kelvin-Helmholtz rolls to the breakdown of the hairpin structures into smaller turbulent structures is similar whether it takes place on the top or side surface of 3D_case1 as shown in Fig. 7-52. The presence of a twisting structure around this geometry with FST is also observed, which is similar to that presented for NFST.

After breakdown of a rectangular ring structure into four Kelvin-Helmholtz rolls, each roll develops topologically on each surface of 3D_case1, forming a hairpin structure in the second half of the separation bubble as shown in the sequential snapshots of the Q-criterion that are presented in Figs. 7-52d - 7-52g. Further downstream, the disappearance of the hairpin structure on each surface is complete at about $x/x_R = 2$ due to their disintegration into smaller turbulent structures as shown in Fig. 7-52.

In general, it can be seen that there is a similarity in the development of the coherent structures for 3D_case2 with NFST, as presented in Section 7.2.3, and with FST, as presented here. For both cases, the coherent structure development is a topological evolution of a Kelvin-Helmholtz roll to a hairpin structure.

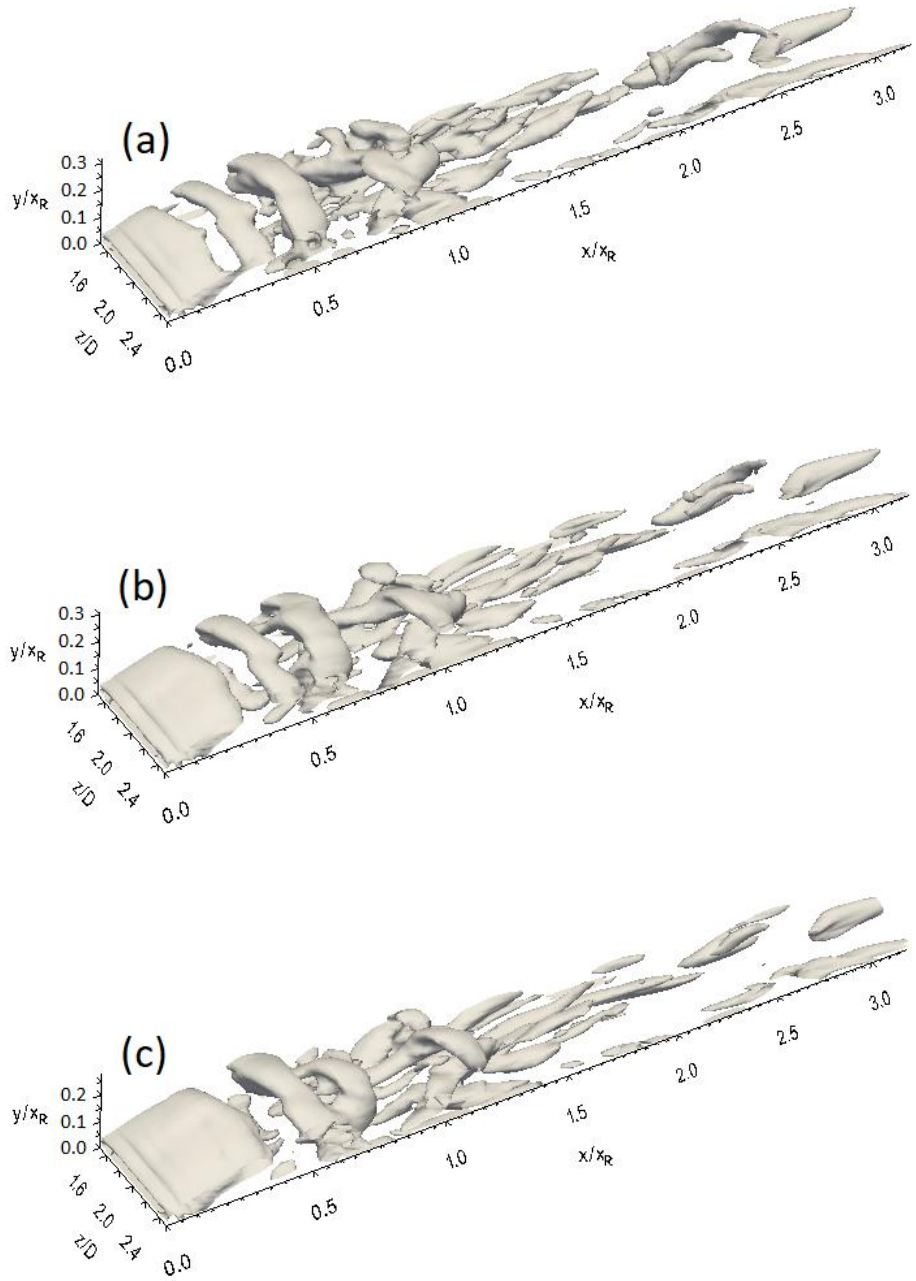

Caption for these figures is on the following page

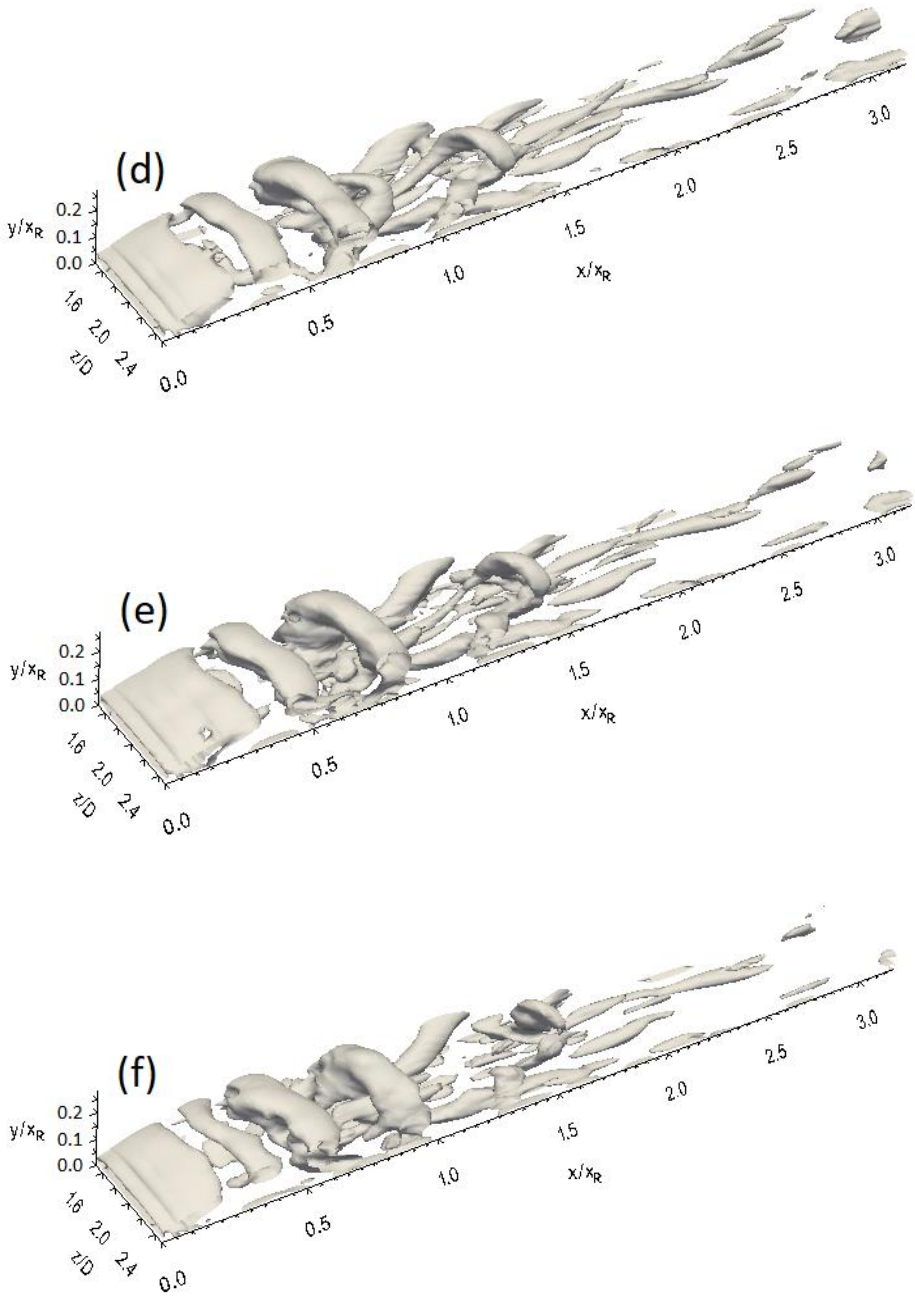
(d)
(e)
(f)
y/x_R
0.2
0.1
0.0
z/D
1.6
2.0
2.4
0.0
0.5
1.0
1.5
2.0
2.5
3.0
x/x_R

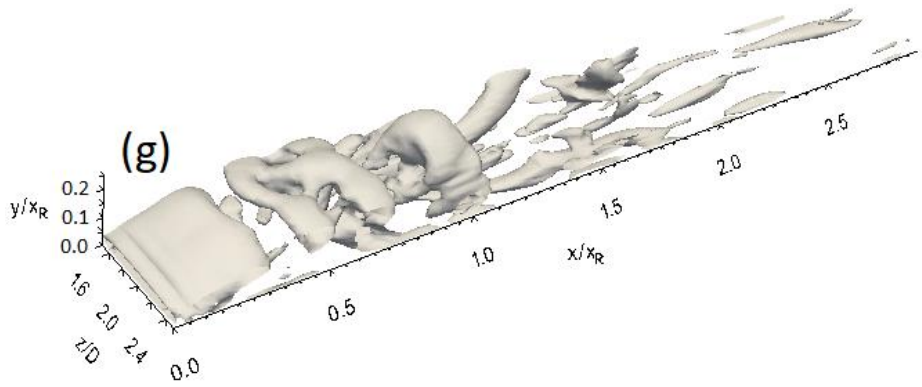
(g)
y/x_R
0.2
0.1
0.0
1.6
2.0
2.4
z/D
0.0
0.5
1.0
1.5
2.0
2.5
x/x_R

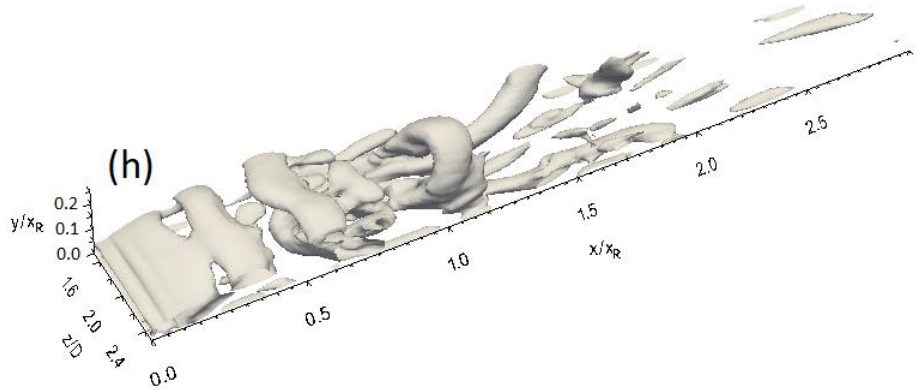
(h)
y/x_R
0.2
0.1
0.0
1.6
2.0
2.4
z/D
0.0
0.5
1.0
1.5
2.0
2.5
x/x_R

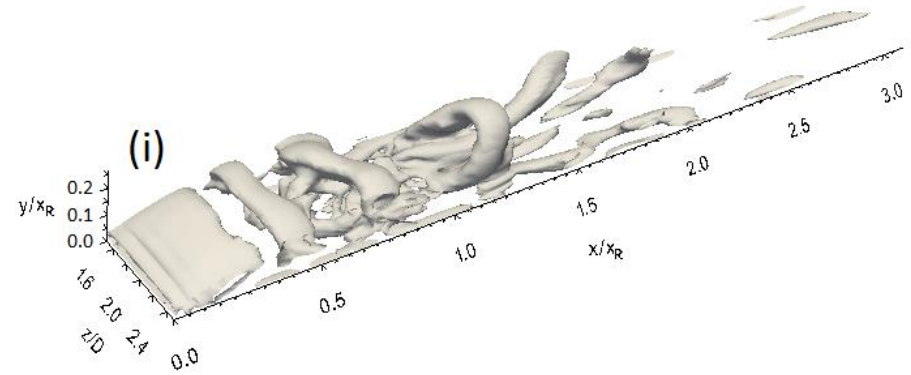
(i)
y/x_R
0.2
0.1
0.0
1.6
2.0
2.4
z/D
0.0
0.5
1.0
1.5
2.0
2.5
3.0
x/x_R

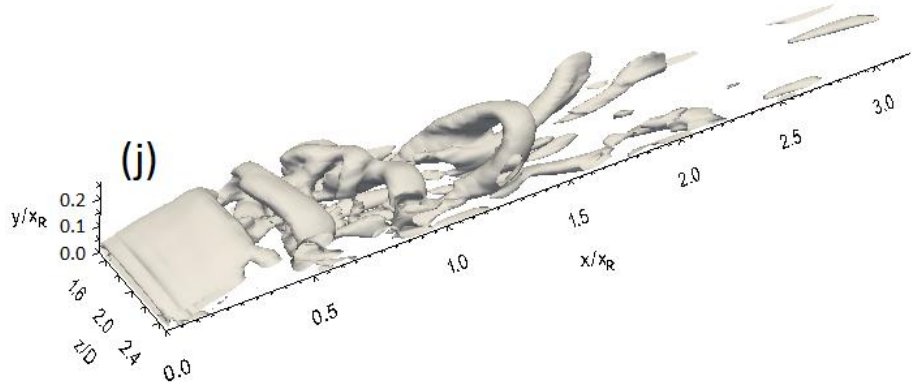
(j)
y/x_R
0.2
0.1
0.0
1.6
2.0
2.4
z/D
0.0
0.5
1.0
1.5
2.0
2.5
3.0
x/x_R

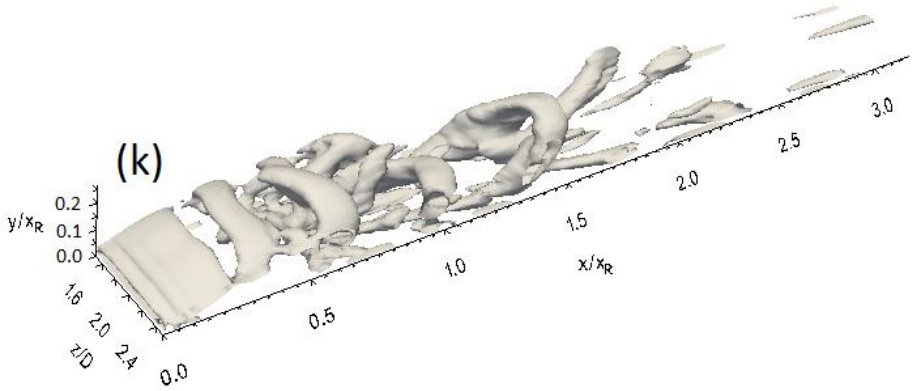
(k)
y/x_R
0.2
0.1
0.0
1.6
2.0
2.4
z/D
0.0
0.5
1.0
1.5
2.0
2.5
3.0
x/x_R

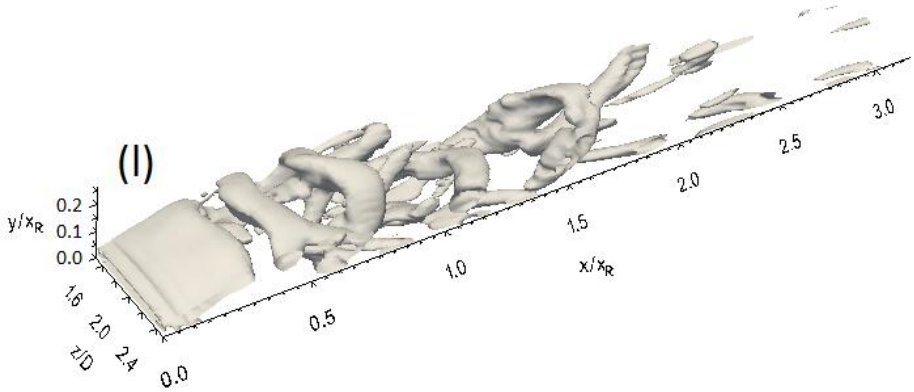
(l)
y/x_R
0.2
0.1
0.0
1.6
2.0
2.4
z/D
0.0
0.5
1.0
1.5
2.0
2.5
3.0
x/x_R

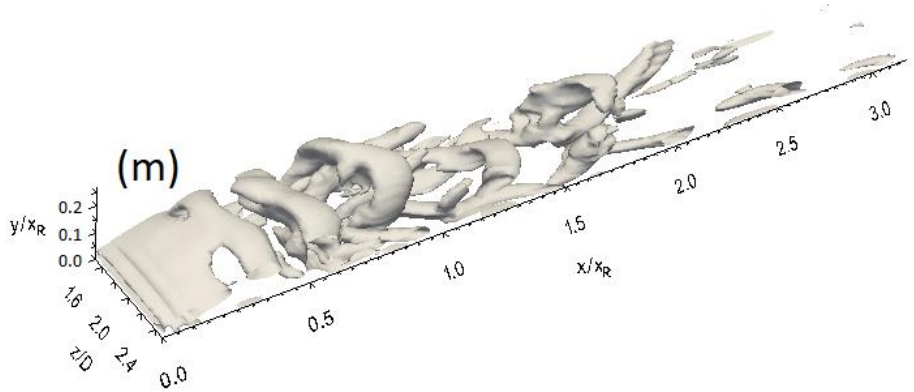
(m)
y/x_R
0.2
0.1
0.0
1.6
2.0
2.4
z/D
0.0
0.5
1.0
1.5
2.0
2.5
3.0
x/x_R

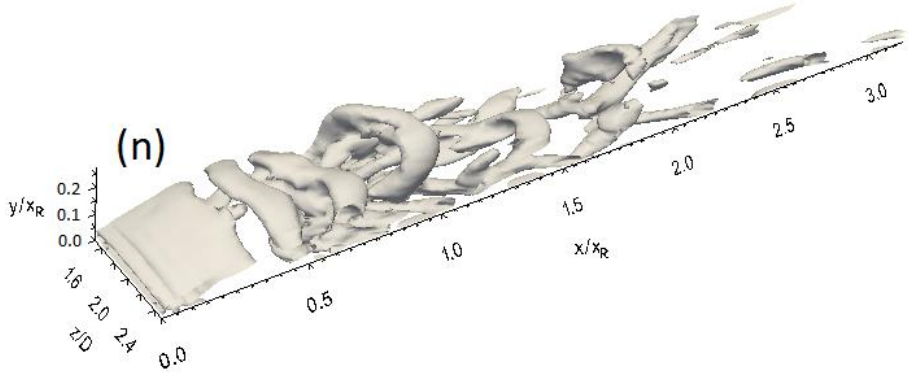
(n)
y/x_R
0.2
0.1
0.0
1.6
2.0
2.4
z/D
0.0
0.5
1.0
1.5
2.0
2.5
3.0
x/x_R

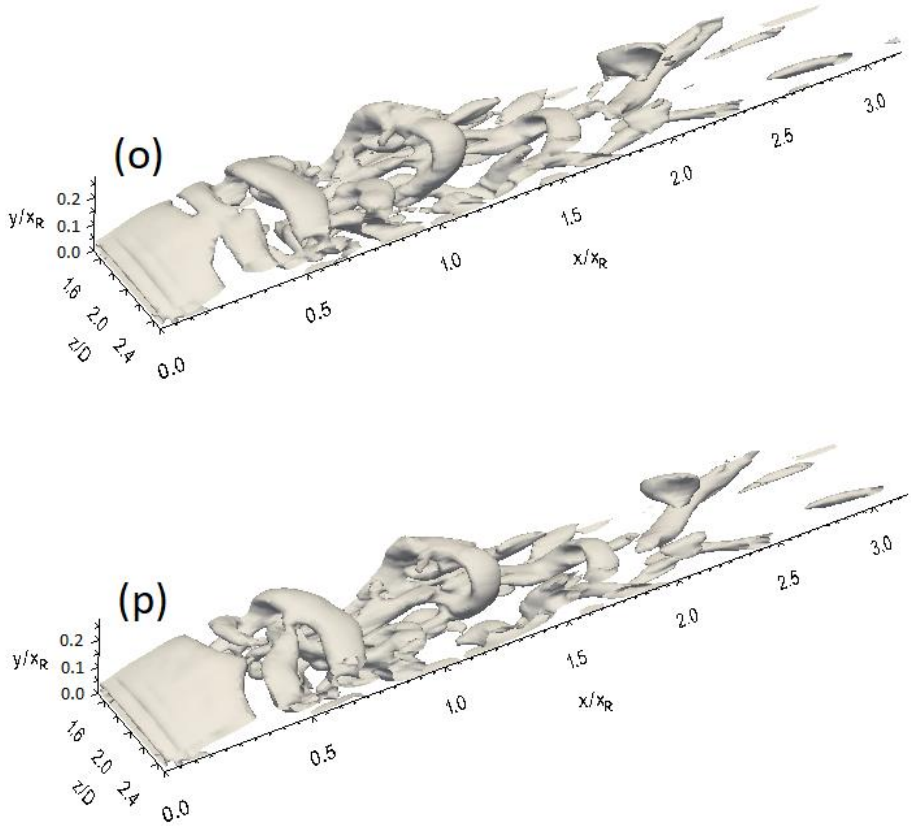

Fig. 7-51. Q-criterion isosurface at sequential times (every 250 time steps) for 3D_case1 with FST

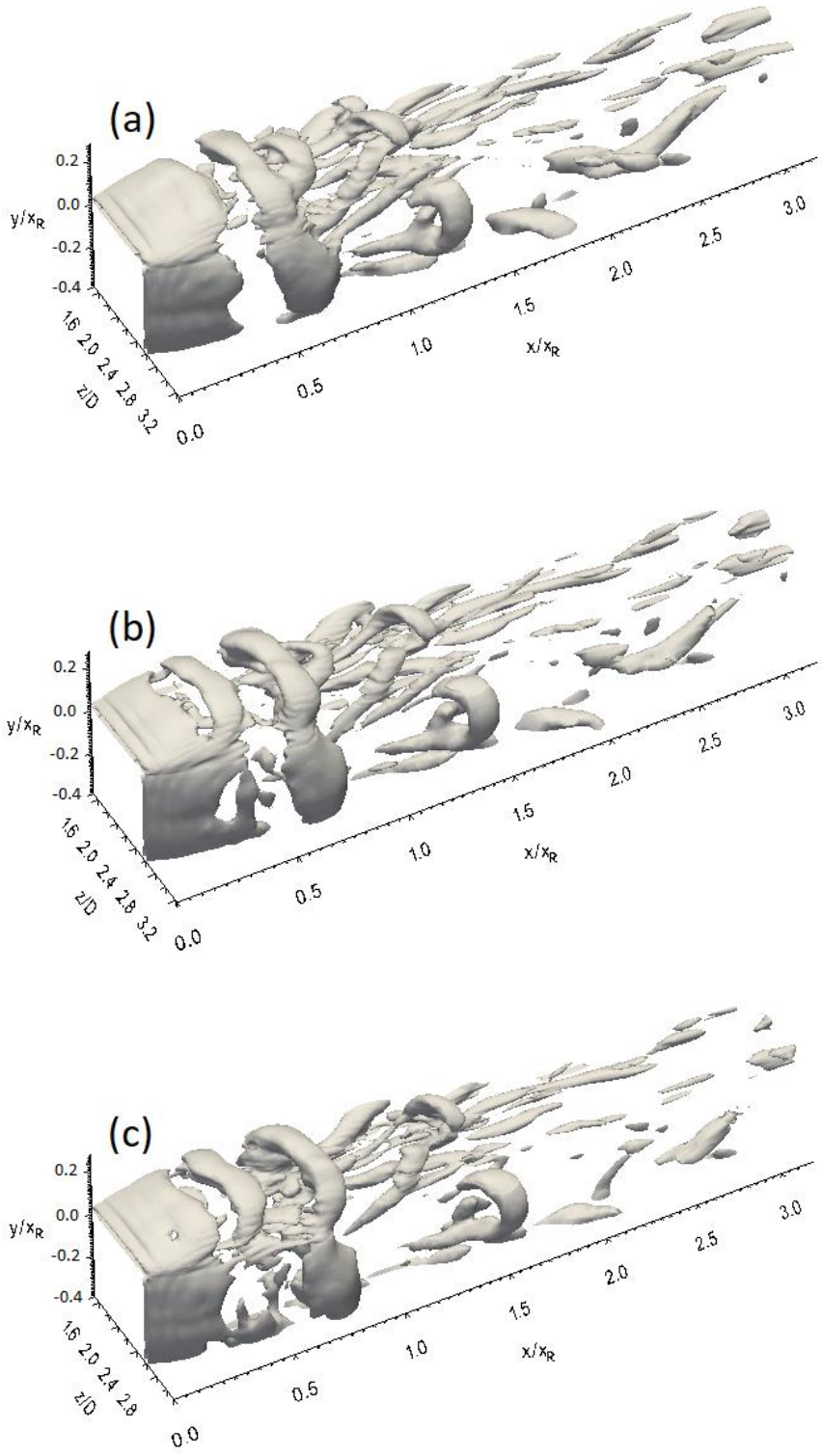

Caption for these figures is on the following page

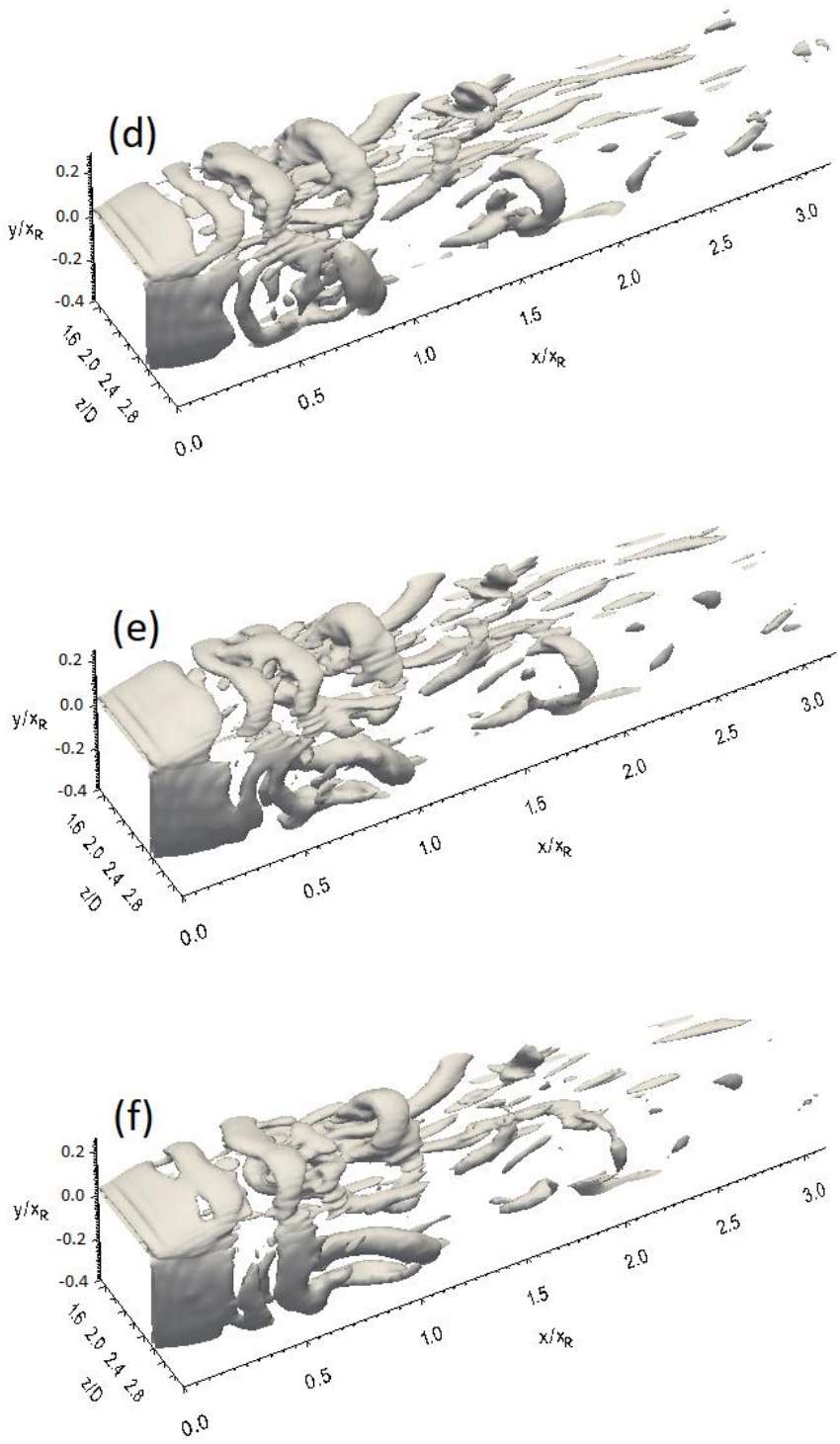
(d)
(e)
(f)
y/x_R
x/x_R
z/D
0.2
0.0
-0.2
-0.4
0.0
0.5
1.0
1.5
2.0
2.5
3.0
1.6
2.0
2.4
2.8

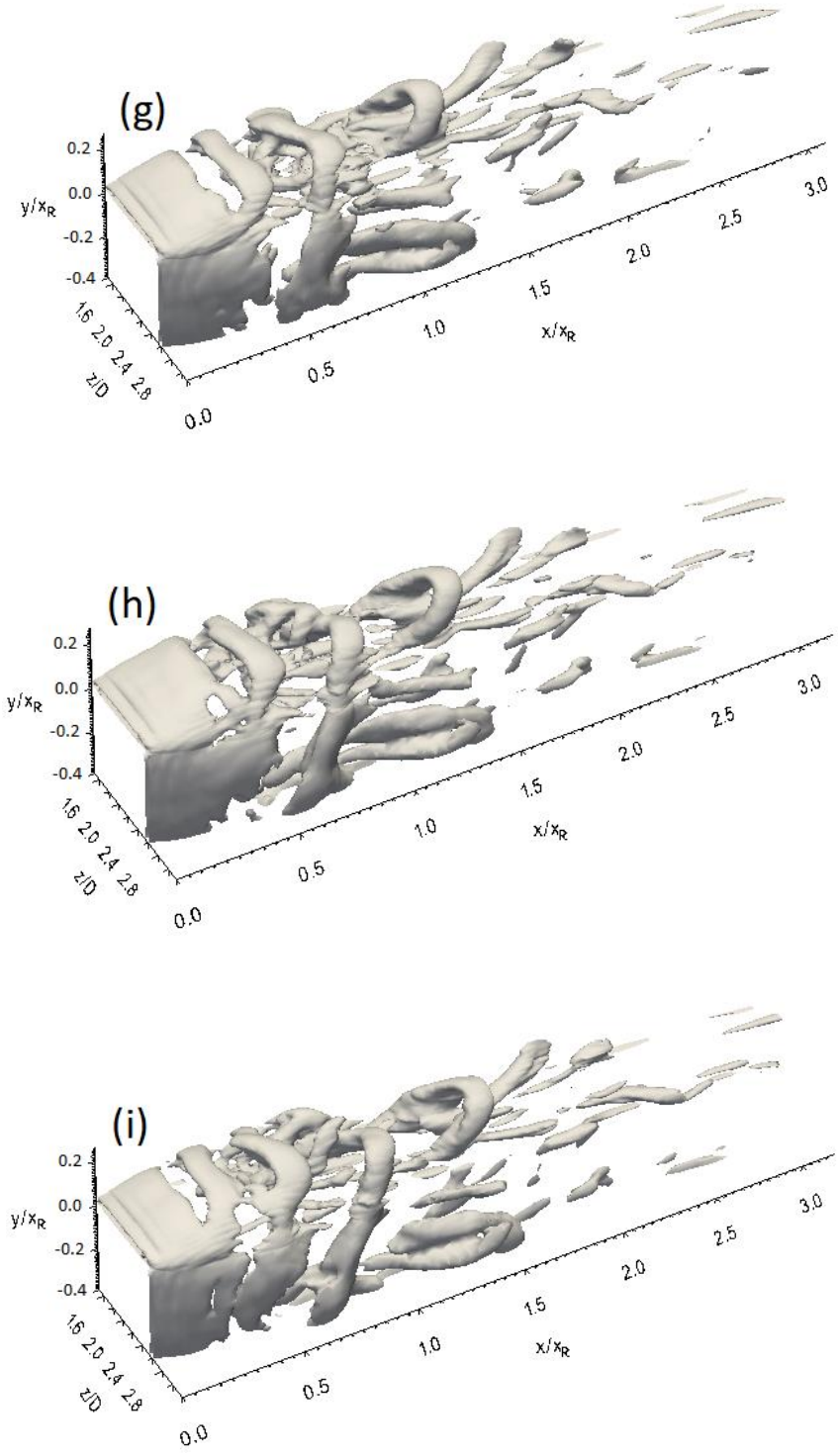
(g)
(h)
(i)
y/x_R
x/x_R
z/D
0.2
0.0
-0.2
-0.4
0.5
1.0
1.5
2.0
2.5
3.0
1.6
2.0
2.4
2.8

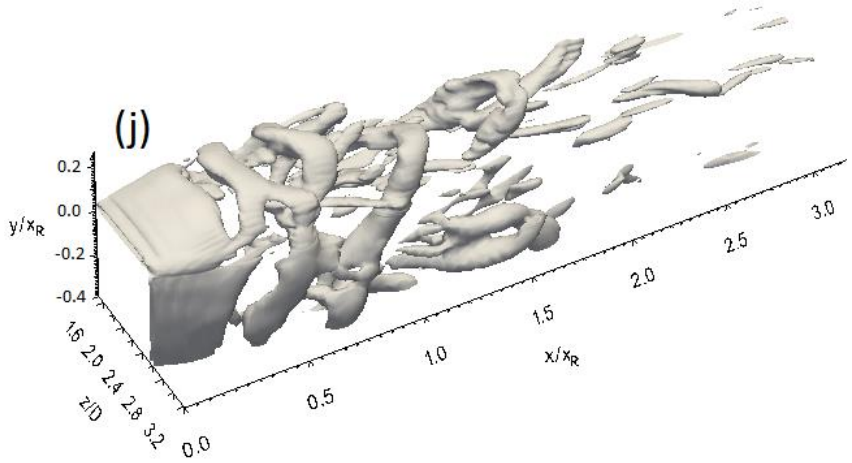

Fig. 7-52. Q-criterion isosurface on the top and side surfaces at sequential times (every 250 time steps) for 3D_case1 with FST

With FST, Q-criterion isosurfaces for 3D_case2, as taken every 250 time steps, are exhibited in Fig. 7-53. It is clearly seen that Kelvin-Helmholtz rolls form downstream of the location at which the unsteadiness starts at x/x_R = 0.2. This is the first stage of the formation and development of coherent structures in this geometry. Despite this stage also occurring with NFST, the difference between the two flow cases is the nature of the Kelvin-Helmholtz roll itself. This roll seems to be smooth and straight with NFST, while it is wavy with FST. This waviness, which is associated with the spanwise motion in a Kelvin-Helmholtz roll, is indeed a consequence of the presence of elevated intensity of the free stream turbulence. However, the existence of Kelvin-Helmholtz rolls in the separated layer indicates the transition in 3D_case2 is driven by the Kelvin-Helmholtz instability mechanism. This is considered as further confirmation to the discussion presented in Chapter 5.

After the formation of Kelvin-Helmholtz rolls and their shedding from the separated layer, they move a certain distance downstream and directly break down into a set of hairpin structures in the second half of the separation bubble as shown in Fig. 7-53. New hairpin structures shed to reattached turbulent boundary layer and vanish at about x/x_R= 1.5 due to their breakdown into smaller turbulent structures, indicating a delay in the recovery of the turbulent boundary layer.

Overall, the development of coherent structures with FST for 3D_case2 presented above is similar to that with NFST with just one difference, which is the nature of Kelvin-Helmholtz rolls.

In order to see if there are any similarities or differences in the evolution of the flow structures with FST on the top and side surfaces of 3D_case2, a number of Q-criterion isosurfaces at the top and side surfaces of this geometry, taken at the same times as those shown in Fig. 7-53, are illustrated in Fig. 7-54. As presented with NFST, the coherent structure also starts here with a twisting nature and breaks down into four Kelvin-Helmholtz rolls on each surface as shown in Figs. 7-54a and 7-54b. Further downstream, the Kelvin-Helmholtz roll on the side surface of 3D_case2 seems to develop topologically to form a hairpin structure in the second half of the separation bubble. However, the side surface hairpin structure is not clearly exhibited in Fig. 7-54. Hence, the Q-criterion isosurface for 3D_case2 is presented for another time period in Fig. 7-55.

Three structures referred to as *A*, *B* and *C* are identified on the side surface of 3D_case2 to illustrate the development of coherent structures on this surface as presented in Fig. 7-55. The Kelvin-Helmholtz roll on this surface develops topologically to form a hairpin structure that sheds to the reattached turbulent boundary layer and disintegrates there. Therefore, it can be concluded that there is a similarity in coherent structure development around 3D_case2 whether the flow condition shows high or low intensity of free stream turbulence.

In general, the evolution of coherent structures from the Kelvin-Helmholtz rolls to the hairpin structures with NFST and FST for 3D_case2 is different on the top and side surfaces of this geometry. On the top surface, the direct breakdown of the Kelvin-Helmholtz rolls to the hairpin structures is observed, while on the side surface, a Kelvin-Helmholtz roll develops topologically to form a hairpin structure.

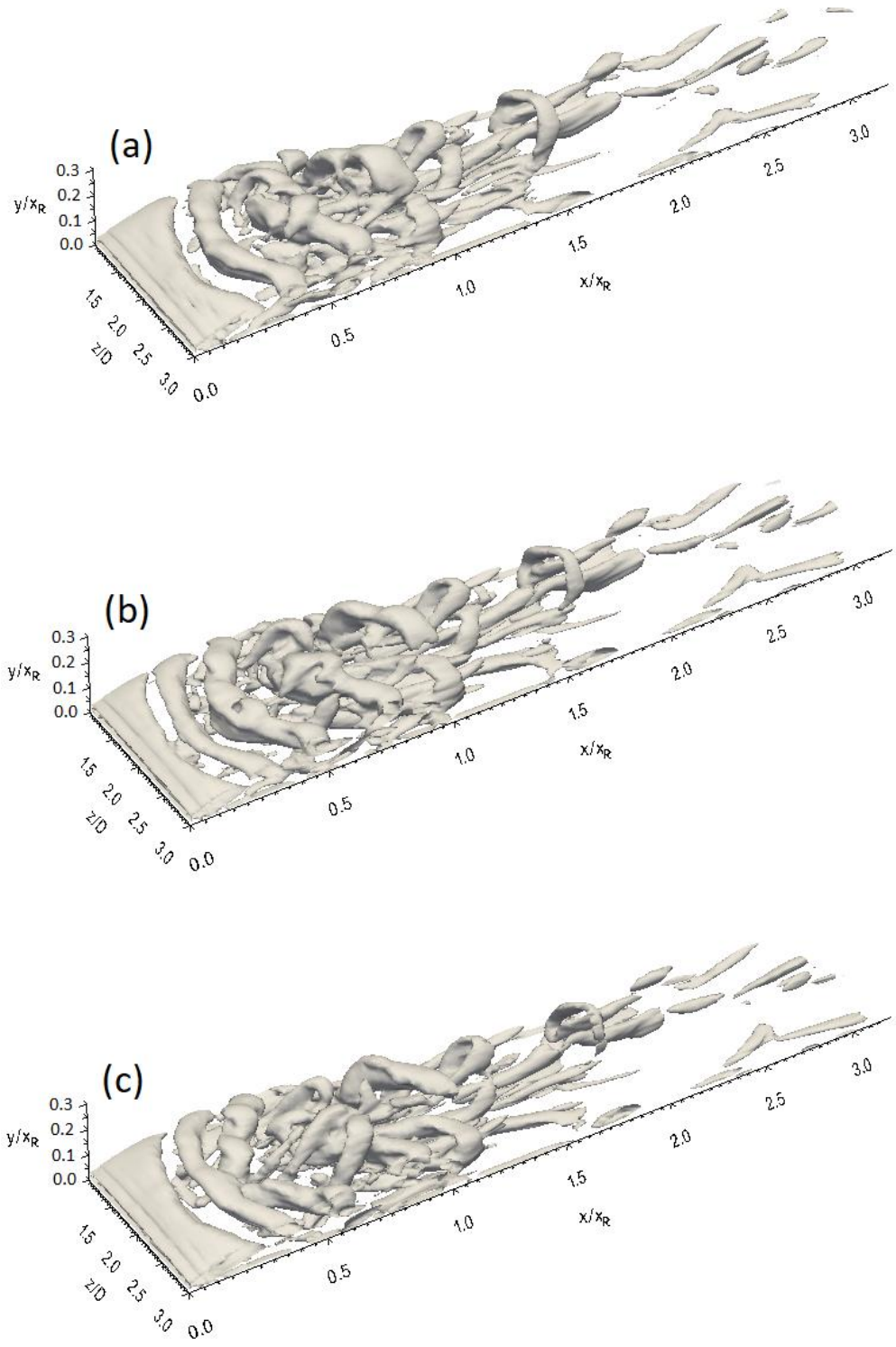

Caption for these figures is on the following page

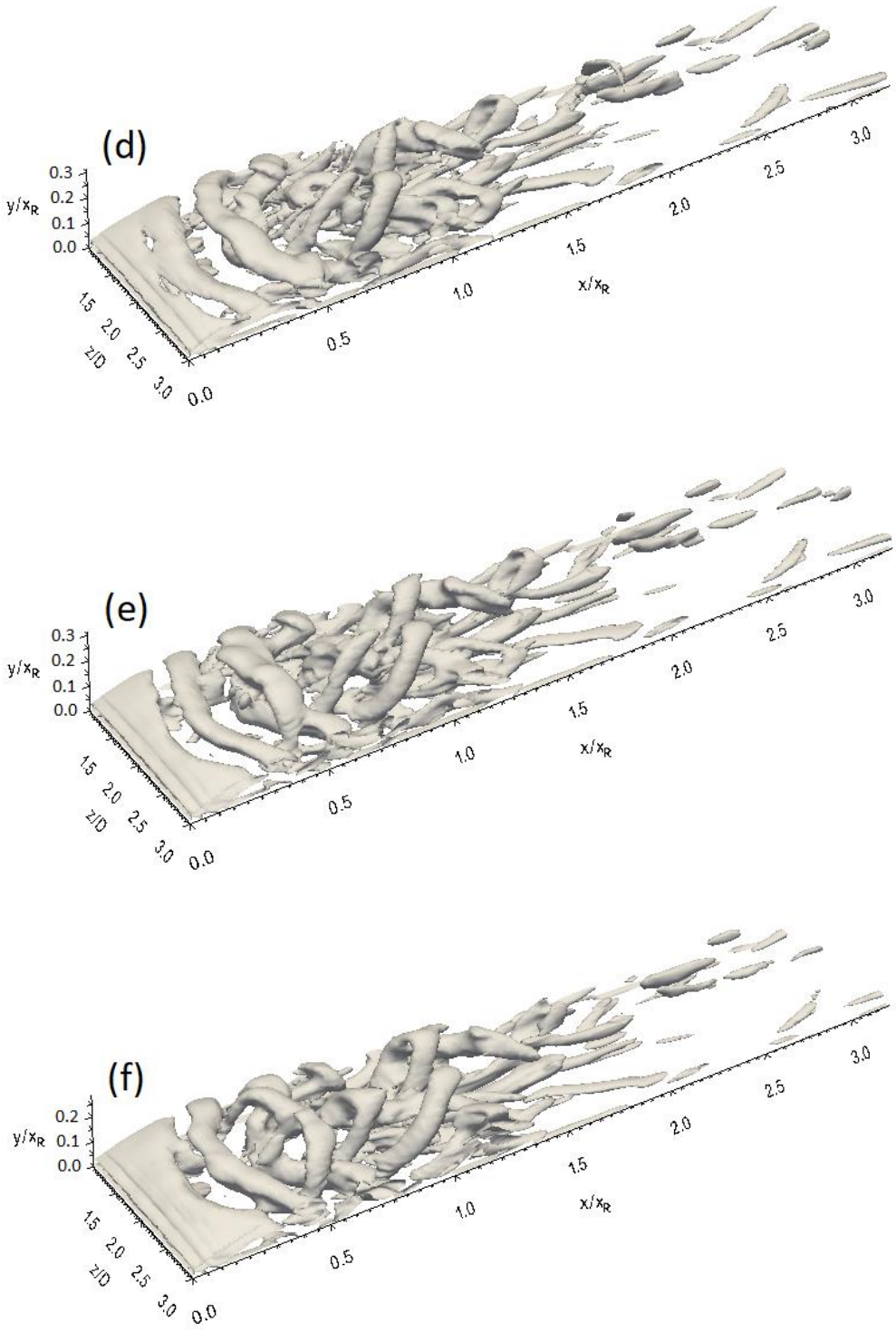
(d)
(e)
(f)
y/x_R
x/x_R
z/D
0.0
0.1
0.2
0.3
0.5
1.0
1.5
2.0
2.5
3.0

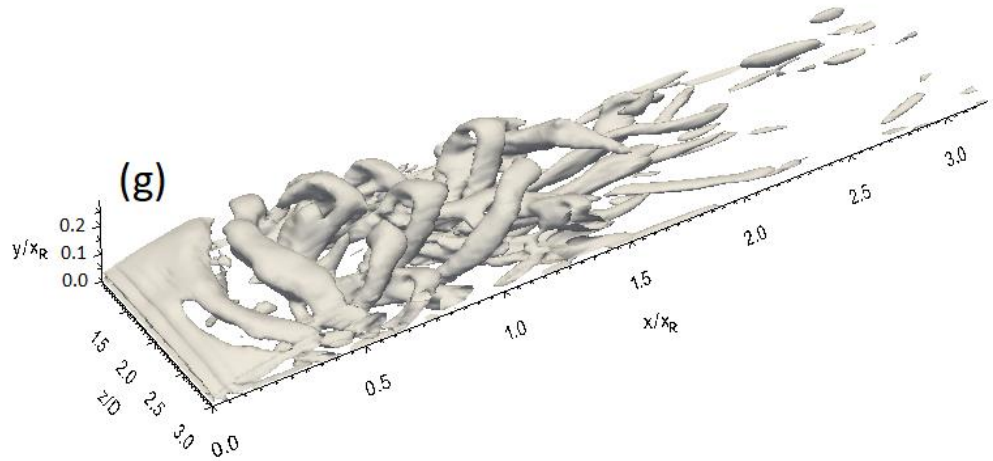
(g)
y/x_R
0.2
0.1
0.0
z/D
1.5
2.0
2.5
3.0
0.0
0.5
1.0
1.5
2.0
2.5
3.0
x/x_R

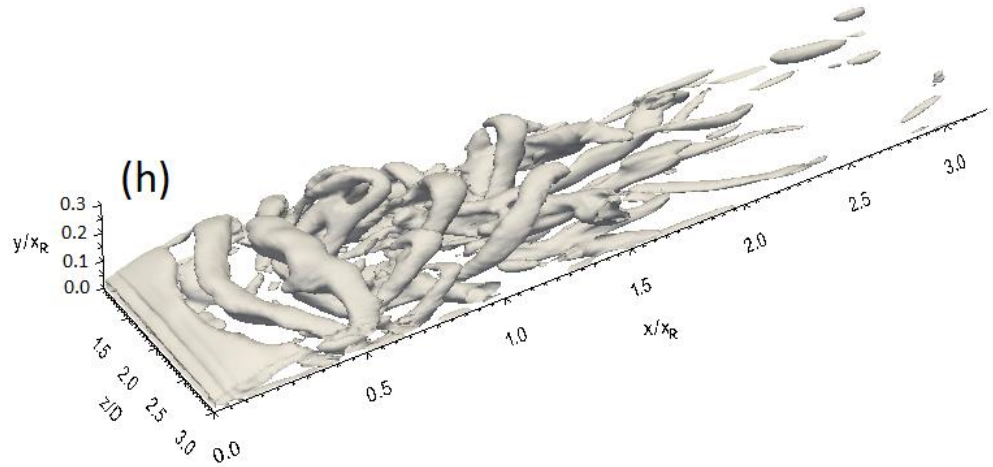
(h)
y/x_R
0.3
0.2
0.1
0.0
z/D
1.5
2.0
2.5
3.0
0.0
0.5
1.0
1.5
2.0
2.5
3.0
x/x_R

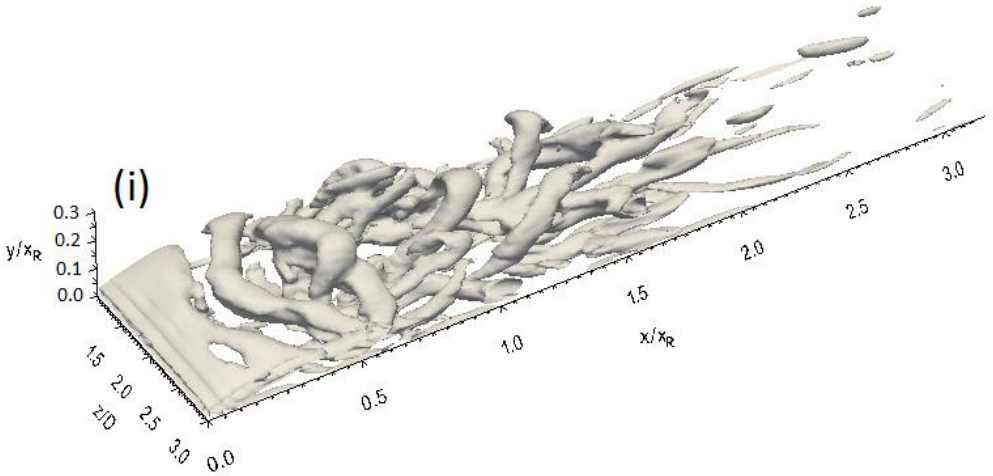
(i)
y/x_R
0.3
0.2
0.1
0.0
z/D
1.5
2.0
2.5
3.0
0.0
0.5
1.0
1.5
2.0
2.5
3.0
x/x_R

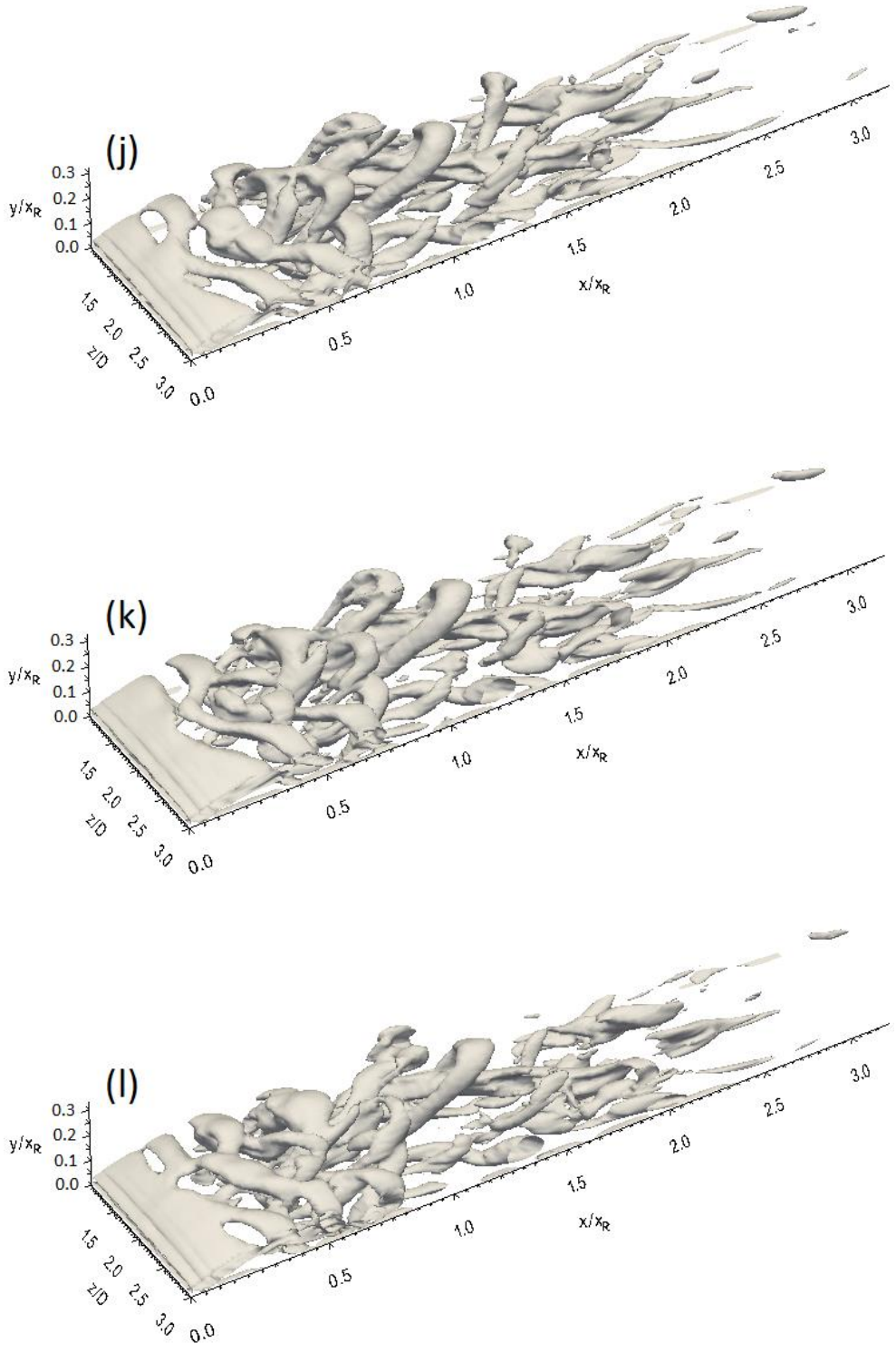

Fig. 7-53. Q-criterion isosurface at sequential times (every 250 time steps) for 3D_case2 with FST

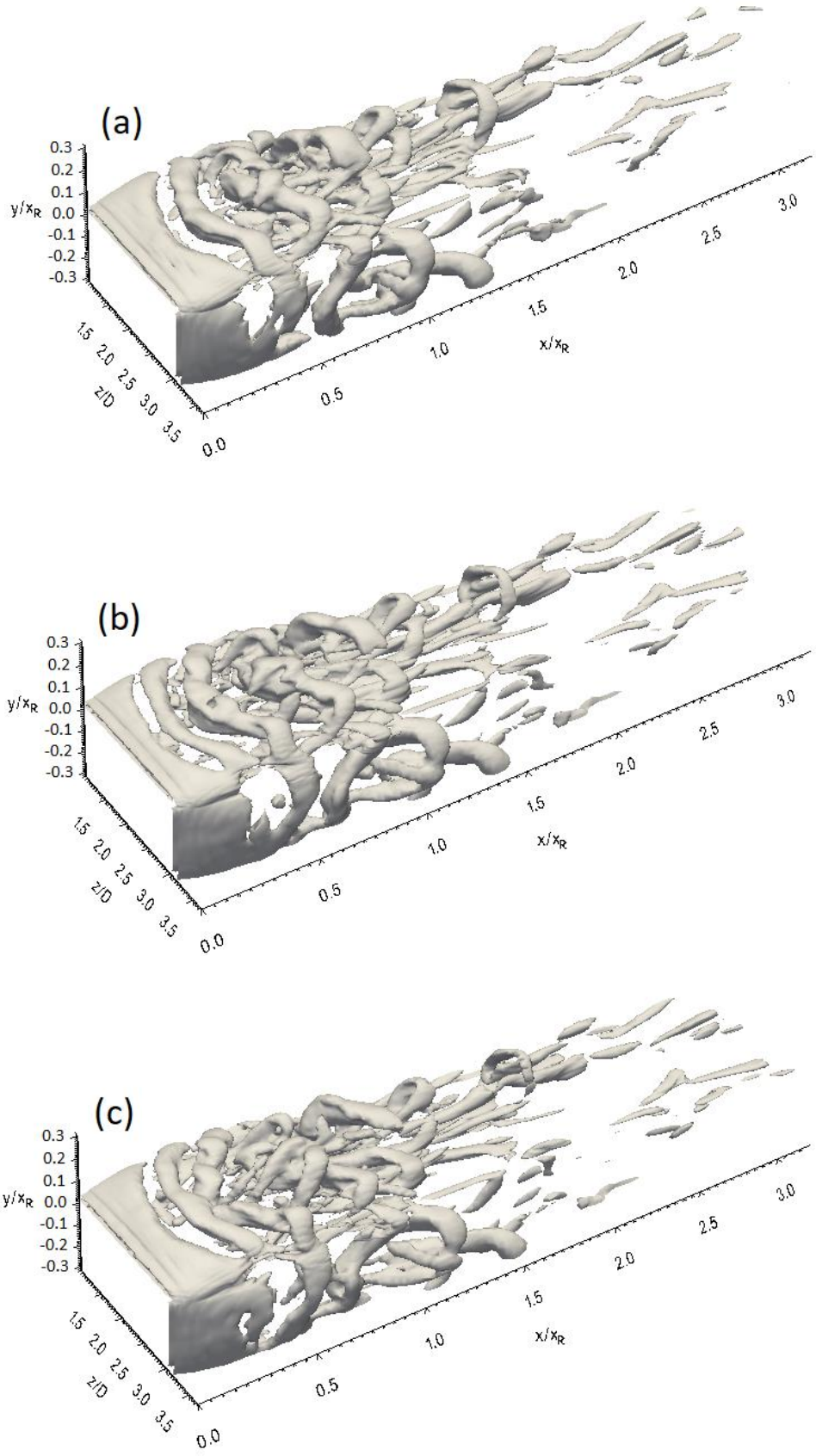

Caption for these figures is on the following page

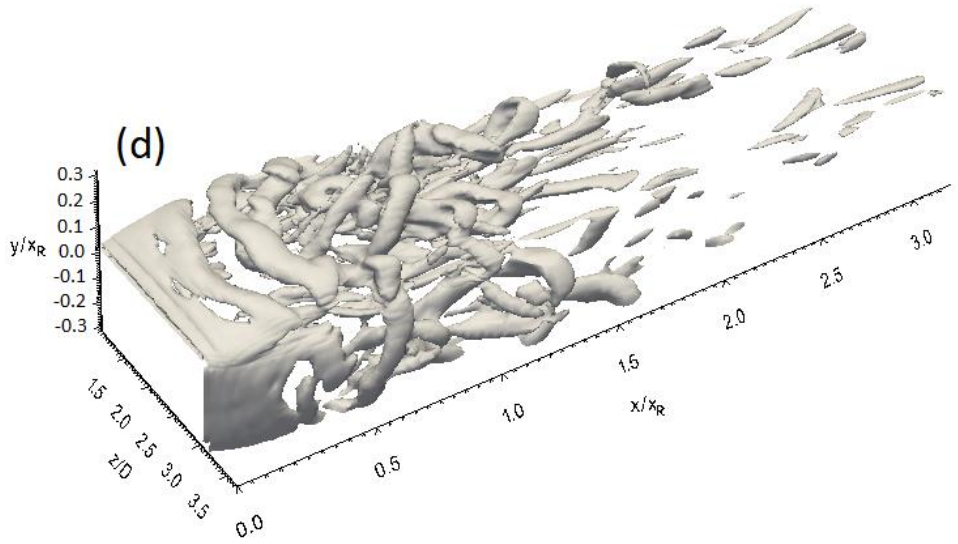
(d)
y/x_R
0.3
0.2
0.1
0.0
-0.1
-0.2
-0.3
z/D
1.5 2.0 2.5 3.0 3.5
x/x_R
0.0 0.5 1.0 1.5 2.0 2.5 3.0

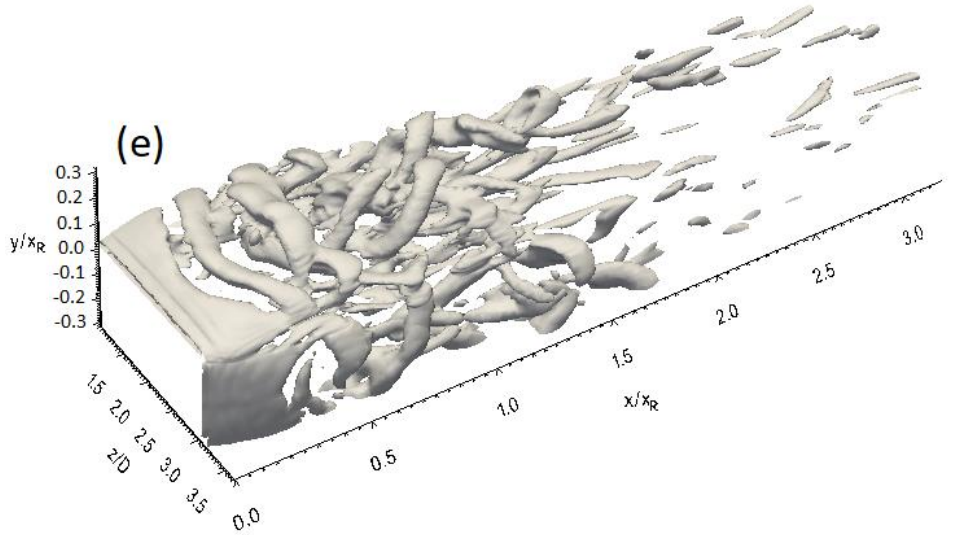
(e)
y/x_R
0.3
0.2
0.1
0.0
-0.1
-0.2
-0.3
z/D
1.5 2.0 2.5 3.0 3.5
x/x_R
0.0 0.5 1.0 1.5 2.0 2.5 3.0

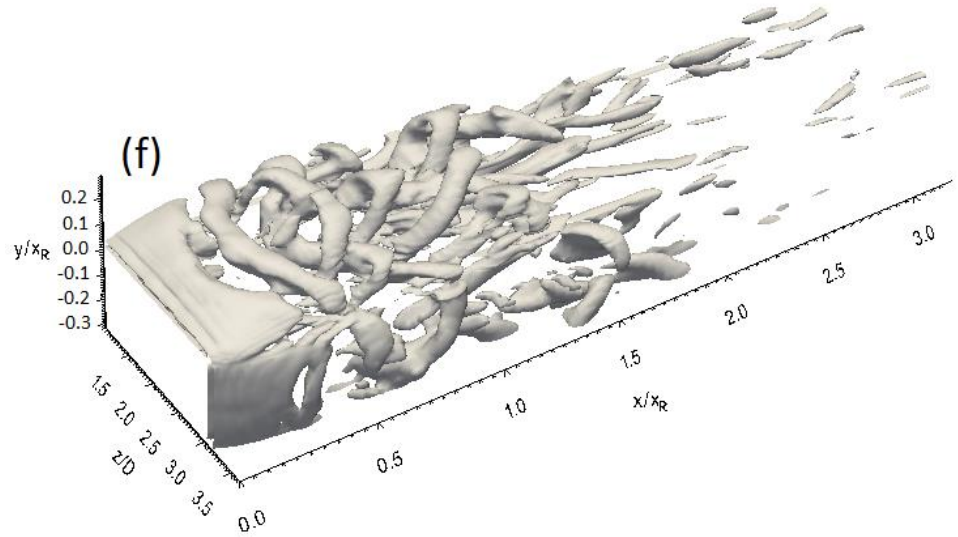
(f)
y/x_R
0.2
0.1
0.0
-0.1
-0.2
-0.3
z/D
1.5 2.0 2.5 3.0 3.5
x/x_R
0.0 0.5 1.0 1.5 2.0 2.5 3.0

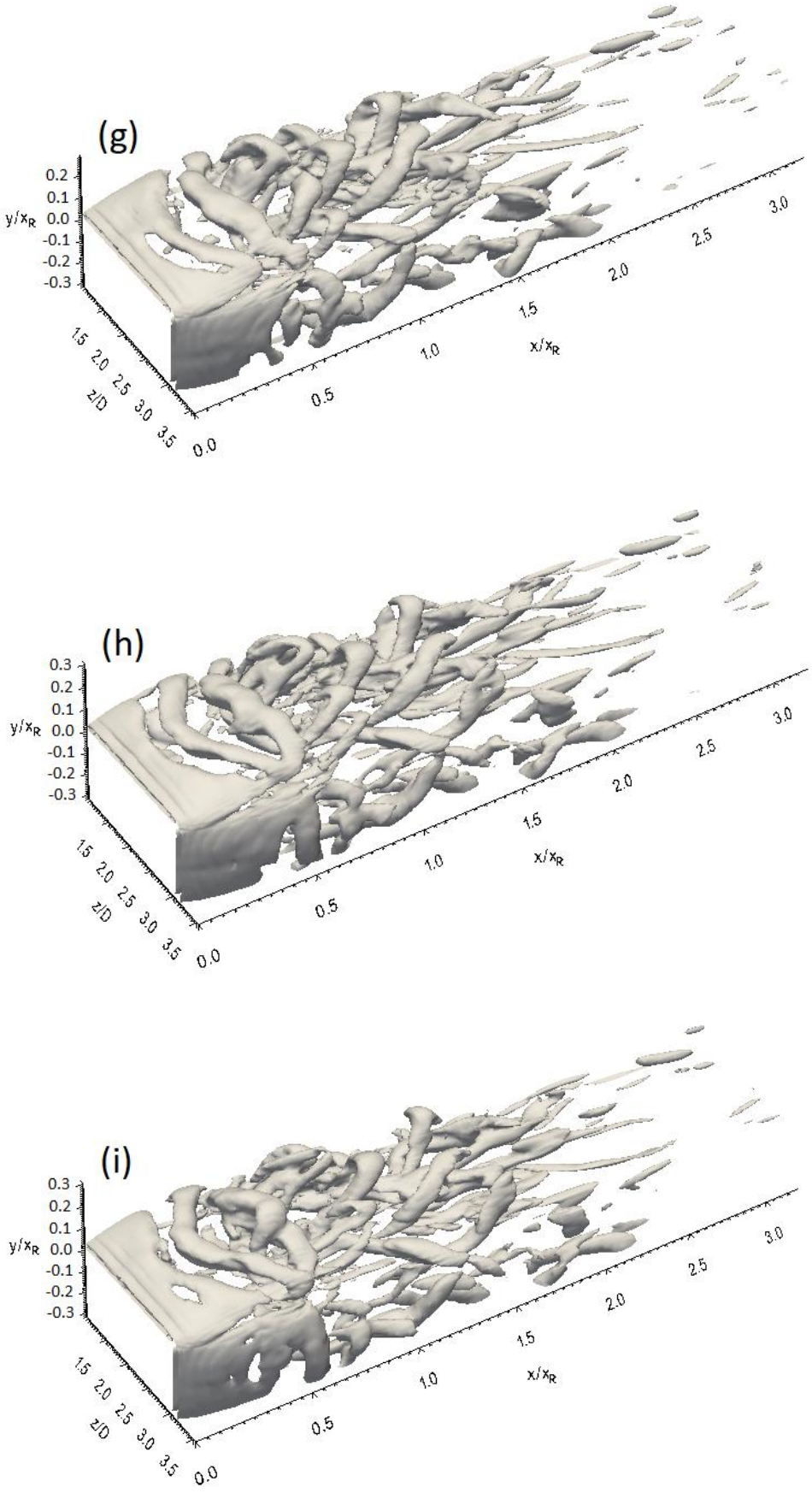
(g)
(h)
(i)
y/x_R
x/x_R
z/D

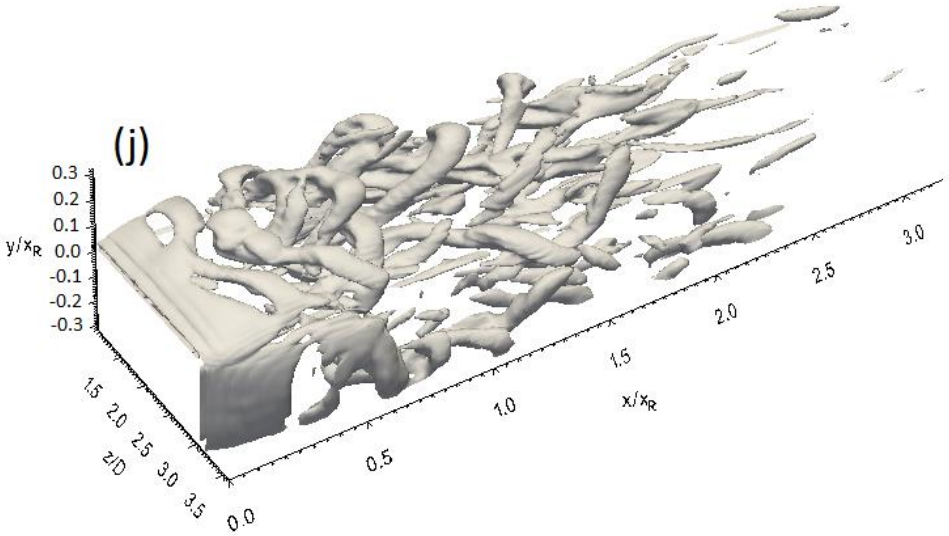

Fig. 7-54. Q-criterion isosurface on the top and side surfaces at sequential times (every 250 time steps) for 3D_case2 with FST (period I)

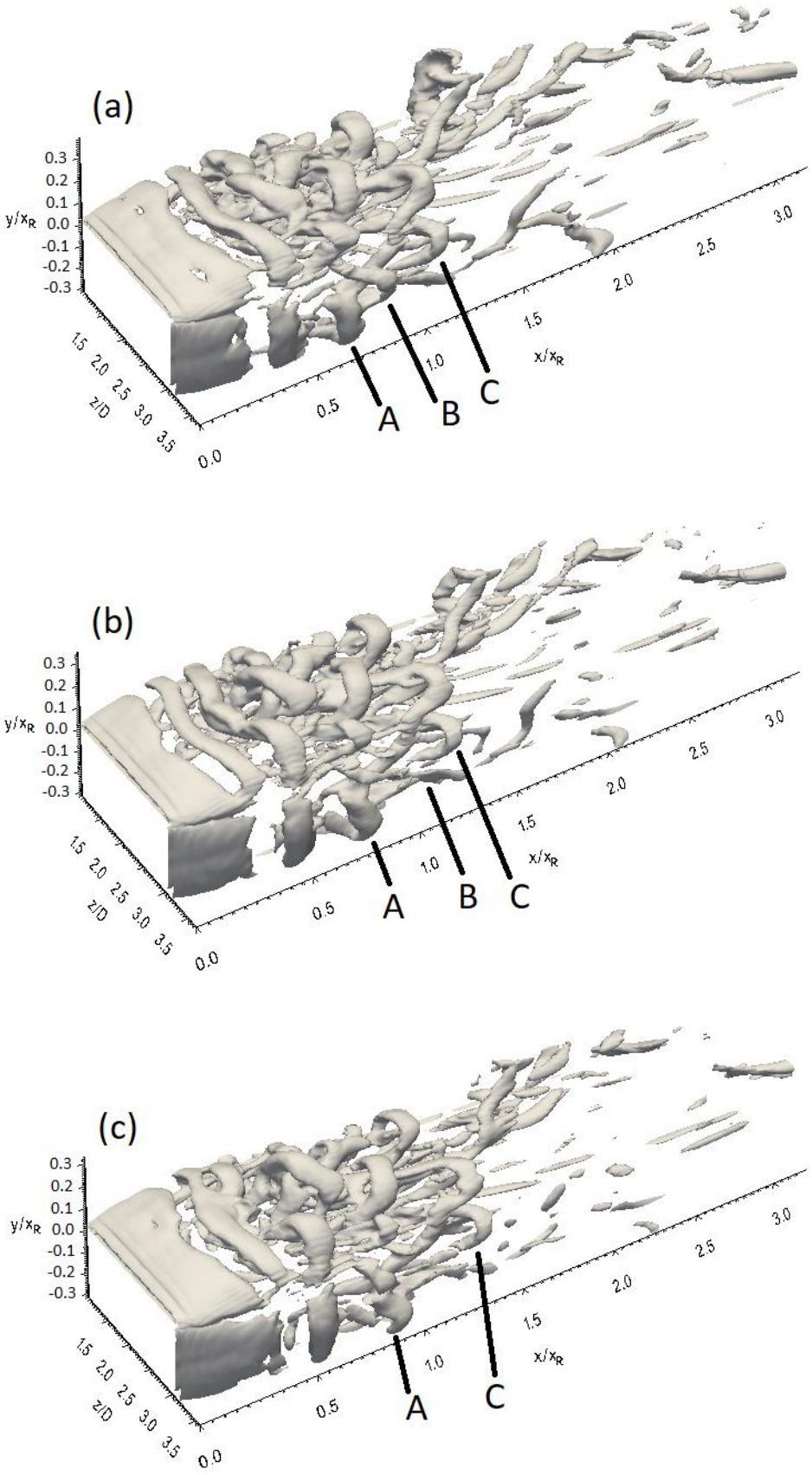

Caption for these figures is on the following page

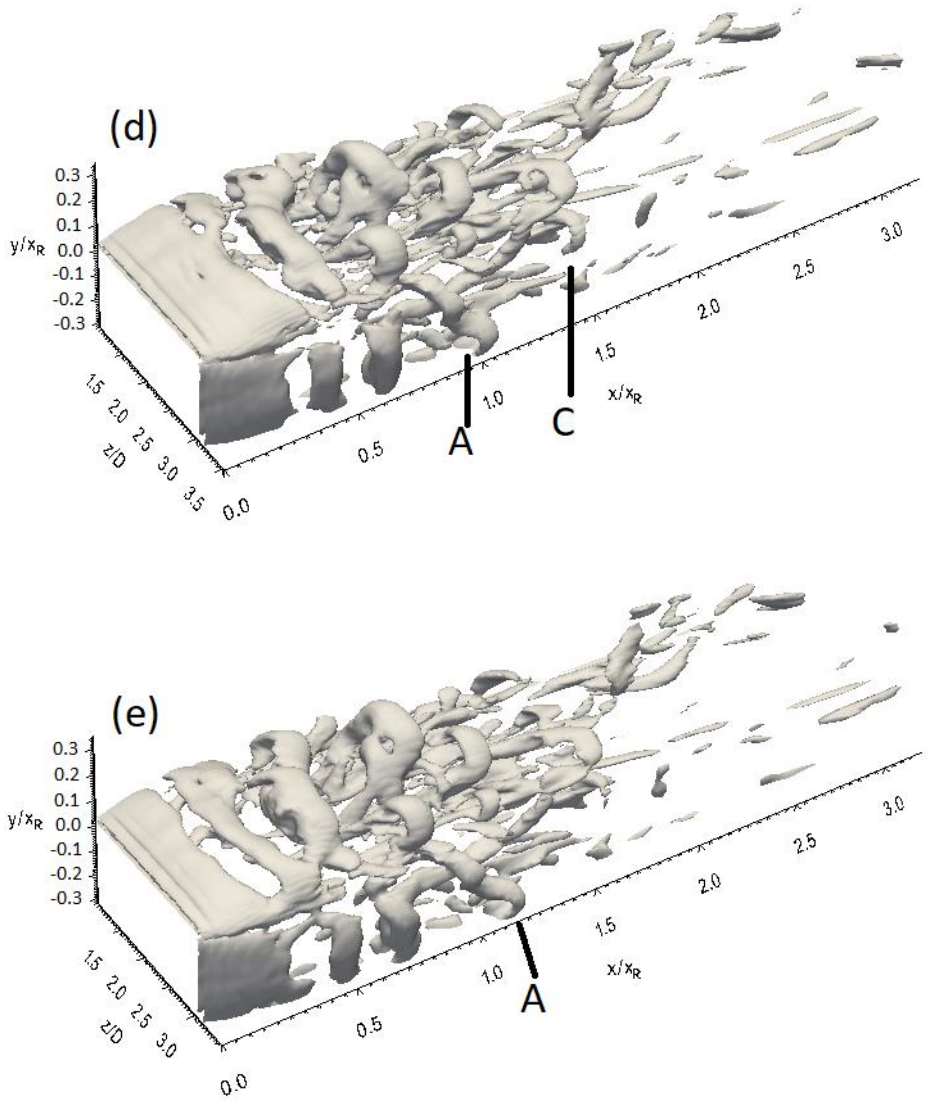

Fig. 7-55. Q-criterion isosurface on the top and side surfaces at sequential times (every 250 time steps) for 3D_case2 with FST (period II)

7.4 Summary

Three flow visualization methods are performed in the current study to shed light on the development of coherent structures and to determine if there are any similarities and differences through the transitional separated-reattached flow over all geometries with NFST and FST. These methods are the low pressure isosurface, vorticity field isosurface, and Q-criterion isosurface. Employing these methods shows that they can capture all, or at least some, of the coherent structure development stages with varying degrees of clarity.

In general, the time and distance for the transition in the flat plate are longer than those in other two geometries, leading to the formation of a longer separation bubble on the flat plate.

With NFST, the stages of coherent structures development for the flat plate are: shedding of Kelvin-Helmholtz rolls downstream from the plate leading edge; increasing in size of these rolls as they move downstream; merging of two Kelvin-Helmholtz structures by winding around each other to form a new large structure which keeps its two-dimensional nature; breaking down of the new structure into a large number of hairpin structures around the mean reattachment line; shedding of these streamwise structures to the reattached turbulent boundary layer; and disintegrating of hairpin structures into smaller structures further downstream.

In the presence of a 3.7% intensity of free stream turbulence, similar development of coherent structures is observed to that described above, with the exception of the stage in which the two Kelvin-Helmholtz rolls merge, where with FST this process is absent. In addition, the Kelvin-Helmholtz rolls' axis is not entirely parallel to the spanwise direction with FST, where a waviness in these rolls is seen.

Different stages of the development of coherent structures are revealed for both three-dimensional geometries. In addition, it is found that the aspect ratio of the three-dimensional geometry influences the coherent structures development.

For 3D_case1 with NFST, after the shedding of Kelvin-Helmholtz rolls from the separation bubble, these rolls grow as they move downstream. It is observed that these rolls develop topologically to form three-dimensional hairpin structures around the mean reattachment line. Further downstream, the breakdown of streamwise structures within the reattached turbulent boundary layer takes place more rapidly than that is observed for other two geometries. No merging of structures is revealed for this geometry.

Similar development to the above coherent structures is captured on both the top and side surfaces of 3D_case1.

Under the influence of the current elevated levels of intensity of free stream turbulence, there is just one difference in the coherent structures development stages which is related to the nature of the Kelvin-Helmholtz rolls after shedding from the separated layer. With

FST, it can be seen that Kelvin-Helmholtz rolls undergo a degree of distortion in the spanwise direction.

For 3D_case2 with NFST, the vortex merging process of structures does not represent one of the stages of coherent structures development. The current LES results show that first type of coherent structures to appear on the top surface of 3D_case2 are spanwise Kelvin-Helmholtz structures shed from the separated layer. These structures move downstream and enlarge. Downstream of x/x_R = 0.7, breakdown of these rolls occurs, leading to the formation of a set of hairpin structures. These three-dimensional structures survive up to x/x_R = 1.5. Further downstream, the hairpin structures disintegrate into smaller turbulent structures.

The coherent structures development on the side surface of 3D_case2 is different from that on the top surface of this geometry. There is no breakdown of the Kelvin-Helmholtz rolls on the side surface of 3D_case2, where it can be observed that Kelvin-Helmholtz rolls develop topologically to form hairpin structures.

Similarly, the evolution of coherent structures in 3D_case2 that is presented with NFST is observed with FST apart from a distortion (waviness) that is dominant for the Kelvin-Helmholtz rolls in the first stages of the transition with FST.

It can be concluded that the aspect ratio of the three-dimensional geometry affects the coherent structures development on the top and side surfaces of this geometry. With an aspect ratio value of 1, there is no difference in coherent structure development on either the top or the side surface. With an aspect ratio value of 2, however, there is a difference between coherent structure development on the top and side surfaces as presented in this chapter.

Flow visualization of the current study indicates a twisting structure at the early stage of the transition over both 3D_case1 and 3D_case2 for both NFST and FST. This structure breaks down quickly into four Kelvin-Helmholtz rolls on each surface of these geometries. This breakdown process is believed to be the reason for the reduced ability of the Kelvin-Helmholtz structures to pair around each other in the three-dimensional geometries.

Chapter Eight

Turbulent Boundary Layer Development

8.1 Introduction

It is clear from the literature review in Chapter 2, the distance for the recovery of the reattached turbulent boundary layer is quite long, but the slowness of its development is quite independent of the nature of the separated flow, where this phenomenon is common with laminar and turbulent separated flows. Moreover, there is no impact of elevated intensity of free stream turbulence on enhancing the recovery of the reattached turbulent boundary layer.

It is worth pointing out that the limited length of the numerical computational box in the present study prevents the identification of the exact distance to reach the canonical form of reattached turbulent boundary layer for all geometries. The main target of the current study is to simulate numerical transitional separated-reattached flow over two and three-dimensional geometries to compare with transition physics. Therefore, the choice of dimensions of the numerical computational box here is purely to focus on the transition flow, not on the distance of reattached turbulent boundary layer recovery.

The purpose of this chapter is to reveal if there is any effect of the nature of the geometry, if it is two- or three-dimensional, on the development of the reattached turbulent boundary layer within a limited distance.

8.2 Boundary layer development after the reattachment for NFST

In order to investigate the development of the reattached turbulent boundary layer in the geometries used in the current study with NFST, a distance of 10*D* starting from the mean reattachment line is chosen as the inspection region for the turbulent boundary layer recovery. This region is divided into four equal distances to involve four inspection stations where, at each station, the profile of the mean streamwise velocity is plotted to check its approach to the log-law profile. Locations of inspection stations are detailed in Tables 8-1 for the flat plate, 8-2 for 3D_case1 and 8-3 for 3D_case2.

It should be noted that the inspection distance for the reattached turbulent boundary layer development is chosen to be just x/D = 10 because of the limited length of the computational box used in the present study. The inspection distance for the flat plate ends at x/D = 16, which is a point close to the outflow boundary of the computational domain. However, for the three-dimensional geometries, it is possible to choose an inspection distance that is longer than x/D = 10 due to the shorter separation bubble mean length compared with that in the flat plate. The main purpose of the present study is to compare flow behaviours among the chosen geometries. Therefore, the inspection distance (x/D = 10) is the same for all geometries.

location 1 (L1)	location 2 (L2)	location 3 (L3)	location 4 (L4)
x/D =8.5	x/D =11	x/D =13.5	x/D =16
x/x_R =1.416	x/x_R =1.833	x/x_R =2.25	x/x_R =2.666

Table 8-1. Positions of the inspection stations for the flat plate with NFST

location 1 (L1)	location 2 (L2)	location 3 (L3)	location 4 (L4)
x/D =5.9	x/D =8.4	x/D =10.9	x/D =13.4
x/x_R =1.735	x/x_R =2.470	x/x_R =3.205	x/x_R =3.941

Table 8-2. Positions of the inspection stations for 3D_case1 with NFST

location 1 (L1)	location 2 (L2)	location 3 (L3)	location 4 (L4)
x/D =6.45	x/D =8.95	x/D =11.45	x/D =13.95
x/x_R =1.632	x/x_R =2.265	x/x_R =2.898	x/x_R =3.531

Table 8-3. Positions of the inspection stations for 3D_case2 with NFST

The mean streamwise velocity profiles in the wall units ($u^+ = U_m/ u_\tau$) at each inspection station are compared with the log-law profile as shown in Figs 8-1, 8-2 and 8-3 for the flat plate, 3D_case1 and 3D_case2, respectively. For all geometries used in the current study, it is clearly seen that the velocity profiles of the turbulent boundary layer show the slowness of the boundary layer development process, where these profiles do not quite establish the log-law profile.

However, it can be seen that the velocity profiles of the reattached turbulent boundary layer in 3D_case1 are more uniform than that for other two geometries. This is clearly shown in Fig. 8-2, where a dip in streamwise velocity profile below the standard log-law does not appear as strongly as for other geometries. This confirms the flow visualizations shown in Chapter 7, where the breakdown of the large coherent structures into small turbulent structures in 3D_case1 is faster than that for other two geometries.

In general, the mean streamwise velocity profiles for all geometries are consistent with the fact that the reattached turbulent boundary layer takes a quite long distance to re-establish. In addition, the current study demonstrates that there is no effect due to the nature of the geometries, if it is two- or three-dimensional, with regards to this phenomenon.

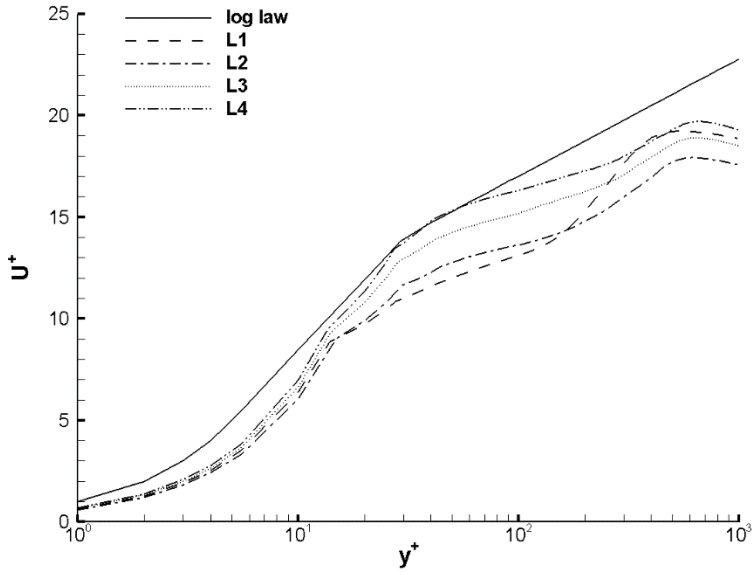

Fig. 8-1. The mean streamwise velocity profiles for the developed boundary layer after reattachment at various streamwise locations for the flat plate with NFST

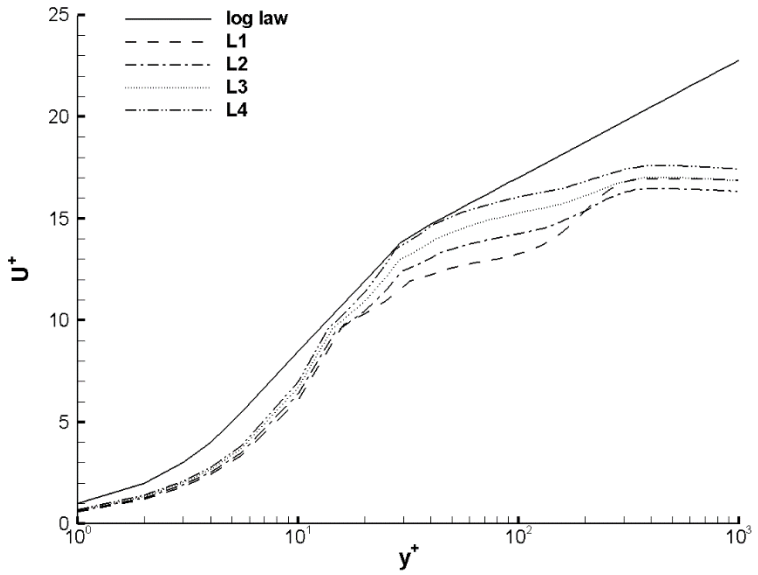

Fig. 8-2. The mean streamwise velocity profiles for the developed boundary layer after reattachment at various streamwise locations for 3D_case1 with NFST

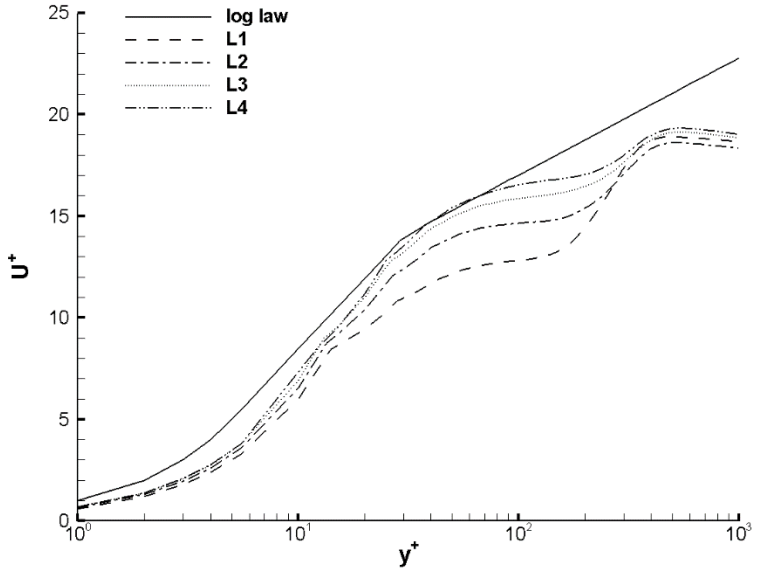

Fig. 8-3. The mean streamwise velocity profiles for the developed boundary layer after reattachment at various streamwise locations for 3D_case2 with NFST

It should be noted that in the current study, the standard log law is defined by Nichols:

$$u^+ = \begin{cases} y^+ & 0 < y^+ < 5 \\ 5\,ln(y^+) - 3.05 & 5 < y^+ < 30 \\ \frac{1}{k}\,ln(y^+) + 5.5 & 30 < y^+ < 1000 \end{cases} \quad (8\text{-}1)$$

where k is the von Karmen constant taken as 0.4.

In order to present further evidence to show the slowness of the re-establishment of the turbulent boundary layer after the reattachment in all geometries studied here, the Clauser parameter (G) can be employed. This parameter predicts the distance of the boundary layer equilibrium, where it is reported that the expected equilibrium value of the Clauser parameter is 6.8 (Alam and Sandham, 2000).

The Clauser parameter profiles for all geometries are shown in Fig. 8-4 for the flat plate, Fig. 8-5 for 3D_case1 and Fig. 8-6 for 3D_case2, respectively. This parameter is plotted as a function of $(x\text{-}x_R)/h_R$, where h_R is the boundary layer thickness on the mean reattachment line. The Clauser parameter is defined as:

$$G = \left(\frac{H-1}{H}\right)\sqrt{\frac{2}{C_f}} \quad (8\text{-}2)$$

where H is the shape factor, which is taken as 1.3, and C_f is the skin fraction coefficient calculated in equation (4-2).

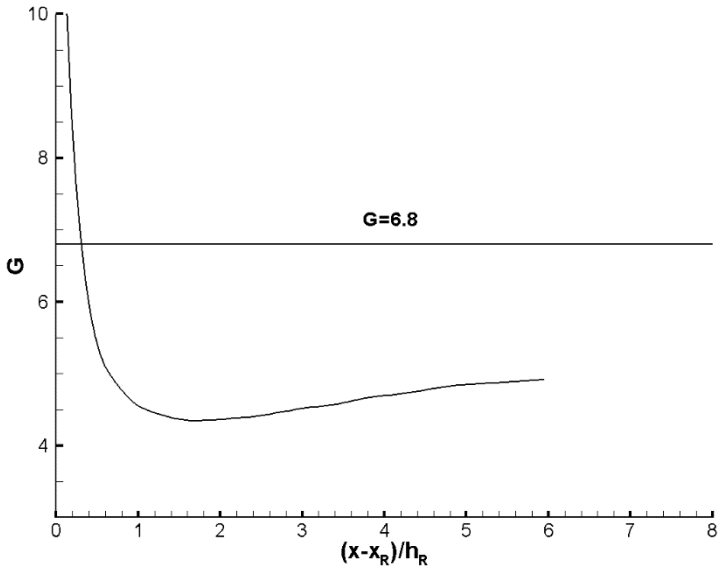

Fig. 8-4. The Clauser parameter profile for the flat plate with NFST

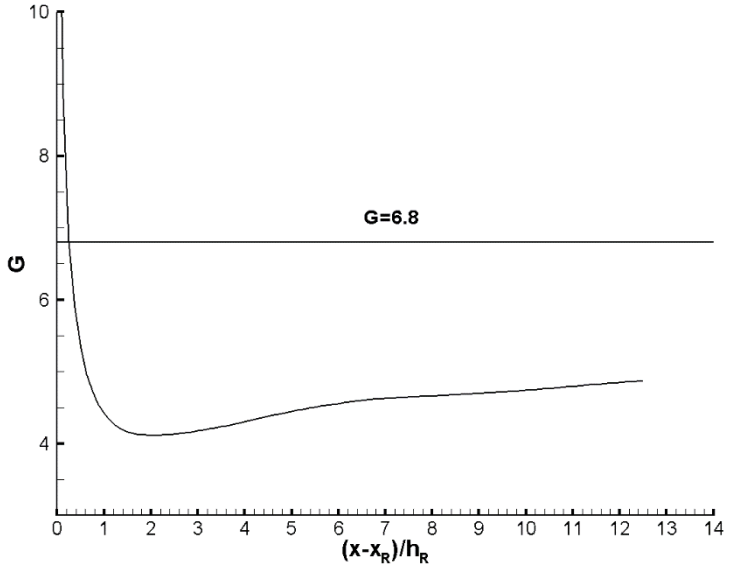

Fig. 8-5. The Clauser parameter profile for 3D_case1 with NFST

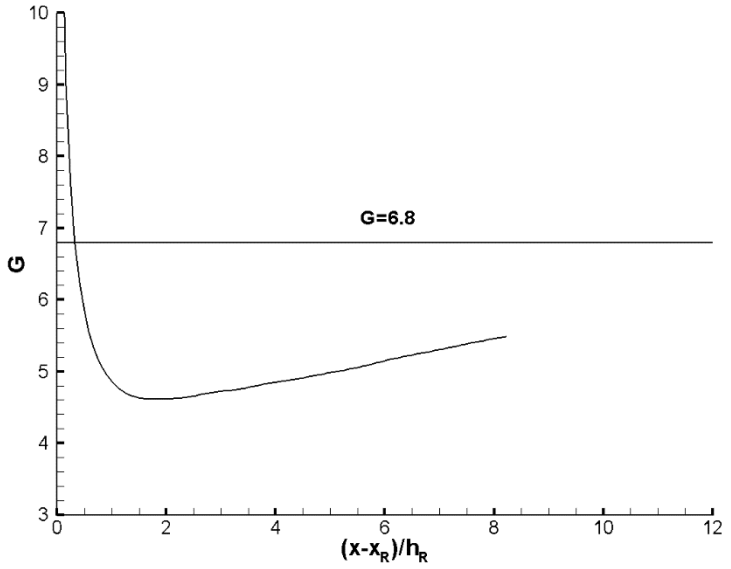

Fig. 8-6. The Clauser parameter profile for 3D_case2 with NFST

As can be seen for all geometries, the Clauser parameter value at the end of the inspection region does not match the standard value of this parameter (G = 6.8). The simulation results show that the Clauser parameter value at the end of the inspection region is 4.918 for the flat plate, 4.871 for 3D_case1 and 5.484 for 3D_case2.

However, the Clauser parameter magnitude in 3D_case2, as shown in Fig. 8-6, is closer to the standard value of this parameter. This may refer to the recovery distance of the turbulent boundary layer for 3D_case2, which may be shorter. However, this is not a guarantee that one can conclude this, because the Clauser parameter value for 3D_case2 does not match the standard value (G = 6.8). Therefore, the length of the numerical computational box must be much longer than that selected in the present study to achieve the standard value of the Clauser parameter and find which of the current geometries will establish the recovered turbulent boundary layer first.

8.3 Boundary layer development after the reattachment for FST

To determine if there is an enhancement of the re-establishment of the turbulent boundary layer after reattachment in the presence of an elevated intensity of free stream turbulence, two investigative methods, which are similar to those used with NFST in Section 8.2, are performed here.

In the present study, an inspection distance, which is between the mean reattachment line and a point at x_R + 10, is chosen. This inspection distance is divided into four spaces corresponding to four inspection locations after the mean reattachment line. Inspection locations are detailed in Tables 8-4, 8-5 and 8-6 for the flat plate, 3D_case1 and 3D_case2, respectively.

location 1 (L1)	location 2 (L2)	location 3 (L3)	location 4 (L4)
x/D =6.7	x/D =9.2	x/D =11.7	x/D =14.2
x/x_R =1.595	x/x_R =2.19	x/x_R =2.785	x/x_R =3.38

Table 8-4. Positions of the inspection stations for the flat plate with FST

location 1 (L1)	location 2 (L2)	location 3 (L3)	location 4 (L4)
x/D =5	x/D =7.5	x/D =10	x/D =12.5
x/x_R =2	x/x_R =3	x/x_R =4	x/x_R =5

Table 8-5. Positions of the inspection stations for 3D_case1 with FST

location 1 (L1)	location 2 (L2)	location 3 (L3)	location 4 (L4)
x/D =5.6	x/D =8.1	x/D =10.6	x/D =13.1
x/x_R =1.417	x/x_R =2.05	x/x_R =2.683	x/x_R =3.316

Table 8-6. Positions of the inspection stations for 3D_case2 with FST

The mean streamwise velocity profiles with FST for all geometries used in the current study show similar behaviour to the reattached turbulent boundary layer for the NFST case regarding the recovery of reattached turbulent boundary layer. Despite the presence of free stream turbulence with an intensity of 3.7%, profiles of the mean streamwise velocity at all inspection stations in all geometries are still below the standard log-law profile, as shown in Fig. 8-7 for the flat plate, Fig. 8-8 for 3D_case1 and Fig. 8-9 for 3D_case2. It is clearly seen that the velocity profiles at the selected inspection stations approach the log-law profile when moving downstream. This indicates that the re-establishment of the turbulent boundary layer takes place at a distance that is longer than the distance of the current inspection.

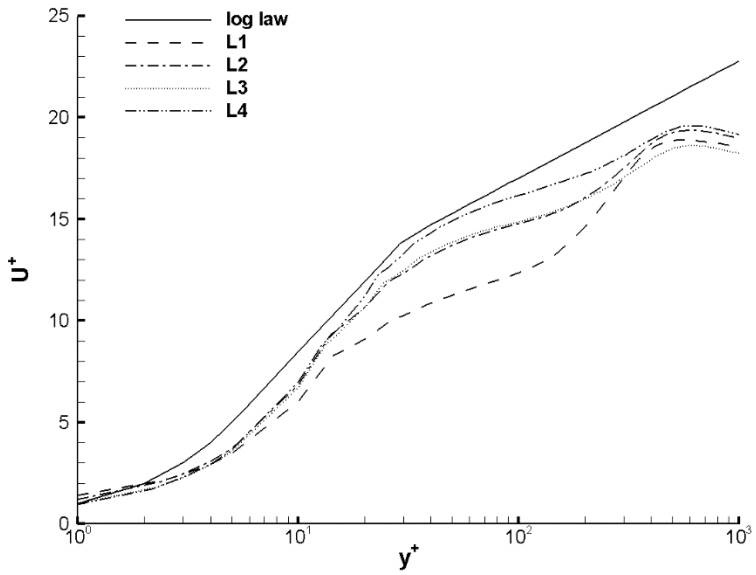

Fig. 8-7. The mean streamwise velocity profiles for the developed boundary layer after reattachment at various streamwise locations for the flat plate with FST

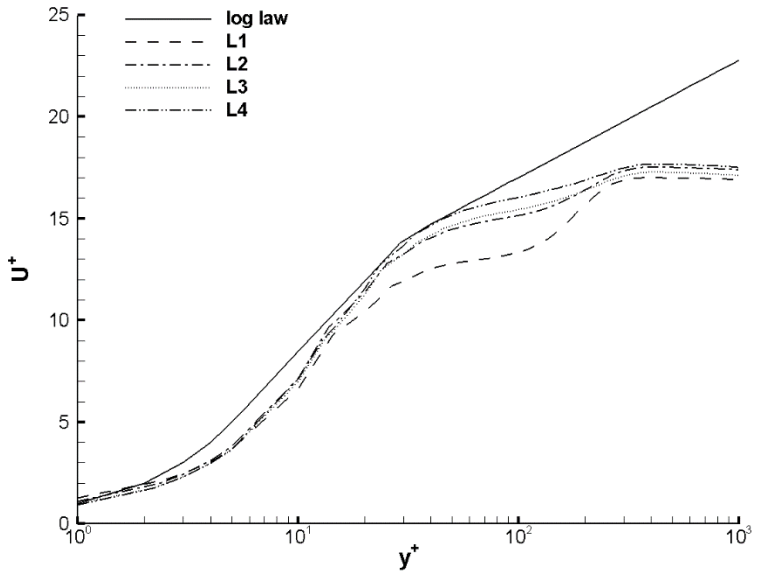

Fig. 8-8. The mean streamwise velocity profiles for the developed boundary layer after reattachment at various streamwise locations for 3D_case1 with FST

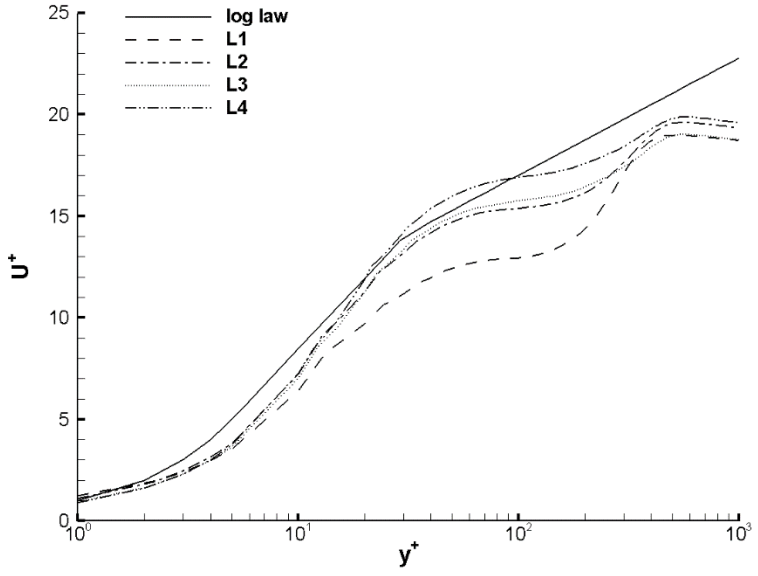

Fig. 8-9. The mean streamwise velocity profiles for the developed boundary layer after reattachment at various streamwise locations for 3D_case2 with FST

The Clauser parameter profiles as a function of $(x-x_R)/h_R$ with FST and NFST are plotted in Fig. 8-10 for the flat plat, Fig. 8-11 for 3D_case1 and Fig. 8-12 for 3D_case2. It is clearly seen that there are inconsiderable differences between the Clauser parameter value

when using FST and NFST, indicating that there is no effect due to the presence of an elevated intensity of free stream turbulence on the development of turbulent boundary layer after the reattachment, where the Clauser parameter value with FST is lower than the standard value (G = 6.8).

Due to an intensity of 3.7% for the free stream turbulence, the Clauser parameter value at end of the inspection distance increases from 4.918 to 4.986 for the flat plate, from 4.871 to 4.923 for 3D_case1 and from 5.484 to 5.49 for 3D_case2. This phenomenon is consistent with the results found in transitional separated-reattached flow on a blunt flat plate by Castro and Epik (1996, 1998), where they reported there was no effect due to increasing the intensity of the free stream turbulence on the Clauser parameter value.

It can be concluded that even with an elevated intensity of free stream turbulence, the recovery distance of the reattached turbulent boundary layer is still long, regardless of whether the geometry is two- or three-dimensional.

In general, the current simulation results show that the change in nature of the geometry that can be associated with an increase in the intensity of the free stream turbulence does not significantly affect the development of the reattached turbulent boundary layer.

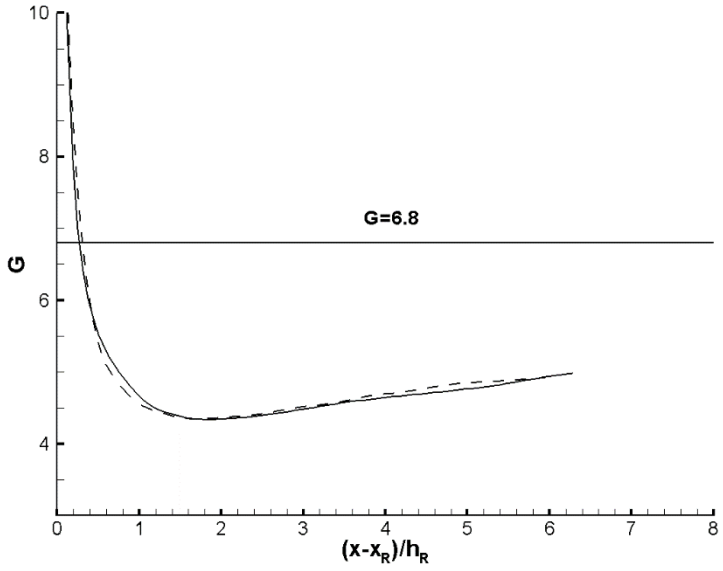

Fig. 8-10. The Clauser parameter profile for the flat plate. With FST: solid line; with NFST: dashed line

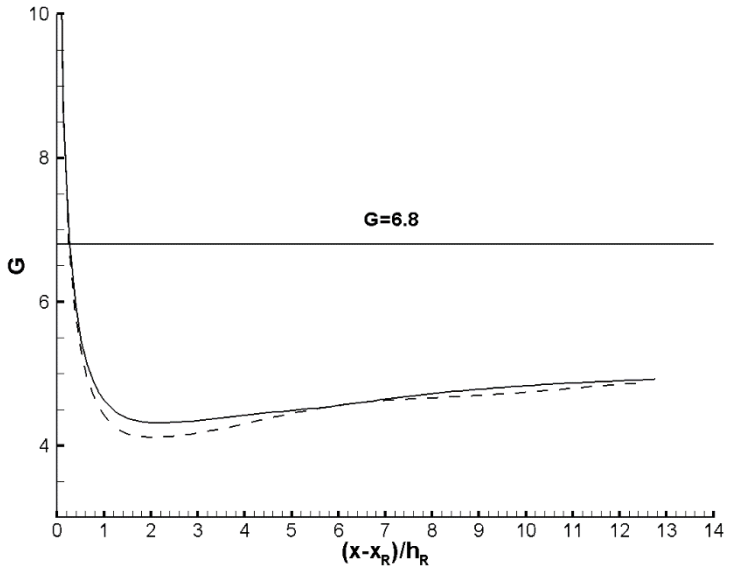

Fig. 8-11. The Clauser parameter profile for 3D_case1. With FST: solid line; with NFST: dashed line

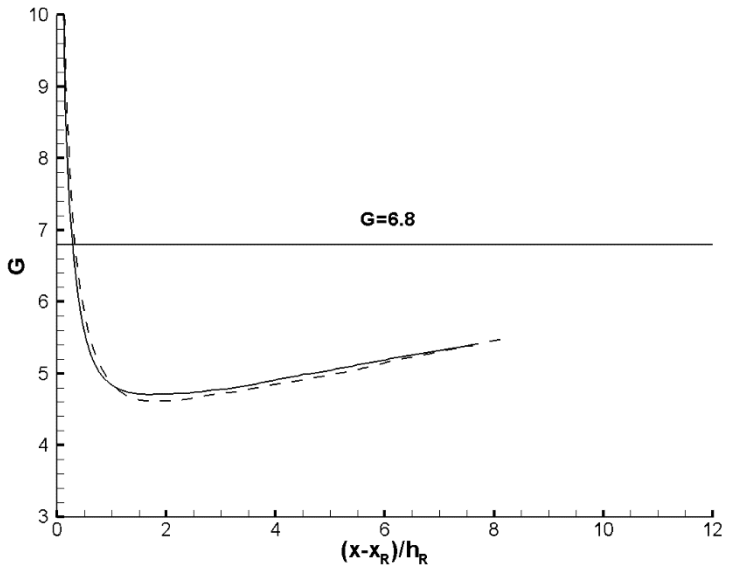

Fig. 8-12. The Clauser parameter profile for 3D_case2. With FST: solid line; with NFST: dashed line

8.4 Summary

As shown in this chapter, the re-establishment of the turbulent boundary layer after the reattachment for the current geometries takes place over a long distance. The length of

the numerical competition box in the present study is considerably shorter than the length necessary to show the recovery of the turbulent boundary layer after the reattachment presented in the literature. The issue remains unclear for any of the current geometries in which the reattached turbulent boundary layers would be re-established first. Two methods are used here to answer this issue: the log-law profile and the Clauser parameter value.

For both NFST and FST cases, the comparison between the mean streamwise velocity profiles and the log-law profile indicates that the recovery of the reattached turbulent boundary layer in 3D_case1 may be faster than that in other geometries due to disappearance of a dip in the velocity profiles. On the other hand, the Clauser parameter profile for 3D_case2 shows that reattached turbulent boundary layer may re-establish first due to the value of the Clauser parameter in this geometry being closer to the standard value than those for other geometries. However, the limited length of the numerical computation box prevents the direct determination in which geometry the re-establishment of the reattached turbulent boundary layer occurs first.

In general, the current study shows that there is no influence due to the nature of geometries, whether it is two or three-dimensional, or whether there is an elevated intensity of free stream turbulence, in terms of enhancing the re-establishment of the turbulent boundary layer after reattachment.

Chapter Nine

Conclusion and Recommendation

9.1 Conclusion

The properties of a transitional separated-reattached flow over six case studies have been investigated in this thesis by employing three geometrical shapes with two disturbance levels in the incoming flows. The geometries are a blunt flat plate (with an infinity aspect ratio) and two three-dimensional geometries characterized by two different aspect ratios (1 and 2). Low level of intensity of free stream turbulence (< 0.2%) and high level of intensity of free stream turbulence (3.7%) are applied in the current study. The numerical simulations are carried out by the commercial OF tool box employing LES with the dynamic localization SGS.

The good agreement obtained from the comparison among the current OF code results and the available experimental data and simulated results for the flat plate with NFST and FST is encouraging in terms of the simulation results obtained for transitional separated-reattached flow over three-dimensional geometries. To the best of the author's knowledge, there are no published results for separated-reattached flow over a three-dimensional geometry. Therefore, the current study is the first to investigate such a flow with low and also high levels of intensity of free stream turbulence over three-dimensional geometries with different aspect ratios.

The current study presents the following similarities and differences in the features of transitional separated-reattached flows:

- With NFST, the separation bubble mean length is 6*D* for the flat plate which reduces to 3.95*D* for 3D_case2 and 3.4*D* for 3D_case1. This indicates that the separation on the flat plate is longer than that on the three-dimensional geometries. In addition, there is no strong effect associated with changing the aspect ratio of the three-dimensional geometry on the mean reattachment length. With FST, there is a reduction in the separation bubble mean length by about 30% for the flat plate, 21.5% for 3D_case2, and 26.47% for 3D_case1.

- For the current geometries, the minimum negative value in the mean streamwise velocity profile is approximately identical for NFST and FST. The peak value in the Reynolds stresses for the flat plate is larger than that in the other two geometries by about 20%-25% with NFST and 30%-35% with FST. The Reynolds stresses profile peaks for 3D_case2 are slightly larger than those for 3D_case1 with both NFST and FST.

- In the current study, the elevated intensity of free stream turbulence enhances the transformation to turbulence by speeding up the transition, which moves upstream. This phenomenon is consistent with results found in the literature.

- For all geometries with NFST and FST, there is no trace of the absolute instability, where the separation bubble is classified as convectively unstable. In addition, the transition in the free shear layer is driven by the inviscid Kelvin-Helmholtz instability, which is dominant as the primary instability mechanism.

- To investigate existing frequency modes, spectral analyses is carried out employing Fourier transform and wavelet power transform methods. Fourier transform spectra show that the regular shedding frequency with NFST and FST for all geometries is in a good agreement with that documented in the literature for different two-dimensional geometries.

- For the geometries studied here, it is found that the selective high shedding frequency mode is absent with NFST, however, this frequency mode clearly appears in frequency spectra with FST.

- The inspection of Fourier transform spectra detects that there is no trace of any low frequency mode (shear layer flapping) for all geometries in the current study with NFST and FST.

- The flow visualizations carried out for all case studies reveal the existence of Kelvin-Helmholtz rolls as the initial coherent structures of the transition. With NFST, these rolls are uniform and totally parallel to the spanwise axis. With FST, a spanwise waviness is clearly shown in the Kelvin-Helmholtz rolls.

- The transition in the flat plate is longer than that for the other geometries with both NFST and FST.

- With NFST, the vortex pairing process represents one of the coherent structures development stages in the transition for the flat plate. However, this process is completely absent for other geometries.

- There is no effect due to an elevated intensity of free stream turbulence on production of hairpin structures for all geometries, while the nature of the geometry was found to have a strong effect on formation of hairpin structures. In the flat plate, it is observed that hairpin structures are formed by the direct breakdown of Kelvin-Helmholtz rolls. In 3D_case1, the coherent structures development is similar on the top and side surfaces. Hairpin structures are formed by a topological evolution of a Kelvin-Helmholtz roll in 3D_case1. However, for 3D_case2, the evolution of the coherent structures on the top surface is different from that on the side surface. On the top surface, there is a direct breakdown of the Kelvin-Helmholtz rolls into hairpin structures, and on the side surface, a topological evolution of the Kelvin-Helmholtz rolls to hairpin structures is a dominant factor.

- Recovery of the reattached turbulent boundary layer is investigated employing two methods: the log law profile method and the Clauser parameter method. For all case studies, it is found that there is a delay in the reestablishment of the reattached turbulent boundary layer. It can be concluded that there is no effect on the development of the turbulent boundary layer after the reattachment due to the change of the geometry nature or the presence of an elevated intensity of free stream turbulence.

9.2 Recommendation

The following suggestions are recommended as a scope for further research:

- Investigate the secondary instability mechanism that associates with the transition later stages and leads to breakdown of the primary coherent structures for all case studies.

- Shed a light on the process that takes place after the secondary instability and leads to breakdown of three-dimensional structures into smaller structure in the reattached turbulent boundary layer for all case studies.

- Employ a higher intensity of free stream turbulence than that used in the current study to identify the threshold at which a bypassed transition occurs.

- Increase the length of the numerical computation box to identify for in any given case study which reattached turbulent boundary layer will recover first.

- Select further case studies by choosing more values of the aspect ratio of the three-dimensional geometries to investigate their effects on the characteristics of transitional separated-reattached flow, in particular, the evolution of the coherent structures.

- Clarify if there is a relationship between increase of the intensity of free stream turbulence and change of aspect ratio of the three-dimensional geometries on the characteristics of transitional separated-reattached flow.

Bibliography

Abdalla, I. E., Yang, Z., and Cook, M. 2007. Numerical Study of Transitional Separated-Reattached Flow over Surface-Mounted Obstacles Using Large Eddy Simulation. *Int. J. Numer. Meth. Fluids*, 54:175-206.

Abdalla, I. E., Yang, Z., and Cook, M. 2009. Computational Analysis and Flow Structure of a Transitional Separated-Reattached Flow over a Surface Mounted Obstacle and a Forward-Facing Step. *International Journal of Computational Fluid Dynamics*, 23 (1): 25-57.

Abdalla, I. E. and Yang, Z. 2004a. Numerical Study of the Instability Mechanism in Transitional Separating-Reattaching Flow. *International Journal of Heat and Fluid Flow*, 25 (4): 593-605.

Abdalla, I. E., Yang, Z. 2004b. Computational Visualisation of Separated/Reattached Transitional Flow on a Blunt Plate. *Journal of Flow Visualization and Image Processing*, 11: 1-28.

Abdalla, I. E. and Yang, Z. 2005. Numerical Study of a Separated-Reattached Flow on a Blunt Plate. *AIAA JOURNAL*, 43 (12): 2465-2474.

Adrian, R. J. 2007. Hairpin Vortex Organization in Wall Turbulence. *Physics of Fluids*, 19: 041301.

Adrian, R. J. Meinhart, C. D, and Tomkins, C. D. 2000. Vortex Organization in the Outer Region of the Turbulent Boundary Layer. *J. Fluid Mech.*, 422: 1-54.

Alam, M. and Sandham, N. D. 2000. Direct Numerical Simulation of Short Laminar Separation Bubbles with Turbulent Reattachment. *Journal of Fluid Mechanics*, 410: 1-28.

Alving A. E. and Fernholz H. H. 1996. Turbulence Measurements around a Mild Separation Bubble and Downstream of Reattachment. *Journal of Fluid Mechanics*, 322: 297-328.

Ba, Y., Pan, C., and Wang, J. 2014. Separated Laminar Shear Layer Transition over a Two-Dimensional Bump. *29th Congress of the International Council of the Aeronautical Sciences*, St. Petersburg, Russia.

Baba-Ahmadi, M. H. and Tabor, G. 2009. Inlet Conditions for LES Using Mapping and Feedback Control. *Computers & Fluids*, 38: 1299-1311.

Baba-Ahmadi, M. H. and Tabor, G. R. 2008. Inlet Conditions for Large Eddy Simulation of Gas-Turbine Swirl Injectors. *AIAA JOURNAL*, 46(7): 1782-1790.

Babu, H. and Sarkar, S. 2012. Study of Inlet Perturbations on Excitation of a Laminar Separation Bubble through LES. *9th International Conference on Heat Transfer, Fluid Mechanics and Thermodynamics 16 – 18 July 2012*, *Malta*: 604-612.

Bak, C., Madsen, H. A., Fuglsang, P., and Rasmussen, F. 1999. Observations and Hypothesis of Double Stall. *Wind Energy*, 2 (1): 195-210.

Balogh, M., Parente, A., and Benocci, C. 2012. RANS Simulation of ABL Flow over Complex Terrains Applying an Enhanced *k*-ε Model and Wall Function Formulation: Implementation and Comparison for Fluent and OpenFOAM. *J. Wind Eng. Ind. Aerodyn*, 104-106: 360-368.

Balzer, W. and Fasel, H. F. 2016. Numerical Investigation of the Role of Free-Stream Turbulence in Boundary-Layer Separation. *J. Fluid Mech.*, 801: 289-321.

Barton, I. E. 1998. Comparison of SIMPLE- and PISO- Type Algorithms for Transient Flows. *International Journal for Numerical Methods in Fluids*, 26 (4): 459-483.

Bearman, P. W. and Morel, T. 1983. Effect of Free Stream Turbulence on the Flow around Bluff Bodies. *Prog. Aerospace Sci.*, 20: 97-123.

Berkooz, G., Elezgaray, J., and Holmes, P. 1992. Coherent Structures in Random Media and Wavelets. *Physica*, D 61: 47-58.

Blair, M. F. 1982. Influence of Free-Stream Turbulence on Boundary Layer Transition in Favorable Pressure Gradients. *J. Eng. Power*, 104: 743-750.

Bradshaw, P. and Wong, F. Y. F. 1972. The Reattachment and Relaxation of a Turbulent Shear Layer, *J. Fluid Mech*, 52: 113-135.

Bressloff, N. W. 2001. A Parallel Pressure Implicit Splitting of Operators Algorithm Applied to Flows at All Speeds. *International Journal for Numerical Methods in Fluids*, 36: 497-518.

Brinkerhoff, J. R. and Yaras, M. I. 2013. Direct Numerical Simulations of Transitional Separation-Bubble Development in Swept-Blade Flow Conditions. *Journal of Turbomachinery*, 135: 041006.

Brinkerhoff, J. R. and Yaras, M. I. 2011. Interaction of Viscous and Inviscid Instability Modes in Separation-Bubble Transition. *Physics of Fluids*, 23, 124102.

Brinkerhoff, J. R. and Yaras, M. I. 2014. Numerical Investigation of the Generation and Growth of Coherent Flow Structures in a Triggered Turbulent Spot. *J. Fluid Mech.*, 759: 257-294.

Brinkerhoff, J. R. and Yaras, M. I. 2015. Numerical Investigation of Transition in a Boundary Layer Subjected to Favourable and Adverse Streamwise Pressure Gradients and Elevated Free Stream Turbulence. *J. Fluid Mech.*, 781: 52-86.

Browand, F. K. and Trout, T. R. 1985. The Turbulent Mixing Layer: Geometry of Large Vortices. *Journal of Fluid Mechanics*, 158: 489-509.

Brown, G. L. and Roshko, A. 1974. On Density Effects and Large Structure in Turbulent Mixing Layers. *Journal of Fluid Mechanics*, 64: 775-816.

Burgmann, S. and Schroder, W. 2008. Investigation of the Vortex Induced Unsteadiness of a Separation Bubble via Time-Resolved and Scanning PIV Measurements. *Experiments in Fluids*, 45(4): 675-691.

Burgmann, S., Brucker, C., and Schroder, W. 2006. Scanning PIV Measurements of a Laminar Separation Bubble. *Experiments in Fluids*, 41(2): 319-326.

Cantwell, B. J. 1981. Organised Motion in Turbulent Flow. *Ann. Rev. Fluid Mech.*, 13: 457-515.

Castro, I. P. 2005. The Stability of Laminar Symmetric Separated Wakes. *Journal of Fluid Mechanics*, 532: 389-411.

Castro, I. P. and Epik, E. 1996. Boundary Layer Relaxation after a Separated Region. *Experimental Thermal and Fluid Science*, 13: 338-348.

Castro, I. P. and Haque, A. 1988. The Structure of a Shear Layer Bounding a Separation Region. Part 2. Effects of Free-Stream Turbulence. *J. Fluid Mech*, 192: 577-595.

Castro, I. P. and Haque, A. 1987. The Structure of a Turbulent Shear Layer Bounding a Separation Region. *Journal of Fluid Mechanics*, 179: 439-468.

Castro, L. P. and Epik, E. 1998. Boundary Layer Development after a Separated Region. *Journal of Fluid Mechanics*, 374: 91-116.

Chandrasekhar, S. 1981. *Hydrodynamic and Hydromagnetic Stability*. Oxford: Clarendon Press.

Chandrsuda, C., Mehta, R. D., Weir, A. D., and Bradshaw, P. 1978. Effects of Free-Stream Turbulence on Large Structures in Turbulent Mixing Layers. *J. Fluid Mech.*, 85: 693-704.

Chernyshenko, S. I. and Baig, M. F. 2005. The Mechanism of Streak Formation in Near-Wall Turbulence. *J. Fluid Mech.*, 544: 99-131.

Cherry, N. J., Hillier, R., and Latour, M.E.M.P. 1983. The Unsteady Structure of Two-Dimensional Separated-and-Reattaching Flows. *Journal of Wind Engineering and Industrial Aerodynamics*, 11: 95-105.

Cherry, N. J., Hillier, R., and Latour, M.E.M.P. 1984. Unsteady Measurements in a Separated and Reattaching Flow. *Journal of Fluid Mechanics*, 144: 13-46.

Comte, P., Lesieur, J. H., and Lamballais, E. 1992. Large- and Small-Scale Stirring of Vorticity and a Passive Scalar in a 3-D Temporal Mixing Layer. *Physics of Fluids*, 4: 2761-2778.

Comte, P., Silvestrini, J. H., and Begou, P. 1998. Streamwise Vortices in Large-Eddy Simulation of Mixing Layers. *Eur. J. Mech. B/Fluids*, 17 (4): 615-637.

Coull, J. D. and Hodson, H. P. 2011. Unsteady Boundary-Layer Transition in Low-Pressure Turbines. *J. Fluid Mech.*, 681: 370-410.

Dahnert, J., Lyko, C., and Peitsch, D. 2012. Transition Mechanisms in Laminar Separated Flow under Simulated Low Pressure Turbine Aerofoil Conditions, *Journal of Turbomachinery*, 135 (1): 011007.

Danaila, I., Dusek, J., and Anselmet, F. 1997. Direct Numerical Simulation of the Free, Unsteady, Round, Unforced Jet at Low Reynolds Number. *Direct and Large-Eddy Simulation II*, 1-10.

Daubechies, C. 1990. The Wavelet Transform Time-Frequency Localization and Signal Analysis. *IEEE Transactions on Information Theory*, 36 (5): 961-1005.

Deguchi, K. and Hall, P. 2015. Free-Stream Coherent Structures in Growing Boundary Layers: A Link to Near-Wall Streaks. *J. Fluid Mech.*, 778: 451-484.

Delcayre, F. 1997. Topology of Coherent Vortices in the Reattachment Region of a Backward Facing Step. *11th Symposium on Turbulent Shear Flows, Grenoble: France*, 3: 6-24.

de Villiers, E. 2006. *The Potential for Large Eddy Simulation for the Modelling of Wall Bounded Flows*. PhD thesis, Imperial College.

Dimaczek, G. Kessler, R. Martinuzzi, R. and Tropea, C. 1989. The Flow over Two-Dimensional Surface-Mounted Obstacles at High Reynolds Numbers. *Turbulence Shear Flow*, 1(A90-35176 15-34): 10.1.1-10.1.6.

Djilali, N. and Gartshore, I. S. 1991. Turbulent Flow Around a Bluff Rectangular Plate. PartI: Experimental Investigation. *ASME Journal of Fluids Engineering*, 113: 51-59.

Dovgal, A. V., Kozlov, V. V., and Michalke, A. 1994. Laminar Boundary Layer Separation: Instability and Associated Phenomena. *Prog. Aerospace Sci*, 30 (1): 61-94.

Driver, D. M., Seegmiller, H. L., and Marvin, J. G. 1987. Time-Dependent Behaviour of Reattaching Shear Layer. *AIAA Journal*, 25 (7): 914–919.

Dubief, Y. and Delcayre, F. 2000. On Coherent-Vortex Identification in Turbulence. *Journal of Turbulence*, 1: 011.

Ducoin, A., Loiseau, J., and Robinet, J. 2016. Numerical Investigation of the Interaction between Laminar to Turbulent Transition and the Wake of an Airfoil. *European Journal of Mechanics B/Fluids*, 57: 231-248.

Eaton, J. K., Johnston, J. P. 1982. Low Frequency Unsteadiness of a Reattaching Turbulent Shear Layer. *Turbulence Shear Flows*, 3: 162-170.

Farge, M. 1992. Wavelet Transforms and their Applications to Turbulence. *Annual Review of Fluid Mechanics,* 24: 395-457.

Gartshore, I. P. and Savill, M. 1982. Some Effects of Free Stream Turbulence on the Flow around Bluff Bodies, *Euromech 160: Periodic Flow and Wake Phenomina,* Berlin.

Germano, P., Piomelli, U., Moin, P., and Cabot, W. H. 1991. A Dynamic Subgrid-Scale Eddy Viscosity Model. *Journal of Physics of Fluids*, A3 (7): 1760-1765.

Ghosal, S., Lund, T. S., Moin, P., and Akselvoll, K. 1995. A Dynamic Localization Model for Large-Eddy Simulation of Turbulent Flow. *J. Fluid Mech*. 286: 229-255.

Giralt, F. and Ferre, J. A. 1993. Structure and flow pattern in turbulent wakes. *Phys. Fluids,* A5 (7): 1783-1789.

Gordeyev, S. V. and Thomas, F. O. 2000. Coherent Structure in the Turbulent Planar Jet. Part 1. Extraction of Proper Orthogonal Decomposition Eigenmodes and their Self-Similarity. *J. Fluid Mech.*, 414: 145-194.

Gordeyev, S. V. and Thomas, F. O. 2002. Coherent Structure in the Turbulent Planar Jet. Part 2. Structural Topology via POD Eigenmode Projection. *J. Fluid Mech.,* 460: 349-380.

Gungora, A. G. and Simens, M. P. 2015. Transition to turbulence in a separated boundary layer with spanwise perturbations. *IUTAM ABCM Symposium on Laminar Turbulent Transition, Science Direct*, 14: 69-77.

Halfon, E., Nishri, B. Seifert, A., and Wygnanski, I. 2004. Effects of Elevated Free-Stream Turbulence on Actively Controlled Separation Bubble. *Journal of Fluids Engineering*, 126: 1015-1024.

Hammond, D. A. and Redekopp, L. G. 1998. Local and Global Instability Properties of Separation Bubbles. *Eur. J. Mech. B/Fluids*, 17: 145-164.

Hancock, P. E. 1995. Reynolds-number effects in separated flows, *Advances in turbulence V*: 184-189.

Hatman, A. and Wang, T. 1999. A Prediction Model for Separated-Flow Transition. *Journal of Turbomachinery*, 121(3): 594-602.

Head, M. R. and Bandyopadhyay, P. 1981. New Aspects of Turbulent Boundary-Layer Structure. *Journal of Fluid Mechanics*, 107: 297-338.

Heenan, A. F., and Morrison, J. F. 1998. Passive Control of Pressure Fluctuations Generated by Separated Flow. *AIAA Journal*, 36 (6): 1014–1022.

Hellstrom, L. O., Ganapathisubramani, B., and Smits, A. J. 2015. The Evolution of Large-Scale Motions in Turbulent Pipe Flow. *J. Fluid Mech.*, 779: 701-715.

Hillier, R., Cherry, N. J. 1981 a. Pressure Fluctuations under a Turbulent Shear Layer. *Proceedings of the Third Symposium on Turbulent Shear Flows, Davis, California, September*: 16.23-16.29.

Hillier, R. and Cherry, N. J. 1981 b. The Effects of Stream Turbulence on Separation Bubbles. *Journal of Wind Engineering and Industrial Aerodynamics*, 8: 49-58.

Ho, C. M. and Huerre, P. 1984. Perturbed Free Shear Layers. *Ann. Rev. Fluid Mech.*, 16: 365-424.

Horton, H. P. 1967. A Semi-Empirical Theory for the Growth and Bursting of Laminar Separation Bubbles, *Aeronautical Research Council Current Papers*, CP 1073, Univ. of London.

Hosseinverdi, S. and Hermann, F. 2016. Direct Numerical Simulations of Laminar-to-Turbulent Transition in Laminar Separation Bubbles in Three-Dimensional Boundary-Layer. *46th AIAA Fluid Dynamics Conference, 13-17 June 2016, Washington, D.C.*: 3793.

Hosseinverdi, S. and Fasel, H. F. 2015. Laminar-Turbulent Transition in a Laminar Separation Bubble in the Presence of Free-Stream Turbulence. *IUTAM ABCM Symposium on Laminar Turbulent Transition, Science Direct*, 14: 570-579.

Huai, X., Joslin, R., and Piomelli, U. 1997. Large-Eddy Simulation of Transition to Turbulence in Boundary Layers. *Theoretical and Computational Fluid Dynamics*, 9(2): 149-163.

Huang, L. S. and Ho, C. M. 1990. Small-Scale Transition in a Plane Mixing Layer. *Journal of Fluid Mechanics*, 210: 475-500.

Hudy, L. M., Naguib, A. M., and Humphreys, W. M. 2003. Wall-Pressure-Array Measurements Beneath a Separating/Reattaching Flow Region. *Phys. Fluid*, 15: 706-717.

Huerre, P., Monkewitz, P. A. 1985. Absolute and Convective Instabilities in Free Shear Layers. *Journal of Fluid Mechanics*, 159: 151-168.

Hunt, J. C. R., A. A. Wary, and P. Moin. 1988. Eddies, Stream, and Convergence Zones in Turbulent Flows. *Center for Turbulence Research, Proceeding of Summer Program*: 193-208.

Hussain, A. K. M. F. 1986. Coherent Structures and Turbulence. *Journal of Fluid Mechanics*, 173: 303-356.

Hussain, A. K. M. F. and Hayakawa, M. 1987. Education of Large-Scale Organized Structures in a Turbulent Plane Wake. *Journal of Fluid Mechanics*, 180: 193-229.

Hussain, F. and Melander, M. V. 1992. Understanding Turbulence via Vortex Dynamics. *Studies in Turbulence*: 157-178.

Hwang, K. S., Sung, H. J., and Hyun, J. M. 2000. Visualizations of Large-Scale Vortices in Flow about a Blunt-Faced Flat Plate. *Experiments in Fluids*, 29: 198-201.

Issa, R. I. 1986. Solution of the Implicitly Discretized Fluid Flow Equations by Operator-Splitting. *Journal of Comput. Phys*, 62: 40-65.

Istvan, M. S. and Yarusevych, S. 2017. Free-Stream Turbulence Effects on Transition within a Laminar Separation Bubble. *47th AIAA Fluid Dynamics Conference, 5-9 June 2017, Denver, Colorado*: 3646.

Jahanmiri, M. 2011. *Laminar Separation Bubble: Its Structure, Dynamics and Control*. Research report: 06.

Jasak, H. 1996. *Error Analysis and Estimation for the Finite Volume Method with Applications to Fluid Flows*. PhD dissertation. Imperial College. London.

Jasak, H., Jemcov, A., and Tukovi, Z. 2007. OpenFOAM: A C++ Library for Complex Physics Simulations. *International Workshop on Coupled Methods in Numerical Dynamics IUC, Dubrovnik, Croatia, September 19th-21st*: 1-20.

Jeong, J. Hussain, F., Schoppa, W., and Kim J. 1997. Coherent Structure Near the Wall in a Turbulent Channel Flow, *J. Fluid Mech.*, 332: 185-214.

Jones, L. E., Sandberg, R. D., and Sandham, N. D. 2008. Direct Numerical Simulations of Forced and Unforced Separation Bubbles on an Airfoil at Incidence. *Journal of Fluid Mechanics*, 602: 175-207.

Kaiser, G. 1999. *A Friendly Guide to Wavelets*. Birkhauser: 6th printing, Cambridge, MA.

Keating, A., Piomelli, U., Balaras, E., and Kaltenbach, H. 2004. A Priori and Posteriori Tests of Inflow Conditions for Large-Eddy Simulation. *Phys. Fluids*, 16 (12): 4696-4712.

Kimbrell, A. B. 2012. *Development and Verification of a Navier-Stokes Solver with Vorticity Confinement Using OpenFOAM*. MSc. Thesis, The University of Tennessee, Knoxville.

Kida, S. and Miura, H. 1998. Identification and Analysis of Vortical Structures. *European Journal of Mechanics - B/Fluids*, 17(4): 471-488.

Kirk, M. T. and Yarusevych, S. 2017. Vortex Shedding within Laminar Separation Bubbles Forming over an Airfoil. *Exp Fluids*, 58: 43.

Kiya, M. and Sasaki, K. 1983. Structure of a Turbulent Separation Bubble. *J. Fluid Mech*., 137: 83-113.

Kiya, M. and Sasaki, K. 1985. Structure of Large-Scale Vortices and Unsteady Reverse Flow in the Reattaching Zone of Turbulent Separation Bubble. *Journal of Fluid Mechanics*, 154: 463-491.

Kiya, M., Moehizuki, O., Ido, Y., and Kosaku, H. 1993. Structure of Turbulent Leading-Edge Separation Bubble of a Blunt Circular Cylinder and Its Response to Sinusoidal Disturbances. *Journal of Wind Engineering and Industrial Aerodynamics*, 49: 227-236.

Kurelek, J. W. and Yarusevych, S. 2016. The Effect of Acoustic Excitation on the Later Stages of Transition in a Laminar Separation Bubble. *46th AIAA Fluid Dynamics Conference, 13-17 June 2016, Washington, D.C.*: 3948.

Kurelek, J. W., Burak, A. T., and Yarusevych, S. 2017. Three-Dimensional Vortex Development in a Laminar Separation Bubble formed over an Airfoil. *47th AIAA Fluid Dynamics Conference, 5-9 June 2017, Denver, Colorado*: 3642.

Kurelek, J. W., Lambert, A. R., and Yarusevych, S. 2016. Coherent Structures in the Transition Process of a Laminar Separation Bubble. *AIAA Journal*, 54(8): 2295–2309.

Lambert, A. R. and Yarusevych, S. 2017. Characterization of Vortex Dynamics in a Laminar Separation Bubble. *AIAA Journal*, 55(8): 2664-2675.

Lane, J. C. and Loehrke, R. I. 1980. Leading Edge Separation from a Blunt Plate at Low Reynolds Number. *Transactions of the ASME,* 102: 494-496.

Lang, M., Rist, U. and Wagner, S. 2004. Investigations on Controlled Transition Development in a Laminar Separation Bubble by Means of LDA and PIV. *Experiments in Fluids*, 36: 43–52.

Langari, M. Yang, Z. 2013. Numerical Study of the Primary Instability in a Separated Boundary Layer Transition under Elevated Free-Stream Turbulence. *Physics of Fluids*, 25: 074106.

Lardeau, S., and Leschziner, M., and Zaki, T. 2012. Large Eddy Simulation of Transitional Separated Flow over a Flat Plate and a Compressor Blade. *Flow, Turbulence and Combustion*, 88(1-2): 19-44.

Lasheras, J. C. and Choi, H. 1988. Three-Dimensional Instability of a Plain, Free Shear Layer: An Experimental Study on the Formation and Evolution of Streamwise Vortices. *Journal of Fluid Mechanics*, 189: 53-86.

Le, H., Moin, P., and Kim, J. 1997. Direct Numerical Simulation of Turbulent Flow over a Backward-Facing Step. *Journal of Fluid Mechanics*, 330: 349-374.

Lee, I., & Sung, H.J., 2001. Characteristics of wall pressure fluctuations in separated and reattaching flow over a backward-facing step. *Exp. Fluid*, 30, pp. 262–272.

Lesieur, M. 1997. *Turbulence in Fluids (Fluid Mechanics and its Applications)*. 3rd Revised and Enlarged Edition, Kluwer Academic Publishers.

Lilly, D. K. 1992. A Proposed Modification of the Germano-Subgrid-Scale Closure Method. *Physics of Fluids a-Fluid Dynamics*, 4 (3): 633-635.

Lin, J. C. M. and Pauley, L. L. 1996. Low-Reynolds-Number Separation on an Airfoil. *AIAA Journal*, 34(8): 1570-1577.

Lopez, A. Nicholls, W., Stickland, M. T., and Dempster, W. M. 2015. CFD Study of Jet Impingement Test Erosion Using Ansys Fluent and OpenFOAM. *Computer Physics Communications*, 197: 88-95.

Lund, T. S., Wu, X., and Squires, K. D. 1998. Generation of Turbulent Inflow Data for Spatially-Developing Boundary Layer Simulations. *JOURNAL OF COMPUTATIONAL PHYSICS*, 140: 233-258.

Lysenko, D. A., Ertesvag, I. S., and Rian, K. E. 2013. Modeling of Turbulent Separated Flows Using OpenFOAM. *Computers & Fluids*, 80: 408-422.

Mabey, D. G. 1972. Analysis and Correlation of Data on Pressure Fluctuations in Separated Flow. *Journal of Aircraft*, 9 (9): 642–645.

Manneville, P. 1990. *Dissipative Structures and Week Turbulence*. Academic Press, New York.

Marxen, O., Lang, M., Rist, U., and Wagner, S. 2003. A Combined Experimental/Numerical Study of Unsteady Phenomena in a Laminar Separation Bubble. *Flow Turbul. Combust.*, 71: 133-146.

Marxen, O., Lang, M., and Rist, U. 2013. Vortex Formation and Vortex Breakup in a Laminar Separation Bubble. *J Fluid Mech*., 728: 58-90.

Marxen, O., Rist, U., and Wagner, S. 2004. Effect of Spanwise-Modulated Disturbances on Transition in a Separated Boundary Layer. *AIAA Journal*, 42: 937-944.

Mayle, R. E. 1991. The role of laminar-turbulent transition in gas turbine engine. ASME J. Turbomach, 113 (4): 509-536.

McAuliffe, B. R. and Yaras, M. I. 2008. Numerical Study of Instability Mechanisms Leading to Transition in Separation Bubbles. *ASME Journal of Turbomachinery*, 130: 021006.

McAuliffe, B. R. and Yaras, M. I. 2009. Passive Manipulation of Separation-Bubble Transition Using Surface Modifications, *Journal Fluids Engineering*, 131 (2): 021201.

McAuliffe, B. R. and Yaras, M. I. 2010.Transition Mechanisms in Separation Bubbles Under Low and Elevated-Freestream Turbulence. *Journal of Turbomachinery*, 132: 011004.

McMullan, W. A. and Garrett, S. J. 2016. Initial Condition Effects on Large Scale Structure in Numerical Simulations of Plane Mixing Layers. *Phys. Fluids*, 28: 015111.

Na, Y. and Moin, P. 1998. Direct Numerical Simulation of a Separated Turbulent Boundary Layer. *Journal of Fluid Mechanics*, 374: 379-405.

Nakamura, Y. and Ohya, Y. 1983. The Effects of Turbulence on the Mean Flow Past Square Rods. *J. Fluid Mech.*, 137: 331-345.

Nakamura, Y. and Ohya, Y. 1984. The Effects of Turbulence on the Mean Flow Past Two Dimensional Rectangular Cylinders. *J. Fluid Mech.*, 149: 255-273.

Nakamura, Y. and Ohya, Y. 1986. Vortex Shedding from Square Prisms in Smooth and Turbulent Flows. *J. Fluid Mech.*, 164: 77-89.

Nakamura, Y. and Ozono, S. 1987. The Effects of Turbulence on a Separated and Reattaching Flow. *J. Fluid Mech.*, 178: 477-490.

Neto, A. S., Grand, D., Metais, O., and Lesieur, M. 1993. A Numerical Investigation of the Coherent Vortices in Turbulence behind a Backward-Facing Step. *Journal of Fluid Mechanics*, 256: 1-25.

Nichols, R. H. *Turbulence models and their application to complex flows*. Universit Alabama at Birmingham, revision 4.01.

Niew, T. R. 1993. *The Stability of the Flow in a Laminar Separation Bubble*. PhD thesis, University of Cambridge.

OpenFOAM 2.3.1 User Guide, 2014. The Open Source CFD Toolbox.

Orellano, A. Wengle, H. 2000. Numerical Simulation (DNS and LES) of Manipulated Turbulent Boundary Layer Flow over a Surface-Mounted Fence. *European Journal of Mechanics B-Fluids*, 19: 765-788.

Perry, A. E. and Chong, M. S. 1982. On the Mechanism of Wall Turbulence. *Journal of Fluid Mechanics*, 119: 173-217.

Piomelli, U. and Liu, J. 1995. Large-Eddy Simulation of Rotating Channel Flows Using a Localized Dynamic Model. *Physics of Fluids*, 7(4): 839-848.

Piomelli, U. 1999. Large-Eddy Simulation: Achievements and Challenges. *Progress in Aerospace Sciences*, 35: 335-362.

Pokora, C. D., McMullan, W. A., Page, G. J., and McGuirk, J. J. 2011. Influence of a Numerical Boundary Layer Trips on Spatio-Temporal Correlations within LES of a Subsonic Jet. *17th AIAA/CEAS Aeroacoustics Conference*: 2920.

Rist, U. and Augustin, K. 2006. Control of Laminar Separation Bubbles Using Instability Waves. *AIAA Journal*, 44 (10): 2217-2223.

Roberts, S. K. and Yaras, M. I. 2006. Large-eddy Simulation of Transition in a Separation Bubble. *ASME Journal of Fluids Engineering*, 128: 232-238.

Robertson, E., Choudhury, V., Bhushan, S. and Walters, D. K. 2015. Validation of OpenFOAM Numerical Methods and turbulence Models for Incompressible Bluff Body Flows. *Computers & Fluids*, 123: 122-145.

Robinet, J. C. 2013. Instabilities in Laminar Separation Bubbles. *J. Fluid Mech.*, 732: 1-4.

Robinson, S. K. 1991a. The Kinematics of Turbulent Boundary Layer Structure, *NASA Technical Memorandum TM 103859*.

Robinson, S. K. 1991b. Coherent Motion in the Turbulent Boundary Layer. *Annu. Rev. of Fluid Mech.*, 23: 601-639.

Rogers, M. and Moser, R. 1993. Direct Numerical Simulation of a Self Similar Turbulent Mixing Layer. *Physics of fluids*, A 6: 903-923.

Ruderich, R. and Fernholz, H. H. 1986. An Experimental Investigation of a Turbulent Shear Flow with Separation, Reverse Flow and Reattachment. *Journal of Fluid Mechanics*, 163: 283-322.

Sasaki, K. and Kiya, M. 1991. Three-Dimensional Vortex Structure in a Leading-Edge Separation Bubble at Moderate Reynolds Numbers. *Journal of Fluids Engineering*, 113: 405-410.

Scarano, F., Benocci, C., and Riethmuller, M. L. 1999. Pattern Recognition Analysis of the Turbulent Flow Past a Backward Facing Step. *Phys. Fluids*, 11 (12): 3808-3818.

Schlatter, P., Brandt, L., de Lange, H. C., and Henningson, D. S. 2008. On Streak Breakdown in Bypass Transition. *Physics of Fluids*, 20: 101505.

Schrader, L., Amin, S., and Brandt, L. 2010. Transition to Turbulence in the Boundary Layer over a Smooth and Rough Swept Plate Exposed to Free-Stream Turbulence. *J. Fluid Mech.*, 646: 297-325.

Schreck, S. J. and Robinson, M. C. 2007. Horizontal Axis Wind Turbine Blade Aerodynamics in Experiments and Modelling. *IEEE Transactions on Energy Conversion*, 22 (1): 61-70.

Serna, J. and Lazaro, B. J. 2015a. Experiments on Natural Transition in Separation Bubbles. *IUTAM ABCM Symposium on Laminar Turbulent Transition, Science Direct*, 14: 496-502.

Serna, J. and Lazaro, B. J. 2015b. On the Laminar Region and the Initial Stages of Transition in Transitional Separation Bubbles. *European Journal of Mechanics B/Fluids*, 49(A): 171-183.

Sharp, G. J. 1994. *Solving problems in fluid dynamics*. 1st published, John Wiley & Sons, Inc., New York.

Simoni, D., Lengani, D., Ubaldi, M., Zunino, P., and Dellacasagrande, M. 2017. Inspection of The Dynamic Properties of Laminar Separation Bubbles: Free‐Stream Turbulence Intensity Effects for Different Reynolds Numbers. *Exp Fluids*, 58: 66.

Simoni, D., Ubaldi, M., Zunino, P., Lengani, D., and Bertini, F. 2012. An Experimental Investigation of the Separated-Flow Transition Under High-Lift Turbine Blade Pressure Gradients. *Flow, Turbulence and Combustion*, 88 (1-2): 45-62.

Spalart, P. R. and Strelets, M. K. 2000. Mechanisms of Transition and Heat Transfer in a Separation Bubble. *J. Fluid Mech.*, 403: 329-349.

Spazzini, P. G., Iuso, G., Onorato, M., Zurlo, N., and Di Cicca, G. M. 2001. Unsteady Behaviour of Back-Facing Step Flow. *Experiments in Fluids*, 30: 551–561.

Suksangpanomrung, A., Djilali, N., and Moinat, P. 2000. Large-Eddy Simulation of Separated Flow over a Bluff Rectangular Plate, *International Journal of Heat and Fluid Flow*, 21: 655-663.

Svizher, A. and Cohen, J. 2006. Holographic Particle Image Velocimetry Measurements of Hairpin Vortices in a Subcortical Air Channel Flow. *Physics of Fluids*, 18: 014105.

Tabor, G. R., Baba-Ahmadi, M. H., de Villiers, E., and Weller, H. G. 2004. Construction of Inlet Conditions for LES of Turbulent Channel Flow. *Proceedings of the ECCOMAS*.

Tabor, G. R. and Baba-Ahmadi, M. H. 2010. Inlet Conditions for Large Eddy Simulation: A Review. *Computers & Fluids*, 39: 553–567.

Tafti, D. K. and Vanka, S. P. 1991. A Three-Dimensional Numerical Study of Flow Separation and Reattachment on a Blunt Plate. *Physics of Fluids*, 3 (12): 2887-2909.

Taghinia, J., Rahman, M., and Siikonen, T. 2015. Large Eddy Simulation of Flow Past a Circular Cylinder with a Novel Sub-Grid Scale Model. *European Journal of Mechanics B/Fluids*, 52: 11-18.

Tani, I. 1964. Low-Speed Flows Involving Bubble Separations. *Progress in Aerospace Sciences*, 5: 70-103.

Tenaud, C., Podvin, B., Fraigneau, Y., and Daru, V. 2016. On Wall Pressure Fluctuations and their Coupling with Vortex Dynamics in a Separated–Reattached Turbulent Flow over a Blunt Flat Plate. *International Journal of Heat and Fluid Flow*, 61(B): 730-748.

Torrence, C., Compo, G. P. 1998. A practical guide to wavelet analysis. *Bulletin of the American Meteorological Society*: 61-77.

Urbain, G. and Metais, O. 1997. Large-Eddy Simulation of Three Dimensional Spatially Developing Round Jets. *Direct and Large-Eddy Simulation II*, 35-46.

Versteeg, H. K. and Malalasekera, W. 2007. *An introduction to computational fluid dynamics: The finite Volume Method*, 2nd ed., ISBN: 978-0-13-127498-3.

Voke, P. R., Yang, Z. 1995. Numerical Study of Bypass Transition. *Phys. Fluids*, 7(9): 2256-2264.

Volino, R. J. 2002. Separated Flow Transition under Simulated Low-Pressure Turbine Airfoil Conditions. Part 1. Mean Flow and Turbulence Statistics. *Trans. Journal of Turbomachinery*, 124: 645-655.

Volino, R. J. and Hultgren, L. S. 2000. Measurements in Separated and Transitional Boundary Layers under Low-Pressure Turbine Airfoil Conditions. *Proceedings of ASME TURBO EXPO, May 8-11, Munich, Germany*: GT-0260.

Watmuff, J. H., Pook, D. A., Sayadi, T., and Wu, X. 2010. Fundamental Physical Processes Associated with Bypass Transition. *Center for Turbulence Research, Proceedings of the Summer Program*: 97-106.

Wei, S. and Ning, T. 1988. Bursting Frequency in Turbulent Boundary Layers. *ACTA MECHANICA SINICA*, 4 (4): 291-296.

Winant, C. D. and Browand, F. K. 1974. Vortex Pairing: The Mechanism of Turbulent Mixing- Layer Growth at Moderate Reynolds Number". *Journal of Fluid Mechanics*, 63: 237-255.

Yang, Z. and Abdalla, I. E. 2009. Effects of Free-Stream Turbulence on a Transitional Separated-Reattached Flow over a Flat Plate with a Sharp Leading Edge. *International Journal of Heat and Fluid Flow*, 30 (5):1026-1035.

Yang, Z. and Abdalla, I. E. 2005. Effects of Free-Stream Turbulence on Large-Scale Coherent Structures of Separated Boundary Layer Transition. *Int. J. Numer. Meth. Fluids*, 49: 331-348.

Yang, Z. and Abdalla, I. E. 2008. On Coherent Structures in a Separated/Reattached Flow. *WSEAS TRANSACTIONS on FLUID MECHANICS*, 3(2):143-153.

Yang, Z. and Voke, P. R. 2000. Large-Eddy Simulation of Separated Leading-Edge Flow in General Co-ordinates. *Int. J. Numer. Meth. Engng*, 49: 681-696.

Yang, Z. and Voke, P. R. 2001. Large-Eddy Simulation of Boundary Layer Separation and Transition at a Change of Surface Curvature. *Journal of Fluid Mechanics*, 439: 305-333.

Yang, Z. 2002. Large-Scale Structures at Various Stages of Separated Boundary Layer Transition. *International Journal of Numerical Methods in Fluids*, 40: 723–733.

Yang, Z. 2013. Numerical Study of Instabilities in Separated-Reattached Flows. *Int. Journal of Comp. Meth. and Exp. Meas.*, 1 (2): 116-131.

Yang, Z. 2012. Numerical Study of Transition Process in a Separated Boundary Layer on a Flat Plate with two Different Leading Edges. *WSEAS Transactions on Applied and Theoretical Mechanics*, 7(1): 49–58.

Yang, Z. 2015. Large-eddy Simulation: Past, Present and the Future. *Chinese Journal of Aeronautics*, 28 (1): 11-24.

Yaras, M. I. 2012. Instability and Transition in a Separation Bubble Under a Three-Dimensional Freestream Pressure Distribution. *Journal of Turbomachinery*, 134: 031019.